Halogen bonds, hydrogen bonds and beyond:

A cryospectroscopic study into competitive noncovalent interactions

Proefschrift voorgelegd tot het behalen van de graad van doctor in de wetenschappen: chemie aan de Universiteit Antwerpen te verdedigen door

Yannick Geboes

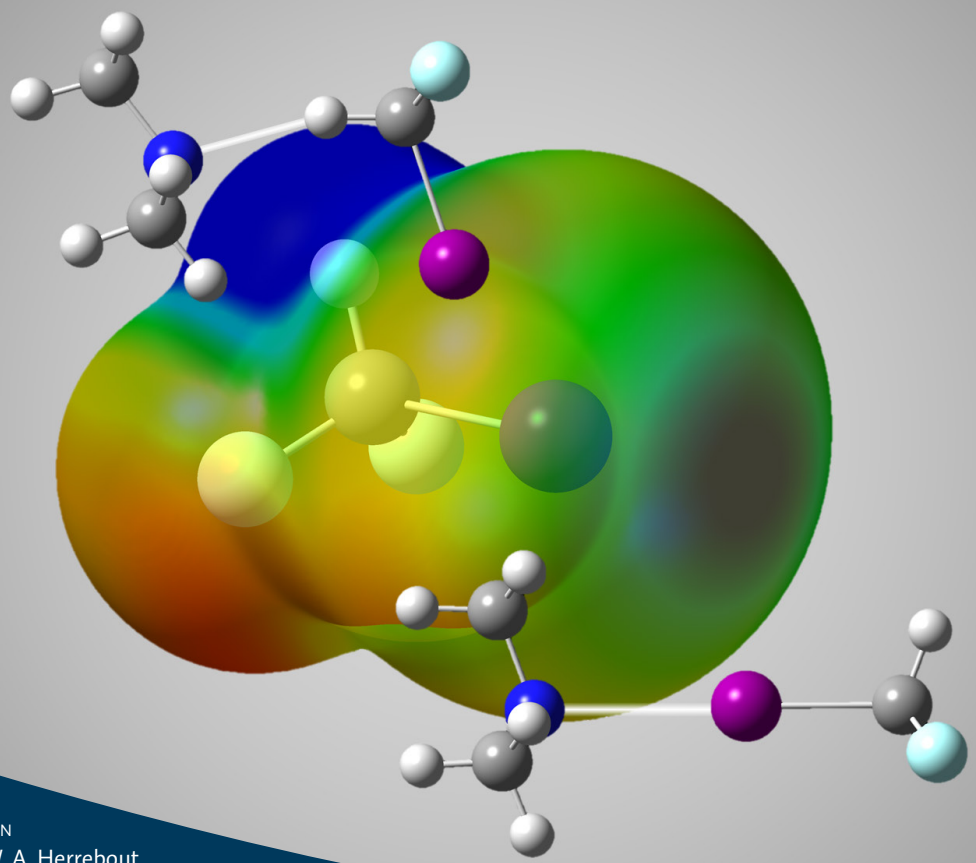

Promotoren
Prof. dr. W. A. Herrebout
Prof. dr. F. De Proft

Faculteit Wetenschappen
Departement Chemie
Antwerpen 2017

VUB VRIJE UNIVERSITEIT BRUSSEL

Universiteit Antwerpen

Faculteit Wetenschappen

Departement Chemie

Halogen bonds, hydrogen bonds and beyond:

A cryospectroscopic study into competitive noncovalent interactions

Proefschrift voorgelegd tot het behalen van de graad
doctor in de wetenschappen: chemie
aan de Universiteit Antwerpen te verdedigen door

Yannick Geboes

Promotoren
Prof. dr. Wouter A. Herrebout
Prof. dr. Frank De Proft

Antwerpen, 2017

I was born not knowing and have had only a little time to change that here and there.

– Richard P. Feynman

Dankwoord

Net geen vijf jaar, stapels papier, dozen inkt, (veel) koffie, bloed, zweet en tranen en vele producten, solventgassen en spectrometeronderdelen heeft het gekost om deze thesis op papier te krijgen. Een doctoraat is echter nooit het werk van één enkel persoon, maar het gevolg van de samenwerking en ondersteuning van een hele hoop mensen. Daarom zou ik iedereen die een bijdrage heeft gemaakt aan het tot stand komen van dit manuscript van harte willen bedanken.

In de eerste plaats wens ik mijn familie te bedanken voor hun aanhoudende hulp en ondersteuning, met mijn ouders in het bijzonder, die mij de gelegenheid gaven om deze studies en een doctoraat aan te vatten terwijl ik thuis kon blijven wonen. Ik zou ook mijn moeder, Titia, specifiek willen bedanken voor de goede zorgen, evenals mijn vader en mededoctor Peter Geboes voor zijn hulp tijdens het doctoraat en voorgaande studies. Vervolgens zou ik ook mijn broer (toekomstige dr.) ir. Yoran Geboes willen bedanken om mij altijd te blijven *pushen*. Tenslotte wens ik ook mijn grootouders Victor en Maria te bedanken voor hun onvoorwaardelijke steun.

Ik zou mijn promotoren prof. Wouter Herrebout en prof. Frank De Proft willen bedanken voor hun hulp en steun bij het tot stand brengen van deze thesis. Verder wens ik ook alle leden van mijn doctoraatsjury te bedanken voor de interessante inzichten en opmerkingen die bijgedragen werden aan deze thesis.

Ik zou ook Carl en Sam willen bedanken voor hun veelvuldige hulp bij het schrijven en *debuggen* van de scripts gebruikt in de berekeningen in deze thesis, evenals Evelien, Liene en Linny voor de vele fijne gesprekken. Verder bedank ik ook Filip voor de technische ondersteuning en Jonathan, Christian en Christophe voor het nalezen van deze thesis. Of course I would also like to thank our foreign group members Roberta, for the very strong Italian espresso which is supposed to be Americano, and Pilar, for the pleasant companionship as an office-buddy. Daarnaast wens ik ook alle leden van

de MolSpec groep nogmaals te bedanken voor de veelvuldige koffiepauzes, lunchpauzes, namiddagpauzes met ijsjes en bijhorende discussies.

Ik zou ook mijn voorganger Nick Nagels willen bedanken voor zijn bijdrage die het startpunt vormde van deze thesis. Ik zou ook Isabelle willen bedanken voor haar bijdrage aan het creëren van een aangename werkplek door het proper houden van de labo's en bureaus gedurende mijn verblijf op V0.

Ik wil ook de leden van de ALGC groep aan de VUB bedanken, in het bijzonder Balazs Pinter en Freija de Vleeschouwer voor hun hulp met de kwantumchemische berekeningen in hoofdstukken 3, 7 en 11.

Ik bedank ook het BOF en het FWO voor de financiële ondersteuning die dit doctoraat mogelijk heeft gemaakt. Ik wens ook het VSC te bedanken voor het beschikbaar stellen van de royale hoeveelheid rekentijd die nodig was voor dit onderzoek, met Franky en Stefan in het bijzonder voor hun technische ondersteuning.

I would also like to take this opportunity to thank the members of the Molecular Spectroscopy group at the University of Bologna, prof. Caminati, prof. Melandri, Lorenzo and Qian for the lovely time I had during my stay, as well as their help and support with the FTMW measurements. Lorenzo is also thanked for his comments on the FTMW chapter. Furthermore, I would like to thank Nick, Chris, John, Dror, Joe and Ethan at Newcastle University for the interesting Friday pub night discussions during my stay in Newcastle upon Tyne.

Tenslotte zou ik ook Elias, Nathan en Sebastian willen bedanken voor hun inzet en bijdrage aan dit manuscript in het kader van hun Bachelor- en/of Masterthesissen.

Table of contents

List of abbreviations

aug-cc-pVDZ	augmented correlation-consistent polarized valence with double zeta
aug-cc-pVTZ	augmented correlation-consistent polarized valence with triple zeta
BSSE	Basis set superposition error
C_2F_3Br	Bromotrifluoroethene
C_2F_3Cl	Chlorotrifluoroethene
C_2F_3I	Trifluoroiodoethene
C_2F_4	Tetrafluoroethene
$C_2F_4S_2$	2,2,4,4-Tetrafluoro-1,3-dithiethane
C_6F_6	Hexafluorobenzene
CBS	Complete basis set
CCSD(T)	Coupled cluster with a full treatment singles and doubles, in which an estimate to the connected triples contribution is calculated non-iteratively using Many-Body Perturbation Theory arguments.
CF_3Br	Bromotrifluoromethane
CF_3Cl	Chlorotrifluoromethane
CF_3I	Trifluoroiodomethane
CH_2FI	Fluoroiodomethane
CH_3Cl	Chloromethane
CH_3F	Fluoromethane
CHF_2Br	Bromodifluoromethane
CHF_2I	Difluoroiodomethane
COF_2	Carbonyl fluoride
COFCl	Carbonyl chloride fluoride
CP-correction	Counterpoise correction
CP-FTMW	Chirped pulse-Fourier transform microwave
DFT	Density Functional Theory
DME	Dimethyl ether
DMS	Dimethyl sulfide
EDA	Energy decomposition analysis
FTIR	Fourier transform infrared
FTMW	Fourier transform microwave
HB	Hydrogen bond / Hydrogen-bonded

HSAB	Hard and soft acids and bases
IR	Infrared
LAr	Liquid argon
LHe	Liquid helium
LKr	Liquid krypton
LN_2	Liquid nitrogen
LNg	Liquid noble gas
lp···π	Lone pair···π
LXe	Liquid xenon
MC-FEP	Monte Carlo-free energy perturbation
MP2	Møller-Plesset second order perturbation theory
NCI index	Noncovalent interactions index
NH_3	Ammonia
NOCV	Natural orbitals for chemical valence
PP	Pseudopotential
SI	Supporting information
TMA	Trimethylamine
TMP	Trimethylphosphine
UAntwerp	University of Antwerp
VUB	Vrije Universiteit Brussel
XB	Halogen bond / Halogen-bonded

Put it before them
briefly so they will read it,
clearly so they will appreciate it,
picturesquely so they will remember it ,
and, above all,
accurately so they will be guided by its light.

– Joseph J. Pulitzer

Chapter 1

Introduction

Ever since the 19th century, the forces between separate atoms and molecules that make up matter has intrigued scientists. One of the first great breakthroughs in this field was the description of non-ideal gases by Johannes Diderik van der Waals using an adapted version of the ideal gas law that included a parameter for the attractive interactions between the gas molecules and the volume these molecules occupy. [1] Up to this day, weak attractive interactions between molecules are still called 'van der Waals' forces when they are the consequence of interacting permanent dipoles, a permanent and induced dipole or instantaneously induced dipoles (i.e. London dispersion force). More generally, the forces between different molecules or groups of atoms are called noncovalent interactions and, apart from the previously mentioned van der Waals forces, also include, among others, electrostatic interactions, hydrophobic effects, etc. The noncovalent interaction that has probably attracted the most interest within the scientific community is the hydrogen bond, often abbreviated as HB. The definition of a hydrogen bond has been defined by the 'IUPAC Working Party on the hydrogen bond' in 2011 as:

"The hydrogen bond is an attractive interaction between a group X–H and an atom or a group of atoms, in the same or different molecule(s), when there is evidence of bond formation." [2]

Within the field of hydrogen bonding, a division is often made based on the strength of the noncovalent interaction, with the strong HB's, such as the O-H···O interactions, on one side and the weaker HB's, where the hydrogen is typically covalently bonded on a carbon atom, e.g. C-H···O interactions, on the other side. In the last couple of decades more and more scientific interest has also gone to other noncovalent interactions, which are able to compete with the latter class of hydrogen bonds.

1.1 Halogen bonding

A definition for halogen bonding (XB) was proposed in 2013 following the IUPAC Project 'Categorizing Halogen Bonding and Other Noncovalent Interactions Involving Halogen Atoms' as:

"A halogen bond occurs when there is evidence of a net attractive interaction between an electrophilic region associated with a halogen atom in a molecular entity and a nucleophilic region in another, or the same, molecular entity" [3]

In other words, it can be described as an attractive interaction between a covalently bonded halogen atom and an electron rich site in the same or another molecule. Despite the fact that the existence of attractive interactions between halogen atoms and electron rich sites has been known ever since the discovery of the $I_2 \cdots NH_3$ complex by Guthrie in 1863, [4] the classification of these interactions as a separate type of noncovalent interaction has come much later, along with the unveiling of their origin. Nevertheless, Remsen and Norris [5] showed the general trend that the dihalogens Cl_2 and Br_2 form complexes with amines in 1896. The first report of halocarbons being used as XB donors comes from O. Roussopoulos, who in 1883 described the adduct between quinolone and iodoform. [6-8] After the identification of the complexes of iodine with different aromatic solvents [9-11] and acetone [12] by Benesi and Hildebrand, Mulliken [13] developed theoretical formalisms in which he described them as a subclass of electron donor-acceptor interactions. A systematic investigation into the interactions formed with halogen atoms followed in the fifties and sixties with the crystallographic studies of Hassel et al., [14] in which X-ray diffraction experiments were conducted on the crystals of addition complexes formed between dihalogens and Lewis bases. A review on the structural chemistry of donor-acceptor interactions was published by Bent in 1968. [15] The first recorded use of the term halogen bond is ascribed to Dumas et al. in 1976, [16] after which the field further expanded in the seventies and eighties by the incorporation of infrared and microwave spectroscopy and the analysis of a large number of crystal structures from the Cambridge Structural Database by, among others, Murray-Rust et al. [17]

Despite these experimental results, the attractive interaction between an electronegative element, such as a halogen atom, and electron rich sites remained counterintuitive. The rationalization of the origin of halogen bonding came with the advancements in computing power and computational chemistry. Theoretical studies have shown that the electron distribution around the covalently bonded halogen atoms is not spherical, but rather anisotropic, with an accumulation of charge density perpendicular to the covalent bond axis. This not only causes the halogen atom to effectively have two different atomic radii, [18-20] one along and one perpendicular to the covalent bond axis, a feature called polar-flattening, [21] but also causes a region of less negative or even positive electrostatic potential opposite to the covalent bond. This region, which is surrounded by a band with more negative electrostatic potential is called the σ-hole (sigma-hole), in reference to the covalent σ-bond it is opposed to. This can be visualized by plotting the electrostatic potential on the molecular surface defined by the 0.001 electrons $Bohr^{-3}$ contour, as proposed by Bader et al. [22] As an example, the electrostatic potentials on the molecular surfaces of CF_3Cl, CF_3Br and CF_3I are shown in Figure 1.1

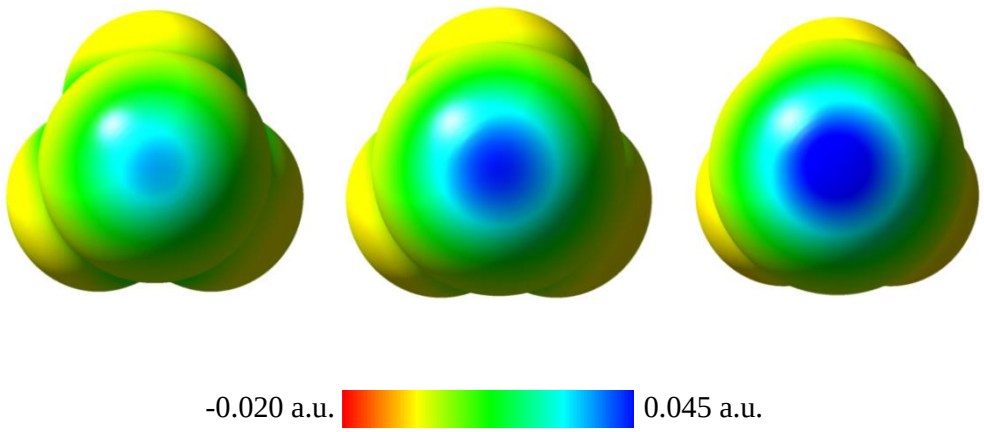

Figure 1.1: Electrostatic potentials of CF_3Cl (left), CF_3Br (middle) and CF_3I (right) on the molecular surface defined by the 0.001 electrons $Bohr^{-3}$ contour of the electron density. The apparent deviation from spherical symmetry of the σ-holes is caused by the lighting used to create a 3D effect.

In general, the strength of the noncovalent interaction formed during σ-hole bonding is related to the size of the σ-hole itself, which, in turn, is dependent on two factors. In this context, the size of the σ-hole refers to both its physical size on the electrostatic potential as well as the maximal potential of the σ-hole, two properties that are strongly correlated to each other.

The first factor is related to the element involved. When going down on the periodic table within a group the size and polarizability of the atom increases, while the electronegativity decreases simultaneously. The lower electronegativity will reduce the charge on the element of interest while the increased size will enhance its polarizability, thus increasing the anisotropy of the electron distribution around the covalently bonded atom. Both interconnected effects lead to an increase of the size of σ-hole when descending down the periodic table, as can be seen in Figure 1.1 when going from chlorine over bromine to iodine.

The second factor determining the size of the σ-hole are the electron withdrawing capabilities of covalently bonded group, as withdrawing charge density from the element containing the σ-hole will enhance the size of the σ-hole. Therefore, the addition of electron withdrawing substituents on the covalently bonded groups, is an often used technique to enhance the stability of the formed noncovalent interactions in the field of halogen bonding. In this context it should also be noted that fluorine only has a discernible σ-hole in very limited cases, when bonded to strongly electron withdrawing groups, e.g. difluoride (F_2), thus making fluorine halogen bonding a rare occurrence. [23] An advantage of this is that fluorine atoms can readily be used to enhance the electron withdrawing properties of the covalently bonded group, making perfluorohalocarbons excellent halogen bond donors. [18, 24]

Apart from the substitution of the covalently bonded group with electron withdrawing groups, the hybridization of the atom to whom the σ-hole carrying atom is covalently bonded has also been mentioned as a factor determining the σ-hole size, the strength of the associated interaction following the order $C(sp)\text{-}X > C(sp^2)\text{-}X > C(sp^3)\text{-}X$. [18, 25-26]

Thanks to the deeper understanding of halogen bonding, these noncovalent interactions are now also in numerous applications such as crystal engineering,[18] liquid crystals,[27-29] supramolecular chemistry,[8, 30-31] molecular recognition processes [25, 32] and rational drug design. [33-36]

Although the halogen bonding concept has been described using a purely electrostatic approach in the previous sections, throughout the years it has become abundantly clear that different contributions play a role in the formation of halogen bonds. Apart from the electrostatic contribution, it is widely established that dispersion, polarization and charge transfer also play a crucial role. [19, 37-39] Indeed, theoretical explanations of the formation of halogen bonds through an orbital σ-hole have already been formulated. [40-41]

The strength of halogen bonding spans a range of around 5 kJ mol^{-1} for weak Cl···Cl interactions to 180 kJ mol^{-1} for the $I^-\cdots I_2$ interaction in I_3^- [25], thus overlapping with the strength range of hydrogen bonds. As halogen bonds and hydrogen bonds occur at about the same strength levels, both noncovalent interactions are able to coexist, cooperate [42-43] or compete [44-45] with each other, as proven in many theoretical [46] and experimental studies. [47-49]

1.2 Lone pair···π interactions

The addition of electron withdrawing substituents to enhance the formed hydrogen or halogen bonds creates molecules that are electron deficient. When these electron deficient molecules are also unsaturated, a region of positive electrostatic potential can be observed above and below the unsaturated part of the molecule. In analogy to the σ-holes, which are located in the plane of the σ-framework of a molecule, these new positive regions, perpendicular to (a part of) the molecular framework, are called π-holes. [50] An example of a π-hole is shown in Figure 1.2.

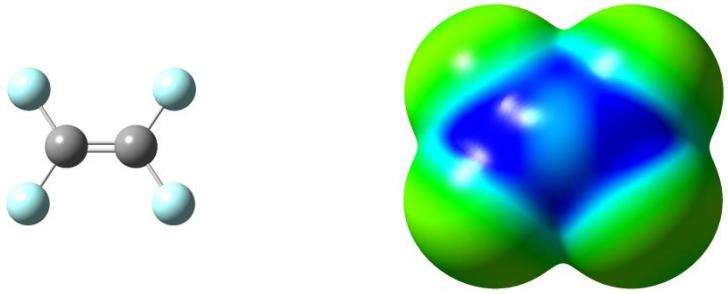

Figure 1.2: Electrostatic potential of tetrafluoroethene (C_2F_4) on the molecular surface defined by the 0.001 electrons Bohr^{-3} contour of the electron density, with positive, neutral and negative regions shown in blue, green and red, respectively, showing the π-hole.

Just as hydrogen bonds and halogen bonds, intermolecular interactions can be formed with electron rich sites such as lone pairs (lp) or anions, thus giving rise to lone pair···π (lp···π) interactions and anion···π interactions. These noncovalent interactions can in turn compete with halogen bonds or hydrogen bonds.

One of the earliest descriptions of lp···π interactions was made by Bürgi et al., by identifying attractive interactions between the carbonyl carbon atom and nucleophiles during a survey of crystal-structure analyses. [51] A first description of a π-hole was made by Murray et al. in 1991 during a theoretical study of the electrostatic potentials of cyclic ureides. [52]

One of the first experimental observations of a lone pair···π interaction in a biochemical system was made by Egli et al. in 1995, when they described the stabilizing effect of a (then unusual) lp···π interaction on the stability of the left-handed Z-DNA duplex, which overcomes the poor base-pair stacking. [53] In later studies, the stabilizing effect of lp···π interactions has also been demonstrated for other biological macromolecules. [54-55] Because of its biological importance, most reports of lp···π interactions involve the oxygen lone pair of a water molecule. A comprehensive study of lp···π interactions was performed by Mooibroek et al. [56] in a systematic analysis of the Cambridge Structural Database.

1.3 Expanding the concept of σ-hole bonding towards chalcogen bonding

The existence of σ-holes is not limited to halogen atoms, but has also been observed for group VI and group V elements, where interactions with electron rich moieties give rise to chalcogen bonds and pnicogen bonds, respectively. [57-58] The number of σ-holes is equal to the number of covalent bonds in which the atom of interest is involved, e.g. for a divalent chalcogen, two σ-holes are observed, while for a trivalent pnicogen three σ-holes will be observed. In some studies, σ-holes have also been described on group IV elements, which can give rise to tetrel bonds,[59-60] although the presence of four covalently bonded groups often obscures the band of more negative potential surrounding the σ-hole, and also sterically hinders the formation of a noncovalent interaction with the σ-hole, thus shrouding the exact nature of the interaction formed. In this context it should also be mentioned that, in order to be a true σ-hole, the region of positive electrostatic potential should be positioned along a covalent bond axis (opposite to the covalent bond itself). [50] Therefore, the interactions formed through the previously mentioned π-holes should not be described as tetrel bonds.

1.4 Studying the competition of weak noncovalent interactions

Within the Molecular Spectroscopy (MolSpec) group (formerly known as the Cryospectroscopy group) at the University of Antwerp, the study of weak noncovalent interactions in cryogenic solutions has been one of the main research subjects for almost 20 years now. Initially starting with the study of van der Waals complexes, [61] the research interest has shifted during the years towards proper and improper hydrogen bonding, [62] hydrogen bonding in anesthetics [63-64] and more recently towards halogen bonding. [65-66]

During these halogen bonding studies mixtures of trifluorohalomethanes (CF_3X, X = Cl, Br, I), which are ideal model systems for halogen bond donors where

the halogen atom is covalently bonded to a carbon atom, with different lone pair carrying Lewis bases and both aromatic and non-aromatic π-electron donors were investigated in liquid noble gas solutions. This yielded, for the first time ever, information on the thermodynamic properties of these XB complexes. The competition of weak noncovalent interactions has been studied before within the research group by investigating mixtures containing Lewis bases with different types of electron rich sites, such as thiophene and furan, which can act as both lone pair and π-electron donors. In the current project, the competition of noncovalent interactions is studied using Lewis acids, often referred to as bond donors in the fields of hydrogen and halogen bonding, with multiple bonding sites.

This thesis is initiated by bringing the previous studies into halogen bonding and hydrogen bonding together in an investigation into the competition of halogen bonds and hydrogen bonds. Therefore, Fourier Transform Infrared (FTIR) and Raman spectroscopic studies are performed on liquid noble gas (LNg) solutions containing a combined halogen and hydrogen bond donor and different Lewis bases. All studies are supported by *ab initio* calculations, in which the energies and vibrational frequencies of the monomers and complexes are calculated, thus aiding assignment of the bands observed in the spectra. Furthermore, statistical thermodynamics calculations and Monte Carlo-free energy perturbation (MC-FEP) simulations are performed to obtain calculated complexation enthalpies in solution which can be compared with the experimental results. In order to rationalize the tendencies observed, conceptual Density Functional Theory (DFT) is used in the form of the noncovalent interactions (NCI) index, natural orbitals for chemical valence (NOCV) and a Ziegler-Rauk type energy decomposition analysis (EDA).

An overview of the experimental setups and methodology as well as the computational details are summarized in chapter 2 of this thesis.

As a starting point, the combined donor difluoroiodomethane (CHF_2I), for which the electrostatic potential is shown in Figure 1.3, is studied with Lewis bases containing a lone pair located on a second period element, namely fluoromethane (CH_3F),

dimethyl ether (DME) and trimethylamine (TMA) in chapter 3. To further investigate the role of the Lewis base involved on the halogen/hydrogen bond competition, this study is expanded in a subsequent chapter by studying the complexes of CHF_2I with chloromethane (CH_3Cl), dimethyl sulfide (DMS) and trimethylphosphine (TMP) in chapter 4.

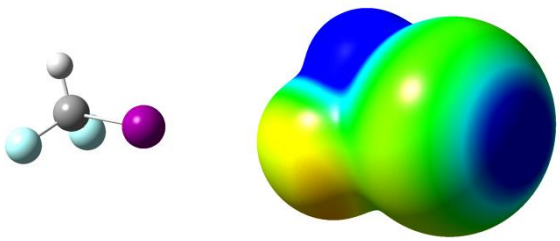

Figure 1.3: Electrostatic potential of CHF_2I on the molecular surface defined by the 0.001 electrons $Bohr^{-3}$ contour of the electron density, with positive, neutral and negative regions shown in blue, green and red, respectively. The σ-hole on the iodine atom is shown on the right while positive region on the hydrogen atom is shown on the left top of the image.

Apart from the influence of the Lewis base on the competition, the influence of the previously mentioned modifications of the bond donor to enhance the σ-hole bonding strength are also studied. To investigate the influence of the addition of electron withdrawing atoms or groups on the covalently bonded molecule, the complexes of the less fluorinated fluoroiodomethane (CH_2FI) with DME and TMA are investigated in chapter 5, while the effect of substitution of the σ-hole carrying halogen atom is evaluated by the study of the bromodifluoromethane (CHF_2Br) complex with TMA in chapter 6.

To investigate the role of the hybridization of the covalently bonded carbon atom on the halogen bond complex stability, the complexes of trifluorohaloethenes (C_2F_3X, X = F, Cl, Br, I) with the Lewis bases DME (chapter 7) and TMA (chapter 8). Furthermore, the use of these unsaturated donor molecules also enables the formation of potentially competing lp···π interactions.

Further evidence of the existence of the relatively new lp···π interactions was gathered from the study of the complexes between the aromatic bond donor hexafluorobenzene (C_6F_6) and the Lewis bases DME and TMA, reported in chapter 9. The concept of lp···π interactions, and its competition with halogen bonding, is further expanded in chapter 10 by the study of the interactions between the electron deficient heterogeneous π-systems of carbonyl fluoride (COF_2) and carbonyl chloride fluoride (COFCl) and DME.

In the final chapter, a first step into the expansion of the σ-hole bonding concept to chalcogen bonding is taken by the study of the 2,2,4,4-tetrafluoro-1,3-dithiethane ($C_2F_4S_2$) DME dimer.

During this Ph.D., Microwave spectroscopy experiments were also performed at the University of Bologna and Newcastle University. In the research group of Prof. Caminati and Prof. Melandri at the University of Bologna, the complexes of chlorotrifluoroethene (C_2F_3Cl) with ammonia (NH_3) and DME were studied to investigate the competition of halogen bonding and lp···π interactions in a jet expansion experiment. The results of these studies have been published in peer reviewed journals, for which the details are included in the publications list at the end of this thesis. At Newcastle University we aimed to study the halogen/hydrogen bond competition involving CHF_2I and the Lewis bases TMA and NH_3, to investigate the influence of methylation of the Lewis base on the competition. Using the chirped-pulse Fourier Transform Microwave spectrometer of dr. Walker, complexes with both Lewis bases were observed, but a full assignment of the observed peaks remains unattainable up to this point due to an off-axis internal rotation for the CHF_2I·TMA complex.

1.5 References

1 J. D. van der Waals, *Z. Physik. Ch.*, 1901, ***38***, 257-288.
2 E. Arunan, G. R. Desiraju, R. A. Klein, J. Sadlej, S. Scheiner, I. Alkorta, D. C. Clary, R. H. Crabtree, J. J. Dannenberg, P. Hobza, H. G. Kjaergaard, A. C. Legon, B. Mennucci, D. J. Nesbitt, *Pure Appl. Chem.*, 2011, ***83***, 1637-1641.
3 G. R. Desiraju, P. S. Ho, L. Kloo, A. C. Legon, R. Marquardt, P. Metrangolo, P. Politzer, G. Resnati, K. Rissanen, *Pure Appl. Chem.*, 2013, ***85***, 1711-1713.
4 F. Guthrie, *J. Chem. Soc.*, 1863, ***16***, 239-244.
5 I. Remsen, J. F. Norris, *Am. Chem. J.*, 1896, ***18***, 90-95.
6 O. Roussopoulos, *Ber.*, 1883, ***16***, 202-203.
7 P. Metrangolo, G. Resnati, *Cryst. Growth Des.*, 2012, ***12***, 5835-5838.
8 G. Resnati, E. Boldyreva, P. Bombicz, M. Kawano, *IUCrJ*, 2015, ***2***, 675-690.
9 H. A. Benesi, J. H. Hildebrand, *J. Am. Chem. Soc.*, 1948, ***70***, 2832-2833.
10 H. A. Benesi, J. H. Hildebrand, *J. Am. Chem. Soc.*, 1949, ***71***, 2703-2707.
11 J. H. Hildebrand, H. A. Benesi, L. M. Mower, *J. Am. Chem. Soc.*, 1950, ***72***, 1017-1020.
12 H. A. Benesi, J. H. Hildebrand, *J. Am. Chem. Soc.*, 1950, ***72***, 2273-2274.
13 R. S. Mulliken, *J. Am. Chem. Soc.*, 1952, ***74***, 811-824.
14 O. Hassel, *Science*, 1970, ***170***, 497-502.
15 H. A. Bent, *Chem. Rev.*, 1968, ***68***, 587-648.
16 J. M. Dumas, C. Geron, H. Peurichard, M. J. Gomel, *Bull. Soc. Chim. Fr.* , 1976, 720-722.
17 P. Murray-Rust, W. D. S. Motherwell, *J. Am. Chem. Soc.*, 1979, ***101***, 4374-4376.
18 P. Metrangolo, G. Resnati, T. Pilati, S. Biella, *Struct. Bond.*, 2008, ***126***, 105-136.
19 M. Fourmigue, *Curr. Opin. Solid State Mater. Sci.*, 2009, ***13***, 36-45.
20 J. P. M. Lommerse, A. J. Stone, R. Taylor, F. H. Allen, *J. Am. Chem. Soc.*, 1996, ***118***, 3108-3116.
21 M. Fourmigué, P. Batail, *Chem. Rev.*, 2004, ***104***, 5379-5418.
22 R. F. W. Bader, M. T. Carroll, J. R. Cheeseman, C. Chang, *J. Am. Chem. Soc.*, 1987, ***109***, 7968-7979.
23 P. Metrangolo, J. S. Murray, T. Pilati, P. Politzer, G. Resnati, G. Terraneo, *CrystEngComm*, 2011, ***13***, 6593-6596.
24 R. W. Troff, T. Mäkelä, F. Topić, A. Valkonen, K. Raatikainen, K. Rissanen, *Eur. J. Org. Chem.*, 2013, ***2013***, 1617-1637.
25 P. Metrangolo, H. Neukirch, T. Pilati, G. Resnati, *Acc. Chem. Res.*, 2005, ***38***, 386-395.
26 J. W. Zou, Y. J. Jiang, M. Guo, G. X. Hu, B. Zhang, H. C. Liu, Q. S. Yu, *Chem. - Eur. J.*, 2005, ***11***, 740-751.
27 D. W. Bruce, *Struct. Bond.*, 2008, ***126***, 161-180.
28 H. L. Nguyen, P. N. Horton, M. B. Hursthouse, A. C. Legon, D. W. Bruce, *J. Am. Chem. Soc.*, 2004, ***126***, 16-17.

29 P. Metrangolo, C. Prasang, G. Resnati, R. Liantonio, A. C. Whitwood, D. W. Bruce, *Chem. Commun. (Cambridge, U. K.)*, 2006, 3290-3292.

30 L. C. Gilday, S. W. Robinson, T. A. Barendt, M. J. Langton, B. R. Mullaney, P. D. Beer, *Chem. Rev.*, 2015, ***115***, 7118-7195.

31 C. B. Aakeröy, M. Baldrighi, J. Desper, P. Metrangolo, G. Resnati, *Chem. - Eur. J.*, 2013, ***19***, 16240-16247.

32 Y. X. Lu, H. Y. Li, X. Zhu, H. L. Liu, W. L. Zhu, *J. Mol. Model.*, 2012, ***18***, 3311-3320.

33 Y. X. Lu, Y. T. Liu, Z. J. Xu, H. Y. Li, H. L. Liu, W. L. Zhu, *Expert Opin. Drug Discovery*, 2012, ***7***, 375-383.

34 S. Sirimulla, J. B. Bailey, R. Vegesna, M. Narayan, *J. Chem. Inf. Model.*, 2013, ***53***, 2781-2791.

35 R. Wilcken, M. O. Zimmermann, A. Lange, A. C. Joerger, F. M. Boeckler, *J. Med. Chem.*, 2012, ***56***, 1363-1388.

36 Y. X. Lu, T. Shi, Y. Wang, H. Y. Yang, X. H. Yan, X. M. Luo, H. L. Jiang, W. L. Zhu, *J. Med. Chem.*, 2009, ***52***, 2854-2862.

37 P. Politzer, J. S. Murray, *ChemPhysChem*, 2013, ***14***, 278-294.

38 A. C. Legon, *Phys. Chem. Chem. Phys.*, 2010, ***12***, 7736-7747.

39 L. P. Wolters, P. Schyman, M. J. Pavan, W. L. Jorgensen, F. M. Bickelhaupt, S. Kozuch, *WIREs Comput. Mol. Sci.*, 2014.

40 B. Pinter, N. Nagels, W. A. Herrebout, F. De Proft, *Chem. - Eur. J.*, 2013, ***19***, 519-530.

41 L. P. Wolters, F. M. Bickelhaupt, *ChemistryOpen*, 2012, ***1***, 96-105.

42 B. Jing, Q. Li, R. Li, B. Gong, Z. Liu, W. Li, J. Cheng, J. Sun, *Comput. Theor. Chem.*, 2011, ***963***, 417-421.

43 M. Solimannejad, M. Malekani, *Comput. Theor. Chem.*, 2012, ***998***, 34-38.

44 C. B. Aakeröy, C. L. Spartz, S. Dembowski, S. Dwyre, J. Desper, *IUCrJ*, 2015, ***2***, 498-510.

45 P. Metrangolo, G. Resnati, *Science*, 2008, ***321***, 918-919.

46 P. Politzer, J. S. Murray, P. Lane, *Int. J. Quantum Chem.*, 2007, ***107***, 3046-3052.

47 C. B. Aakeröy, S. Panikkattu, P. D. Chopade, J. Desper, *CrystEngComm*, 2013, ***15***, 3125-3136.

48 C. B. Aakeröy, M. Fasulo, N. Schultheiss, J. Desper, C. Moore, *J. Am. Chem. Soc.*, 2007, ***129***, 13772-13773.

49 E. Corradi, S. V. Meille, M. T. Messina, P. Metrangolo, G. Resnati, *Angew. Chem., Int. Ed.*, 2000, ***39***, 1782-1786.

50 J. S. Murray, P. Lane, T. Clark, K. E. Riley, P. Politzer, *J. Mol. Model.*, 2012, ***18***, 541-548.

51 H. B. Bürgi, J. D. Dunitz, E. Shefter, *J. Am. Chem. Soc.*, 1973, ***95***, 5065-5067.

52 J. S. Murray, P. Lane, T. Brinck, P. Politzer, P. Sjoberg, *J. Phys. Chem.*, 1991, ***95***, 844-848.

53 M. Egli, R. V. Gessner, *Proc. Natl. Acad. Sci. USA*, 1995, ***92***, 180-184.

54 S. Sarkhel, A. Rich, M. Egli, *J. Am. Chem. Soc.*, 2003, ***125***, 8998-8999.

55 E. J. Stollar, J. L. Gelpí, S. Velankar, A. Golovin, M. Orozco, B. F. Luisi, *Proteins: Struct., Funct., Bioinf.*, 2004, ***57***, 1-8.

56 T. J. Mooibroek, P. Gamez, J. Reedijk, *CrystEngComm*, 2008, ***10***, 1501-1515.
57 J. S. Murray, P. Lane, P. Politzer, *J. Mol. Model.*, 2009, ***15***, 723-729.
58 J. S. Murray, P. Lane, T. Clark, P. Politzer, *J. Mol. Model.*, 2007, ***13***, 1033-1038.
59 S. J. Grabowski, *Phys. Chem. Chem. Phys.*, 2014, ***16***, 1824-1834.
60 A. Bauzá, T. J. Mooibroek, A. Frontera, *ChemPhysChem*, 2015, ***16***, 2496-2517.
61 P. Van Ginderen, *PhD Thesis: Studie van de van der Waals complexen gevormd tussen zwakke Lewiszuren en verschillende Lewisbasen in vloeibare edelgassen.*, University of Antwerp **2005**.
62 S. N. Delanoye, *PhD Thesis: Cryospectroscopic Study of Proper and Improper C-H···O Hydrogen Bonds: the van der Waals Complexes of Dimethyl Ether, Acetone and Oxirane with Diverse Proton Donors*, University of Antwerp **2004**.
63 J. J. J. Dom, *PhD Thesis: Anaesthetics Directed via Weak Hydrogen Bonds? An Infrared and Raman Spectroscopic Study Towards Target Molecules and Computational Accuracy*, University of Antwerp **2011**.
64 B. Michielsen, *PhD Thesis: Molecular Interactions with Halothane: a Spectroscopic Study*, University of Antwerp **2011**.
65 D. Hauchecorne, *PhD Thesis: C-X···Y Halogen Bonding: a Spectroscopic Study*, University of Antwerp **2011**.
66 N. Nagels, *PhD Thesis: Building Cryospectroscopic Bridges: Halogen Bonding, Hydrogen Bonding and Lone Pair···π Interactions*, University of Antwerp **2013**.

Chapter 2

Experimental and computational details

Thanks to the chemical inert nature of noble gases and the low temperature of their liquid phase, cryogenic solutions form an excellent medium for the study of weak intermolecular interactions. The studies of complexes in cryogenic solutions, which are supported by *ab initio* calculations, typically consist of a few different phases, for which an overview is given in Figure 2.1.

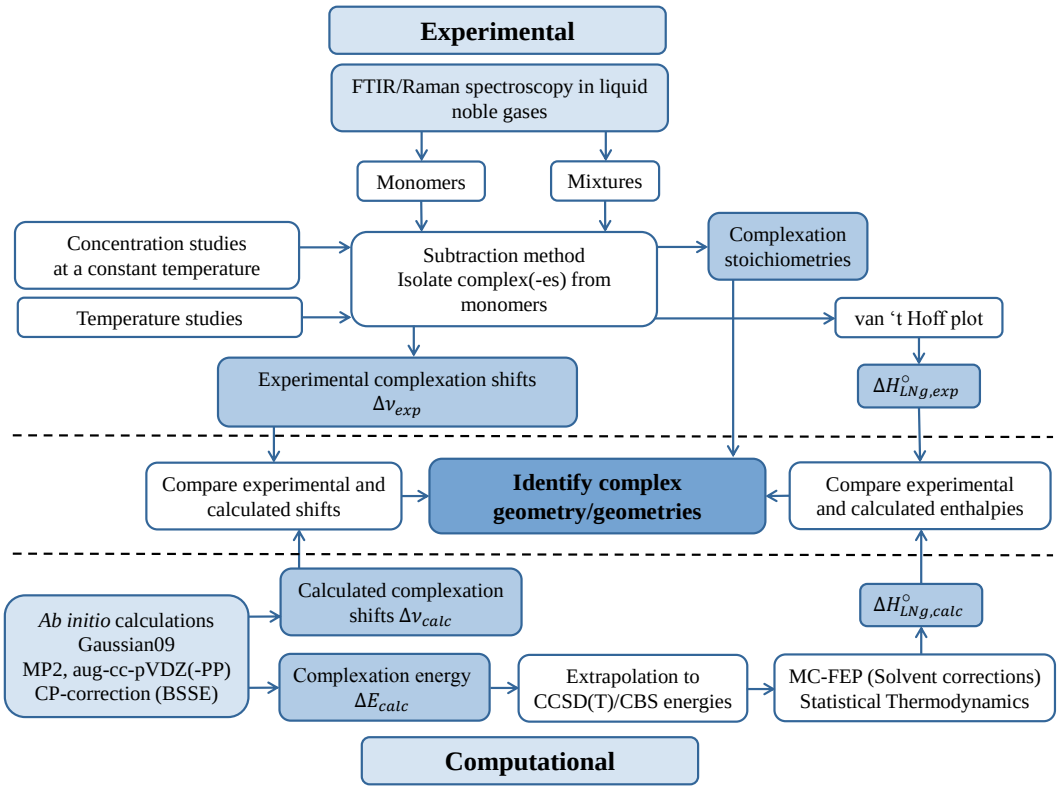

Figure 2.1 A schematic overview of the methodology followed for the FTIR and Raman measurements and the supporting calculations performed at the University of Antwerp (UAntwerp). Additionally, conceptual quantum chemical calculations are performed at the Vrije Universiteit Brussel (VUB) to rationalize the observed tendencies (not included in this overview, *vide infra*).

During the first phase, spectra of monomers and mixtures of the molecules are compared, and new bands due to complexation interactions are identified.

In the following phase, spectra of the monomers are multiplied by a scaling factor and subsequently subtracted from the spectrum of the mixture. The value of this scaling

factor is such that, after subtraction of the rescaled monomer spectra, no further signal due to the monomer is withheld, in order to obtain a spectrum which solely contains bands from the formed complexes. Comparison of the observed complexation shifts $\Delta\nu_{exp}$ and the *ab initio* calculated values $\Delta\nu_{calc}$ for the possible complex isomers gives information on the geometry of the formed complexes.

Subsequently, the stoichiometry of the observed complexes is determined by analysing the concentration dependent behaviour of the complex bands, in which the intensity of a complex band is compared to the product of rescaled monomer band intensities.

In the last phase, the relative stability, expressed as an enthalpy difference, is derived from temperature studies, in which spectra of the monomers and the mixture are recorded over a specified temperature interval, determined by the liquid properties of the noble gas used. During the processing of these spectra, the van 't Hoff isochore is used to determine the complexation enthalpies $\Delta H^{\circ}_{LNg,exp}$ of the formed complexes. These values are then also compared with the calculated complexation enthalpies $\Delta H^{\circ}_{LNg,calc}$ to further aid assignment of the complex geometries present in the solutions.

2.1 Experimental section

2.1.1 Cryospectroscopy in liquid noble gases

In the past couple of decades, cryospectroscopy in liquid noble gases has been proven to be an ideal technique for the study of weak noncovalent interactions. The technique combines the advantage of working at relatively low temperatures, aiding complex formation and avoiding thermally excited states, with the advantages of working in the liquid phase, which suppresses the rotation of the solutes and the associated rotation fine structure. Furthermore, as opposed to the matrix isolation technique, no site effects occur in the liquid phase. Within the group of cryogenic liquids, noble gases are the ideal solvents for these studies as they are chemically inert, form only weak interactions with the molecules and complexes, thus not disrupting the interactions of interest, and have no infrared or Raman intensity which might inhibit the study of

certain spectral regions. Moreover, since the cryogenic solutions are in chemical equilibrium, they provide the possibility to determine thermodynamic properties of the formed complexes. Due to the limited liquid range at atmospheric pressure, as shown in Figure 2.2, cryosolutions must be studied at increased pressures of up to 45 bars, which requires specific expertise and a dedicated experimental setup.

A disadvantage to the use of liquid noble gases is the limited solubility of many compounds, the maximal mole fractions typically lying in the 10^{-4} to 10^{-6} region for the more polar compounds. As the solubility increases drastically with the size of the noble gas used, the use of krypton or xenon over argon is often required. As shown in Figure 2.2 the use of different noble gases also allows to conduct studies at different temperature intervals.

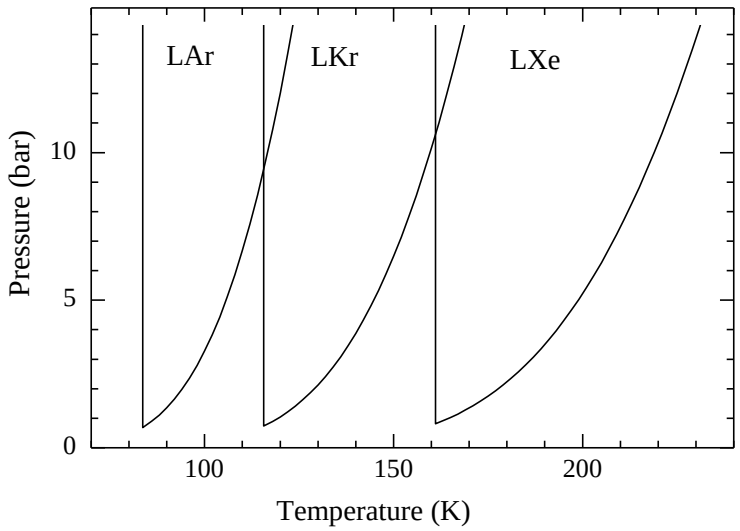

Figure 2.2 : Liquid ranges of the different noble gases used: liquid argon (LAr), liquid krypton (LKr) and liquid xenon (LXe).

2.1.2 Infrared spectroscopy

The infrared spectra were recorded on Bruker 66v and 66v/S FTIR vacuum spectrometers, both equipped with a globar source, a Ge/KBr beam splitter and MCT detector, cooled with LN_2. A photograph of one of the used experimental setups is given in Figure 2.3.

Figure 2.3: Overview of the used experimental FTIR setup: (1) Bruker 66v FTIR vacuum spectrometer, (2) vacuum manifold, (3) PID controller and (4) two-stage pump group.

Measurements were conducted in cells equipped with Si windows and a path length of 10 mm or a cell with ZnSe windows and 20 mm path length to obtain spectra between 6500 cm^{-1} and 450 cm^{-1}. Single channel spectra and photographs of the cells used are given in Figure 2.4. To avoid condensation of water and carbon dioxide on the cell windows, the cells are placed in a vacuum shroud with KBr windows. The temperature of the LN_2 cooled cells is kept constant at a given value using a built-in heating element controlled by a PID controller, which operates using the information of a Pt-100 sensor. The Pt-100 sensor is also built into the brass cell body and is connected to the PID controller through a Wheatstone bridge circuit.

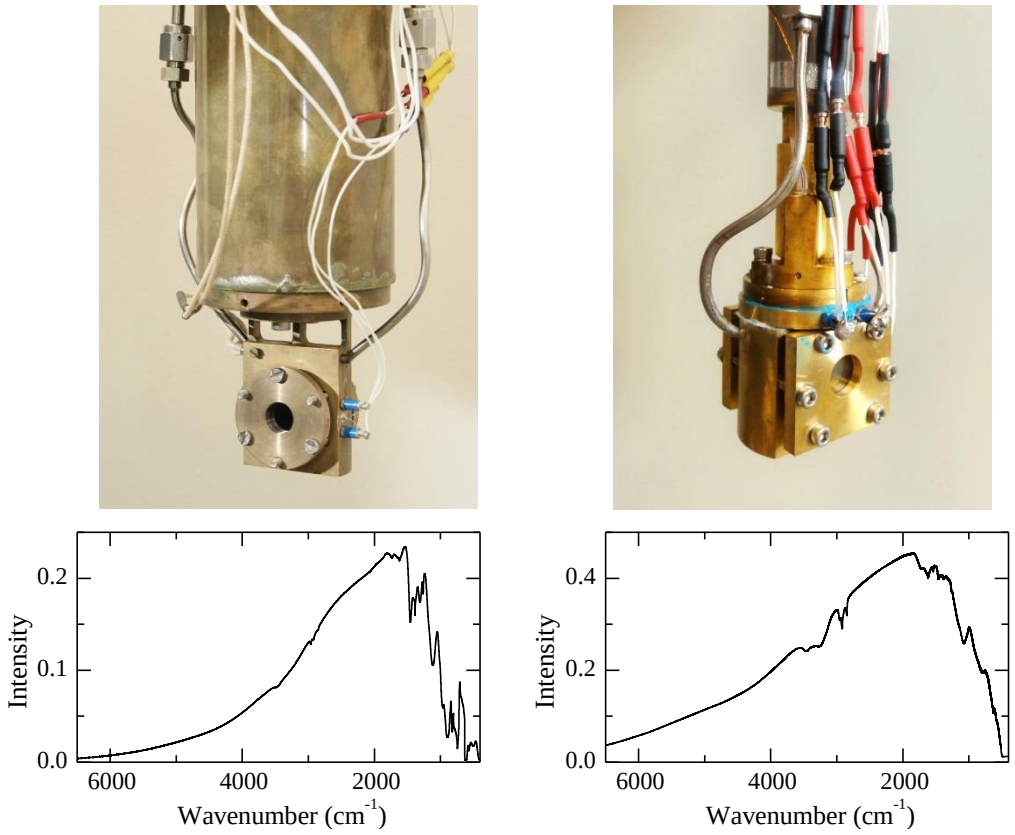

Figure 2.4: Photographs of the cells used in the FTIR measurements. A 10 mm path length cell with Si windows (and without its heat shield) is shown on the left-hand side, while the 20 mm cell equipped with ZnSe windows is shown on the right. Single channel spectra of both evacuated cells, suspended in vacuum shrouds with KBr windows, are shown under the respective photographs.

All interferograms were averaged over 500 scans, Blackman-Harris 3-term apodised and Fourier transformed with a zero filling factor of 8 to yield spectra with a resolution of 0.5 cm^{-1}.

The cells were filled using custom-made vacuum manifolds, based on ¼ inch stainless steel Swagelock components. Each of the manifolds is equipped with a Pirani vacuum gauge, used during evacuation of the manifold, a Bourdon type manometer, used to monitor the pressure in the cell during measurements and during filling of the solvent gas and a gas independent capacitance manometer gauge operating in the mbar range, used during filling of the solutes. As the experimental setup does not allow for

verification of full solubility of the compounds, or verification of the fluid level in the filling tube, exact concentrations are not known and the mole fractions reported are estimates. The vacuum manifold and vacuum shroud are evacuated using a two-stage pump group, consisting of a rotary vane pump as a pre-pump and an oil diffusion pump for high vacuum with a by-pass.

In principle, the used spectrometer allows the complete IR spectrum to be recorded between 10 and 25000 cm^{-1}. [1] Expansion to the near-IR (NIR) involves the use of a tungsten light source, Si/CaF_2 and quartz beam splitters and an InSb detector and allows the study of higher frequency transitions, which for the compounds studied in this thesis solely involve overtones and combination bands that are of little interest in the current project. Far-IR (FIR) measurements can also be performed using the globar light source, a Mylar beam splitter, polyethylene windows for the vacuum shroud, and a LHe cooled bolometer, although much of this spectral information is also easily obtainable using the available Raman setup.

2.1.3 Raman spectroscopy

Whereas infrared spectroscopy is based on the absorption of infrared radiation, during Raman spectroscopy the inelastic scattered photons of monochromatic light, generated by a laser, are detected. [2] Raman spectra were recorded using a TriVista 557 triple-stage spectrometer with two f = 50 cm spectrographs equipped with 300/900/2000 lines mm^{-1} gratings and a f = 70 cm spectrograph equipped with 500/1800/2400 lines mm^{-1} gratings and a back-end illuminated LN_2 cooled CCD detector. For low wavenumber measurements, the three spectrographs are used in series in a subtractive way, to reduce the amount of Rayleigh radiation reaching the detector. Other measurements are performed using solely the third stage f = 70 cm spectrograph to optimize the amount of Stokes scattered light reaching the detector. The 514.5 nm line of a Spectra-Physics argon ion laser was used for Raman excitation, and the power of the incident laser beam was set to 0.8 W. A plasma filter is placed between the laser and the cell to eliminate the plasma lines of the laser. To reduce the amount of Rayleigh radiation

entering the spectrometer, a notch filter is also placed after the cell. Frequencies were calibrated using Ne emission lines, and are expected to be accurate to 0.5 cm^{-1}. The full widths at half height of the most intense Ne lines studied typically varied between 0.5 and 0.6 cm^{-1}. The liquid cell, equipped with four quartz windows at right angles, is placed in a multipass setup to increase the amount of Raman scattered radiation. A schematic overview of the Raman setup is given in Figure 2.5.

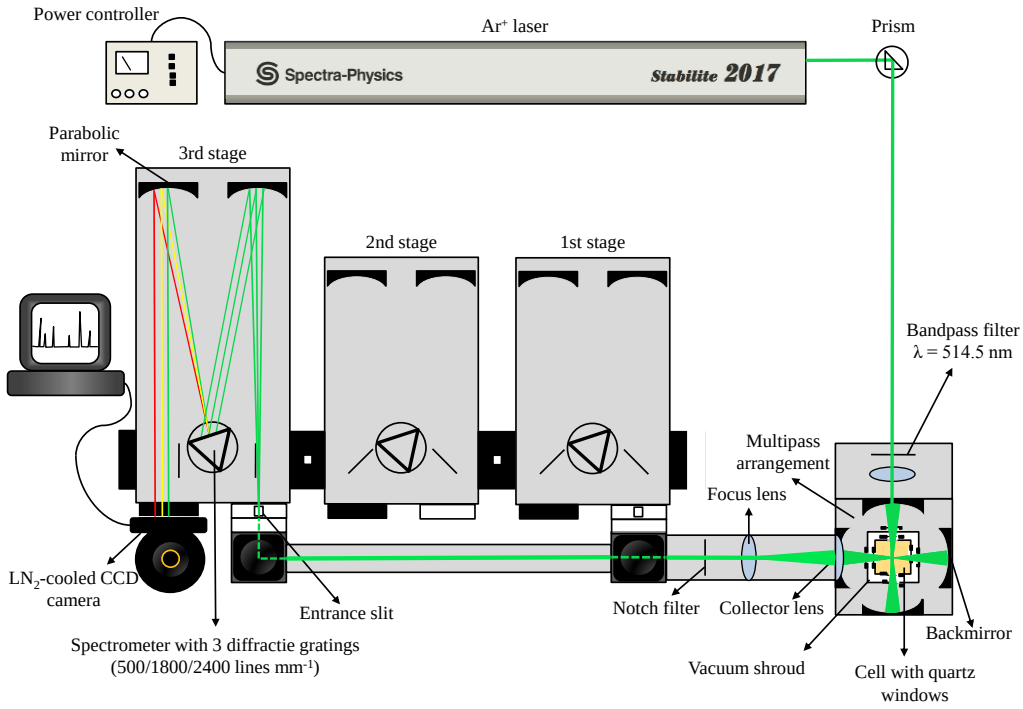

Figure 2.5: Schematic overview of the Raman setup used for cryospectroscopic measurements with the TriVista 557 spectrometer operating in 3rd stage mode. [3]

The temperature of the cell, which is cooled with LN_2, is controlled by a PID controlled heating element. A vacuum manifold similar to those of the FTIR setups was used to fill and evacuate the Raman cell. The two-stage pump group uses a turbopump for high vacuum instead of an oil diffusion pump to evacuate the manifold, while the high vacuum of the vacuum shroud is maintained using a second, identical pump group. An overview of the Raman cell and setup is given in Figure 2.6

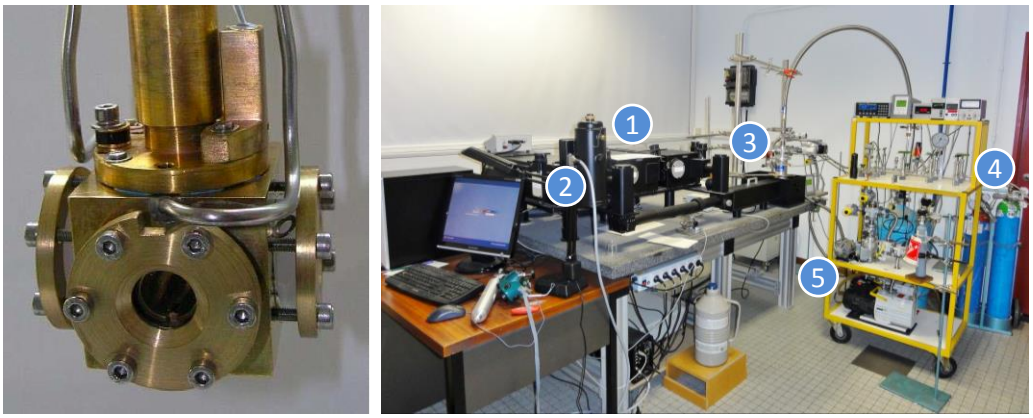

Figure 2.6: Raman cell for cryogenic solutions (left) and overview of the experimental Raman setup (right): (1) TriVista 557 spectrometer, (2) LN_2 cooled CCD (3) Raman cell, (4) vacuum manifold and (5) two-stage pumping group.

2.1.4 Processing of experimental measurements

Complex formation influences the electron distribution of the monomers involved, which in turn influences the covalent bond strengths of said molecules. This leads to changes in the frequencies of the vibrational modes, which can be observed in infrared and Raman spectroscopy in the form of redshifted or blueshifted bands in the spectra of mixtures of compounds alongside the monomer bands. To fully analyse these complex bands, they have to be isolated from the bands belonging to the monomers. Therefore, spectra of the individual monomers are recorded under the same conditions as the measurements of the mixtures. These spectra are then rescaled, using a scale factor determined in a spectral region where a distinction can be made between the monomer and complex band, and subtracted from the spectrum of the mixture to obtain a spectrum that contains solely bands due to the complex or complexes present. This procedure allows differentiation between monomer and complex bands which are located at frequency differences smaller than the resolution of the spectrometer and thus largely overlapping. From these rescaled and subtracted spectra, the intensities of the different compounds, which are needed for the processing of the concentration and temperature studies, can be integrated numerically, or can be obtained from a band fit analysis if complex bands are found to be (partially) overlapping. When the complex

bands of multiple complex isomers are overlapping and cannot be deconvoluted, the isomers are assigned to the same band and the intensity is not used during further analyses.

2.1.4.1 Complexation interactions at thermodynamic equilibrium

Intermolecular interactions between two or more molecules can generally be described by the equilibrium equation of the monomers A and B and the complex A_nB_m

$$nA + mB \rightleftharpoons A_nB_m \tag{2.1}$$

for which the corresponding equilibrium constant $K_{A_nB_m}$ is given by

$$K_{A_nB_m} = \frac{a_{A_nB_m}}{(a_A)^n(a_B)^m} \tag{2.2}$$

Assuming an ideal solution, as is common for diluted systems, in which all activity coefficients are equal to one, this equilibrium constant can be rewritten as a function of the mole fractions

$$K_{A_nB_m} = \frac{x_{A_nB_m}}{(x_A)^n(x_B)^m} \tag{2.3}$$

Furthermore, the complexation interaction is described thermodynamically by the equation

$$-RTlnK_{A_nB_m} = \Delta G^{\circ}_{A_nB_m} = \Delta H^{\circ}_{A_nB_m} - T\,\Delta S^{\circ}_{A_nB_m} \tag{2.4}$$

in which $\Delta G^{\circ}_{A_nB_m}$ is the standard free energy of complexation, $\Delta H^{\circ}_{A_nB_m}$ is the standard complexation enthalpy and $\Delta S^{\circ}_{A_nB_m}$ is the standard complexation entropy. As the latter value is negative, due to the loss of freedom upon complexation, the standard complexation enthalpy also has to be negative in order to obtain an attractive interaction. This also implies that complex formation is aided by working at lower temperatures.

2.1.4.2 Concentration studies and complex stoichiometry

Complexation stoichiometries can be determined experimentally by performing an isothermal concentration study in which the concentrations of the solutes are

systematically varied. The concentration of a solute can be determined by applying the Lambert-Beer law

$$C_i = \frac{I_i}{\varepsilon_i d} \tag{2.5}$$

in which I_i is the integrated intensity and ε_i is the extinction coefficient of component *i* and *d* the path length of the sample studied. Furthermore, the concentration of a solute can also be described as

$$C_i = \frac{n_i}{V} = \frac{n_i \rho}{N M_a} = x_i \frac{\rho}{M_a} \tag{2.6}$$

in which n_i is the number of solute molecules in the solution, V is the volume of the solution, ρ is the density of the solution, *N* is the sum of the number of solute and solvent molecules and M_a is the average molar mass of the solute and solvent molecules in solution. Using this equation, the equilibrium constant can be written as

$$K_{A_nB_m} = \frac{C_{A_nB_m}}{(C_A)^n (C_B)^m} \frac{\rho^{n+m-1}}{{M_a}^{n+m-1}} \tag{2.7}$$

after which implementation of the Lambert-Beer law yields

$$K_{A_nB_m} = \frac{(\varepsilon_A)^n (\varepsilon_B)^m}{\varepsilon_{A_nB_m}} \left(\frac{d\rho}{M_a}\right)^{n+m-1} \frac{I_{A_nB_m}}{(I_A)^n (I_B)^m} \tag{2.8}$$

which describes the relationship between the equilibrium constant and the integrated band intensities of the complex and monomers involved. Furthermore, as the concentration study is performed at a constant temperature, the density of the solution remains constant, thus reducing the equation to

$$I_{A_mB_n} = C (I_A)^m (I_B)^n \tag{2.9}$$

in which $C = K_{A_nB_m} \frac{\varepsilon_{A_nB_m}}{(\varepsilon_A)^n (\varepsilon_B)^m} \left(\frac{M_a}{d\rho}\right)^{n+m-1}$ is a constant.

When plotting the integrated intensity of the complex $I_{A_mB_n}$ against the product of the integrated monomer intensities $(I_A)^x (I_B)^y$ a linear relationship will thus only be found when $x = m$ and $y = n$. [1] By preparing a series of plots for various integer values of *x* and *y* and evaluating their linearity, the complex stoichiometry can be determined experimentally.

2.1.4.3 Temperature studies, van ‘t Hoff plots and complex enthalpies

Apart from the complex stoichiometry, the standard complexation enthalpy can also be determined by creating a van ‘t Hoff plot based on measurements performed at different temperatures.

The underlying theory is based on a rewritten version of equation 2.4

$$lnK_{A_nB_m} = -\frac{\Delta H^{\circ}_{A_nB_m}}{RT} + \frac{\Delta S^{\circ}_{A_nB_m}}{R} \tag{2.10}$$

which is also called the van ‘t Hoff equation and gives the relationship between the complexation enthalpy and the inverse temperature. Substitution of the equilibrium constant, based on equation 2.8, yields

$$-\frac{\Delta H^{\circ}_{A_nB_m}}{RT} = ln\left(\frac{I_{A_nB_m}}{(I_A)^n(I_B)^m}\right) + (n+m-1)ln\rho + C \tag{2.11}$$

where

$$C = ln\left(\frac{(\varepsilon_A)^n(\varepsilon_B)^m}{\varepsilon_{A_nB_m}}\left(\frac{d}{M_a}\right)^{n+m-1}\right) - \frac{\Delta S^{\circ}_{A_nB_m}}{R} \tag{2.12}$$

Equation 2.11 demonstrates that, when a substantial thermal expansion occurs within the temperature range studied, the complexation enthalpy cannot be determined directly. To account for this, the density of the liquid noble gases is approximated as

$$ln\rho = a + \frac{b}{T} \tag{2.13}$$

where a and b are temperature independent constants. [4]

This enables equation 2.11 to be rewritten as

$$ln\left(\frac{I_{A_nB_m}}{(I_A)^n(I_B)^m}\right) = -\left(\frac{\Delta H^{\circ}_{A_nB_m} + (n+m-1)Rb}{R}\right)\frac{1}{T} - (C + (n+m-1)a) \tag{2.14}$$

so that the complexation enthalpy can be determined from the gradient of the plot of $ln\left(\frac{I_{A_nB_m}}{(I_A)^n(I_B)^m}\right)$ against the inverse temperature.

2.1.5 Product overview

An overview of all products used within this thesis is given in Table 2.1. Depending on the container the product was delivered in, the samples were either used without purification or transferred into a glass sample tube and degassed using a freeze-thaw cycle procedure.

Table 2.1: Overview of all used chemical during the FTIR and Raman measurements in this PhD thesis, including their abbreviation, supplier and purity specifications and the protocol utilized to prepare the samples.

Compound	CAS	Supplier	Purity specification	Protocol
Difluoroiodomethane (CHF_2I)	1493-03-4	ABCR	97%	(1)
Fluoroiodomethane (CH_2FI)	373-53-5	ABCR	99%	(2)
Bromodifluoromethane (CHF_2Br)	1511-62-2	Fluorochem		(1)
Tetrafluoroethene (C_2F_4)	116-14-3	ABCR	99%	(1)
Chlorotrifluoroethene (C_2F_3Cl)	79-38-9	ABCR	99%	(1)
Bromotrifluoroethene (C_2F_3Br)	598-73-2	ABCR	98%	(1)
Trifluoroiodoethene (C_2F_3I)	359-37-5	Lancaster	97%	(1)
Hexafluorobenzene (C_6F_6)	392-56-3	Sigma-Aldrich	+99.5%	(2)
Carbonyl fluoride (COF_2)	353-50-4	ABCR	97%	(1)
Carbonyl chloride fluoride (COFCl)	353-49-1	ABCR	97%	(1)
2,2,4,4-tetrafluoro-1,3-dithiethane ($C_2F_4S_2$)	1717-50-6	Alfa Aesar	97%	(2)
Trimethylamine (TMA)	75-50-3	Sigma-Aldrich	99%	(1)
Trimethylamine-d_9 (TMA-d_9)	13960-80-0	Sigma-Aldrich	+99%d	(1)
Dimethyl ether (DME)	115-10-6	Sigma-Aldrich	99+%	(1)
Dimethyl ether-d_6 (DME-d_6)	17222-37-6	Aldrich	+98%d	(1)
Fluoromethane (CH_3F)	593-53-3	ABCR	98%	(1)
Fluoromethane-d_3 (CH_3F-d_3 / CD_3F)	558-21-4	Sigma-Aldrich	99%d	(1)
Trimethylphosphine (TMP)	594-09-2	Sigma-Aldrich	99%	(2)
Trimethylphosphine-d_9 (TMP-d_9)	22529-57-3	Sigma-Aldrich	99%d	(2)
Dimethyl sulfide (DMS)	75-18-3	Sigma-Aldrich	99%	(2)
Dimethyl sulfide-d_6 (DMS-d_6)	926-09-0	Sigma-Aldrich	99%d	(2)
Chloromethane (CH_3Cl)	74-87-3	Sigma-Aldrich	+99.5%	(1)
Krypton (Kr /LKr)	7439-90-9	Air Liquide	99.9995%	(1)
Argon (Ar / Lar)	7440-37-1	Air Liquide	99.9999%	(1)
Xenon (Xe / LXe)	4770-63-3	Linde	99.999%	(1)

(1) Sample was used without further purification.
(2) Sample was transferred into a glass sample tube and degassed using a freeze-thaw cycle procedure.

To aid assignments and avoid spectral congestion, measurements are often performed for both the undeuterated and the fully deuterated Lewis base. When referring to (measurements or results of) both undeuterated and fully deuterated Lewis bases the abbreviation of the product followed by ($-d_x$) in parentheses is used in the remainder of this thesis.

2.1.6 Microwave spectroscopy

During this PhD, Fourier Transform Microwave (FTMW) spectroscopic measurements were performed at the universities of Bologna and Newcastle. Whereas the molecules and complexes are investigated through their vibrational energy levels during infrared and Raman measurements, the rotational energy levels are studied in microwave spectroscopy. Using this technique, direct information on the geometry of the studied species can be obtained through the rotational constants, which are related the moments of inertia of the species. Therefore, this technique is highly complementary with the FTIR and Raman measurements, which only yield indirect evidence on the geometry of complexes through comparison of the experimental shifts with those of *ab initio* calculations. Another important difference with the earlier discussed techniques is the fact that FTMW measurements are not performed at thermodynamic equilibrium, as the sample undergoes supersonic expansion upon introduction to the vacuum cavity through a nozzle. During this supersonic expansion, rotational temperatures decrease to about 2 K, which means that these measurements are performed at far lower temperatures than those used for the FTIR and Raman measurements.

The measurements at the University of Bologna, which involved the complexes of C_2F_3Cl with NH_3 and DME, were performed on a Balle-Flygare type FTMW spectrometer, [5] which covers the 6.5-18 GHz range. In this spectrometer, which is shown in Figure 2.7, the sample, which is mixed with helium at a pressure of 5 bar, is introduced into a Fabry-Pérot cavity through a solenoid valve with a nozzle diameter of 0.5 mm. The gas pulses expand supersonically into the vacuum chamber, after which

the molecules are excited to higher rotational levels using an antenna which is coaxially mounted to the nozzle. On the other side of the vacuum chamber, the subsequently emitted microwave radiation of the free induction decay (FID) is measured using another antenna, yielding spectra of about 1 MHz bandwidth. In order for the Fabry-Pérot cavity to act as a resonator, the aluminium mirror on the side of the receiving antenna is movable, so that its position can be tuned for each measured frequency. As the antennae and gas pulse nozzle are mounted coaxially, the supersonic expansion of the sample propagates along the same axis as the detected microwave radiation and each rotational transition appears as a Doppler doublet. The line position of the transition is then calculated as the arithmetic mean of the frequencies of the Doppler components. The entire sequence of gas and radiation pulses and measurements is controlled by a 10 MHz rubidium oscillator, which acts as an internal clock for the spectrometer. A more detailed description of the spectrometer, for which most details have been taken from the spectrometer at the University of Valladolid [6] can be found in a previous paper by Caminati et al. [7]

Figure 2.7: Photograph of the Balle-Flygare type FTMW spectrometer used at the University of Bologna, with the controllers and amplifiers on the left-hand side and the Fabry-Pérot cavity on the right.

The development of faster digitizers has allowed the construction of broadband microwave spectrometers, the first of which was developed by Prof. Brooks Pate at the University of Virginia and reported in 2008. [8] In the scope of this thesis, chirped-pulse Fourier transform microwave (CP-FTMW) measurements have been performed at Newcastle University. A detailed description of the used spectrometer, shown in Figure 2.8, and frequency mixing regime can be found in a publication by Stephens and Walker, [9] and only a short description is given here. A circuit diagram of the CP-FTMW spectrometer has also been included in Figure 2.9. Just as with the FTMW instrument described above, the FID is recorded and Fourier transformed in CP-FTMW spectroscopy. The introduced microwave pulse and detected FID however span a bandwidth of 12 GHz, thus measuring hundreds of transitions simultaneously, allowing spectra to be recorded in a fraction of the time necessary for measurements with Balle-Flygare type FTMW spectrometers with a bandwidth of 1 MHz. In this spectrometer, the sample is still introduced in a vacuum chamber in a carrier gas (argon in the measurements discussed) where it undergoes supersonic expansion, thus cooling down to about 2 K rotational temperature. The pulsed nozzle is however positioned perpendicularly to the horn antennae on either side of the vacuum chamber, which either introduce the chirped pulse of microwave radiation or record the FID, so that the rotational transitions are no longer observed as Doppler doublets. Furthermore, as a wide bandwidth of radiation is simultaneously emitted and recorded by the horns, the vacuum chamber must no longer be resonant, thus eliminating the need for a (movable) mirror of a Fabry-Pérot cavity. The current setup allows the recording of spectra in the 7 - 18 GHz range, although lower ranges can in principle be measured by changing the horn antennae and the microwave generator. A major drawback of the use of chirped-pulse FTMW spectrometers is the reduced resolution, the linewidth (full width at half maximum, FWHM) being approximately 80 kHz [9] as compared to less than 10 kHz for FTMW spectrometers of the Balle-Flygare type. [10]

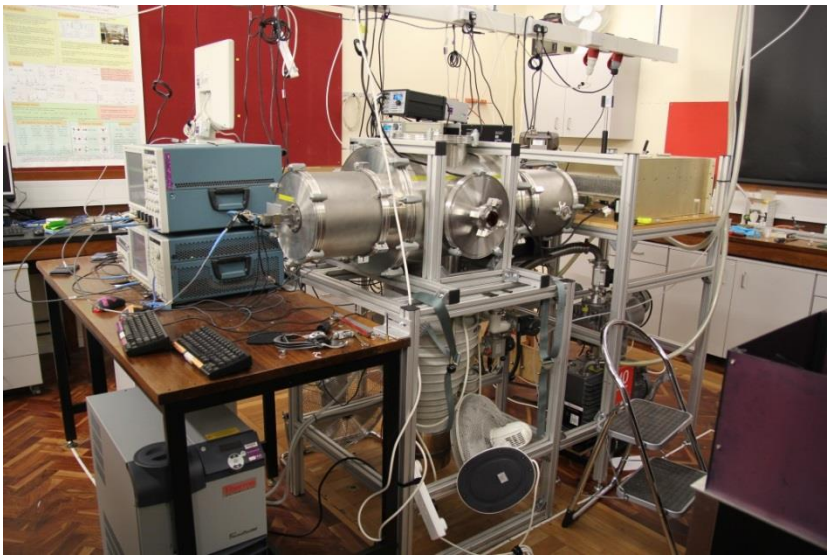

Figure 2.8: Photograph of the CP-FTMW spectrometer used at Newcastle University, with the vacuum chamber in the centre of the image and the oscilloscope on the left.

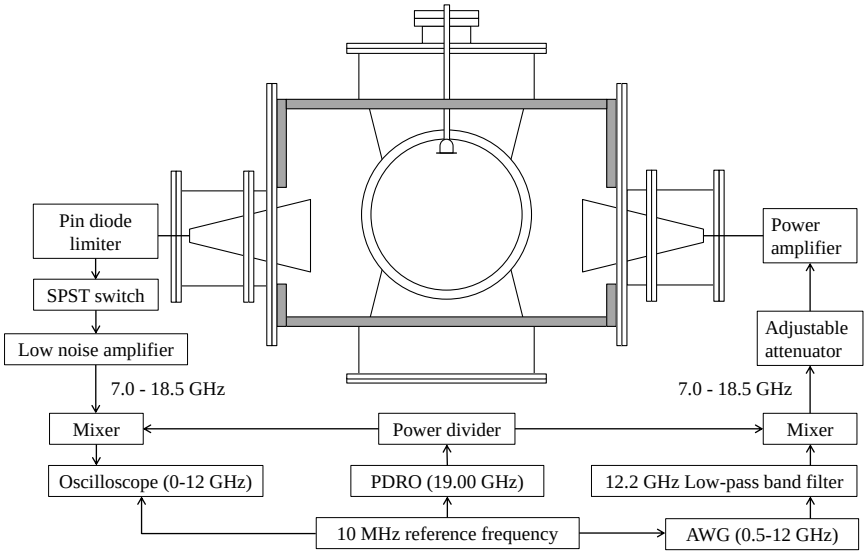

Figure 2.9: Circuit diagram of the CP-FTMW spectrometer, including a top view of the vacuum chamber. The pulsed nozzle comes in through the top of the image, with the emitting (right) and recording (left) horn antennae on either side of the chamber. The circle in the middle represents the oil diffusion pump maintaining the high vacuum in the chamber. [9]

2.2 Computational details

2.2.1 *Ab initio* calculations

To support the experimental measurements, *ab initio* calculations were performed to determine the properties of atoms and molecules in a theoretical way from the principles of quantum mechanics. This involves solving the time-independent Schrödinger equation

$$\hat{H}\Psi(R_1, R_2, \dots R_N, r_1, r_2, \dots r_n) = E\Psi(R_1, R_2, \dots R_N, r_1, r_2, \dots r_n) \quad (2.15)$$

in which $\hat{H}$ is the Hamiltonian operator, Ψ is the wave function of all nuclei and electrons and E is the energy associated with the wave function. [11] Using the Born-Oppenheimer approximation, which states that, as the electrons move much faster than the nuclei, they can instantly respond to any change in the relative positions of the nuclei and they can thus be considered as moving in a field of fixed nuclei, the variables due to the nuclei and electrons can be separated in an electronic wave function ψ and nuclear wave function Φ.

$$\Psi(R_1, R_2, \dots R_N, r_1, r_2, \dots r_n) = \Phi(R_1, R_2, \dots R_N)\psi(r_1, r_2, \dots r_n; R_1, R_2, \dots R_N) \quad (2.16)$$

The electronic wave function depends only parametrically on the nuclear coordinates, so that for a certain geometry, the Schrödinger equation can then be solved by looking at the electronic wave function ψ.

In the Hartree-Fock method, the electronic wave function is then written as the simplest combination of one-electron functions $\phi_1(r_1)$, which are called molecular orbitals, that satisfies the antisymmetry property of the total wave function, i.e. a Slater determinant:

$$\psi(r_1, r_2, \dots r_N) = \frac{1}{\sqrt{N!}} \begin{vmatrix} \phi_i(r_1) & \phi_j(r_1) & \dots & \phi_k(r_1) \\ \phi_i(r_2) & \phi_j(r_2) & \dots & \phi_k(r_2) \\ \vdots & \vdots & & \vdots \\ \phi_i(r_N) & \phi_j(r_N) & \dots & \phi_k(r_N) \end{vmatrix} \quad (2.17)$$

with N the number of electrons.

The Hartree-Fock equations are then obtained by minimizing the energy of this Slater determinant with respect to variations in these molecular orbitals, subject to the

constraint that these orbitals remain orthonormal during the minimization process. One of the major disadvantages when adopting the Hartree-Fock approximation is the fact that it turns out that the motion of electrons with opposite spin is not correlated in this method.

In post-Hartree-Fock methods the instantaneous electron-electron repulsion, known as electron correlation, is taken into account. One such method is Rayleigh-Schrödinger perturbation theory (RS-PT), in which the Hamiltonian is decomposed into an operator of which the eigenvectors and eigenvalues are exactly known and a perturbation which covers the difference with the true operator. This perturbation is then expanded as a power series in terms of the energy levels and eigenstates of the old Hamiltonian.

Møller and Plesset divided the full Hamiltonian of a molecular system into the Hartree-Fock Hamiltonian (for which the eigenvectors and eigenvalues are exactly known, i.e. the sum of Fock operators) and a perturbation covering the electron correlation, thus creating Møller-Plesset (MP) perturbation theory:

$$\hat{H}_{MP} = \hat{H}_0 + \hat{V} \qquad \hat{H}_0 = \sum \hat{F}_v \tag{2.18}$$

Here, zeroth-order MP perturbation theory yields the sum of the orbital energies

$$E^{(0)} = \langle \Psi_0 | \hat{H}_0 | \Psi_0 \rangle = \sum_i \varepsilon_i \tag{2.19}$$

while first-order MP perturbation theory yields the HF energy

$$E^{(1)} = \langle \Psi_0 | \hat{V} | \Psi_0 \rangle \qquad E^{HF} = E^{(0)} + E^{(1)} \tag{2.20}$$

Typically, the series expansion is truncated after the second-order correction, giving rise to Møller-Plesset second order perturbation theory (MP2). Here, the single excitation terms are 0, so that the expression only contains double excitations, as described in equation 2.21. [12]

$$E^{(2)} = E^{HF} - \sum_{s \neq 0} \frac{\left| \langle \Psi_0 | \hat{V} | \Psi_s \rangle \right|^2}{E_s - E_0} = E^{HF} - \frac{1}{4} \sum_{ijab} \frac{|\langle ij \| ab \rangle|^2}{\varepsilon_a + \varepsilon_b - \varepsilon_i - \varepsilon_j} \tag{2.21}$$

To support the experimental measurements, *ab initio* MP2 calculations were performed using Dunning's augmented correlation consistent basis sets of double (aug-cc-pVDZ)

or triple (aug-cc-pVTZ) zeta quality in Gaussian09. [13] For bromine and iodine, aug-cc-pVDZ-PP and aug-cc-pVTZ-PP basis sets including a small-core energy-consistent relativistic pseudopotential (PP) were used, while the standard aug-cc-pVDZ and aug-cc-pVTZ basis sets were used for all other atoms. [14-15] The counterpoise technique as proposed by Boys and Bernardi [16] was used during all *ab initio* calculations to account for basis set superposition error.

2.2.2 CCSD(T)/CBS extrapolation scheme

To obtain complexation energies at a higher level of theory at a reasonable computational cost, energies at the basis set limit were calculated with Molpro [17] using the extrapolation scheme of Truhlar [18]. The starting point of these calculations is always the MP2/aug-cc-pVDZ(-PP) optimized complex geometry, for which multiple single point calculations at different levels of theory are performed. In this extrapolation scheme, the complexation energy at the complete basis set limit at the Hartree-Fock level is extrapolated using the formula

$$E_{CBS}^{HF} = \frac{3^{\alpha}}{3^{\alpha} - 2^{\alpha}} E_3^{HF} - \frac{2^{\alpha}}{3^{\alpha} - 2^{\alpha}} E_2^{HF} \tag{2.22}$$

where $\alpha = 3.4$ [18]. The energies with subscript 2 and 3 are obtained from single point calculations using the aug-cc-pVDZ(-PP) and aug-cc-pVTZ(-PP) basis sets respectively. Furthermore, the effect of electron correlation is obtained from MP2 calculations, for which the correction factor at the basis set limit is obtained from

$$E_{CBS}^{cor,MP2} = \frac{3^{\beta}}{3^{\beta} - 2^{\beta}} E_3^{cor,MP2} - \frac{2^{\beta}}{3^{\beta} - 2^{\beta}} E_2^{cor,MP2} \tag{2.23}$$

in which $\beta=2.2$ [18] while energies with subscript 2 and 3 are calculated using the aug-cc-pVDZ(-PP) and aug-cc-pVTZ(-PP) basis sets respectively.

Furthermore, a correction for higher order correlation effects is made using the method of Jurečka and Hobza [19, 20], yielding results of $E_{CBS}^{CCSD(T)}$ quality.

$$\Delta E^{CCSD(T)} = \left| E^{CCSD(T)} - E^{MP2} \right|_{aug-cc-pVDZ(-PP)} \tag{2.24}$$

$$E_{CBS}^{CCSD(T)} = E_{CBS}^{HF} + E_{CBS}^{cor,MP2} + \Delta E^{CCSD(T)} \tag{2.25}$$

This last correction is based on the observation that for calculations using Dunning's basis sets the difference in correlation energy between MP2 and CCSD(T) calculations, calculated using the same basis set size, remains stable throughout the expanding basis set size, as depicted graphically in Figure 2.10.

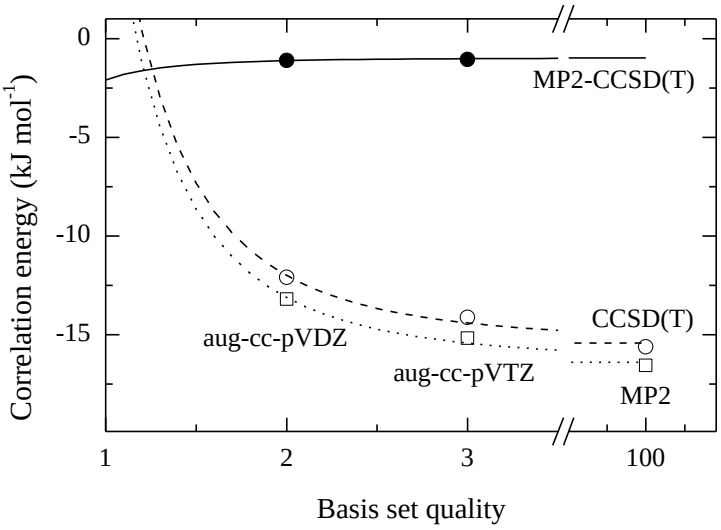

Figure 2.10: 2-point extrapolations of MP2 and CCSD(T) correlation energies and MP2 to CCSD(T) difference (MP2-CCSD(T)) using aug-cc-pVDZ and aug-cc-pVTZ basis sets. Calculations were made for the CF_3Cl·TMA XB complex.

2.2.3 Statistical thermodynamics

To compare the experimentally obtained complexation enthalpy in the liquid noble gas with the theoretically obtained complexation energy of the isolated complex at 0 K, several corrections have to applied to the latter value. By using statistical thermodynamics based on the regularly used standard rigid rotor/harmonic oscillator model, thermal effects and zero-point vibrations can be accounted for, in order to obtain a complexation enthalpy value in the gas-phase at the temperature used during the experimental measurements. The enthalpy value of a molecule at a temperature T can be written as the sum of the electronic ground state without incorporation of the zero-point energy (E_e^0), the zero-point energy itself (E_{vib}^0), the labour term (PV) and the classical translation (E_{trans}^T), rotation (E_{rot}^T) and vibration (E_{vib}^0) terms.

$$H^T = E_e^0 + E_{vib}^0 + PV + E_{trans}^T + E_{rot}^T + E_{vib}^T \tag{2.26}$$

As the complexation energy is defined as the difference in enthalpy between the complex A_nB_m and the monomers A and B

$$\Delta H_{Complex}^T = H_{A_nB_m}^T - (nH_A^T + mH_B^T) \tag{2.27}$$

equation 2.26 can be rewritten as

$$\Delta H_{Complex}^T = \Delta E_e^0 + \Delta E_{trans}^T + \Delta E_{rot}^T + \Delta E_{vib}^T + \Delta E_{vib}^0 + \Delta(PV) \tag{2.28}$$

where the latter five terms are the thermodynamic corrections.

The classical translation and rotation terms ΔE_{trans}^T and ΔE_{rot}^T are $-\frac{1}{2}RT$ for each degree of freedom that is lost upon complexation, while the decrease of free molecules also influences the labour term $\Delta(PV) = \Delta nRT$, in which Δn is one minus the number of molecules involved in the complex.

The zero-point vibrational energy difference ΔE_{vib}^0 can be calculated as

$$\Delta E_{vib}^0 = \frac{1}{2}\sum_{i=1}^{\substack{complex\\vibrations}} h\nu_i - \frac{1}{2}\sum_{j=1}^{\substack{monomer\\vibrations}} h\nu_j \tag{2.29}$$

while the remaining classical (thermal) vibrational term ΔE_{vib}^T represents the difference in vibrational energy between 0 K and the temperature T.

$$\Delta E_{vib}^{T} = N_A h \left(\sum_{i=1}^{\substack{complex \\ vibrations}} \frac{\nu_i}{e^{\frac{h\nu_i}{k_B T}} - 1} - \sum_{j=1}^{\substack{monomer \\ vibrations}} \frac{\nu_j}{e^{\frac{h\nu_j}{k_B T}} - 1} \right) \quad (2.30)$$

These calculations were performed at 103 K for Ar, 138 K for Kr and 193 K for Xe, i.e. at the midpoint of the temperature intervals used during the experimental studies.

2.2.4 Solvent corrections: Monte Carlo-free energy perturbation theory

By including the thermal effects and zero-point vibrations in the previous section, a complex enthalpy value is obtained at a temperature T is the gas-phase. Even though liquid noble gas solutions were originally described as pseudo-gas-phases, it is now generally accepted that significant solute-solvent interactions can occur, which have to be taken into account. To enable comparison of the calculated complexation enthalpy with the experimental results, Monte Carlo-free energy perturbation (MC-FEP) simulations are performed using an in-house modified version of BOSS 4.0 by Jorgensen [21], which also takes into account the polarization of the noble gas molecules by the solute, resulting in dipole-induced dipole interactions.

To calculate the solvation of a molecule or complex using free energy perturbation theory, a reference system of pure solvent (system A) is compared with a system where a single molecule (or complex), which is treated as a perturbation, is solvated (system B). To avoid numerical instabilities, the introduction of the solute molecule is carried out in multiple steps, involving *k* intermediate (virtual) states between systems A and B introduced by a coupling parameter λ_i ($0 \leq \lambda_i \leq 1$), rather than a single step. It should be stressed that the intermediate steps do not correspond to a physically realizable state. A schematic overview of the gradual perturbation of the reference system towards the perturbed system is given in Figure 2.11.

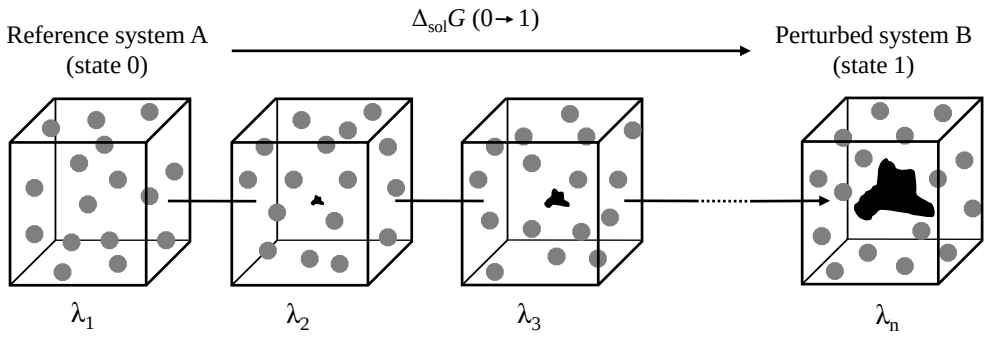

Figure 2.11: Schematic overview for the calculation of $\Delta_{sol}G$ by gradual perturbation of the reference system. [22]

The change in free energy of solvation is then written as the sum of all intermediate energy differences:

$$\Delta_{sol}G = \sum_{i=1}^{k-1} \Delta_{sol}G(\lambda_i \rightarrow \lambda_{i+1}) = -k_B T \sum_{i=1}^{k-1} ln\langle e^{-\frac{H_{\lambda_{i+1}} - H_{\lambda_i}}{k_B T}} \rangle \qquad (2.31)$$

where the angle brackets indicate averaging over the ensemble and H is the Hamiltonian describing the unperturbed (λ_i) and perturbed (λ_{i+1}) systems. In order to obtain free energy values, the calculations are performed in the isothermal-isobaric (NPT) ensemble, where the volume of the system is evaluated every 250 steps. The calculations are done using the binary approximation, in which the interaction potential between any two species is assumed not to be affected by the presence of other species in their proximity. Because of the nature of noble gases, the solvent-solvent interactions are described adequately within this approximation by Lennard-Jones potentials, accounting for long-range dispersion and short range exchange repulsion. Solute-solvent interactions are described by two contributions, the first obtained by using a Lennard-Jones potential between each solvent atom and each atom in the solute molecule, while the second accounts for the polarization of the solvent atoms by the solute, as mentioned previously. This contribution is calculated in a non-iterative first-order approximation as

$$E_{pol} = -\frac{1}{2}\vec{\mu}_{ind}.\vec{E} = -\frac{1}{2}\alpha_{solvent}(\vec{E}.\vec{E}) \qquad (2.32)$$

in which $\alpha_{solvent}$ is the polarizability of the noble gas and $\vec{E}$ is the electric field generated by the solute. To simulate the electric field created by the solute, charges based on the electrostatic potential using a grid based method (CHELPG) are placed on the solute atoms. The ε and σ parameters for the Lennard–Jones potentials are taken from the OPLS (Optimized Potentials for Liquid Simulation) all-atom force field, which can be altered for interactions between two different atoms *i* and *j* using the mixing rules

$$\varepsilon_{ij} = \sqrt{\varepsilon_{ii}\varepsilon_{jj}} \tag{2.33}$$

and

$$\sigma_{ij} = \frac{1}{2}\left(\sigma_{ii} + \sigma_{jj}\right) \tag{2.34}$$

Using this procedure, the free energy of solvation $\Delta_{sol}G$ for the monomers and complexes is calculated at different temperatures, varying between 88 K and 128 K for solutions in LAr, 118 K and 170 K for solutions in LKr and 168 K and 223 K for solutions in LXe at a pressure of 28 bar. The free energy is then decomposed in an enthalpy and entropy contribution by using the expressions

$$\Delta_{sol}G = \Delta_{sol}H - T\Delta_{sol}S \tag{2.35}$$

and

$$\left(\frac{\partial \Delta_{sol}G}{\partial T}\right)_p = -\Delta_{sol}S \tag{2.36}$$

from which the values of $\Delta_{sol}H$ and $\Delta_{sol}S$ are then obtained from the intercept and the slope, respectively, of a linear regression of the plot of free energies at different temperatures.

2.2.5 Noncovalent interactions index: NCI-Plot

For many years, the computational characterization of covalent and noncovalent interactions has been based on theories like the Atoms in Molecules (AIM) theory of R.F.W. Bader. [23] Within this theory, minima and maxima in the electron density $\rho(\vec{r})$, called critical points, are used as indicators for interactions. These critical points are further classified based on the second derivatives (curvatures) of the density at these points. Local maxima in the electron density, associated with the presence of nuclei, have three negative curvatures and are indicated with a (3,-3) critical point. Here, the first number between the parentheses indicates the evaluation of three curvatures (as expected in a three dimensional space), while the second number is the sum of the number of positive curvatures minus the number of negative curvatures. When one of the three curvatures in a critical point is positive, a (3,-1) *bond critical point* is found. Two or even three positive curvatures in a 3D space are associated with (repulsive) (3,1) *ring critical points* and (3,3) *cage critical points*.

The limitations of this theory for the study of noncovalent interactions lies in the fact that only points where the electron density gradient is exactly zero are detected. As the density accumulation associated with noncovalent interactions is typically a lot smaller than that of covalent interactions the charge density of these interactions might not have a location where the gradient is exactly zero and will thus not be detected in the Atoms in Molecules theory.

Therefore a new approach was developed to visualize noncovalent interactions, based on the analysis of the electron density and its reduced gradient $s(\vec{r})$, which highlights interactions in the low-density regime, i.e. noncovalent interactions. The reduced gradient, which is based on the electron density ρ is calculated as

$$s = \frac{1}{2(3\pi^2)^{1/3}} \frac{|\nabla\rho|}{\rho^{4/3}} \tag{2.37}$$

This reduced gradient can then be calculated for a grid of points surrounding the molecule(-s) of interest. The noncovalent interactions (NCI) index is based on a two-

dimensional plot of this reduced gradient and the electron density. In this $s(\rho)$ plot, troughs appear that are associated with density critical points. Furthermore, by multiplying the electron density with the sign of the second eigenvalue λ_2 of the electron density Hessian matrix $\nabla^2\rho = \lambda_1 + \lambda_2 + \lambda_3$ where $\lambda_1 < \lambda_2 < \lambda_3$ a distinction can be made between bonding interactions (associated with electron accumulation in the region, so that $\lambda_2 < 0$) and nonbonding interactions (electron depletion, $\lambda_2 > 0$). It should, however, be noted that for the very weak noncovalent interactions that are studied within this thesis, the electron accumulation between the noncovalently bonded moieties is often very small, especially for secondary interactions, so that the sign of the second eigenvalue λ_2 is sometimes positive for interactions which are clearly bonding.

Using this reduced gradient, noncovalent interactions can also be visualized by plotting the points of the gradient isosurface, i.e. all points on a horizontal line in the two-dimensional plot, in the low electron density region in the three dimensional space of the calculated complex geometry (based on the grid of points mentioned above). To further aid correlation between the two-dimensional plot and the three-dimensional space, the isosurfaces are also coloured based on the value on the horizontal axis of the two-dimensional plot. Here, points with the lowest electron densities are coloured green, while points with higher densities are coloured blue or red, based on whether the sign of λ_2 is negative or positive, respectively.

An example of the plot of the reduced density gradient versus the electron density multiplied by the sign of the second Hessian eigenvalue and gradient isosurface is given in Figure 2.12.

Although this methodology has shown to also yield good results when using promolecular electron densities, for the small systems studied within this thesis the more exact MP2/aug-cc-pVDZ(-PP) densities were used as they carry only a small computational cost.

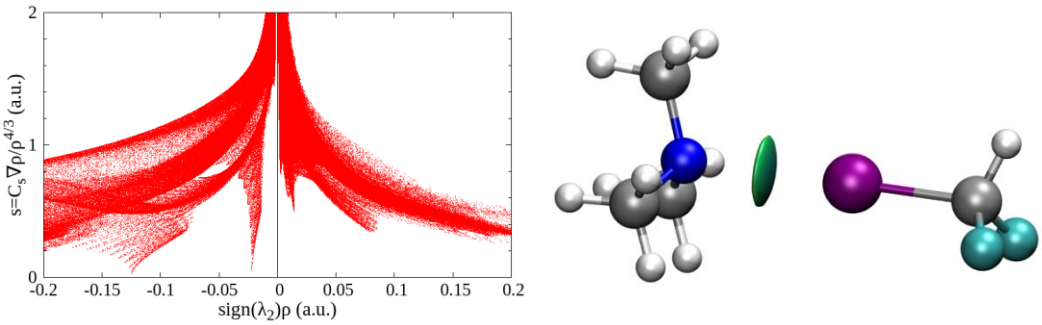

Figure 2.12: Plot of the reduced density gradient versus the electron density multiplied by the sign of the second Hessian eigenvalue (left) and gradient isosurfaces (s = 0.5 a.u., right) for the XB complex between CHF_2I and TMA.

2.2.6 Rationalizing results using a DFT energy decomposition analysis

To rationalize the tendencies of the complex strengths observed within and across the different studies, Ziegler-Rauk-type energy decomposition analyses (EDAs) [24-26] were performed on the MP2/aug-cc-pVDZ(-PP) optimized structures using the PBE functional [27-28] and TZ2P (small core) basis set, as implemented in ADF2013.01. [29] Relativistic effects were taken into account using the zeroth-order regular approximation (ZORA), [30-31] whereas the dispersion energy was calculated using Grimme's revised DFT-D method. [32] Using this methodology, the interaction energy (ΔE_{int}) between the monomers can be decomposed in the following contributions:

$$\Delta E_{int} = \Delta E_{Pauli} + \Delta V_{elst} + \Delta E_{oi} + E_{disp} \qquad (2.38)$$

where ΔE_{Pauli}, ΔV_{elst} and ΔE_{oi} are the Pauli repulsion, electrostatic interaction and orbital interaction energies between the monomers, respectively and E_{disp} is the dispersion energy. Here, ΔE_{Pauli} corresponds the repulsive filled-filled orbital interaction, which is the origin of the steric effect, [33] while ΔE_{oi} represents the stabilizing inter- and intrafragment occupied-vacant orbital mixing upon formation of the complex from the predefined fragments. The strain energy ΔE_{strain} is then calculated as the difference in energy between the monomers in their equilibrium geometry and the monomers in their geometry within the complex. As weak

noncovalent interactions are studied here, which cause only minor strain in the monomers involved, and MP2/aug-cc-pVDZ(-PP) optimized geometries are used, ΔE_{strain} values can be negative in some cases.

This particular EDA was chosen in this PhD thesis since it is rooted in Density Functional Theory and allows to decompose interactions into charge transfer and electrostatic components, in analogy with the perturbation expansions from conceptual DFT, [34-43] where the interaction energy between two chemical species is written as contributions from their changes in number of electrons and external potentials.

2.3 References

1 W. A. Herrebout, *Top. Curr. Chem.*, 2015, ***358***, 79-154.

2 C. N. Banwell, *Fundamentals of Molecular Spectroscopy*, third ed., McGraw-Hill Book Company, London, U.K., **1972**.

3 L. I. De Beuckeleer, *Master Thesis: N-H⋯π Interacties met Pyrrool: een Cryospectroscopisch Onderzoek*, University of Antwerp **2010**.

4 B. J. van der Veken, *J. Phys. Chem.*, 1996, ***100***, 17436-17438.

5 T. J. Balle, W. H. Flygare, *Rev. Sci. Instrum.*, 1981, ***52***, 33-45.

6 J. L. Alonso, F. J. Lorenzo, J. C. López, A. Lesarri, S. Mata, H. Dreizler, *Chem. Phys.*, 1997, ***218***, 267-275.

7 W. Caminati, A. Millemaggi, J. L. Alonso, A. Lesarri, J. C. López, S. Mata, *Chem. Phys. Lett.*, 2004, ***392***, 1-6.

8 G. G. Brown, B. C. Dian, K. O. Douglass, S. M. Geyer, S. T. Shipman, B. H. Pate, *Rev. Sci. Instrum.*, 2008, ***79***, 053103.

9 S. L. Stephens, N. R. Walker, *J. Mol. Spectrosc.*, 2010, ***263***, 27-33.

10 Q. Gou, G. Feng, L. Evangelisti, W. Caminati, *Angew. Chem. Int. Ed.*, 2013, ***52***, 11888-11891.

11 S. M. Bachrach, *Computational Organic Chemistry*, John Wiley & Sons, Inc., Hoboken, NJ, USA, **2007**.

12 J. B. Foresman, Æ. Frisch, *Exploring Chemistry with Electronic Structure Methods*, Third ed., Gaussian, Inc., Wallingford, CT, USA, **2015**.

13 M. J. Frisch, G. W. Trucks, H. B. Schlegel, G. E. Scuseria, M. A. Robb, J. R. Cheeseman, G. Scalmani, V. Barone, B. Mennucci, G. A. Petersson, H. Nakatsuji, M. Caricato, X. Li, H. P. Hratchian, A. F. Izmaylov, J. Bloino, G. Zheng, J. L. Sonnenberg, M. Hada, M. Ehara, K. Toyota, R. Fukuda, J. Hasegawa, M. Ishida, T. Nakajima, Y. Honda, O. Kitao, H. Nakai, T. Vreven, J. A. Montgomery, Jr., J. E. Peralta, F. Ogliaro, M. Bearpark, J. J. Heyd, E. Brothers, K. N. Kudin, V. N. Staroverov, R. Kobayashi, J. Normand, K.

Raghavachari, A. Rendell, J. C. Burant, S. S. Iyengar, J. Tomasi, M. Cossi, N. Rega, N. J. Millam, M. Klene, J. E. Knox, J. B. Cross, V. Bakken, C. Adamo, J. Jaramillo, R. Gomperts, R. E. Stratmann, O. Yazyev, A. J. Austin, R. Cammi, C. Pomelli, J. W. Ochterski, R. L. Martin, K. Morokuma, V. G. Zakrzewski, G. A. Voth, P. Salvador, J. J. Dannenberg, S. Dapprich, A. D. Daniels, Ö. Farkas, J. B. Foresman, J. V. Ortiz, J. Cioslowski, D. J. Fox, *Gaussian 09, Revision D.01*, Wallingford, CT, USA, 2009.

14 D. Feller, *J. Comput. Chem.*, 1996, ***17***, 1571-1586.

15 K. L. Schuchardt, B. T. Didier, T. Elsethagen, L. Sun, V. Gurumoorthi, J. Chase, J. Li, T. L. Windus, *J. Chem. Inf. Model.*, 2007, ***47***, 1045-1052.

16 S. F. Boys, F. Bernardi, *Mol. Phys.*, 1970, ***19***, 553-566.

17 H.-J. Werner, P. J. Knowles, G. Knizia, F. R. Manby, M. Schütz, P. Celani, T. Korona, R. Lindh, A. Mitrushenkov, G. Rauhut, K. R. Shamasundar, T. B. Adler, R. D. Amos, A. Bernhardsson, A. Berning, D. L. Cooper, M. J. O. Deegan, A. J. Dobbyn, F. Eckert, E. Goll, C. Hampel, A. Hesselmann, G. Hetzer, T. Hrenar, G. Jansen, C. Köppl, Y. Liu, A. W. Lloyd, R. A. Mata, A. J. May, S. J. McNicholas, W. Meyer, M. E. Mura, A. Nicklass, D. O'Neill, P. Palmieri, D. Peng, K. Pflüger, R. Pitzer, M. Reiher, T. Shiozaki, H. Stoll, A. J. Stone, R. Tarroni, T. Thorsteinsson, M. Wang, *MOLPRO, version 2012.1, A Package of Ab Initio Programs*, 2012.

18 D. G. Truhlar, *Chem. Phys. Lett.*, 1998, ***294***, 45-48.

19 P. Jurečka, P. Hobza, *J. Am. Chem. Soc.*, 2003, ***125***, 15608-15613.

20 P. Jurečka, P. Hobza, *Chem. Phys. Lett.*, 2002, ***365***, 89-94.

21 W. L. Jorgensen, *BOSS - Biochemical and Organic Simulation System*, John Wiley & Sons Ltd., New York, NY, USA, **1998**.

22 L. I. De Beuckeleer, *PhD Thesis: Exploring the Boundaries of Cryospectroscopy: A New Approach towards Separating Monomer and Complex Spectra*, **2016**.

23 R. F. W. Bader, *Atoms in Molecules - A Quantum Theory*, Oxford University Press, Oxford, U.K., **1990**.

24 F. M. Bickelhaupt, E. J. Baerends, *Rev. Comput. Chem.*, 2000, ***15***, 1-86.

25 T. Ziegler, A. Rauk, *Theor. Chim. Acta*, 1977, ***46***, 1-10.

26 B. Pinter, N. Nagels, W. A. Herrebout, F. De Proft, *Chem. - Eur. J.*, 2013, ***19***, 519-530.

27 J. P. Perdew, K. Burke, M. Ernzerhof, *Phys. Rev. Lett.*, 1996, ***77***, 3865-3868.

28 J. P. Perdew, K. Burke, M. Ernzerhof, *Phys. Rev. Lett.*, 1997, ***78***, 1396-1396.

29 E. J. Baerends, J. Autschbach, D. Bashford, A. Børces, F. M. Bickelhaupt, C. Bo, P. M. Boerrigter, L. Cavallo, D. P. Chong, L. Deng, R. M. Dickson, D. E. Ellis, M. van Faassen, M. Fan, T. H. Fischer, C. Fonseca Guerra, A. Ghysels, A. Giammona, S. J. A. van Gisbergen, A. W. Gotz, J. A. Groeneveld, O. V. Gritsenko, M. Grüning, F. E. Harris, P. Harris, P. van den Hoek, C. R. Jacob, H. Jacobsen, L. Jensen, G. van Kessel, F. Kootstra, M. V. Krykunov, E. van Lenthe, D. A. McCormack, A. Michalak, M. Mitoraj, J. Neugebauer, V. P. Nicu, L. Noodleman, V. P. O. Osinga, S. Patchkovskii, P. H. T. Philipsen, D. Post, C. C. Pye, W. Ravenek, J. I. Rodriguez, P. Ros, P. R. T. Schipper, G. Schreckenbach, M. Seth, J. G. Snijders, M. Solà, M. Swart, D. Swerhone, G. te

Velde, P. Vernooijs, L. Versluis, L. Visscher, O. Visser, F. Wang, T. A. Wesolowski, E. M. van Wezenbeek, G. Wiesenekker, S. K. Wolff, T. K. Woo, Y. A. L., T. Ziegler, *ADF2013.01*, Amsterdam (The Netherlands), 2013.
30 E. van Lenthe, R. van Leeuwen, E. J. Baerends, J. G. Snijders, *Int. J. Quant. Chem.*, 1996, ***57***, 281-293.
31 E. van Lenthe, E. J. Baerends, J. G. Snijders, *J. Chem. Phys.*, 1993, ***99***, 4597-4610.
32 S. Grimme, J. Antony, S. Ehrlich, H. Krieg, *J. Chem. Phys.*, 2010, ***132***, 154104.
33 B. Pinter, T. Fievez, F. M. Bickelhaupt, P. Geerlings, F. De Proft, *Phys. Chem. Chem. Phys.*, 2012, ***14***, 9846-9854.
34 R. G. Parr, W. Yang, *Density-Functional Theory of Atoms and Molecules*, Oxford University Press, Oxford, U.K., **1989**.
35 R. G. Parr, W. Yang, *Annu. Rev. Phys. Chem.*, 1995, ***46***, 701-728.
36 W. Kohn, A. D. Becke, R. G. Parr, *J. Phys. Chem.*, 1996, ***100***, 12974-12980.
37 H. Chermette, *J. Comput. Chem.*, 1999, ***20***, 129-154.
38 P. Geerlings, F. De Proft, W. Langenaeker, *Adv. Quantum Chem.*, 1998, ***33***, 303-328.
39 P. Geerlings, F. De Proft, W. Langenaeker, *Chem. Rev.*, 2003, ***103***, 1793-1874.
40 P. W. Ayers, J. S. M. Anderson, L. J. Bartolotti, *Int. J. Quantum Chem.*, 2005, ***101***, 520-534.
41 J. L. Gázquez, *J. Mex. Chem. Soc.*, 2008, ***52***, 3-10.
42 P. Geerlings, F. De Proft, *Phys. Chem. Chem. Phys.*, 2008, ***10***, 3028-3042.
43 S. B. Liu, *Acta Phys.-Chim. Sin.*, 2009, ***25***, 590-600.

The difference between the impossible and the possible is merely a measure of man's determination.

– Captain James Thain

Chapter 3

Can halogen bonds compete or coexist with hydrogen bonds?

Complexes of CHF_2I with TMA, DME and CH_3F.

The results in this chapter have been published as:

Nagels, N.; Geboes, Y.; Pinter, B.; De Proft, F.; Herrebout, W. A., Tuning the Halogen/Hydrogen Bond Competition: A Spectroscopic and Conceptual DFT Study of Some Model Complexes Involving CHF_2I, *Chemistry - A European Journal* **2014**, *20*, 8433-8443.

Abstract

Insight into the key factors driving the competition of halogen and hydrogen bonds is obtained by studying the affinity of the Lewis bases TMA, DME and CH_3F towards CHF_2I. Analysis of the IR and Raman spectra of solutions in LKr containing mixtures of TMA and CHF_2I and of DME and CHF_2I reveals that for these Lewis bases HB and XB complexes appear simultaneously. In contrast, only a HB complex is formed for the mixtures of CHF_2I and CH_3F. The complexation enthalpies for the C-H···Y HB complexes with TMA, DME and CH_3F are determined to be -14.7(2), -10.5(5) and -5.1(6) kJ mol^{-1}, respectively. The values for the C-I···Y XB isomers are -19.0(3) kJ mol^{-1} for TMA and -11.5(6) kJ mol^{-1} for DME. Generalization of the observed trends suggests that, at least for the bases studied here, softer Lewis bases such as TMA favour halogen bonding, while harder bases such as CH_3F show a substantial preference for hydrogen bonding.

3.1 Introduction

Due to the growing awareness of its useful applications in the fields of supramolecular chemistry, [1-3] crystal engineering, [4-7] biochemistry [8-11] and drug design, [12-15] the noncovalent interaction of a covalently bonded halogen atom and an electron rich region in a Lewis base, also known as halogen bonding, has recently gained a tremendous increase of interest. Also, similarities and differences of the fundamental intrinsic properties of halogen and hydrogen bonds have been extensively studied theoretically. [16-31] Although some co-crystallization experiments, combined with X-ray diffraction [32-34], NMR [35] and IR studies [35] have been published, experimental data on the competition, [36-42] cooperation [9] and coexistence [32, 35, 43] between halogen and hydrogen bonds still remains scarce. Even though observed simultaneously in crystals, it is thus still unclear whether isolated halogen bonds can indeed compete with or prevail over equivalent hydrogen bonds in a thermodynamically stable liquid system. In this experimentally driven study, we provide fundamental thermodynamical data on the coexistence and competition of these two types of noncovalent interactions under chemical equilibrium conditions by an IR and Raman study of mixtures containing a mixed HB/XB donor molecule and different Lewis bases. To this end, mixtures of the Lewis bases TMA, DME and CH_3F with CHF_2I, dissolved in LKr have been studied. The choice of the model compounds was based on earlier observations showing that different Lewis bases including TMA, DME, and CH_3F form weak to moderately strong HB complexes with typical C-H proton donors such as fluoroform (CHF_3) [44-48], chlorodifluoromethane (CHF_2Cl) [47-52] and halothane ($CHClBrCF_3$) [53] and, at the same time, give rise to relatively strong C-I···Y XB complexes with perfluorinated iodine containing hydrocarbons such as CF_3I. [54-59]

The experimental study, which is supported by *ab initio* calculations, MC-FEP simulations and statistical thermodynamics, reveals that for the Lewis bases TMA and DME HB and XB complexes with CHF_2I are formed simultaneously, while for CH_3F only the HB complex is present. Inspection of the experimental complexation enthalpies of the HB and the XB complexes suggests that, for the bases studied here,

the competition between hydrogen and halogen bonding is dominated by the chemical hardness of the Lewis base.

3.2 Results

3.2.1 *Ab initio* calculations

The MP2/aug-cc-pVDZ-PP geometries for the XB and HB complexes of CHF_2I with TMA, DME and CH_3F are shown in Figure 3.1, while Cartesian coordinates of all monomers and complexes are given in Tables S3.1 and S3.2 of the SI at the end of this chapter. The intermolecular parameters and energetics for all complexes are summarized in Table 3.1. For the HB complex with CH_3F, the calculations lead to two different, energetically very similar, geometries involving a $C(F_2I)$-H⋯F hydrogen bond and a secondary interaction between either the fluorine or iodine atom of CHF_2I and a hydrogen atom of CH_3F. The occurrence of secondary interactions for the HB complexes, and the lack of such interactions in the XB complexes is in line with previous reports [60] and can be ascribed to the lack of linearity of the HB complexes as compared with the XB complexes, which can clearly be seen in Table 3.1. Whereas the XB complexes exhibit a nearly linear geometry, with $\varphi_{C\text{-}I\cdots Y}$ between 179.5° and 172.4°, the HB complexes deviate from this linear geometry, with bonding angles between 164.4° and 126.7°.

The data also shows that for both the aug-cc-pVDZ-PP and CCSD(T)/CBS extrapolated calculations, the XB complex with TMA is calculated to be intrinsically stronger than the HB isomer, while for DME and CH_3F an opposite trend is predicted. The harmonic vibrational frequencies and IR intensities for the monomers and for the different complexes with TMA, DME and CH_3F, as well as their fully deuterated counterparts, typically used to avoid overlap of monomer and complex bands related to the acceptor and the donor molecules, are summarized in Tables S3.3 to S3.9.

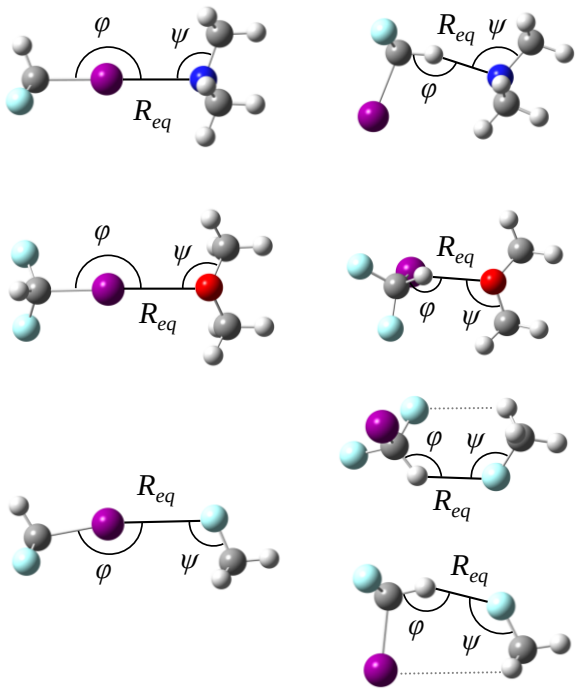

Figure 3.1: *Ab initio* calculated MP2/aug-cc-pVDZ-PP geometries for the XB (left) and HB (right) complexes of CHF_2I with TMA (top), DME (middle) and CH_3F (bottom). For CH_3F, the HB complex with a secondary C-H···F interaction is shown on the top, while the HB complex with a secondary C-H···I interaction is shown in the bottom. Both secondary interactions are indicated by a grey dotted line.

It is worth mentioning that the two types of complexes can be detected and assigned individually in the vibrational spectra only if the species are formed during a longer timeframe, the minimum required life time at 150 K being in the order of several tenths of picoseconds. [61] This implies that rapid interconversion or tunnelling from one minimum to another should be avoided. To shed light on the different aspects related to a possible tunnelling motion, for all Lewis bases studied the transition state between both isomers was searched for using the Synchronous Transit-Guided Quasi-Newton method. [62-63] The geometries derived for the complexes with TMA and DME, and the energy profiles derived are shown in Figure S3.1. It can be seen that for both bases, the transition state is characterized by a complexation energy close to 5 kJ mol^{-1}, while the values for the HB and the XB complexes are much larger. From this, it can safely be assumed that little or no tunnelling between the HB and the XB isomers of TMA and

DME will occur in the (cryo-)solutions. For the complexes formed with CH_3F, various geometry optimizations were attempted using different initial guesses for the transition state searched, but no first order saddle point could be found.

Table 3.1: Intermolecular distance R_{eq} (Å), bond angles (°), MP2/aug-cc-pVDZ-PP ΔE(DZ) and CCSD(T)/CBS ΔE(CCSD(T)) extrapolated complexation energies, calculated vapour phase complexation enthalpies $\Delta H°$ (vap,calc), the calculated complexation enthalpies in liquid krypton ($\Delta H°$ (LKr,calc)) and the corresponding experimentally obtained complexation enthalpies ($\Delta H°$ (LKr)) (kJ mol^{-1}) for the complexes of CHF_2I with TMA, DME and CH_3F. (X = H, I; Y = F, O, N)

	TMA		DME		CH_3F		
	XB	HB	XB	HB	XB	HB (F)[b]	HB (I)[c]
$R_{eq}=R_{X\cdots Y}$ [a]	2.93	2.21	3.04	2.24	3.20	2.35	2.25
$\varphi_{C\text{-}X\cdots Y}$ [a]	179.5	164.4	176.2	140.7	172.4	126.7	153.2
$\psi_{C\text{-}Y\cdots X}$ [a]	109.2/108.3/108.3	112.0/107.6/107.6	108.7/108.7	121.5/111.1	110.0	122.8	130.0
ΔE (DZ)	-28.3	-24.6	-17.1	-19.9	-8.7	-13.0	-12.6
ΔE (CCSD(T))	-28.0	-25.3	-17.8	-21.4	-9.7	-14.3	-13.5
$\Delta H°$ (vap,calc)	-26.4	-22.5	-15.3	-18.6	-7.4	-11.7	-10.8
$\Delta H°$ (LKr,calc)	-23.4	-16.6	-12.4	-12.0	-6.5	-7.8	-8.0
Experimental $\Delta H°$ (LKr)	-19.0(3)	-14.7(2)	-11.5(6)	-10.5(5)		-5.1(6)	

[a] X = I, H, Y = F, O, N
[b] HB (F): HB complex with secondary C-H···F interaction.
[c] HB (I): HB complex with secondary C-H···I interaction.

3.2.2 Infrared and Raman measurements

The vibrational spectra of TMA($-d_9$), DME($-d_6$), $CH_3F(-d_3)$ dissolved in liquid rare gases, have been reported before. [53-56, 64-65] The characteristic frequencies for CHF_2I in LKr and their assignments based on the MP2/aug-cc-pVDZ-PP frequencies are included in Tables 3.2-3.4. It is worth noting that, apart from the ν_1 C-H stretching mode at 3003 cm^{-1}, a weak shoulder is observed near 2994 cm^{-1}. This band most plausibly corresponds to a Fermi resonance between the ν_1 fundamental and the $\nu_5 + \nu_7 + \nu_8$ combination band and is assigned accordingly.

To characterize the XB and/or HB complexes of CHF_2I with TMA($-d_9$), DME($-d_6$) and $CH_3F(-d_3)$, IR and Raman spectra of solutions in LKr, containing mixtures of the donor and acceptor molecules were recorded, at temperatures between 120 and 156 K. For the IR measurements, the mole fractions for CHF_2I and the Lewis bases were typically varied between 1.9×10^{-5} and 9.4×10^{-3} and between 9.4×10^{-5} and 5.6×10^{-3}. The Raman spectra were recorded with mole fractions varying between 1.4×10^{-3} and 8.5×10^{-3} for CHF_2I and between 2.4×10^{-3} and 7.1×10^{-3} for the Lewis bases. The frequencies, assignments and complexation shifts derived are summarized in Tables 3.2 (TMA), 3.3 (DME) and 3.4 (CH_3F). The frequencies for the C-H stretching region of CHF_2I were obtained using the fully deuterated isotopomers.

Comparison of the spectral data calculated for the HB and XB complexes, summarized in Tables S3.3 to S3.9, reveals that complexation shifts with a substantial difference between the envisaged types of complexes are predicted for both the C-H stretching mode ν_1 and the C-I stretching mode ν_4 of CHF_2I. These vibrations were considered excellent candidates to experimentally distinguish between the two types of complexes formed in the solutions. As a consequence, during the analysis of the spectral data, special attention was paid to these regions in IR and Raman.

The C-H stretching region for the IR spectra of mixed solutions containing CHF_2I and TMA-d_9, DME-d_6 or CD_3F are shown in panels A, B and C of Figure 3.2.

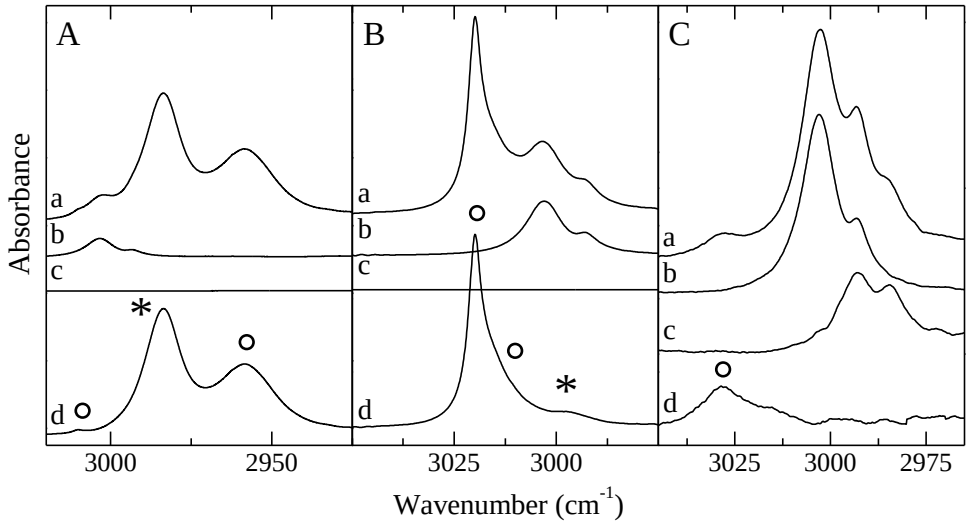

Figure 3.2: Infrared spectra of the C-H stretching region for solutions in LKr, at 120 K, obtained for mixtures of CHF_2I with TMA-d_9 (panel A), DME-d_6 (panel B) and CD_3F (panel C). In each panel trace *a* represents the mixed solution, while traces *b* and *c* show the solution containing only CHF_2I and the Lewis base, respectively. Trace *d* is obtained by subtracting the rescaled monomer in traces *b* and *c* from the mixture trace *a*. Bands due to the XB or HB complexes observed in traces *d* are marked with an asterisk (*) or open circle (°), respectively.

Inspection of the spectral data in panel 3.2A shows that, apart from the absorptions due to the ν_1 and $\nu_7 + \nu_8 + \nu_9$ monomer bands, two intense, well separated absorptions appear near 2984 and 2960 cm^{-1}. Inspection of the integrated band areas obtained during isothermal concentration studies in which spectra of solutions containing a variety of monomer concentrations are studied shows that the relative intensity of both bands is not affected by changes in the relative monomer concentrations. Both bands should, therefore, be correlated with molecular complexes having at least the same stoichiometry. Further evidence allowing the assignment of the spectral features was obtained from temperature studies in which spectra of solutions were recorded at different temperatures, and in which the relative intensities of the observed complex bands were studied. These studies showed that the relative intensity of the 2983.9 and 2959.7 cm^{-1} bands is strongly affected by temperature. These bands must, therefore, be assigned to two different complexes having the same stoichiometry but a different relative stability. This result, obviously, supports the idea of the simultaneous

formation of XB and HB complexes. The small blueshifted complex band at 3010.2 cm^{-1} is assigned to the HB complex for the $\nu_5 + \nu_7 + \nu_8$ combination band.

Further evidence allowing the identification of the 2983.9 and 2959.7 cm^{-1} bands was obtained by comparing the observed and calculated complexation shifts, the latter values being -18.7 cm^{-1} for the XB complex and -80.0 cm^{-1} for the HB complex. The first value agrees excellently with the experimental value of -19.4 cm^{-1} observed for the 2983.9 cm^{-1} band and allows this band to be assigned to the XB complex. The second value is significantly larger than the experimental value of -43.6 cm^{-1} observed for the 2959.7 cm^{-1} band. However, taking into account the relative position of both bands and considering the fact that the predicted complexation shifts of C-H···Y HB complexes are often largely overestimated due to changes in anharmonicity, [46-47, 66] this band can safely be assigned to the C-H···N bonded complex.

Before moving on to the description of the C-H stretching regions observed for the solutions containing DME or CH_3F, it is of interest to note that, although the two bands have similar IR intensities, this does not immediately imply that both complexes are present in a similar concentration. Inspection of the calculated intensities indeed shows that, upon complexation, the IR intensity in the XB complex is only slightly increased by a factor of 3, while the IR intensity of the same mode in the HB complex increases by a factor close to 30. In view of these results, it might therefore be realistic that the equilibrium concentration of the XB complex is significantly larger than that of the HB complex. As the Raman scattering activities, given in Tables S3.3 and S3.4, are only slightly influenced upon complexation with TMA, experimental evidence for a significantly larger concentration of the XB complex can be obtained using from Raman spectroscopy. Therefore, Raman spectra of solutions containing similar concentrations of the monomers as the IR spectra shown in Figure 3.2A were obtained. These Raman spectra, shown in Figure 3.3, reveal that, apart from the monomer transition and the intense band assigned to the XB complex, only a relatively weak band due to the HB complex is observed, thus yielding experimental evidence for a significantly larger concentration of the XB complex.

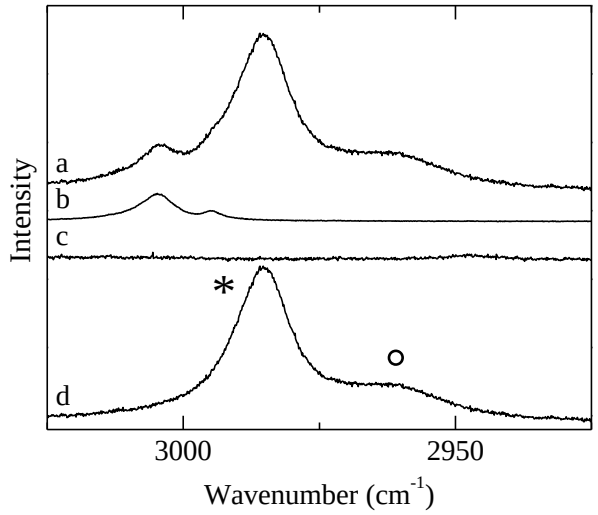

Figure 3.3: Raman spectra for the C-H stretching region obtained for solutions in LKr solutions, at 120 K, containing mixtures of CHF_2I and TMA-d_9. Trace a shows the spectrum of the mixed solution, while traces *b* and *c* refer to the solutions containing only CHF_2I or TMA-d_9, respectively. Trace *d* is obtained by subtracting the rescaled monomer traces *b* and *c* from trace *a*. Bands appearing in trace *d* are assigned to the XB or HB complexes and are marked with an asterisk (*) or open circle (°), respectively.

Further experimental evidence supporting the observation of a larger equilibrium concentration of the XB complexes was obtained by analysing the data obtained for ν_4 spectral region of CHF_2I, shown in Figure 3.4. Inspection of trace *d* in panel 3.4A reveals that for the mixture with TMA, a single, slightly asymmetric band is observed near 630.5 cm^{-1}, i.e. at a frequency redshifted from the monomer transition by -3.1 cm^{-1}. In agreement with the suggestions above, as well as the calculated shifts of -4.8 and -0.6 cm^{-1} and the predicted infrared intensities of 0.5 and 1.1 km mol^{-1} for the XB and HB complexes, this band is assigned primarily to the ν_4 mode of the XB complex. The weak asymmetry showing a tailing toward higher frequencies and smaller complexation shifts can, on the other hand, be interpreted as evidence for the presence of some HB complex.

Table 3.2: Experimental vibrational frequencies and complexation shifts, in cm^{-1}, for the XB and HB complexes of CHF_2I with TMA dissolved in LKr at 130 K. The *ab initio* complexation shifts are derived from the MP2/aug-cc-pVDZ-PP harmonic vibrational frequencies.

Assignment		$\nu_{monomer}$	$\nu_{complex,XB}$	$\Delta\nu_{exp,XB}$	$\Delta\nu_{calc,XB}$	$\nu_{complex,HB}$	$\Delta\nu_{exp,HB}$	$\Delta\nu_{calc,HB}$
CHF_2I	ν_1	3003.3	2983.9 [a]	-19.4	-18.7	2959.7 [a]	-43.6	-80.0
	$\nu_5+\nu_7+\nu_8$	2993.9	-		-36.8	3010.2 [a]	16.3	50.4
	ν_7	1337.2	1335.1	-2.1	-2.9	-		61.7
	ν_2	1247.6	1247.7	0.1	0.6	1268.9	21.3	40.7
	ν_8	1107.6	1079.7	-27.9	-26.8	1096.6	-11.0	-11.4
	ν_3	1077.1	1069.0	-8.1	-7.7	1069.0	-8.1	-11.0
	ν_4	633.6	630.5	-3.1	-4.8	630.5	-3.1	-0.6
	ν_5	567.8	561.7	-6.1	-7.4	567.2	-0.6	0.2
	ν_9	268.8	269.7	0.9	3.9	265.0	-3.8	-1.9
	ν_6	268.8	265.0	-3.8	-5.0	265.0	-3.8	-4.7
TMA	ν_{12}	2976.7	2980.8	4.1	2.9	2980.8	4.1	0.9
	ν_1	2944.2	2947.5	3.3	5.5	2947.5	3.3	2.9
	ν_{13}	2944.2	2947.5	3.3	5.6	2947.5	3.3	3.0
	$2\nu_4$	2818.3	-		-0.3	-		2.4
	ν_2	2768.6	-		23.1	-		16.6
	ν_{14}	2768.6	-		25.5	-		19.0
	$\nu_{20}+\nu_{21}$	1474.7	1472.1	-2.6	-6.3	1472.1	-2.6	-6.8
	ν_{15}	1467.5	1467.9	0.4	0.0	1467.9	0.4	1.2
	ν_3	1454.8	1452.3	-2.5	0.3	1452.3	-2.5	1.9
	ν_4	1438.8	1439.9	1.1	-0.1	1439.9	1.1	1.2
	ν_{16}	1438.8	1439.9	1.1	-1.2	1439.9	1.1	0.7
	ν_{17}	1405.2	-		0.7	-		1.4
	ν_{18}	1273.2	1268.9	-4.3	-2.1	1268.9	-4.3	-5.2
	ν_5	1184.1	1193.6	9.5	9.1	1193.6	9.5	8.4
	ν_{19}	1098.5	1096.6	-1.9	-1.9	1096.6	-1.9	-0.6
	ν_{20}	1041.4	1036.7	-4.7	-3.9	1036.7	-4.7	-4.6
	ν_6	827.9	824.4	-3.5	-6.6	824.4	-3.5	-4.2
	ν_{21}	424.0	422.7	-1.3	-2.4	422.7	-1.3	-2.3
	ν_7	372.3	392.6	20.3	18.8	392.6	20.3	17.0

[a] Complex bands derived by studying mixed solutions of CHF_2I and TMA-d_9 in LKr, at 130 K.

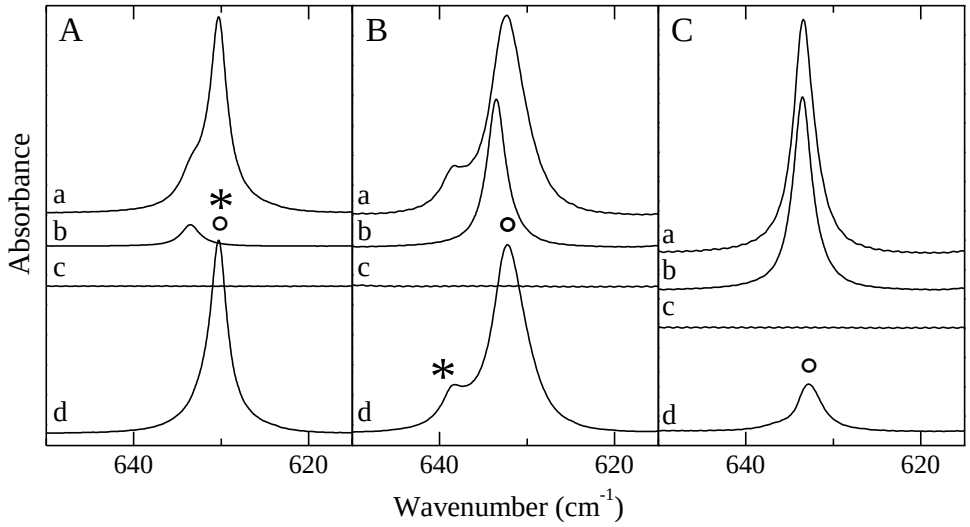

Figure 3.4: Infrared spectra for the ν_4 region of CHF_2I obtained for solutions in LKr solutions, at 120 K, containing mixtures of CHF_2I with TMA (panel A), DME-d_6 (panel B) and CH_3F (panel C). In each panel the trace *a* shows the spectrum of the mixed solution, while traces b and c refer to the solutions containing only CHF_2I or the Lewis base, respectively. Trace *d* is obtained by subtracting the rescaled monomers, traces *b* and *c*, from trace *a*. Bands appearing in trace *d* are assigned to the XB or HB complexes and are marked with an asterisk (*) or open circle (°), respectively.

Another spectral region of interest is found for the C-F stretches of CHF_2I, which is shown in Figure 3.5 for the mixtures involving TMA-d_9. Upon subtraction, the presence of four complex bands is revealed in this spectral region, of which the band with the lowest frequency can be assigned to the ν_4 and ν_{16} modes of TMA-d_9 by comparison with the spectra of the undeuterated TMA. The remaining three bands, which are present in the spectra of mixtures with TMA and TMA-d_9, can thus be ascribed to the C-F stretching vibrations of CHF_2I. For both the asymmetric C-F stretch ν_8 and the symmetric C-F stretch ν_3, sizeable redshifts are predicted, as shown in Tables S3.3 and S3.4 of the SI. Inspection of the spectrum shows that two of the complex bands are blueshifted compared to the ν_3 vibrational mode and are could therefore be assigned to the ν_8 vibrational mode, which lies at a higher frequency. When assigning these bands to the ν_8 mode in the complexes, the experimental shifts of -10.6 and -28.1 cm^{-1} are in excellent agreement with the calculated shifts of -10.7 cm^{-1} for the HB complex and -26.5 cm^{-1} for the XB complex, thus further

demonstrating the simultaneous coexistence of both complex geometries in LKr solutions.

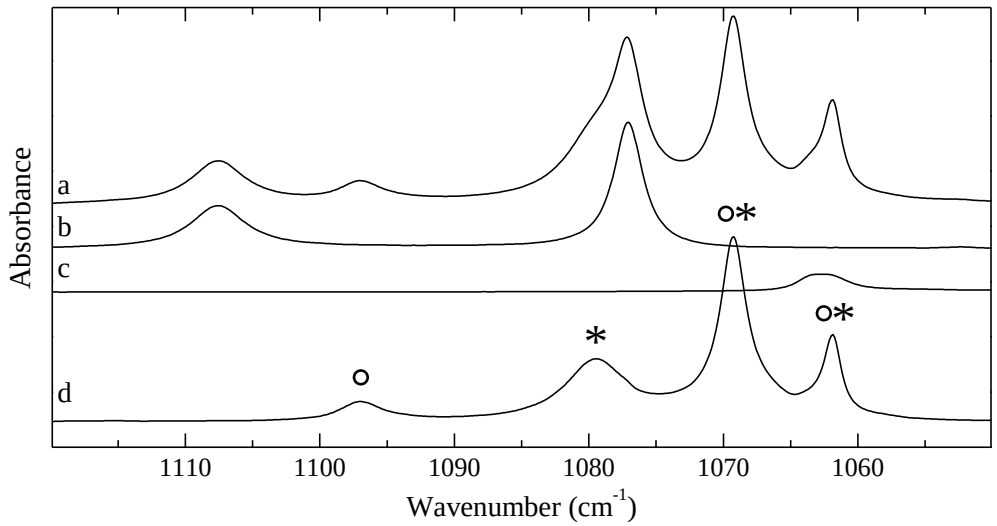

Figure 3.5: Infrared spectra for the C-F stretching region of CHF_2I obtained for solutions in LKr solutions, at 120 K. Trace *a* represents the mixed solution of CHF_2I and TMA-d_9, while traces *b* and *c* show the rescaled spectra of the solutions containing only CHF_2I or TMA-d_9, respectively. Trace *d* represents the spectrum of the complex which is obtained by subtracting the rescaled traces *b* and *c* from trace *a*. Bands appearing in trace *d* are assigned to the XB or HB complexes and are marked with an asterisk (*) or open circle (°), respectively.

For the complexes with DME, a blueshift of 14.3 cm^{-1} and redshift of -8.4 cm^{-1} is predicted for the C-H stretching fundamental in the HB and the XB complex. Similar, albeit significantly smaller, shifts showing a different sign for the HB and XB complex are also calculated for the ν_4 vibration. In agreement with the predictions, and with the idea that both complexes are formed simultaneously in the solutions, the subtraction procedures reveal that for both the ν_1 and the ν_4 spectral regions, two separate complex bands can be identified. Comparison of the data in panel 3.2B shows that for the C-H stretching mode, a relatively intense band is observed at 3017.5 cm^{-1}, i.e. at a frequency 13.9 cm^{-1} higher than that of the monomer. In addition, a weaker feature redshifted from the monomer transition by -6.7 cm^{-1} is observed at 2996.9 cm^{-1}. The observed shifts of these features are in good agreement with the predicted values for the HB and the XB isomers, making the assignment of these features straightforward.

Table 3.3: Experimental vibrational frequencies and complexation shifts, in cm^{-1}, for the XB and HB complexes of CHF_2I with DME dissolved in LKr at 120 K. The *ab initio* complexation shifts are derived from the MP2/aug-cc-pVDZ-PP harmonic vibrational frequencies.

Assignment		$\nu_{monomer}$	$\nu_{complex,XB}$	$\Delta\nu_{exp,XB}$	$\Delta\nu_{calc,XB}$	$\nu_{complex,HB}$	$\Delta\nu_{exp,HB}$	$\Delta\nu_{calc,HB}$
CHF_2I	ν_1	3003.6	2996.9 [a]	-6.7	-8.4	3017.5 [a]	13.9	14.3
	$\nu_5+\nu_7+\nu_8$	2993.3	-		-21.1	3009.2 [a]	15.9	18.5
	$\nu_3+\nu_8$	2170.7	2157.0	-13.7	-20.8	2157.0	-13.7	-13.0
	$2\nu_3$	2143.7	2130.8	-12.9	-9.0	2130.8	-12.9	-14.0
	ν_7	1337.3	1336.4	-0.9	-1.1	1340.5	3.2	23.9
	$2\nu_4$	1272.2	1278.9	6.7	8.5			-3.2
	ν_2	1247.6	1254.5	6.9	3.8	1247.2	-0.4	-0.1
	ν_8	1107.3	1090.7	-16.6	-16.3	1100.1	-7.2	-6.1
	ν_3	1077.1	1070.3	-6.8	-4.5	1070.3	-6.8	-7.0
	$\nu_3(^{13}C)$	1052.2	1046.1	-6.1	-4.5	1046.1	-6.1	-7.0
	ν_4	633.6	638.3	4.7	4.2	631.9	-1.7	-1.6
	ν_5	567.7	564.5	-3.2	-3.7	567.8	0.1	0.6
	ν_9	268.8	-		4.4	270.1	1.3	0.4
	ν_6	268.8	-		1.6	266.8	-2.0	-2.9
DME	ν_1	2990.2	2993.4	3.2	2.9	2993.4	3.2	0.5
	ν_{16}	2990.2	2993.4	3.2	2.9	2993.4	3.2	0.5
	$2\nu_3$	2950.4	2952.1	1.7	-4.4	2952.1	1.7	-3.0
	$\nu_3+\nu_{18}$	2932.9	2931.8	-1.1	-4.2	2931.8	-1.1	-2.7
	ν_{12}	2916.4	2921.0	4.6	14.6	2921.0	4.6	14.9
	$\nu_3+\nu_{19}$	2905.2	2906.9	1.7	-2.6	2906.9	1.7	-0.6
	$\nu_{18}+\nu_{19}$	2886.1	2882.6	-3.5	-2.4	2882.6	-3.5	-0.3
	$\nu_4+\nu_{19}$	2880.5	-		-1.0	2888.1	7.6	2.7
	ν_2	2811.6	2819.5	7.9	7.7	2819.5	7.9	8.1
	$\nu_6+\nu_{20}$	2092.6	2082.0	-10.6	-21.2	2082.0	-10.6	-16.8
	ν_{18}	1457.5	1458.4	0.9	-2.0	1458.4	0.9	-1.2
	ν_{13}	1454.6	1455.1	0.5	-0.5	1455.1	0.5	-0.7
	ν_{19}	1426.2	1428.4	2.2	-0.4	1428.4	2.2	0.9
	ν_5	1245.1	-		-0.1			2.0
	ν_{20}	1172.1	1167.5	-4.6	-9.3	1167.5	-4.6	-8.2
	ν_6	929.4	-		-11.9	922.8	-6.6	-8.7
	$\nu_6(^{13}C)$	918.7	-		-11.9	912.3	-6.4	-8.7

[a] Complex bands derived by studying mixed solutions of CHF_2I and DME-d_6 in LKr, at 120 K.

An important remark that has to be made here is the fact that, in contrast to the results obtained for TMA-d_9, only a very weak spectral feature due to the XB complex is observed for the mixtures involving DME-d_6. In view of the predicted IR intensities, it is therefore not unrealistic to assume that in the studied cryosolutions, the majority of the formed complex is of the HB type. One could also note that, apart from the bands reported above, a weak shoulder can be envisaged near 3009 cm^{-1}. In agreement with the predicted shifts for the constituent modes, given in Table 3.3, this feature is assigned to the $\nu_5 + \nu_7 + \nu_8$ combination in the HB complex.

Experimental evidence supporting the conclusion that in the cryosolutions containing DME and CHF_2I mainly HB complex is formed, is obtained from the ν_4 region. Comparison of the data in panel 3.4B indeed shows that careful scaling and subtraction of the monomer spectra reveals two complex bands. In agreement with the above assumption and with the predicted complexation shifts and IR intensities showing that the intensities for ν_4 are hardly perturbed during complexation, the intense band at 631.9 cm^{-1} is assigned to the HB complex while the weaker blue-shifted transition at 638.3 cm^{-1} is assigned to the XB isomer.

The general trend showing that for the softer Lewis base TMA the XB complex is preferred while for the harder DME the HB interaction takes over, motivates further extrapolation towards even harder Lewis bases such as CH_3F. The ν_1 and ν_4 regions for solutions containing CH_3F and CHF_2I are given in panels 3.2C and 3.4C, respectively. In agreement with the predictions showing that for CH_3F the HB complex is strongly preferred, experimental evidence was found for the HB complex only, the experimental shifts of for ν_1 and ν_4 being 24.5 and -1.2 cm^{-1} respectively. In contrast to the results obtained for TMA and DME, it must thus be concluded that under equilibrium conditions, little or no XB complexes are formed in the solutions. It is also of interest to note that although two different HB isomers were calculated for the complex with CH_3F, no experimental information allowing the identification of and discrimination between these isomers was obtained.

Table 3.4: Experimental vibrational frequencies and complexation shifts, in cm^{-1}, for the HB complex of CHF_2I with CH_3F dissolved in LKr at 120 K. The *ab initio* complexation shifts of the two conformers with secondary C-H···F (F) or C-H···I (I) interactions, are derived from the MP2/aug-cc-pVDZ-PP harmonic vibrational frequencies. For completeness, the MP2/aug-cc-pVDZ-PP complexation shifts of the XB complex ($\Delta\nu_{calc,XB}$) have been included.

	Assignment	$\nu_{monomer}$	$\nu_{complex}$	$\Delta\nu_{exp}$	$\Delta\nu_{calc,HB(F)}$	$\Delta\nu_{calc,HB(I)}$	$\Delta\nu_{calc,XB}$
CHF_2I	ν_1	3003.6	3028.1 [a]	24.5	28.8	31.2	-3.3
	$\nu_5 + \nu_7 + \nu_8$	2993.3	-		15.3	-4.4	-12.2
	$\nu_3 + \nu_8$	2170.7	2164.5	-6.2	-3.4	-8.5	-12.0
	$2\nu_3$	2143.7	2137.1	-6.6	-4.0	-11.0	-4.8
	ν_7	1337.3	-		15.3	-1.6	-0.8
	$2\nu_4$	1272.2	-		-4.2	-4.8	8.8
	ν_2	1247.6	1256.9	9.3	3.2	4.4	3.3
	ν_8	1107.3	1104.0	-3.3	-1.4	-3.0	-9.6
	ν_3	1077.1	1072.8	-4.3	-2.0	-5.5	-2.4
	$\nu_3(^{13}C)$	1052.2	-		-2.0	-5.5	-2.4
	ν_4	633.6	632.4	-1.2	-2.1	-2.4	4.4
	ν_5	567.7	568.0	0.3	1.4	0.2	-1.8
	$2\nu_6$	536.3	534.5	-1.8	-4.6	-2.8	4.2
	ν_9	268.8	269.9	1.1	-0.7	1.6	2.5
	ν_6	268.8	266.8	-2.0	-2.3	-1.4	2.1
CH_3F	ν_4	3000.9	-		11.4	10.1	7.1
	ν_1	2956.5	2959.8	3.3	6.5	5.5	3.5
	$2\nu_3$	2054.9	2024.5	-30.4	-39.0	-37.2	-31.2
	ν_5	1459.5	1449.2	-10.3	-3.2	-2.0	-2.1
	ν_2	1457.1	-		-0.6	-1.0	-1.4
	ν_6	1178.9	-		-1.4	-0.9	-1.4
	ν_3	1035.5	1020.3	-15.2	-19.5	-18.6	-15.6

[a] Complex bands derived by studying mixed solutions of CHF_2I and CD_3F in LKr, at 120 K.

3.2.3 Experimental complexation enthalpies

The standard complexation enthalpies for the observed complexes were obtained from temperature studies [67] in which the IR spectra of various mixed solutions were recorded at different temperatures, the temperature interval typically ranging from 120 to 156 K. Typical van 't Hoff plots obtained for the complexes studied are shown in Figure 3.6. The complexation enthalpies for the XB complexes, obtained by analysing and averaging out the data for a series of solutions, are -19.0(3) kJ mol^{-1} for TMA and -11.5(6) kJ mol^{-1} for DME. The complexation enthalpies for the HB complexes are -14.7(2) kJ mol^{-1} for TMA, -10.5(5) kJ mol^{-1} for DME and -5.1(6) kJ mol^{-1} for CH_3F.

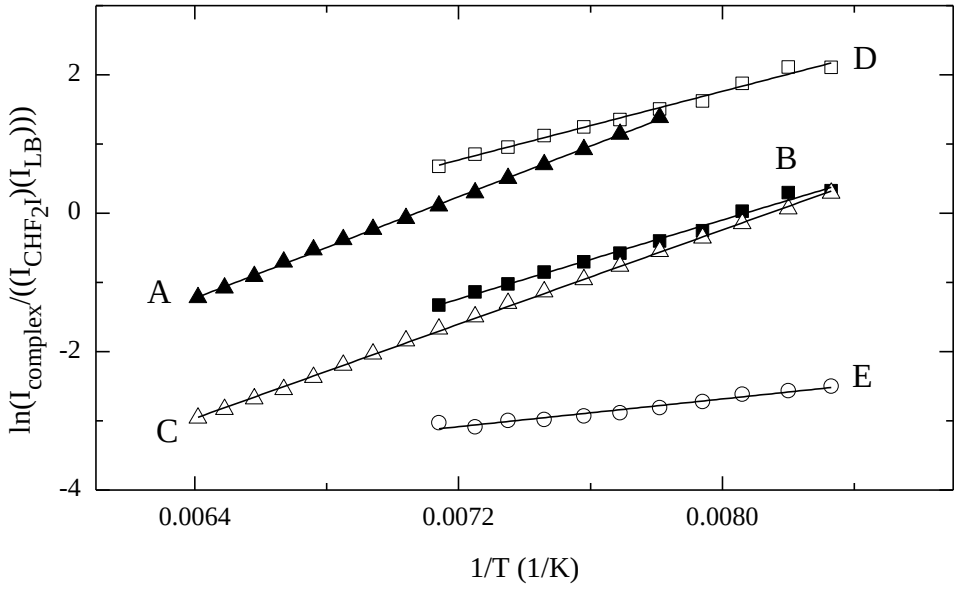

Figure 3.6: van 't Hoff plots for the XB complexes of CHF_2I with TMA (A) and DME (B) and for the HB complexes of CHF_2I with TMA (C), DME (D) and CH_3F (E). All data were obtained using LKr as a solvent.

3.3 Discussion

Comparison of the experimental and calculated complexation enthalpies shows that, in agreement with previous data, [54-56, 68] the predicted stabilities in solution are on average slightly overestimated. Nevertheless, the experimentally derived complexation enthalpies confirm the computed trend that the interactions with TMA are in general the strongest ones, while the complexes with CH_3F are the weakest. The experimental stabilities also clearly support the general trends deduced from the spectra, showing that for both TMA and DME, both HB and XB complexes are formed, albeit with a difference in the preference towards complex formation. The complexation enthalpies therefore support the general idea that the competition of HB and XB complexes can be tuned by changing the chemical hardness of the chosen Lewis base.

It is worth comparing the complexation enthalpies for the XB complexes obtained in this study with the previously reported data on the XB complexes $CF_3I{\cdot}TMA$ (-28.7(1) kJ mol^{-1}) and $CF_3I{\cdot}DME$ (-15.5(1) kJ mol^{-1}). This comparison reveals that the extra fluorine atom of CF_3I results in an excess stabilization of approximately 50 and 35%, respectively. These relatively large differences in stability, observed for the complexes of CHF_2I and CF_3I with TMA and DME, combined with the experimentally derived value of -7.6(1) kJ mol^{-1} for $CF_3I{\cdot}CH_3F$, support the assumption that the XB complex of CHF_2I and CH_3F is too weak to be observed.

DFT based calculations of the complexes discussed in this chapter in which the origins and manifestations of the interactions studied are scrutinized based on the Ziegler-Rauk type EDA, [69-70] the NOCV framework, [71-73] and the NCI index [74-75] can be found in the paper mentioned on the cover page of this chapter. Details of these analyses can be found in a previous publication by Pinter et al. [76] Furthermore, the results of the Ziegler-Rauk type EDA are also reported and expanded in the following chapter, where they are put into context with Pearson's HSAB concept.

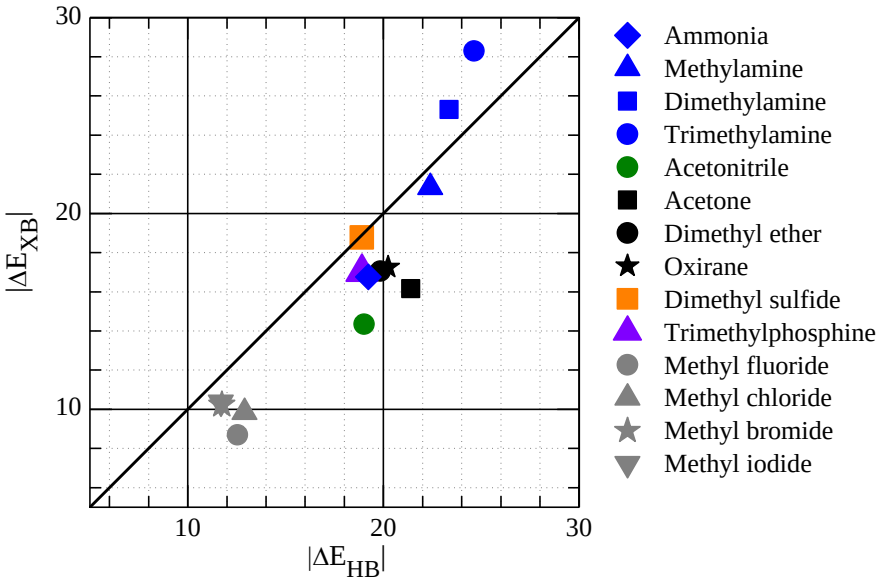

Figure 3.7: MP2/aug-cc-pVDZ-PP complexation energies, in kJ mol^{-1}, of the C-I···X XB and C-H···X HB complexes of CHF_2I with a selection of oxygen, nitrogen, sulphur, phosphorus and halogen containing Lewis bases.

The finding that the competition between hydrogen and halogen bonding can be tuned by the choice of the Lewis base, and the fact that, at least for the bases studied in this chapter, the preference for halogen or hydrogen bonding seems to be correlated by the chemical hardness of the base molecule used, triggers to expand the current data set. To this end, additional calculations were initiated for different complexes of CHF_2I with various nitrogen, oxygen, sulphur, phosphorus and halogen containing Lewis bases. The complexation energies for the various XB and HB isomers are summarized in Figure 3.7. It can be seen at the used computational level, TMA is by far the most effective XB acceptor and gives rise to a complexation energy that is approximately 15% higher than that of the corresponding HB complex. CH_3F, on the other hand, is by far the most effective HB acceptor, with a difference in complexation energies of 44%. The data further shows that also for the complexes with dimethylamine a preference is observed for halogen bonding, while for the complex with methylamine, the HB and XB complexes are predicted to have a similar stability. Experimental studies for these complexes, unfortunately, are limited due to the occurrence of N-H···N HB dimers and higher associations and the limited solubility of these species in LKr and LXe. Other

interesting trends that can be deduced are related to the observations that when passing from TMA to TMP, the HB is predicted to take over, while for DME and DMS an opposite trend is observed. A detailed study of the XB-HB competition involving CHF_2I as a bond donor with the Lewis bases CH_3Cl, DMS and TMP is reported in the following chapter.

3.4 Conclusions

A cryospectroscopic infrared and Raman study of LKr solutions of mixtures of CHF_2I and the Lewis bases TMA and DME revealed the simultaneous formation of HB and XB complexes. For the mixtures of CHF_2I and CH_3F, only the HB complex was detected. The experimental complexation enthalpies of the HB complexes with TMA, DME and CH_3F were found to be -14.7(2), -10.5(5) and -5.1(6) kJ mol^{-1}, respectively. The complexation enthalpies for the XB complexes with TMA and DME are -19.0(3) and -11.5(6) kJ mol^{-1}. The experimental data supports the idea that TMA shows a greater affinity to form XB complex, while CH_3F prefers HB interactions. Overall, a good agreement between the experimental and the calculated shifts and complexation enthalpies was observed. Comparison of the experimental complexation enthalpies for the XB interactions with those obtained for XB complexes with CF_3I reveals an additional stabilization of approximately 50 % for TMA and 35 % for DME for the complexes with CF_3I. In general, we can conclude that the present study is one of the first to report experimental thermodynamical data on the simultaneous formation of XB and HB complexes. Moreover, it has theoretically and experimentally been shown that the competition of HB and XB complexes can be tuned by changing the chemical hardness of the chosen Lewis base.

3.5 References

1 C. B. Aakeröy, M. Baldrighi, J. Desper, P. Metrangolo, G. Resnati, *Chem. - Eur. J.*, 2013, ***19***, 16240-16247.

2 R. W. Troff, T. Mäkelä, F. Topić, A. Valkonen, K. Raatikainen, K. Rissanen, *Eur. J. Org. Chem.*, 2013, ***2013***, 1617-1637.

3 A. Priimagi, G. Cavallo, A. Forni, M. Gorynsztejn-Leben, M. Kaivola, P. Metrangolo, R. Milani, A. Shishido, T. Pilati, G. Resnati, G. Terraneo, *Adv. Funct. Mater.*, 2012, ***22***, 2572-2579.

4 L. Meazza, J. A. Foster, K. Fucke, P. Metrangolo, G. Resnati, J. W. Steed, *Nature Chemistry*, 2013, ***5***, 42-47.

5 P. Metrangolo, F. Meyer, T. Pilati, G. Resnati, G. Terraneo, *Angew. Chem., Int. Ed.*, 2008, ***47***, 6114-6127.

6 P. Metrangolo, G. Resnati, T. Pilati, S. Biella, *Struct. Bond.*, 2008, ***126***, 105-136.

7 C. B. Aakeröy, P. D. Chopade, J. Desper, *Cryst. Growth Des.*, 2013, ***13***, 4145-4150.

8 N. F. Valadares, L. B. Salum, I. Polikarpov, A. D. Andricopulo, R. C. Garratt, *J. Chem. Inf. Model.*, 2009, ***49***, 2606-2616.

9 H. Duan, W. Zhang, J. Zhao, D. Liang, X. Yang, S. Jin, *J. Mol. Model.*, 2012, ***18***, 3867-3875.

10 M. R. Scholfield, C. M. Zanden, M. Carter, P. S. Ho, *Protein Sci.*, 2013, ***22***, 139-152.

11 P. Auffinger, F. A. Hays, E. Westhof, P. S. Ho, *Proc. Natl. Acad. Sci. U. S. A.*, 2004, ***101***, 16789-16794.

12 Y. X. Lu, T. Shi, Y. Wang, H. Y. Yang, X. H. Yan, X. M. Luo, H. L. Jiang, W. L. Zhu, *J. Med. Chem.*, 2009, ***52***, 2854-2862.

13 Y. X. Lu, H. Y. Li, X. Zhu, H. L. Liu, W. L. Zhu, *J. Mol. Model.*, 2012, ***18***, 3311-3320.

14 S. Sirimulla, J. B. Bailey, R. Vegesna, M. Narayan, *J. Chem. Inf. Model.*, 2013, ***53***, 2781-2791.

15 D. Manna, G. Roy, G. Mugesh, *Acc. Chem. Res.*, 2013, ***46***, 2706-2715.

16 P. Politzer, K. E. Riley, F. A. Bulat, J. S. Murray, *Comput. Theor. Chem.*, 2012, ***998***, 2-8.

17 P. Metrangolo, G. Resnati, *Science*, 2008, ***321***, 918-919.

18 P. Metrangolo, H. Neukirch, T. Pilati, G. Resnati, *Acc. Chem. Res.*, 2005, ***38***, 386-395.

19 Z. P. Shields, J. S. Murray, P. Politzer, *Int. J. Quantum Chem.*, 2010, ***110***, 2823-2832.

20 P. Politzer, J. S. Murray, T. Clark, *Phys. Chem. Chem. Phys.*, 2010, ***12***, 7748-7757.

21 J. W. Zou, Y. J. Jiang, M. Guo, G. X. Hu, B. Zhang, H. C. Liu, Q. S. Yu, *Chem. - Eur. J.*, 2005, ***11***, 740-751.

22 L. P. Wolters, F. M. Bickelhaupt, *ChemistryOpen*, 2012, ***1***, 96-105.

23 I. Alkorta, F. Blanco, M. Solimannejad, J. Elguero, *J. Phys. Chem. A*, 2008, ***112***, 10856-10863.

24 M. Domagała, P. Matczak, M. Palusiak, *Comput. Theor. Chem.*, 2012, ***998***, 26-33.

25 B. Jing, Q. Li, R. Li, B. Gong, Z. Liu, W. Li, J. Cheng, J. Sun, *Comput. Theor. Chem.*, 2011, ***963***, 417-421.

26 P. Politzer, J. S. Murray, P. Lane, *Int. J. Quantum Chem.*, 2007, ***107***, 3046-3052.

27 Q. Li, H. Li, J. Gong, W. Li, J. Cheng, *Int. J. Quantum Chem.*, 2012, ***112***, 2429-2434.

28 Q. Li, Q. Lin, W. Li, J. Cheng, B. Gong, J. Sun, *ChemPhysChem*, 2008, ***9***, 2265-2269.

29 Q. Li, X. Xu, T. Liu, B. Jing, W. Li, J. Cheng, B. Gong, J. Sun, *Phys. Chem. Chem. Phys.*, 2010, ***12***, 6837-6843.

30 A. R. Voth, P. Khuu, K. Oishi, P. S. Ho, *Nat. Chem.*, 2009, ***1***, 74-79.

31 P. Politzer, J. S. Murray, *ChemPhysChem*, 2013, ***14***, 278-294.

32 H. D. Arman, R. L. Gieseking, T. W. Hanks, W. T. Pennington, *Chem. Commun.*, 2010, ***46***, 1854-1856.

33 E. Corradi, S. V. Meille, M. T. Messina, P. Metrangolo, G. Resnati, *Angew. Chem., Int. Ed.*, 2000, ***39***, 1782-1786.

34 K. Raatikainen, M. Cametti, K. Rissanen, *Beilstein J. Org. Chem.*, 2010, ***6***.

35 C. B. Aakeröy, N. Schultheiss, A. Rajbanshi, J. Desper, C. Moore, *Cryst. Growth Des.*, 2009, ***9***, 432-441.

36 T. Di Paolo, C. Sandorfly, *Can. J. Chem.*, 1974, ***52***, 3612-3622.

37 R. Massuda, C. Sandorfy, *Can. J. Chem.*, 1977, ***55***, 3211-3217.

38 J. Lieffrig, O. Jeannin, T. Guizouarn, P. Auban-Senzier, M. Fourmigué, *Cryst. Growth Des.*, 2012, ***12***, 4248-4257.

39 C. B. Aakeröy, M. Fasulo, N. Schultheiss, J. Desper, C. Moore, *J. Am. Chem. Soc.*, 2007, ***129***, 13772-13773.

40 C. B. Aakeröy, S. Panikkattu, P. D. Chopade, J. Desper, *CrystEngComm*, 2013, ***15***, 3125-3136.

41 G. Minguez Espallargas, F. Zordan, L. Arroyo Marin, H. Adams, K. Shankland, J. van de Streek, L. Brammer, *Chem. - Eur. J.*, 2009, ***15***, 7554-7568.

42 S. Y. Oh, C. W. Nickels, F. Garcia, W. Jones, T. Friščić, *CrystEngComm*, 2012, ***14***, 6110-6114.

43 C. B. Aakeröy, J. Desper, B. A. Helfrich, P. Metrangolo, T. Pilati, G. Resnati, A. Stevenazzi, *Chem. Commun. (Cambridge, U. K.)*, 2007, ***41***, 4236-4238.

44 B. J. van der Veken, W. A. Herrebout, R. Szostak, D. N. Shchepkin, Z. Havlas, P. Hobza, *J. Am. Chem. Soc.*, 2001, ***123***, 12290-12293.

45 T. Van den Kerkhof, A. Bouwen, E. Goovaerts, W. A. Herrebout, B. J. van der Veken, *Phys. Chem. Chem. Phys.*, 2004, ***6***, 358-362.

46 W. A. Herrebout, S. M. Melikova, S. N. Delanoye, K. S. Rutkowski, D. N. Shchepkin, B. J. van der Veken, *J. Phys. Chem. A*, 2005, ***109***, 3038-3044.

47 W. A. Herrebout, S. N. Delanoye, B. J. van der Veken, *J. Phys. Chem. A*, 2004, ***108***, 6059-6064.

48 S. N. Delanoye, W. A. Herrebout, B. J. van der Veken, *J. Am. Chem. Soc.*, 2002, ***124***, 11854-11855.

49 S. N. Delanoye, W. A. Herrebout, B. J. van der Veken, *J. Am. Chem. Soc.*, 2002, ***124***, 7490-7498.

50 K. S. Rutkowski, W. A. Herrebout, S. M. Melikova, B. J. van der Veken, A. Koll, *Chem. Phys.*, 2008, ***354***, 71-79.

51 K. S. Rutkowski, S. M. Melikova, P. Rodziewicz, W. A. Herrebout, B. J. van der Veken, A. Koll, *J. Mol. Struct.*, 2008, ***880***, 64-68.

52 K. S. Rutkowski, A. Karpfen, S. M. Melikova, W. A. Herrebout, A. Koll, P. Wolschann, B. J. van der Veken, *Phys. Chem. Chem. Phys.*, 2009, ***11***, 1551-1563.

53 B. Michielsen, W. A. Herrebout, B. J. van der Veken, *ChemPhysChem*, 2007, ***8***, 1188-1198.

54 D. Hauchecorne, B. J. van der Veken, A. Moiana, W. A. Herrebout, *Chem. Phys.*, 2010, ***374***, 30-36.

55 D. Hauchecorne, R. Szostak, W. A. Herrebout, B. J. van der Veken, *ChemPhysChem*, 2009, ***10***, 2105-2115.

56 D. Hauchecorne, W. A. Herrebout, *J. Phys. Chem. A*, 2013, ***117***, 11548-11557.

57 D. Hauchecorne, N. Nagels, B. J. van der Veken, W. A. Herrebout, *Phys. Chem. Chem. Phys.*, 2012, ***14***, 681-690.

58 N. Nagels, D. Hauchecorne, W. A. Herrebout, *Molecules*, 2013, ***18***, 6829-6851.

59 D. Hauchecorne, A. Moiana, B. J. van der Veken, W. A. Herrebout, *Phys. Chem. Chem. Phys.*, 2011, ***13***, 10204-10213.

60 A. C. Legon, *Phys. Chem. Chem. Phys.*, 2010, ***12***, 7736-7747.

61 W. Vanspeybrouck, W. A. Herrebout, B. J. van der Veken, J. Lundell, R. N. Perutz, *J. Phys. Chem. B*, 2003, ***107***, 13855-13861.

62 C. Peng, H. B. Schlegel, *Isr. J. Chem.*, 1993, ***33***, 449-454.

63 C. Peng, P. Y. Ayala, H. B. Schlegel, M. J. Frisch, *J. Comput. Chem.*, 1996, ***17***, 49-56.

64 B. Michielsen, W. A. Herrebout, B. J. van der Veken, *ChemPhysChem*, 2008, ***9***, 1693-1701.

65 B. J. van der Veken, S. N. Delanoye, B. Michielsen, W. A. Herrebout, *J. Mol. Struct.*, 2010, ***976***, 97-104.

66 P. R. Shirhatti, D. K. Maity, S. Bhattacharyya, S. Wategaonkar, *ChemPhysChem*, 2014, ***15***, 109-117.

67 B. J. van der Veken, *J. Phys. Chem.*, 1996, ***100***, 17436-17438.

68 S. N. Delanoye, W. A. Herrebout, B. J. van der Veken, *J. Phys. Chem. A*, 2005, ***109***, 9836-9843.

69 T. Ziegler, A. Rauk, *Theor. Chim. Acta*, 1977, ***46***, 1-10.

70 F. M. Bickelhaupt, E. J. Baerends, *Rev. Comput. Chem.*, 2000, ***15***, 1-86.

71 M. P. Mitoraj, M. Parafiniuk, M. Srebro, M. Handzlik, A. Buczek, A. Michalak, *J. Mol. Model.*, 2011, ***17***, 2337-2352.

72 M. P. Mitoraj, A. Michalak, T. Ziegler, *J. Chem. Theory Comput.*, 2009, ***5***, 962-975.

73 M. P. Mitoraj, A. Michalak, *J. Mol. Model.*, 2007, ***13***, 347-355.

74 J. Contreras-García, E. R. Johnson, S. Keinan, R. Chaudret, J.-P. Piquemal, D. N. Beratan, W. Yang, *J. Chem. Theory Comput.*, 2011, ***7***, 625-632.
75 E. R. Johnson, S. Keinan, P. Mori-Sánchez, J. Contreras-García, A. J. Cohen, W. Yang, *J. Am. Chem. Soc.*, 2010, ***132***, 6498-6506.
76 B. Pinter, N. Nagels, W. A. Herrebout, F. De Proft, *Chem. - Eur. J.*, 2013, ***19***, 519-530.

3.6 Supporting information

Table S3.1.1: Cartesian coordinates of the MP2/aug-cc-pVDZ-PP optimized geometry of CHF_2I.

C_s	X	Y	Z
CHF_2I			
C	0.461801	-1.276126	0.000000
H	1.552810	-1.382611	0.000000
F	-0.060896	-1.882815	1.101579
F	-0.060896	-1.882815	-1.101579
I	-0.060896	0.810001	0.000000

Table S3.1.2: Cartesian coordinates of the MP2/aug-cc-pVDZ optimized geometry of TMA.

C_{3v}	X	Y	Z
TMA			
N	0.000000	0.000000	0.410619
C	0.000000	1.379959	-0.066347
H	-0.892330	1.901918	0.309142
H	0.892330	1.901918	0.309142
H	0.000000	1.440847	-1.178318
C	1.195079	-0.689979	-0.066347
H	2.093274	-0.178178	0.309142
H	1.200944	-1.723740	0.309142
H	1.247810	-0.720423	-1.178318
C	-1.195079	-0.689979	-0.066347
H	-1.200944	-1.723740	0.309142
H	-2.093274	-0.178178	0.309142
H	-1.247810	-0.720423	-1.178318

Table S3.1.3: Cartesian coordinates of the MP2/aug-cc-pVDZ optimized geometry of DME.

C_{2v}	X	Y	Z
DME			
O	0.000000	0.000000	0.607066
C	0.000000	1.169581	-0.202099
H	0.000000	2.032636	0.474896
H	0.898418	1.208635	-0.845282
H	-0.898418	1.208635	-0.845282
C	0.000000	-1.169581	-0.202099
H	0.898418	-1.208635	-0.845282
H	0.000000	-2.032636	0.474896
H	-0.898418	-1.208635	-0.845282

Table S3.1.4: Cartesian coordinates of the MP2/aug-cc-pVDZ optimized geometry of CH_3F.

C_{3v}	X	Y	Z
CH_3F			
C	0.000000	0.000000	-0.646104
H	0.000000	1.041664	-0.991672
H	-0.902108	-0.520832	-0.991672
H	0.902108	-0.520832	-0.991672
F	0.000000	0.000000	0.761293

Table S3.2.1: Cartesian coordinates of the MP2/aug-cc-pVDZ-PP optimized geometry of the HB complex between CHF_2I and TMA.

C_s	X	Y	Z
CHF_2I			
C	0.642426	-1.130002	0.000000
H	1.147834	-0.151321	0.000000
F	0.984576	-1.859033	1.101290
F	0.984576	-1.859033	-1.101290
I	-1.492535	-0.791141	0.000000
TMA			
N	1.595699	2.013850	0.000000
C	0.984576	2.592977	1.197800
H	-0.094911	2.382464	1.200288
H	1.431047	2.141955	2.096381
H	1.130721	3.694111	1.247510
C	3.035468	2.276065	0.000000
H	3.494095	1.826639	0.893043
H	3.494095	1.826639	-0.893043
H	3.260101	3.364980	0.000000
C	0.984576	2.592977	-1.197800
H	1.431047	2.141955	-2.096381
H	-0.094911	2.382464	-1.200288
H	1.130721	3.694111	-1.247510

Table S3.2.2: Cartesian coordinates of the MP2/aug-cc-pVDZ-PP optimized geometry of the XB complex between CHF_2I and TMA.

C_s	X	Y	Z
CHF_2I			
C	0.077175	-2.606913	0.000000
H	1.096720	-3.012779	0.000000
F	-0.587693	-3.073256	1.104876
F	-0.587693	-3.073256	-1.104876
I	0.101990	-0.449926	0.000000
TMA			
N	0.109853	2.476047	0.000000
C	-0.587693	2.936661	1.200962
H	-1.615594	2.545466	1.202157
H	-0.069782	2.559360	2.094879
H	-0.629598	4.045724	1.256325
C	1.492405	2.954472	0.000000
H	2.012316	2.577183	0.892794
H	2.012316	2.577183	-0.892794
H	1.547442	4.064397	0.000000
C	-0.587693	2.936661	-1.200962
H	-0.069782	2.559360	-2.094879
H	-1.615594	2.545466	-1.202157
H	-0.629598	4.045724	-1.256325

Table S3.2.3: Cartesian coordinates of the MP2/aug-cc-pVDZ-PP optimized geometry of the HB complex between CHF_2I and DME.

C_1	X	Y	Z
CHF_2I			
C	0.422381	1.262195	0.286858
H	-0.583419	1.225610	0.720110
F	0.404415	1.970865	-0.879460
F	1.303380	1.870211	1.129217
I	1.077574	-0.754264	-0.112438
DME			
O	-2.599621	0.333498	0.341380
C	-3.001557	-0.889345	0.955838
H	-2.742630	-0.819018	2.019602
H	-4.090938	-1.040486	0.852634
H	-2.473015	-1.748220	0.505095
C	-2.899948	0.318157	-1.053892
H	-3.986935	0.212841	-1.219382
H	-2.557575	1.273619	-1.470652
H	-2.375340	-0.512081	-1.559867

Table S3.2.4: Cartesian coordinates of the MP2/aug-cc-pVDZ-PP optimized geometry of the XB complex between CHF_2I and DME.

C_s	X	Y	Z
CHF_2I			
C	-0.189143	-2.390401	0.000000
H	-1.200211	-2.815109	0.000000
F	0.486455	-2.833703	1.103335
F	0.486455	-2.833703	-1.103335
I	-0.275850	-0.244447	0.000000
DME			
O	-0.196033	2.791227	0.000000
C	0.486455	3.229885	-1.174260
H	-0.083613	2.861418	-2.035942
H	0.535871	4.332663	-1.208894
H	1.512608	2.821630	-1.209905
C	0.486455	3.229885	1.174260
H	0.535871	4.332663	1.208894
H	-0.083613	2.861418	2.035942
H	1.512608	2.821630	1.209905

Table S3.2.5: Cartesian coordinates of the MP2/aug-cc-pVDZ-PP optimized geometry of the HB complex with a secondary C-H···F between CHF_2I and CH_3F.

C_1	X	Y	Z
CHF_2I			
C	0.051120	1.231334	-0.167891
H	0.819405	1.143550	-0.942383
F	-0.824403	2.229711	-0.469011
F	0.633385	1.533751	1.028692
I	-1.011363	-0.635055	0.005013
CH_3F			
C	3.174738	-0.834283	0.338424
H	4.265554	-0.949658	0.339853
H	2.677354	-1.809321	0.267112
H	2.836716	-0.289230	1.228324
Cl	2.818581	-0.076764	-0.802104

Table S3.2.6: Cartesian coordinates of the MP2/aug-cc-pVDZ-PP optimized geometry of the HB complex with a secondary C-H···I between CHF_2I and CH_3F.

C_s	X	Y	Z
CHF_2I			
C	-1.148940	0.695687	0.000000
H	-1.609299	-0.297830	0.000000
F	-1.533021	1.399323	1.101091
F	-1.533021	1.399323	-1.101091
I	0.997562	0.478027	0.000000
CH_3F			
C	-0.419710	-3.424009	0.000000
H	-0.799161	-4.453105	0.000000
H	0.170570	-3.222906	0.902200
H	0.170570	-3.222906	-0.902200
F	-1.533021	-2.550729	0.000000

Table S3.2.7: Cartesian coordinates of the MP2/aug-cc-pVDZ-PP optimized geometry of the XB complex between CHF_2I and CH_3F.

C_s	X	Y	Z
CHF_2I			
C	-0.066973	-2.146617	0.000000
H	0.875331	-2.707020	0.000000
F	-0.798003	-2.484278	1.102384
F	-0.798003	-2.484278	-1.102384
I	0.330139	-0.036860	0.000000
CH_3F			
C	-0.798003	3.713723	0.000000
H	-0.700788	4.806339	0.000000
H	-1.317109	3.368107	0.902696
H	-1.317109	3.368107	-0.902696
F	0.501801	3.159158	0.000000

Table S3.3A: MP2/aug-cc-pVDZ-PP vibrational frequencies, in cm^{-1}, infrared intensities, in km mol^{-1}, and Raman intensities, in $Å^4$ amu^{-1}, for the HB complex of CHF_2I and TMA and both monomers, as well as the complexation shift Δν.

	Monomer			HB complex			
	Frequency	IR int.	Raman int.	Frequency	Δν	IR int.	Raman int.
CHF_2I							
ν_1 (A')	3192.4	3.6	94.4	3112.3	-80.2	91.6	248.0
ν_2 (A')	1279.7	99.2	7.5	1320.4	40.7	158.8	17.3
ν_3 (A')	1074.1	300.4	3.2	1063.1	-11.0	260.6	5.3
ν_4 (A')	652.5	81.8	18.4	651.9	-0.6	93.3	17.0
ν_5 (A')	549.4	2.9	1.8	549.6	0.2	7.3	1.7
ν_6 (A')	276.0	0.2	6.6	271.3	-4.7	0.007	6.7
ν_7 (A")	1346.0	4.1	2.7	1407.6	61.6	6.3	0.7
ν_8 (A")	1096.9	186.9	1.9	1085.5	-11.4	163.9	2.0
ν_9 (A")	277.0	0.0004	1.2	275.1	-1.9	0.006	0.9
TMA							
ν_1 (A_1)	3111.8	42.4	235.1	3114.8	2.9	67.2	173.2
ν_2 (A_1)	2962.3	167.2	390.2	2978.9	16.7	178.4	429.2
ν_3 (A_1)	1499.0	23.4	0.4	1500.9	1.9	26.2	0.3
ν_4 (A_1)	1464.0	1.6	2.3	1465.3	1.3	2.3	3.7
ν_5 (A_1)	1204.0	24.9	5.6	1212.3	8.4	23.7	5.1
ν_6 (A_1)	853.0	22.9	12.0	848.8	-4.3	37.6	11.3
ν_7 (A_1)	383.8	7.6	1.1	400.7	16.9	14.0	0.8
ν_8 (A_2)	3163.7	0.0	0.0	3164.9	1.2	0.2	1.6
ν_9 (A_2)	1477.8	0.0	0.0	1478.1	0.3	0.004	0.005
ν_{10} (A_2)	1057.3	0.0	0.0	1057.9	0.6	0.03	0.03
ν_{11} (A_2)	243.9	0.0	0.0	239.2	-4.7	0.004	0.03
ν_{12} (E)	3166.9	34.6	87.1	3167.8	1.0	25.7	67.0
ν_{13} (E)	3111.1	26.1	27.8	3114.2	3.1	18.3	48.7
ν_{14} (E)	2955.2	44.4	18.3	2974.3	19.1	36.4	21.5
ν_{15} (E)	1500.8	9.8	5.5	1502.0	1.2	11.7	6.4
ν_{16} (E)	1475.1	5.7	8.8	1475.8	0.7	3.0	7.9
ν_{17} (E)	1421.1	0.7	1.6	1422.5	1.4	0.2	1.7
ν_{18} (E)	1303.4	14.9	1.7	1298.2	-5.2	16.6	1.5
ν_{19} (E)	1115.9	9.1	0.4	1115.3	-0.6	9.4	0.6
ν_{20} (E)	1066.2	13.6	2.7	1061.7	-4.6	25.9	1.6
ν_{21} (E)	423.7	0.006	0.7	421.4	-2.3	0.07	0.6
ν_{22} (E)	290.9	0.4	0.6	290.3	-0.7	0.3	0.4

Van der Waals vibrations: 5.0 cm^{-1}, 0.1 km mol^{-1}, 0.07 $Å^4$ amu^{-1}, 28.9 cm^{-1}, 0.07 km mol^{-1}, 0.04 $Å^4$ amu^{-1}, 32.3 cm^{-1}, 0.06 km mol^{-1}, 0.5 $Å^4$ amu^{-1}, 51.8 cm^{-1}, 0.3 km mol^{-1}, 0.3 $Å^4$ amu^{-1}, 68.8 cm^{-1}, 0.5 km mol^{-1}, 0.3 $Å^4$ amu^{-1}, 84.6 cm^{-1}, 0.6 km mol^{-1}, 0.8 $Å^4$ amu^{-1}.

Table S3.3B: MP2/aug-cc-pVDZ-PP vibrational frequencies, in cm^{-1}, infrared intensities, in km mol^{-1}, and Raman intensities, in $Å^4$ amu^{-1}, for the HB complex of CHF_2I and TMA-d_9 and both monomers, as well as the complexation shift Δν.

	Monomer			HB complex			
	Frequency	IR int.	Raman int.	Frequency	Δν	IR int.	Raman int.
CHF_2I							
ν_1 (A')	3192.4	3.6	94.4	3112.2	-80.3	133.9	280.7
ν_2 (A')	1279.7	99.2	7.5	1320.8	41.1	162.1	16.3
ν_3 (A')	1074.1	300.4	3.2	1061.6	-12.4	205.8	3.6
ν_4 (A')	652.5	81.8	18.4	651.9	-0.6	93.2	17.2
ν_5 (A')	549.4	2.9	1.8	549.6	0.1	7.0	1.7
ν_6 (A')	276.0	0.2	6.6	271.2	-4.7	0.002	6.6
ν_7 (A")	1346.0	4.1	2.7	1407.9	61.9	6.2	0.7
ν_8 (A")	1096.9	186.9	1.9	1086.2	-10.7	146.7	1.2
ν_9 (A")	277.0	0.0004	1.2	275.1	-1.9	0.006	0.9
TMA-d_9							
ν_1 (A_1)	2286.9	51.7	81.2	2292.3	5.4	48.2	65.3
ν_2 (A_1)	2142.3	72.7	232.7	2152.0	9.7	72.2	251.4
ν_3 (A_1)	1151.7	0.2	5.9	1149.2	-2.5	2.2	7.0
ν_4 (A_1)	1079.2	12.6	0.2	1080.8	1.6	19.0	0.2
ν_5 (A_1)	1018.9	33.5	3.4	1029.3	10.4	33.1	2.9
ν_6 (A_1)	756.9	12.4	9.6	754.1	-2.8	21.0	8.9
ν_7 (A_1)	323.0	4.6	0.8	337.9	14.9	9.4	0.6
ν_8 (A_2)	2345.4	0.0	0.0	2346.4	1.0	0.04	0.57
ν_9 (A_2)	1067.7	0.0	0.0	1067.3	-0.5	0.008	0.012
ν_{10} (A_2)	801.3	0.0	0.0	801.9	0.6	0.001	0.009
ν_{11} (A_2)	173.1	0.0	0.0	169.9	-3.3	0.002	0.02
ν_{12} (E)	2349.0	17.4	46.2	2350.0	1.0	13.0	35.3
ν_{13} (E)	2287.5	8.1	21.2	2293.2	5.7	5.5	17.5
ν_{14} (E)	2135.6	36.1	4.2	2146.7	11.2	28.7	5.9
ν_{15} (E)	1252.4	33.4	1.0	1243.5	-8.9	32.7	1.1
ν_{16} (E)	1078.6	2.1	2.4	1078.2	-0.4	8.4	2.9
ν_{17} (E)	1073.1	0.2	0.4	1073.5	0.3	1.7	0.4
ν_{18} (E)	1063.4	1.6	3.7	1064.3	0.9	44.4	3.3
ν_{19} (E)	886.2	7.4	2.6	885.6	-0.7	6.8	2.4
ν_{20} (E)	839.0	0.03	1.0	838.2	-0.8	0.008	1.1
ν_{21} (E)	352.0	0.007	0.5	350.7	-1.3	0.09	0.4
ν_{22} (E)	210.6	0.2	0.3	210.1	-0.4	0.2	0.2

Van der Waals vibrations: 4.6 cm^{-1}, 0.1 km mol^{-1}, 0.09 $Å^4$ amu^{-1}, 26.2 cm^{-1}, 0.07 km mol^{-1}, 0.04 $Å^4$ amu^{-1}, 31.1 cm^{-1}, 0.06 km mol^{-1}, 0.4 $Å^4$ amu^{-1}, 45.3 cm^{-1}, 0.2 km mol^{-1}, 0.2 $Å^4$ amu^{-1}, 64.9 cm^{-1}, 0.5 km mol^{-1}, 0.2 $Å^4$ amu^{-1}, 81.0 cm^{-1}, 0.6 km mol^{-1}, 0.8 $Å^4$ amu^{-1}.

Table S3.4A: MP2/aug-cc-pVDZ-PP vibrational frequencies, in cm^{-1}, infrared intensities, in km mol^{-1}, and Raman intensities, in $Å^4$ amu^{-1}, for the XB complex of CHF_2I and TMA and both monomers, as well as the complexation shift Δν.

	Monomer			XB complex			
	Frequency	IR int.	Raman int.	Frequency	Δν	IR int.	Raman int.
CHF_2I							
ν_1 (A')	3192.4	3.6	94.4	3173.7	-18.7	11.2	142.3
ν_2 (A')	1279.7	99.2	7.5	1280.3	0.6	127.4	10.1
ν_3 (A')	1074.1	300.4	3.2	1066.5	-7.6	316.2	4.2
ν_4 (A')	652.5	81.8	18.4	647.7	-4.8	37.5	67.3
ν_5 (A')	549.4	2.9	1.8	542.0	-7.4	1.9	5.4
ν_6 (A')	276.0	0.2	6.6	271.0	-5.0	8.3	23.4
ν_7 (A")	1346.0	4.1	2.7	1343.1	-2.8	3.3	3.0
ν_8 (A")	1096.9	186.9	1.9	1070.4	-26.5	182.2	1.8
ν_9 (A")	277.0	0.0004	1.2	280.9	3.9	0.05	1.0
TMA							
ν_1 (A_1)	3111.8	42.4	235.1	3117.4	5.5	33.3	142.8
ν_2 (A_1)	2962.3	167.2	390.2	2985.6	23.3	211.0	513.9
ν_3 (A_1)	1499.0	23.4	0.4	1499.3	0.3	25.5	1.3
ν_4 (A_1)	1464.0	1.6	2.3	1464.0	0.0	0.2	21.8
ν_5 (A_1)	1204.0	24.9	5.6	1213.0	9.1	18.9	23.7
ν_6 (A_1)	853.0	22.9	12.0	846.5	-6.5	77.0	11.3
ν_7 (A_1)	383.8	7.6	1.1	402.5	18.7	34.5	0.9
ν_8 (A_2)	3163.7	0.0	0.0	3166.6	2.9	0.3	0.7
ν_9 (A_2)	1477.8	0.0	0.0	1476.2	-1.5	0.002	0.006
ν_{10} (A_2)	1057.3	0.0	0.0	1059.1	1.8	0.001	0.0004
ν_{11} (A_2)	243.9	0.0	0.0	235.4	-8.5	0.0	0.0
ν_{12} (E)	3166.9	34.6	87.1	3169.8	2.9	22.2	56.3
ν_{13} (E)	3111.1	26.1	27.8	3116.7	5.7	14.7	33.3
ν_{14} (E)	2955.2	44.4	18.3	2980.8	25.6	36.5	33.4
ν_{15} (E)	1500.8	9.8	5.5	1500.8	0.0	14.2	5.9
ν_{16} (E)	1475.1	5.7	8.8	1473.9	-1.2	1.7	7.7
ν_{17} (E)	1421.1	0.7	1.6	1421.8	0.7	0.0	1.8
ν_{18} (E)	1303.4	14.9	1.7	1301.3	-2.1	12.1	1.2
ν_{19} (E)	1115.9	9.1	0.4	1114.0	-2.0	6.7	0.8
ν_{20} (E)	1066.2	13.6	2.7	1062.3	-3.9	13.8	2.8
ν_{21} (E)	423.7	0.006	0.7	421.2	-2.4	0.004	0.7
ν_{22} (E)	290.9	0.4	0.6	284.4	-6.5	0.3	1.1

Van der Waals vibrations: 2.8 cm^{-1}, 0.7 km mol^{-1}, 0.02 $Å^4$ amu^{-1}, 36.8 cm^{-1}, 0.3 km mol^{-1}, 0.3 $Å^4$ amu^{-1}, 36.9 cm^{-1}, 0.3 km mol^{-1}, 0.2 $Å^4$ amu^{-1}, 80.8 cm^{-1}, 5.8 km mol^{-1}, 1.3 $Å^4$ amu^{-1}, 96.7 cm^{-1}, 0.008 km mol^{-1}, 0.1 $Å^4$ amu^{-1}, 98.0 cm^{-1}, 0.6 km mol^{-1}, 0.1 $Å^4$ amu^{-1}.

Table S3.4B: MP2/aug-cc-pVDZ-PP vibrational frequencies, in cm^{-1}, infrared intensities, in km mol^{-1}, and Raman intensities, in $Å^4$ amu^{-1}, for the XB complex of CHF_2I and TMA-d_9 and both monomers, as well as the complexation shift Δν.

	Monomer			XB complex			
	Frequency	IR int.	Raman int.	Frequency	Δν	IR int.	Raman int.
CHF_2I							
ν_1 (A')	3192.4	3.6	94.4	3173.7	-18.7	11.4	141.4
ν_2 (A')	1279.7	99.2	7.5	1280.4	0.7	127.0	10.9
ν_3 (A')	1074.1	300.4	3.2	1066.4	-7.7	317.2	2.8
ν_4 (A')	652.5	81.8	18.4	647.6	-4.9	37.3	67.3
ν_5 (A')	549.4	2.9	1.8	542.0	-7.4	2.0	5.4
ν_6 (A')	276.0	0.2	6.6	270.9	-5.1	8.4	23.6
ν_7 (A")	1346.0	4.1	2.7	1343.1	-2.8	3.4	3.0
ν_8 (A")	1096.9	186.9	1.9	1070.3	-26.5	179.7	1.7
ν_9 (A")	277.0	0.0004	1.2	281.0	4.0	0.0001	1.7
TMA-d_9							
ν_1 (A_1)	2286.9	51.7	81.2	2295.3	8.4	40.4	88.0
ν_2 (A_1)	2142.3	72.7	232.7	2155.7	13.4	94.8	259.8
ν_3 (A_1)	1151.7	0.2	5.9	1147.9	-3.8	6.1	17.6
ν_4 (A_1)	1079.2	12.6	0.2	1080.0	0.7	8.4	0.4
ν_5 (A_1)	1018.9	33.5	3.4	1029.8	10.9	60.9	14.6
ν_6 (A_1)	756.9	12.4	9.6	752.4	-4.5	42.6	9.1
ν_7 (A_1)	323.0	4.6	0.8	340.2	17.2	25.4	1.0
ν_8 (A_2)	2345.4	0.0	0.0	2347.7	2.3	0.06	0.2
ν_9 (A_2)	1067.7	0.0	0.0	1065.9	-1.8	0.0002	0.0007
ν_{10} (A_2)	801.3	0.0	0.0	802.9	1.7	0.0	0.0001
ν_{11} (A_2)	173.1	0.0	0.0	167.0	-6.1	0.0	0.0
ν_{12} (E)	2349.0	17.4	46.2	2351.4	2.4	11.0	29.9
ν_{13} (E)	2287.5	8.1	21.2	2296.4	8.9	6.5	23.1
ν_{14} (E)	2135.6	36.1	4.2	2150.4	14.8	27.8	10.6
ν_{15} (E)	1252.4	33.4	1.0	1247.2	-5.2	28.5	0.7
ν_{16} (E)	1078.6	2.1	2.4	1077.0	-1.6	4.6	2.6
ν_{17} (E)	1073.1	0.2	0.4	1073.7	0.6	0.1	0.4
ν_{18} (E)	1063.4	1.6	3.7	1062.7	-0.7	0.9	3.1
ν_{19} (E)	886.2	7.4	2.6	885.9	-0.3	6.6	2.4
ν_{20} (E)	839.0	0.03	1.0	836.9	-2.1	0.01	1.4
ν_{21} (E)	352.0	0.007	0.5	350.8	-1.2	0.007	0.6
ν_{22} (E)	210.6	0.2	0.3	206.1	-4.5	0.2	0.4

Van der Waals vibrations: 2.7 cm^{-1}, 0.8 km mol^{-1}, 0.02 $Å^4$ amu^{-1}, 34.4 cm^{-1}, 0.3 km mol^{-1}, 0.3 $Å^4$ amu^{-1}, 34.6 cm^{-1}, 0.2 km mol^{-1}, 0.3 $Å^4$ amu^{-1}, 76.1 cm^{-1}, 4.9 km mol^{-1}, 1.2 $Å^4$ amu^{-1}, 88.0 cm^{-1}, 0.03 km mol^{-1}, 0.07 $Å^4$ amu^{-1}, 89.5 cm^{-1}, 0.8 km mol^{-1}, 0.1 $Å^4$ amu^{-1}.

Table S3.5A: MP2/aug-cc-pVDZ-PP vibrational frequencies, in cm^{-1}, infrared intensities, in km mol^{-1}, and Raman intensities, in $Å^4$ amu^{-1}, for the HB complex of CHF_2I and DME and both monomers, as well as the complexation shift Δν.

	Monomer			HB complex			
	Frequency	IR int.	Raman int.	Frequency	Δν	IR int.	Raman int.
CHF_2I							
ν_1 (A')	3192.4	3.6	94.4	3206.7	14.3	14.0	103.0
ν_2 (A')	1279.7	99.2	7.5	1279.6	-0.1	117.7	11.6
ν_3 (A')	1074.1	300.4	3.2	1067.1	-7.0	275.3	3.2
ν_4 (A')	652.5	81.8	18.4	650.9	-1.6	81.1	15.6
ν_5 (A')	549.4	2.9	1.8	550.0	0.6	4.9	1.6
ν_6 (A')	276.0	0.2	6.6	273.1	-2.9	0.1	6.0
ν_7 (A")	1346.0	4.1	2.7	1369.9	23.9	6.4	2.7
ν_8 (A")	1096.9	186.9	1.9	1090.8	-6.1	187.6	2.3
ν_9 (A")	277.0	0.0004	1.2	277.4	0.4	0.3	1.3
DME							
ν_1 (A_1)	3188.7	20.1	87.6	3189.1	0.5	16.1	61.7
ν_2 (A_1)	3024.8	58.6	320.3	3032.9	8.1	46.3	308.2
ν_3 (A_1)	1505.9	2.9	5.6	1504.4	-1.5	8.3	5.7
ν_4 (A_1)	1473.5	0.0008	2.2	1475.3	1.8	0.03	1.8
ν_5 (A_1)	1261.1	6.6	0.5	1263.1	2.0	6.6	0.4
ν_6 (A_1)	942.4	34.7	9.8	933.7	-8.7	40.0	9.7
ν_7 (A_1)	416.8	2.3	1.0	417.7	0.9	2.0	0.8
ν_8 (A_2)	3096.2	0.0	14.7	3110.7	14.5	0.4	11.8
ν_9 (A_2)	1474.8	0.0	11.4	1473.4	-1.4	0.4	9.6
ν_{10} (A_2)	1157.2	0.0	1.5	1156.4	-0.9	0.002	1.8
ν_{11} (A_2)	195.2	0.0	0.2	191.1	-4.1	0.004	0.1
ν_{12} (B_1)	3089.5	107.8	94.2	3104.5	14.9	95.8	85.9
ν_{13} (B_1)	1489.2	13.0	0.04	1488.5	-0.7	16.2	0.3
ν_{14} (B_1)	1187.2	7.2	0.04	1187.6	0.4	4.2	0.4
ν_{15} (B_1)	260.2	5.1	0.002	262.2	2.0	8.1	0.1
ν_{16} (B_2)	3187.3	24.6	59.2	3187.8	0.5	15.4	41.3
ν_{17} (B_2)	3018.4	55.2	0.6	3027.9	9.5	42.1	3.3
ν_{18} (B_2)	1490.1	10.3	1.0	1488.8	-1.2	6.8	0.6
ν_{19} (B_2)	1441.5	2.5	1.3	1442.4	0.9	0.7	1.2
ν_{20} (B_2)	1191.9	98.1	0.7	1183.7	-8.2	81.8	0.5
ν_{21} (B_2)	1113.8	35.0	1.6	1110.1	-3.7	50.1	1.8

Van der Waals vibrations: 16.0 cm^{-1}, 0.3 km mol^{-1}, 0.3 $Å^4$ amu^{-1}, 33.4 cm^{-1}, 0.5 km mol^{-1}, 0.3 $Å^4$ amu^{-1}, 34.7 cm^{-1}, 0.5 km mol^{-1}, 0.4 $Å^4$ amu^{-1}, 59.9 cm^{-1}, 0.5 km mol^{-1}, 0.3 $Å^4$ amu^{-1}, 72.9 cm^{-1}, 4.5 km mol^{-1}, 0.1 $Å^4$ amu^{-1}, 100.4 cm^{-1}, 5.2 km mol^{-1}, 0.2 $Å^4$ amu^{-1}.

Table S3.5B: MP2/aug-cc-pVDZ-PP vibrational frequencies, in cm^{-1}, infrared intensities, in km mol^{-1}, and Raman intensities, in $Å^4$ amu^{-1}, for the HB complex of CHF_2I and DME-d_6 and both monomers, as well as the complexation shift Δν.

	Monomer			HB complex			
	Frequency	IR int.	Raman int.	Frequency	Δν	IR int.	Raman int.
CHF_2I							
ν_1 (A')	3192.4	3.6	94.4	3206.7	14.3	14.3	100.6
ν_2 (A')	1279.7	99.2	7.5	1280.3	0.6	115.2	10.8
ν_3 (A')	1074.1	300.4	3.2	1068.1	-5.9	193.0	3.0
ν_4 (A')	652.5	81.8	18.4	650.9	-1.6	80.9	15.6
ν_5 (A')	549.4	2.9	1.8	550.0	0.6	4.8	1.6
ν_6 (A')	276.0	0.2	6.6	273.0	-2.9	0.05	6.0
ν_7 (A")	1346.0	4.1	2.7	1370.1	24.1	6.3	2.6
ν_8 (A")	1096.9	186.9	1.9	1091.6	-5.3	180.2	2.5
ν_9 (A")	277.0	0.0004	1.2	277.2	0.2	0.1	1.3
DME-d_6							
ν_1 (A_1)	2364.1	17.0	37.1	2365.5	1.4	13.0	28.9
ν_2 (A_1)	2171.1	32.1	166.2	2176.1	5.0	25.8	157.0
ν_3 (A_1)	1153.5	5.3	2.6	1148.8	-4.7	4.8	3.3
ν_4 (A_1)	1085.9	0.09	2.5	1084.9	-1.0	1.2	2.2
ν_5 (A_1)	1058.5	17.5	1.8	1060.2	1.6	11.3	1.8
ν_6 (A_1)	834.8	16.9	7.7	830.2	-4.6	20.2	7.4
ν_7 (A_1)	351.5	1.5	0.7	353.0	1.5	1.4	0.6
ν_8 (A_2)	2297.2	0.0	7.5	2308.4	11.2	0.2	6.0
ν_9 (A_2)	1065.8	0.0	4.2	1063.2	-2.6	59.0	3.6
ν_{10} (A_2)	877.6	0.0	2.2	876.7	-1.0	0.01	2.2
ν_{11} (A_2)	139.5	0.0	0.1	137.1	-2.4	0.002	0.06
ν_{12} (B_1)	2290.4	65.1	51.2	2302.1	11.7	58.0	46.7
ν_{13} (B_1)	1077.4	4.3	0.003	1076.1	-1.2	14.9	0.1
ν_{14} (B_1)	937.8	9.9	0.1	937.8	0.0	9.3	0.4
ν_{15} (B_1)	200.5	4.6	0.0	206.2	5.7	8.5	0.02
ν_{16} (B_2)	2360.7	10.6	31.7	2362.1	1.4	6.7	21.8
ν_{17} (B_2)	2164.0	44.9	0.03	2170.1	6.1	34.3	1.2
ν_{18} (B_2)	1170.3	134.3	0.9	1158.0	-12.3	124.3	1.0
ν_{19} (B_2)	1077.4	0.5	0.2	1076.7	-0.7	1.7	0.09
ν_{20} (B_2)	1066.1	1.6	1.1	1065.8	-0.3	40.2	0.8
ν_{21} (B_2)	860.9	0.08	0.9	861.1	0.2	0.2	0.8

Van der Waals vibrations: 14.8 cm^{-1}, 0.3 km mol^{-1}, 0.3 $Å^4$ amu^{-1}, 31.8 cm^{-1}, 0.8 km mol^{-1}, 0.3 $Å^4$ amu^{-1}, 32.5 cm^{-1}, 0.05 km mol^{-1}, 0.4 $Å^4$ amu^{-1}, 54.4 cm^{-1}, 0.5 km mol^{-1}, 0.3 $Å^4$ amu^{-1}, 61.5 cm^{-1}, 3.6 km mol^{-1}, 0.1 $Å^4$ amu^{-1}, 93.5 cm^{-1}, 2.3 km mol^{-1}, 0.3 $Å^4$ amu^{-1}.

Table S3.6A: MP2/aug-cc-pVDZ-PP vibrational frequencies, in cm^{-1}, infrared intensities, in km mol^{-1}, and Raman intensities, in $Å^4$ amu^{-1}, for the XB complex of CHF_2I and DME and both monomers, as well as the complexation shift Δν.

	Monomer			XB complex			
	Frequency	IR int.	Raman int.	Frequency	Δν	IR int.	Raman int.
CHF_2I							
ν_1 (A')	3192.4	3.6	94.4	3184.2	-8.2	6.8	115.7
ν_2 (A')	1279.7	99.2	7.5	1283.5	3.8	117.0	7.3
ν_3 (A')	1074.1	300.4	3.2	1069.5	-4.5	302.7	2.7
ν_4 (A')	652.5	81.8	18.4	656.7	4.2	61.2	29.1
ν_5 (A')	549.4	2.9	1.8	545.7	-3.7	2.4	2.4
ν_6 (A')	276.0	0.2	6.6	277.5	1.6	4.6	10.1
ν_7 (A")	1346.0	4.1	2.7	1344.9	-1.1	3.6	2.8
ν_8 (A")	1096.9	186.9	1.9	1080.6	-16.3	180.4	1.9
ν_9 (A")	277.0	0.0004	1.2	281.4	4.4	0.0007	1.4
DME							
ν_1 (A_1)	3188.7	20.1	87.6	3191.5	2.9	17.6	60.5
ν_2 (A_1)	3024.8	58.6	320.3	3032.5	7.7	57.1	308.3
ν_3 (A_1)	1505.9	2.9	5.6	1503.7	-2.2	6.6	5.6
ν_4 (A_1)	1473.5	0.0008	2.2	1472.9	-0.6	0.7	4.1
ν_5 (A_1)	1261.1	6.6	0.5	1260.9	-0.1	7.4	0.5
ν_6 (A_1)	942.4	34.7	9.8	930.5	-11.9	62.0	11.6
ν_7 (A_1)	416.8	2.3	1.0	416.3	-0.5	3.7	0.8
ν_8 (A_2)	3096.2	0.0	14.7	3110.3	14.1	0.4	14.2
ν_9 (A_2)	1474.8	0.0	11.4	1473.3	-1.6	0.6	9.2
ν_{10} (A_2)	1157.2	0.0	1.5	1155.8	-1.5	0.003	1.6
ν_{11} (A_2)	195.2	0.0	0.2	190.2	-5.1	0.003	0.1
ν_{12} (B_1)	3089.5	107.8	94.2	3104.2	14.6	92.4	123.2
ν_{13} (B_1)	1489.2	13.0	0.04	1488.7	-0.5	16.8	0.1
ν_{14} (B_1)	1187.2	7.2	0.04	1187.8	0.7	5.5	0.2
ν_{15} (B_1)	260.2	5.1	0.002	265.0	4.8	11.0	0.03
ν_{16} (B_2)	3187.3	24.6	59.2	3190.2	2.9	13.9	39.8
ν_{17} (B_2)	3018.4	55.2	0.6	3027.5	9.2	41.9	3.8
ν_{18} (B_2)	1490.1	10.3	1.0	1488.1	-2.0	8.7	0.6
ν_{19} (B_2)	1441.5	2.5	1.3	1441.1	-0.4	0.4	1.4
ν_{20} (B_2)	1191.9	98.1	0.7	1182.6	-9.3	76.1	0.4
ν_{21} (B_2)	1113.8	35.0	1.6	1107.6	-6.2	42.6	2.1

Van der Waals vibrations: 6.3 cm^{-1}, 2.0 km mol^{-1}, 0.1 $Å^4$ amu^{-1}, 29.0 cm^{-1}, 2.9 km mol^{-1}, 0.2 $Å^4$ amu^{-1}, 32.2 cm^{-1}, 0.2 km mol^{-1}, 0.5 $Å^4$ amu^{-1}, 64.0 cm^{-1}, 0.2 km mol^{-1}, 0.4 $Å^4$ amu^{-1}, 79.8 cm^{-1}, 0.08 km mol^{-1}, 0.1 $Å^4$ amu^{-1}, 99.2 cm^{-1}, 13.1 km mol^{-1}, 0.5 $Å^4$ amu^{-1}.

Table S3.6B: MP2/aug-cc-pVDZ-PP vibrational frequencies, in cm^{-1}, infrared intensities, in km mol^{-1}, and Raman intensities, in $Å^4$ amu^{-1}, for the XB complex of CHF_2I and DME-d_6 and both monomers, as well as the complexation shift Δν.

	Monomer			XB complex			
	Frequency	IR int.	Raman int.	Frequency	Δν	IR int.	Raman int.
CHF_2I							
ν_1 (A')	3192.4	3.6	94.4	3184.2	-8.2	6.9	115.5
ν_2 (A')	1279.7	99.2	7.5	1283.5	3.8	116.3	7.4
ν_3 (A')	1074.1	300.4	3.2	1069.4	-4.6	298.5	2.7
ν_4 (A')	652.5	81.8	18.4	656.7	4.2	61.1	29.1
ν_5 (A')	549.4	2.9	1.8	545.7	-3.7	2.4	2.4
ν_6 (A')	276.0	0.2	6.6	277.4	1.4	3.1	10.0
ν_7 (A")	1346.0	4.1	2.7	1344.9	-1.1	3.5	2.8
ν_8 (A")	1096.9	186.9	1.9	1080.6	-16.3	182.5	1.9
ν_9 (A")	277.0	0.0004	1.2	281.4	4.4	0.0009	1.5
DME-d_6							
ν_1 (A_1)	2364.1	17.0	37.1	2367.2	3.1	14.2	28.2
ν_2 (A_1)	2171.1	32.1	166.2	2175.8	4.7	33.4	155.2
ν_3 (A_1)	1153.5	5.3	2.6	1147.6	-5.9	9.6	5.8
ν_4 (A_1)	1085.9	0.09	2.5	1084.0	-1.9	1.3	2.5
ν_5 (A_1)	1058.5	17.5	1.8	1057.5	-1.0	39.0	1.7
ν_6 (A_1)	834.8	16.9	7.7	828.2	-6.6	30.3	8.3
ν_7 (A_1)	351.5	1.5	0.7	351.7	0.2	2.8	0.6
ν_8 (A_2)	2297.2	0.0	7.5	2308.1	10.9	0.2	7.1
ν_9 (A_2)	1065.8	0.0	4.2	1064.4	-1.3	0.2	3.3
ν_{10} (A_2)	877.6	0.0	2.2	876.4	-1.3	0.008	2.0
ν_{11} (A_2)	139.5	0.0	0.1	136.0	-3.5	0.001	0.1
ν_{12} (B_1)	2290.4	65.1	51.2	2301.9	11.5	54.5	65.8
ν_{13} (B_1)	1077.4	4.3	0.003	1076.7	-0.6	0.01	0.1
ν_{14} (B_1)	937.8	9.9	0.1	938.8	1.0	11.9	0.2
ν_{15} (B_1)	200.5	4.6	0.0	209.7	9.2	13.1	0.1
ν_{16} (B_2)	2360.7	10.6	31.7	2363.8	3.1	5.9	22.0
ν_{17} (B_2)	2164.0	44.9	0.03	2169.9	6.0	34.2	1.1
ν_{18} (B_2)	1170.3	134.3	0.9	1156.6	-13.7	114.8	0.9
ν_{19} (B_2)	1077.4	0.5	0.2	1075.6	-1.8	0.1	0.06
ν_{20} (B_2)	1066.1	1.6	1.1	1065.6	-0.6	3.3	1.1
ν_{21} (B_2)	860.9	0.08	0.9	859.5	-1.4	0.2	0.9

Van der Waals vibrations: 5.9 cm^{-1}, 1.8 km mol^{-1}, 0.07 $Å^4$ amu^{-1}, 26.8 cm^{-1}, 2.5 km mol^{-1}, 0.2 $Å^4$ amu^{-1}, 30.3 cm^{-1}, 0.2 km mol^{-1}, 0.5 $Å^4$ amu^{-1}, 59.5 cm^{-1}, 0.2 km mol^{-1}, 0.5 $Å^4$ amu^{-1}, 73.0 cm^{-1}, 0.03 km mol^{-1}, 0.07 $Å^4$ amu^{-1}, 87.0 cm^{-1}, 7.9 km mol^{-1}, 0.4 $Å^4$ amu^{-1}.

Table S3.7A: MP2/aug-cc-pVDZ-PP vibrational frequencies, in cm^{-1}, infrared intensities, in km mol^{-1}, and Raman intensities, in $Å^4$ amu^{-1}, for the HB complex with a secondary F···H-C interaction of CHF_2I and CH_3F and both monomers, as well as the complexation shift Δν.

	Monomer			HB complex (C-H···F + F···H-C)			
	Frequency	IR int.	Raman int.	Frequency	Δν	IR int.	Raman int.
CHF_2I							
ν_1 (A')	3192.4	3.6	94.4	3223.6	31.2	1.7	78.4
ν_2 (A')	1279.7	99.2	7.5	1284.1	4.4	104.4	7.8
ν_3 (A')	1074.1	300.4	3.2	1068.6	-5.5	278.4	3.2
ν_4 (A')	652.5	81.8	18.4	650.1	-2.4	81.9	17.1
ν_5 (A')	549.4	2.9	1.8	549.6	0.2	3.4	1.6
ν_6 (A')	276.0	0.2	6.6	274.5	-1.4	0.1	6.4
ν_7 (A")	1346.0	4.1	2.7	1344.4	-1.6	1.3	3.7
ν_8 (A")	1096.9	186.9	1.9	1093.9	-3.0	207.4	2.1
ν_9 (A")	277.0	0.0004	1.2	278.6	1.6	0.1	1.2
CH_3F							
ν_1 (A)	3095.0	32.1	161.3	3100.6	5.5	24.0	148.9
ν_2 (A)	1473.3	1.3	0.4	1472.3	-1.0	0.2	0.5
ν_3 (A)	1039.1	105.8	7.2	1020.5	-18.6	103.5	6.4
ν_4 (E)	3209.0	23.5	40.8	3219.1	10.1	17.9	35.9
ν_5 (E)	1491.9	4.4	4.1	1489.9	-2.0	7.6	3.4
ν_6 (E)	1188.8	1.3	1.7	1187.9	-0.9	1.0	1.7

Van der Waals vibrations: 24.7 cm^{-1}, 1.2 km mol^{-1}, 0.3 $Å^4$ amu^{-1}, 33.5 cm^{-1}, 2.0 km mol^{-1}, 0.08 $Å^4$ amu^{-1}, 44.3 cm^{-1}, 0.4 km mol^{-1}, 0.07 $Å^4$ amu^{-1}, 49.3 cm^{-1}, 4.2 km mol^{-1}, 0.1 $Å^4$ amu^{-1}, 70.7 cm^{-1}, 5.8 km mol^{-1}, 0.2 $Å^4$ amu^{-1}, 94.7 cm^{-1}, 7.0 km mol^{-1}, 0.1 $Å^4$ amu^{-1}.

Table S3.7B: MP2/aug-cc-pVDZ-PP vibrational frequencies, in cm^{-1}, infrared intensities, in km mol^{-1}, and Raman intensities, in $Å^4$ amu^{-1}, for the HB complex with a secondary F···D-C interaction of CHF_2I and CD_3F and both monomers, as well as the complexation shift Δν.

	Monomer			HB complex (C-H···F + F···D-C)			
	Frequency	IR int.	Raman int.	Frequency	Δν	IR int.	Raman int.
CHF_2I							
ν_1 (A')	3192.4	3.6	94.4	3223.6	31.2	1.4	79.8
ν_2 (A')	1279.7	99.2	7.5	1284.3	4.6	104.5	7.8
ν_3 (A')	1074.1	300.4	3.2	1067.4	-6.6	269.6	3.1
ν_4 (A')	652.5	81.8	18.4	650.1	-2.4	81.9	17.1
ν_5 (A')	549.4	2.9	1.8	549.6	0.2	3.4	1.6
ν_6 (A')	276.0	0.2	6.6	274.5	-1.4	0.08	6.4
ν_7 (A")	1346.0	4.1	2.7	1344.7	-1.3	1.3	3.6
ν_8 (A")	1096.9	186.9	1.9	1094.5	-2.4	197.6	2.7
ν_9 (A")	277.0	0.0004	1.2	278.6	1.6	0.09	1.2
CD_3F							
ν_1 (A)	2213.6	25.3	80.8	2217.0	3.5	19.4	74.3
ν_2 (A)	1132.6	37.4	1.2	1124.1	-8.5	25.0	1.0
ν_3 (A)	986.8	65.9	6.1	976.0	-10.8	72.9	5.7
ν_4 (E)	2383.6	15.7	21.7	2391.6	8.0	12.2	18.8
ν_5 (E)	1082.3	1.2	1.5	1080.9	-1.4	12.5	1.0
ν_6 (E)	909.9	2.6	1.6	908.2	-1.6	2.6	1.5

Van der Waals vibrations: 21.6 cm^{-1}, 1.1 km mol^{-1}, 0.2 $Å^4$ amu^{-1}, 30.4 cm^{-1}, 0.3 km mol^{-1}, 0.2 $Å^4$ amu^{-1}, 36.3 cm^{-1}, 1.7 km mol^{-1}, 0.03 $Å^4$ amu^{-1}, 47.1 cm^{-1}, 3.5 km mol^{-1}, 0.2 $Å^4$ amu^{-1}, 63.5 cm^{-1}, 4.9 km mol^{-1}, 0.1 $Å^4$ amu^{-1}, 93.2 cm^{-1}, 5.6 km mol^{-1}, 0.1 $Å^4$ amu^{-1}.

Table S3.8A: MP2/aug-cc-pVDZ-PP vibrational frequencies, in cm^{-1}, infrared intensities, in km mol^{-1}, and Raman intensities, in $Å^4$ amu^{-1}, for the HB complex with a secondary I···H-C interaction of CHF_2I and CH_3F and both monomers, as well as the complexation shift Δν.

	Monomer			HB complex (C-H···F + I···H-C)			
	Frequency	IR int.	Raman int.	Frequency	Δν	IR int.	Raman int.
CHF_2I							
ν_1 (A')	3192.4	3.6	94.4	3221.3	28.8	10.3	75.5
ν_2 (A')	1279.7	99.2	7.5	1282.9	3.2	111.0	9.5
ν_3 (A')	1074.1	300.4	3.2	1072.0	-2.0	303.6	3.4
ν_4 (A')	652.5	81.8	18.4	650.4	-2.1	84.0	17.2
ν_5 (A')	549.4	2.9	1.8	550.8	1.4	4.6	1.8
ν_6 (A')	276.0	0.2	6.6	273.7	-2.3	0.1	6.6
ν_7 (A")	1346.0	4.1	2.7	1361.3	15.3	5.1	2.0
ν_8 (A")	1096.9	186.9	1.9	1095.5	-1.4	181.8	1.9
ν_9 (A")	277.0	0.0004	1.2	276.3	-0.7	0.0	1.1
CH_3F							
ν_1 (A)	3095.0	32.1	161.3	3101.5	6.5	23.2	151.2
ν_2 (A)	1473.3	1.3	0.4	1472.7	-0.6	0.3	0.5
ν_3 (A)	1039.1	105.8	7.2	1019.6	-19.5	106.8	7.3
ν_4 (E)	3209.0	23.5	40.8	3220.4	11.4	16.3	46.6
ν_5 (E)	1491.9	4.4	4.1	1488.7	-3.2	8.7	3.2
ν_6 (E)	1188.8	1.3	1.7	1187.4	-1.4	0.9	1.6

Van der Waals vibrations: 9.5 cm^{-1}, 0.8 km mol^{-1}, 0.2 $Å^4$ amu^{-1}, 33.1 cm^{-1}, 0.1 km mol^{-1}, 0.4 $Å^4$ amu^{-1}, 33.9 cm^{-1}, 5.3 km mol^{-1}, 0.002 $Å^4$ amu^{-1}, 41.3 cm^{-1}, 1.0 km mol^{-1}, 0.03 $Å^4$ amu^{-1}, 62.9 cm^{-1}, 5.4 km mol^{-1}, 0.1 $Å^4$ amu^{-1}, 88.6 cm^{-1}, 6.3 km mol^{-1}, 0.1 $Å^4$ amu^{-1}.

Table S3.8B: MP2/aug-cc-pVDZ-PP vibrational frequencies, in cm^{-1}, infrared intensities, in km mol^{-1}, and Raman intensities, in $Å^4$ amu^{-1}, for the HB complex with a secondary I···D-C interaction of CHF_2I and CD_3F and both monomers, as well as the complexation shift Δν.

	Monomer			HB complex (C-H···F + I···D-C)			
	Frequency	IR int.	Raman int.	Frequency	Δν	IR int.	Raman int.
CHF_2I							
ν_1 (A')	3192.4	3.6	94.4	3221.2	28.8	5.0	93.6
ν_2 (A')	1279.7	99.2	7.5	1283.3	3.6	111.9	9.4
ν_3 (A')	1074.1	300.4	3.2	1071.7	-2.4	306.8	3.7
ν_4 (A')	652.5	81.8	18.4	650.4	-2.2	83.9	17.3
ν_5 (A')	549.4	2.9	1.8	550.8	1.4	4.6	1.8
ν_6 (A')	276.0	0.2	6.6	273.7	-2.3	0.05	6.6
ν_7 (A")	1346.0	4.1	2.7	1361.3	15.3	5.2	2.0
ν_8 (A")	1096.9	186.9	1.9	1095.5	-1.4	180.0	1.8
ν_9 (A")	277.0	0.0004	1.2	276.3	-0.7	0.0007	1.1
CD_3F							
ν_1 (A)	2213.6	25.3	80.8	2217.7	4.1	19.0	75.9
ν_2 (A)	1132.6	37.4	1.2	1123.9	-8.7	19.7	1.4
ν_3 (A)	986.8	65.9	6.1	975.5	-11.3	73.2	6.3
ν_4 (E)	2383.6	15.7	21.7	2392.7	9.1	12.7	19.7
ν_5 (E)	1082.3	1.2	1.5	1080.1	-2.3	6.9	1.0
ν_6 (E)	909.9	2.6	1.6	907.9	-2.0	2.8	1.5

Van der Waals vibrations: 8.9 cm^{-1}, 0.6 km mol^{-1}, 0.1 $Å^4$ amu^{-1}, 27.5 cm^{-1}, 0.7 km mol^{-1}, 0.003 $Å^4$ amu^{-1}, 32.4 cm^{-1}, 0.1 km mol^{-1}, 0.4 $Å^4$ amu^{-1}, 34.9 cm^{-1}, 4.4 km mol^{-1}, 0.02 $Å^4$ amu^{-1}, 56.6 cm^{-1}, 4.7 km mol^{-1}, 0.1 $Å^4$ amu^{-1}, 86.7 cm^{-1}, 4.9 km mol^{-1}, 0.1 $Å^4$ amu^{-1}.

Table S3.9A: MP2/aug-cc-pVDZ-PP vibrational frequencies, in cm^{-1}, infrared intensities, in km mol^{-1}, and Raman intensities, in $Å^4$ amu^{-1}, for the XB complex of CHF_2I and CH_3F and both monomers, as well as the complexation shift Δν.

	Monomer			XB complex			
	Frequency	IR int.	Raman int.	Frequency	Δν	IR int.	Raman int.
CHF_2I							
ν_1 (A')	3192.4	3.6	94.4	3189.1	-3.3	4.9	104.1
ν_2 (A')	1279.7	99.2	7.5	1283.0	3.3	107.3	6.8
ν_3 (A')	1074.1	300.4	3.2	1071.6	-2.4	296.0	3.1
ν_4 (A')	652.5	81.8	18.4	656.9	4.4	71.8	20.6
ν_5 (A')	549.4	2.9	1.8	547.7	-1.8	2.6	1.9
ν_6 (A')	276.0	0.2	6.6	278.1	2.1	1.0	6.9
ν_7 (A")	1346.0	4.1	2.7	1345.2	-0.8	3.8	2.7
ν_8 (A")	1096.9	186.9	1.9	1087.3	-9.6	185.2	1.9
ν_9 (A")	277.0	0.0004	1.2	279.5	2.5	0.0	1.3
CH_3F							
ν_1 (A)	3095.0	32.1	161.3	3098.6	3.5	27.0	157.4
ν_2 (A)	1473.3	1.3	0.4	1471.9	-1.4	0.7	0.4
ν_3 (A)	1039.1	105.8	7.2	1023.5	-15.6	117.0	7.4
ν_4 (E)	3209.0	23.5	40.8	3216.1	7.1	19.5	40.7
ν_5 (E)	1491.9	4.4	4.1	1489.8	-2.1	6.7	3.6
ν_6 (E)	1188.8	1.3	1.7	1187.4	-1.4	1.3	1.7

Van der Waals vibrations: 6.6 cm^{-1}, 6.0 km mol^{-1}, 0.1 $Å^4$ amu^{-1}, 9.5 cm^{-1}, 0.1 km mol^{-1}, 0.01 $Å^4$ amu^{-1}, 22.5 cm^{-1}, 3.5 km mol^{-1}, 0.4 $Å^4$ amu^{-1}, 39.7 cm^{-1}, 2.1 km mol^{-1}, 0.3 $Å^4$ amu^{-1}, 50.7 cm^{-1}, 0.4 km mol^{-1}, 0.2 $Å^4$ amu^{-1}, 79.8 cm^{-1}, 12.8 km mol^{-1}, 0.1 $Å^4$ amu^{-1}.

Table S3.9B: MP2/aug-cc-pVDZ-PP vibrational frequencies, in cm^{-1}, infrared intensities, in km mol^{-1}, and Raman intensities, in $Å^4$ amu^{-1}, for the XB complex of CHF_2I and CD_3F and both monomers, as well as the complexation shift Δν.

	Monomer			XB complex			
	Frequency	IR int.	Raman int.	Frequency	Δν	IR int.	Raman int.
CHF_2I							
ν_1 (A')	3192.4	3.6	94.4	3189.1	-3.3	4.9	103.6
ν_2 (A')	1279.7	99.2	7.5	1283.1	3.3	106.7	6.9
ν_3 (A')	1074.1	300.4	3.2	1071.1	-2.9	298.7	2.7
ν_4 (A')	652.5	81.8	18.4	656.9	4.4	71.7	20.6
ν_5 (A')	549.4	2.9	1.8	547.7	-1.8	2.6	1.9
ν_6 (A')	276.0	0.2	6.6	278.1	2.1	1.0	6.9
ν_7 (A")	1346.0	4.1	2.7	1345.2	-0.8	3.8	2.7
ν_8 (A")	1096.9	186.9	1.9	1087.3	-9.6	185.2	1.9
ν_9 (A")	277.0	0.0004	1.2	279.5	2.5	0.0	1.3
CD_3F							
ν_1 (A)	2213.6	25.3	80.8	2215.7	2.1	22.1	78.4
ν_2 (A)	1132.6	37.4	1.2	1125.9	-6.7	33.6	1.5
ν_3 (A)	986.8	65.9	6.1	977.4	-9.4	79.0	6.6
ν_4 (E)	2383.6	15.7	21.7	2389.3	5.7	13.0	21.7
ν_5 (E)	1082.3	1.2	1.5	1080.8	-1.6	1.4	1.3
ν_6 (E)	909.9	2.6	1.6	908.3	-1.5	3.0	1.6

Van der Waals vibrations: 6.2 cm^{-1}, 5.1 km mol^{-1}, 0.09 $Å^4$ amu^{-1}, 6.8 cm^{-1}, 0.08 km mol^{-1}, 0.007 $Å^4$ amu^{-1}, 21.4 cm^{-1}, 3.3 km mol^{-1}, 0.4 $Å^4$ amu^{-1}, 38.6 cm^{-1}, 1.5 km mol^{-1}, 0.2 $Å^4$ amu^{-1}, 47.5 cm^{-1}, 0.3 km mol^{-1}, 0.2 $Å^4$ amu^{-1}, 77.2 cm^{-1}, 10.7 km mol^{-1}, 0.1 $Å^4$ amu^{-1}.

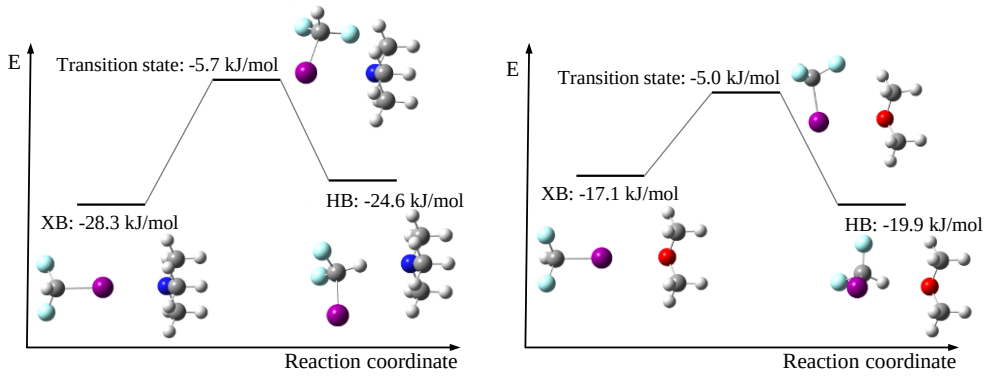

Figure. S3.1: MP2/aug-cc-pVDZ-PP reaction coordinate describing the tunnelling motion between the XB and HB isomers for CHF_2I with TMA (left) and DME (right). All energies given refer to the complexation energy obtained by using the energies for the two non-interacting species. For the complexes of CHF_2I with CH_3F, similar calculations were attempted, but no transition state was found.

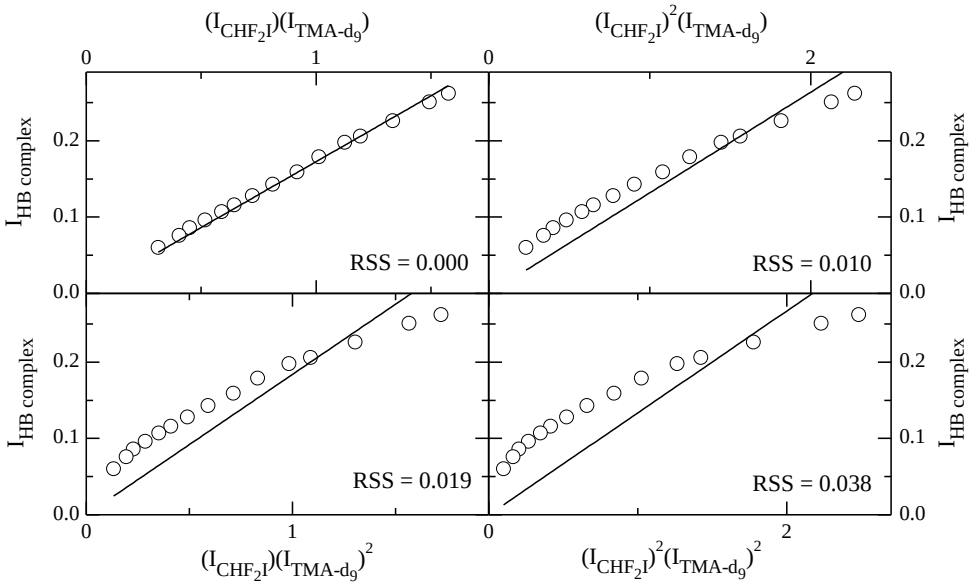

Figure S3.2: Concentration study plots of the $CHF_2I{\cdot}TMA\text{-}d_9$ HB complex at 130 K in LKr. Integrated intensity of the complex is plotted against the product of monomer intensities $\left(I_{CHF_2I}\right)^x\left(I_{TMA-d_9}\right)^y$. Top left: $x = 1, y = 1$, top right: $x = 2, y = 1$, bottom left $x = 1, y = 2$ and bottom right $x = 2, y = 2$. Additionally, residual sum of square values (RSS) have been included.

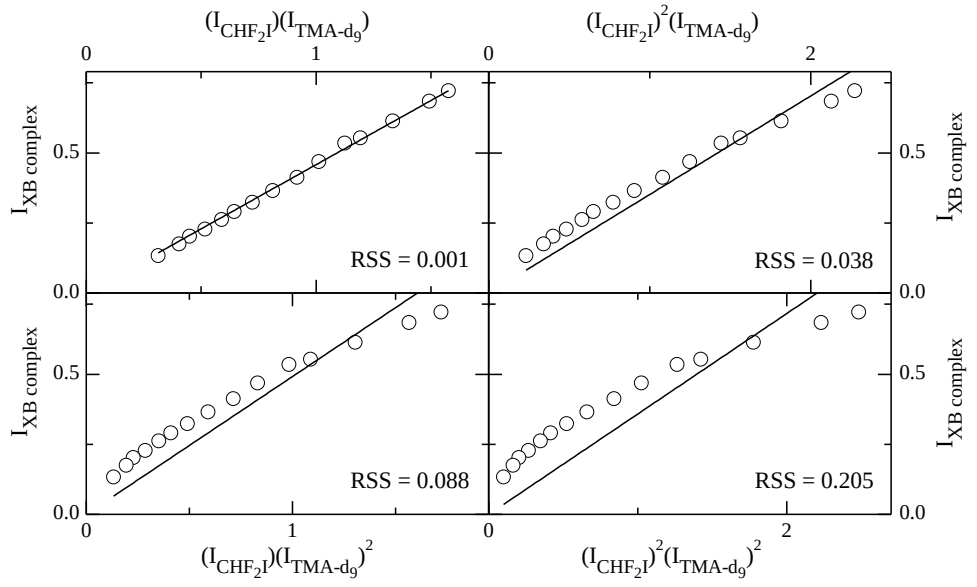

Figure S3.3: Concentration study plots of the $CHF_2I{\cdot}TMA\text{-}d_9$ XB complex at 130 K in LKr. Integrated intensity of the complex is plotted against the product of monomer intensities $\left(I_{CHF_2I}\right)^x\left(I_{TMA-d_9}\right)^y$. Top left: $x = 1, y = 1$, top right: $x = 2, y = 1$, bottom left $x = 1, y = 2$ and bottom right $x = 2, y = 2$. Additionally, residual sum of square values (RSS) have been included.

Chapter 4

How does the Lewis base influence the halogen bond/hydrogen bond competition?

Complexes of CHF_2I with TMP, DMS and CH_3Cl.

This chapter has been published as:

Geboes, Y.; De Proft, F.; Herrebout, W. A., Taking the halogen bonding-hydrogen bonding competition one step further: Complexes of difluoroiodomethane with trimethylphosphine, dimethyl sulfide and chloromethane, *Acta Crystallographica B* **2017**, *B73*, 168-178.

Abstract

To rationalize the driving factors in the competition of halogen bonding and hydrogen bonding, the complexes of the combined halogen/hydrogen bond donor CHF_2I with the Lewis bases TMP, DMS and CH_3Cl are studied. For all Lewis bases, *ab initio* calculations lead to XB and HB complexes. FTIR experiments involving solutions of mixtures of CHF_2I with TMP($-d_9$) or DMS($-d_6$) in LKr confirm the coexistence of XB and HB complex. Also for solutions containing CH_3Cl, evidence for formation of binary associations is found, but no definitive assignment of the multiple complex bands could be made. Using van 't Hoff plots, the experimental complexation enthalpies for the XB and HB complex of CHF_2I with TMP are determined to be -15.4(4) and -10.5(3) kJ mol^{-1}, respectively, while for the XB and HB complexes with DMS, the values are -11.3(5) and -7.7(6) kJ mol^{-1}, respectively. The experimental observation that for both TMP and DMS the XB complex is more stable than the HB complex supports the finding that softer Lewis bases tend to favour iodine halogen bonding over hydrogen bonding.

4.1 Introduction

In recent years, the competition between the halogen bonding and hydrogen bonding has been subject of various experimental and theoretical studies. [1-17] However, a systematic approach investigating the driving factors of the XB-HB bond competition at thermodynamic equilibrium has not yet been reported. In chapter 3, this investigation is initiated by performing an experimental study on the IR and Raman spectra of LKr solutions containing the combined hydrogen/halogen bond donor CHF_2I and one of the Lewis bases TMA, DME or CH_3F. For the solutions containing CHF_2I and TMA, it was found that the XB complex had a higher complexation enthalpy than the HB complex, whereas complexes of similar strength were found for the mixtures containing DME and only HB complex was observed in the solutions of MF. The experimental data were found to be in line with, *ab initio* calculations for complexes of CHF_2I with a series of lone pair containing Lewis bases suggesting that softer Lewis bases tend to favour C-I···Y halogen bonding over C-H···Y hydrogen bonding. To further build on this hypothesis, we have now expanded the experimental data towards complexes with additional (softer) Lewis bases containing a second period element with a lone pair, namely TMP, DMS and CH_3Cl. To avoid spectral congestion and aid assignment of the complex bands, measurements are performed using the regular (DMS, TMP) and fully deuterated (DMS-d_6, TMP-d_9) Lewis bases.

4.2 Results

4.2.1 *Ab initio* calculations

For both the complexes of CHF_2I with DMS and TMP, *ab initio* MP2/aug-cc-pVDZ-PP calculations lead to a stable XB and HB complex geometry. For CH_3Cl, a single XB complex geometry and two different HB complex geometries are obtained. Apart from the C-H···Cl hydrogen bond, the latter geometries are discriminated by the appearance of an additional C-H···F or C-H···I secondary interaction, (*vide infra*). All

complex geometries are shown in Figure 4.1, while Cartesian coordinates of all monomers and complexes are given in Tables S4.1 and S4.2 of the SI. The intermolecular parameters and energetics for all complexes are summarized in Table 4.1.

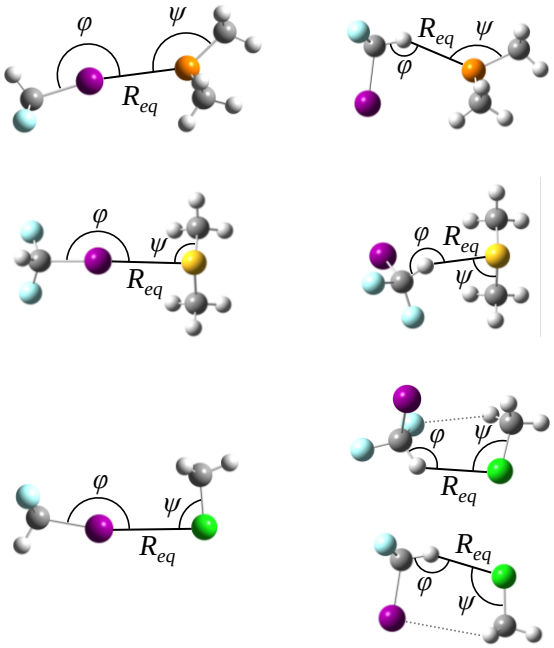

Figure 4.1: *Ab initio* calculated MP2/aug-cc-pVDZ-PP geometries for the XB (left) and HB (right) complexes of CHF_2I with TMP (top), DMS (middle) and CH_3Cl (bottom). For CH_3Cl, the HB complex with a secondary C-H···F interaction is shown on the top, while the HB complex with a secondary C-H···I interaction is shown in the bottom. Both secondary interactions are indicated by a grey dotted line.

For the XB complexes, geometries are found in which the C-I···Y angles are close to 170°. This is consistent with earlier observations that halogen bonds, due to the location and shape of the σ-hole in the electrostatic potential, form nearly linear complexes. [18] For the HB complexes, a larger deviation from linear behaviour is observed, with C-H···Y bonding angles lying between 125.9° and 153.1°. This deviation can be explained by the possibility to form additional secondary stabilizing interactions with the Lewis base due to the absence of nonbonding valence electrons on the hydrogen atom, leading to a reduced directionality compared to halogen bonding. [19]

Table 4.1: Intermolecular distance R_{eq} (Å), bond angles (°), MP2/aug-cc-pVDZ-PP ΔE(DZ) and CCSD(T)/CBS ΔE(CCSD(T)) extrapolated complexation energies, calculated vapour phase complexation enthalpies $\Delta H°$ (vap,calc), the calculated complexation enthalpies in LKr ($\Delta H°$ (LKr,calc)) and the corresponding experimentally obtained complexation enthalpies ($\Delta H°$ (LKr)) (kJ mol^{-1}) for the complexes of CHF_2I with TMP, DMS and CH_3Cl.

	TMP		DMS		CH_3Cl		
	XB	HB	XB	HB	XB	HB (F)[b]	HB (I)[c]
$R_{eq}=R_{X\cdots Y}$ [a]	3.50	2.84	3.45	2.84	3.64	2.86	2.78
$\varphi_{C\text{-}X\cdots Y}$ [a]	170.4	145.2	170.3	128.5	169.1	125.9	153.1
$\psi_{C\text{-}Y\cdots X}$ [a]	143.7/103.8/103.8	131.3/111.7/111.7	90.8/90.8	97.0/110.2	86.4	99.5	107.9
ΔE (DZ)	-17.0	-18.9	-18.8	-18.9	-9.9	-12.9	-11.7
ΔE (CCSD(T))	-18.3	-20.4	-19.5	-20.6	-10.9	-14.6	-13.0
$\Delta H°$ (vap,calc)	-16.0	-17.8	-17.2	-18.0	-8.6	-12.1	-10.5
$\Delta H°$ (LKr,calc)	-14.9	-13.2	-15.3	-11.9	-7.1	-7.2	-6.9
Experimental $\Delta H°$ (LKr)	-15.4(4)	-10.5(3)	-11.3(5)	-7.7(6)			

[a] X = I, H, Y = Cl, S, P
[b] HB (F): HB complex with secondary C-H···F interaction,
[c] HB (I): HB complex with secondary C-H···I interaction.

The presence of secondary interactions was studied using the NCI index visualized using NCIPLOT [20-21]. Plots of the reduced density gradient versus the electron density multiplied by the sign of the second Hessian eigenvalue and figures showing the gradient isosurfaces are given in Figures S4.1 to S4.3 of the SI. For the complexes involving TMP, a single isosurface between iodine and phosphorus is observed for the XB complex, whereas in the HB complex, apart from the isosurface between the hydrogen and phosphorus atom, a second isosurface between iodine and the methyl groups of TMP is observed. In the HB complex with DMS an additional part of the isosurface is observed between the fluorine atom and the methyl group of DMS (at the backside of the image), explaining the tilted position of CHF_2I with a C-H···S angle of 128.5°. In the XB complex, two small circular isosurfaces are also observed between the fluorine atoms and the methyl groups of DMS. These surfaces are caused by the

proximity of both entities due to the nearly perpendicular position of the lone pair on the sulfide atom to the C-S-C plane. For the XB complex with CH_3Cl a single isosurface is observed with an appendage between iodine and the methyl group due to the small C-Cl···I angle. In the HB complexes additional isosurfaces between the methyl group and the fluorine or iodine atom are observed as the CHF_2I molecule is tilted towards CH_3Cl in both complexes. It is noteworthy that the electrophilic donor molecule interacts with the chlorine atom almost perpendicular to the C-Cl bonding axis, the C-Cl···X bonding angles lying between 86.4° and 107.9°, due to the accumulated electron density on chlorine in this region.

Comparison of the calculated complexation energies yields a higher complexation energy for the HB complex than the XB complex for all three Lewis bases at all levels of theory. Upon application of the solvent effects from MC-FEP, this strength order changes for the complexes with TMP and DMS, whereas similar complexation enthalpies are found for the complex with CH_3Cl.

4.2.2 Infrared measurements

To allow full characterization of the spectral features observed in the C-H stretching region of CHF_2I and avoid overlap with the modes from the Lewis bases, the spectra and assignments involving the deuterated Lewis bases DMS-d_6 and TMP-d_9 are reported in this chapter. Spectra and assignments of the non-deuterated species are included in Figures S4.4 and S4.5 and Tables S4.10 and S4.11 of the SI. For CH_3Cl the non-deuterated species was used, as spectral congestion was not an issue for this Lewis base. The assignment of CHF_2I, [17] TMP, [22] TMP-d_9, [23] DMS, [24] DMS-d_6 [23] and CH_3Cl [25-28] is primarily based on experimental studies available in the literature, aided by *ab initio* calculations, for which the results can be found in Tables S4.3 to S4.9 of the SI.

In the spectra of mixtures with TMP-d_9 and TMP, shown in Figures 4.2 and S4.4 respectively, a clear distinction between both calculated complex geometries can be made in the C-F stretching region around 1100 cm^{-1}. In panel 4.2B, the spectrum of the

mixture (trace *a*), rescaled monomer spectra (traces *b* and *c*) and the resulting complex spectrum (trace *d*) are shown for this region. In trace *d*, the presence of both complex geometries is clearly visible for ν_8 ($\nu_{C\text{-}F,as}$) with redshifts of -19.9 cm^{-1} and -5.8 cm^{-1} for the XB and HB complex respectively. Also in the C-I stretching region and CF_2-bending region, shown in panels C and D respectively, two complex bands are observed with complexation shifts agreeing favourably with the calculated values. For the CHF_2I C-H stretching region shown in panel A, however, no clear distinction between the complexes, which both have a predicted redshift, could be made. An overview of experimentally observed monomer bands, complexation shifts and the corresponding calculated shifts is given in Table 4.2 for TMP-d_9 and Table S4.10 for TMP.

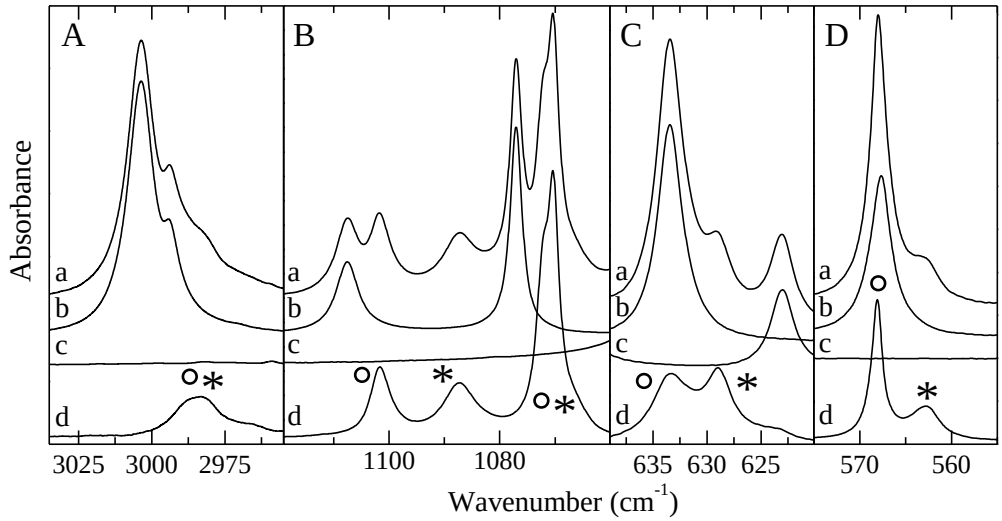

Figure 4.2: Infrared spectra of selected spectral regions for the mixtures of CHF_2I with TMP-d_9 dissolved in LKr at 130 K. In each panel, trace *a* represents the mixed solution, while traces *b* and *c* show the rescaled spectra of the solutions containing only CHF_2I or TMP-d_9, respectively. Trace *d* represents the spectrum of the complex which is obtained by subtracting the rescaled traces *b* and *c* from trace *a*. Bands due to the XB and HB complexes observed in traces *d* are marked with an asterisk (*) or open circle (°), respectively. Estimated mole fractions of the solutions of the mixtures are 5.6×10^{-3} for CHF_2I and 2.8×10^{-3} for TMP-d_9 in panel A, 5.6×10^{-5} for CHF_2I and 3.8×10^{-3} for TMP-d_9 in panel B, 6.6×10^{-5} for CHF_2I and 2.4×10^{-3} for TMP-d_9 in panel C and 1.9×10^{-3} for CHF_2I and 4.7×10^{-3} for TMP-d_9 in panel D.

As with the spectra from TMP-d_9, a clear distinction between both complex geometries formed with DMS-d_6 can be made when looking at the ν_8 mode of CHF_2I, shown in panel B of Figure 4.3, with a complexation shift of -14.7 cm^{-1} for the XB complex and -3.4 cm^{-1} for the HB complex. Also in the spectral region of the CF_2-bending mode, shown in panel 4.3C, two complex bands are observed with shifts of 0.2 cm^{-1} and -3.0 cm^{-1}, corresponding to the HB and XB complex respectively. When looking to the CHF_2I C-H stretching mode (ν_1) for the mixture with DMS-d_6, shown in panel 4.3A, only a redshifted band is observed, even though a blueshift is predicted for the HB complex. An overview of experimentally observed monomer bands, complexation shifts and the corresponding calculated shifts is given in Table 4.3 for DMS-d_6 and Table S4.11 for DMS.

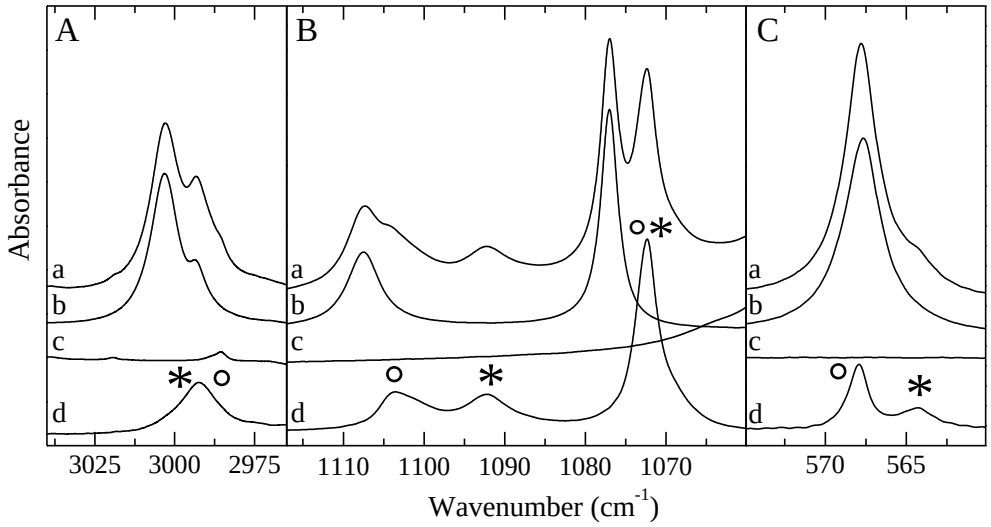

Figure 4.3: Infrared spectra of selected spectral regions for the mixtures of CHF_2I with DMS-d_6 dissolved in LKr at 130 K. In each panel, trace *a* represents the mixed solution, while traces *b* and *c* show the rescaled spectra of the solutions containing only CHF_2I or DMS-d_6, respectively. Trace *d* represents the spectrum of the complex which is obtained by subtracting the rescaled traces *b* and *c* from trace *a*. Bands due to the XB and HB complexes observed in traces *d* are marked with an asterisk (*) or open circle (°), respectively. Estimated mole fractions of the solutions of the mixtures are 9.4×10^{-4} for CHF_2I and 1.9×10^{-3} for DMS-d_6 in panel A, 5.6×10^{-5} for CHF_2I and 5.6×10^{-3} for DMS-d_6 in panel B and 9.4×10^{-4} for CHF_2I and 1.9×10^{-3} for DMS-d_6 in panel C.

For the mixtures of CH_3Cl with CHF_2I, several complex bands are observed in multiple spectral region upon subtraction. For both the symmetrical and asymmetrical C-F stretches (ν_3 and ν_8), shown in Figure 4.4C, at least two redshifted bands are observed. The assignment of the complex bands to specific complex geometries is however complicated by the small values of the experimental and calculated complexation shifts for most bands, which is typical for rather weak noncovalent interactions. For the CHF_2I C-H stretching mode, shown in panel 4.4A, a redshift of -3.0 cm^{-1} is calculated for the XB complex whereas blueshifts of 15.7 cm^{-1} and 12.7 cm^{-1} are calculated for the HB complexes. Upon inspection of the spectrum, a redshifted band is observed with a blueshifted shoulder on the left. Using a band fit analysis, shifts of -0.4 cm^{-1} and 8.3 cm^{-1} were obtained. Due to the limited spectral intensity, which is consistent with the calculated low infrared intensities for the CHF_2I ν_1 mode in HB complexes, given in Tables S4.7 and S4.8, the assignment of the HB complexes should be taken with the necessary prudence. For none of the complex bands of the CH_3Cl vibrational modes a distinction between the different geometries could be made experimentally. Furthermore, in none of the spectral regions complex bands were sufficiently resolved to construct a van 't Hoff plot to obtain complexation enthalpies of the complexes. An overview of experimentally observed monomer bands, complexation shifts and the corresponding calculated shifts for the CHF_2I·CH_3Cl complex is given in Table 4.4.

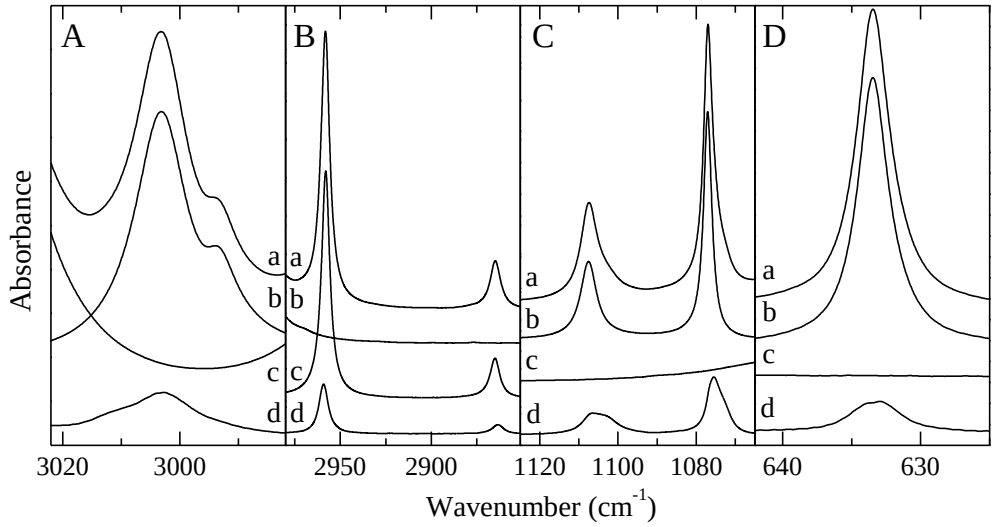

Figure 4.4: Infrared spectra of selected spectral regions for the mixtures of CHF_2I with CH_3Cl dissolved in LKr at 130 K. In each panel, trace *a* represents the mixed solution, while traces *b* and *c* show the rescaled spectra of the solutions containing only CHF_2I or CH_3Cl, respectively. Trace *d* represents the spectrum of the complex which is obtained by subtracting the rescaled traces *b* and *c* from trace *a*. Estimated mole fractions of the solutions of the mixtures are 9.4×10^{-3} for CHF_2I and 1.9×10^{-2} for CH_3Cl in panel A, 9.4×10^{-3} for CHF_2I and 2.3×10^{-3} for CH_3Cl in panel B, 5.6×10^{-5} for CHF_2I and 1.8×10^{-2} for CH_3Cl in panel C and 1.2×10^{-4} for CHF_2I and 1.9×10^{-2} for CH_3Cl in panel D.

Table 4.2: Experimental vibrational frequencies for the monomers and complexes, as well as experimental complexation shifts ($\Delta\nu_{exp}$) and MP2/aug-cc-pVDZ-PP calculated complexation shifts ($\Delta\nu_{calc}$), in cm^{-1}, for the XB complex and HB complex of CHF_2I with TMP-d_9 dissolved in LKr at 130 K.

Assignment		$\nu_{monomer}$	$\nu_{complex,XB}$	$\Delta\nu_{exp,XB}$	$\Delta\nu_{calc,XB}$	$\nu_{complex,HB}$	$\Delta\nu_{exp,HB}$	$\Delta\nu_{calc,HB}$
CHF_2I	ν_1	3003.3	2984.8	-18.5	-12.1	2984.8	-18.5	-19.6
	$\nu_5 + \nu_7 + \nu_8$	2993.9	-		-24.3	-		21.0
	$\nu_3 + \nu_8$	2171.2	2144.0	-27.2	-23.4	2160.0	-11.2	-8.1
	$2\nu_3$	2144.1	2128.4	-15.7	-12.3	2134.2	-9.9	-7.8
	ν_7	1337.2	1335.6	-1.6	-2.3	-		23.5
	ν_2	1247.6	1243.5	-4.1	-1.1	1248.3	0.7	0.9
	ν_8	1107.6	1087.7	-19.9	-17.2	1101.8	-5.8	-4.2
	ν_3	1077.1	1070.5	-6.6	-6.1	1072.5	-4.6	-3.9
	ν_4	633.6	629.2	-4.4	-5.4	633.5	-0.1	-1.3
	ν_5	567.8	562.9	-4.9	-4.7	568.2	0.4	1.6
	$2\nu_6$	536.8	-		-7.6	-		-6.3
TMP-d_9	ν_{12}	2227.6	2229.8	2.2	2.3	2229.8	2.2	1.9
	ν_1	2217.1	2219.8	2.7	2.7	2219.8	2.7	2.4
	ν_{13}	2217.1	2219.8	2.7	2.8	2219.8	2.7	2.4
	ν_{14}	2219.5	2120.8	1.3	1.6	2120.8	1.3	1.5
	ν_2	2218.0	2119.5	1.5	1.6	2119.5	1.5	1.5
	ν_3	1047.8	1047.3	-0.5	-1.1	1074.3	-0.5	-0.4
	ν_{15}	1042.8	1042.1	-0.7	-1.1	1042.1	-0.7	-0.8
	ν_{16}	1035.4	1035.1	-0.3	-1.0	1035.1	-0.3	-0.4
	ν_4	1015.0	1016.3	1.3	0.3	1016.3	1.3	0.2
	ν_{17}	1004.3	1006.2	1.9	1.1	1006.2	1.9	0.7
	ν_5	782.5	782.6	0.1	0.2	782.6	0.1	1.5
	ν_{18}	756.6	759.3	2.7	3.0	759.3	2.7	2.3
	ν_{19}	646.1	651.3	5.2	5.7	649.9	3.8	3.9
	ν_{20}	623.0	623.8	0.8	0.5	623.8	0.8	1.5

Table 4.3: Experimental vibrational frequencies for the monomers and complexes, as well as experimental complexation shifts ($\Delta\nu_{exp}$) and MP2/aug-cc-pVDZ-PP calculated complexation shifts ($\Delta\nu_{calc}$), in cm^{-1}, for the XB complex and HB complex of CHF_2I with DMS-d_6 dissolved in LKr at 130 K.

Assignment		$\nu_{monomer}$	$\nu_{complex,XB}$	$\Delta\nu_{exp,XB}$	$\Delta\nu_{calc,XB}$	$\nu_{complex,HB}$	$\Delta\nu_{exp,HB}$	$\Delta\nu_{calc,HB}$
CHF_2I	ν_1	3003.3	2992.8	-10.5	-9.3	2992.8	-10.5	9.7
	$\nu_5 + \nu_7 + \nu_8$	2993.9	-		-20.3	-		-3.8
	$\nu_3 + \nu_8$	2170.7	2150.6	-20.1	-19.3	2162.3	-8.4	-8.0
	$2\nu_3$	2143.7	2131.0 [a]	-12.7	-9.4	2131.0 [a]	-12.7	-9.3
	ν_7	1337.3	1335.8	-1.5	-1.8	1335.8	-1.5	-1.1
	ν_2	1247.6	1247.8	0.2	-0.2	1247.8	0.2	-2.6
	ν_8	1107.3	1092.6	-14.7	-14.6	1103.9	-3.4	-3.4
	ν_3	1077.1	1072.4	-4.7	-4.7	1072.4	-4.7	-4.6
	ν_4	633.6	632.2	-1.4	-2.1	632.2	-1.4	-2.1
	ν_5	567.7	564.7	-3.0	-3.8	567.9	0.2	0.7
	$2\nu_6$	536.3	532.6	-3.7	-3.9	532.6	-3.7	-5.0
DMS-d_6	ν_1	2243.9	2246.3	2.4	1.9	2246.3	2.4	2.3
	ν_{16}	2243.9	2246.3	2.4	1.7	2246.3	2.4	1.2
	ν_{12}	2226.7	2230.2	3.5	2.8	2230.2	3.5	3.9
	ν_{17}	2131.6	2131.0	-0.6	-0.3	2131.0	-0.6	0.5
	ν_2	2129.7	2129.3	-0.4	-0.2	2131.0	1.3	0.8
	ν_3	1064.3	-		-2.4	-		-1.1
	ν_{18}	1050.4	1048.4	-2.0	-2.3	1049.7	-0.7	-1.5
	ν_{13}	1044.4	1043.9	-0.5	-1.2	1043.9	-0.5	-2.1
	ν_4	1025.5	1025.4	-0.1	-1.4	1025.4	-0.1	-1.4
	ν_{19}	1009.0	1008.7	-0.3	-1.3	1008.7	-0.3	-1.4
	ν_5	828.1	828.0	-0.1	-0.3	828.0	-0.1	0.2
	ν_{14}	744.8	746.4	1.6	2.1	746.4	1.6	2.1
	ν_6	642.1	640.9	-1.2	-1.4	640.9	-1.2	-1.2

[a] Overlap with complex bands of DMS-d_6 modes ν_{17} and ν_2.

Table 4.4: Experimental vibrational frequencies for the monomers and complexes, as well as experimental complexation shifts ($\Delta\nu_{exp}$) and MP2/aug-cc-pVDZ-PP calculated complexation shifts ($\Delta\nu_{calc}$), in cm^{-1}, for the XB complex and HB complexes with a secondary C-H···F interaction (F) or secondary C-H···I interaction (I) of CHF_2I with CH_3Cl dissolved in LKr at 130 K.

Assignment	$\nu_{monomer}$	$\nu_{complex,XB}$	$\Delta\nu_{exp,XB}$	$\Delta\nu_{calc,XB}$	$\nu_{complex,HB(F)}$	$\Delta\nu_{exp,HB(F)}$	$\Delta\nu_{calc,HB(F)}$	$\nu_{complex,HB(I)}$	$\Delta\nu_{exp,HB(I)}$	$\Delta\nu_{calc,HB(I)}$
CHF_2I										
ν_1	3003.3	3002.9	-0.4	-3.0	3011.6	8.3	15.7	3011.6	8.3	12.7
$\nu_5 + \nu_7 + \nu_8$	2993.9	-		-9.6	-		-6.1	-		10.4
$\nu_3 + \nu_8$	2171.2	2166.0	-5.2	-9.8	2166.0	-5.2	-9.4	-		-0.7
$2\nu_3$	2144.1	2140.2	-3.9	-5.0	2133.9	-10.2	-12.6	2140.2	-3.9	-2.2
ν_7	1337.2	-		-0.9	-		-3.2	-		8.7
ν_2	1247.6	1249.4	1.8	1.5	1249.4	1.8	1.1	1247.3	-0.3	-0.6
ν_8	1107.6	1103.0	-4.6	-7.3	1103.0	-4.6	-3.1	1107.0	-0.6	0.4
ν_3	1077.1	1075.6	-1.5	-2.5	1072.9	-4.2	-6.3	1075.6	-1.5	-1.1
ν_4	633.6	634.2	0.6	2.0	632.6	-1.0	-2.5	632.6	-1.0	-2.3
ν_5	567.8	568.0	0.2	-1.4	568.0	0.2	0.2	568.0	0.2	1.4
$2\nu_6$	536.8	-		2.0	-		-2.0	-		-4.1
CH_3Cl										
ν_4[a]	3037.6	-			-			-		
ν_4	3032.0	3033.9	1.9	2.2	3033.9	1.9	5.0	3033.9	1.9	5.5
ν_1	2958.0	2959.2	1.2	-0.3	2959.2	1.2	1.7	2959.2	1.2	2.0
$2\nu_5$	2865.3	2863.5	-1.8	-6.0	2863.5	-1.8	-4.9	2863.5	-1.8	-8.3
ν_5	1444.5	1443.3[b]	-1.2	-3.0	1443.3[b]	-1.2	-2.5	1443.3[b]	-1.2	-4.2
ν_2	1348.8	1349.1	0.3	-0.4	1349.1	0.3	0.3	1349.1	0.3	0.2
ν_6	1016.2	1017.3	1.1	0.7	1017.3	1.1	2.2	1017.3	1.1	1.6
ν_3 (^{35}Cl)	726.2	720.0	-6.2	-7.2	720.0	-6.2	-8.9	720.0	-6.2	-8.5
ν_3 (^{37}Cl)	720.6	714.4	-6.2	-7.2	714.4	-6.2	-8.9	714.4	-6.2	-8.5

[a] Partially resolved dimer band. [25]

[b] Exact frequency could not be determined due to an impurity in the CHF_2I sample.

4.2.3 Complexation stoichiometries and enthalpies

To experimentally verify the complex stoichiometries of the complexes formed with TMP and DMS, concentration studies were performed at 130 K. Estimated mole fractions of the solutions varied between 3.8×10^{-5} and 5.6×10^{-3} for CHF_2I, 9.4×10^{-4} and 4.7×10^{-3} for TMP, 1.9×10^{-3} and 5.6×10^{-3} for DMS and 2.3×10^{-4} and 2.1×10^{-2} for CH_3Cl.The results are shown in Figures S4.6 to S4.9 of the SI, and confirm a 1:1 complex stoichiometry for all four complexes.

Complexation enthalpies for the complexes with DMS and TMP were determined by measurements of solutions between 120 K and 156 K to create van 't Hoff plots. An illustration of these van 't Hoff plots is given in Figure S4.10 of the SI. For the XB and HB complex of $CHF_2I{\cdot}TMP(-d_9)$, average complexation enthalpies of -15.4(4) kJ mol^{-1} and -10.5(3) kJ mol^{-1} respectively were determined in LKr. For the $CHF_2I{\cdot}DMS(-d_6)$ complexes average complexation enthalpies of -11.3(5) kJ mol^{-1} and -7.7(6) kJ mol^{-1} were determined in LKr. For mixtures of CHF_2I and CH_3Cl no complexation enthalpies could be determined due to a lack of separation of the observed complex bands. The average experimental complexation enthalpies are given in Table 4.1, while an overview of the parameters used in the van 't Hoff plots is given in Tables S4.12 to S4.15 of the SI.

4.3 Discussion

The spectral data reported above clearly illustrate the occurrence of XB and HB complexes in solutions of CHF_2I with $TMP(-d_9)$. The experimental complexation enthalpies derived from the van 't Hoff plots, -15.4(4) kJ mol^{-1} for the XB complex and -10.5(3) kJ mol^{-1} for the HB complex, are in agreement with the calculated values of -14.9 kJ mol^{-1} and -13.2 kJ mol^{-1}. This experimental data thus confirms the computational prediction that the XB complex is more stable than the HB complex in a LKr solution when using TMP as a Lewis base.

Also for the mixtures of CHF_2I with DMS or DMS-d_6, the presence of two different types of complexes can be deduced for several vibrational modes. By combining the experimental data with *ab initio* harmonic vibrational frequencies, the complex bands observed can be assigned confidently to the XB or the HB complex. The experimental complexation enthalpies derived from the van 't Hoff plots, -11.3(5) kJ mol^{-1} and -7.7(6) kJ mol^{-1}, again are in agreement with the calculated values of -15.3 and -11.9 kJ mol^{-1}. As before, the XB complex is found to be the most stable complex geometry both experimentally and computationally.

One of the main discrepancies between the observed spectra and the calculated complexation shifts of the CHF_2I·DMS(-d_6) complexes is the absence of the blueshifted band in the CHF_2I C-H stretching region (ν_1) for the HB complex. Furthermore, the calculated blueshifted band for the HB complex also strongly contrasts with the data for TMP(-d_9), where both the calculations and the experiments lead to a weakening of the C-H bond and a redshift of its stretching frequency in the complex. The differences between experiment and theory can, in principle, be related to various phenomena including, amongst others, differences in anharmonicity perturbing the frequencies in monomer and complexes. Also, different effects of solvation leading to the different solvent induced frequency shifts in the cryosolutions studied might be envisaged.

It should be noted that a very similar behaviour as that observed for CHF_2I·DMS was also observed for the complexes of halothane ($CF_3CHBrCl$) with benzene by Michielsen, et al. [29], the blueshift for the C-H stretching fundamental of halothane derived from the *ab initio* data and the redshift from spectroscopic data in liquid krypton being 10.2 and -1.1 cm^{-1}. Based on complementary data derived using FTIR and Raman studies of the same complex formed in supersonic jet expansion showing that at significantly lower temperatures a blueshift of 7.7 cm^{-1} is observed, the discrepancies between the cryosolution experiments and the calculated (*ab initio*) data were proposed to be due to the increase of the population of the low-frequency van der Waals modes of the complex with the temperature. The driving force of the model is the observation that, due to strong anharmonicity of the van der Waals stretching

mode, the molecules in the complex tend to move away from each other, yielding an intramolecular distance that on average is somewhat larger than that of the equilibrium geometry.

To support the idea that also in the HB complex of CHF_2I with DMS the complexation shift for the C-H stretching mode is largely affected by temperature effects, two different model calculations were initiated in this study. In the first approach, different geometries for the complex were obtained by changing the C···S intermolecular distance. Subsequently, for all geometries obtained, partial geometry optimizations were initiated in which the intermolecular distance was fixed and harmonic vibrational frequencies and complexation shifts were derived for all vibrational modes. Typical results for the CHF_2I ν_1 and ν_8 modes derived using this procedure are given in Figure 4.5. The data for the C-H stretching mode clearly illustrate that upon decreasing the C···S intermolecular distance, the blueshift for the C-H stretching mode is predicted to further increase, while an increase of the intermolecular distance first leads to a decrease of the blueshift and then changes it into a redshift. Most notably, the behaviour of the CHF_2I ν_1 mode does not change continually, but rather jumps from -3.9 cm^{-1} to -13.0 cm^{-1} between 3.83 and 3.84 Å. Comparison of the geometries obtained shows that at this distance, the secondary C-H···F interaction is disrupted, causing the CHF_2I molecule to turn away from the DMS molecule, yielding a complex of C_s symmetry. The relationship between this change in geometry and frequency shift was further analysed by freezing the C-H···S or C-H···S and C-H···S-C angles during optimization, which led to continuous C···S distance-ν_1 frequency curves with minima of -3.8 cm^{-1} and -3.0 cm^{-1} at a C···S distance of 4.3 Å, as shown in Figure S4.11 of the SI. Furthermore, by restricting the HB complex to C_s symmetry during optimization, a redshift of -11.4 cm^{-1} is calculated at a C···S distance of 3.77 Å.

Comparison of the data for the CHF_2I ν_1 and ν_8 modes clearly shows that not all modes are affected in the same way. This observation is in line with the fact that in most cases the calculated and experimentally observed frequency shifts agree favourably, and that only in specific cases, such as a C-H stretching mode in blue-shifting hydrogen bonds, strong temperature effects could be expected to appear.

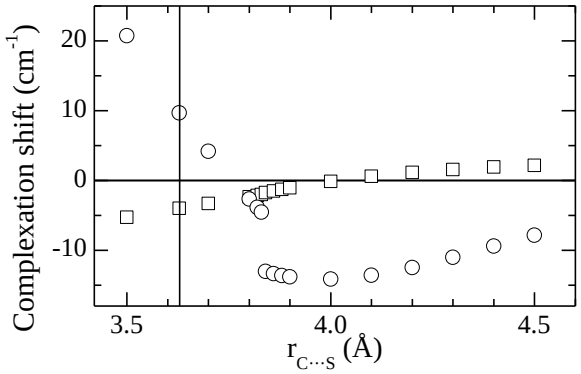

Figure 4.5: Complexation shifts (in cm^{-1}) of the CHF_2I ν_1 mode (○) and CHF_2I ν_8 mode (□) of the HB complex plotted against the C···S distance (in Å). For reference, the C···S equilibrium distance of 3.63 Å is indicated by a vertical line.

In the second model used, the above procedure was adopted to take into account the influence of the other van der Waals vibrations as well. To this end, a Monte Carlo simulation of the dynamical behaviour of the complex was set up in which the intermolecular distance and the relative orientation of the rigid monomers were varied simultaneously, and the energy of the complex was calculated using MP2/aug-cc-pVDZ-PP calculations. Corrections for BSSE were avoided in order to keep the amount of CPU-time acceptable. Random distance variations between 0.05 to 0.15 Å and random angle variations between 5.0° to 15° resulted, *via* application of the Metropolis algorithm to the MP2 energies, in an acceptance ratio of 45%. Of the accepted structures, one in every eight was used for further analysis. The latter consisted in optimizing the structure of both moieties of the complex, at the same level as above, while keeping the van der Waals parameters fixed. For the structure thus obtained, the C-H stretching frequency was determined by determining the corresponding Hessian. By using appropriate binning of the obtained frequencies, the distribution shown in Figure S4.12 of the SI was obtained at a temperature of 130 K. The infrared intensity weighted average over the distribution yielded a complexation shift of -29.4 cm^{-1} for the C-H stretching mode, as compared to a shift of 9.7 cm^{-1} for the same mode in the equilibrium geometry. The data clearly shows that also in the second model, significant temperature effects are predicted and that also in this model, the blueshift obtained for the equilibrium geometry is converted in a redshift when

temperature effects are corrected for. A further analysis of the data was not pursued, as all data were obtained without corrections for BSSE, and thus should only be considered as approximate.

When studying mixtures of CHF_2I with CH_3Cl, multiple complex bands are observed in several spectral regions, as shown in Figure 4.4. By comparing experimental complexation shifts with computational shifts, definitive assignment of all bands was deemed impossible, and the assignments given in Table 4.4 should thus be interpreted with the necessary prudence. Although it is clear that at least two different complexes are present in the solutions, the absence of the third complex geometry cannot be confirmed. Furthermore, due to the overlap of the complex bands in all observed spectral regions, no van 't Hoff plots could be constructed to aid the assignments.

Combining the experimental complexation enthalpies with those of the study involving CH_3F, DME and TMA, a halogen bond strength order N > P > O ≈ S is obtained for these Lewis bases, while the strength order for hydrogen bonding is found to be N > O ≈ P > S > F. It should be noted that these strength orders are in agreement with the previously determined halogen bond strength order N > S > O and hydrogen bond strength order N > O > S. [30-34]

From the previous results, it becomes abundantly clear that secondary interactions often play a major role in the competition of noncovalent interactions. The formation of secondary interactions in HB complexes is aided by two factors, when comparing to XB complexes. Firstly, the directionality of hydrogen bonds is far less stringent than in halogen bonds, which nearly always occur at a bonding angle approaching 180° as a consequence of the localization of the σ-hole, whereas hydrogen bond angles can be considerably less. [19, 35-37] Secondly, due to the increased size of the halogen atom as compared to hydrogen, the C-X···B bonding distance in XB complexes is significantly larger than the C-H···B bonding distance, which aids the formation of secondary interactions in the latter complexes. Even though the high directionality and lack of secondary interactions yields highly predictable structures for XB complexes, which is a major strong suit in several fields of applications such as crystal engineering, the lack

of secondary interactions may well be their biggest weakness when having to compete with other noncovalent interactions, such as hydrogen bonds.

Apart from the ability to form secondary interactions, the chemical hardness/softness of the Lewis base also seems to play a major role in the competition of these noncovalent interactions, as mentioned in our previous study [17], which has shown that halogen bonding seems to prevail over hydrogen bonding when softer Lewis bases are involved. The results from this study support this finding, as the XB complex clearly prevails over the HB complex in mixtures of CHF_2I with TMP($-d_9$) or DMS($-d_6$), whereas a similar complexation enthalpy was found for the harder Lewis base DME. The ratio of the XB/HB complexation enthalpy rises from 1.29(3) for TMA($-d_9$) and 1.10(8) for DME($-d_6$) to 1.47(6) for TMP($-d_9$) and 1.47(13) for DMS($-d_6$) when descending from the second to third row of the periodic table. This seems consistent with the general HSAB theory, as the iodine atom through which the halogen bond is formed is softer than the hydrogen atom. To evaluate this tendency, values for the chemical hardness of the different Lewis bases were calculated using the method of Tozer and De Prof, based on the MP2/aug-cc-pVDZ structures. [38] An overview of the complexation enthalpies and chemical hardnesses for all Lewis bases is given in Table 4.5, while a plot of the enthalpy ratio of $\frac{\Delta H^\circ_{XB}}{\Delta H^\circ_{HB}}$ versus chemical hardness η is given in Figure S4.13 of the SI. From these data it becomes clear that for the three softest Lewis bases, with a nearly identical global chemical hardness, TMA, TMP and DMS, the complexation enthalpy of the XB complex is 1.29 to 1.47 times higher than for the HB complex, while for the slightly harder Lewis base DME (η = 6.6 eV) this ratio diminishes to 1.10. For the hardest Lewis base studied, CH_3F (η = 8.5 eV), no XB complex was observed, [17] whereas for the slightly softer Lewis base CH_3Cl (η = 7.1 eV) traces of XB complex are still observed. It should however be noted that this analysis is based on the use of the global hardness of the base, rather than a local hardness so that, e.g., TMA and TMP have almost the same global hardness, whereas one expects that locally, the nitrogen atom in TMA represents a harder site than the P atom in TMP, in accordance with the higher atomic hardness of N vs. P.

Table 4.5: Overview of the experimental complexation enthalpies (in kJ mol^{-1}) for the XB ($\Delta H°_{XB}$) and HB complexes ($\Delta H°_{HB}$) with CHF_2I in liquid krypton, enthalpy ratio $\frac{\Delta H°_{XB}}{\Delta H°_{HB}}$ and chemical hardness η (in eV) for TMA, DME, CH_3F, TMP, DMS and CH_3Cl.

Lewis base	$\Delta H°_{XB}$ (LKr)	$\Delta H°_{HB}$ (LKr)	$\frac{\Delta H°_{XB}}{\Delta H°_{HB}}$	η (eV) [b]
TMA [a]	-19.0(3)	-14.7(2)	1.29(3)	5.6
DME [a]	-11.5(6)	-10.5(5)	1.10(8)	6.6
CH_3F [a]		-5.1(6)		8.5
TMP	-15.4(4)	-10.5(3)	1.47(6)	5.5
DMS	-11.3(5)	-7.7(6)	1.47(13)	5.7
CH_3Cl				7.1

[a] Results from Nagels, et al. [17]
[b] Calculated using the method described by Tozer and De Proft [38]

In order to gain more insight into the driving forces of halogen and hydrogen bonding, an EDA was performed, for which details can be found in previous publications by Nagels, et al. [17,] Pinter, et al. [39] and an overview of the results can be found in Table 4.6. From these data it is clear that the electrostatic (ΔV_{elst}) and orbital interaction (ΔE_{oi}) components of the interaction energy for the HB complexes increase towards the softer Lewis bases at the bottom of the table. For the XB complexes this tendency is even more outspoken, the complex with TMA being an outlier. The stronger increase in ΔV_{elst} and ΔE_{oi} for the XB complex also means that these values are about 1.5-2 times higher than for the HB complexes for the softest Lewis bases DMS, TMA and TMP, whereas comparable values for ΔV_{elst} and ΔE_{oi} are found for the XB and HB complexes with the hardest Lewis bases. When comparing ΔV_{elst} and ΔE_{oi} directly, it can be seen that the relative contribution of ΔE_{oi} increases towards the softer Lewis bases for both types of complexes, but remains consistently higher for the XB complexes as compared to the equivalent HB complexes. However, the Pauli repulsion energy (ΔE_{Pauli}) also increases more rapidly for the XB complex than the HB complex, thus reducing the effect of the increase in stabilization energy to the interaction energy (ΔE_{int}). Dispersion contributions remain relatively constant throughout the series of Lewis bases studied, although the contributions are consistently higher for the HB

complexes, a consequence of the fact that they are more readily able to form secondary interactions than their XB counterparts, as shown in the NCI-plots in Figures S4.1-S4.3 of the SI. Furthermore, as expected for relatively weak noncovalent interactions, all strain energies are negligible, the values being less than 1 kJ mol^{-1}. The negative strain energies for the HB complexes with CH_3Cl and TMP are a consequence of the difference in computational method used for the optimization (MP2/aug-cc-pVDZ-PP) and single point calculations in this analysis (PBE/TZ2P).

T**able 4.6:** Interaction energy (ΔE_{int}) and its components, ΔE_{Pauli}, ΔV_{elst}, ΔE_{oi} and dispersion (E_{disp}), strain energy ΔE_{strain} and complexation energy (ΔE^{DFT}) obtained at PBE/TZ2P level in kJ mol^{-1} of the complexes between CHF_2I and several Lewis bases, including their chemical hardness η (in eV).

	η (eV) [a]		ΔE_{Pauli}	ΔV_{elst} [b]	ΔE_{oi} [b]	E_{disp}	ΔE_{int}	ΔE_{strain}	ΔE^{DFT}
CH_3F	8.5	HB (H···I)	9.1	-14.1 (70)	-6.0 (30)	-4.7	-15.6	0.4	-15.2
		HB (H···F)	9.1	-13.9 (73)	-5.2 (27)	-5.8	-15.8	0.6	-15.3
		XB	9.1	-11.3 (70)	-4.9 (30)	-3.1	-10.2	0.7	-9.6
CH_3Cl	7.1	HB (H···I)	9.0	-11.2 (63)	-6.5 (37)	-5.8	-14.6	-0.2	-14.7
		HB (H···F)	9.9	-12.1 (67)	-6.0 (33)	-7.2	-15.5	0.0	-15.5
		XB	11.4	-11.3 (61)	-7.2 (39)	-4.0	-11.0	0.1	-10.9
DME	6.6	HB	19.0	-23.0 (68)	-10.8 (32)	-8.7	-23.5	0.3	-23.2
		XB	29.1	-27.5 (65)	-15.0 (35)	-5.8	-19.1	0.8	-18.4
DMS	5.7	HB	17.8	-19.6 (63)	-11.4 (37)	-9.8	-23.0	0.0	-22.9
		XB	35.0	-29.6 (56)	-23.4 (44)	-6.1	-24.1	0.3	-23.9
TMA	5.6	HB	30.8	-33.5 (64)	-18.6 (36)	-9.5	-30.8	0.3	-30.7
		XB	75.4	-63.4 (63)	-37.1 (37)	-8.5	-33.7	0.6	-33.1
TMP	5.5	HB	19.8	-22.5 (62)	-13.8 (38)	-7.9	-24.3	-0.1	-24.4
		XB	37.3	-32.0 (56)	-24.8 (44)	-5.3	-24.7	0.4	-24.4

[a] Calculated using the method of Tozer and De Proft [38]

[b] The relative contributions of the electrostatic and orbital interaction energies to the stabilization are indicated in brackets in percentages.

4.4 Conclusions

Ab initio calculations of the interactions between CHF_2I and TMP, DMS or CH_3Cl yielded both XB complexes and HB complexes for all three Lewis bases. For all Lewis bases, the highest complexation energies are found for the HB complexes at the MP2/aug-cc-pVDZ(-PP) and extrapolated CCSD(T)/CBS levels of theory. By application of solvent corrections and statistical thermodynamics, this strength order is reversed, yielding higher complex enthalpies in LKr for the XB complexes with TMP and DMS, as well as similar complex enthalpies for CH_3Cl. By analysis of the NCI index, the existence of secondary interactions in all three HB complexes is revealed, whereas these are largely absent in the XB complex geometries.

The experimental FTIR study of mixtures of CHF_2I with these Lewis bases in LKr, combined with the *ab initio* calculated frequency shifts revealed the coexistence of XB and HB complex in mixtures of TMP($-d_9$) and DMS($-d_6$). For the mixtures involving CH_3Cl, no definitive assignment of the complex bands belonging to at least two complex isomers could be made. The absence of a blueshifted band for the CHF_2I C-H stretching mode in the mixtures of CHF_2I with DMS-d_6, corresponding to the HB complex, has been rationalized as a temperature dependent behaviour due to the anharmonicity of the van der Waals stretching mode. Complexation enthalpies of -15.4(4) kJ mol^{-1} and -10.5(3) kJ mol^{-1} were determined for the XB and HB complex of CHF_2I with TMP($-d_9$) respectively by construction of a van ‘t Hoff plot. For the XB and HB complexes of CHF_2I with DMS($-d_6$), complexation enthalpies of -11.3(5) and -7.7(6) kJ mol^{-1} have been measured. These measurements confirm that the XB complexes have a higher complexation enthalpy than the corresponding HB complexes, as predicted by the calculated complexation enthalpies.

The experimental complexation enthalpies further confirm the observation that softer Lewis bases tend to favour iodine halogen bonding over hydrogen bonding at thermodynamic equilibrium. Furthermore, it can be concluded that the lack of ability to form secondary interactions, due to its linearity and increased intermolecular distance, hinders halogen bonding in its competition with HB at equilibrium conditions.

4.5 References

1 M. D. Perera, J. Desper, A. S. Sinha, C. B. Aakeroy, *CrystEngComm*, 2016, ***18***, 8631-8636.

2 C. B. Aakeröy, C. L. Spartz, S. Dembowski, S. Dwyre, J. Desper, *IUCrJ*, 2015, ***2***, 498-510.

3 T. Shirman, M. Boterashvili, M. Orbach, D. Freeman, L. J. W. Shimon, M. Lahav, M. E. van der Boom, *Cryst. Growth Des.*, 2015, ***15***, 4756-4759.

4 S. W. L. Hogan, T. van Mourik, *J. Comput. Chem.*, 2016, ***37***, 763-770.

5 M. Domagała, P. Matczak, M. Palusiak, *Comput. Theor. Chem.*, 2012, ***998***, 26-33.

6 S. Y. Oh, C. W. Nickels, F. Garcia, W. Jones, T. Friščić, *CrystEngComm*, 2012, ***14***, 6110-6114.

7 J. Marti-Rujas, L. Colombo, J. Lu, A. Dey, G. Terraneo, P. Metrangolo, T. Pilati, G. Resnati, *Chem. Commun.*, 2012, ***48***, 8207-8209.

8 J. Lieffrig, O. Jeannin, T. Guizouarn, P. Auban-Senzier, M. Fourmigué, *Cryst. Growth Des.*, 2012, ***12***, 4248-4257.

9 H. D. Arman, R. L. Gieseking, T. W. Hanks, W. T. Pennington, *Chem. Commun.*, 2010, ***46***, 1854-1856.

10 G. Minguez Espallargas, F. Zordan, L. Arroyo Marin, H. Adams, K. Shankland, J. van de Streek, L. Brammer, *Chem. - Eur. J.*, 2009, ***15***, 7554-7568.

11 C. B. Aakeröy, N. Schultheiss, A. Rajbanshi, J. Desper, C. Moore, *Cryst. Growth Des.*, 2009, ***9***, 432-441.

12 I. Alkorta, F. Blanco, M. Solimannejad, J. Elguero, *J. Phys. Chem. A*, 2008, ***112***, 10856-10863.

13 C. B. Aakeröy, M. Fasulo, N. Schultheiss, J. Desper, C. Moore, *J. Am. Chem. Soc.*, 2007, ***129***, 13772-13773.

14 C. B. Aakeröy, J. Desper, B. A. Helfrich, P. Metrangolo, T. Pilati, G. Resnati, A. Stevenazzi, *Chem. Commun. (Cambridge, U. K.)*, 2007, ***41***, 4236-4238.

15 S. Zhu, C. Xing, W. Xu, Z. Li, *Tetrahedron Lett.*, 2004, ***45***, 777-780.

16 E. Corradi, S. V. Meille, M. T. Messina, P. Metrangolo, G. Resnati, *Angew. Chem., Int. Ed.*, 2000, ***39***, 1782-1786.

17 N. Nagels, Y. Geboes, B. Pinter, F. De Proft, W. A. Herrebout, *Chem. - Eur. J.*, 2014, ***20***, 8433-8443.

18 P. Metrangolo, H. Neukirch, T. Pilati, G. Resnati, *Acc. Chem. Res.*, 2005, ***38***, 386-395.

19 Z. P. Shields, J. S. Murray, P. Politzer, *Int. J. Quantum Chem.*, 2010, ***110***, 2823-2832.

20 E. R. Johnson, S. Keinan, P. Mori-Sánchez, J. Contreras-García, A. J. Cohen, W. Yang, *J. Am. Chem. Soc.*, 2010, ***132***, 6498-6506.

21 J. Contreras-García, E. R. Johnson, S. Keinan, R. Chaudret, J.-P. Piquemal, D. N. Beratan, W. Yang, *J. Chem. Theory Comput.*, 2011, ***7***, 625-632.

22 D. C. McKean, G. P. McQuillan, W. F. Murphy, F. Zerbetto, *J. Phys. Chem.*, 1990, ***94***, 4820-4831.

23 B. Michielsen, C. Verlackt, B. J. van der Veken, W. A. Herrebout, *J. Mol. Struct.*, 2012, ***1023***, 90-95.
24 D. Hauchecorne, A. Moiana, B. J. van der Veken, W. A. Herrebout, *Phys. Chem. Chem. Phys.*, 2011, ***13***, 10204-10213.
25 Y. Futami, S. Kudoh, F. Ito, T. Nakanaga, M. Nakata, *J. Mol. Struct.*, 2004, ***690***, 9-16.
26 J. L. Duncan, M. M. Law, *J. Mol. Spectrosc.*, 1990, ***140***, 13-30.
27 A. J. Barnes, H. E. Hallam, J. D. R. Howells, G. F. Scrimshaw, *J. Chem. Soc., Faraday Trans. 2*, 1973, ***69***, 738-749.
28 E. W. Jones, R. J. L. Popplewell, H. W. Thompson, *Spectrochim. Acta*, 1966, ***22***, 669-680.
29 B. Michielsen, J. J. J. Dom, B. J. van der Veken, S. Hesse, Z. Xue, M. A. Suhm, W. A. Herrebout, *Phys. Chem. Chem. Phys.*, 2010, ***12***, 14034-14044.
30 H. A. Bent, *Chem. Rev.*, 1968, ***68***, 587-648.
31 J. P. Sheridan, D. E. Martire, Y. B. Tewari, *J. Am. Chem. Soc.*, 1972, ***94***, 3294-3298.
32 D. E. Martire, J. P. Sheridan, J. W. King, S. E. O'Donnell, *J. Am. Chem. Soc.*, 1976, ***98***, 3101-3106.
33 J. F. Bertrán, M. Rodríguez, *Org. Magn. Reson.*, 1979, ***12***, 92-94.
34 J. F. Bertrán, M. Rodríguez, *Org. Magn. Reson.*, 1980, ***14***, 244-246.
35 A. C. Legon, *Phys. Chem. Chem. Phys.*, 2010, ***12***, 7736-7747.
36 A. C. Legon, *Struct. Bond.*, 2008, ***126***, 17-64.
37 P. Politzer, K. E. Riley, F. A. Bulat, J. S. Murray, *Comput. Theor. Chem.*, 2012, ***998***, 2-8.
38 D. J. Tozer, F. De Proft, *J. Phys. Chem. A*, 2005, ***109***, 8923-8929.
39 B. Pinter, N. Nagels, W. A. Herrebout, F. De Proft, *Chem. - Eur. J.*, 2013, ***19***, 519-530.

4.6 Supporting information

Table S4.1.1: Cartesian coordinates of the MP2/aug-cc-pVDZ-PP optimized geometry of CHF_2I.

C_s	X	Y	Z
CHF_2I			
C	0.461801	-1.276126	0.000000
H	1.552810	-1.382611	0.000000
F	-0.060896	-1.882815	1.101579
F	-0.060896	-1.882815	-1.101579
I	-0.060896	0.810001	0.000000

Table S4.1.2: Cartesian coordinates of the MP2/aug-cc-pVDZ optimized geometry of TMP.

C_{3v}	X	Y	Z
TMP			
P	0.000000	0.000000	0.618978
C	0.000000	1.626598	-0.285498
H	-0.889964	2.208825	-0.001487
H	0.889964	2.208825	-0.001487
H	0.000000	1.481355	-1.378927
C	-1.408675	-0.813299	-0.285498
H	-1.467917	-1.875144	-0.001487
H	-2.357881	-0.333681	-0.001487
H	-1.282891	-0.740678	-1.378927
C	1.408675	-0.813299	-0.285498
H	2.357881	-0.333681	-0.001487
H	1.467917	-1.875144	-0.001487
H	1.282891	-0.740678	-1.378927

Table S4.1.3: Cartesian coordinates of the MP2/aug-cc-pVDZ optimized geometry of DMS.

C_{2v}	X	Y	Z
DMS			
S	0.000000	0.674247	0.000000
C	-1.370330	-0.522675	0.000000
H	-2.309643	0.047454	0.000000
H	-1.334542	-1.152689	-0.900834
H	-1.334542	-1.152688	0.900834
C	1.370330	-0.522675	0.000000
H	1.334542	-1.152689	-0.900834
H	2.309643	0.047454	0.000000
H	1.334542	-1.152689	0.900834

Table S4.1.4: Cartesian coordinates of the MP2/aug-cc-pVDZ optimized geometry of CH_3Cl.

C_{3v}	X	Y	Z
CH_3Cl			
C	0.000000	0.000000	-1.134242
H	0.000000	1.040001	-1.477217
H	-0.900667	-0.520001	-1.477217
H	0.900667	-0.520001	-1.477217
Cl	0.000000	0.000000	0.661006

Table S4.2.1: Cartesian coordinates of the MP2/aug-cc-pVDZ-PP optimized geometry of the HB complex between CHF_2I and TMP.

C_s	X	Y	Z
CHF_2I			
C	-1.216105	1.353406	-0.000007
H	-0.132928	1.531390	-0.000019
F	-1.797300	1.906772	-1.100901
F	-1.797275	1.906778	1.100897
I	-1.556091	-0.778530	0.000002
TMP			
P	2.433219	0.310927	-0.000005
C	2.626429	-0.879781	-1.413081
H	1.740677	-1.530608	-1.468765
H	2.700723	-0.323563	-2.360047
H	3.527461	-1.503794	-1.290861
C	4.140404	1.046128	-0.000009
H	4.271464	1.679600	-0.890422
H	4.271460	1.679624	0.890387
H	4.915127	0.261437	0.000003
C	2.626421	-0.879749	1.413099
H	2.700709	-0.323510	2.360052
H	1.740667	-1.530573	1.468791
H	3.527452	-1.503766	1.290898

Table S4.2.2: Cartesian coordinates of the MP2/aug-cc-pVDZ-PP optimized geometry of the XB complex between CHF_2I and TMP.

C_s	X	Y	Z
CHF_2I			
C	3.039329	0.000074	-0.120817
H	3.521408	0.000128	-1.106167
F	3.443285	-1.103496	0.579305
F	3.443117	1.103684	0.579340
I	0.894182	-0.000089	-0.330647
TMP			
P	-2.597960	-0.000069	-0.084146
C	-2.962250	1.415033	1.061597
H	-2.183466	1.468763	1.837625
H	-2.946416	2.360742	0.498785
H	-3.946593	1.299233	1.545139
C	-4.168149	-0.000761	-1.076796
H	-4.197578	0.889428	-1.723114
H	-4.197437	-0.891692	-1.722098
H	-5.055548	-0.000457	-0.422101
C	-2.962026	-1.413920	1.063213
H	-2.946027	-2.360269	0.501483
H	-2.183240	-1.466632	1.839308
H	-3.946393	-1.297731	1.546613

Table S4.2.3: Cartesian coordinates of the MP2/aug-cc-pVDZ-PP optimized geometry of the HB complex between CHF_2I and DMS.

C_1	X	Y	Z
CHF_2I			
C	-0.785959	1.258032	-0.381791
H	0.079193	1.257115	-1.054250
F	-0.488219	1.947842	0.756259
F	-1.860138	1.858460	-0.964421
I	-1.281284	-0.778912	0.124298
DMS			
S	2.745384	0.432273	-0.507237
C	2.637149	0.518652	1.308262
H	2.514127	1.574865	1.584687
H	1.767347	-0.049505	1.669318
H	3.559797	0.130779	1.763817
C	2.888789	-1.375358	-0.664189
H	2.002971	-1.868460	-0.238243
H	2.953370	-1.612667	-1.735166
H	3.800441	-1.730811	-0.162384

Table S4.2.4: Cartesian coordinates of the MP2/aug-cc-pVDZ-PP optimized geometry of the XB complex between CHF_2I and DMS.

C_s	X	Y	Z
CHF_2I			
C	-2.639583	0.000071	-0.002747
H	-3.199738	0.000218	-0.945700
F	-2.982435	-1.103272	0.727881
F	-2.982301	1.103281	0.728144
I	-0.520886	-0.000012	-0.388345
DMS			
S	2.929895	-0.000077	-0.424875
C	2.967183	1.372335	0.770366
H	2.930865	2.310712	0.199858
H	2.094133	1.323466	1.437999
H	3.896366	1.343011	1.357619
C	2.967139	-1.372225	0.770669
H	2.094094	-1.323176	1.438295
H	2.930784	-2.310727	0.200369
H	3.896326	-1.342805	1.357911

Table S4.2.5: Cartesian coordinates of the MP2/aug-cc-pVDZ-PP optimized geometry of the HB complex with a secondary C-H···F between CHF_2I and CH_3Cl.

C_1	X	Y	Z
CHF_2I			
C	-0.341590	1.277646	-0.128791
H	0.442884	1.290430	-0.893239
F	-1.301935	2.198920	-0.414227
F	0.193498	1.594957	1.086312
I	-1.222580	-0.684963	-0.035059
CH_3Cl			
C	2.847452	-0.704367	0.946920
H	2.382405	0.045316	1.595374
H	3.855860	-0.952773	1.294024
H	2.222981	-1.601401	0.880877
Cl	2.990197	-0.003711	-0.704497

Table S4.2.6: Cartesian coordinates of the MP2/aug-cc-pVDZ-PP optimized geometry of the HB complex with a secondary C-H···I between CHF_2I and CH_3Cl.

C_s	X	Y	Z
CHF_2I			
C	-0.676612	1.305798	-0.000004
H	0.402006	1.498825	-0.000030
F	-1.257116	1.857254	-1.101066
F	-1.257061	1.857249	1.101089
I	-1.011921	-0.824659	0.000000
CH_3Cl			
C	3.096877	-1.100970	0.000022
H	2.582231	-1.451300	-0.900496
H	2.582225	-1.451256	0.900554
H	4.146207	-1.414069	0.000033
Cl	3.060303	0.697955	-0.000023

Table S4.2.7: Cartesian coordinates of the MP2/aug-cc-pVDZ-PP optimized geometry of the XB complex between CHF_2I and CH_3Cl.

C_s	X	Y	Z
CHF_2I			
C	2.439103	-0.010448	-0.000231
H	2.987805	-0.959635	-0.001505
F	2.782525	0.717958	-1.101619
F	2.782955	0.715250	1.102809
I	0.322673	-0.385166	-0.000280
CH_3Cl			
C	-3.173743	1.461749	0.000851
H	-4.185999	1.879482	0.001089
H	-2.627700	1.761309	-0.899947
H	-2.627660	1.760383	0.901930
Cl	-3.313505	-0.331435	-0.000066

Table S4.3A: MP2/aug-cc-pVDZ-PP vibrational frequencies, in cm^{-1}, infrared intensities, in km mol^{-1}, and Raman intensities, in $Å^4$ amu^{-1}, for the HB complex of CHF_2I and TMP and both monomers, as well as the complexation shift Δν.

	Monomer			HB complex			
	Frequency	IR int.	Raman int.	Frequency	Δν	IR int.	Raman int.
CHF_2I							
ν_1 (A')	3192.4	3.6	94.4	3172.8	-19.6	18.9	210.1
ν_2 (A')	1279.7	99.2	7.5	1280.3	0.6	129.6	31.5
ν_3 (A')	1074.1	300.4	3.2	1070.1	-3.9	309.6	3.5
ν_4 (A')	652.5	81.8	18.4	651.0	-1.5	72.8	10.9
ν_5 (A')	549.4	2.9	1.8	551.0	1.6	5.3	2.0
ν_6 (A')	276.0	0.2	6.6	272.7	-3.3	0.01	6.2
ν_7 (A")	1346.0	4.1	2.7	1369.5	23.5	8.9	1.0
ν_8 (A")	1096.9	186.9	1.9	1092.7	-4.2	164.9	1.5
ν_9 (A")	277.0	0.0004	1.2	275.5	-1.5	0.002	0.9
TMP							
ν_1 (A_1)	3148.5	33.6	160.8	3151.3	2.7	28.5	148.6
ν_2 (A_1)	3043.5	29.4	528.4	3045.9	2.3	30.0	526.0
ν_3 (A_1)	1469.0	9.2	1.5	1468.7	-0.3	8.0	0.9
ν_4 (A_1)	1314.7	5.1	7.3	1315.6	1.0	9.0	5.5
ν_5 (A_1)	957.8	20.1	5.0	959.4	1.5	34.9	4.2
ν_6 (A_1)	660.9	0.5	26.5	662.8	1.9	0.9	28.0
ν_7 (A_1)	287.5	1.0	1.5	287.8	0.3	0.9	1.4
ν_8 (A_2)	3168.1	0.0	0.0	3170.5	2.4	0.2	3.3
ν_9 (A_2)	1440.1	0.0	0.0	1439.3	-0.8	0.2	0.3
ν_{10} (A_2)	776.6	0.0	0.0	779.5	2.9	0.0001	0.03
ν_{11} (A_2)	164.1	0.0	0.0	164.5	0.4	0.007	0.01
ν_{12} (E)	3167.9	11.5	95.9	3170.2	2.3	8.6	78.4
ν_{13} (E)	3149.3	3.0	18.4	3152.4	3.1	2.6	23.2
ν_{14} (E)	3046.9	16.7	4.2	3049.3	2.4	14.1	14.8
ν_{15} (E)	1456.7	8.7	3.0	1456.0	-0.7	6.8	3.9
ν_{16} (E)	1446.2	3.1	9.5	1445.9	-0.3	2.6	8.4
ν_{17} (E)	1290.0	2.3	0.7	1290.6	0.7	2.4	0.7
ν_{18} (E)	946.6	16.5	0.5	948.9	2.3	16.4	0.9
ν_{19} (E)	831.0	0.2	0.3	833.2	2.2	0.2	0.4
ν_{20} (E)	718.3	11.6	11.8	722.8	4.5	9.4	13.0
ν_{21} (E)	249.8	0.2	2.8	248.2	-1.6	0.2	2.3
ν_{22} (E)	207.4	0.0009	0.6	207.3	-0.1	0.003	0.4

Van der Waals vibrations: 6.3 cm^{-1}, 0.07 km mol^{-1}, 0.1 $Å^4$ amu^{-1}, 27.1 cm^{-1}, 0.2 km mol^{-1}, 0.06 $Å^4$ amu^{-1}, 33.3 cm^{-1}, 0.2 km mol^{-1}, 0.5 $Å^4$ amu^{-1}, 46.7 cm^{-1}, 0.8 km mol^{-1}, 0.5 $Å^4$ amu^{-1}, 50.3 cm^{-1}, 0.8 km mol^{-1}, 0.2 $Å^4$ amu^{-1}, 65.4 cm^{-1}, 0.2 km mol^{-1}, 0.7 $Å^4$ amu^{-1}.

Table S4.3B: MP2/aug-cc-pVDZ-PP vibrational frequencies, in cm^{-1}, infrared intensities, in km mol^{-1}, and Raman intensities, in $Å^4$ amu^{-1}, for the HB complex of CHF_2I and TMP-d_9 and both monomers, as well as the complexation shift Δν.

	Monomer			HB complex			
	Frequency	IR int.	Raman int.	Frequency	Δν	IR int.	Raman int.
CHF_2I							
ν_1 (A')	3192.4	3.6	94.4	3172.8	-19.6	17.5	200.9
ν_2 (A')	1279.7	99.2	7.5	1280.6	0.9	129.8	28.9
ν_3 (A')	1074.1	300.4	3.2	1070.2	-3.9	307.3	3.7
ν_4 (A')	652.5	81.8	18.4	651.2	-1.3	74.5	13.3
ν_5 (A')	549.4	2.9	1.8	551.0	1.6	5.3	2.0
ν_6 (A')	276.0	0.2	6.6	272.8	-3.2	0.008	6.5
ν_7 (A")	1346.0	4.1	2.7	1369.5	23.5	8.7	1.0
ν_8 (A")	1096.9	186.9	1.9	1092.7	-4.2	164.2	1.4
ν_9 (A")	277.0	0.0004	1.2	275.5	-1.5	0.002	0.9
TMP-d_9							
ν_1 (A_1)	2330.8	15.5	84.8	2333.2	2.4	13.1	87.2
ν_2 (A_1)	2184.5	10.3	254.0	2186.0	1.5	10.6	250.2
ν_3 (A_1)	1058.7	8.5	0.9	1058.4	-0.4	7.1	0.6
ν_4 (A_1)	1021.8	3.7	15.4	1022.0	0.2	6.6	16.3
ν_5 (A_1)	779.8	14.3	2.3	781.3	1.5	22.5	1.7
ν_6 (A_1)	597.0	0.0	20.0	598.6	1.6	0.2	18.6
ν_7 (A_1)	246.1	0.5	1.1	246.9	0.8	0.4	0.8
ν_8 (A_2)	2344.5	0.0	0.0	2346.4	1.9	0.001	0.2
ν_9 (A_2)	1041.0	0.0	0.0	1040.1	-0.9	0.002	0.2
ν_{10} (A_2)	582.2	0.0	0.0	584.4	2.3	0.002	0.02
ν_{11} (A_2)	116.8	0.0	0.0	117.2	0.4	0.003	0.006
ν_{12} (E)	2345.4	3.7	50.1	2347.3	1.9	2.9	43.6
ν_{13} (E)	2332.7	1.4	11.4	2335.1	2.4	1.0	12.2
ν_{14} (E)	2186.9	6.7	0.7	2188.5	1.5	5.5	5.3
ν_{15} (E)	1052.1	4.8	1.2	1051.3	-0.8	5.4	1.5
ν_{16} (E)	1044.7	0.2	4.5	1044.4	-0.4	0.2	3.9
ν_{17} (E)	1009.0	8.5	3.5	1009.7	0.7	8.9	3.5
ν_{18} (E)	760.6	15.4	1.8	762.9	2.3	15.1	2.7
ν_{19} (E)	652.0	3.6	6.9	655.9	3.9	1.9	7.7
ν_{20} (E)	625.1	0.5	0.7	626.6	1.5	0.2	0.8
ν_{21} (E)	208.8	0.1	2.3	207.9	-0.8	0.09	1.8
ν_{22} (E)	150.6	0.01	0.1	150.3	-0.2	0.01	0.1

Van der Waals vibrations: 5.9 cm^{-1}, 0.08 km mol^{-1}, 0.1 $Å^4$ amu^{-1}, 25.3 cm^{-1}, 0.1 km mol^{-1}, 0.04 $Å^4$ amu^{-1}, 32.2 cm^{-1}, 0.2 km mol^{-1}, 0.4 $Å^4$ amu^{-1}, 43.5 cm^{-1}, 0.7 km mol^{-1}, 0.5 $Å^4$ amu^{-1}, 45.3 cm^{-1}, 0.6 km mol^{-1}, 0.2 $Å^4$ amu^{-1}, 63.6 cm^{-1}, 0.2 km mol^{-1}, 0.7 $Å^4$ amu^{-1}.

Table S4.4A: MP2/aug-cc-pVDZ-PP vibrational frequencies, in cm^{-1}, infrared intensities, in km mol^{-1}, and Raman intensities, in $Å^4$ amu^{-1}, for the XB complex of CHF_2I and TMP and both monomers, as well as the complexation shift Δν.

	Monomer			XB complex			
	Frequency	IR int.	Raman int.	Frequency	Δν	IR int.	Raman int.
CHF_2I							
ν_1 (A')	3192.4	3.6	94.4	3180.3	-12.1	8.7	168.9
ν_2 (A')	1279.7	99.2	7.5	1278.5	-1.2	147.4	9.0
ν_3 (A')	1074.1	300.4	3.2	1068.1	-6.0	349.6	4.6
ν_4 (A')	652.5	81.8	18.4	647.5	-5.0	45.4	95.4
ν_5 (A')	549.4	2.9	1.8	544.7	-4.7	2.7	6.1
ν_6 (A')	276.0	0.2	6.6	272.0	-4.0	4.5	31.1
ν_7 (A")	1346.0	4.1	2.7	1343.7	-2.3	4.2	3.6
ν_8 (A")	1096.9	186.9	1.9	1079.6	-17.2	183.7	1.7
ν_9 (A")	277.0	0.0004	1.2	278.6	1.6	0.04	1.5
TMP							
ν_1 (A_1)	3148.5	33.6	160.8	3151.6	3.1	31.3	188.2
ν_2 (A_1)	3043.5	29.4	528.4	3046.0	2.5	35.6	563.3
ν_3 (A_1)	1469.0	9.2	1.5	1467.7	-1.3	7.4	1.6
ν_4 (A_1)	1314.7	5.1	7.3	1315.4	0.7	3.9	17.1
ν_5 (A_1)	957.8	20.1	5.0	957.6	-0.3	72.2	22.1
ν_6 (A_1)	660.9	0.5	26.5	662.3	1.4	0.9	26.5
ν_7 (A_1)	287.5	1.0	1.5	286.2	-1.4	0.7	2.3
ν_8 (A_2)	3168.1	0.0	0.0	3170.0	1.9	3.9	32.9
ν_9 (A_2)	1440.1	0.0	0.0	1439.0	-1.1	0.01	0.05
ν_{10} (A_2)	776.6	0.0	0.0	779.1	2.6	0.0	0.01
ν_{11} (A_2)	164.1	0.0	0.0	163.9	-0.2	0.0008	0.002
ν_{12} (E)	3167.9	11.5	95.9	3170.9	3.0	6.2	65.4
ν_{13} (E)	3149.3	3.0	18.4	3152.8	3.5	2.3	29.9
ν_{14} (E)	3046.9	16.7	4.2	3049.4	2.5	13.4	18.5
ν_{15} (E)	1456.7	8.7	3.0	1455.5	-1.2	9.2	4.2
ν_{16} (E)	1446.2	3.1	9.5	1445.0	-1.2	2.2	8.5
ν_{17} (E)	1290.0	2.3	0.7	1290.9	0.9	4.0	1.2
ν_{18} (E)	946.6	16.5	0.5	948.9	2.3	16.0	0.8
ν_{19} (E)	831.0	0.2	0.3	832.1	1.2	0.8	0.6
ν_{20} (E)	718.3	11.6	11.8	724.7	6.4	8.7	16.0
ν_{21} (E)	249.8	0.2	2.8	245.3	-4.5	0.2	2.8
ν_{22} (E)	207.4	0.0009	0.6	207.0	-0.3	0.02	0.4

Van der Waals vibrations: 3.7 cm^{-1}, 1.0 km mol^{-1}, 0.009 $Å^4$ amu^{-1}, 12.0 cm^{-1}, 0.7 km mol^{-1}, 0.6 $Å^4$ amu^{-1}, 12.4 cm^{-1}, 1.5 km mol^{-1}, 0.5 $Å^4$ amu^{-1}, 52.0 cm^{-1}, 2.4 km mol^{-1}, 3.7 $Å^4$ amu^{-1}, 52.9 cm^{-1}, 0.004 km mol^{-1}, 0.2 $Å^4$ amu^{-1}, 57.7 cm^{-1}, 0.8 km mol^{-1}, 0.4 $Å^4$ amu^{-1}.

Table S4.4B: MP2/aug-cc-pVDZ-PP vibrational frequencies, in cm^{-1}, infrared intensities, in km mol^{-1}, and Raman intensities, in $Å^4$ amu^{-1}, for the XB complex of CHF_2I and TMP-d_9 and both monomers, as well as the complexation shift Δν.

	Monomer			XB complex			
	Frequency	IR int.	Raman int.	Frequency	Δν	IR int.	Raman int.
CHF_2I							
ν_1 (A')	3192.4	3.6	94.4	3180.3	-12.1	8.7	168.6
ν_2 (A')	1279.7	99.2	7.5	1278.6	-1.1	150.6	9.4
ν_3 (A')	1074.1	300.4	3.2	1067.9	-6.1	359.8	3.8
ν_4 (A')	652.5	81.8	18.4	647.2	-5.4	43.9	100.5
ν_5 (A')	549.4	2.9	1.8	544.7	-4.7	2.7	6.1
ν_6 (A')	276.0	0.2	6.6	272.2	-3.8	4.0	32.0
ν_7 (A")	1346.0	4.1	2.7	1343.7	-2.3	4.2	3.6
ν_8 (A")	1096.9	186.9	1.9	1079.6	-17.2	184.0	1.7
ν_9 (A")	277.0	0.0004	1.2	278.5	1.6	0.04	1.4
TMP-d_9							
ν_1 (A_1)	2330.8	15.5	84.8	2333.6	2.7	12.5	127.0
ν_2 (A_1)	2184.5	10.3	254.0	2186.1	1.6	12.7	263.2
ν_3 (A_1)	1058.7	8.5	0.9	1057.6	-1.1	9.3	0.7
ν_4 (A_1)	1021.8	3.7	15.4	1022.1	0.3	3.7	20.8
ν_5 (A_1)	779.8	14.3	2.3	780.1	0.2	46.1	10.8
ν_6 (A_1)	597.0	0.0	20.0	598.2	1.2	0.0	21.2
ν_7 (A_1)	246.1	0.5	1.1	245.7	-0.4	0.5	1.3
ν_8 (A_2)	2344.5	0.0	0.0	2346.3	1.8	0.5	6.4
ν_9 (A_2)	1041.0	0.0	0.0	1040.0	-1.0	0.0001	0.04
ν_{10} (A_2)	582.2	0.0	0.0	584.3	2.1	0.0003	0.008
ν_{11} (A_2)	116.8	0.0	0.0	116.7	-0.1	0.0004	0.001
ν_{12} (E)	2345.4	3.7	50.1	2347.7	2.3	2.2	39.4
ν_{13} (E)	2332.7	1.4	11.4	2335.4	2.8	0.7	14.5
ν_{14} (E)	2186.9	6.7	0.7	2188.5	1.6	5.1	6.1
ν_{15} (E)	1052.1	4.8	1.2	1051.0	-1.1	4.5	1.8
ν_{16} (E)	1044.7	0.2	4.5	1043.7	-1.0	0.2	4.0
ν_{17} (E)	1009.0	8.5	3.5	1010.1	1.1	8.0	5.0
ν_{18} (E)	760.6	15.4	1.8	763.7	3.0	13.5	3.3
ν_{19} (E)	652.0	3.6	6.9	657.7	5.7	3.6	5.7
ν_{20} (E)	625.1	0.5	0.7	625.6	0.5	0.3	1.6
ν_{21} (E)	208.8	0.1	2.3	206.0	-2.7	0.1	2.2
ν_{22} (E)	150.6	0.01	0.1	149.8	-0.8	0.04	0.1

Van der Waals vibrations: 3.6 cm^{-1}, 1.0 km mol^{-1}, 0.007 $Å^4$ amu^{-1}, 11.0 cm^{-1}, 0.6 km mol^{-1}, 0.6 $Å^4$ amu^{-1}, 11.4 cm^{-1}, 1.2 km mol^{-1}, 0.5 $Å^4$ amu^{-1}, 50.2 cm^{-1}, 2.5 km mol^{-1}, 3.5 $Å^4$ amu^{-1}, 50.8 cm^{-1}, 0.02 km mol^{-1}, 0.1 $Å^4$ amu^{-1}, 54.9 cm^{-1}, 0.4 km mol^{-1}, 0.3 $Å^4$ amu^{-1}.

Table S4.5A: MP2/aug-cc-pVDZ-PP vibrational frequencies, in cm^{-1}, infrared intensities, in km mol^{-1}, and Raman intensities, in $Å^4$ amu^{-1}, for the HB complex of CHF_2I and DMS and both monomers, as well as the complexation shift Δν.

	Monomer			HB complex			
	Frequency	IR int.	Raman int.	Frequency	Δν	IR int.	Raman int.
CHF_2I							
ν_1 (A')	3192.4	3.6	94.4	3202.1	9.7	3.0	99.6
ν_2 (A')	1279.7	99.2	7.5	1276.8	-2.9	100.4	17.0
ν_3 (A')	1074.1	300.4	3.2	1068.2	-5.9	269.8	3.3
ν_4 (A')	652.5	81.8	18.4	650.5	-2.0	72.7	14.0
ν_5 (A')	549.4	2.9	1.8	550.1	0.7	4.0	1.5
ν_6 (A')	276.0	0.2	6.6	273.5	-2.5	0.03	5.9
ν_7 (A")	1346.0	4.1	2.7	1344.4	-1.6	6.7	5.2
ν_8 (A")	1096.9	186.9	1.9	1092.9	-4.0	209.0	3.1
ν_9 (A")	277.0	0.0004	1.2	277.6	0.7	0.09	1.0
DMS							
ν_1 (A_1)	3186.3	9.8	92.1	3187.8	1.4	5.8	74.2
ν_2 (A_1)	3062.2	31.8	338.0	3063.7	1.5	24.5	329.7
ν_3 (A_1)	1473.5	0.3	7.6	1472.7	-0.8	2.1	7.8
ν_4 (A_1)	1352.5	0.8	0.9	1353.1	0.6	1.2	1.0
ν_5 (A_1)	1046.4	8.6	0.4	1047.9	1.5	8.0	0.3
ν_6 (A_1)	713.3	2.8	22.1	710.9	-2.4	2.8	19.3
ν_7 (A_1)	260.8	0.03	3.0	260.6	-0.2	0.05	2.4
ν_8 (A_2)	3168.0	0.0	16.5	3172.0	4.0	0.2	12.1
ν_9 (A_2)	1450.1	0.0	10.3	1448.3	-1.8	0.4	9.3
ν_{10} (A_2)	945.6	0.0	0.1	948.8	3.2	0.01	0.5
ν_{11} (A_2)	171.2	0.0	0.1	174.2	3.0	0.04	0.06
ν_{12} (B_1)	3159.9	21.3	119.4	3165.0	5.1	17.2	99.4
ν_{13} (B_1)	1462.5	12.9	0.02	1460.7	-1.8	10.7	0.5
ν_{14} (B_1)	982.7	4.1	0.006	985.7	3.0	10.9	0.4
ν_{15} (B_1)	187.1	0.8	0.09	188.5	1.4	1.1	0.1
ν_{16} (B_2)	3187.4	3.4	42.0	3190.0	2.6	2.7	43.4
ν_{17} (B_2)	3066.9	26.3	2.8	3068.0	1.1	20.5	6.1
ν_{18} (B_2)	1464.2	13.6	0.03	1462.9	-1.2	8.0	0.2
ν_{19} (B_2)	1326.0	6.5	0.1	1325.9	-0.1	4.2	0.1
ν_{20} (B_2)	912.7	0.2	0.2	915.2	2.5	0.1	0.1
ν_{21} (B_2)	765.1	0.1	8.5	762.7	-2.3	0.4	7.0

Van der Waals vibrations: 24.5 cm^{-1}, 0.6 km mol^{-1}, 0.5 $Å^4$ amu^{-1}, 31.4 cm^{-1}, 0.3 km mol^{-1}, 0.4 $Å^4$ amu^{-1}, 36.8 cm^{-1}, 1.1 km mol^{-1}, 0.2 $Å^4$ amu^{-1}, 61.8 cm^{-1}, 0.04 km mol^{-1}, 1.2 $Å^4$ amu^{-1}, 72.7 cm^{-1}, 0.3 km mol^{-1}, 0.5 $Å^4$ amu^{-1}, 91.6 cm^{-1}, 7.3 km mol^{-1}, 0.2 $Å^4$ amu^{-1}.

Table S4.5B: MP2/aug-cc-pVDZ-PP vibrational frequencies, in cm^{-1}, infrared intensities, in km mol^{-1}, and Raman intensities, in $Å^4$ amu^{-1}, for the HB complex of CHF_2I and DMS-d_6 and both monomers, as well as the complexation shift Δν.

	Monomer			HB complex			
	Frequency	IR int.	Raman int.	Frequency	Δν	IR int.	Raman int.
CHF_2I							
ν_1 (A')	3192.4	3.6	94.4	3202.1	9.7	2.9	99.6
ν_2 (A')	1279.7	99.2	7.5	1277.1	-2.6	101.4	16.0
ν_3 (A')	1074.1	300.4	3.2	1069.4	-4.6	254.4	3.3
ν_4 (A')	652.5	81.8	18.4	650.4	-2.1	73.4	13.1
ν_5 (A')	549.4	2.9	1.8	550.1	0.7	4.0	1.5
ν_6 (A')	276.0	0.2	6.6	273.5	-2.5	0.03	5.9
ν_7 (A")	1346.0	4.1	2.7	1344.9	-1.1	6.1	4.9
ν_8 (A")	1096.9	186.9	1.9	1093.5	-3.4	201.8	3.2
ν_9 (A")	277.0	0.0004	1.2	277.6	0.6	0.09	1.1
DMS-d_6							
ν_1 (A_1)	2361.4	4.6	45.5	2363.7	2.3	2.1	35.0
ν_2 (A_1)	2194.1	16.7	162.8	2195.0	0.8	12.9	158.2
ν_3 (A_1)	1064.3	0.5	3.0	1063.2	-1.1	13.1	3.4
ν_4 (A_1)	1037.4	1.2	5.6	1036.0	-1.4	0.3	5.5
ν_5 (A_1)	837.1	3.9	1.7	837.4	0.2	3.0	1.3
ν_6 (A_1)	655.7	2.7	17.4	654.5	-1.2	2.2	16.3
ν_7 (A_1)	223.6	0.0	2.2	223.7	0.1	0.05	1.8
ν_8 (A_2)	2350.5	0.0	8.5	2353.5	3.0	0.08	6.2
ν_9 (A_2)	1046.5	0.0	4.3	1044.4	-2.1	7.6	3.7
ν_{10} (A_2)	708.3	0.0	0.4	710.6	2.3	0.008	0.7
ν_{11} (A_2)	122.8	0.0	0.1	126.3	3.5	0.04	0.09
ν_{12} (B_1)	2344.4	10.8	63.9	2348.2	3.9	8.6	53.5
ν_{13} (B_1)	1056.3	7.2	0.0	1054.2	-2.1	17.7	0.4
ν_{14} (B_1)	751.1	0.9	0.1	753.2	2.1	2.8	0.4
ν_{15} (B_1)	136.8	0.8	0.1	139.4	2.6	1.9	0.1
ν_{16} (B_2)	2360.9	1.2	22.7	2362.1	1.2	1.6	25.8
ν_{17} (B_2)	2197.7	15.2	0.5	2198.2	0.5	11.8	2.4
ν_{18} (B_2)	1060.2	7.9	0.1	1058.7	-1.5	0.7	0.2
ν_{19} (B_2)	1017.4	2.5	0.6	1016.0	-1.4	0.9	0.5
ν_{20} (B_2)	720.2	0.0	7.3	718.8	-1.3	0.1	6.0
ν_{21} (B_2)	686.0	0.0	0.1	687.8	1.8	0.003	0.05

Van der Waals vibrations: 22.5 cm^{-1}, 0.5 km mol^{-1}, 0.4 $Å^4$ amu^{-1}, 31.0 cm^{-1}, 0.3 km mol^{-1}, 0.4 $Å^4$ amu^{-1}, 36.2 cm^{-1}, 1.0 km mol^{-1}, 0.2 $Å^4$ amu^{-1}, 54.5 cm^{-1}, 0.07 km mol^{-1}, 0.9 $Å^4$ amu^{-1}, 67.1 cm^{-1}, 0.9 km mol^{-1}, 0.5 $Å^4$ amu^{-1}, 83.8 cm^{-1}, 4.6 km mol^{-1}, 0.1 $Å^4$ amu^{-1}.

Table S4.6A: MP2/aug-cc-pVDZ-PP vibrational frequencies, in cm^{-1}, infrared intensities, in km mol^{-1}, and Raman intensities, in $Å^4$ amu^{-1}, for the XB complex of CHF_2I and DMS and both monomers, as well as the complexation shift Δν.

	Monomer			XB complex			
	Frequency	IR int.	Raman int.	Frequency	Δν	IR int.	Raman int.
CHF_2I							
ν_1 (A')	3192.4	3.6	94.4	3183.2	-9.3	7.2	148.4
ν_2 (A')	1279.7	99.2	7.5	1279.5	-0.2	135.6	8.0
ν_3 (A')	1074.1	300.4	3.2	1069.0	-5.0	327.5	2.8
ν_4 (A')	652.5	81.8	18.4	650.5	-2.0	54.0	58.5
ν_5 (A')	549.4	2.9	1.8	545.6	-3.8	2.6	4.0
ν_6 (A')	276.0	0.2	6.6	274.1	-1.9	3.1	20.1
ν_7 (A")	1346.0	4.1	2.7	1344.2	-1.8	3.8	3.2
ν_8 (A")	1096.9	186.9	1.9	1082.2	-14.6	181.7	1.7
ν_9 (A")	277.0	0.0004	1.2	279.3	2.3	0.01	1.5
DMS							
ν_1 (A_1)	3186.3	9.8	92.1	3188.3	1.9	6.6	89.9
ν_2 (A_1)	3062.2	31.8	338.0	3062.3	0.1	24.3	311.5
ν_3 (A_1)	1473.5	0.3	7.6	1471.5	-2.0	2.8	9.7
ν_4 (A_1)	1352.5	0.8	0.9	1352.2	-0.3	0.2	7.5
ν_5 (A_1)	1046.4	8.6	0.4	1047.4	1.1	6.5	0.6
ν_6 (A_1)	713.3	2.8	22.1	710.5	-2.8	3.3	19.0
ν_7 (A_1)	260.8	0.03	3.0	261.1	0.3	0.03	2.5
ν_8 (A_2)	3168.0	0.0	16.5	3170.6	2.6	0.4	14.5
ν_9 (A_2)	1450.1	0.0	10.3	1448.3	-1.8	0.3	8.6
ν_{10} (A_2)	945.6	0.0	0.1	948.9	3.3	0.003	0.4
ν_{11} (A_2)	171.2	0.0	0.1	173.6	2.4	0.02	0.09
ν_{12} (B_1)	3159.9	21.3	119.4	3163.6	3.7	16.3	113.3
ν_{13} (B_1)	1462.5	12.9	0.02	1461.2	-1.4	13.6	0.5
ν_{14} (B_1)	982.7	4.1	0.006	984.9	2.3	13.6	0.7
ν_{15} (B_1)	187.1	0.8	0.09	188.0	0.9	1.8	0.4
ν_{16} (B_2)	3187.4	3.4	42.0	3189.3	1.9	1.7	32.6
ν_{17} (B_2)	3066.9	26.3	2.8	3066.7	-0.2	18.7	7.5
ν_{18} (B_2)	1464.2	13.6	0.03	1461.5	-2.6	8.0	0.4
ν_{19} (B_2)	1326.0	6.5	0.1	1326.0	0.1	3.5	0.09
ν_{20} (B_2)	912.7	0.2	0.2	914.9	2.2	0.2	0.2
ν_{21} (B_2)	765.1	0.1	8.5	762.3	-2.8	0.4	7.2

Van der Waals vibrations: 6.3 cm^{-1}, 2.5 km mol^{-1}, 0.05 $Å^4$ amu^{-1}, 32.2 cm^{-1}, 0.0002 km mol^{-1}, 1.0 $Å^4$ amu^{-1}, 32.5 cm^{-1}, 2.0 km mol^{-1}, 0.6 $Å^4$ amu^{-1}, 63.9 cm^{-1}, 1.5 km mol^{-1}, 1.8 $Å^4$ amu^{-1}, 67.2 cm^{-1}, 0.007 km mol^{-1}, 0.8 $Å^4$ amu^{-1}, 106.5 cm^{-1}, 12.3 km mol^{-1}, 2.9 $Å^4$ amu^{-1}.

Table S4.6B: MP2/aug-cc-pVDZ-PP vibrational frequencies, in cm^{-1}, infrared intensities, in km mol^{-1}, and Raman intensities, in $Å^4$ amu^{-1}, for the XB complex of CHF_2I and DMS-d_6 and both monomers, as well as the complexation shift Δν.

	Monomer			XB complex			
	Frequency	IR int.	Raman int.	Frequency	Δν	IR int.	Raman int.
CHF_2I							
ν_1 (A')	3192.4	3.6	94.4	3183.2	-9.3	7.2	148.8
ν_2 (A')	1279.7	99.2	7.5	1279.5	-0.2	136.1	7.9
ν_3 (A')	1074.1	300.4	3.2	1069.4	-4.7	311.5	2.1
ν_4 (A')	652.5	81.8	18.4	650.4	-2.1	52.9	60.6
ν_5 (A')	549.4	2.9	1.8	545.6	-3.8	2.6	4.0
ν_6 (A')	276.0	0.2	6.6	274.0	-1.9	3.1	20.0
ν_7 (A")	1346.0	4.1	2.7	1344.2	-1.8	3.9	3.2
ν_8 (A")	1096.9	186.9	1.9	1082.2	-14.6	181.4	1.7
ν_9 (A")	277.0	0.0004	1.2	279.3	2.3	0.01	1.5
DMS-d_6							
ν_1 (A_1)	2361.4	4.6	45.5	2363.2	1.9	2.9	46.5
ν_2 (A_1)	2194.1	16.7	162.8	2194.0	-0.2	13.0	148.8
ν_3 (A_1)	1064.3	0.5	3.0	1062.0	-2.4	20.4	5.5
ν_4 (A_1)	1037.4	1.2	5.6	1036.0	-1.4	0.6	9.2
ν_5 (A_1)	837.1	3.9	1.7	836.9	-0.3	2.6	1.5
ν_6 (A_1)	655.7	2.7	17.4	654.3	-1.4	4.6	13.0
ν_7 (A_1)	223.6	0.0	2.2	224.3	0.7	0.05	1.9
ν_8 (A_2)	2350.5	0.0	8.5	2352.4	1.9	0.2	7.2
ν_9 (A_2)	1046.5	0.0	4.3	1045.1	-1.4	0.2	3.6
ν_{10} (A_2)	708.3	0.0	0.4	710.9	2.6	0.004	0.8
ν_{11} (A_2)	122.8	0.0	0.1	126.4	3.6	0.01	0.1
ν_{12} (B_1)	2344.4	10.8	63.9	2347.2	2.8	7.8	58.6
ν_{13} (B_1)	1056.3	7.2	0.0	1055.1	-1.2	8.8	0.1
ν_{14} (B_1)	751.1	0.9	0.1	753.1	2.1	2.2	0.9
ν_{15} (B_1)	136.8	0.8	0.1	140.3	3.5	4.3	1.1
ν_{16} (B_2)	2360.9	1.2	22.7	2362.6	1.7	0.6	17.5
ν_{17} (B_2)	2197.7	15.2	0.5	2197.3	-0.3	10.9	3.0
ν_{18} (B_2)	1060.2	7.9	0.1	1057.9	-2.3	4.7	0.2
ν_{19} (B_2)	1017.4	2.5	0.6	1016.1	-1.3	1.7	0.5
ν_{20} (B_2)	720.2	0.0	7.3	718.5	-1.6	0.1	5.9
ν_{21} (B_2)	686.0	0.0	0.1	687.8	1.8	0.0008	0.1

Van der Waals vibrations: 6.0 cm^{-1}, 2.2 km mol^{-1}, 0.03 $Å^4$ amu^{-1}, 30.2 cm^{-1}, 0.002 km mol^{-1}, 1.0 $Å^4$ amu^{-1}, 31.4 cm^{-1}, 1.9 km mol^{-1}, 0.6 $Å^4$ amu^{-1}, 61.0 cm^{-1}, 0.009 km mol^{-1}, 0.5 $Å^4$ amu^{-1}, 61.3 cm^{-1}, 1.3 km mol^{-1}, 1.6 $Å^4$ amu^{-1}, 94.9 cm^{-1}, 8.4 km mol^{-1}, 2.2 $Å^4$ amu^{-1}.

Table S4.7: MP2/aug-cc-pVDZ-PP vibrational frequencies, in cm^{-1}, infrared intensities, in km mol^{-1}, and Raman intensities, in $Å^4$ amu^{-1}, for the HB complex with a secondary C-H···F interaction of CHF_2I and CH_3Cl and both monomers, as well as the complexation shift Δν.

	Monomer			HB complex (C-H···Cl + F···H-C)			
	Frequency	IR int.	Raman int.	Frequency	Δν	IR int.	Raman int.
CHF_2I							
ν_1 (A')	3192.4	3.6	94.4	3208.2	15.7	0.8	82.7
ν_2 (A')	1279.7	99.2	7.5	1280.8	1.1	101.4	8.9
ν_3 (A')	1074.1	300.4	3.2	1067.8	-6.3	266.0	3.0
ν_4 (A')	652.5	81.8	18.4	650.1	-2.5	75.2	15.9
ν_5 (A')	549.4	2.9	1.8	549.6	0.2	3.4	1.5
ν_6 (A')	276.0	0.2	6.6	275.0	-1.0	0.09	6.0
ν_7 (A")	1346.0	4.1	2.7	1342.8	-3.2	0.7	5.1
ν_8 (A")	1096.9	186.9	1.9	1093.8	-3.1	216.3	2.6
ν_9 (A")	277.0	0.0004	1.2	278.2	1.2	0.07	1.1
CH_3Cl							
ν_1 (A)	3109.9	24.4	147.2	3111.6	1.7	17.0	139.7
ν_2 (A)	1369.8	13.2	0.006	1370.0	0.3	11.1	0.1
ν_3 (A)	750.4	25.3	17.9	741.4	-8.9	23.8	14.7
ν_4 (E)	3230.5	3.6	48.9	3235.5	5.0	2.6	40.3
ν_5 (E)	1474.7	5.0	4.0	1472.3	-2.5	9.6	3.7
ν_6 (E)	1031.9	2.1	0.6	1034.2	2.2	3.5	0.6

Van der Waals vibrations: 22.8 cm^{-1}, 2.2 km mol^{-1}, 0.9 $Å^4$ amu^{-1}, 26.6 cm^{-1}, 0.8 km mol^{-1}, 0.5 $Å^4$ amu^{-1}, 41.9 cm^{-1}, 1.3 km mol^{-1}, 0.2 $Å^4$ amu^{-1}, 56.6 cm^{-1}, 0.3 km mol^{-1}, 0.2 $Å^4$ amu^{-1}, 70.2 cm^{-1}, 0.7 km mol^{-1}, 0.3 $Å^4$ amu^{-1}, 80.7 cm^{-1}, 7.3 km mol^{-1}, 1.0 $Å^4$ amu^{-1}.

Table S4.8: MP2/aug-cc-pVDZ-PP vibrational frequencies, in cm^{-1}, infrared intensities, in km mol^{-1}, and Raman intensities, in $Å^4$ amu^{-1}, for the HB complex with a secondary C-H···I interaction of CHF_2I and CH_3Cl and both monomers, as well as the complexation shift Δν.

	Monomer			HB complex (C-H···Cl + I···H-C)			
	Frequency	IR int.	Raman int.	Frequency	Δν	IR int.	Raman int.
CHF_2I							
ν_1 (A')	3192.4	3.6	94.4	3205.2	12.7	1.6	115.7
ν_2 (A')	1279.7	99.2	7.5	1279.1	-0.6	104.5	13.2
ν_3 (A')	1074.1	300.4	3.2	1073.0	-1.1	309.9	3.3
ν_4 (A')	652.5	81.8	18.4	650.2	-2.3	75.8	15.9
ν_5 (A')	549.4	2.9	1.8	550.8	1.4	4.5	1.8
ν_6 (A')	276.0	0.2	6.6	273.9	-2.1	0.04	6.3
ν_7 (A")	1346.0	4.1	2.7	1354.6	8.7	6.5	1.6
ν_8 (A")	1096.9	186.9	1.9	1097.2	0.4	176.1	1.8
ν_9 (A")	277.0	0.0004	1.2	276.2	-0.8	0.0	1.0
CH_3Cl							
ν_1 (A)	3109.9	24.4	147.2	3111.9	2.0	16.4	142.6
ν_2 (A)	1369.8	13.2	0.006	1369.9	0.2	12.0	0.1
ν_3 (A)	750.4	25.3	17.9	741.9	-8.5	24.1	14.5
ν_4 (E)	3230.5	3.6	48.9	3236.0	5.5	3.3	42.6
ν_5 (E)	1474.7	5.0	4.0	1470.6	-4.2	11.1	3.5
ν_6 (E)	1031.9	2.1	0.6	1033.6	1.6	3.1	0.6

Van der Waals vibrations: 5.7 cm^{-1}, 0.6 km mol^{-1}, 0.6 $Å^4$ amu^{-1}, 18.5 cm^{-1}, 3.7 km mol^{-1}, 0.1 $Å^4$ amu^{-1}, 28.5 cm^{-1}, 0.2 km mol^{-1}, 0.6 $Å^4$ amu^{-1}, 57.2 cm^{-1}, 0.04 km mol^{-1}, 0.03 $Å^4$ amu^{-1}, 61.1 cm^{-1}, 0.04 km mol^{-1}, 0.4 $Å^4$ amu^{-1}, 72.2 cm^{-1}, 6.2 km mol^{-1}, 0.7 $Å^4$ amu^{-1}.

Table S4.9: MP2/aug-cc-pVDZ-PP vibrational frequencies, in cm^{-1}, infrared intensities, in km mol^{-1}, and Raman intensities, in $Å^4$ amu^{-1}, for the XB complex of CHF_2I and CH_3Cl and both monomers, as well as the complexation shift Δν.

	Monomer			XB complex			
	Frequency	IR int.	Raman int.	Frequency	Δν	IR int.	Raman int.
CHF_2I							
ν_1 (A')	3192.4	3.6	94.4	3189.4	-3.0	4.6	113.8
ν_2 (A')	1279.7	99.2	7.5	1281.2	1.5	119.1	6.8
ν_3 (A')	1074.1	300.4	3.2	1071.6	-2.5	312.1	2.8
ν_4 (A')	652.5	81.8	18.4	654.5	2.0	72.8	26.5
ν_5 (A')	549.4	2.9	1.8	548.0	-1.4	2.8	2.1
ν_6 (A')	276.0	0.2	6.6	276.9	1.0	0.8	8.9
ν_7 (A")	1346.0	4.1	2.7	1345.1	-0.9	4.1	2.8
ν_8 (A")	1096.9	186.9	1.9	1089.6	-7.3	185.1	1.8
ν_9 (A")	277.0	0.0004	1.2	278.7	1.7	0.01	1.4
CH_3Cl							
ν_1 (A)	3109.9	24.4	147.2	3109.6	-0.3	17.3	144.7
ν_2 (A)	1369.8	13.2	0.006	1369.3	-0.4	8.2	0.7
ν_3 (A)	750.4	25.3	17.9	743.2	-7.2	23.6	15.4
ν_4 (E)	3230.5	3.6	48.9	3232.7	2.2	3.3	46.1
ν_5 (E)	1474.7	5.0	4.0	1471.7	-3.0	9.2	3.5
ν_6 (E)	1031.9	2.1	0.6	1032.7	0.7	4.1	0.8

Van der Waals vibrations: 5.0 cm^{-1}, 4.6 km mol^{-1}, 0.7 $Å^4$ amu^{-1}, 22.5 cm^{-1}, 2.1 km mol^{-1}, 0.8 $Å^4$ amu^{-1}, 26.5 cm^{-1}, 0.6 km mol^{-1}, 0.3 $Å^4$ amu^{-1}, 43.6 cm^{-1}, 0.02 km mol^{-1}, 0.05 $Å^4$ amu^{-1}, 51.2 cm^{-1}, 0.1 km mol^{-1}, 0.5 $Å^4$ amu^{-1}, 69.5 cm^{-1}, 7.3 km mol^{-1}, 1.1 $Å^4$ amu^{-1}.

Table S4.10: Experimental vibrational frequencies for the monomer and complexes, as well as experimental complexation shifts ($\Delta\nu_{exp}$) and MP2/aug-cc-pVDZ-PP calculated complexation shifts ($\Delta\nu_{calc}$), in cm^{-1}, for the XB complex and HB complex of CHF_2I with TMP dissolved in LKr at 130 K.

	Assignment	$\nu_{monomer}$	$\nu_{complex,XB}$	$\Delta\nu_{exp,XB}$	$\Delta\nu_{calc,XB}$	$\nu_{complex,HB}$	$\Delta\nu_{exp,HB}$	$\Delta\nu_{calc,HB}$
CHF_2I	ν_1	3003.3	2989.9[a]	-13.4	-12.1	2989.9[a]	-13.4	-19.6
	$\nu_5 + \nu_7 + \nu_8$	2993.9	-		-24.3	-		21.0
	$\nu_3 + \nu_8$	2171.2	2145.2	-26.0	-23.2	2160.6	-10.6	-8.1
	$2\nu_3$	2144.1	2129.0	-15.1	-11.9	2133.9	-10.2	-7.9
	ν_7	1337.2	1335.5	-1.7	-2.3			23.5
	ν_2	1247.6	1244.0	-3.6	-1.2	1247.8	0.2	0.6
	ν_8	1107.6	1087.7	-19.9	-17.2	1101.8	-5.8	-4.2
	ν_3	1077.1	1070.7	-6.4	-6.0	1072.5	-4.6	-3.9
	ν_4	633.6	628.5	-5.1	-5.0	633.1	-0.5	-1.5
	ν_5	567.8	563.2	-4.6	-4.7	568.3	0.5	-1.6
	$2\nu_6$	536.8	-			-		
TMP	ν_{12}	2971.9	2974.6	2.7	3.0	2974.6	2.7	2.3
	ν_1	2957.7	2961.0	3.3	3.1	2961.0	3.3	2.7
	ν_{13}	2957.7	2961.0	3.3	3.5	2961.0	3.3	3.1
	ν_2	2897.2	2899.2	2.0	2.5	2899.2	2.0	2.3
	ν_{14}	2897.2	2899.2	2.0	2.5	2899.2	2.0	2.4
	ν_3	1436.6	1436.2	-0.4	-1.3	1436.2	-0.4	-0.3
	ν_{15}	1426.9	1426.1	-0.8	-1.2	1426.1	-0.8	-0.7
	ν_{16}	1418.3	1417.9	-0.4	-1.2	1417.9	-0.4	-0.3
	$\nu_6 + \nu_{20}$	1359.4	1366.9	7.5	7.8	1366.9	7.5	6.4
	$2\nu_6$	1310.9	1314.5	3.6	2.7	1314.5	3.6	3.8
	ν_4	1295.1	1297.7	2.6	0.7	1297.7	2.6	1.0
	ν_{17}	1278.7	1280.8	2.1	0.9	1280.8	2.1	0.7
	ν_5	949.0	948.8	-0.2	-0.3	950.5	1.5	1.5
	ν_{18}	937.6	939.8	2.2	2.3	939.8	2.2	2.3
	ν_{19}	825.3	827.2	1.9	1.2	827.2	1.9	2.2
	ν_{20}	708.7	715.0	6.3	6.4	713.1	4.4	4.5
	ν_6	654.1	656.0	1.9	1.4	656.0	1.9	1.9

[a] Shoulder of TMP complex band

Table S4.11: Experimental vibrational frequencies for the monomer and complexes, as well as experimental complexation shifts ($\Delta\nu_{exp}$) and MP2/aug-cc-pVDZ-PP calculated complexation shifts ($\Delta\nu_{calc}$), in cm^{-1}, for the XB complex and HB complex of CHF_2I with DMS dissolved in LKr at 130 K.

	Assignment	$\nu_{monomer}$	$\nu_{complex,XB}$	$\Delta\nu_{exp,XB}$	$\Delta\nu_{calc,XB}$	$\nu_{complex,HB}$	$\Delta\nu_{exp,HB}$	$\Delta\nu_{calc,HB}$
CHF_2I	ν_1	3003.3	2994.5	-8.8	-9.3	2994.5	-8.8	9.7
	$\nu_5 + \nu_7 + \nu_8$	2993.9	-		-20.3	-		-4.9
	$\nu_3 + \nu_8$	2170.7	2150.9	-19.8	-19.7	2163.0	-7.7	-9.9
	$2\nu_3$	2143.7	2132.7	-11.0	-10.1	2132.7	-11.0	-11.7
	ν_7	1337.3	1336.2	-1.1	-1.8	1336.2	-1.1	-1.6
	ν_2	1247.6	1247.9	0.3	-0.2	1247.9	0.3	-2.9
	ν_8	1107.3	1092.7	-14.6	-14.6	1103.6	-3.7	-4.0
	ν_3	1077.1	1072.5	-4.6	-5.0	1072.5	-4.6	-5.9
	ν_4	633.6	632.3	-1.3	-2.0	632.3	-1.3	-2.0
	ν_5	567.7	564.3	-3.4	-3.8	568.0	0.3	0.7
	$2\nu_6$	536.3	533.0	-3.3	-3.8	533.0	-3.3	-5.0
DMS	ν_1	2992.0	2994.4	2.4	1.9	2994.4	2.4	1.4
	ν_{16}	2992.0	2994.4	2.4	1.9	2994.4	2.4	2.6
	ν_{12}	2965.5	2970.3	4.8	3.7	2970.3	4.8	5.1
	ν_{17}	2920.4	2921.9	1.5	-0.2	2921.9	1.5	1.1
	ν_2	2917.3	2918.9	1.6	0.1	2918.9	1.6	1.5
		2883.8	-			-		
		2864.6	2862.4	-2.2		2862.4	-2.2	
		2856.5	2855.3	-1.2		2855.3	-1.2	
	$2\nu_9$	2838.4	2836.3	-2.1	-3.5	2836.3	-2.1	-3.7
	ν_3	1444.4	1442.8	-1.6	-2.0	1444.4	0.0	-0.8
	ν_{18}	1438.9	1437.2	-1.7	-2.6	1437.2	-1.7	-1.2
	ν_{13}	1432.8	1432.2	-0.6	-1.4	1432.2	-0.6	-1.8
	ν_4	1331.8	-		-0.3	-		0.6
	ν_{19}	1310.4	1311.5	1.1	0.1	1311.5	1.1	-0.1
	ν_5	1030.8	1032.0	1.2	1.1	1032.0	1.2	1.5
	ν_{14}	973.3	975.3	2.0	2.3	975.3	2.0	3.0
	ν_{20}	901.8	904.0	2.2	2.2	904.0	2.2	2.5
	ν_6	696.2	694.0	-2.2	-2.8	694.0	-2.2	-2.4

Table S4.12: Overview of the different van 't Hoff plots constructed for the XB complex between CHF_2I and TMP or TMP-d_9 in LKr in the 120-156 K temperature interval, showing the estimated mole fractions of each monomer, range of the integrated monomer and complex bands and complex enthalpies $\Delta H°$ (LKr).

x_{CHF_2I}	x_{TMP}	Integrated CHF_2I band (cm^{-1})	Integrated TMP band (cm^{-1})	Integrated Complex band (cm^{-1})	$\Delta H°$ (LKr) [a]
1.1×10^{-4}	1.9×10^{-3}	1128-1093	3000-2930	1095-1080	-15.6(2)
6.1×10^{-5}	9.4×10^{-4}	646-622	834.4-819.5	1095-1080	-15.6(3)
1.9×10^{-4}	1.9×10^{-3} [b]	1128-1093	2263-2185	1095-1080	-15.0(1)

[a] Values are given with the standard deviation of the linear regression in parentheses.

[b] Measurement involving TMP-d_9, rather than TMP.

Table S4.13: Overview of the different van 't Hoff plots constructed for the HB complex between CHF_2I and TMP or TMP-d_9 in LKr in the 120-156 K temperature interval, showing the estimated mole fractions of each monomer, range of the integrated monomer and complex bands and complex enthalpies $\Delta H°$ (LKr).

x_{CHF_2I}	x_{TMP}	Integrated CHF_2I band (cm^{-1})	Integrated TMP band (cm^{-1})	Integrated Complex band (cm^{-1})	$\Delta H°$ (LKr) [a]
1.1×10^{-4}	1.9×10^{-3}	1128-1093	3000-2930	1110-1095	-10.40(5)
6.1×10^{-5}	9.4×10^{-4}	646-622	834.4-819.5	1109-1095	-10.3(1)
1.9×10^{-4}	1.9×10^{-3} [b]	1128-1093	2263-2185	1110-1095	-10.8(1)

[a] Values are given with the standard deviation of the linear regression in parentheses.
[b] Measurement involving TMP-d_9, rather than TMP.

Table S4.14: Overview of the different van 't Hoff plots constructed for the XB complex between CHF_2I and DMS or DMS-d_6 in LKr in the 120-156 K temperature interval, showing the estimated mole fractions of each monomer, range of the integrated monomer and complex bands and complex enthalpies $\Delta H°$ (LKr).

x_{CHF_2I}	x_{DMS}	Integrated CHF_2I band (cm^{-1})	Integrated DMS band (cm^{-1})	Integrated Complex band (cm^{-1})	$\Delta H°$ (LKr) [a]
3.8×10^{-5}	1.9×10^{-3}	1263-1234	997-955	CHF_2I ν_8 (1092.6)	-12.0(2)
1.1×10^{-4}	1.9×10^{-3} [b]	1263-1232	2275-2195	CHF_2I ν_8 (1092.6) [c]	-11.3(3)
1.9×10^{-4}	1.9×10^{-3}	1262-1238	1322-1302	CHF_2I ν_8 (1092.6) [c]	-10.8(2)
1.9×10^{-4}	1.9×10^{-3} [b]	1262.5-1235	2280-2185	CHF_2I ν_8 (1092.6) [c]	-11.1(1)

[a] Values are given with the standard deviation of the linear regression in parentheses.
[b] Measurement involving DMS-d_6, rather than DMS.
[c] Intensity obtained from a band fit analysis.

Table S4.15: Overview of the different van 't Hoff plots constructed for the HB complex between CHF_2I and DMS or DMS-d_6 in LKr in the 120-156 K temperature interval, showing the estimated mole fractions of each monomer, range of the integrated monomer and complex bands and complex enthalpies $\Delta H°$ (LKr).

x_{CHF_2I}	x_{DMS}	Integrated CHF_2I band (cm^{-1})	Integrated DMS band (cm^{-1})	Integrated Complex band (cm^{-1})	$\Delta H°$ (LKr) [a]
3.8×10^{-5}	1.9×10^{-3}	1263-1234	997-955	1114-1090	-8.0(2)
1.1×10^{-4}	1.9×10^{-3} [b]	1124-1093	2275-2195	1118-1090	-7.1(3)
1.9×10^{-4}	1.9×10^{-3}	1262.1238	1322-1302	1116-1091	-7.4(1)
1.9×10^{-4}	1.9×10^{-3} [b]	1262.5-1235	2280-2185	1114-1089	-8.3(2)

[a] Values are given with the standard deviation of the linear regression in parentheses.
[b] Measurement involving DMS-d_6, rather than DMS.

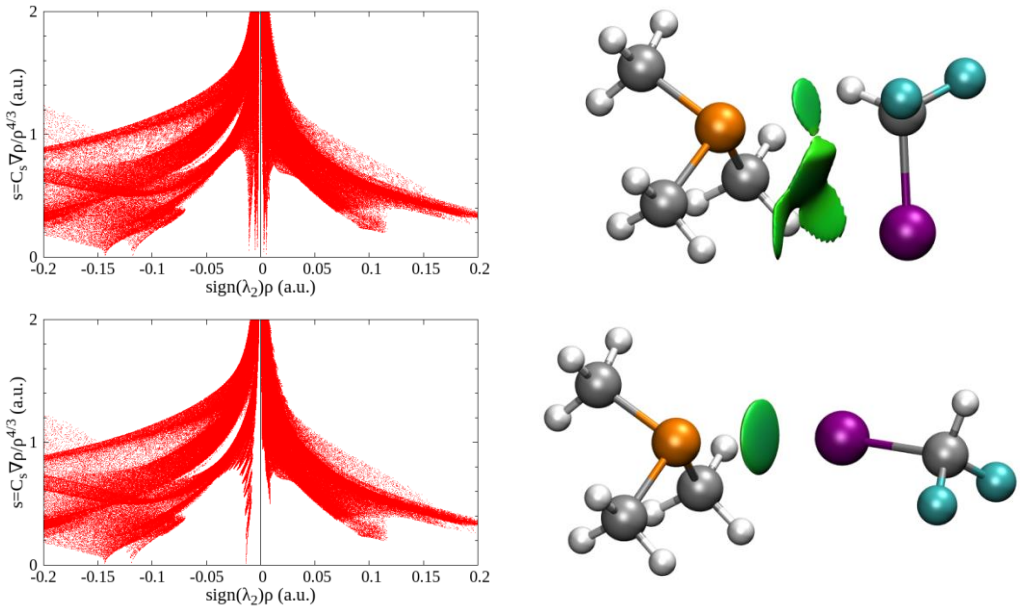

Figure S4.1: Plots of the reduced density gradient versus the electron density multiplied by the sign of the second Hessian eigenvalue (left) and gradient isosurfaces (s = 0.5 a.u., right) for the HB complex (top) and the XB complex (bottom) between CHF_2I and TMP.

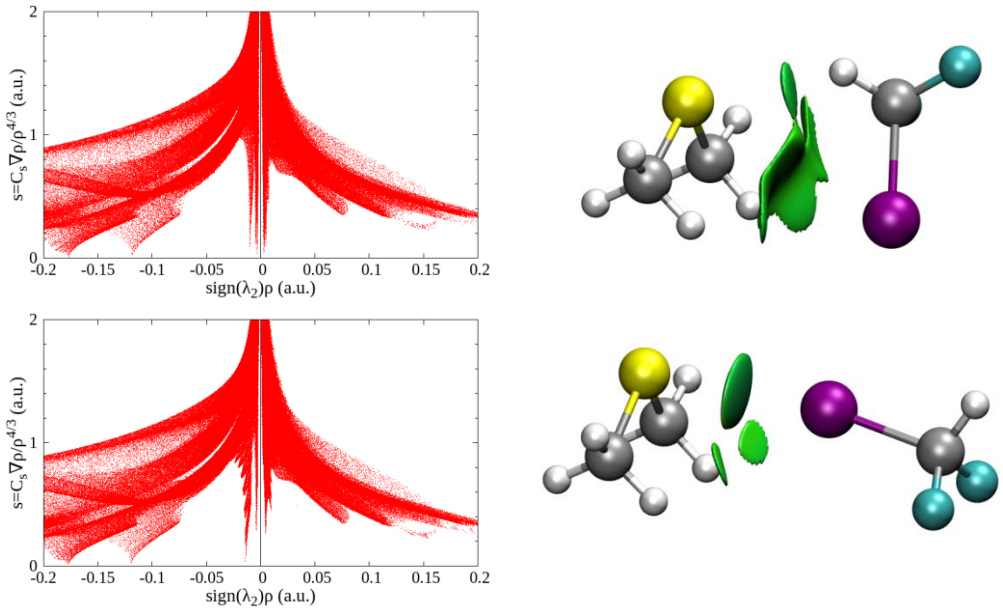

Figure S4.2: Plots of the reduced density gradient versus the electron density multiplied by the sign of the second Hessian eigenvalue (left) and gradient isosurfaces (s = 0.5 a.u., right) for the HB complex (top) and the XB complex (bottom) between CHF_2I and DMS.

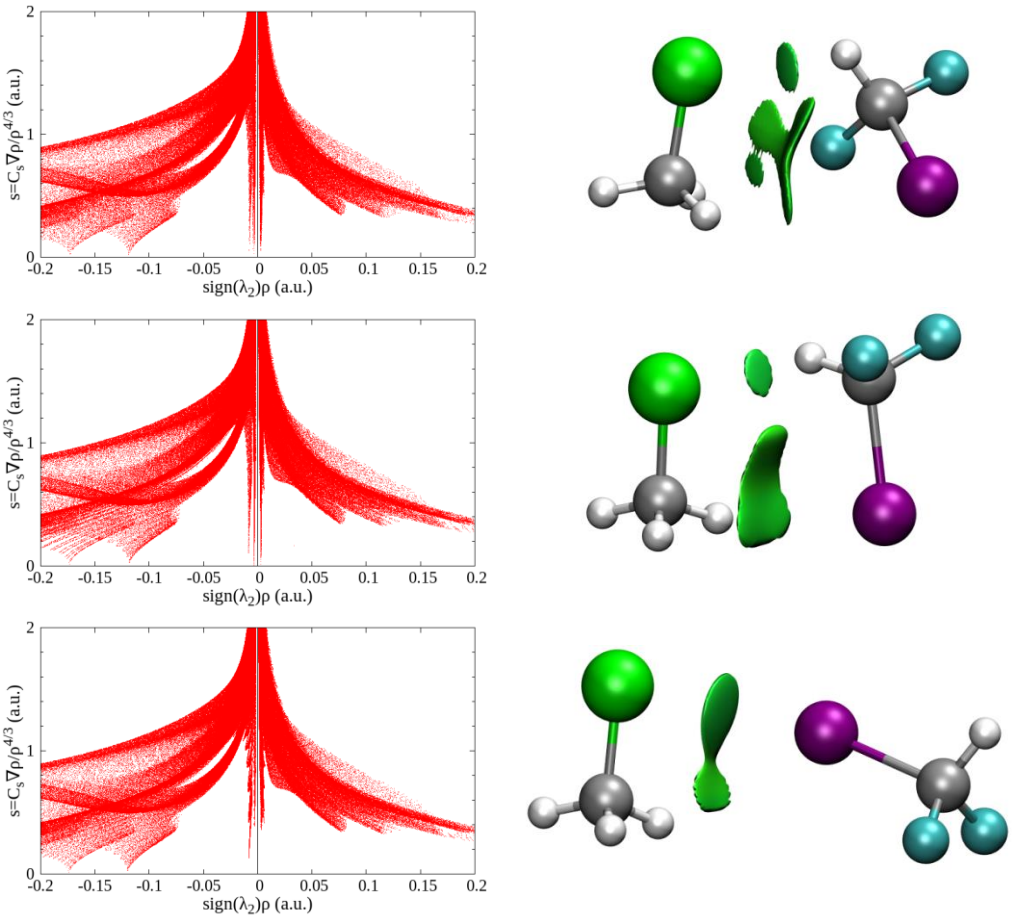

Figure S4.3: Plots of the reduced density gradient versus the electron density multiplied by the sign of the second Hessian eigenvalue (left) and gradient isosurfaces (s = 0.5 a.u., right) for the HB complexes with a secondary C-H···F (top) or C-H···I interaction (middle) and the XB complex (bottom) between CHF_2I and CH_3Cl.

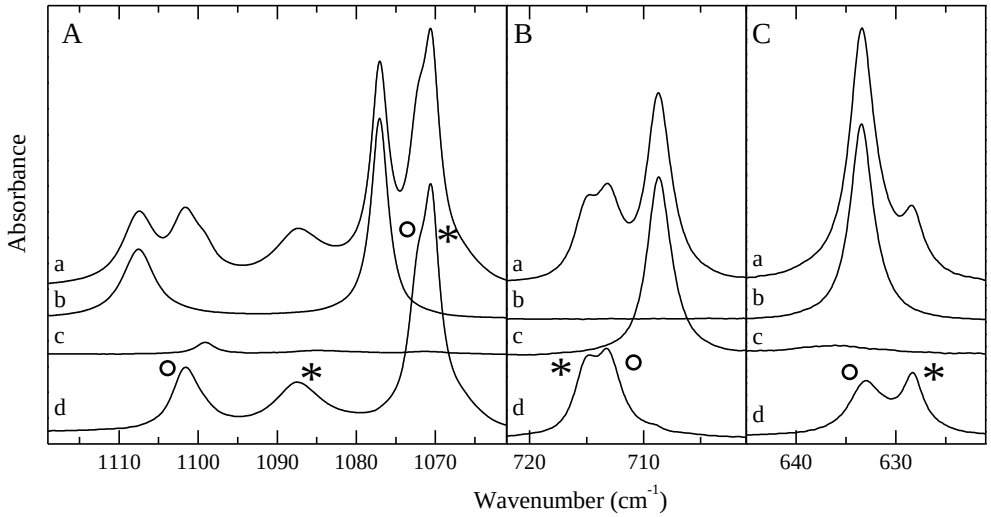

Figure S4.4: Infrared spectra of selected spectral regions for the mixtures of CHF_2I with TMP dissolved in LKr at 130 K. In each panel, trace *a* represents the mixed solution, while traces *b* and *c* show the rescaled spectra of the solutions containing only CHF_2I or TMP, respectively. Trace *d* represents the spectrum of the complex which is obtained by subtracting the rescaled traces *b* and *c* from trace *a*. Bands due to the XB and HB complexes observed in traces *d* are marked with an asterisk (*) or open circle (°), respectively. Estimated mole fractions of the solutions of the mixtures are 5.6×10^{-5} for CHF_2I and 3.8×10^{-3} for TMP in panel A, 9.4×10^{-4} for CHF_2I and 9.4×10^{-4} for TMP in panel B and 5.6×10^{-5} for CHF_2I and 2.4×10^{-3} for TMP-d_9 in panel C.

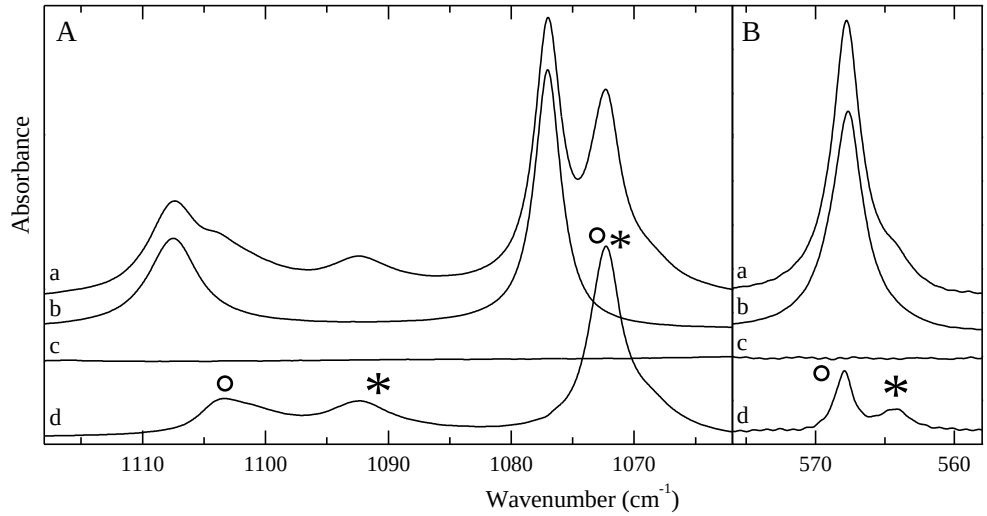

Figure S4.5: Infrared spectra of selected spectral regions for the mixtures of CHF_2I with DMS dissolved in LKr at 130 K. In each panel, trace *a* represents the mixed solution, while traces *b* and *c* show the rescaled spectra of the solutions containing only CHF_2I or DMS, respectively. Trace *d* represents the spectrum of the complex which is obtained by subtracting the rescaled traces *b* and *c* from trace *a*. Bands due to the XB and HB complexes observed in traces *d* are marked with an asterisk (*) or open circle (°), respectively. Estimated mole fractions of the solutions of the mixtures are 5.6×10^{-5} for CHF_2I and 3.8×10^{-3} for DMS in panel A and 9.4×10^{-4} for CHF_2I and 1.9×10^{-3} for DMS in panel B.

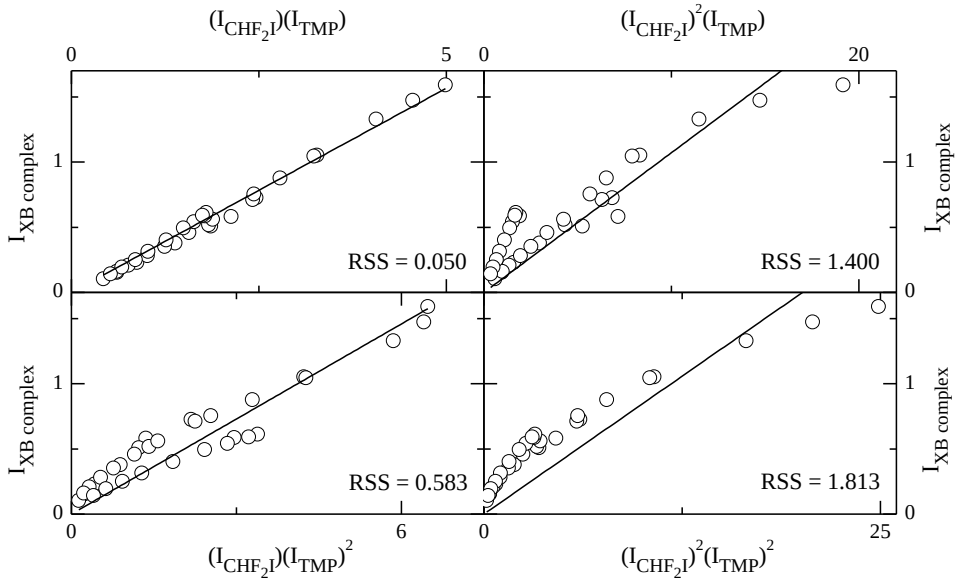

Figure S4.6: Concentration study plots of the CHF_2I·TMP XB complex at 130 K in LKr. Integrated intensity of the complex is plotted against the product of monomer intensities $\left(I_{CHF_2I}\right)^x (TMP)^y$. Top left: $x = 1, y = 1$, top right: $x = 2, y = 1$, bottom left $x = 1, y = 2$ and bottom right $x = 2, y = 2$. Additionally, residual sum of square values (RSS) have been included.

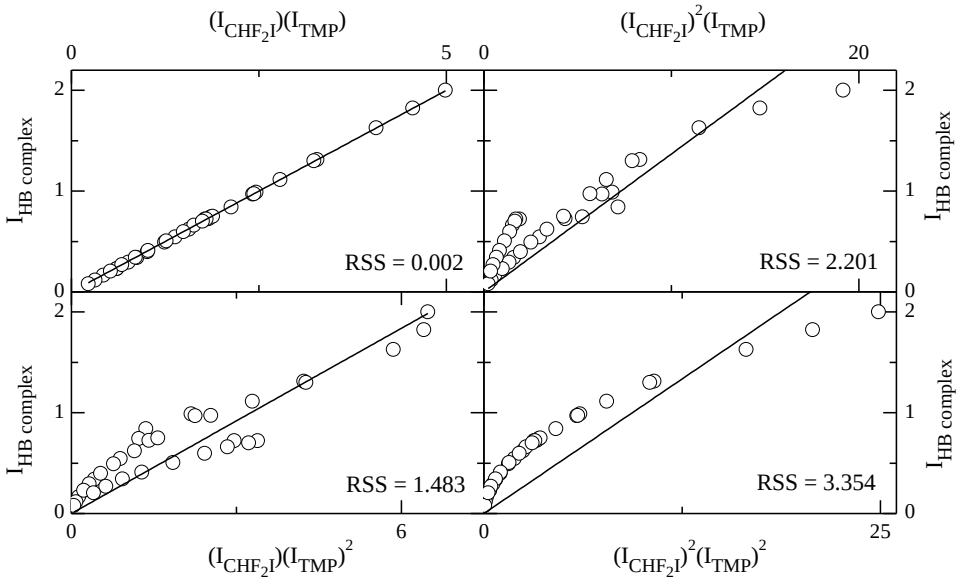

Figure S4.7: Concentration study plots of the CHF_2I·TMP HB complex at 130 K in LKr. Integrated intensity of the complex is plotted against the product of monomer intensities $\left(I_{CHF_2I}\right)^x (TMP)^y$. Top left: $x = 1, y = 1$, top right: $x = 2, y = 1$, bottom left $x = 1, y = 2$ and bottom right $x = 2, y = 2$. Additionally, residual sum of square values (RSS) have been included.

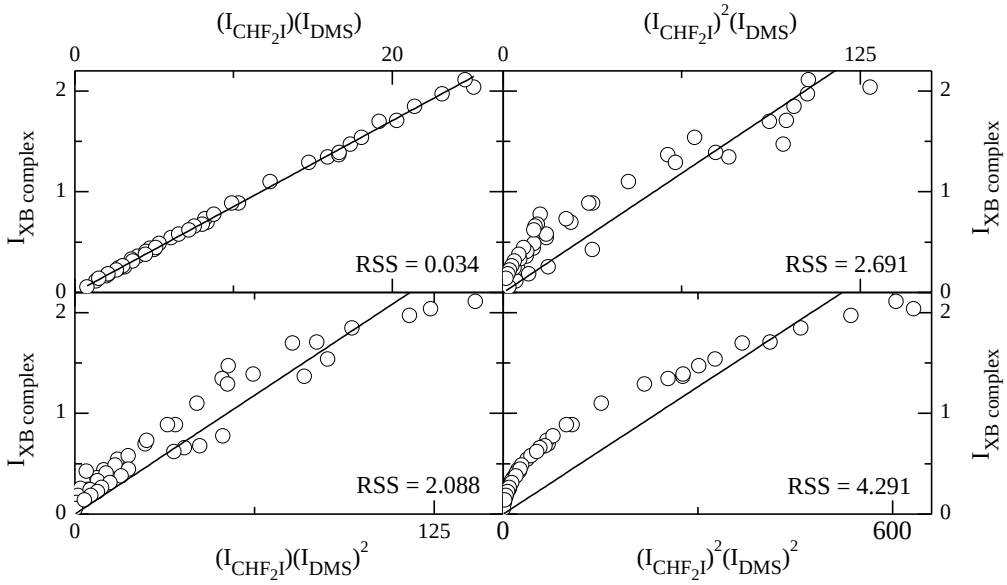

Figure S4.8: Concentration study plots of the CHF_2I·DMS XB complex at 130 K in LKr. Integrated intensity of the complex is plotted against the product of monomer intensities $\left(I_{CHF_2I}\right)^x(DMS)^y$. Top left: $x = 1, y = 1$, top right: $x = 2, y = 1$, bottom left $x = 1, y = 2$ and bottom right $x = 2, y = 2$. Additionally, residual sum of square values (RSS) have been included.

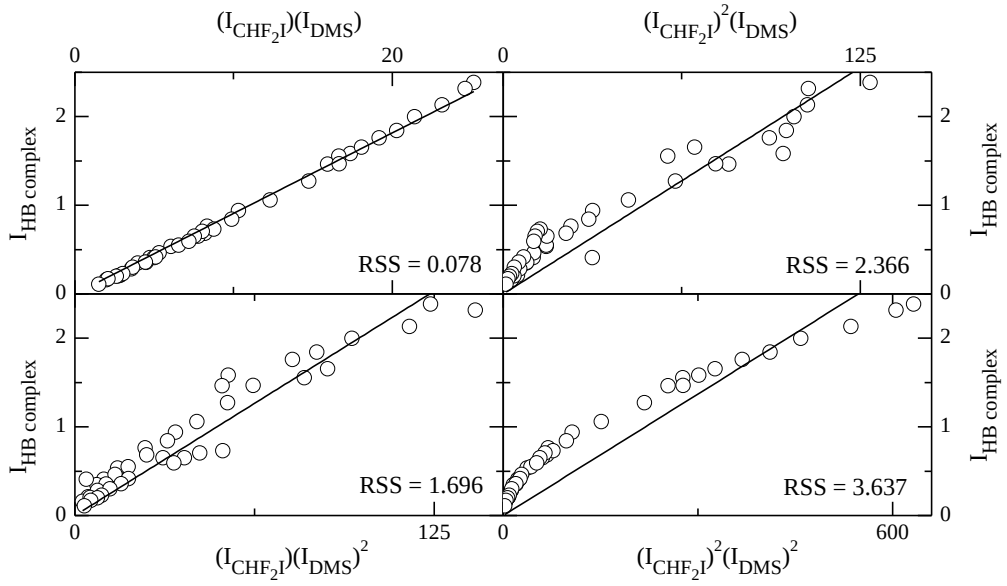

Figure S4.9: Concentration study plots of the CHF_2I·DMS HB complex at 130 K in LKr. Integrated intensity of the complex is plotted against the product of monomer intensities $\left(I_{CHF_2I}\right)^x(DMS)^y$. Top left: $x = 1, y = 1$, top right: $x = 2, y = 1$, bottom left $x = 1, y = 2$ and bottom right $x = 2, y = 2$. Additionally, residual sum of square values (RSS) have been included.

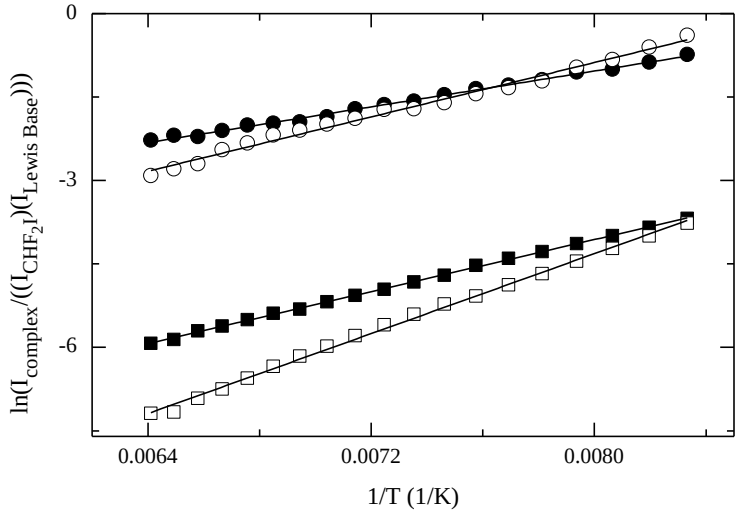

Figure S4.10: Typical van 't Hoff plots of the HB complexes (filled) and XB complexes (hollow) of CHF_2I with DMS (round) and TMP (square) in LKr.

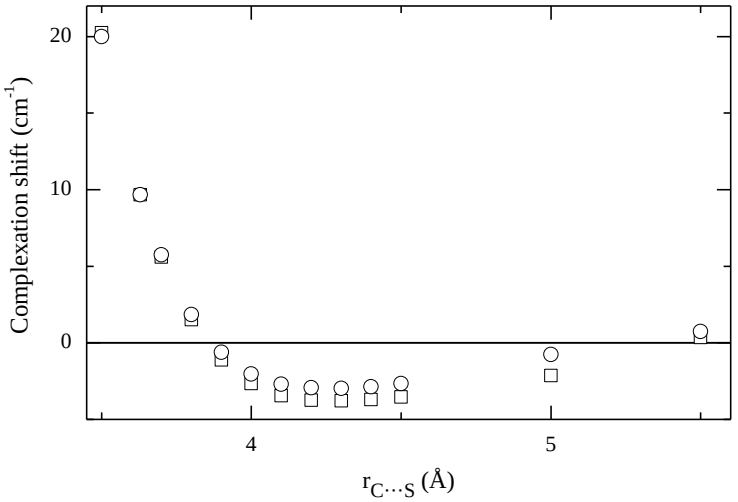

Figure S4.11: Complexation shifts (in cm^{-1}) of the CHF_2I ν_1 mode plotted against the C···S distance (in Å) for the partially optimized CHF_2I·DMS-d_6 HB complex with the C-H···S angle (□) and C-H···S angle and C-H···S-C dihedral angle (○) from the equilibrium geometry.

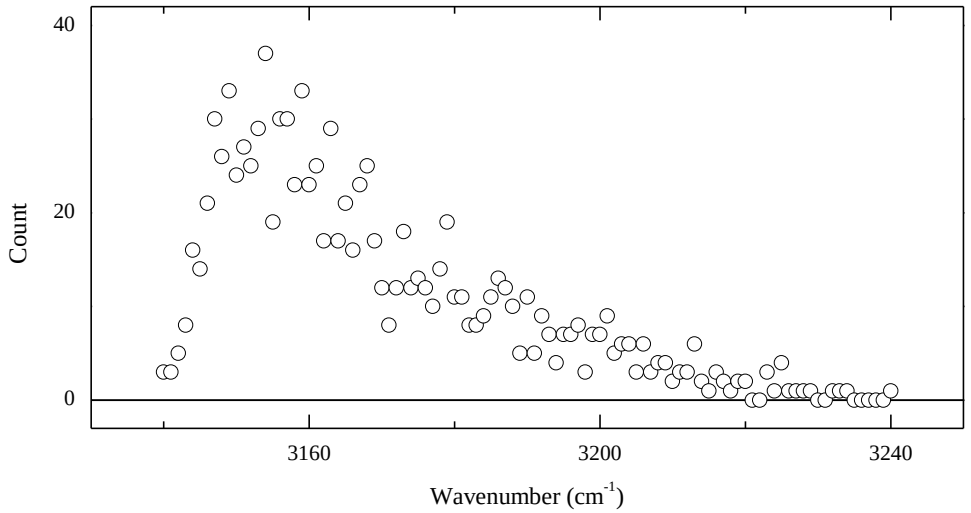

Figure S4.12: Distribution of MP2/aug-cc-pVDZ-PP *ab initio* frequencies for the C-H stretching mode of the HB complex between CHF_2I and DMS-d_6 at 130 K, obtained from a Monte Carlo sample of the internal coordinates describing the relative orientation of both molecules. Division of the frequencies was made using a bin-width of 1 cm^{-1}.

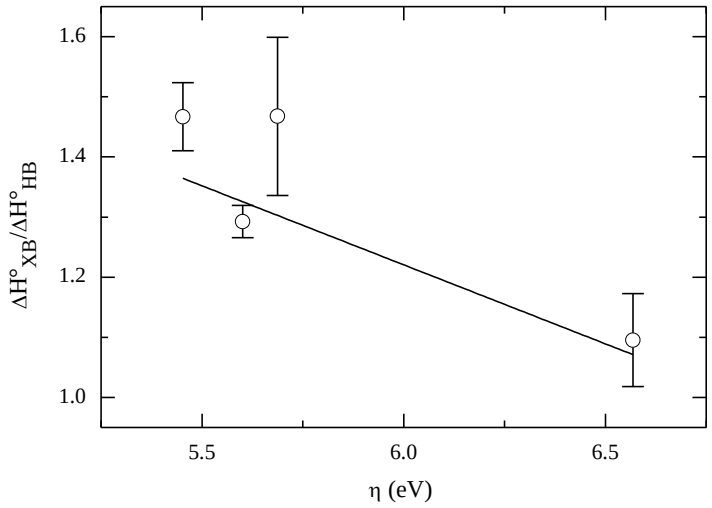

Figure S4.13: Plot of the enthalpy ratio of $\frac{\Delta H°_{XB}}{\Delta H°_{HB}}$ versus chemical hardness η (in eV), as calculated using the method of Tozer et al. for the complexes formed between CHF_2I and the Lewis bases TMA, DME, TMP and DMS.

Chapter 5

The effect of bond donor fluorination on the halogen bonding/hydrogen bonding competition.

Complexes of fluoroiodomethane with DME and TMA.

This chapter has been published as:

Geboes, Y.; De Proft, F.; Herrebout, W. A., The effect of fluorination on the competition of halogen bonding and hydrogen bonding: Complexes of fluoroiodomethane with dimethyl ether and trimethylamine, *The Journal of Physical Chemistry A* **2017**, *121*(21), 4180-4188.

Abstract

To further rationalize the competition between halogen and hydrogen bonding, a combined experimental and theoretical study on the weakly bound molecular complexes formed between the combined halogen bond/hydrogen bond donor CH_2FI and the Lewis bases DME and TMA (in standard and fully deuterated form) is presented. The experimental data are obtained by recording IR and Raman spectra of mixtures of the compounds in LKr, at temperatures between 120 K and 156 K. The experiments are supported by *ab initio* calculations at the MP2/aug-cc-pVDZ-PP level, statistical thermodynamics and MC-FEP simulations. For the mixtures containing CH_2FI and DME a HB complex with an experimental complexation enthalpy of -7.0(2) kJ mol^{-1} is identified. Only a single weak spectral feature is observed which can be tentatively assigned to the XB. For the mixtures involving TMA, both XB and HB complexes are observed, the experimental complexation enthalpies being -12.5(1) and -9.6(2) kJ mol^{-1} respectively. To evaluate the influence of fluorination on the competition between halogen and hydrogen bonding, the results obtained for CH_2FI are compared with those of a previous study involving CHF_2I.

5.1 Introduction

Halogen bonds, the noncovalent interactions between covalently bonded halogen atoms and electron rich sites in the same or in another molecule, have been widely studied as a consequence of their applicability in, among other, the fields of rational drug design, molecular recognition, supramolecular chemistry and crystal engineering. One of the main aspects studied in this field is the relationship between this noncovalent interaction and the ubiquitous hydrogen bonding. It has been demonstrated that both noncovalent interactions can coexist, [1-3] compete [4-10] or cooperate [11] with each other in multiple theoretical and experimental studies.

To be able to rationalize the competition between halogen bonding and hydrogen bonding, a combined experimental and computational study on the weakly bound bimolecular complexes formed between CHF_2I, which can simultaneously act as a halogen and hydrogen bond donor, and several Lewis bases including DME, TMA, DMS and TMP has been pursued in the previous chapters. [12-13] The cornerstones of these studies were the infrared and Raman measurements of liquefied noble gas solutions containing mixtures of CHF_2I and one of the Lewis bases, thereby exploiting the advantage that the weakly bonded complexes can be studied at thermodynamic equilibrium with the monomers. It was found that for some Lewis bases the XB complex was stronger than the HB complex, while for other electron donors the HB complex prevailed over the XB isomer. Rationalization of the results, supported by DFT calculations, suggested that iodine halogen bonding is generally preferred by the softer Lewis bases, while harder Lewis bases tend to favour HB complexes.

To get a more general view of the competition between both types of bonding, it is of interest to understand whether the tendencies observed for CHF_2I hold up when the nature of the combined donor molecule is altered by substituting the electron withdrawing groups present. Such information can, for example, be deduced by comparing data for CH_2FI and CHF_2I.

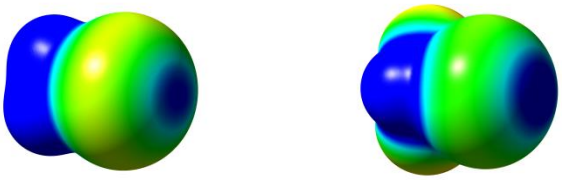

Figure 5.1: Electrostatic potential on the molecular surface of CH_2FI (left) and CHF_2I (right), defined by the 0.001 electrons $Bohr^{-3}$ contour of the electron density. Positive, neutral and negative regions are shown in blue, green and red, respectively.

The molecular electrostatic potentials of both species are presented in Figure 5.1. It can be seen that, upon additional fluorination, the size of the σ-hole on the iodine atom increases significantly. The increase for the σ-hole, influencing the halogen bond capabilities of both species, is also illustrated by the maximum values for the electrostatic potential mapped on the 0.001 electrons $Bohr^{-3}$ electron density isosurface, the values being 0.0292 a.u. for CH_2FI and 0.0377 a.u. for CHF_2I. Also for the hydrogen atom(-s) an increase of the maximal potential is observed upon additional fluorination, the values for the maxima localized near the hydrogen atoms in CH_2FI being 0.0424 a.u. and that for the remaining hydrogen atom in CHF_2I being 0.0547 a.u.

To further investigate the effect of fluorination on the strength of these noncovalent interactions and their competition, experimental data for the complexes between CH_2FI and the Lewis bases DME and TMA are obtained in this study using FTIR on solutions in liquid krypton. The interpretation of the data is supported by *ab initio* and statistical thermodynamics calculations, and MC-FEP simulations. The results reported and tendencies observed will be compared with the data recently reported for the complexes with CHF_2I.

5.2 Results

5.2.1 *Ab initio* calculations

Ab initio calculations at the MP2/aug-cc-pVDZ-PP level of theory yielded two stable complex geometries between CH_2FI and each of the Lewis bases DME and TMA. The equilibrium geometries of the complexes are shown in Figure 5.2. Cartesian coordinates of monomers and complexes are given in Tables S5.1 and S5.2 of the SI. The intermolecular parameters defined in Figure 5.2 and energetics for all complexes are summarized in Table 5.1. The XB complexes, formed through the interaction between iodine and the lone pair on the oxygen or nitrogen atom, are both characterized by a C_s symmetry. The HB complexes, in which one of the hydrogen atoms of CH_2FI interacts with the oxygen or nitrogen atom have C_1 symmetry.

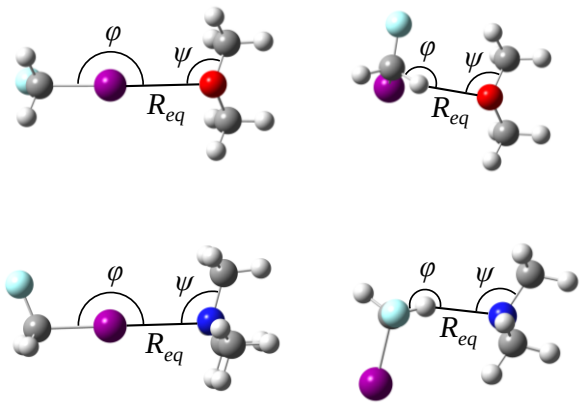

Figure 5.2: MP2/aug-cc-pVDZ-PP equilibrium geometries for the XB and HB complexes of CH_2FI with DME and TMA.

For both XB complexes, nearly linear geometries are obtained, the C-I···Y angles being 174.7° for DME and 179.2° for TMA. For the HB complexes, the C-H···Y angles are reduced to 143.4° and 156.0° for DME and TMA, respectively. In agreement with tendencies observed and described in chapters, these deviations from linearity enable the formation of secondary interaction between the halogen atoms of CH_2FI and the methyl groups of the Lewis bases in the HB complexes. To aid

characterization of such interactions, in this study, additional information supporting their role was obtained using the NCI index visualized using NCIPLOT [14-15]. These plots are given in Figures S5.1 and S5.2 of the SI. For both XB complexes, a single isosurface is observed between the iodine atom and the lone pair carrying atom of the Lewis base. Inspection of the result for the HB complex with DME in Figure S5.1 reveals the presence of isosurfaces between iodine and a hydrogen atom of both methyl groups, as well as an isosurface between fluorine and a hydrogen atom in addition to the isosurface between the CH_2FI hydrogen atom and the oxygen atom. Similar secondary interactions are also observed in the HB complex with TMA, shown in Figure S5.2.

Table 5.1: Intermolecular distance R_{eq} (Å), bond angles (°), MP2/aug-cc-pVDZ-PP ΔE(DZ) and CCSD(T)/CBS extrapolated complexation energies ΔE(CCSD(T)), calculated vapour phase complexation enthalpies $\Delta H°$ (vap,calc), the calculated complexation enthalpies in liquid krypton ($\Delta H°$ (LKr,calc)) and the corresponding experimentally obtained complexation enthalpies ($\Delta H°$ (LKr)) (kJ mol^{-1}) for the complexes of CH_2FI with DME and TMA. For comparison, calculated ($\Delta H°$ (CHF_2I, LKr, calc)) and experimental ($\Delta H°$ (CHF_2I, LKr)) [12] complexation enthalpies for the complexes with CHF_2I are also given (kJ mol^{-1}).

	DME		TMA	
	XB	HB	XB	HB
$R_{eq}=R_{X\cdots Y}$ [a]	3.10	2.29	2.99	2.31
$\varphi_{C\text{-}X\cdots Y}$ [a]	174.7	143.4	179.2	156.0
$\psi_{C\text{-}Y\cdots X}$ [a]	106.5	105.0/123.0	107.5/109.1/109.1	96.2/114.4/115.8
ΔE (DZ)	-14.5	-17.4	-23.6	-20.8
ΔE (CCSD(T))	-15.4	-19.0	-22.8	-21.9
$\Delta H°$ (vap,calc)	-13.0	-16.1	-20.4	-19.0
$\Delta H°$ (LKr,calc)	-9.4	-10.1	-16.4	-12.7
Experimental				
$\Delta H°$ (LKr)		-7.0(2)	-12.5(1)	-9.6(2)
$\Delta H°$ (CHF_2I, LKr, calc)	-12.4	-12.0	-23.4	-16.6
$\Delta H°$ (CHF_2I, LKr) [b]	-11.5(6)	-10.5(5)	-19.0(3)	-14.7(2)

[a] X = I, H; Y = O, N
[b] Values from Nagels et al. [12]

5.3.2 Infrared measurements

The assignment of the vibrational modes of DME(-d_6) and TMA(-d_9) observed in liquefied noble gases has been discussed in detail in previous chapters and is not repeated here. The assignment of the vibrational modes of CH_2FI given is based on *ab initio* calculations and the Raman study reported by Feller et al. [16] In order to assess the presence of XB and/or HB complex, the complexation shifts of the bands in the subtracted spectra are compared to those obtained from *ab initio* calculations, given in Tables S5.3 to S5.6 of the SI. Due to the limited solubility of CH_2FI, a comprehensive study over a wide concentration interval was not feasible. As a result, some complex bands of the vibrational modes with the lowest IR intensities could not be observed. Estimated mole fractions of the components in solution varied between 7.5×10^{-5} and 1.9×10^{-3} for CH_2FI, 1.3×10^{-4} and 4.9×10^{-3} for DME(-d_6) and 2.8×10^{-4} and 1.9×10^{-3} for TMA(-d_9).

5.2.2.1 CH_2FI·DME infrared spectra

The *ab initio* calculations suggest that a distinction between the XB and HB complex between CH_2FI and DME can be made in the ν_5, ν_7, ν_8 and ν_3 spectral regions of CH_2FI, whereas no DME modes are suitable for distinction between both dimer geometries.

An overview of experimentally observed monomer bands, complex bands, complexation shifts and the corresponding calculated shifts is given in Table 5.2 for the complexes with DME and Table S5.7 for the complexes with DME-d_6. Selected spectral regions for the mixtures between CH_2FI and DME or DME-d_6 are given in Figures 5.3 and S5.3 of the SI, respectively.

For the ν_5 mode of CH_2FI, shown in panel C of Figure 5.3, a -2.8 cm^{-1} redshifted band corresponding to the HB complex with a calculated value of -3.5 cm^{-1} is observed. No blueshifted band corresponding to the XB complex, with a calculated shift of 2.9 cm^{-1}, is observed. Further evidence for the presence of a HB complex is found for CH_2FI ν_7 mode, which, due to overlap with the C-H stretches of DME and its low IR intensity, is

shown for a mixture with DME-d_6 in panel S5.3A of the SI. For this spectral region, a 7.4 cm^{-1} blueshifted band corresponding to the calculated value of 7.1 cm^{-1} is observed. As before, no band corresponding to the -8.0 cm^{-1} redshifted XB complex was observed.

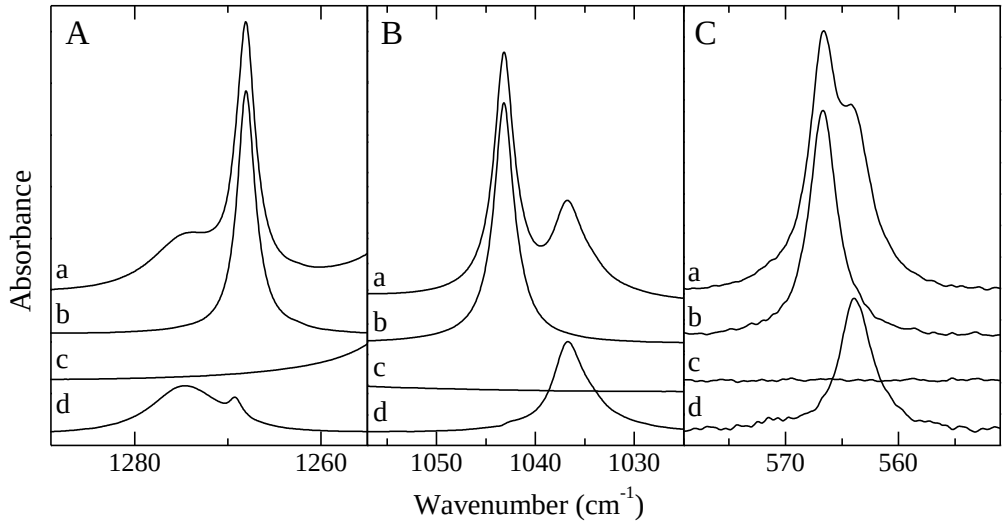

Figure 5.3: Infrared spectra of selected spectral regions for the mixtures of CH_2FI with DME dissolved in LKr at 130 K. In each panel, trace *a* represents the mixed solution, while traces *b* and *c* show the rescaled spectra of the solutions containing only CH_2FI or DME, respectively. Trace *d* represents the spectrum of the complex which is obtained by subtracting the rescaled traces *b* and *c* from trace *a*. Estimated mole fractions of the solutions of the mixtures are 1.2×10^{-4} for CH_2FI and 4.9×10^{-3} for DME in panel A, 1.3×10^{-4} for CH_2FI and 4.7×10^{-3} for DME in panel B and 1.2×10^{-4} for CH_2FI and 4.9×10^{-3} for DME in panel C.

It is worth noting that the complex bands of the ν_7 mode and ν_1 mode (shown on the right-hand side in the same panel) have similar intensities, whereas the intensity of the ν_1 mode of the monomer is far more intense than the ν_7 mode (trace *b*). This can be explained by the increase of intensity of the ν_7 mode upon hydrogen bond formation, as predicted in the calculations given in Table S5.4B, where an intensity of 0.5 km mol^{-1} is calculated for this mode in the monomer and 7.8 km mol^{-1} for the same mode in the HB complex. For the XB complex, a less pronounced intensity enhancement to 1.4 km mol^{-1} is predicted, as seen in Table S5.3B. To explore whether the low infrared intensity might be a reason for the absence of a XB complex band in the spectra

studied, Raman experiments were also initiated. Unfortunately, due to the low solubility and the larger bandwidth of the ν_7 mode, no complex bands were observed for this mode.

For the ν_8 mode of CH_2FI a very weak 5.3 cm^{-1} blueshifted band is observed, corresponding to the 13.5 cm^{-1} blueshift calculated for the HB complex, whereas no trace of a redshifted band for the XB complex ($\Delta\nu_{calc}$ = -0.8 cm^{-1}) was observed.

Up to this point, all complex bands observed corresponded well to the HB complex, whereas no bands corresponding to the XB complex were detected. For the CH_2FI ν_3 mode, shown in panel 5.3A, a clear 6.5 cm^{-1} blueshifted band is observed, which is again in excellent correspondence with the calculated value of 8.0 cm^{-1} for the HB complex. However, apart from this band, a weaker spectral feature with a blueshift of 1.3 cm^{-1} is also observed. To evaluate whether this feature originates from the Lewis base involved, mixtures involving DME-d_6 were also investigated. As shown in panel B of Figure S5.3 of the SI, this spectral feature is also present when using the fully deuterated Lewis base. It must therefore be considered that this spectral feature can come from the presence of a small amount of XB complex ($\Delta\nu_{calc}$ = -0.7 cm^{-1}) in the solution.

5.2.2.2 CH_2FI·DME van ‘t Hoff plots and experimental complexation enthalpies

By performing measurements of CH_2FI·DME(-d_6) mixtures within the 120 K - 156 K temperature interval, four van ‘t Hoff plots were constructed, yielding an average complexation enthalpy of -7.0(2) kJ mol^{-1}. An overview of the concentrations and integration intervals used, as well as the resulting complexation enthalpies, is given in Table S5.9 of the SI. An example of a typical van ‘t Hoff plot for this complex is given in Figure S5.6 of the SI. It should be noted that for the van ‘t Hoff plots constructed using the complex band intensities of the ν_3 mode of CH_2FI, the small additional band intensity was integrated separately and subtracted from the total intensity. Apart from the complex intensities of the ν_3 mode of CH_2FI, the integrated intensities of the

complex band of the CH_2FI ν_4 mode, shown in panel 5.3B, were also used for the construction of a van 't Hoff plot.

Table 5.2: Experimental infrared frequencies for the monomers and complexes, as well as experimental complexation shifts ($\Delta\nu_{exp}$) and MP2/aug-cc-pVDZ-PP calculated complexation shifts ($\Delta\nu_{calc}$), in cm^{-1}, for the XB complex and HB complex of CH_2FI with DME dissolved in LKr at 130 K.

Assignment		$\nu_{monomer}$	$\nu_{complex,HB}$	$\Delta\nu_{exp,HB}$	$\Delta\nu_{calc,HB}$	$\Delta\nu_{calc,XB}$
CH_2FI	ν_7	3043.0	[a]		7.1	-8.0
	ν_1	2981.5	[a]		-3.0	-5.0
		2975.7	-			
	$2\nu_2$	2877.3	[a]		-1.6 [b]	-2.1
	$2\nu_4$	2070.0	2057.0	-13.0	-21.3	-21.1
	ν_2	1448.1	-		-0.8 [b]	-1.0
	ν_3	1268.0	1274.5	6.5	8.0	-0.7
	ν_8	1219.8	1225.1	5.3	13.5	-0.8
	$2\nu_5$	1130.1	1124.4	-5.7	-7.0	5.8
	ν_4	1043.2	1036.7	-6.5	-10.7	-10.5
	ν_4 (^{13}C)	1020.6	1014.4	-6.2	-10.7	-10.5
	ν_9	855.1	-			
	ν_5	566.7	563.9	-2.8	-3.5	2.9
DME	ν_1	2990.0	2991.7	1.7	1.2	2.0
	ν_{16}	2990.0	2991.7	1.7	-0.6	2.0
	$2\nu_3$	2950.6	-		-3.1	-4.8
	$\nu_3 + \nu_{18}$	2932.8	2931.2	-1.6	-2.9	-4.6
	$\nu_3 + \nu_{13}$	2929.5	2931.2	1.7	-2.6	-3.3
	ν_{12}	2916.5	2919.2	2.7	11.9	11.1
	$\nu_3 + \nu_{19}$	2905.5	-		-1.1	-3.1
	$\nu_4 + \nu_{19}$	2880.5	2885.4	4.9	3.8	-1.6
	ν_2	2811.6	2816.6	5.0	6.1	5.6
	$\nu_6 + \nu_{20}$	2092.6	2084.5	-8.1	-15.1	-17.7
	$\nu_6 + \nu_{21}$	2020.4	2012.6	-7.8	-10.7	-15.0
	ν_3	1474.9	1474.8	-0.1	-1.6	-2.4
	ν_{18}	1457.4	1457.8	0.4	-1.4	-2.2
	ν_{13}	1455.1	1455.0	-0.1	-1.1	-0.9
	ν_{19}	1426.2	-		0.4	-0.7
	ν_5	1244.9	1246.5	1.6	1.6	-0.4
	ν_{20}	1172.2	1168.4	-3.8	-7.6	-8.0
	ν_{21}	1099.1	1096.8	-2.3	-3.1	-5.3
	ν_6	929.3	924.2	-5.1	-7.6	-9.7

[a] Modes could not be assigned due to overlap with DME modes.

[b] Vibrational mode is degenerate with DME modes in *ab initio* calculations.

5.2.2.3 CH_2FI·TMA infrared spectra

As TMA vibrational modes are found in the same regions as the CH_2FI ν_3 and ν_4 modes, the mixtures involving the fully deuterated TMA-d_9 will be discussed here, while spectra and assignments for the mixtures involving TMA are given in the SI.

An overview of experimentally observed monomer bands, complex bands, complexation shifts and the corresponding calculated shifts is given in Table 5.3 for the complexes with TMA-d_9 and Table S5.8 for the complexes with TMA, while selected spectral regions of CH_2FI·TMA mixtures are shown in Figure S5.4. In order to avoid saturation of the detector in the spectral regions where vibrational modes of CHF_2I and TMA overlap, the spectra shown in panels S5.4A and S5.4B were obtained using reduced concentrations of both monomers.

In several of the spectral regions discussed for the CH_2FI·DME mixtures, two distinct complex bands are observed for CH_2FI·TMA-d_9 mixtures. In the CH_2FI ν_3 region near 1268 cm^{-1}, a broad band with a 12.8 cm^{-1} blueshift as well as a narrower band with a -3.2 cm^{-1} redshift are observed upon subtraction, as shown in panel A of Figure 5.4. These complex bands can be assigned to the HB complex and XB complex with calculated shifts of 24.2 cm^{-1} and -6.4 cm^{-1} respectively.

In the CH_2FI ν_5 spectral region, shown in panel 5.4C, two overlapping redshifted bands are observed, the experimental complexation shifts being -4.1 cm^{-1} and -1.4 cm^{-1}. Although redshifts were calculated for both complex geometries (-5.9 cm^{-1} for the HB and -5.4 cm^{-1} for the XB complex), the difference between experimental complexation shifts of -1.4 cm^{-1} and -4.1 cm^{-1} is noticeably larger than predicted. The assignment of the band with the largest redshift to the HB complex and the band with the smallest redshift to the XB complex, given in Tables 5.3 and S5.8 of the SI, should therefore be interpreted with the necessary prudence. It should also be noted that the assignment of the least intense band to the XB complex is in line with the calculated reduction in IR intensity for this mode in the XB complex, as given in Table S5.5B.

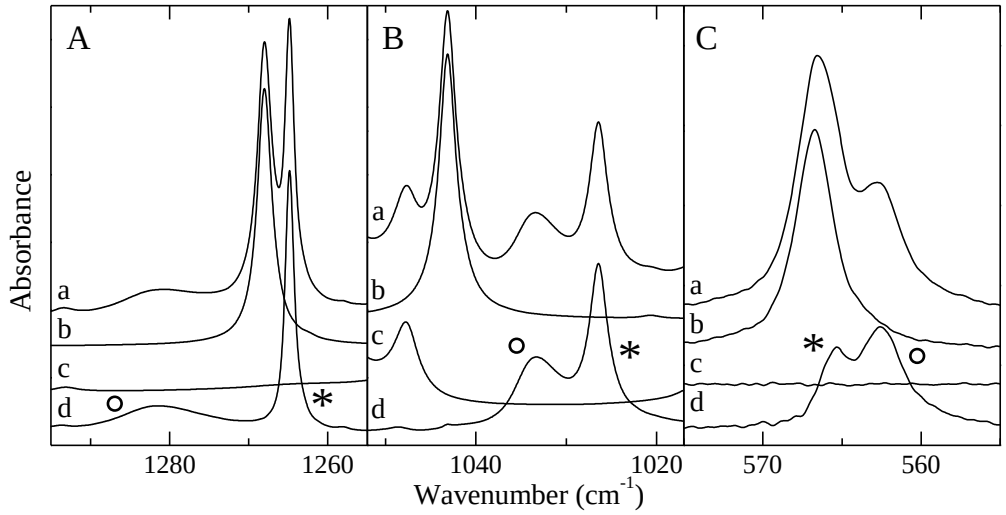

Figure 5.4: Infrared spectra of selected spectral regions for the mixtures of CH_2FI with TMA-d_9 dissolved in LKr at 130 K. In each panel, trace *a* represents the mixed solution, while traces *b* and *c* show the rescaled spectra of the solutions containing only CH_2FI or TMA-d_9, respectively. Trace *d* represents the spectrum of the complex which is obtained by subtracting the rescaled traces *b* and *c* from trace *a*. Bands due to the XB and HB complexes observed in traces *d* are marked with an asterisk (*) or open circle (°), respectively. Estimated mole fractions of the solutions of the mixtures are 1.3×10^{-4} for CH_2FI and 1.9×10^{-3} for TMA-d_9 in panel A, 7.1×10^{-5} for CH_2FI and 1.9×10^{-3} for TMA-d_9 in panel B and 1.3×10^{-4} for CH_2FI and 1.9×10^{-3} for TMA-d_9 in panel C.

Also in the spectral region of the CH_2FI ν_4 mode shown in panel 5.4B, two partially overlapping redshifted bands are observed with experimental complexation shifts of -16.7 cm^{-1} and -9.9 cm^{-1} corresponding to the XB complex ($\Delta\nu_{calc}$ = -18.5 cm^{-1}) and HB complex ($\Delta\nu_{calc}$ = -13.5 cm^{-1}) respectively.

Another interesting spectral feature is the presence of a sharp complex band at 1136.4 cm^{-1} in the spectra of $CH_2FI{\cdot}$TMA-d_9 mixtures, shown in panel B of Figure 5.5, which is absent in the spectra of $CH_2FI{\cdot}$TMA mixtures, shown in panel A of the same Figure. Even though no vibrational modes with appreciable infrared intensities are present for the TMA-d_9 monomer in this spectral region, as shown in trace *c* in Figure 5.5B, Raman measurements have revealed the presence of the ν_3 mode of TMA-d_9 at 1138.7 cm^{-1}. Investigation of the *ab initio* calculated IR intensities for the

CH_2FI·TMA-d_9 complexes, given in Tables S5.5B and S5.6B, shows that for the XB complex the calculated IR intensity for the ν_3 mode of TMA-d_9 rises from 0.2 km mol^{-1} to 5.8 km mol^{-1}. For the HB complex a rise of the infrared intensity is also observed for this vibrational mode, albeit less noticeable to a value of 0.7 km mol^{-1}. For both complexes redshifts are calculated (-2.3 cm^{-1} for the HB complex and -3.1 cm^{-1} for the XB complex), which are in agreement with the experimental shift of -2.3 cm^{-1} when taking into account the monomer band frequency from the Raman measurements. Therefore, this additional complex band is assigned to the TMA-d_9 ν_3 mode in the XB and HB complexes.

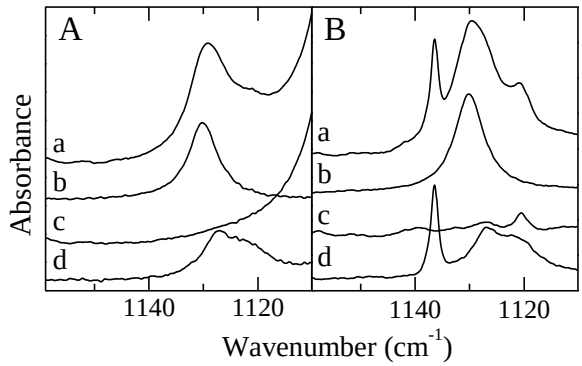

Figure 5.5: Infrared spectra for the mixtures of CH_2FI with TMA (left) or TMA-d_9 (right) dissolved in LKr at 130 K. In each panel, trace *a* represents the mixed solution, while traces *b* and *c* show the rescaled spectra of the solutions containing only CH_2FI or TMA(-d_9), respectively. Trace *d* represents the spectrum of the complex which is obtained by subtracting the rescaled traces *b* and *c* from trace *a*. Estimated mole fractions of the solutions of the mixtures are 9.4×10^{-5} for CH_2FI and 1.9×10^{-3} for TMA in panel A and 1.3×10^{-4} for CH_2FI and 1.9×10^{-3} for TMA-d_9 in panel B.

Furthermore, when studying the C-H stretching region for solutions containing CH_2FI, apart from the antisymmetric C-H stretch ν_7 and the symmetric C-H stretch ν_1, a third band is found at 2877.3 cm^{-1}. Inspection of the CH_2FI·TMA-d_9 mixtures shows the existence of two complex bands, with a broad 8.0 cm^{-1} blueshifted band and a narrow -4.6 cm^{-1} redshifted band as shown in Figure S5.5 of the SI. The presence of these two complex bands is consistent with the *ab initio* calculated shifts of -5.9 cm^{-1}

for the XB complex and 25.3 cm^{-1} for the HB complex for the first overtone of ν_2, an assignment previously made by Feller et al. [16]

Table 5.3: Experimental infrared frequencies for the monomers and complexes, as well as experimental complexation shifts ($\Delta\nu_{exp}$) and MP2/aug-cc-pVDZ-PP calculated complexation shifts ($\Delta\nu_{calc}$), in cm^{-1}, for the XB complex and HB complex of CH_2FI with TMA-d_9 dissolved in LKr at 130 K.

Assignment		$\nu_{monomer}$	$\nu_{complex,HB}$	$\Delta\nu_{exp,HB}$	$\Delta\nu_{calc,HB}$	$\nu_{complex,XB}$	$\Delta\nu_{exp,XB}$	$\Delta\nu_{calc,XB}$
CH_2FI	ν_7	3043.0	3031.5	-11.5	-17.1	3031.5	-11.5	-16.0
	ν_1	2981.5	2965.8	-15.7	-41.1	2975.5	-6.0	-11.7
		2975.7	-			-		
	$2\nu_2$	2877.3	2885.3	8.0	25.3	2872.7	-4.6	-5.9
	$2\nu_4$	2070.0	[a]		-27.0	[a]		-37.0
	ν_2	1448.1	1455.9	7.8	12.6	1446.3	-1.8	-3.0
	ν_3	1268.0	1280.8	12.8	24.2	1264.8	-3.2	-6.4
	ν_8	1219.8	-		18.6	1217.8 [b]	-2.0	-2.7
	$2\nu_5$	1130.1	1126.9	-3.2	-11.8	1126.9	-3.2	-10.7
	ν_4	1043.2	1033.3	-9.9	-13.5	1026.5	-16.7	-18.5
	ν_4 (^{13}C)	1020.6	-		-13.5	-		-18.5
	ν_5	566.7	562.6	-4.1	-5.9	565.3	-1.4	-5.4
TMA-d_9	ν_{12}	2232.7	2234.0	1.3	0.5	2234.0	1.3	1.3
	ν_1	2181.9	2186.6	4.7	2.6	2186.6	4.7	5.8
	ν_{13}	2181.9	2186.6	4.7	4.2	2186.6	4.7	6.2
	ν_2	2029.4	2036.7	7.3	6.5	2036.7	7.3	9.9
	ν_{14}	2029.4	2036.7	7.3	7.6	2036.7	7.3	10.9
	$\nu_{19} + \nu_{21}$	1226.3	1225.2	-1.1	-1.4	1225.2	-1.1	-1.0
	ν_{15}	1220.8	1217.8	-3.0	-7.3	1217.8	-3.0	-2.7
	ν_3	1138.7 [c]	1136.4 [d]	-2.3	-2.3	1136.4 [d]	-2.3	-3.1
	ν_4	1063.1	1063.2	0.1	1.1	1063.2	0.1	0.0
	ν_{16}	1062.4	1061.7	-0.7	-0.6	1061.7	-0.7	-1.7
	ν_{17}	1055.7	-		0.1	-		0.4
	ν_{18}	1047.8	1048.6	0.8	0.4	1048.6	0.8	-1.0
	ν_5	1003.7	1011.2	7.5	7.5	1011.2	7.5	9.9
	ν_{19}	873.8	873.6	-0.2	-0.4	873.6	-0.2	0.1
	ν_6	741.0	738.6	-2.4	-2.3	738.6	-2.4	-3.6

[a] Band could not be assigned due to overlap with TMA-d_9 modes.

[b] Overlap with the complex bands of the TMA-d_9 ν_{15} mode.

[c] Obtained from a Raman measurement at 130 K in LKr.

[d] Tentatively assigned from IR measurements.

5.2.2.4 CH_2FI·TMA van ‘t Hoff plots and experimental complexation enthalpies

Due to the band overlaps of CH_2FI and TMA in the regions of interest, solutions with reduced concentrations of both species had to be used for the CHF_2I·TMA mixtures to avoid saturation of the detector. As a consequence, only limited amounts of the complexes are observed in the CHF_2I·TMA solutions. Therefore, all experimental enthalpies are determined from measurements involving TMA-d_9, recorded in the 120 - 156 K temperature interval. Furthermore, as the complex bands of the CH_2FI ν_4 mode had a significant overlap, which inhibits the use of direct numerical integrations to obtain the intensities needed in the van ‘t Hoff plots, the band intensities for these complex bands were obtained using least-squares band fitting.

Average experimental complexation enthalpies of -12.5(1) kJ mol^{-1} for the XB complex and -9.6(2) kJ mol^{-1} for the HB complex were obtained from four van ‘t Hoff plots for each complex, the details of which are given in Tables S5.10 and S5.11 of the SI. Typical van ‘t Hoff plots obtained for both complexes are given in Figure S5.6 of the SI.

5.3 Discussion

Despite calculations indicating that the complexation enthalpies of the XB and HB complex between CH_2FI and DME(-d_6) are separated by a mere 0.7 kJ mol^{-1}, the HB complex being slightly stronger, from the cryosolutions experiments only clear indications were found for the presence of a HB complex. Especially the absence of the blueshifted band of the ν_5 CH_2FI mode near 567 cm^{-1} and the redshifted band for the ν_3 CH_2FI mode near 1268 cm^{-1}, which are calculated for the XB complex, is noteworthy. The absence of XB complex is remarkable, as complexes with differences in relative stability of up to -7.5(7) kJ mol^{-1} were found simultaneously in liquefied noble gas solutions in previous studies. [12] The weak blueshifted feature in the ν_3 spectral region might indicate the presence of a limited amount of XB complex, but the band is found to be too weak for further analysis.

For the mixtures involving the Lewis base TMA(-d_9), both HB and XB complexes are observed, with clearly resolved complex bands occurring in several spectral regions. Consistent with a strong increase of IR intensity predicted upon complexation, a complex band is also observed for the ν_3 mode of TMA-d_9, while this mode is too weak to be observed in IR in the monomer.

As expected from the electrostatic potentials shown in Figure 5.1, reduction of the number electron withdrawing fluorine atoms decreased the binding strength of both the XB and HB complex with both Lewis bases. For the HB complex with DME the complexation enthalpy is reduced from -10.5(5) to -7.0(2) kJ mol^{-1} when going from CHF_2I to CH_2FI, while no XB complex could be assigned decisively. For TMA the complexation energy of the HB complex is reduced from -14.7(2) kJ mol^{-1} to -9.6(2) kJ mol^{-1} when going from CHF_2I to CH_2FI, while the complexation enthalpy of the XB complex diminishes from -19.0(3) to -12.5(1) kJ mol^{-1}. Closer inspection of these values reveals that the ratio of the halogen and hydrogen bond complexation enthalpies of 1.29(3) for CHF_2I and 1.30(3) for CH_2FI remains constant for the complexes with TMA. This indicates that enhancing the noncovalent interactions by addition of electron withdrawing fluorine atoms does not promote the formation of XB complexes over HB complexes or *vice versa*. Increasing fluorination of the bond donor molecule is therefore most likely not a suitable method to influence the bond strength order of both noncovalent interactions when interacting with a nitrogen electron donor. It should also be noted that despite the HB site having the greater electrostatic potential, the largest complexation energies and enthalpies are predicted for the XB complexes when TMA is used as a Lewis base. Furthermore, the order of the complexation strengths is also not upheld when switching to DME as a Lewis base, as the CHF_2I·DME XB complex has a slightly higher theoretical and experimental complexation enthalpy than the CHF_2I·DME HB complex, while the CH_2FI·DME HB complex has a higher calculated complexation enthalpy than the CH_2FI·DME XB complex.

These observations confirm that, even though the electrostatic potentials on the donor molecules give a good indication of the complexes that might be formed in solution,

they do not tell the full story, as the Lewis base involved in the interaction also plays a significant role through its chemical hardness and ability to form secondary interactions.

To further rationalize these results, the different contributions to the interaction energy were analysed using a Ziegler-Rauk-type EDA [17-19] on the complexes of CH_2FI and CHF_2I with DME and TMA. An overview of the results of this analysis is given in Table 5.4, which for comparison also includes the results of the complexes of DME and TMA with CHF_2I.

Table 5.4: Interaction energy (ΔE_{int}) and its components, ΔE_{Pauli}, ΔV_{elst}, ΔE_{oi} and dispersion (E_{disp}), strain energy ΔE_{strain} and complexation energy (ΔE^{DFT}) obtained at PBE/TZ2P level in kJ mol^{-1} for the complexes of CH_2FI and CHF_2I with DME or TMA. [a]

			ΔE_{Pauli}	ΔV_{elst} [b]	ΔE_{oi} [b]	E_{disp}	ΔE_{int}	ΔE_{strain}	ΔE^{DFT}
CH_2FI	DME	HB	16.0	-19.4 (68)	-9.0 (32)	-8.7	-21.1	0.4	-20.7
		XB	24.0	-22.6 (65)	-12.2 (35)	-5.8	-16.6	0.6	-16.0
	TMA	HB	23.9	-26.1 (65)	-13.8 (35)	-9.9	-25.9	0.3	-25.6
		XB	61.6	-52.2 (64)	-29.7 (36)	-8.3	-28.6	0.4	-28.2
CHF_2I	DME	HB	19.0	-23.0 (68)	-10.8 (32)	-8.7	-23.5	0.3	-23.2
		XB	29.1	-27.5 (65)	-15.0 (35)	-5.8	-19.1	0.8	-18.4
	TMA	HB	30.8	-33.5 (64)	-18.6 (36)	-9.5	-30.8	0.3	-30.7
		XB	75.4	-63.4 (63)	-37.1 (37)	-8.5	-33.7	0.6	-33.1

[a] Single point PBE/TZ2P calculations were performed based on MP2/aug-cc-pVDZ-PP optimized geometries.
[b] The relative contributions of the electrostatic and orbital interaction energies to the stabilization energy are indicated in brackets in percentages.

From this analysis it becomes clear that both the stabilizing electrostatic and orbital interaction contributions and the destabilizing Pauli repulsion increase between 19 and 35 % when changing the donor molecule CH_2FI to the more fluorinated CHF_2I. This implies that a purely electrostatic description, i.e. based on the electrostatic potential, will give an incomplete picture of the effect of the addition of fluorine atoms on the bond donor on the noncovalent interactions formed. It should, however, also be noted that, when comparing the equivalent complexes formed with both bond donors, the

relative contributions of both stabilizing forces remain remarkably similar, differing at most 1 %. Furthermore, the absolute contributions of the dispersion energies remain stable when going from CH_2FI to CHF_2I. The increased stability of the complexes formed with the more fluorinated donor is therefore not the consequence of one single contribution, but of the combination of both the stabilizing ΔV_{elst} and ΔE_{oi} and repulsive ΔE_{Pauli} contributions. From this analysis it is therefore clear that, although fluorination of the bond donor increases the strength of the noncovalent interactions formed, it does not change the nature of the interactions themselves, as the relative contributions of ΔV_{elst} and ΔE_{oi} and the absolute contributions of E_{disp} remain constant.

Reviewing the relative contributions of ΔV_{elst} and ΔE_{oi} (which contains the stabilization caused by interactions between the occupied molecular orbitals on one fragment and the unoccupied molecular orbitals of the other fragment) shows that the former dominates over the latter for both types of noncovalent interactions between all donor-acceptor pairs studied. Moreover, the relative contributions of ΔV_{elst} and ΔE_{oi} for the HB and XB complexes are very similar. This is somewhat different from the previous studies performed by Shaik and co-workers where, based on a different decomposition, Charge Transfer (CT) was found to be the dominant contribution for XBs, while its role in HBs was minor. [20-21] Not only is such dominance in XB complexes not observed in the current study, but also the difference in energetic contributions between XB and HB complexes is also absent.

Within these results also no indication is found as to the reason why no XB complex is observed in the infrared spectra of the CH_2FI·DME mixtures, despite the small difference in calculated complexation enthalpy. As the concentration ratio of the XB and HB complexes in the liquid noble gas solutions is linked to the free energy of both complexes through the equilibrium constant, the low relative concentration of XB complex most probably must be ascribed to a more unfavourable entropic contribution to this complex compared to the HB complex. The reason for this is not understood but might be correlated with the fact that in the solutions studied, all complexes are extremely non-rigid and are thus characterized by several strongly anharmonic large amplitude intermolecular motions. Unfortunately, a reliable approach allowing the

thermodynamic contributions of these motions to be correctly estimated encounters large difficulties as the intermolecular motions cannot be reduced to a set of (an-)harmonic motions and internal rotations. [22-23] This limitation, obviously, limits the use of the rigid rotor harmonic oscillator approximation often used in statistical thermodynamics. The floppy character of the complexes further limits the use of anharmonic corrections based on perturbation theory based approaches [24-27] as harmonic frequencies and corrections for anharmonicity in these types of calculations are obtained for specific, well defined equilibrium geometries only.

5.4 Conclusions

The competition between halogen and hydrogen bonding was assessed using infrared spectroscopy on solutions in liquid krypton containing mixtures of the Lewis bases DME or TMA (including their fully deuterated counterparts) and CH_2FI.

Despite calculations on the CH_2FI·DME dimers indicating that both the XB and HB complex would have very similar complexation enthalpy, the HB complex being stronger by a mere -0.7 kJ mol^{-1}, only clear complex bands assigned to the HB complex were observed. An experimental complexation enthalpy in solution $\Delta H°$(LKr) for this HB complex was obtained of -7.0(2) kJ mol^{-1} using the van 't Hoff isochore. Additionally, a single, weak spectral feature was also observed in the CH_2FI ν_4 spectral region, which can be tentatively assigned to a small amount of XB complex.

For the solutions in liquid krypton containing CH_2FI and TMA(-d_9) both the XB and HB complex were observed in several spectral regions. As complex bands due to both complexes were sufficiently resolved, complexation enthalpies could be determined of -12.5(1) kJ mol^{-1} for the XB complex and -9.6(2) kJ mol^{-1} for the HB complex. As suggested by the *ab initio* calculations, the XB complex is indeed found to be more stable than its HB counterpart.

Comparison of these results with the results from a previous study on the complexes of DME and TMA with CHF_2I, using a Ziegler-Rauk-type EDA, also shows that although fluorination of the bond donor enhances the stability of the noncovalent interactions formed, the nature of the interactions formed is not altered, as the different contributions to the interaction energy remain similar.

5.5 References

1 J. Marti-Rujas, L. Colombo, J. Lu, A. Dey, G. Terraneo, P. Metrangolo, T. Pilati, G. Resnati, *Chem. Commun.*, 2012, ***48***, 8207-8209.
2 A. R. Voth, P. Khuu, K. Oishi, P. S. Ho, *Nat. Chem.*, 2009, ***1***, 74-79.
3 S. Zhu, C. Xing, W. Xu, Z. Li, *Tetrahedron Lett.*, 2004, ***45***, 777-780.
4 C. B. Aakeröy, M. Fasulo, N. Schultheiss, J. Desper, C. Moore, *J. Am. Chem. Soc.*, 2007, ***129***, 13772-13773.
5 C. B. Aakeröy, S. Panikkattu, P. D. Chopade, J. Desper, *CrystEngComm*, 2013, ***15***, 3125-3136.
6 C. B. Aakeröy, C. L. Spartz, S. Dembowski, S. Dwyre, J. Desper, *IUCrJ*, 2015, ***2***, 498-510.
7 Q. Li, X. Xu, T. Liu, B. Jing, W. Li, J. Cheng, B. Gong, J. Sun, *Phys. Chem. Chem. Phys.*, 2010, ***12***, 6837-6843.
8 J. Lieffrig, O. Jeannin, T. Guizouarn, P. Auban-Senzier, M. Fourmigué, *Cryst. Growth Des.*, 2012, ***12***, 4248-4257.
9 P. Metrangolo, G. Resnati, *Science*, 2008, ***321***, 918-919.
10 P. Politzer, J. S. Murray, P. Lane, *Int. J. Quantum Chem.*, 2007, ***107***, 3046-3052.
11 Q. Li, Q. Lin, W. Li, J. Cheng, B. Gong, J. Sun, *ChemPhysChem*, 2008, ***9***, 2265-2269.
12 N. Nagels, Y. Geboes, B. Pinter, F. De Proft, W. A. Herrebout, *Chem. - Eur. J.*, 2014, ***20***, 8433-8443.
13 Y. Geboes, F. De Proft, W. A. Herrebout, *Acta Cryst.*, 2017, 168-178.
14 E. R. Johnson, S. Keinan, P. Mori-Sánchez, J. Contreras-García, A. J. Cohen, W. Yang, *J. Am. Chem. Soc.*, 2010, ***132***, 6498-6506.
15 J. Contreras-García, E. R. Johnson, S. Keinan, R. Chaudret, J.-P. Piquemal, D. N. Beratan, W. Yang, *J. Chem. Theory Comput.*, 2011, ***7***, 625-632.
16 M. Feller, K. Lux, A. Kornath, *Eur. J. Inorg. Chem.*, 2015, ***2015***, 5357-5362.
17 B. Pinter, N. Nagels, W. A. Herrebout, F. De Proft, *Chem. - Eur. J.*, 2013, ***19***, 519-530.
18 T. Ziegler, A. Rauk, *Theor. Chim. Acta*, 1977, ***46***, 1-10.
19 F. M. Bickelhaupt, E. J. Baerends, *Rev. Comput. Chem.*, 2000, ***15***, 1-86.
20 C. Wang, D. Danovich, Y. Mo, S. Shaik, *J. Chem. Theory Comput.*, 2014, ***10***, 3726-3737.
21 C. Wang, L. Guan, D. Danovich, S. Shaik, Y. Mo, *J. Comput. Chem.*, 2016, ***37***, 34-45.
22 A. Riganelli, W. Wang, A. J. C. Varandas, *J. Phys. Chem. A*, 1999, ***103***, 8303-8308.
23 S. K. Ignatov, N. N. Vyshinskii, A. G. Razuvaev, *Russ. J. Phys. Chem. B*, 2010, ***4***, 44-52.
24 B. Temelso, G. C. Shields, *J. Chem. Theory Comput.*, 2011, ***7***, 2804-2817.
25 V. Barone, *Wiley Interdiscip. Rev.: Comput. Mol. Sci.*, 2016, ***6***, 86-110.
26 V. Barone, *J. Chem. Phys.*, 2004, ***120***, 3059-3065.
27 V. Barone, J. Bloino, C. A. Guido, F. Lipparini, *Chem. Phys. Lett.*, 2010, ***496***, 157-161.

5.6 Supporting information

Table S5.1.1: Cartesian coordinates of the MP2/aug-cc-pVDZ-PP optimized geometry of CH_2FI.

C_s	X	Y	Z
CH_2FI			
C	-0.536137	-1.469079	0.000000
H	-1.106997	-1.662637	0.914403
H	-1.106997	-1.662637	-0.914403
F	0.603424	-2.258519	0.000000
I	0.000000	0.612574	0.000000

Table S5.1.2: Cartesian coordinates of the MP2/aug-cc-pVDZ optimized geometry of DME.

C_{2v}	X	Y	Z
DME			
O	0.000000	0.000000	0.607066
C	0.000000	1.169581	-0.202099
H	0.000000	2.032636	0.474896
H	0.898418	1.208635	-0.845282
H	-0.898418	1.208635	-0.845282
C	0.000000	-1.169581	-0.202099
H	0.898418	-1.208635	-0.845282
H	0.000000	-2.032636	0.474896
H	-0.898418	-1.208635	-0.845282

Table S5.1.3: Cartesian coordinates of the MP2/aug-cc-pVDZ optimized geometry of TMA.

C_{3v}	X	Y	Z
TMA			
N	0.000000	0.000000	0.410619
C	0.000000	1.379959	-0.066347
H	-0.892330	1.901918	0.309142
H	0.892330	1.901918	0.309142
H	0.000000	1.440847	-1.178318
C	1.195079	-0.689979	-0.066347
H	2.093274	-0.178178	0.309142
H	1.200944	-1.723740	0.309142
H	1.247810	-0.720423	-1.178318
C	-1.195079	-0.689979	-0.066347
H	-1.200944	-1.723740	0.309142
H	-2.093274	-0.178178	0.309142
H	-1.247810	-0.720423	-1.178318

Table S5.2.1: Cartesian coordinates of the MP2/aug-cc-pVDZ-PP optimized geometry of the XB complex between CH_2FI and DME.

C_s	X	Y	Z
CH_2FI			
C	-0.460142	2.602075	0.000000
H	-0.978026	2.918326	0.912224
H	-0.978026	2.918326	-0.912224
F	0.820697	3.147717	0.000000
I	-0.360534	0.455758	0.000000
DME			
O	0.068618	-2.615536	0.000000
C	0.820697	-2.919865	-1.173111
H	1.074674	-3.994444	-1.208687
H	0.192801	-2.663019	-2.035116
H	1.753329	-2.328069	-1.208842
C	0.820697	-2.919865	1.173111
H	1.753329	-2.328069	1.208842
H	0.192801	-2.663019	2.035116
H	1.074674	-3.994444	1.208687

Table S5.2.2: Cartesian coordinates of the MP2/aug-cc-pVDZ-PP optimized geometry of the HB complex between CH_2FI and DME.

C_1	X	Y	Z
CH_2FI			
C	-0.386073	1.271767	0.839189
H	0.623038	0.985344	1.154151
H	-1.055746	1.566405	1.654190
F	-0.301447	2.315680	-0.074435
I	-1.249640	-0.460203	-0.104708
DME			
O	2.594135	0.087985	0.412919
C	2.737780	0.566208	-0.923945
H	2.056972	0.029684	-1.608956
H	2.479426	1.632414	-0.917347
H	3.777488	0.439950	-1.275825
C	2.886379	-1.305453	0.481092
H	3.927070	-1.505087	0.167711
H	2.755389	-1.614275	1.525691
H	2.198684	-1.883810	-0.161570

Table S5.2.3: Cartesian coordinates of the MP2/aug-cc-pVDZ-PP optimized geometry of the XB complex between CH_2FI and TMA.

C_s	X	Y	Z
CH_2FI			
C	0.441539	2.832276	0.000000
H	0.978372	3.120143	0.911327
H	0.978372	3.120143	-0.911327
F	-0.803977	3.462466	0.000000
I	0.200057	0.689365	0.000000
TMA			
N	-0.176394	-2.278145	0.000000
C	0.441539	-2.839479	-1.200143
H	-0.012258	-2.386518	-2.093844
H	1.517493	-2.610897	-1.201599
H	0.313669	-3.942478	-1.257974
C	0.441539	-2.839479	1.200143
H	1.517493	-2.610897	1.201599
H	-0.012258	-2.386518	2.093844
H	0.313669	-3.942478	1.257974
C	-1.615150	-2.538870	0.000000
H	-2.071343	-2.085621	0.892334
H	-2.071343	-2.085621	-0.892334
H	-1.841147	-3.627483	0.000000

Table S5.2.4: Cartesian coordinates of the MP2/aug-cc-pVDZ-PP optimized geometry of the HB complex between CH_2FI and TMA.

C_1	X	Y	Z
CH_2FI			
C	-0.467376	1.248030	-0.698891
H	0.554484	0.858317	-0.803737
H	-0.925692	1.603616	-1.628250
F	-0.473856	2.282721	0.230022
I	-1.675291	-0.387617	0.017001
TMA			
N	2.510889	-0.139132	-0.102619
C	2.547100	-1.590665	-0.281552
H	1.609777	-2.031192	0.088190
H	2.648029	-1.829732	-1.350554
H	3.397384	-2.056388	0.264224
C	3.745910	0.456329	-0.610694
H	3.855323	0.227383	-1.681033
H	3.708413	1.548891	-0.488057
H	4.644184	0.074625	-0.076862
C	2.352931	0.181493	1.316974
H	2.298378	1.272525	1.447094
H	1.418761	-0.260306	1.693960
H	3.198494	-0.205727	1.927099

Table S5.3A: MP2/aug-cc-pVDZ-PP vibrational frequencies, in cm^{-1}, infrared intensities, in km mol^{-1}, and Raman intensities, in $Å^4$ amu^{-1}, for the XB complex between CH_2FI and DME and both monomers, as well as the complexation shift Δν.

	Monomer			XB complex			
	Frequency	IR int.	Raman int.	Frequency	Δν	IR int.	Raman int.
CHF_2I							
ν_1 (A')	3144.9	8.6	115.8	3139.9	-5.0	12.5	135.3
ν_2 (A')	1469.3	0.4	6.4	1468.3	-1.0	0.3	7.0
ν_3 (A')	1307.7	54.8	6.8	1307.0	-0.7	62.9	7.1
ν_4 (A')	1042.6	191.1	3.1	1032.1	-10.5	189.0	3.2
ν_5 (A')	591.6	38.5	25.5	594.5	2.9	24.6	38.9
ν_6 (A')	271.2	0.8	4.3	274.8	3.6	5.3	5.8
ν_7 (A")	3243.7	0.5	51.7	3235.7	-8.0	1.4	58.2
ν_8 (A")	1233.0	2.3	1.7	1232.2	-0.8	2.2	1.7
ν_9 (A")	874.7	0.7	0.4	871.2	-3.5	0.2	0.6
DME							
ν_1 (A_1)	3188.7	20.1	87.6	3190.7	2.0	17.7	62.7
ν_2 (A_1)	3024.8	58.6	320.3	3030.4	5.6	57.2	312.4
ν_3 (A_1)	1505.9	2.9	5.6	1503.5	-2.4	7.1	5.7
ν_4 (A_1)	1473.5	0.0	2.2	1472.6	-0.9	0.4	3.3
ν_5 (A_1)	1261.1	6.6	0.5	1260.7	-0.4	6.5	0.4
ν_6 (A_1)	942.4	34.7	9.8	932.7	-9.7	51.4	11.2
ν_7 (A_1)	416.8	2.3	1.0	416.3	-0.5	2.8	0.9
ν_8 (A_2)	3096.2	0.0	14.7	3106.8	10.6	0.4	14.4
ν_9 (A_2)	1474.8	0.0	11.4	1472.9	-1.9	0.6	9.1
ν_{10} (A_2)	1157.2	0.0	1.5	1155.9	-1.3	0.03	1.6
ν_{11} (A_2)	195.2	0.0	0.2	191.9	-3.3	0.003	0.1
ν_{12} (B_1)	3089.5	107.8	94.2	3100.6	11.1	99.4	117.2
ν_{13} (B_1)	1489.2	13.0	0.0	1488.3	-0.9	17.3	0.1
ν_{14} (B_1)	1187.2	7.2	0.0	1187.6	0.5	5.5	0.2
ν_{15} (B_1)	260.2	5.1	0.0	264.6	4.3	9.7	0.08
ν_{16} (B_2)	3187.3	24.6	59.2	3189.3	2.0	15.2	41.1
ν_{17} (B_2)	3018.4	55.2	0.6	3025.0	6.7	43.3	3.9
ν_{18} (B_2)	1490.1	10.3	1.0	1487.8	-2.2	8.1	0.6
ν_{19} (B_2)	1441.5	2.5	1.3	1440.8	-0.7	0.5	1.4
ν_{20} (B_2)	1191.9	98.1	0.7	1183.9	-8.0	77.3	0.4
ν_{21} (B_2)	1113.8	35.0	1.6	1108.5	-5.3	38.7	2.0

Van der Waals vibrations: 6.6 cm^{-1}, 4.5 km mol^{-1}, 0.4 $Å^4$ amu^{-1}, 30.1 cm^{-1}, 3.4 km mol^{-1}, 0.3 $Å^4$ amu^{-1}, 44.9 cm^{-1}, 3.8 km mol^{-1}, 1.7 $Å^4$ amu^{-1}, 63.7 cm^{-1}, 0.1 km mol^{-1}, 0.5 $Å^4$ amu^{-1}, 82.6 cm^{-1}, 0.7 km mol^{-1}, 0.1 $Å^4$ amu^{-1}, 95.3 cm^{-1}, 12.4 km mol^{-1}, 0.5 $Å^4$ amu^{-1}.

Table S5.3B: MP2/aug-cc-pVDZ-PP vibrational frequencies, in cm^{-1}, infrared intensities, in km mol^{-1}, and Raman intensities, in $Å^4$ amu^{-1}, for the XB complex between CH_2FI and DME-d_6 and both monomers, as well as the complexation shift Δν.

	Monomer			XB complex			
	Frequency	IR int.	Raman int.	Frequency	Δν	IR int.	Raman int.
CHF_2I							
ν_1 (A')	3144.9	8.6	115.8	3139.9	-5.0	12.6	134.9
ν_2 (A')	1469.3	0.4	6.4	1468.3	-1.0	0.3	6.9
ν_3 (A')	1307.7	54.8	6.8	1307.0	-0.7	62.3	7.3
ν_4 (A')	1042.6	191.1	3.1	1031.8	-10.8	189.2	2.9
ν_5 (A')	591.6	38.5	25.5	594.5	2.9	24.6	38.9
ν_6 (A')	271.2	0.8	4.3	274.4	3.2	3.2	5.8
ν_7 (A")	3243.7	0.5	51.7	3235.7	-8.0	1.4	58.3
ν_8 (A")	1233.0	2.3	1.7	1232.2	-0.8	2.2	1.7
ν_9 (A")	874.7	0.7	0.4	871.0	-3.7	0.2	1.0
DME-d_6							
ν_1 (A_1)	2364.1	17.0	37.1	2366.3	2.2	14.3	29.0
ν_2 (A_1)	2171.1	32.1	166.2	2174.4	3.3	33.0	157.3
ν_3 (A_1)	1153.5	5.3	2.6	1148.3	-5.2	9.0	5.1
ν_4 (A_1)	1085.9	0.09	2.5	1083.9	-1.9	1.2	2.3
ν_5 (A_1)	1058.5	17.5	1.8	1057.8	-0.7	23.2	1.9
ν_6 (A_1)	834.8	16.9	7.7	829.4	-5.3	25.8	8.2
ν_7 (A_1)	351.5	1.5	0.7	351.6	0.1	2.0	0.6
ν_8 (A_2)	2297.2	0.0	7.5	2305.5	8.2	0.2	7.3
ν_9 (A_2)	1065.8	0.0	4.2	1064.2	-1.6	0.4	3.3
ν_{10} (A_2)	877.6	0.0	2.2	876.8	-0.8	0.0	1.6
ν_{11} (A_2)	139.5	0.0	0.1	137.4	-2.1	0.0009	0.09
ν_{12} (B_1)	2290.4	65.1	51.2	2299.1	8.8	58.9	63.1
ν_{13} (B_1)	1077.4	4.3	0.003	1076.4	-1.0	5.6	0.08
ν_{14} (B_1)	937.8	9.9	0.1	938.6	0.8	11.8	0.2
ν_{15} (B_1)	200.5	4.6	0.0	208.7	8.2	12.3	0.2
ν_{16} (B_2)	2360.7	10.6	31.7	2362.9	2.2	6.4	22.6
ν_{17} (B_2)	2164.0	44.9	0.03	2168.2	4.3	35.2	1.2
ν_{18} (B_2)	1170.3	134.3	0.9	1158.6	-11.8	113.7	0.9
ν_{19} (B_2)	1077.4	0.5	0.2	1075.6	-1.8	0.4	0.07
ν_{20} (B_2)	1066.1	1.6	1.1	1065.4	-0.7	3.1	1.0
ν_{21} (B_2)	860.9	0.08	0.9	859.6	-1.3	0.2	1.0

Van der Waals vibrations: 6.3 cm^{-1}, 4.1 km mol^{-1}, 0.3 $Å^4$ amu^{-1}, 28.2 cm^{-1}, 3.1 km mol^{-1}, 0.3 $Å^4$ amu^{-1}, 41.8 cm^{-1}, 3.5 km mol^{-1}, 1.5 $Å^4$ amu^{-1}, 59.2 cm^{-1}, 0.07 km mol^{-1}, 0.5 $Å^4$ amu^{-1}, 77.3 cm^{-1}, 1.1 km mol^{-1}, 0.2 $Å^4$ amu^{-1}, 82.9 cm^{-1}, 7.4 km mol^{-1}, 0.4 $Å^4$ amu^{-1}.

Table S5.4A: MP2/aug-cc-pVDZ-PP vibrational frequencies, in cm^{-1}, infrared intensities, in km mol^{-1}, and Raman intensities, in $Å^4$ amu^{-1}, for the HB complex between CH_2FI and DME and both monomers, as well as the complexation shift Δν.

	Monomer			HB complex			
	Frequency	IR int.	Raman int.	Frequency	Δν	IR int.	Raman int.
CHF_2I							
ν_1 (A')	3144.9	8.6	115.8	3141.9	-3.0	18.6	139.4
ν_2 (A')	1469.3	0.4	6.4	1468.5	-0.8	2.6	5.9
ν_3 (A')	1307.7	54.8	6.8	1315.7	8.0	54.5	8.0
ν_4 (A')	1042.6	191.1	3.1	1032.0	-10.7	166.1	2.8
ν_5 (A')	591.6	38.5	25.5	588.1	-3.5	37.6	22.5
ν_6 (A')	271.2	0.8	4.3	269.8	-1.4	0.7	3.8
ν_7 (A")	3243.7	0.5	51.7	3250.8	7.1	7.8	49.5
ν_8 (A")	1233.0	2.3	1.7	1246.5	13.5	4.1	1.7
ν_9 (A")	874.7	0.7	0.4	889.2	14.4	3.9	0.6
DME							
ν_1 (A_1)	3188.7	20.1	87.6	3189.9	1.2	13.6	51.4
ν_2 (A_1)	3024.8	58.6	320.3	3030.9	6.1	49.3	313.8
ν_3 (A_1)	1505.9	2.9	5.6	1504.3	-1.6	9.1	5.7
ν_4 (A_1)	1473.5	0.0	2.2	1476.9	3.4	0.9	2.8
ν_5 (A_1)	1261.1	6.6	0.5	1262.7	1.6	5.4	0.4
ν_6 (A_1)	942.4	34.7	9.8	934.8	-7.6	34.3	9.5
ν_7 (A_1)	416.8	2.3	1.0	417.8	1.0	2.3	0.8
ν_8 (A_2)	3096.2	0.0	14.7	3107.8	11.6	1.1	12.1
ν_9 (A_2)	1474.8	0.0	11.4	1473.3	-1.6	0.5	9.4
ν_{10} (A_2)	1157.2	0.0	1.5	1156.5	-0.8	0.0004	1.9
ν_{11} (A_2)	195.2	0.0	0.2	191.4	-3.8	0.01	0.07
ν_{12} (B_1)	3089.5	107.8	94.2	3101.4	11.9	100.2	81.6
ν_{13} (B_1)	1489.2	13.0	0.0	1488.2	-1.1	15.7	0.4
ν_{14} (B_1)	1187.2	7.2	0.0	1187.6	0.5	5.6	0.4
ν_{15} (B_1)	260.2	5.1	0.0	262.8	2.6	10.4	0.05
ν_{16} (B_2)	3187.3	24.6	59.2	3186.7	-0.6	18.3	53.4
ν_{17} (B_2)	3018.4	55.2	0.6	3025.6	7.2	43.8	5.1
ν_{18} (B_2)	1490.1	10.3	1.0	1488.7	-1.4	6.9	0.5
ν_{19} (B_2)	1441.5	2.5	1.3	1441.9	0.4	0.9	1.0
ν_{20} (B_2)	1191.9	98.1	0.7	1184.3	-7.6	78.4	0.5
ν_{21} (B_2)	1113.8	35.0	1.6	1110.7	-3.1	40.5	1.7

Van der Waals vibrations: 24.6 cm^{-1}, 1.4 km mol^{-1}, 0.6 $Å^4$ amu^{-1}, 33.3 cm^{-1}, 0.03 km mol^{-1}, 0.5 $Å^4$ amu^{-1}, 46.4 cm^{-1}, 2.4 km mol^{-1}, 0.2 $Å^4$ amu^{-1}, 58.5 cm^{-1}, 0.5 km mol^{-1}, 0.3 $Å^4$ amu^{-1}, 73.9 cm^{-1}, 5.4 km mol^{-1}, 0.1 $Å^4$ amu^{-1}, 147.3 cm^{-1}, 18.1 km mol^{-1}, 1.2 $Å^4$ amu^{-1}.

Table S5.4B: MP2/aug-cc-pVDZ-PP vibrational frequencies, in cm^{-1}, infrared intensities, in km mol^{-1}, and Raman intensities, in $Å^4$ amu^{-1}, for the HB complex between CH_2FI and DME-d_6 and both monomers, as well as the complexation shift Δν.

	Monomer			HB complex			
	Frequency	IR int.	Raman int.	Frequency	Δν	IR int.	Raman int.
CHF_2I							
ν_1 (A')	3144.9	8.6	115.8	3141.9	-3.0	19.1	135.0
ν_2 (A')	1469.3	0.4	6.4	1470.8	1.5	4.5	6.0
ν_3 (A')	1307.7	54.8	6.8	1315.9	8.2	53.3	7.8
ν_4 (A')	1042.6	191.1	3.1	1031.5	-11.1	167.9	2.8
ν_5 (A')	591.6	38.5	25.5	588.1	-3.5	37.5	22.5
ν_6 (A')	271.2	0.8	4.3	269.8	-1.4	0.7	3.8
ν_7 (A")	3243.7	0.5	51.7	3250.8	7.1	7.8	49.3
ν_8 (A")	1233.0	2.3	1.7	1246.5	13.5	3.9	1.6
ν_9 (A")	874.7	0.7	0.4	889.3	14.5	2.9	0.5
DME-d_6							
ν_1 (A_1)	2364.1	17.0	37.1	2365.4	1.3	11.7	27.4
ν_2 (A_1)	2171.1	32.1	166.2	2174.8	3.7	26.6	160.4
ν_3 (A_1)	1153.5	5.3	2.6	1149.4	-4.1	5.2	2.8
ν_4 (A_1)	1085.9	0.09	2.5	1084.7	-1.2	1.4	2.4
ν_5 (A_1)	1058.5	17.5	1.8	1059.8	1.3	19.6	1.6
ν_6 (A_1)	834.8	16.9	7.7	830.8	-3.9	18.1	7.4
ν_7 (A_1)	351.5	1.5	0.7	353.0	1.4	1.7	0.6
ν_8 (A_2)	2297.2	0.0	7.5	2306.1	8.9	0.5	6.2
ν_9 (A_2)	1065.8	0.0	4.2	1064.2	-1.6	1.2	3.0
ν_{10} (A_2)	877.6	0.0	2.2	876.8	-0.8	0.02	2.3
ν_{11} (A_2)	139.5	0.0	0.1	137.4	-2.2	0.002	0.06
ν_{12} (B_1)	2290.4	65.1	51.2	2299.7	9.3	60.9	45.6
ν_{13} (B_1)	1077.4	4.3	0.003	1076.3	-1.0	4.6	0.1
ν_{14} (B_1)	937.8	9.9	0.1	937.8	0.0	9.4	0.4
ν_{15} (B_1)	200.5	4.6	0.0	207.6	7.1	12.9	0.07
ν_{16} (B_2)	2360.7	10.6	31.7	2361.4	0.7	8.4	24.2
ν_{17} (B_2)	2164.0	44.9	0.03	2168.6	4.6	35.2	1.8
ν_{18} (B_2)	1170.3	134.3	0.9	1159.2	-11.2	115.5	1.0
ν_{19} (B_2)	1077.4	0.5	0.2	1076.6	-0.8	0.5	0.09
ν_{20} (B_2)	1066.1	1.6	1.1	1066.4	0.3	1.4	1.6
ν_{21} (B_2)	860.9	0.08	0.9	861.1	0.3	0.2	0.8

Van der Waals vibrations: 22.3 cm^{-1}, 1.2 km mol^{-1}, 0.5 $Å^4$ amu^{-1}, 31.9 cm^{-1}, 0.004 km mol^{-1}, 0.4 $Å^4$ amu^{-1}, 44.5 cm^{-1}, 2.3 km mol^{-1}, 0.1 $Å^4$ amu^{-1}, 52.8 cm^{-1}, 0.9 km mol^{-1}, 0.3 $Å^4$ amu^{-1}, 60.4 cm^{-1}, 3.2 km mol^{-1}, 0.08 $Å^4$ amu^{-1}, 142.8 cm^{-1}, 13.8 km mol^{-1}, 1.2 $Å^4$ amu^{-1}.

Table S5.5A: MP2/aug-cc-pVDZ-PP vibrational frequencies, in cm^{-1}, infrared intensities, in km mol^{-1}, and Raman intensities, in $Å^4$ amu^{-1}, for the XB complex between CH_2FI and TMA and both monomers, as well as the complexation shift Δν.

	Monomer			XB complex			
	Frequency	IR int.	Raman int.	Frequency	Δν	IR int.	Raman int.
CHF_2I							
ν_1 (A')	3144.9	8.6	115.8	3133.2	-11.7	17.6	163.8
ν_2 (A')	1469.3	0.4	6.4	1466.5	-2.8	0.3	12.3
ν_3 (A')	1307.7	54.8	6.8	1301.1	-6.6	61.9	11.4
ν_4 (A')	1042.6	191.1	3.1	1026.0	-16.6	197.8	3.2
ν_5 (A')	591.6	38.5	25.5	586.3	-5.3	10.5	88.0
ν_6 (A')	271.2	0.8	4.3	272.6	1.3	5.6	12.6
ν_7 (A")	3243.7	0.5	51.7	3227.7	-16.0	2.7	66.5
ν_8 (A")	1233.0	2.3	1.7	1230.3	-2.7	1.8	1.7
ν_9 (A")	874.7	0.7	0.4	860.5	-14.3	0.2	0.8
TMA							
ν_1 (A_1)	3111.8	42.4	235.1	3115.4	3.6	28.9	109.9
ν_2 (A_1)	2962.3	167.2	390.2	2979.5	17.2	222.5	508.2
ν_3 (A_1)	1499.0	23.4	0.4	1498.7	-0.4	26.2	1.3
ν_4 (A_1)	1464.0	1.6	2.3	1463.7	-0.3	0.1	16.5
ν_5 (A_1)	1204.0	24.9	5.6	1210.7	6.8	20.3	20.9
ν_6 (A_1)	853.0	22.9	12.0	847.7	-5.3	68.4	11.7
ν_7 (A_1)	383.8	7.6	1.1	397.0	13.3	30.2	1.3
ν_8 (A_2)	3163.7	0.0	0.0	3165.1	1.5	0.2	0.4
ν_9 (A_2)	1477.7	0.0	0.0	1476.1	-1.7	0.001	0.003
ν_{10} (A_2)	1057.3	0.0	0.0	1059.0	1.7	0.0003	0.0004
ν_{11} (A_2)	243.9	0.0	0.0	236.4	-7.5	0.0	0.0
ν_{12} (E)	3166.8	34.6	87.1	3168.3	1.5	23.7	58.1
ν_{13} (E)	3111.1	26.1	27.8	3114.5	3.5	18.8	50.7
ν_{14} (E)	2955.2	44.4	18.3	2974.2	19.0	39.0	34.6
ν_{15} (E)	1500.8	9.8	5.5	1500.4	-0.4	13.8	5.9
ν_{16} (E)	1475.1	5.7	8.8	1473.5	-1.5	1.9	7.7
ν_{17} (E)	1421.1	0.7	1.6	1421.3	0.3	0.003	1.7
ν_{18} (E)	1303.4	14.9	1.7	1302.7	-0.7	14.8	1.7
ν_{19} (E)	1115.9	9.1	0.4	1114.1	-1.8	7.6	0.7
ν_{20} (E)	1066.2	13.6	2.7	1063.9	-2.3	12.7	2.7
ν_{21} (E)	423.6	0.006	0.7	421.7	-2.0	0.01	0.7
ν_{22} (E)	290.9	0.4	0.6	283.9	-7.0	0.4	0.8

Van der Waals vibrations: 4.1 cm^{-1}, 2.3 km mol^{-1}, 0.1 $Å^4$ amu^{-1}, 34.8 cm^{-1}, 0.6 km mol^{-1}, 0.4 $Å^4$ amu^{-1}, 44.5 cm^{-1}, 2.8 km mol^{-1}, 1.4 $Å^4$ amu^{-1}, 75.3 cm^{-1}, 4.1 km mol^{-1}, 1.7 $Å^4$ amu^{-1}, 88.7 cm^{-1}, 0.9 km mol^{-1}, 0.2 $Å^4$ amu^{-1}, 102.4 cm^{-1}, 2.0 km mol^{-1}, 0.3 $Å^4$ amu^{-1}.

Table S5.5B: MP2/aug-cc-pVDZ-PP vibrational frequencies, in cm^{-1}, infrared intensities, in km mol^{-1}, and Raman intensities, in $Å^4$ amu^{-1}, for the XB complex between CH_2FI and TMA-d_9 and both monomers, as well as the complexation shift Δν.

	Monomer			XB complex			
	Frequency	IR int.	Raman int.	Frequency	Δν	IR int.	Raman int.
CHF_2I							
ν_1 (A')	3144.9	8.6	115.8	3133.2	-11.7	17.5	161.8
ν_2 (A')	1469.3	0.4	6.4	1466.4	-3.0	0.4	8.3
ν_3 (A')	1307.7	54.8	6.8	1301.3	-6.4	66.2	13.0
ν_4 (A')	1042.6	191.1	3.1	1024.1	-18.5	213.1	9.7
ν_5 (A')	591.6	38.5	25.5	586.2	-5.4	10.3	88.1
ν_6 (A')	271.2	0.8	4.3	272.5	1.3	5.6	12.8
ν_7 (A")	3243.7	0.5	51.7	3227.7	-16.0	2.7	66.5
ν_8 (A")	1233.0	2.3	1.7	1230.3	-2.7	1.5	1.6
ν_9 (A")	874.7	0.7	0.4	860.6	-14.2	0.1	0.7
TMA-d_9							
ν_1 (A_1)	2286.9	51.7	81.2	2292.7	5.8	46.6	90.7
ν_2 (A_1)	2142.3	72.7	232.7	2152.1	9.9	100.3	260.9
ν_3 (A_1)	1151.7	0.2	5.9	1148.7	-3.1	5.8	17.1
ν_4 (A_1)	1079.2	12.6	0.2	1079.2	0.0	18.4	0.5
ν_5 (A_1)	1018.9	33.5	3.4	1028.8	9.9	31.9	4.6
ν_6 (A_1)	756.9	12.4	9.6	753.3	-3.6	38.2	9.3
ν_7 (A_1)	323.0	4.6	0.8	335.5	12.6	22.1	1.4
ν_8 (A_2)	2345.4	0.0	0.0	2346.6	1.1	0.04	0.1
ν_9 (A_2)	1067.7	0.0	0.0	1065.9	-1.8	0.0001	0.0002
ν_{10} (A_2)	801.3	0.0	0.0	802.9	1.6	0.0	0.0001
ν_{11} (A_2)	173.1	0.0	0.0	167.7	-5.4	0.0	0.0
ν_{12} (E)	2349.0	17.4	46.2	2350.2	1.3	11.8	30.8
ν_{13} (E)	2287.5	8.1	21.2	2293.7	6.2	5.2	20.4
ν_{14} (E)	2135.6	36.1	4.2	2146.5	10.9	29.7	10.9
ν_{15} (E)	1252.4	33.4	1.0	1249.6	-2.7	29.5	0.8
ν_{16} (E)	1078.6	2.1	2.4	1076.9	-1.7	3.6	2.5
ν_{17} (E)	1073.1	0.2	0.4	1073.5	0.4	0.3	0.4
ν_{18} (E)	1063.4	1.6	3.7	1062.5	-1.0	0.3	3.1
ν_{19} (E)	886.2	7.4	2.6	886.3	0.1	6.6	2.4
ν_{20} (E)	839.0	0.03	1.0	837.2	-1.8	0.005	1.4
ν_{21} (E)	352.0	0.007	0.5	350.9	-1.1	0.02	0.6
ν_{22} (E)	210.6	0.2	0.3	205.8	-4.7	0.2	0.4

Van der Waals vibrations: 4.0 cm^{-1}, 2.4 km mol^{-1}, 0.09 $Å^4$ amu^{-1}, 32.5 cm^{-1}, 0.5 km mol^{-1}, 0.5 $Å^4$ amu^{-1}, 40.6 cm^{-1}, 2.3 km mol^{-1}, 1.3 $Å^4$ amu^{-1}, 71.0 cm^{-1}, 3.3 km mol^{-1}, 1.4 $Å^4$ amu^{-1}, 81.6 cm^{-1}, 1.2 km mol^{-1}, 0.2 Å amu^{-1}, 97.0 cm^{-1}, 2.4 km mol^{-1}, 0.5 $Å^4$ amu^{-1}.

Table S5.6A: MP2/aug-cc-pVDZ-PP vibrational frequencies, in cm^{-1}, infrared intensities, in km mol^{-1}, and Raman intensities, in $Å^4$ amu^{-1}, for the HB complex between CH_2FI and TMA and both monomers, as well as the complexation shift Δν.

	Monomer			HB complex			
	Frequency	IR int.	Raman int.	Frequency	Δν	IR int.	Raman int.
CHF_2I							
ν_1 (A')	3144.9	8.6	115.8	3103.9	-41.0	60.8	235.6
ν_2 (A')	1469.3	0.4	6.4	1482.7	13.4	3.9	5.5
ν_3 (A')	1307.7	54.8	6.8	1331.7	24.0	65.6	10.0
ν_4 (A')	1042.6	191.1	3.1	1029.5	-13.1	165.2	3.0
ν_5 (A')	591.6	38.5	25.5	585.7	-5.9	37.4	22.4
ν_6 (A')	271.2	0.8	4.3	268.9	-2.3	0.6	3.8
ν_7 (A")	3243.7	0.5	51.7	3226.7	-17.1	23.0	74.3
ν_8 (A")	1233.0	2.3	1.7	1251.3	18.2	5.1	1.5
ν_9 (A")	874.7	0.7	0.4	907.1	32.3	1.9	0.2
TMA							
ν_1 (A_1)	3111.8	42.4	235.1	3114.0	2.2	35.1	125.4
ν_2 (A_1)	2962.3	167.2	390.2	2973.8	11.5	175.6	419.4
ν_3 (A_1)	1499.0	23.4	0.4	1500.0	1.0	23.6	1.1
ν_4 (A_1)	1464.0	1.6	2.3	1464.1	0.09	1.3	5.0
ν_5 (A_1)	1204.0	24.9	5.6	1210.2	6.3	23.3	5.3
ν_6 (A_1)	853.0	22.9	12.0	849.3	-3.7	33.3	11.2
ν_7 (A_1)	383.8	7.6	1.1	397.5	13.7	14.8	0.9
ν_8 (A_2)	3163.7	0.0	0.0	3163.7	0.1	4.3	12.7
ν_9 (A_2)	1477.7	0.0	0.0	1477.8	0.0	0.06	0.1
ν_{10} (A_2)	1057.3	0.0	0.0	1057.7	0.4	0.3	0.06
ν_{11} (A_2)	243.9	0.0	0.0	241.2	-2.7	0.007	0.04
ν_{12} (E)	3166.8	34.6	87.1	3167.3	0.4	24.4	64.0
ν_{13} (E)	3111.1	26.1	27.8	3112.5	1.4	21.2	49.9
ν_{14} (E)	2955.2	44.4	18.3	2968.2	13.0	42.3	30.0
ν_{15} (E)	1500.8	9.8	5.5	1501.5	0.8	13.1	6.2
ν_{16} (E)	1475.1	5.7	8.8	1475.0	-0.1	4.2	7.9
ν_{17} (E)	1421.1	0.7	1.6	1421.8	0.7	0.4	1.6
ν_{18} (E)	1303.4	14.9	1.7	1299.1	-4.3	13.9	1.4
ν_{19} (E)	1115.9	9.1	0.4	1115.6	-0.4	7.8	0.6
ν_{20} (E)	1066.2	13.6	2.7	1062.8	-3.4	14.6	2.5
ν_{21} (E)	423.6	0.006	0.7	421.8	-1.8	0.1	0.6
ν_{22} (E)	290.9	0.4	0.6	291.2	0.3	0.3	0.4

Van der Waals vibrations: 20.1 cm^{-1}, 0.4 km mol^{-1}, 0.2 $Å^4$ amu^{-1}, 30.1 cm^{-1}, 0.2 km mol^{-1}, 0.4 $Å^4$ amu^{-1}, 40.4 cm^{-1}, 0.4 km mol^{-1}, 0.2 $Å^4$ amu^{-1}, 52.4 cm^{-1}, 2.5 km mol^{-1}, 0.2 $Å^4$ amu^{-1}, 64.8 cm^{-1}, 0.2 km mol^{-1}, 0.2 $Å^4$ amu^{-1}, 145.9 cm^{-1}, 17.6 km mol^{-1}, 2.4 $Å^4$ amu^{-1}.

Table S5.6B: MP2/aug-cc-pVDZ-PP vibrational frequencies, in cm^{-1}, infrared intensities, in km mol^{-1}, and Raman intensities, in $Å^4$ amu^{-1}, for the HB complex between CH_2FI and TMA-d_9 and both monomers, as well as the complexation shift $\Delta\nu$.

	Monomer			HB complex			
	Frequency	IR int.	Raman int.	Frequency	$\Delta\nu$	IR int.	Raman int.
CHF_2I							
ν_1 (A')	3144.9	8.6	115.8	3103.8	-41.1	68.6	221.9
ν_2 (A')	1469.3	0.4	6.4	1482.0	12.6	6.2	5.8
ν_3 (A')	1307.7	54.8	6.8	1331.9	24.2	65.8	9.6
ν_4 (A')	1042.6	191.1	3.1	1029.1	-13.5	165.4	2.7
ν_5 (A')	591.6	38.5	25.5	585.7	-5.9	37.4	22.5
ν_6 (A')	271.2	0.8	4.3	268.9	-2.3	0.6	3.8
ν_7 (A")	3243.7	0.5	51.7	3226.6	-17.1	23.3	73.6
ν_8 (A")	1233.0	2.3	1.7	1251.6	18.6	8.6	1.8
ν_9 (A")	874.7	0.7	0.4	907.2	32.5	2.0	0.2
TMA-d_9							
ν_1 (A_1)	2286.9	51.7	81.2	2289.6	2.6	30.0	49.7
ν_2 (A_1)	2142.3	72.7	232.7	2148.8	6.5	75.6	250.5
ν_3 (A_1)	1151.7	0.2	5.9	1149.5	-2.3	0.7	6.8
ν_4 (A_1)	1079.2	12.6	0.2	1080.3	1.1	16.4	0.4
ν_5 (A_1)	1018.9	33.5	3.4	1026.4	7.5	37.4	3.4
ν_6 (A_1)	756.9	12.4	9.6	754.6	-2.3	19.2	8.9
ν_7 (A_1)	323.0	4.6	0.8	335.3	12.3	10.4	0.6
ν_8 (A_2)	2345.4	0.0	0.0	2345.6	0.2	0.9	3.5
ν_9 (A_2)	1067.7	0.0	0.0	1067.0	-0.7	0.02	0.01
ν_{10} (A_2)	801.3	0.0	0.0	801.8	0.5	0.002	0.01
ν_{11} (A_2)	173.1	0.0	0.0	171.3	-1.8	0.006	0.02
ν_{12} (E)	2349.0	17.4	46.2	2349.4	0.5	13.0	35.4
ν_{13} (E)	2287.5	8.1	21.2	2291.7	4.2	15.5	26.3
ν_{14} (E)	2135.6	36.1	4.2	2143.1	7.6	30.9	7.5
ν_{15} (E)	1252.4	33.4	1.0	1245.1	-7.3	29.2	0.9
ν_{16} (E)	1078.6	2.1	2.4	1077.9	-0.6	1.7	2.8
ν_{17} (E)	1073.1	0.2	0.4	1073.2	0.1	0.2	0.5
ν_{18} (E)	1063.4	1.6	3.7	1063.8	0.4	1.8	3.4
ν_{19} (E)	886.2	7.4	2.6	885.8	-0.4	6.9	2.4
ν_{20} (E)	839.0	0.03	1.0	838.3	-0.7	0.002	1.1
ν_{21} (E)	352.0	0.007	0.5	351.0	-1.0	0.1	0.4
ν_{22} (E)	210.6	0.2	0.3	210.8	0.3	0.2	0.2

Van der Waals vibrations: 18.4 cm^{-1}, 0.4 km mol^{-1}, 0.2 $Å^4$ amu^{-1}, 28.8 cm^{-1}, 0.2 km mol^{-1}, 0.3 $Å^4$ amu^{-1}, 36.6 cm^{-1}, 0.2 km mol^{-1}, 0.2 $Å^4$ amu^{-1}, 47.1 cm^{-1}, 2.1 km mol^{-1}, 0.1 $Å^4$ amu^{-1}, 59.6 cm^{-1}, 0.3 km mol^{-1}, 0.2 $Å^4$ amu^{-1}, 144.1 cm^{-1}, 17.5 km mol^{-1}, 2.4 $Å^4$ amu^{-1}.

Table S5.7: Experimental vibrational frequencies for the monomers and HB complex ($\nu_{complex,HB}$), as well as experimental complexation shifts ($\Delta\nu_{exp,HB}$) and MP2/aug-cc-pVDZ-PP calculated complexation shifts, in cm^{-1}, for the HB complex ($\Delta\nu_{calc,HB}$) and XB complex ($\Delta\nu_{calc,XB}$) of CH_2FI with DME-d_6 dissolved in LKr at 130 K.

Assignment		$\nu_{monomer}$	$\nu_{complex,HB}$	$\Delta\nu_{exp,HB}$	$\Delta\nu_{calc,HB}$	$\Delta\nu_{calc,XB}$
CH_2FI	ν_7	3043.0	3050.4	7.4	7.1	-8.0
	ν_1	2981.5	2978.9	-2.6	-3.0	-5.0
		2975.7	2962.2	-13.5		
	$2\nu_2$	2877.3	-		3.0	-2.0
	$2\nu_4$	2070.0	[a]		-22.3	-21.5
	ν_2	1448.1	-		1.5	-1.0
	ν_3	1268.0	1274.9	6.9	8.2	-0.7
	ν_8	1219.8	-		13.5	-0.8
	$2\nu_5$	1130.1	1123.8	-6.3	-7.0	5.8
	ν_4	1043.2	1036.4	-6.8	-11.1	-10.8
	ν_4 (^{13}C)	1020.6	1014.2	-6.4	-11.1	-10.8
	ν_9	855.1	-			
	ν_5	566.7	563.9	-2.8	-3.5	2.9
DME-d_6	ν_1	2243.4	2245.4	2.0	1.3	2.2
	ν_{16}	2243.4	2245.4	2.0	0.7	2.2
	ν_{12}	2179.9	2186.5	6.6	9.3	8.8
	ν_2	2054.4	2057.1	2.7	3.7	3.3
	ν_{17}	2049.6	2053.0	3.4	4.6	4.3
	ν_{18}	1153.5	1146.9	-6.6	-11.2	-11.8
	ν_3	1144.7	-		-4.1	-5.2
	ν_{13}	1060.9	1061.2	0.3	-1.0	-1.0
	ν_{19}	1057.7	1058.3	0.6	-0.8	-1.8
	ν_{20}	1057.7	1058.3	0.6	0.3	-0.7
	ν_5	1050.6	1051.7	1.1	1.3	-0.7
	ν_{14}	929.0	928.9	-0.1	0.0	0.8
	ν_{21}	857.8	-		0.3	-1.3
	ν_6	826.3	823.9	-2.4	-3.9	-5.3

[a] Modes could not be assigned due to overlap with DME-d_6 modes.

Table S5.8: Experimental vibrational frequencies for the monomers and complexes, as well as experimental complexation shifts ($\Delta\nu_{exp}$) and MP2/aug-cc-pVDZ-PP calculated complexation shifts ($\Delta\nu_{calc}$), in cm^{-1}, for the XB complex and HB complex of CH_2FI with TMA dissolved in LKr at 130 K.

Assignment		$\nu_{monomer}$	$\nu_{complex,HB}$	$\Delta\nu_{exp,HB}$	$\Delta\nu_{calc,HB}$	$\nu_{complex,XB}$	$\Delta\nu_{exp,XB}$	$\Delta\nu_{calc,XB}$
CH_2FI	ν_7	3043.0	-		-17.1	-		-16.0
	ν_1	2981.5	[a]		-41.0	[a]		-11.7
		2975.7	-		-41.0	-		-11.7
	$2\nu_2$	2877.3	[a]		26.9	[a]		-5.6
	$2\nu_4$	2070.0	2050.9	-19.1	-26.2	2035.8	-34.2	-33.3
	ν_2	1448.1	overlap		13.4	1446.3	-1.8	-2.8
	ν_3	1268.0	1280.8	12.8	24.0	1264.8	-3.2	-6.6
	ν_8	1219.8	-		18.2	1218.7	-1.1	-2.7
	$2\nu_5$	1130.1	1127.1	-3.0	-11.8	1127.1	-3.0	-10.6
	ν_4	1043.2	1033.8	-9.4	-13.1	1026.4	-16.8	-16.6
	ν_4 (^{13}C)	1020.6	-		-13.1	1004.1	-16.5	-16.6
	ν_5	566.7	562.7	-4.0	-5.9	565.5	-1.2	-5.3
TMA	ν_{12}	2976.6	2979.2	2.6	0.4	2979.2	2.6	1.5
	ν_1	2944.2	2945.9	1.7	2.2	2945.9	1.7	3.6
	ν_{13}	2944.2	2945.9	1.7	1.4	2945.9	1.7	3.5
	$2\nu_4$	2818.3	2825.6	7.3	0.2	2818.3	0.0	-0.7
	ν_2	2768.6	2776.6	8.0	11.5	2776.6	8.0	17.2
	ν_{14}	2768.6	2776.6	8.0	13.0	2776.6	8.0	19.0
	$\nu_{20} + \nu_{21}$	1474.7	1472.7	-2.0	-5.2	1472.7	-2.0	-4.3
	ν_{15}	1467.5	1467.5	0.0	0.8	1467.5	0.0	-0.4
	ν_3	1454.7	1453.3	-1.4	1.0	1453.3	-1.4	-0.4
	ν_4	1438.8	1439.4	0.6	0.1	1439.4	0.6	-0.3
	ν_{16}	1438.8	1439.4	0.6	-0.1	1439.4	0.6	-1.5
	ν_{17}	1405.2	-		0.7	-		0.3
	ν_{18}	1273.2	1269.5	-3.7	-4.3	1269.5	-3.7	-0.7
	ν_5	1184.1	1189.6	5.5	6.3	1190.9	6.8	6.8
	ν_{19}	1098.4	1098.6	0.2	-0.4	1098.6	0.2	-1.8
	ν_{20}	1041.4	1038.1	-3.3	-3.4	1038.1	-3.3	-2.3
	ν_6	827.9	825.1	-2.8	-3.7	825.1	-2.8	-5.3

[a] Modes could not be assigned due to overlap with TMA modes.

Table S5.9: Overview of the different van 't Hoff plots constructed for the HB complex between CH_2FI and DME in LKr in the 120 - 156 K temperature interval, showing the estimated mole fractions of each monomer, range of the integrated monomer and complex bands and complex enthalpies $\Delta H°$ (LKr).

x_{CH_2FI}	x_{DME}	Integrated CH_2FI band (cm^{-1})	Integrated DME band (cm^{-1})	Integrated Complex band (cm^{-1})	$\Delta H°$ (LKr) [a]
1.1×10^{-3}	4.9×10^{-3}	1283 - 1253	2125 - 2068	1292 - 1258 [c]	-7.1(2)
1.9×10^{-3}	4.7×10^{-3}	1283 - 1253	2125 - 2068	1290 - 1260 [c]	-7.2(1)
3.8×10^{-4}	4.7×10^{-3}	1288 - 1252	2127 - 2065	1056 - 1020	-6.9(2)
3.8×10^{-4}	4.7×10^{-3} [b]	1291 - 1252	968 – 889 [b]	1293 - 1254 [c]	-7.0(1)

[a] Values are given with the standard deviation of the linear regression in parentheses.
[b] Measurement involving DME-d_6.
[c] Intensity of the additional band was integrated numerically and deducted from the intensity of the band assigned to the HB complex.

Table S5.10: Overview of the different van 't Hoff plots constructed for the XB complex between CH_2FI and TMA-d_9 in LKr in the 120-156 K temperature interval, showing the estimated mole fractions of each monomer, range of the integrated monomer and complex bands and complex enthalpies $\Delta H°$ (LKr).

x_{CH_2FI}	x_{TMA-d_9}	Integrated CH_2FI band (cm^{-1})	Integrated TMA-d_9 band (cm^{-1})	Integrated Complex band (cm^{-1})	$\Delta H°$ (LKr) [a]
5.6×10^{-4}	1.9×10^{-3}	1290 - 1248	1974 - 1948	1270-1259	-12.56(3)
5.6×10^{-4}	1.9×10^{-3}	1290 - 1248	1974 - 1948	ν_4 (1026.4) [b]	-12.39(3)
2.3×10^{-4}	1.9×10^{-3}	1290 - 1248	1974 - 1948	1269 - 1259	-12.57(2)
2.3×10^{-4}	1.9×10^{-3}	1290 - 1248	1974 - 1948	ν_4 (1026.4) [b]	-12.44(1)

[a] Values are given with the standard deviation of the linear regression in parentheses.
[b] Due to overlap between both complex bands, the intensity used is obtained from a band fit analysis.

Table S5.11: Overview of the different van 't Hoff plots constructed for the HB complex between CH_2FI and TMA-d_9 in LKr in the 120-156 K temperature interval, showing the estimated mole fractions of each monomer, range of the integrated monomer and complex bands and complex enthalpies $\Delta H°$ (LKr).

x_{CH_2FI}	x_{TMA-d_9}	Integrated CH_2FI band (cm^{-1})	Integrated TMA-d_9 band (cm^{-1})	Integrated Complex band (cm^{-1})	$\Delta H°$ (LKr) [a]
5.6×10^{-4}	1.9×10^{-3}	1290 - 1248	1974 - 1948	1292 - 1270	-9.80(7)
5.6×10^{-4}	1.9×10^{-3}	1290 - 1248	1974 - 1948	ν_4 (1033.8) [b]	-9.57(3)
2.3×10^{-4}	1.9×10^{-3}	1290 - 1248	1974 - 1948	1292 - 1269	-9.5(1)
2.3×10^{-4}	1.9×10^{-3}	1290 - 1248	1974 - 1948	ν_4 (1033.8) [b]	-9.33(5)

[a] Values are given with the standard deviation of the linear regression in parentheses.
[b] Due to overlap between both complex bands, the intensity used is obtained from a band fit analysis.

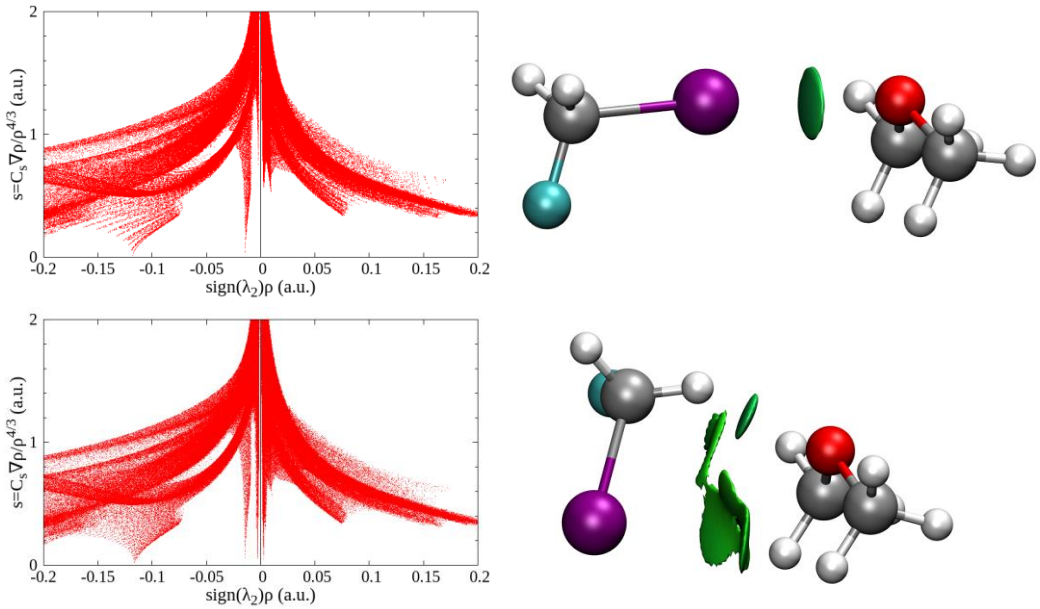

Figure S5.1: Plots of the reduced density gradient versus the electron density multiplied by the sign of the second Hessian eigenvalue (left) and gradient isosurfaces (s = 0.5 a.u., right) for the XB complex (top) and the HB complex (bottom) between CH_2FI and DME.

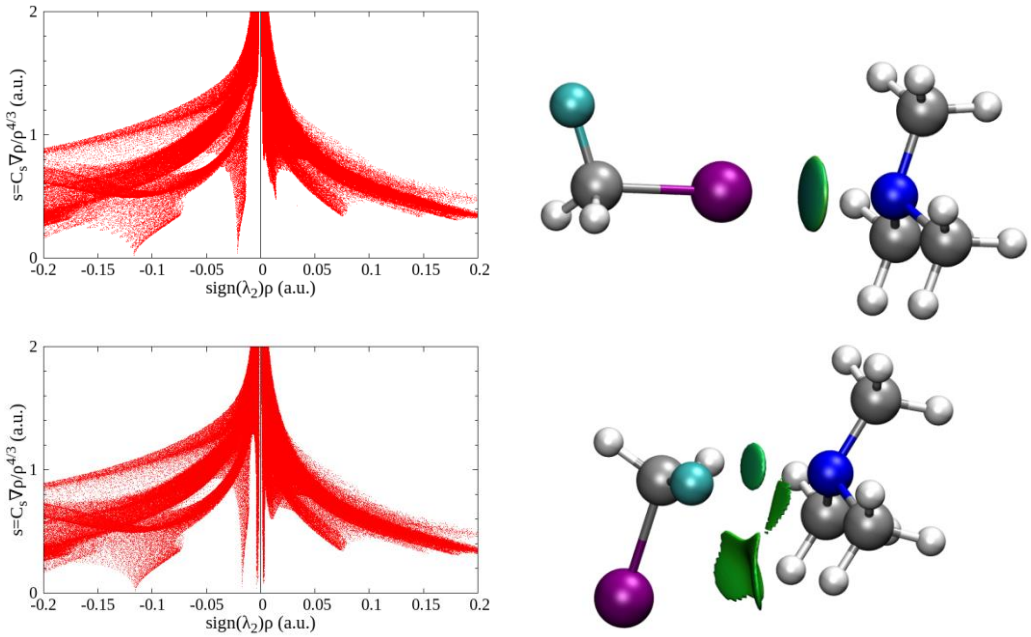

Figure S5.2: Plots of the reduced density gradient versus the electron density multiplied by the sign of the second Hessian eigenvalue (left) and gradient isosurfaces (s = 0.5 a.u., right) for the XB complex (top) and the HB complex (bottom) between CH_2FI and TMA.

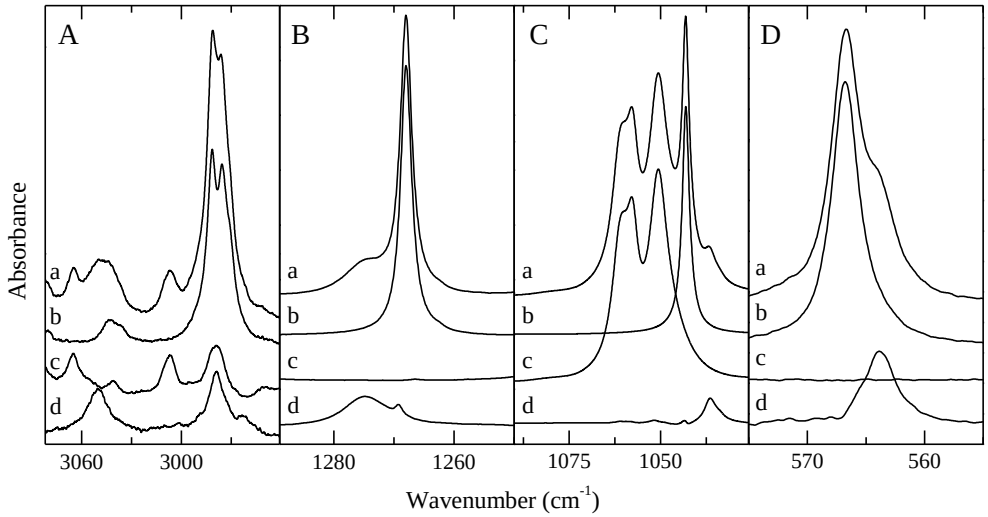

Figure S5.3: Infrared spectra of selected spectral regions for the mixtures of CH_2FI with DME-d_6 dissolved in LKr at 130 K. In each panel, trace *a* represents the mixed solution, while traces *b* and *c* show the rescaled spectra of the solutions containing only CH_2FI or DME-d_6, respectively. Trace *d* represents the spectrum of the complex which is obtained by subtracting the rescaled traces *b* and *c* from trace *a*. Estimated mole fractions of the solutions of the mixtures are 1.9×10^{-4} for CH_2FI and 4.7×10^{-3} for DME-d_6 in panel A, 9.4×10^{-5} for CH_2FI and 4.7×10^{-3} for DME-d_6 in panel B, 6.8×10^{-5} for CH_2FI and 2.8×10^{-3} for DME-d_6 in panel C and 1.9×10^{-4} for CH_2FI and 4.7×10^{-3} for DME-d_6 in panel D.

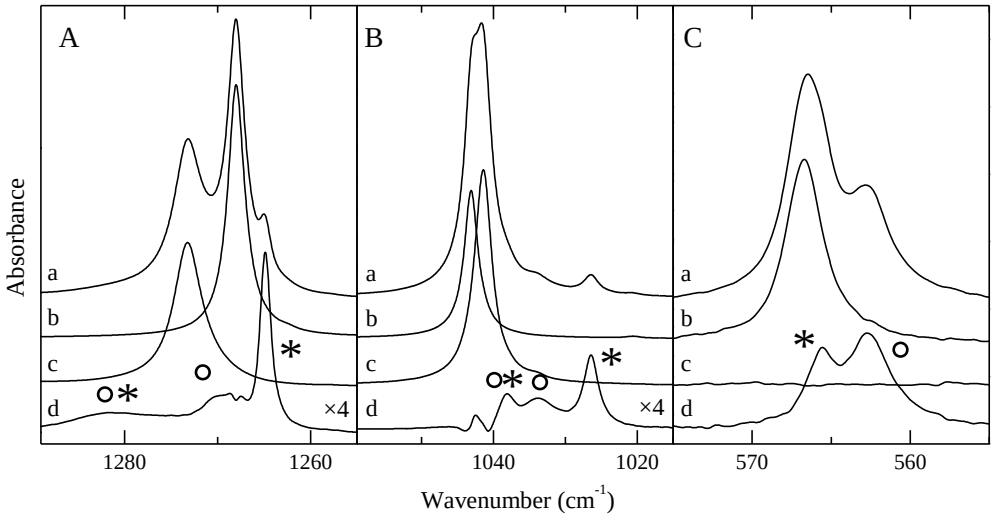

Figure S5.4: Infrared spectra of selected spectral regions for the mixtures of CH_2FI with TMA dissolved in LKr at 130 K. In each panel, trace *a* represents the mixed solution, while traces *b* and *c* show the rescaled spectra of the solutions containing only CH_2FI or TMA, respectively. Trace *d* represents the spectrum of the complex which is obtained by subtracting the rescaled traces *b* and *c* from trace *a*. For clarity, trace *d* has been multiplied by a factor of 4 in panels A and B. Bands due to the XB and HB complexes observed in traces *d* are marked with an asterisk (*) or open circle (°), respectively. Estimated mole fractions of the solutions of the mixtures are 2.9×10^{-4} for CH_2FI and 3.8×10^{-4} for TMA in panel A, 4.7×10^{-5} for CH_2FI and 3.8×10^{-4} for TMA in panel B and 9.4×10^{-5} for CH_2FI and 1.9×10^{-3} for TMA in panel C.

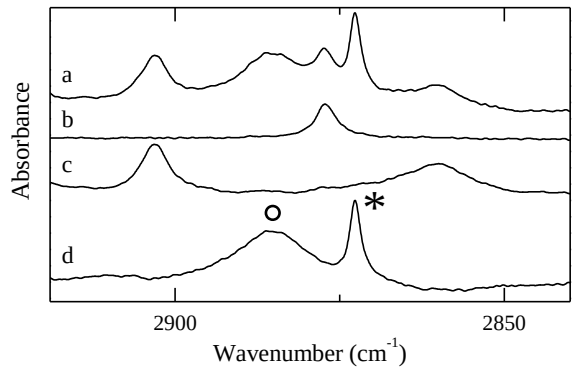

Figure S5.5: Infrared spectra of the $2\nu_2$ spectral region for the mixtures of CH_2FI with TMA-d_9 dissolved in LKr at 130 K. Trace *a* represents the mixed solution, while traces *b* and *c* show the rescaled spectra of the solutions containing only CH_2FI or TMA-d_9, respectively. Trace *d* represents the spectrum of the complex which is obtained by subtracting the rescaled traces *b* and *c* from trace *a*. Bands due to the XB and HB complexes observed in trace *d* are marked with an asterisk (*) or open circle (°), respectively. Estimated mole fractions of the solution of the mixture is 1.3×10^{-4} for CH_2FI and 1.9×10^{-3} for TMA-d_9.

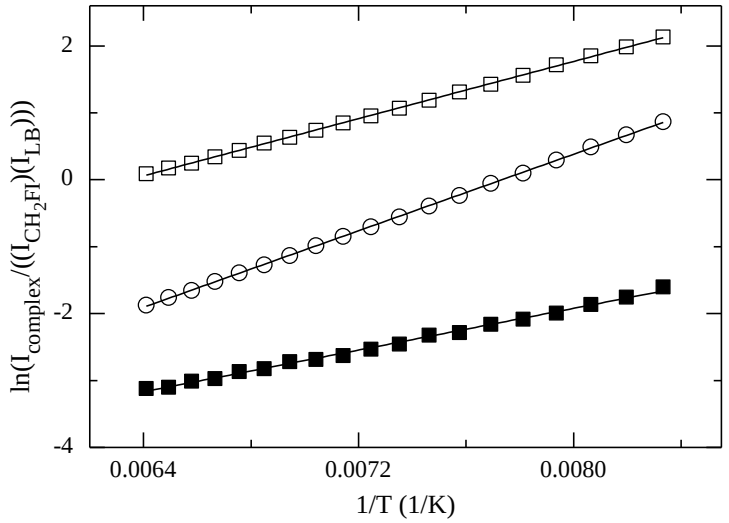

Figure S5.6: Typical van 't Hoff plots of the HB complexes (squares) and XB complex (circles) between CH_2FI and DME (filled) or TMA (open) in LKr in the 120 - 156 K temperature interval.

Chapter 6

Bromine halogen bonding vs. hydrogen bonding:

Can the weaker sibling of iodine halogen bonding stand up for itself? Complexes of bromodifluoromethane with TMA.

This chapter will be submitted as:

Geboes, Y.; De Proft, F.; Herrebout, W. A., On the competition of bromine halogen bonding and hydrogen bonding: Complexes of bromodifluoromethane with trimethylamine, to *Journal of Molecular Structure* as a part of the *Proceedings of HBOND2017*.

Abstract

Previous experimental and theoretical studies of various model compounds dissolved in liquid noble gases have shown that iodine halogen bonding can compete with hydrogen bonding and that experimental information on the thermodynamic equilibria present can be derived. To get a more general grasp of the competition between halogen bonding and hydrogen bonding, and to expand the set of experimental data to other, weaker, halogen donors, solutions in LKr containing mixtures of CHF_2Br with TMA or the fully deuterated TMA-d_9 are studied using FTIR spectroscopy. Analysis of the experimental data obtained is supported by *ab initio* calculations, statistical thermodynamics and MC-FEP simulations. Careful comparison of the spectra of the monomers and of the mixtures studied, shows that for all solutions studied, only features due to a HB complex are observed. The experimental complexation enthalpy for this species is determined to be -14.2(4) kJ mol^{-1}.

6.1 Introduction

Halogen bonding, the noncovalent interaction in which covalently bonded halogen atoms interact with electron rich moieties through a region with positive electrostatic potential along the covalent bond axis, the σ-hole, has been widely studied in the past decades. [1-3] Within these studies, it was found that the strength of the noncovalent interactions correlates well with the size of the σ-hole on the halogen atom involved. [4] Ways to increase the size of the σ-hole, and thus strengthen the noncovalent interactions formed, include enhancing the electron withdrawing properties of the covalently bonded molecule [5] and increasing the size of the halogen atom involved. [6] Another aspect relevant to the field of halogen bonding is its relationship with the more ubiquitous hydrogen bonds. [7] It has been demonstrated that these noncovalent interactions are able to coexist, [8-10] cooperate [11] and compete [12-15] with each other in several theoretical and experimental studies.

In the previous chapters, we have investigated the competition between iodine halogen bonding and hydrogen bonding by performing IR and Raman measurements on liquid noble gas solutions containing one of several Lewis bases and the combined donor molecules CHF_2I [16-17] or CH_2FI [18]. The experimental measurements, performed at thermodynamic equilibrium, were supported by *ab initio* calculations to assign the complex bands observed and rationalize the results. In these studies, it was demonstrated that softer Lewis bases tend to prefer iodine halogen bonding over hydrogen bonding, while decreasing the number of fluorine atoms on the donor molecule weakens both noncovalent interactions.

As the size of the halogen atom involved is one of the key factors determining the strength of the halogen bond formed, we wish to investigate the effect of using a bromine atom (instead of an iodine atom) as a halogen bond donor on the competition with hydrogen bonding. Therefore, in the current study, the complexes formed between CHF_2Br and TMA in LKr solutions are studied using FTIR. The choice for CHF_2Br is motivated by the fact that the use of a small molecule avoids complications in the spectra associated with internal rotations, while the presence of two fluorine atoms

enhances the strength of the noncovalent interactions formed. Since it was shown in a previous study [16] that for the combination of CHF_2I with TMA the XB complex is significantly more stable than the HB complex, the same Lewis base is used within this study to give the XB complex the best possible chance to compete with its HB counterpart.

The results obtained within this study will be compared with the results of previous studies involving TMA with CHF_2I to assess how substituting the iodine atom with a bromine atom influences the strength of both noncovalent interactions. Furthermore, an additional comparison with the results for the complex between fluoroform (CF_3H) and TMA will yield information on the influence of the third halogen atom of a CHF_2X (X = F, Br, I) molecule on the formed hydrogen bond. To reveal the effect of adding fluorine atoms to the covalently bonded molecule on halogen bonding, the results are also compared with those of the XB complex between TMA and CF_3Br.

6.2 Results

6.2.1 *Ab initio* calculations

Two stable complex geometries were obtained from *ab initio* calculations at the MP2/aug-cc-pVDZ-PP level for the CHF_2Br·TMA dimer. In the first complex, CHF_2Br interacts through its bromine atom with the nitrogen atom in TMA, thus forming a XB complex, while in the second dimer the hydrogen atom of CHF_2Br interacts with the nitrogen atom, forming a HB complex. Both equilibrium geometries have C_s symmetry and are shown in Figure 6.1. The main intermolecular structural parameters and relative energies are summarized in Table 6.1. Cartesian coordinates of both monomers and complexes are given in Tables S6.1 and S6.2 of the SI.

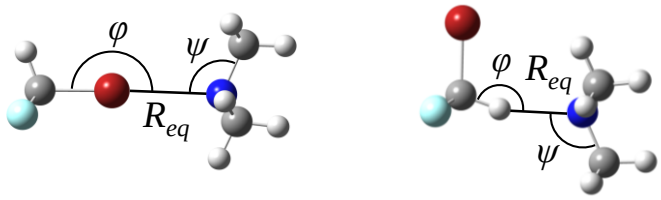

Figure 6.1: *Ab initio* calculated MP2/aug-cc-pVDZ-PP geometries for the XB (left) and HB complex (right) of CHF_2Br with TMA.

Table 6.1: Intermolecular distance R_{eq} (Å), bond angles (°), MP2/aug-cc-pVDZ-PP ΔE(DZ) and CCSD(T)/CBS ΔE(CCSD(T)) extrapolated complexation energies, calculated vapour phase complexation enthalpies $\Delta H°$ (vap,calc), the calculated complexation enthalpies in liquid krypton ($\Delta H°$ (LKr,calc)) and the corresponding experimentally obtained complexation enthalpies ($\Delta H°$ (LKr)) (kJ mol^{-1}) for the complexes of CHF_2Br with TMA. For comparison, the $\Delta H°$ (LKr,calc) and ($\Delta H°$ (LKr) values for the CHF_2I·TMA complexes are also included (kJ mol^{-1}).

	CHF_2Br	
	XB	HB
$R_{eq}=R_{X\cdots N}$ [a]	2.94	2.22
$\varphi_{C\text{-}X\cdots N}$ [a]	178.4	162.3
$\psi_{C\text{-}N\cdots X}$ [a]	111.8/107.1/107.1	115.5/105.8/105.8
ΔE (DZ)	-19.0	-23.8
ΔE (CCSD(T))	-19.1	-24.8
$\Delta H°$ (vap,calc)	-16.7	-22.0
$\Delta H°$ (LKr,calc)	-13.6	-16.5
Experimental		
$\Delta H°$ (LKr)	-	-14.2(4)
$\Delta H°$ (CHF_2I, LKr,calc) [b]	-23.4	-16.6
$\Delta H°$ (CHF_2I , LKr) [c]	-19.0(3)	-14.7(2)

[a] X = Br (in XB), H (in HB)
[b] values calculated using identical parameters, reported by Geboes et al. [18]
[c] values reported by Nagels et al. [16]

For the XB complex between CHF_2Br and TMA a nearly linear geometry is found (φ = 178.43°), while for the HB complex the C-H···N angle φ decreases to 162.3°. As

before for the complexes formed with CHF_2I, [16-17] this deviation from a linear geometry can be explained by the ability to form secondary interactions in the HB complex, which have been revealed by the NCI index visualized using NCIPLOT [19-20]. Plots of the reduced density gradient versus the electron density multiplied by the sign of the second Hessian eigenvalue and figures showing the gradient isosurfaces are given in Figure 6.2. Indeed, for the XB complex a single disk-like surface is observed between bromine and the nitrogen atom, whereas for the HB complex, apart from the disk-like surface between hydrogen and nitrogen, a broad surface is observed between the diffuse bromine atom and hydrogen atoms of two of the methyl groups of TMA.

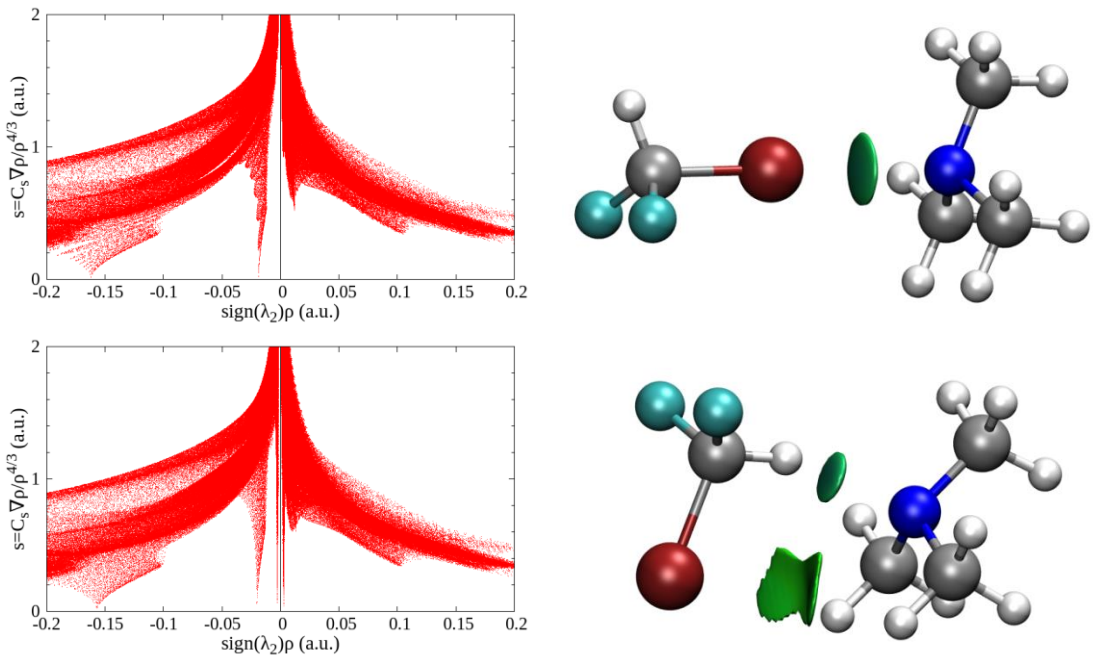

Figure 6.2: Plots of the reduced density gradient versus the electron density multiplied by the sign of the second Hessian eigenvalue (left) and gradient isosurfaces (s = 0.5 a.u., right) for the XB complex (top) and the HB complex (bottom) between CHF_2Br and TMA.

6.2.2 Infrared measurements

An overview of experimentally observed monomer bands, complexation shifts and the corresponding calculated shifts is given in Table 6.2 for TMA and Table 6.3 for TMA-d_9. A selection of the spectral regions discussed in this manuscript is given in Figure 6.3 for CHF_2Br·TMA mixtures and Figure 6.4 for CHF_2Br·TMA-d_9 mixtures. The assignments of the experimental frequencies of TMA and TMA-d_9 are based on previous studies, whereas the assignment of the CHF_2Br bands and complex bands is based on *ab initio* calculations at the MP2/aug-cc-pVDZ-PP level of theory, for which the results are given in Tables S6.3 and S6.4 of the SI. Estimated mole fractions of the solutions varied between 1.3×10^{-4} and 2.3×10^{-3} for CHF_2Br and 5.6×10^{-4} and 1.5×10^{-3} for TMA($-d_9$).

6.2.2.1 CH_2FBr·TMA infrared spectra

Investigation of the subtracted spectra of the mixtures of CHF_2Br with TMA reveals clear complex bands in several spectral regions. To assess whether these bands can be assigned to XB or HB complex, spectral regions where both complex isomers have opposing calculated shifts are the first focus of this study. One such region is found for the CHF_2Br ν_4 spectral region, shown in panel 6.3C, for which a redshift of -8.0 cm^{-1} is calculated for the HB complex and a blueshift of 0.2 cm^{-1} for the XB complex. Upon subtraction, using a subtraction factor for CHF_2Br determined in another spectral region, only a -8.2 cm^{-1} redshifted band corresponding to the HB complex is retained.

For the CHF_2Br ν_2 vibrational mode a 43.0 cm^{-1} blueshifted band is predicted for the HB complex, while a -0.3 cm^{-1} redshift has been calculated for the XB complex. Upon subtraction, a large 32.3 cm^{-1} blueshifted band is retained, as can be seen in panel 6.3B, which is assigned to the HB complex. The second complex band in this panel at 1268 cm^{-1} is assigned to the ν_{18} mode of TMA, for which the experimental shift of -5.1 cm^{-1} corresponds well to the calculated value of -4.9 cm^{-1} for the HB complex. Finally, the absence of XB complex can also be observed in the CHF_2Br ν_7 spectral region, shown in panel 6.3A, where a 33.5 cm^{-1} blueshifted band is observed corresponding to the HB complex with a calculated shift of 59.9 cm^{-1}. On the right-hand side of this panel, the

more intense HB complex band of the ν_2 mode of CHF_2Br can also be seen in part, but no complex band corresponding to the XB complex, for which a redshift of -2.5 cm^{-1} is calculated, is observed in the spectra.

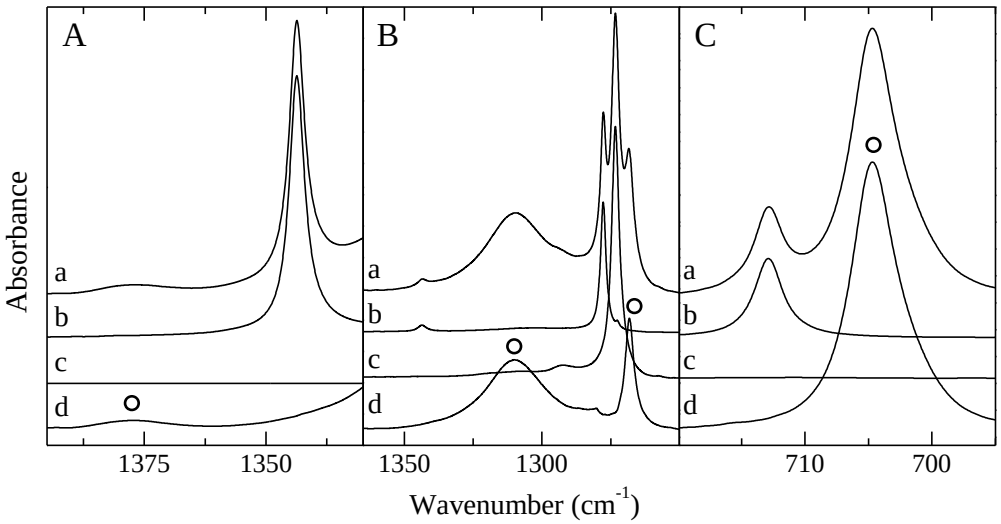

Figure 6.3: Infrared spectra of selected spectral regions for the mixtures of CHF_2Br with TMA dissolved in LKr at 120 K. In each panel, trace *a* represents the mixed solution, while traces *b* and *c* show the rescaled spectra of the solutions containing only CHF_2Br or TMA, respectively. Trace *d* represents the spectrum of the complex which is obtained by subtracting the rescaled traces *b* and *c* from trace *a*. Bands due to the HB complex observed in traces *d* are marked with an open circle (°). Estimated mole fractions of the solutions of the mixtures are 2.3×10^{-3} for CHF_2Br and 5.6×10^{-4} for TMA-d_9 in panel A and 3.8×10^{-4} for CHF_2Br and 7.5×10^{-4} for TMA-d_9 in panels B and C.

Table 6.2: Experimental vibrational frequencies for the monomers and complex, experimental complexation shifts ($\Delta\nu_{exp,HB}$) and MP2/aug-cc-pVDZ-PP calculated complexation shifts, in cm^{-1}, for the HB complex ($\Delta\nu_{calc,HB}$) and XB complex ($\Delta\nu_{calc,XB}$) of CHF_2Br with TMA dissolved in LKr at 120 K.

Assignment		$\nu_{monomer}$	$\nu_{complex}$	$\Delta\nu_{exp,HB}$	$\Delta\nu_{calc,HB}$	$\Delta\nu_{calc,XB}$
CHF_2Br		3025.4	-			
	ν_1	3014.4	[a]		-74.1	-12.1
	ν_7	1343.6	1377.1	33.5	59.9	-2.5
	ν_2	1277.8	1310.1	32.3	43.0	-0.3
	ν_8	1119.7	1107.5	-12.2	-12.3	-19.3
	ν_3	1093.5	1080.9	-12.6	-13.1	-6.7
	ν_4	712.9	704.7	-8.2	-8.0	0.2
	ν_5	578.0	576.8	-1.2	-0.8	-4.9
TMA	ν_{12}	2977.0	2980.8	3.8	1.2	0.1
	ν_1	2944.4	2947.5	3.1	3.0	1.6
	ν_{13}	2944.4	2947.5	3.1	3.3	1.5
	$2\,\nu_4$	2818.6	2821.9	3.3	2.9	0.9
	ν_2	2769.0	2778.2	9.2	16.9	12.4
	ν_{14}	2769.0	2778.2	9.2	19.3	13.7
	$\nu_{20} + \nu_{21}$	1474.8	1472.5	-2.3	-6.4	-2.7
	ν_{15}	1467.6	1469.6	2.0	1.4	0.1
	ν_3	1454.8	1453.8	-1.0	2.0	-0.4
	ν_4	1438.8	1440.6	1.8	1.4	0.4
	ν_{16}	1438.8	1440.6	1.8	1.0	-1.1
	ν_{18}	1273.3	1268.2	-5.1	-4.9	0.0
	ν_5	1184.3	1192.9	8.6	8.4	5.0
	ν_{19}	1098.5	1099.3	0.8	-0.5	-1.3
	ν_{20}	1041.5	1036.3	-5.2	-4.2	-1.2
	ν_6	828.1	826.2	-1.9	-3.9	-3.5

[a] Band could not be assigned due to overlap with TMA C-H stretching modes.

6.2.2.2 CH_2FBr·TMA-d_9 infrared spectra

In addition to the spectral regions discussed for mixtures with TMA, the use of TMA-d_9 also enables the inspection of the C-H stretching mode of CHF_2Br. For this CHF_2Br ν_1 spectral region, shown in Panel A of Figure 6.4, a complex band with a redshift of -42.7 cm^{-1} is observed, corresponding to the HB complex with a calculated shift of -74.3 cm^{-1}. No second redshifted band, corresponding to the predicted redshift of -12.1 cm^{-1} for the HB complex is observed. For the other three spectral regions discussed for the CHF_2Br·TMA mixtures, analogous results were obtained, confirming the absence of XB complex. These spectral regions are also shown in Figure 6.4, while an overview of the experimental and calculated shifts is given in Table 6.3.

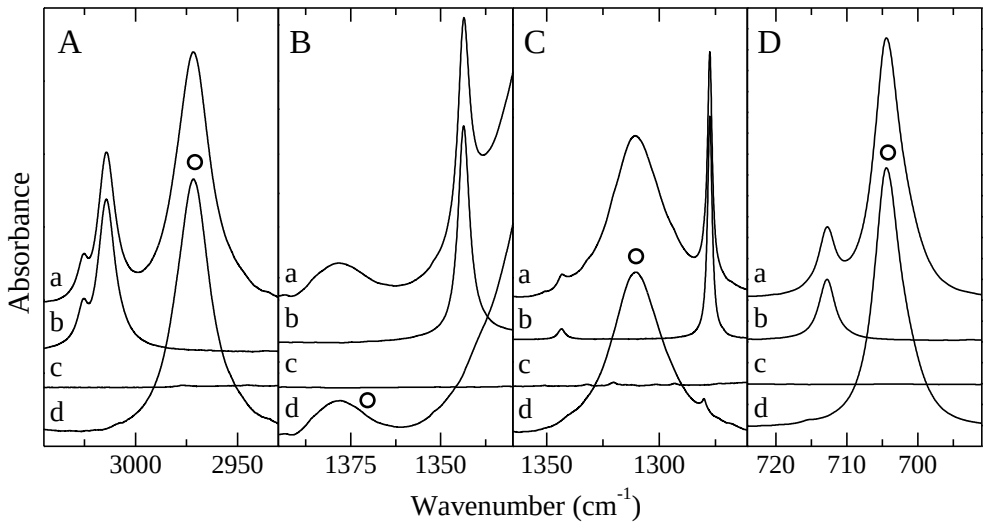

Figure 6.4: Infrared spectra of selected spectral regions for the mixtures of CHF_2Br with TMA-d_9 dissolved in LKr at 120 K. In each panel, trace *a* represents the mixed solution, while traces *b* and *c* show the rescaled spectra of the solutions containing only CHF_2Br or TMA-d_9, respectively. Trace *d* represents the spectrum of the complex which is obtained by subtracting the rescaled traces *b* and *c* from trace *a*. Bands due to the HB complex observed in traces *d* are marked with an open circle (°). Estimated mole fractions of the solutions of the mixtures are 2.3×10^{-3} for CHF_2Br and 5.6×10^{-4} for TMA-d_9 in panel A, 2.3×10^{-3} for CHF_2Br and 1.5×10^{-3} for TMA-d_9 in panel B and 3.8×10^{-4} for CHF_2Br and 7.5×10^{-4} for TMA-d_9 in panels C and D.

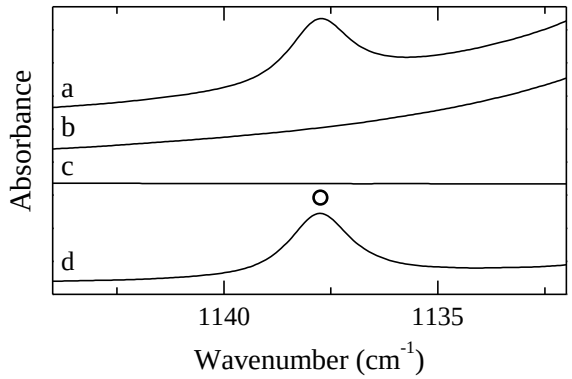

Figure 6.5: Infrared spectrum of the spectral region of the ν_3 mode of TMA-d_9 for mixtures of CHF_2Br with TMA-d_9 dissolved in LKr at 120 K. Trace *a* represents the mixed solution, while traces *b* and *c* show the rescaled spectra of the solutions containing only CHF_2Br or TMA-d_9, respectively. Trace *d* represents the spectrum of the complex which is obtained by subtracting the rescaled traces *b* and *c* from trace *a*. The complex band due to the HB complex observed in trace *d* is marked with an open circle (°). Estimated mole fractions of the solution of the mixture are 2.3×10^{-3} for CHF_2Br and 1.5×10^{-3} for TMA-d_9.

Just as in the previous study of the CH_2FI·TMA(-d_9) complexes, [18] a complex band for the ν_3 mode of TMA-d_9 is observed in the infrared spectrum, despite the fact that this mode has too low an intensity to be observed for the monomer, as shown in Figure 6.5. As shown in Table S6.4B of the SI, upon complexation, the calculated infrared intensity rises from 0.2 km mol^{-1} for the monomer to 1.3 km mol^{-1} for the HB complex. To determine the experimental complexation shift, the vibrational frequency of the monomer is determined using Raman spectroscopy in LKr at the same temperature as the FTIR measurements.

Table 6.3: Experimental vibrational frequencies for the monomers and complex, experimental complexation shifts ($\Delta\nu_{exp,HB}$) and MP2/aug-cc-pVDZ-PP calculated complexation shifts, in cm^{-1}, for the HB complex ($\Delta\nu_{calc,HB}$) and XB complex ($\Delta\nu_{calc,XB}$) of CHF_2Br with TMA-d_9 dissolved in LKr at 120 K.

Assignment		$\nu_{monomer}$	$\nu_{complex}$	$\Delta\nu_{exp}$	$\Delta\nu_{calc,HB}$	$\Delta\nu_{calc,XB}$
CHF_2Br		3025.4	-			
	ν_1	3014.4	2971.7	-42.7	-74.3	-12.1
	ν_7	1343.6	1378.0	34.4	60.2	-2.5
	ν_2	1277.8	1311.0	33.2	43.3	-5.6 [a]
	ν_8	1119.7	1107.7	-12.0	-11.8	-19.3
	ν_3	1093.5	1081.0	-12.5	-14.3	-5.6
	ν_4	712.9	704.5	-8.4	-8.2	0.1
	ν_5	578.0	576.8	-1.2	-0.8	-4.9
TMA-d_9	ν_{12}	2233.0	2235.3	2.3	1.1	0.2
	ν_1	2182.2	2187.9	5.7	3.3	5.5
	ν_{13}	2182.2	2187.9	5.7	3.9	5.8
	ν_2	2029.5	2030.0	0.5	9.9	7.1
	ν_{14}	2029.5	2038.6	9.1	11.3	7.9
	ν_{19} + ν_{21}	1226.5	1224.7	-1.8	-1.8	-0.8
	ν_{15}	1220.8	1224.7	3.9	-8.5	-1.1
	ν_3	1139.4 [b]	1137.8	-1.6	-2.2	-1.6
	ν_4	1063.0	1063.6	0.6	1.7	-1.3
	ν_{16}	1063.0	1063.6	0.6	0.2	-1.0
	ν_{17}	1055.7	-		0.7	0.4
	ν_{18}	1047.7	-		0.6	-0.7
	ν_5	1004.0	1014.0	10.0	10.3	6.0
	ν_{19}	873.9	873.5	-0.4	-0.6	0.1
	ν_{20}	832.8	-		-0.7	-1.0
	ν_6	741.1	739.6	-1.5	-2.5	-2.4

[a] Mode is degenerate with TMA-d_9 modes in the *ab initio* calculations.

[b] Frequency obtained from a Raman measurement at 120 K.

6.2.2.3 van ‘t Hoff plots and experimental complexation enthalpies

The van ’t Hoff plots based on measurements in the 120 - 156 K temperature interval of CHF_2Br·TMA($-d_9$) mixtures, for which details are given in Table S6.5 of the SI, yielded twelve experimental complexation enthalpies with an average value of -14.2(4) kJ mol^{-1}. An example of one of these van ‘t Hoff plots is given in Figure 6.6.

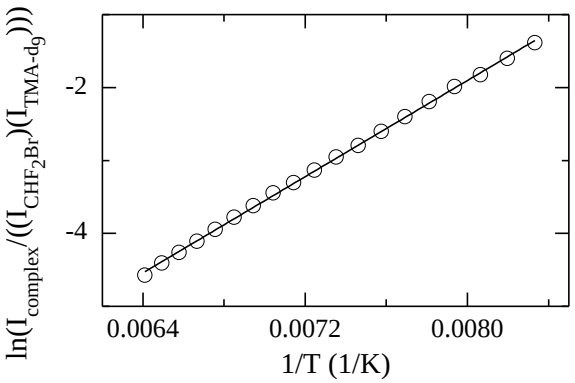

Figure 6.6: van ‘t Hoff plot of the HB complex between CHF_2Br and TMA-d_9 in LKr in the 120 - 156 K temperature interval.

6.3 Discussion

For the mixtures involving CHF_2Br and TMA, all observed complex bands were assigned to the HB complex, whereas no evidence for the presence of XB complex was observed. Furthermore, an average experimental complexation enthalpy of -14.2(4) kJ mol^{-1} was determined from van ‘t Hoff plots for the HB complex, which is in good agreement with the calculated value of -16.5 kJ mol^{-1}. Comparison with the *ab initio* results of the CHF_2I·TMA complexes [16] also reveals that the transition from iodine to bromine strongly decreases the strength of the XB complex, the calculated complexation enthalpies being -23.4 kJ mol^{-1} and -13.6 kJ mol^{-1}. For the HB complexes, nearly identical calculated complexation enthalpies are computed, amounting to -16.6 kJ mol^{-1} for the CHF_2I·TMA HB complex and -16.5 kJ mol^{-1} for the CHF_2Br·TMA HB complex, thus demonstrating that the nature of the heavier halogen present in the molecule has very little effect on the HB complex. The

negligible influence of this halogen atom on the hydrogen bond strength is also confirmed experimentally, where the observed complexation enthalpy of -14.2(4) kJ mol^{-1} for the HB complex between CHF_2Br and TMA is nearly identical to the complexation enthalpy of -14.7(2) kJ mol^{-1} for the HB complex between CHF_2I and TMA. Furthermore, these values are also very comparable to the complexation enthalpy of -14.6(8) kJ mol^{-1} reported for the complex between TMA and fluoroform (CF_3H) in liquid argon and liquid krypton by Bertsev et al. [21-22], thus confirming that the exact nature of the third halogen atom in CHF_2X molecules does not influence the strength of the HB complex with TMA noticeably.

Also worth noting is the fact that the XB complex between CF_3Br and TMA, reported previously with a complexation enthalpy in liquid argon of -18.3(1) kJ mol^{-1} [22], is noticeably stronger than the HB complex with fluoroform. Comparison with the results of the current study show that replacing one of the fluorine atoms of CF_3Br with a hydrogen atom reduced the potential strength of the bromine halogen bond sufficiently for it no longer being able to compete with the hydrogen bond.

Even though the absence of the XB complex comes as a bit of a surprise considering its calculated enthalpy in solution is only 2.9 kJ mol^{-1} higher than that of the HB complex, which corresponds with a relative population estimated to be in the order of 5 to 10 % at 138 K, it is consistent with observations in a previous study involving halothane (1-bromo-1-chloro-2,2,2-trifluoroethane) and TMA, where the XB complex was also not observed. [23] The reason for this, most probably, is related to the fact that in both halothane and CHF_2Br, the bromine and hydrogen atom are covalently bonded to the same carbon atom, along with two electron withdrawing groups (i.e. a chlorine atom and trifluoromethyl group for halothane). The absence of XB complex for both donor molecules in mixtures containing TMA, a Lewis base that has proven to be an excellent target for halogen bonding in previous studies, [16, 18] is a good indicator for the fact that bromine halogen bonding is significantly weaker than hydrogen bonding when both donor atoms are covalently bonded to the same carbon atom. It would therefore be interesting to see whether this tendency holds up when both donor atoms are covalently bonded to different carbon atoms in larger molecules, such as

1-bromo-1,2,2-trifluoroethane or 1-bromo-2,3,5,6-tetrafluorobenzene. *Ab initio* calculations at the MP2/aug-cc-pVDZ-PP level of theory yielded complexation energies of -24.9 kJ mol^{-1} for the HB complex and -23.2 kJ mol^{-1} for the XB complex with the former donor and -22.3 kJ mol^{-1} for the HB complex and -25.1 kJ mol^{-1} for the XB complex with the latter donor.

The absence of the XB complex has also been observed in a preliminary study by Delanoye et al. [24] investigating mixtures of CHF_2Br with DME, acetone or oxirane in liquid krypton. Furthermore, with an experimental complexation enthalpy in LKr of -12.0(1) kJ mol^{-1}, the CHF_2Br·DME HB complex is weaker than the currently studied HB complex with TMA ($\Delta H°$(LKr) = -14.2(4) kJ mol^{-1}). This tendency has also been observed in the study of the complexes with CHF_2I [16], where the HB complexes with DME and TMA had experimental complexation enthalpies of -10.5(5) kJ mol^{-1} and -14.7(2) kJ mol^{-1} respectively and the study with the bond donor molecule CH_2FI [18], with complexation enthalpies of -7.0(2) kJ mol^{-1} for the HB complex with DME and -9.6(2) kJ mol^{-1} for the HB complex with TMA.

6.4 Conclusions

Ab initio calculations yielded both a stable HB an XB complex between CHF_2Br and TMA($-d_9$), the complexation enthalpies in liquid krypton being -16.5 and -13.6 kJ mol^{-1} respectively, upon correction for thermal and solvent effects on the complexation energies of CCSD(T)/CBS quality. Infrared spectroscopy on mixtures of both compounds in LKr revealed that only HB complex is present, for which an experimental complexation enthalpy was determined of -14.2(4) kJ mol^{-1}. Comparison with the complexes of CHF_2I with TMA shows that the transition from iodine to bromine greatly diminishes the strength of the XB complex, as expected for smaller halogen atoms, while the influence on the strength of the HB complex is negligible.

6.5 References

1 P. Politzer, J. S. Murray, *ChemPhysChem*, 2013, ***14***, 278-294.
2 P. Metrangolo, G. Resnati, *Cryst. Growth Des.*, 2012, ***12***, 5835-5838.
3 A. C. Legon, *Phys. Chem. Chem. Phys.*, 2010, ***12***, 7736-7747.
4 T. Clark, M. Hennemann, J. S. Murray, P. Politzer, *J. Mol. Model.*, 2007, ***13***, 291-296.
5 K. E. Riley, J. S. Murray, J. Fanfrlik, J. Rezac, R. J. Sola, M. C. Concha, F. M. Ramos, P. Politzer, *J. Mol. Model.*, 2011, ***17***, 3309-3318.
6 P. Metrangolo, G. Resnati, T. Pilati, S. Biella, *Struct. Bond.*, 2008, ***126***, 105-136.
7 P. Metrangolo, G. Resnati, *Science*, 2008, ***321***, 918-919.
8 S. Zhu, C. Xing, W. Xu, Z. Li, *Tetrahedron Lett.*, 2004, ***45***, 777-780.
9 J. Marti-Rujas, L. Colombo, J. Lu, A. Dey, G. Terraneo, P. Metrangolo, T. Pilati, G. Resnati, *Chem. Commun.*, 2012, ***48***, 8207-8209.
10 A. R. Voth, P. Khuu, K. Oishi, P. S. Ho, *Nat. Chem.*, 2009, ***1***, 74-79.
11 B. Jing, Q. Li, R. Li, B. Gong, Z. Liu, W. Li, J. Cheng, J. Sun, *Comput. Theor. Chem.*, 2011, ***963***, 417-421.
12 C. B. Aakeröy, M. Fasulo, N. Schultheiss, J. Desper, C. Moore, *J. Am. Chem. Soc.*, 2007, ***129***, 13772-13773.
13 C. B. Aakeröy, C. L. Spartz, S. Dembowski, S. Dwyre, J. Desper, *IUCrJ*, 2015, ***2***, 498-510.
14 P. Politzer, J. S. Murray, P. Lane, *Int. J. Quantum Chem.*, 2007, ***107***, 3046-3052.
15 T. Shirman, M. Boterashvili, M. Orbach, D. Freeman, L. J. W. Shimon, M. Lahav, M. E. van der Boom, *Cryst. Growth Des.*, 2015, ***15***, 4756-4759.
16 N. Nagels, Y. Geboes, B. Pinter, F. De Proft, W. A. Herrebout, *Chem. - Eur. J.*, 2014, ***20***, 8433-8443.
17 Y. Geboes, F. De Proft, W. A. Herrebout, *Acta Cryst.*, 2017, 168-178.
18 Y. Geboes, F. De Proft, W. A. Herrebout, *J. Phys. Chem. A*, 2017, ***121***, 4180-4188.
19 E. R. Johnson, S. Keinan, P. Mori-Sánchez, J. Contreras-García, A. J. Cohen, W. Yang, *J. Am. Chem. Soc.*, 2010, ***132***, 6498-6506.
20 J. Contreras-García, E. R. Johnson, S. Keinan, R. Chaudret, J.-P. Piquemal, D. N. Beratan, W. Yang, *J. Chem. Theory Comput.*, 2011, ***7***, 625-632.
21 V. V. Bertsev, N. S. Golubev, D. N. Shchepkin, *Opt. Spectrosc.*, 1976, ***40***, 543-544.
22 D. Hauchecorne, B. J. van der Veken, A. Moiana, W. A. Herrebout, *Chem. Phys.*, 2010, ***374***, 30-36.
23 B. Michielsen, *PhD Thesis: Molecular Interactions with Halothane: a Spectroscopic Study*, University of Antwerp **2011**.
24 S. N. Delanoye, *PhD Thesis: Cryospectroscopic Study of Proper and Improper C-H···O Hydrogen Bonds: the van der Waals Complexes of Dimethyl Ether, Acetone and Oxirane with Diverse Proton Donors*, University of Antwerp **2004**.

6.6 Supporting information

Table S6.1.1: Cartesian coordinates of the MP2/aug-cc-pVDZ-PP optimized geometry of CHF_2Br.

C_s	X	Y	Z
CHF_2Br			
C	-0.433091	-0.895575	0.000000
H	-1.525631	-0.976671	0.000000
F	0.077815	-1.511025	1.099089
F	0.077815	-1.511025	-1.099089
Br	0.077815	0.958530	0.000000

Table S6.1.2: Cartesian coordinates of the MP2/aug-cc-pVDZ optimized geometry of TMA.

C_{3v}	X	Y	Z
TMA			
N	0.000000	0.000000	0.410619
C	0.000000	1.379959	-0.066347
H	-0.892330	1.901918	0.309142
H	0.892330	1.901918	0.309142
H	0.000000	1.440847	-1.178318
C	1.195079	-0.689979	-0.066347
H	2.093274	-0.178178	0.309142
H	1.200944	-1.723740	0.309142
H	1.247810	-0.720423	-1.178318
C	-1.195079	-0.689979	-0.066347
H	-1.200944	-1.723740	0.309142
H	-2.093274	-0.178178	0.309142
H	-1.247810	-0.720423	-1.178318

Table S6.2.1: Cartesian coordinates of the MP2/aug-cc-pVDZ-PP optimized geometry of the XB complex between CHF_2Br and TMA.

C_s	X	Y	Z
CHF_2Br			
C	0.090520	-2.528910	0.000000
H	1.106390	-2.940993	0.000000
F	-0.580762	-2.979121	1.101228
F	-0.580762	-2.979121	-1.101228
Br	0.140726	-0.606028	0.000000
TMA			
N	0.136761	2.331979	0.000000
C	-0.580762	2.760778	1.198700
H	-1.589375	2.321875	1.201443
H	-0.046321	2.410199	2.093945
H	-0.676939	3.867487	1.255691
C	1.492628	2.876287	0.000000
H	2.031128	2.525444	0.892729
H	2.031128	2.525444	-0.892729
H	1.497858	3.988711	0.000000
C	-0.580762	2.760778	-1.198700
H	-0.046321	2.410199	-2.093945
H	-1.589375	2.321875	-1.201443
H	-0.676939	3.867487	-1.255691

Table S6.2.2: Cartesian coordinates of the optimized MP2/aug-cc-pVDZ-PP geometry of the HB complex between CHF_2Br and TMA.

C_s	X	Y	Z
CHF_2Br			
C	0.278772	-1.282807	0.000000
H	0.812252	-0.320239	0.000000
F	0.598091	-2.021474	1.099089
F	0.598091	-2.021474	-1.099089
Br	-1.623932	-0.935742	0.000000
TMA			
N	1.247718	1.858523	0.000000
C	0.598091	2.394406	1.197607
H	-0.463959	2.108431	1.201130
H	1.075867	1.976997	2.096296
H	0.665981	3.503134	1.246268
C	2.666006	2.218589	0.000000
H	3.154254	1.801524	0.892953
H	3.154254	1.801524	-0.892953
H	2.815669	3.320348	0.000000
C	0.598091	2.394406	-1.197607
H	1.075867	1.976997	-2.096296
H	-0.463959	2.108431	-1.201130
H	0.665981	3.503134	-1.246268

Table S6.3A: MP2/aug-cc-pVDZ-PP vibrational frequencies, in cm^{-1}, infrared intensities, in km mol^{-1}, and Raman intensities, in $Å^4$ amu^{-1}, for the XB complex of CHF_2Br and TMA and both monomers, as well as the complexation shift Δν.

	Monomer			XB complex			
	Frequency	IR int.	Raman int.	Frequency	Δν	IR int.	Raman int.
CHF_2Br							
ν_1 (A')	3202.7	5.3	83.4	3190.6	-12.1	10.8	109.4
ν_2 (A')	1299.1	80.8	3.4	1298.7	-0.3	105.8	4.4
ν_3 (A')	1086.1	252.4	1.5	1079.5	-6.7	278.7	1.6
ν_4 (A')	731.8	107.9	12.8	731.9	0.2	73.8	46.3
ν_5 (A')	561.7	4.1	2.1	556.8	-4.9	3.0	5.4
ν_6 (A')	329.0	0.1	4.3	326.6	-2.4	4.1	15.6
ν_7 (A")	1350.5	6.4	2.5	1348.1	-2.5	5.8	2.8
ν_8 (A")	1104.5	207.4	2.0	1085.2	-19.3	202.9	2.0
ν_9 (A")	318.0	0.06	1.1	323.7	5.7	0.09	1.3
TMA							
ν_1 (A_1)	3111.8	42.4	235.1	3113.4	1.6	38.0	157.7
ν_2 (A_1)	2962.3	167.2	390.2	2974.7	12.4	205.4	480.7
ν_3 (A_1)	1499.0	23.4	0.4	1498.6	-0.4	25.2	0.7
ν_4 (A_1)	1464.0	1.6	2.3	1464.5	0.4	0.07	10.7
ν_5 (A_1)	1204.0	24.9	5.6	1208.9	5.0	22.4	12.9
ν_6 (A_1)	853.0	22.9	12.0	849.5	-3.5	54.5	10.8
ν_7 (A_1)	383.8	7.6	1.1	392.6	8.8	23.0	1.2
ν_8 (A_2)	3163.7	0.0	0.0	3163.7	0.1	0.4	1.0
ν_9 (A_2)	1477.7	0.0	0.0	1477.0	-0.8	0.006	0.008
ν_{10} (A_2)	1057.3	0.0	0.0	1058.5	1.2	0.002	0.001
ν_{11} (A_2)	243.9	0.0	0.0	237.5	-6.4	0.0	0.0002
ν_{12} (E)	3166.8	34.6	87.1	3166.9	0.1	26.9	66.0
ν_{13} (E)	3111.1	26.1	27.8	3112.6	1.5	19.0	35.8
ν_{14} (E)	2955.2	44.4	18.3	2968.9	13.7	41.0	29.4
ν_{15} (E)	1500.8	9.8	5.5	1500.9	0.1	12.6	6.0
ν_{16} (E)	1475.1	5.7	8.8	1474.0	-1.1	2.9	8.2
ν_{17} (E)	1421.1	0.7	1.6	1421.5	0.4	0.04	1.7
ν_{18} (E)	1303.4	14.9	1.7	1303.4	0.0	13.8	1.5
ν_{19} (E)	1115.9	9.1	0.4	1114.6	-1.3	7.1	0.7
ν_{20} (E)	1066.2	13.6	2.7	1065.1	-1.2	12.8	2.7
ν_{21} (E)	423.6	0.006	0.7	422.1	-1.6	0.01	0.7
ν_{22} (E)	290.9	0.4	0.6	284.2	-6.7	0.4	0.6

Van der Waals vibrations: 2.3 cm^{-1}, 0.8 km mol^{-1}, 0.01 $Å^4$ amu^{-1}, 22.3 cm^{-1}, 0.5 km mol^{-1}, 0.3 $Å^4$ amu^{-1}, 25.5 cm^{-1}, 0.4 km mol^{-1}, 0.2 $Å^4$ amu^{-1}, 69.3 cm^{-1}, 1.4 km mol^{-1}, 0.9 $Å^4$ amu^{-1}, 77.1 cm^{-1}, 0.02 km mol^{-1}, 0.05 $Å^4$ amu^{-1}, 80.3 cm^{-1}, 1.2 km mol^{-1}, 0.3 $Å^4$ amu^{-1}.

Table S6.3B: MP2/aug-cc-pVDZ-PP vibrational frequencies, in cm^{-1}, infrared intensities, in km mol^{-1}, and Raman intensities, in $Å^4$ amu^{-1}, for the XB complex of CHF_2Br and TMA-d_9 and both monomers, as well as the complexation shift Δν.

	Monomer			XB complex			
	Frequency	IR int.	Raman int.	Frequency	Δν	IR int.	Raman int.
CHF_2Br							
ν_1 (A')	3202.7	5.3	83.4	3190.6	-12.1	10.9	109.0
ν_2 (A')	1299.1	80.8	3.4	1298.9	-0.2	106.6	4.8
ν_3 (A')	1086.1	252.4	1.5	1080.5	-5.6	108.0	0.5
ν_4 (A')	731.8	107.9	12.8	731.9	0.1	76.6	46.0
ν_5 (A')	561.7	4.1	2.1	556.8	-4.9	3.0	5.4
ν_6 (A')	329.0	0.1	4.3	326.3	-2.7	1.5	14.2
ν_7 (A")	1350.5	6.4	2.5	1348.1	-2.5	5.8	2.8
ν_8 (A")	1104.5	207.4	2.0	1085.2	-19.3	201.6	2.0
ν_9 (A")	318.0	0.06	1.1	323.4	5.4	0.09	1.3
TMA-d_9							
ν_1 (A_1)	2286.9	51.7	81.2	2290.2	3.3	38.7	68.0
ν_2 (A_1)	2142.3	72.7	232.7	2149.4	7.1	91.0	259.9
ν_3 (A_1)	1151.7	0.2	5.9	1150.1	-1.6	2.5	10.5
ν_4 (A_1)	1079.2	12.6	0.2	1078.0	-1.3	185.0	1.3
ν_5 (A_1)	1018.9	33.5	3.4	1024.9	6.0	48.3	7.0
ν_6 (A_1)	756.9	12.4	9.6	754.4	-2.4	27.1	9.3
ν_7 (A_1)	323.0	4.6	0.8	331.9	9.0	18.8	2.5
ν_8 (A_2)	2345.4	0.0	0.0	2345.5	0.1	0.09	0.2
ν_9 (A_2)	1067.7	0.0	0.0	1066.7	-1.0	0.0001	0.0007
ν_{10} (A_2)	801.3	0.0	0.0	802.5	1.2	0.0	0.0002
ν_{11} (A_2)	173.1	0.0	0.0	168.5	-4.6	0.0	0.0001
ν_{12} (E)	2349.0	17.4	46.2	2349.1	0.2	13.5	35.2
ν_{13} (E)	2287.5	8.1	21.2	2291.4	3.9	11.4	27.3
ν_{14} (E)	2135.6	36.1	4.2	2143.4	7.9	31.9	8.6
ν_{15} (E)	1252.4	33.4	1.0	1251.2	-1.1	30.3	0.8
ν_{16} (E)	1078.6	2.1	2.4	1077.6	-1.0	2.4	2.4
ν_{17} (E)	1073.1	0.2	0.4	1073.6	0.4	0.5	0.4
ν_{18} (E)	1063.4	1.6	3.7	1062.8	-0.7	0.5	3.4
ν_{19} (E)	886.2	7.4	2.6	886.3	0.1	6.8	2.5
ν_{20} (E)	839.0	0.03	1.0	838.0	-1.0	0.02	1.3
ν_{21} (E)	352.0	0.007	0.5	351.2	-0.8	0.03	0.6
ν_{22} (E)	210.6	0.2	0.3	206.0	-4.6	0.2	0.3

Van der Waals vibrations: 2.2 cm^{-1}, 0.9 km mol^{-1}, 0.01 $Å^4$ amu^{-1}, 20.2 cm^{-1}, 0.4 km mol^{-1}, 0.3 $Å^4$ amu^{-1}, 23.3 cm^{-1}, 0.3 km mol^{-1}, 0.2 $Å^4$ amu^{-1}, 65.6 cm^{-1}, 1.1 km mol^{-1}, 0.8 $Å^4$ amu^{-1}, 72.3 cm^{-1}, 0.05 km mol^{-1}, 0.02 $Å^4$ amu^{-1}, 76.1 cm^{-1}, 1.3 km mol^{-1}, 0.3 $Å^4$ amu^{-1}.

Table S6.4A: MP2/aug-cc-pVDZ-PP vibrational frequencies, in cm^{-1}, infrared intensities, in km mol^{-1}, and Raman intensities, in $Å^4$ amu^{-1}, for the HB complex of CHF_2Br and TMA and both monomers, as well as the complexation shift Δν.

	Monomer			HB complex			
	Frequency	IR int.	Raman int.	Frequency	Δν	IR int.	Raman int.
CHF_2Br							
ν_1 (A')	3202.7	5.3	83.4	3128.6	-74.1	99.5	243.9
ν_2 (A')	1299.1	80.8	3.4	1342.0	43.0	117.0	7.7
ν_3 (A')	1086.1	252.4	1.5	1073.1	-13.1	259.8	2.1
ν_4 (A')	731.8	107.9	12.8	723.8	-8.0	111.7	11.7
ν_5 (A')	561.7	4.1	2.1	560.9	-0.8	8.9	2.1
ν_6 (A')	329.0	0.1	4.3	323.9	-5.1	0.02	4.3
ν_7 (A")	1350.5	6.4	2.5	1410.4	59.9	8.5	0.7
ν_8 (A")	1104.5	207.4	2.0	1092.1	-12.3	180.0	2.1
ν_9 (A")	318.0	0.06	1.1	315.8	-2.2	0.02	0.8
TMA							
ν_1 (A_1)	3111.8	42.4	235.1	3114.8	3.0	40.9	176.8
ν_2 (A_1)	2962.3	167.2	390.2	2979.1	16.9	169.4	426.6
ν_3 (A_1)	1499.0	23.4	0.4	1501.1	2.0	24.6	0.5
ν_4 (A_1)	1464.0	1.6	2.3	1465.5	1.4	2.0	2.9
ν_5 (A_1)	1204.0	24.9	5.6	1212.3	8.4	24.2	4.9
ν_6 (A_1)	853.0	22.9	12.0	849.1	-3.9	35.4	10.7
ν_7 (A_1)	383.8	7.6	1.1	400.1	16.3	13.2	1.0
ν_8 (A_2)	3163.7	0.0	0.0	3165.1	1.4	0.01	0.09
ν_9 (A_2)	1477.7	0.0	0.0	1478.3	0.6	0.001	0.05
ν_{10} (A_2)	1057.3	0.0	0.0	1057.9	0.7	0.01	0.02
ν_{11} (A_2)	243.9	0.0	0.0	239.1	-4.7	0.003	0.02
ν_{12} (E)	3166.8	34.6	87.1	3168.0	1.2	26.3	69.9
ν_{13} (E)	3111.1	26.1	27.8	3114.3	3.3	15.8	21.2
ν_{14} (E)	2955.2	44.4	18.3	2974.5	19.3	36.8	18.9
ν_{15} (E)	1500.8	9.8	5.5	1502.2	1.4	12.0	6.0
ν_{16} (E)	1475.1	5.7	8.8	1476.1	1.0	3.3	8.0
ν_{17} (E)	1421.1	0.7	1.6	1422.6	1.5	0.2	1.6
ν_{18} (E)	1303.4	14.9	1.7	1298.5	-4.9	14.8	1.4
ν_{19} (E)	1115.9	9.1	0.4	1115.4	-0.5	10.5	0.6
ν_{20} (E)	1066.2	13.6	2.7	1062.0	-4.2	11.6	2.6
ν_{21} (E)	423.6	0.006	0.7	421.5	-2.2	0.09	0.6
ν_{22} (E)	290.9	0.4	0.6	290.1	-0.9	0.3	0.4

Van der Waals vibrations: 5.6 cm^{-1}, 0.1 km mol^{-1}, 0.07 $Å^4$ amu^{-1}, 29.3 cm^{-1}, 0.1 km mol^{-1}, 0.02 $Å^4$ amu^{-1}, 35.6 cm^{-1}, 0.2 km mol^{-1}, 0.3 $Å^4$ amu^{-1}, 53.1 cm^{-1}, 0.3 km mol^{-1}, 0.3 $Å^4$ amu^{-1}, 69.2 cm^{-1}, 0.6 km mol^{-1}, 0.3 $Å^4$ amu^{-1}, 84.3 cm^{-1}, 0.6 km mol^{-1}, 0.4 $Å^4$ amu^{-1}.

Table S6.4B: MP2/aug-cc-pVDZ-PP vibrational frequencies, in cm^{-1}, infrared intensities, in km mol^{-1}, and Raman intensities, in $Å^4$ amu^{-1}, for the HB complex of CHF_2Br and TMA-d_9 and both monomers, as well as the complexation shift $\Delta\nu$.

	Monomer			HB complex			
	Frequency	IR int.	Raman int.	Frequency	$\Delta\nu$	IR int.	Raman int.
CHF_2Br							
ν_1 (A')	3202.7	5.3	83.4	3128.4	-74.3	106.1	222.9
ν_2 (A')	1299.1	80.8	3.4	1342.4	43.3	117.6	7.1
ν_3 (A')	1086.1	252.4	1.5	1071.8	-14.3	194.9	1.5
ν_4 (A')	731.8	107.9	12.8	723.6	-8.2	112.0	12.6
ν_5 (A')	561.7	4.1	2.1	560.8	-0.8	8.6	2.1
ν_6 (A')	329.0	0.1	4.3	323.6	-5.4	0.06	3.9
ν_7 (A")	1350.5	6.4	2.5	1410.8	60.2	8.4	0.7
ν_8 (A")	1104.5	207.4	2.0	1092.6	-11.8	174.6	1.4
ν_9 (A")	318.0	0.06	1.1	315.8	-2.2	0.02	0.8
TMA-d_9							
ν_1 (A_1)	2286.9	51.7	81.2	2292.5	5.5	49.5	67.6
ν_2 (A_1)	2142.3	72.7	232.7	2152.1	9.9	69.3	248.0
ν_3 (A_1)	1151.7	0.2	5.9	1149.5	-2.2	1.3	5.6
ν_4 (A_1)	1079.2	12.6	0.2	1081.0	1.7	20.3	0.2
ν_5 (A_1)	1018.9	33.5	3.4	1029.2	10.3	33.2	3.0
ν_6 (A_1)	756.9	12.4	9.6	754.4	-2.5	19.1	7.6
ν_7 (A_1)	323.0	4.6	0.8	337.6	14.7	8.7	1.1
ν_8 (A_2)	2345.4	0.0	0.0	2346.6	1.1	0.004	0.09
ν_9 (A_2)	1067.7	0.0	0.0	1067.4	-0.3	0.02	0.003
ν_{10} (A_2)	801.3	0.0	0.0	802.0	0.7	0.0005	0.007
ν_{11} (A_2)	173.1	0.0	0.0	169.8	-3.3	0.002	0.01
ν_{12} (E)	2349.0	17.4	46.2	2350.1	1.1	13.2	36.8
ν_{13} (E)	2287.5	8.1	21.2	2293.3	5.8	4.8	17.4
ν_{14} (E)	2135.6	36.1	4.2	2146.9	11.3	29.3	5.0
ν_{15} (E)	1252.4	33.4	1.0	1243.9	-8.5	32.9	1.1
ν_{16} (E)	1078.6	2.1	2.4	1078.8	0.2	15.0	3.0
ν_{17} (E)	1073.1	0.2	0.4	1073.8	0.7	21.6	0.3
ν_{18} (E)	1063.4	1.6	3.7	1064.0	0.6	2.3	3.6
ν_{19} (E)	886.2	7.4	2.6	885.6	-0.6	7.1	2.5
ν_{20} (E)	839.0	0.03	1.0	838.2	-0.7	0.01	1.1
ν_{21} (E)	352.0	0.007	0.5	350.8	-1.2	0.1	0.5
ν_{22} (E)	210.6	0.2	0.3	210.0	-0.6	0.2	0.2

Van der Waals vibrations: 5.2 cm^{-1}, 0.1 km mol^{-1}, 0.08 $Å^4$ amu^{-1}, 26.7 cm^{-1}, 0.1 km mol^{-1}, 0.02 $Å^4$ amu^{-1}, 34.2 cm^{-1}, 0.2 km mol^{-1}, 0.3 $Å^4$ amu^{-1}, 47.0 cm^{-1}, 0.2 km mol^{-1}, 0.3 $Å^4$ amu^{-1}, 65.2 cm^{-1}, 0.6 km mol^{-1}, 0.2 $Å^4$ amu^{-1}, 80.8 cm^{-1}, 0.6 km mol^{-1}, 0.4 $Å^4$ amu^{-1}.

Table S6.5: Overview of the different van 't Hoff plots constructed for the HB complex between CHF_2Br and TMA in LKr in the 120-156 K temperature interval, showing the estimated mole fractions of each monomer, range of the integrated monomer and complex bands and complex enthalpies $\Delta H°$ (LKr).

x_{CHF_2Br}	x_{TMA}	Integrated CHF_2Br band (cm^{-1})	Integrated TMA band (cm^{-1})	Integrated Complex band (cm^{-1})	$\Delta H°$ (LKr) [a]
1.3×10^{-4}	5.6×10^{-4}	726 - 700	1196 - 1172	1093 - 1066	-13.51(8)
1.3×10^{-4}	5.6×10^{-4}	726 - 700	1500 - 1425	831 - 821	-13.6(1)
1.3×10^{-4}	5.6×10^{-4} [b]	725 -698	890 - 860	1120 - 1097	-13.96(4)
1.3×10^{-4}	5.6×10^{-4} [b]	1143 - 1078	1022 - 985	714 - 692	-14.1(1)
3.8×10^{-4}	7.5×10^{-4}	1294 - 1268	1200 - 1170	1201 -1185.5	-14.15(6)
3.8×10^{-4}	7.5×10^{-4}	1294 - 1268	1505 -1420	720 - 690	-14.00(7)
3.8×10^{-4}	7.5×10^{-4} [b]	730 - 700	1236 - 1206	1027 - 998	-14.39(8)
3.8×10^{-4}	7.5×10^{-4} [b]	730 - 700	890 - 860	2250 -2221	-14.09(9)
3.8×10^{-4}	7.5×10^{-4} [b]	730 -700	1236 -1206	718 - 690	-14.13(5)
2.3×10^{-3}	5.6×10^{-4} [b]	1365 - 1325	2075 - 1985	3027 - 2922	-14.97(7)
2.3×10^{-3}	5.6×10^{-4} [b]	3050 - 2985	1238 - 1206	886 -862	-14.9(1)
2.3×10^{-3}	1.5×10^{-3} [b]	1365 - 1325	887 -860	3027 - 2916	-14.68(5)

[a] Values are given with the standard deviation of the linear regression in parentheses.

[b] Measurement involving TMA-d_9.

Chapter 7

The influence of hybridization of the donor on halogen bonding strength and competitive lone pair···π interactions.

Complexes of C_2F_3X (X = F, Cl, Br, I) with DME.

This chapter has been published as:

Geboes, Y.; Nagels, N.; Pinter, B; De Proft, F.; Herrebout, W. A., Competition of $C(sp^2)$–X···O Halogen Bonding and Lone Pair···π Interactions: Cryospectroscopic Study of the Complexes of C_2F_3X (X = F, Cl, Br, and I) and Dimethyl Ether, *The Journal of Physical Chemistry A* **2015**, *119*, 2502-2516.

Abstract

Inspection of the electrostatic potential of C_2F_3X (X = F, Cl, Br, I) revealed a second electropositive region in the immediate vicinity of the C=C double bond apart from the σ-hole of chlorine, bromine and iodine, leading to $C(sp^2)$-X···Y halogen bonding, through which complexes stabilized by so-called lone pair···π (lp···π) interactions can be formed. Consequently, the experimental studies for the complexes of DME with C_2F_3X (X = F, Cl, Br, I) not only allowed to experimentally characterize and rationalize the effects of hybridization on halogen bonding but, for the first time, also allowed the competition of C-X···Y halogen bonding and lp···π interactions to be studied at thermodynamic equilibrium. Analysis of the infrared and Raman spectra reveals that in the cryosolutions of DME and C_2F_3I, solely the XB complex is present, whereas C_2F_3Br and C_2F_3Cl give rise to a lp···π complex as well as a XB complex. Mixtures of DME with C_2F_4 solely yield a lp···π complex. The experimentally derived complexation enthalpies for the XB complexes are found to be -14.2(5) kJ mol^{-1} for C_2F_3I·DME and -9.3(5) kJ mol^{-1} for C_2F_3Br·DME. For the complexes of C_2F_3Cl with DME no experimental complexation enthalpy could be obtained, whereas the C_2F_4·DME complex has a complexation enthalpy of -5.5(3) kJ mol^{-1}. The observed trends have been rationalized with the aid of an EDA coupled to a NOCV analysis and also using the NCI index method.

7.1 Introduction

The potential of C-X···Y halogen bonding as a valuable tool to tune key interactions in crystal engineering processes and supramolecular self-assembly is now well recognized. [1-2] Therefore and because of the awareness of its importance in various biochemical processes, [3] in molecular recognition [4] and in drug design, [5-6] the phenomenon of halogen bonding has gained a tremendous increase in interest by theoreticians and experimentalists. [7]

The majority of the papers dealing with C-X···Y halogen bonding so far mainly concentrated on halogen bond donor molecules in which the carbon atoms involved are sp^3 hybridized. As a consequence, little information has been reported on other halogen bonding motifs involving, e.g. sp^2 or sp hybridized carbon atoms. A theoretical study on the influence of the hybridization of the carbon atom has been reported by Zou *et al.*, [8] in which a series of *ab initio* calculations was initiated with the aim of describing the interactions of a variety of halogen bond donors including, amongst others, HC≡CX, H_2C=CHX and CH_3X (X = Cl, Br and I) with the nitrogen lone pair of ammonia. The results obtained by Zou and co-workers led to the theoretical observation that, within a series of halogen bond donor molecules, the halogen bonds formed tend to strengthen with increasing *s* character, and led to general assumption that $C(sp^3)$-X < $C(sp^2)$-X < C(sp)-X.

The trends reported by Zou *et al.* [8] are in line with data reported by Li *et al.* [9] suggesting that also for the C-Br···F XB complexes of CH≡CBr, CH_2=CHBr and CH_3Br with HArF a substantial difference can be observed if the hybridization of the carbon atom is changed. It should however be stressed that, in the same study, the authors also reported a series of calculations for the corresponding fluorinated compounds and that these calculations for CF_3Br and CF_2=CFBr led to complexes with HArF with a very similar interaction energy. The results therefore suggest that, although some calculations reveal that halogen bonding can be affected by the hybridization of the carbon atom involved, this definitely does not lead to a general rule of thumb.

Driven by the fact that C(sp^2)-X and C(sp)-X halogen bond donors show great potential in the field of crystal engineering and supramolecular chemistry, [10-13] and by the fact that the theoretical data reported so far did not lead to an unequivocal description of the intrinsic properties of this kind of interactions, we have initiated an experimental study of the XB complexes of C_2F_3X (X = F, Cl, Br and I) with DME, using IR and Raman spectroscopy on LAr and LKr solutions. As reported in previous studies, [14-16] the experimental approaches are supported by *ab initio* calculations, statistical thermodynamics calculations and MC-FEP simulations. To be able to rationalize the trends observed when passing from C(sp^3)-X donors to C(sp^2)-X systems, the results presented will be compared with the previous data on the XB complexes of CF_3X (X = Cl, Br, I) with DME [17] and with the theoretical results for the XB complexes reported by Zou *et al.* [8] and by Li *et al.* [9]

The choice of the trifluoroethylene derivatives CF_2=CFX (X = Cl, Br, and I) as model systems for the study of C(sp^2)-X···Y halogen bonding was further motivated by the observation that, apart from the σ-hole observed for the chlorine, the bromine or the iodine atoms, a second electropositive region was detected in the immediate vicinity of the C=C double bonds for all four compounds. These regions are clearly visible in the electrostatic potentials shown in Figure 7.1. These results are also in agreement with the theoretical results reported for other complexes involving hexafluorobenzene and typical Lewis bases, such as water, DME and ammonia [18-19] as well as the experimental observation of the $C_6F_6 \cdot H_2O$ complex by Amicangelo *et al.* [20]. Furthermore, in a recent study by Caminati *et al.* [21], the existence of a $C_2F_3Cl \cdot H_2O$ lp···π complex was demonstrated using Pulsed-Jet FTMW spectroscopy. The experimental study for the complexes of DME with C_2F_3X (X = F, Cl, Br, I) therefore does not only allow to experimentally characterize and rationalize the effects of hybridization on halogen bonding but, for the first time ever, also allows the competition of C-X···Y halogen bonding and lp···π interactions to be studied experimentally at thermodynamic equilibrium.

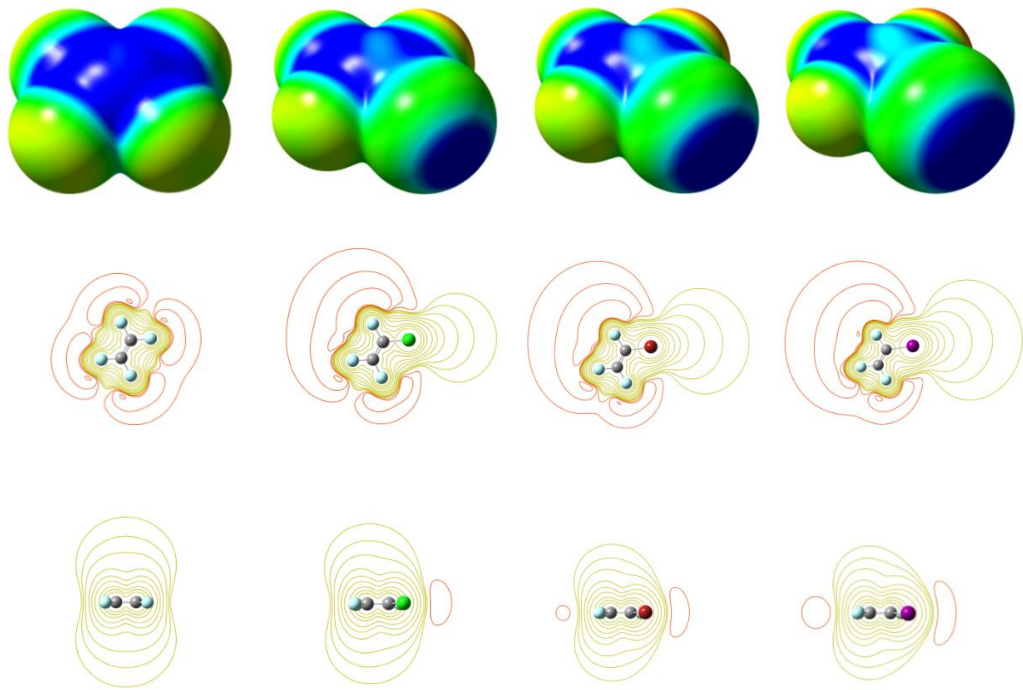

Figure 7.1: Electrostatic potential (top) of C_2F_4 (left), C_2F_3Cl, C_2F_3Br and C_2F_3I (right) on the molecular surface defined by the 0.001 electrons $Bohr^{-3}$ contour of the electron density, with positive, neutral and negative regions shown in blue, green and red, respectively. Contour plots of the electrostatic potential of the respective halogen bond donors are also given in red (negative) and green (positive), in the molecular plane (middle) and the plane perpendicular to the first one, along the C=C bond (bottom).

7.2 Results

7.2.1 *Ab initio* calculations

The isodensity surfaces and contour plots for the electrostatic potential of C_2F_3Cl, C_2F_3Br and C_2F_3I given in Figure 7.1 show the presence of two electrophilic regions. The first region is located at the outermost portion of the halogen's surface, and allows the formation of $C(sp^2)$-X···Y XB complexes. The second region, further noted as the π-hole, is located in the immediate vicinity of the C=C double bond and allows the formation of complexes stabilized by so-called lp···π interactions.

Table 7.1: Intermolecular distance R_{eq} (Å), bond angles (°) and the MP2/aug-cc-pVDZ(-PP) ΔE(DZ) and CCSD(T)/CBS complexation energies ΔE(CCSD(T)) (kJ mol^{-1}) for the complexes of C_2F_3X (X = F, Cl, Br, I) with DME. For completeness, the corresponding values for the complexes of CF_3X (X = Cl, Br, I) with DME are also given, geometric parameters for these complexes have been defined in Figure S7.1.

lp···π	C_2F_4·DME	C_2F_3Cl·DME	C_2F_3Br·DME	C_2F_3I·DME
$R_{eq}=R_{C=C\cdots O}$	2.93	2.91	2.91	2.90
θ	103.5	100.5	100.4	100.9
φ	56.5	64.7	63.7	61.9
ψ	130.0	-18.0	-20.9	-21.9
ΔE (DZ) / kJ mol^{-1}	-12.0	-14.1	-14.5	-14.9
ΔE (CCSD(T)) / kJ mol^{-1}	-13.7	-15.9	-16.4	-16.7
XB	C_2F_3Cl·DME	C_2F_3Br·DME	C_2F_3I·DME	
$R_{eq}=R_{X\cdots O}$	2.97	2.91	2.94	
$\theta_{C\text{-}X\cdots O}$	171.4	175.0	176.6	
φ	68.0	56.9	49.6	
ΔE (DZ) / kJ mol^{-1}	-11.0	-16.3	-21.8	
ΔE (CCSD(T)) / kJ mol^{-1}	-11.7	-16.8	-22.5	
XB	CF_3Cl·DME	CF_3Br·DME	CF_3I·DME	
$R_{eq}=R_{X\cdots O}$	2.96	2.90	2.94	
$\theta_{C\text{-}X\cdots O}$	173.0	176.2	177.7	
φ	66.3	56.3	49.8	
ΔE (DZ) / kJ mol^{-1}	-11.2	-16.1	-21.5	
ΔE (CCSD(T)) / kJ mol^{-1}	-11.9	-16.6	-22.1	

The σ-hole representing the ability of the molecules to act as halogen bond donors strongly increases from chlorine to iodine. These results are in line with the results obtained for C(sp^3)-X···Y halogen bonding suggesting that the strength of the interaction increases when replacing the chlorine atom by the more polarizable bromine and iodine atoms. In the case of C_2F_4 no σ-hole is observed and the molecule is expected to interact solely through its π-hole. [22] Inspection of the data in Figure 7.1 shows that the size of the π-hole remains largely unaffected by the substitution pattern.

In contrast to the trends derived for the halogen bonds, it can be concluded that the different lp···π interactions will have a similar strength throughout the series of halogen bond donors studied.

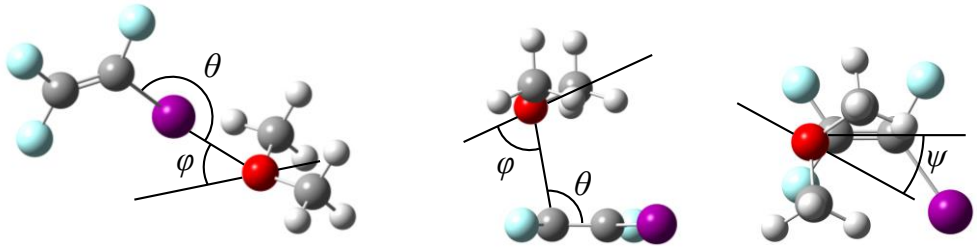

Figure 7.2: MP2/aug-cc-pVDZ(-PP) equilibrium geometries for the XB (left) and lp···π complex (middle and right) of C_2F_3X (X = F, Cl, Br and I) with DME.

The MP2/aug-cc-pVDZ(-PP) geometries for the complexes of C_2F_3X (X = F, Cl, Br, I) and DME are shown schematically in Figure 7.2. The intermolecular structural parameters of the XB and the lp···π complexes are summarized in Table 7.1. For the XB complexes, the calculations lead to a structure with C_s symmetry. The geometries for the lp···π are characterized by C_1 symmetry. For the combination of C_2F_4 with DME, no stationary point was found for the XB complex and multiple optimization attempts using geometries similar to the expected XB complex converged to the lp···π complex geometry. To allow comparison with data obtained for C(sp^3)-X···O XB complexes, the MP2/aug-cc-pVDZ(-PP) geometries obtained for complexes of DME with the trifluorohalomethanes CF_3X (X = Cl, Br or I) are reproduced in Figure S7.1 of the SI at the end of this chapter. Cartesian coordinates of the monomer and complex geometries are given in Tables S7.1 and S7.2 of the SI.

From the data in Figure 7.2 and Table 7.1 it can be seen that for all halogen bond donors studied, a XB complex is obtained in which the halogen atom is shifted away from the C-O-C bisector, the value of the angle φ between the C-O-C bisector and the line connecting the oxygen and the halogen atoms being approximately 68.0° for C_2F_3Cl, 56.9° for C_2F_3Br and 49.6° for C_2F_3I. These results are similar to those obtained for the complexes of DME with the various trifluorohalomethanes with the

values of 66.2°, 56.2° and 49.8° and further support the rabbit ear configuration of the two oxygen lone pairs. [17] Similar structural parameters of the complexes between DME and CF_3X or C_2F_3X are also found for the C-X···O bond angles, the values being 173.0, 176.2 and 177.7 degrees for CF_3X, and 171.4, 175.0 and 176.6 degrees for C_2F_3X, respectively. For the lp···π complexes a significant change in torsion angle ψ to 130.0° between the C=C bond and the C-O-C bisector can be noticed for the complex with C_2F_4, indicating that DME has rotated in respect to the C_2F_3X moiety. Furthermore, the decrease of the angle φ between C···O and the C-O-C bisector to 56.5° for the complex with C_2F_4 indicates that the hydrogen atoms of the methyl groups are rotated farther away from the C_2F_3X moiety. The cause of this deviation will be discussed in more detail below.

The MP2/aug-cc-pVDZ(-PP) and CCSD(T)/CBS extrapolated complexation energies for the C(sp^2)-X···O bonded and the lp···π complexes formed with the various trifluorohaloethenes and the corresponding values for the C(sp^3)-X···O bonded complexes formed with the trifluorohalomethanes are given in Table 7.1. In agreement with the results reported for CF_3X, a comparison of the different C(sp^2)-X···O bonded complexes revealed a significant increase in complexation energy when moving to the higher halogen atoms at all levels of calculation, the values being -11.7 kJ mol^{-1}, -16.8 kJ mol^{-1} and -22.5 kJ mol^{-1} at the CCSD(T)/CBS level, the most accurate method considered. These trends are in line with the general trends deduced from the molecular electrostatic potentials. These values resemble those of the C(sp^3)-X···O bonded complexes and are in line with the data reported by Li *et al.*,[9] suggesting that little or no effects due to changes in hybridization are to be expected for the complexes of HArF and the perfluorinated bromine donors CF≡CBr, CF_2=CFBr.

For all lp···π interactions similar values for the complexation energy are obtained, the CCSD(T)/CBS for the fluorine, chlorine, bromine and iodine derivatives being -13.7, -15.9, -16.4 and -16.7 kJ mol^{-1}, respectively. Comparison of these data at the CCSD(T)/CBS level with the data obtained for the C(sp^2)-X···O XB complexes reveals an intriguing trend in which the lp···π interaction leads to a significantly

stronger complex in the case of C_2F_3Cl (-15.9 vs. -11.7 kJ mol^{-1}), but gradually loses the competition for C_2F_3Br (-16.4 vs. -16.8 kJ mol^{-1}) and C_2F_3I (-16.7 vs. -22.5 kJ mol^{-1}).

The MP2/aug-cc-pVDZ(-PP) harmonic vibrational frequencies and infrared intensities obtained for the monomers and for the complexes under study are listed in Tables S7.3-S7.9 of the SI. From this data it is clear to see that both complex geometries of C_2F_3X·DME (X= Cl, Br, I) can be distinguished in the C=C stretching mode area of the spectrum, as well as the antisymmetrical CF_2 stretch. These vibrational modes will be used in the experimental section to asses which of the complex geometries are found in the noble gas solutions.

In order to differentiate between both geometries in IR and Raman, the complexes should have a sufficient lifetime and tunnelling between both should be avoided. To this end, transition point searches were performed involving the two stable complex geometries of C_2F_3Cl·DME, C_2F_3Br·DME and C_2F_3I·DME. To verify these results, frequency calculations of the proposed first order saddle points were performed to ensure these give rise to only one imaginary frequency. Energy diagrams of the stable geometries and transition points of C_2F_3Cl, C_2F_3Br and C_2F_3I are given in Figures S7.2, S7.3 and S7.4 of the SI respectively, which clearly show that the transition point is much higher in energy (on average about 8 kJ mol^{-1} higher than the lp···π complex), so no tunnelling is expected to occur.

7.2.2 Statistical thermodynamics and MC-FEP simulations

To allow comparison with the experimental complexation enthalpies derived from the cryosolutions measurements, the CCSD(T)/CBS complexation energies ΔE(CCSD(T)) were transformed into vapour phase complexation enthalpies $\Delta H°$(vap,calc), by accounting for thermal and zero-point vibrational contributions. In addition, to estimate the complexation enthalpies in solutions, further noted as $\Delta H°$(LKr,calc), corrections related to the solute-solvent interactions in the solutions were accounted for. The original values for the CCSD(T)/CBS complexation energies, and the calculated values for the vapour phase and solution complexation enthalpies obtained for the different types of complexes of C_2F_3X (X = Cl, Br, I) are collected in Table 7.2. For completeness, the experimental complexation enthalpies, which are discussed in more detail in the discussion section, and the corresponding values for the XB complexes of CF_3X (X = Cl, Br, I) with DME, determined in LAr, are also given.[17]

Table 7.2: The values for the CCSD(T)/CBS complexation energies, the calculated vapour phase complexation enthalpies and the calculated liquid krypton and liquid argon complexation enthalpies for the complexes of C_2F_3X (X = F, Cl, Br, I) with DME in kJ mol^{-1}. For completeness, the corresponding experimentally obtained complexation enthalpies, determined in LKr or LAr, and the corresponding values for the XB complexes of CF_3X (X = Cl, Br, I) with DME, determined in LAr, are also given.[17]

	lp···π				XB			XB		
	C_2F_4	C_2F_3Cl	C_2F_3Br	C_2F_3I	C_2F_3Cl	C_2F_3Br	C_2F_3I	CF_3Cl	CF_3Br	CF_3I
ΔE (CCSD(T))	-13.7	-15.9	-16.4	-16.7	-11.7	-16.8	-22.5	-11.9	-16.6	-22.1
$\Delta H°$ (vap,calc)	-11.2	-13.4	-13.8	-13.1	-9.2	-14.3	-18.9	-9.9	-14.6	-20.1
$\Delta H°$ (LKr,calc)	-5.6	-6.4	-6.5	-5.5	-5.9	-10.4	-14.6			
$\Delta H°$ (LAr,calc)	-5.4							-6.7	-10.7	-16.3
Experimental										
$\Delta H°$ (LKr)						-9.3(5)	-14.2(5)			
$\Delta H°$ (LAr)	-5.5(3)							-6.8(3)	-10.2(1)	-15.5(1)

7.2.3 Infrared and Raman measurements

The vibrational spectrum of DME dissolved in liquid noble gases has been extensively studied. [17, 23-26] The assignments for C_2F_4 are based on the harmonic vibrational frequencies derived at the MP2/aug-cc-pVDZ level, and the assignments made by Shimanouchi. [27] For the assignment of the many combination bands and overtones, anharmonic frequency calculations were performed as well. The numbering scheme as proposed by Herzberg was used for the numbering of the fundamental bands. [28] The assignment of the C_2F_3Cl bands is mainly based on the study reported by Gambi et al. [29] who recently reported a detailed experimental and theoretical study of its harmonic and anharmonic force fields. The assignments for C_2F_3Br and C_2F_3I were based on the harmonic vibrational frequencies derived at the MP2/aug-cc-pVDZ-PP level, as very few spectroscopic studies have yet been performed for these species. [30]

To characterize the different complexes formed between DME and the trifluorohaloethenes, infrared and Raman spectra of solutions in LKr containing mixtures of the acceptor and donor molecules and containing only monomers were recorded, at temperatures between 120 K and 156 K, using different concentrations and ratio for DME and the trifluorohaloethenes.

Inspection of the calculated harmonic vibrational frequencies obtained for the $C(sp^2)\cdots O$ XB and lp···π complexes in Tables S7.14-S7.19 shows that for the ν_1 C=C stretching modes in C_2F_3Cl, C_2F_3Br and C_2F_3I the formation of a XB complex with DME leads to a significant redshift of -2.8 , -4.1 and -5.3 cm^{-1}, respectively, while complexation via the π-system induces a small blueshift of 2.7, 3.0 and 3.1 cm^{-1}. A similar trend, with redshifts of -4.3, -6.7 and -8.9 cm^{-1} for the XB complex and blueshifts of 6.7, 7.0 and 7.4 cm^{-1} for the second type of complex is observed for the CF_2 antisymmetric stretching mode ν_2. These modes are predicted to have large infrared and medium Raman intensities in monomers and complexes, as shown in Tables S7.3 to S7.9, and were considered as the most promising candidates to experimentally observe and distinguish the complexes formed.

For the lp···π complex with C_2F_4, of which the calculated harmonic vibrational frequencies are given in Table S7.3, a slightly different behaviour is found for these vibrational modes, with a slightly larger calculated shift of 5.8 cm^{-1} for the IR inactive ν_1 C=C stretching mode and a redshift of -2.2 cm^{-1} for the CF_2 antisymmetric stretching mode ν_5, which however has B_{1g} symmetry and is also IR inactive, where a blueshift is found for the other lp···π complexes.

The C=C stretching regions of the infrared (panels A, C, E and G) and Raman (panels B, D, F and H) spectra obtained for mixed solutions containing DME and C_2F_4 (panels A and B), DME and C_2F_3Cl (panels C and D), DME and C_2F_3Br (panels E and F), and DME and C_2F_3I (panels G and H) are shown in Figure 7.3. In each panel, the spectrum for the mixed solution, at 120 K, is given in the top trace *a*, while the rescaled spectra of the C_2F_3X and DME monomers, are given in the traces *b* and *c*, respectively. To allow a more thorough analysis, the spectrum of the isolated complex obtained by subtracting rescaled monomer spectra from the spectrum of the mixed solution, is also given (trace *d*). Bands assigned to the 1:1 C(sp^2)···O XB and the 1:1 lp···π complexes are marked with an asterisk (*) and an open circle (°), respectively.

Since the C=C stretching mode has no IR intensity (as can be seen in panel 7.3A) for C_2F_4 due to symmetry restrictions, this region was studied using Raman spectroscopy. For this region, shown in panel 7.3B, an additional band, blueshifted by 4.4 cm^{-1} from the C=C stretching mode of the C_2F_4 monomer, can be observed in the spectrum of the mixture. This observation is in agreement with the predicted blueshift of 5.8 cm^{-1} for the lp···π complex. The irregular pattern in the subtracted spectrum near the top of the C_2F_4 monomer band is ascribed to an artefact of the subtraction, and has no physical meaning.

For mixtures of DME with C_2F_3Cl, subtraction of the spectrum of the mixture clearly reveals two additional bands, one blueshifted and one redshifted from the C=C stretching mode band of the monomer, as can be seen in panels 7.3C (IR) and 7.3D (Raman). With experimental shifts of 4.6 cm^{-1} and -1.8 cm^{-1}, these bands can be assigned to the lp···π complex and XB complex respectively. During the subtraction

process, an additional feature is observed near the monomer band in both the IR and Raman spectra, making subtraction based on this region difficult. Though the nature of this feature is not fully understood, it is consistent with the presence of 1:2 complex including two DME molecules and will be discussed in more detail in a further paragraph.

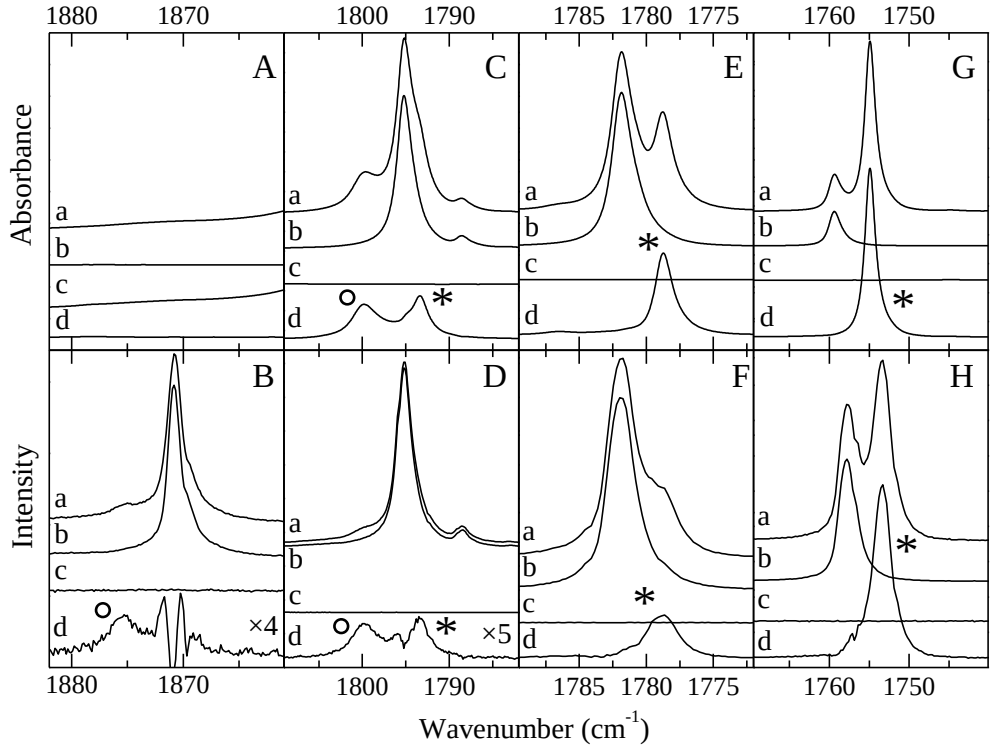

Figure 7.3: Infrared spectra (panels A, C, E and G) and Raman spectra (panels B, D, F and H) of the $\nu_{C=C}$ spectral region of C_2F_3X (X = F, Cl, Br, I) for solutions of mixtures of DME with C_2F_4 (panels A and B), C_2F_3Cl (panels C and D), C_2F_3Br (panels E and F) and C_2F_3I (panels G and H) dissolved in liquid krypton at 120 K. In each panel, trace *a* represents the mixed solution, while traces *b* and *c* show the solution containing only C_2F_3X or DME, respectively. Trace *d* represents the spectrum of the complex and is obtained by subtracting the rescaled traces *b* and *c* from trace *a*. New bands due to the 1:1 C(sp^2)-X···O XB and the 1:1 lp···π complexes are marked with an asterisk (*) and an open circle (°), respectively.

At first sight, only a redshifted band is observed for the mixture of C_2F_3Br and DME, shown in Figures 7.3E (IR) and 7.3F (Raman), which can be ascribed to the presence of XB complex. However, when the concentration of DME is increased, two weak blueshifted bands can also be observed. A detailed spectrum of this region with an elevated DME concentration is shown in Figure 7.4. The band with the largest blueshift (4.4 cm^{-1}) can be ascribed to the presence of a small amount of lp···π complex, while the origin of the band with the smaller blueshift is not fully understood.

Finally, for mixtures of C_2F_3I with DME, shown in Figures 7.3G (IR) and 7.3H (Raman), a single complex band with a -4.5 cm^{-1} redshift, assigned to XB complex, is observed in the C=C stretching region. The observed frequencies, their assignments and their complexation shifts are collected in Tables 7.3 to 7.6.

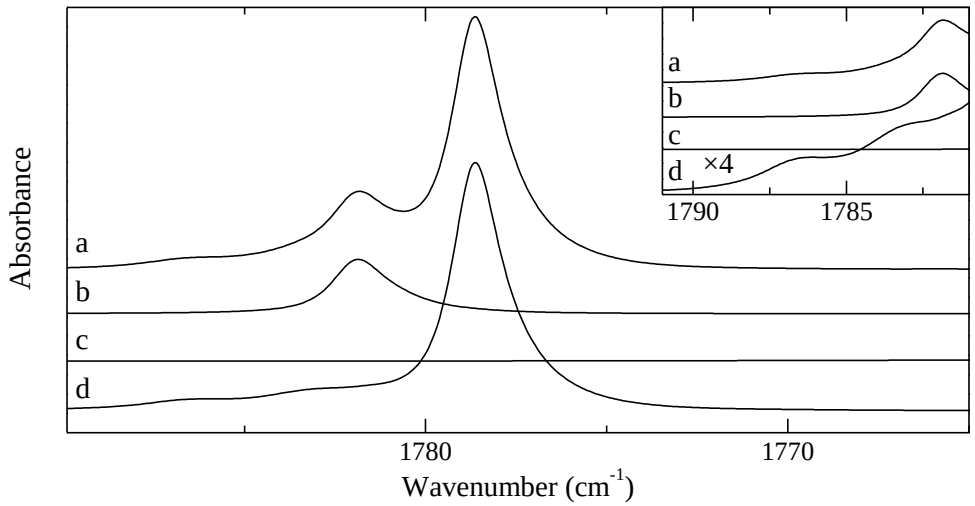

Figure 7.4: IR spectrum of the C=C stretching region of C_2F_3Br for a mixture with an elevated DME concentration (trace *a*), corresponding rescaled monomer spectra (C_2F_3Br in trace *b* and DME in trace *c*) and the resulting subtracted spectrum, solely containing bands due to complexation (trace *d*). The insert at the right top side of the image shows an enlarged image of the blueshifted bands.

Table 7.3: Experimental vibrational frequencies for the monomers and complex, as well as experimental complexation shifts ($\Delta\nu_{exp}$) and MP2/aug-cc-pVDZ calculated complexation shifts ($\Delta\nu_{calc,\ lp\cdots\pi}$), in cm^{-1}, for lp···π complex of C_2F_4 with DME dissolved in LKr at 120 K.

Assignment		$\nu_{monomer}$	$\nu_{complex}$	$\Delta\nu_{exp}$	$\Delta\nu_{calc,\ lp\cdots\pi}$
C_2F_4	$\nu_1 + \nu_9$	3196.6	3198.6	2.0	0.7
	$\nu_1 + \nu_{11}$	3045.3	3049.3	4.0	3.4
	ν_1	1870.8	1875.2	4.4	5.8
	ν_9	1330.5	1328.4	-2.1	-5.1
	ν_{11}	1179.5	[a]		-2.5
	ν_2	778.1	777.8	-0.3	-1.6
	ν_{12}	554.7	554.4	-0.3	0.2
	ν_6	549.9	-		-0.2
	ν_8	505.5	-		-4.3
	ν_3	395.5	-		-0.7
DME	ν_1	2990.4	2992.0	1.6	1.5
	ν_{16}	2990.4	2992.0	1.6	-4.7
	$2\nu_3$	2950.7	2952.8	2.1	-1.6
	ν_{12}	2916.6	2921.8	5.2	6.4
	ν_2	2811.9	2814.6	2.7	3.5
	ν_3	1474.9	1475.7	0.8	-0.8
	ν_{18}	1457.7	1458.3	0.6	-0.5
	ν_{13}	1454.9	1455.5	0.6	-0.6
	ν_{19}	1426.3	1427.2	0.9	-0.2
	ν_5	1245.1	-		0.2
	ν_{20}	1172.1	-		
	ν_{21}	1099.1	-		
	ν_6	929.4	927.6	-1.8	-3.9

[a] Band could not be observed due to overlap with DME modes.

Table 7.4: Experimental vibrational frequencies for the monomers and complexes, as well as experimental complexation shifts ($\Delta\nu_{exp}$) and MP2/aug-cc-pVDZ calculated complexation shifts ($\Delta\nu_{calc}$), in cm^{-1}, for the XB complex and lp···π complex of C_2F_3Cl with DME dissolved in LKr at 120 K. For completeness, the MP2/aug-cc-pVDZ calculated complexation shifts for C_2F_3Cl for the 1:2 complex with two DME molecules has also been included.

Assignment		$\nu_{monomer}$	$\nu_{complex,XB}$	$\Delta\nu_{calc,XB}$	$\Delta\nu_{calc,XB}$	$\nu_{complex,lp\cdots\pi}$	$\Delta\nu_{exp,lp\cdots\pi}$	$\Delta\nu_{calc,lp\cdots\pi}$	$\Delta\nu_{calc,1:2}$
C_2F_3Cl	ν_1	1795.2	1793.4	-1.8	-2.8	1799.8	4.6	2.7	0.2
	ν_2	1328.1	1323.5	-4.6	-4.3	[a]	> 0	6.7	1.7
	ν_3	1214.3	1212.8	-1.5	-6.2	1212.8	-1.5	-5.9	-9.6
	$2\nu_{10}$	1074.8	1073.4	-1.4	-0.4	[b]		7.4	5.6
	ν_4	1053.7	1053.4	-0.3	-0.6	1054.2	0.5	0.3	-0.3
	ν_5 (^{35}Cl)	691.2	691.1	-0.1	-1.8	691.1	-0.1	-1.0	-2.5
	ν_5 (^{37}Cl)	689.6	689.5	-0.1	-1.8	689.5	-0.1	-1.0	-2.5
	ν_{10}	535.0	534.5	-0.5	-0.2	538.4	3.4	3.7	2.8
	ν_6	516.3	516.5	0.2	0.7	516.5	0.2	0.3	0.9
	ν_7 (^{35}Cl)	462.4	462.0	-0.4	-1.3	462.0	-0.4	-0.7	-1.9
	ν_7 (^{37}Cl)	456.5	456.1	-0.4	-1.3	456.1	-0.4	-0.7	-1.9
DME	ν_1	2990.4	2992.2	1.8	0.5	2992.2	1.8	1.0	
	ν_{16}	2990.4	2992.2	1.8	0.5	2992.2	1.8	-1.2	
	ν_{12}	2916.6	2918.4	1.8	6.2	2918.4	1.8	2.5	
	ν_2	2811.9	2814.8	2.9	3.0	2814.8	2.9	0.3	
	ν_3	1474.9	1475.1	0.2	-1.0	1475.1	0.2	-0.3	
	ν_{18}	1457.7	1458.0	0.3	-1.0	1458.0	0.3	-0.4	
	ν_{13}	1454.9	1455.1	0.2	-0.6	1455.1	0.2	-1.5	
	ν_{19}	1426.3	1427.3	1.0	-0.2	1427.3	1.0	-0.4	
	ν_5	1245.1	-			-			
	ν_6	929.4	927.1	-2.3	-5.0	927.1	-2.3	-4.4	

[a] Exact frequency could not be determined due to subtraction artefact.

[b] Band could not be assigned due to overlap with DME.

Table 7.5: Experimental vibrational frequencies for the monomers and complex, experimental complexation shifts ($\Delta\nu_{exp}$) and MP2/aug-cc-pVDZ-PP calculated complexation shifts ($\Delta\nu_{calc,XB}$), in cm^{-1}, for the XB complex of C_2F_3Br with DME dissolved in LKr at 120 K. For completeness, the MP2/aug-cc-pVDZ-PP calculated complexation shifts of the lp···π complexes ($\Delta\nu_{calc,lp\cdots\pi}$) are also given.

Assignment		$\nu_{monomer}$	$\nu_{complex}$	$\Delta\nu_{exp}$	$\Delta\nu_{calc,XB}$	$\Delta\nu_{calc,lp\cdots\pi}$
C_2F_3Br	ν_1	1781.8	1778.7	-3.1	-4.1	3.0
	$2\nu_5$	1330.2	1329.8	-0.4	-4.2	-0.9
		1326.9	1325.6	-1.3		
	ν_2	1319.8	1313.9	-5.9	-6.7	7.0
	ν_3	1197.2	1191.0	-6.2	-8.3	-6.6
	$2\nu_{10}$	1072.6	1071.4	-1.2	0.7	7.0
	$\nu_5 + \nu_7$ (^{79}Br)	1034.4	1032.1	-2.3	-6.7	-0.4
	$\nu_5 + \nu_7$ (^{81}Br)	1033.3	1031.0	-2.3	-6.7	-0.4
	$2\nu_6$	1018.8	1019.3	0.5	1.2	0.7
	ν_4	1016.6	1016.3	-0.3	-1.2	1.2
	$\nu_5 + \nu_{11}$	998.8	999.0	0.2	5.7	4.3
	$\nu_5 + \nu_8$	980.3	979.4	-0.9	-1.0	-1.1
	ν_5	663.9	663.0	-0.9	-2.1	-0.5
	ν_{10}	535.2	535.1	-0.1	0.3	3.5
	ν_6	509.2	509.7	0.5	0.6	0.3
	ν_7	365.8	363.3	-2.5	-4.6	0.0
	ν_8	311.1	312.1	1.0	1.1	-0.6
	ν_9	162.2	166.0	3.8	5.0	0.4
DME	ν_1	2990.4	2991.8	1.4	2.4	0.6
	ν_{16}	2990.4	2991.8	1.4	2.4	-1.7
	ν_{12}	2916.6	2918.3	1.7	12.3	2.4
	ν_2	2811.9	2817.3	5.4	6.5	0.2
	ν_3	1474.9	1475.2	0.3	-1.6	-0.7
	ν_{18}	1457.7	1458.1	0.4	-1.5	-0.6
	ν_{13}	1454.9	1455.3	0.4	-0.4	-1.8
	ν_{19}	1426.3	1427.1	0.8	-0.1	-0.6
	ν_5	1245.1	1246.6	1.5	0.1	-0.6
	ν_{20}	1172.1	1168.6	-3.5	-7.5	-3.7
	ν_{21}	1099.1	1096.3	-2.8	-5.0	-3.2
	ν_6	929.4	923.7	-5.7	-9.0	-4.4

Table 7.6: Experimental vibrational frequencies for the monomers and complex, experimental complexation shifts ($\Delta\nu_{exp}$) and MP2/aug-cc-pVDZ-PP calculated complexation shifts ($\Delta\nu_{calc,XB}$), in cm^{-1}, for the XB complex of C_2F_3I with DME dissolved in LKr at 120 K. For completeness, the MP2/aug-cc-pVDZ-PP calculated complexation shifts of the lp···π complexes ($\Delta\nu_{calc,lp\cdots\pi}$) are also given.

	Assignment	$\nu_{monomer}$	$\nu_{complex}$	$\Delta\nu_{exp}$	$\Delta\nu_{calc,XB}$	$\Delta\nu_{calc,lp\cdots\pi}$
C_2F_3I	ν_1	1759.4	1754.9	-4.5	-5.3	3.1
	ν_1 (^{13}C)	1743.8	1739.3	-4.5	-5.3	3.1
	$\nu_4 + \nu_7$	1326.4	1322.0	-4.4	-5.8	2.4
	ν_2	1312.9	1306.4	-6.5	-8.9	7.4
	$2\nu_5$	1302.8	1298.0	-4.8	-4.3	-0.5
	ν_3	1175.5	1167.7	-7.8	-10.2	-5.5
	$\nu_5 + \nu_6$	1156.2	1153.2	-3.0	-1.7	0.1
	$2\nu_{10}$	1080.2	1079.2	-1.0	1.2	7.8
	$2\nu_6$	1013.2	1012.2	-1.0	0.9	0.7
	ν_4	1002.6	1002.2	-0.4	-1.4	1.9
	$\nu_5 + \nu_7$	973.4	968.8	-4.6	-6.6	0.3
	$\nu_5 + \nu_8$	938.7	936.1	-2.6	-3.4	-0.9
	$\nu_{10} + \nu_{11}$	887.4	893.4	6.0	8.9	12.8
	ν_5	651.5	650.4	-1.1	-2.1	-0.2
	ν_{10}	539.4	538.8	-0.6	0.6	3.9
	ν_6	506.7	506.1	-0.6	0.4	0.4
	ν_{11}	349.1	355.4	6.3	8.3	4.7
	ν_7	321.8	318.6	-3.2	-4.4	0.6
	ν_8	287.5	286	-1.5	-1.3	-0.7
	ν_9	145.5	149.4	3.9	5.1	0.7
DME	ν_1	2990.4	2994.0	3.6	4.7	0.0
	ν_{16}	2990.4	2994.0	3.6	4.7	-2.1
	ν_{12}	2916.6	2920.4	3.8	19.6	2.3
	ν_2	2811.9	2820.6	8.7	10.8	-0.1
	ν_{18}	1457.7	1457.5	-0.2	-1.9	-1.0
	ν_{13}	1454.9	1455.0	0.1	-0.2	-2.0
	ν_{19}	1426.3	-		0.1	-0.7
	ν_5	1245.1	1247.4	2.3	0.6	-0.6
	ν_{20}	1172.1	1166.4	-5.7	-10.8	-4.3
	ν_{21}	1099.1	1093.8	-5.3	-7.5	-3.2
	ν_6	929.4	919.0	-10.4	-14.1	-4.5

It was noted above that apart from the trends observed for the C=C stretching mode, new vibrational bands characteristic for the different types of complexes present should also be expected for the antisymmetric CF_2 stretching mode. The corresponding spectral regions obtained by studying the IR spectra of solutions in LKr, at 120 K, containing mixtures of DME with C_2F_4, C_2F_3Cl, C_2F_3Br and C_2F_3I are shown in panels 7.5A, 7.5B, 7.5C and 7.5D, respectively.

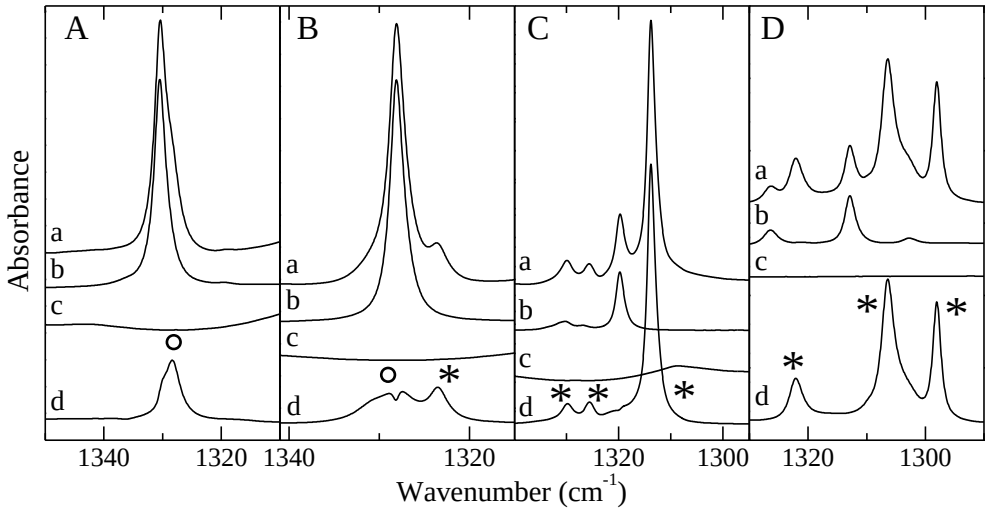

Figure 7.5: IR spectra of solutions in the ν_2 spectral region of C_2F_3X (X = Cl, Br, I) and the ν_9 spectral region of C_2F_4 of mixtures DME and C_2F_4 (panel A), C_2F_3Cl (panel B), C_2F_3Br (panel C) and C_2F_3I (panel D), dissolved in liquid krypton at 120 K. In each panel, trace *a* represents the mixed solution, while traces *b* and *c* show the solution containing only C_2F_3X or DME, respectively, and trace *d* shows the resulting subtracted spectrum. New bands due to the 1:1 C(sp^2)-X···O XB and the 1:1 lp···π complexes are marked with an asterisk (*) and an open circle (°), respectively.

For the solutions containing C_2F_3I, panel 7.5D, bands assigned to the antisymmetric CF_2 stretching mode in the monomer and in the complex are observed at 1312.9 cm^{-1} and 1306.4 cm^{-1}, respectively. For the solutions containing C_2F_3Br, panel 7.5C, the vibrational frequency is redshifted from 1319.8 cm^{-1} in the monomer to 1313.9 cm^{-1} in the complex. The redshifts of -6.5 and -5.9 cm^{-1} observed for C_2F_3I and C_2F_3Br again are in agreement with the calculated values -8.9 and -6.7 cm^{-1}. Despite the large concentration of DME, no blueshifted spectral feature due to lp···π complex could be observed for the mixture with C_2F_3Br. For the mixtures of DME with C_2F_3Cl, panel

7.5B, the subtraction process reveals the presence of a redshifted band (-4.6 cm^{-1}), assigned to the XB complex, as well as a broader, slightly blueshifted band, ascribed to the lp···π complex. However, a small depression is observed in the spectrum resulting from the subtraction process. The origin of this effect remains unclear, but is probably linked to the presence of 1:2 complex, leading to a slight overestimation of the subtraction factor for the C_2F_3Cl monomer. For the mixtures involving C_2F_4, shown in panel 7.5A, a single complex band is observed with a redshift of -2.1 cm^{-1}, which is slightly smaller but still consistent with the predicted redshift of -5.1 cm^{-1}. It should however be noted that the antisymmetric CF_2 stretching mode of C_2F_3X (X = Cl, Br or I), ν_2, corresponds to mode ν_5 of C_2F_4, which has no IR intensity. The observed band in the spectra containing C_2F_4, ν_9, corresponds to mode ν_3 of the other trifluorohaloethenes (which lie at a lower frequency due to the presence of a heavier halogen atom), for which both the XB and lp···π complex have a predicted redshift. It is therefore no surprise that the complex band due to the formation of lp···π complex in this region is redshifted for C_2F_4, whereas it is blueshifted for C_2F_3Cl.

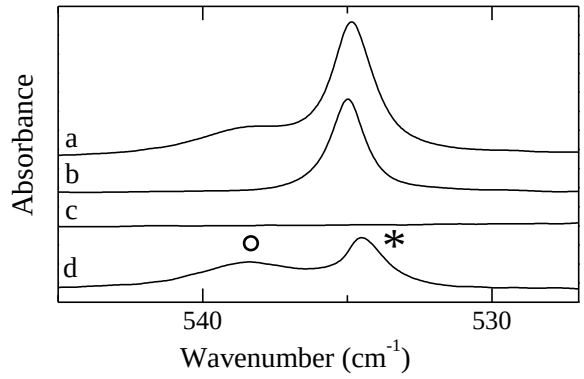

Figure 7.6: IR spectra of the ν_{10} spectral region of C_2F_3Cl. Trace *a* represents the mixed solution, traces *b* and *c* show the rescaled spectra containing only C_2F_3Cl and DME, respectively, while trace *d* shows the subtracted spectrum. Bands due to the XB and the lp···π complexes are marked with an asterisk (*) and an open circle (°), respectively.

Finally, a third region for which a distinction between both complexes with C_2F_3Cl can be made is found in the antisymmetric out-of-plane C=C bending mode, ν_{10}, shown in Figure 7.6. Subtraction yields two distinctive complex bands with shifts of 3.4 cm^{-1} and

-0.5 cm^{-1}, which are in good agreement with the calculated frequency shifts of 3.7 cm^{-1} for the lp···π complex and -0.2 cm^{-1} for the XB complex.

7.2.4 van 't Hoff plots and complexation enthalpies

The standard complexation enthalpy of the complexes observed was established from temperature studies in which spectra of the mixed solution were recorded as a function of temperature, with the temperature being typically varied between 120 and 156 K. Typical van 't Hoff plots obtained for the C(sp^2)-X···O XB complexes involving C_2F_3I and C_2F_3Br are shown in Figure 7.7.

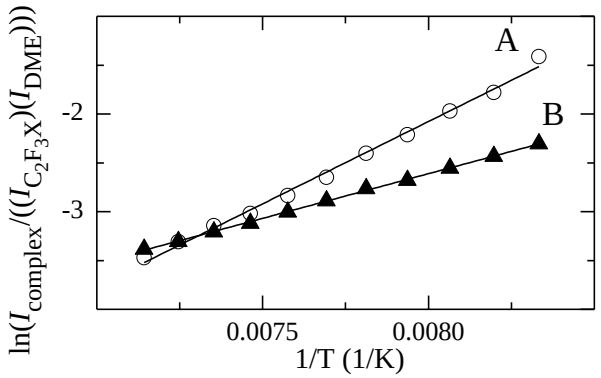

Figure 7.7: Typical van 't Hoff plots for the XB complexes of DME with C_2F_3I (A) and C_2F_3Br (B).

The average complexation enthalpies for the XB complexes, obtained by analysing and averaging out the data for a series of solutions and by correcting the slopes of the different plots for density variations in the temperature intervals used, are -14.2(5) kJ mol^{-1} for C_2F_3I·DME and -9.3(5) kJ mol^{-1} for C_2F_3Br·DME. Even though a small band was observed for the lowest temperatures in the mixture of C_2F_3Br·DME, consistent with the presence of lp···π complex, no experimental complexation enthalpy could be obtained for this type of complex. The spectra of the mixed solutions containing DME and C_2F_3Cl clearly showed the presence of two distinct complexation bands in several regions. However, since both bands were not fully separated in any of the spectral regions, integration of these bands proved to be

difficult. Hence, no experimental complexation enthalpies could be obtained for the C_2F_3Cl·DME complexes. In the case of C_2F_4, a single band was obtained after subtraction, making its integration straightforward. An experimental complexation enthalpy of -5.5(3) kJ mol^{-1} was obtained, which is in excellent agreement with the calculated value of -5.4 kJ mol^{-1} for the lp···π complex at the CCSD(T)/CBS level.

7.2.5 EDA, NOCV and NCI index analysis

Table 7.7 shows that the dispersion included DFT-based interaction energies (ΔE_{DFT}) are in agreement with the *ab initio* results in general. Moreover, the stability order and trends obtained for ΔE_{int} is the same as for *ab initio* based stabilities (ΔE (CCSD(T))) allowing us to analyse the origin of the stability difference between XB and lp···π complexes in detail using the physically meaningful components of ΔE_{int}, namely steric repulsion (ΔE_{Pauli}), electrostatic interaction (ΔV_{elst}), orbital interaction (ΔE_{oi}) and dispersion (E_{disp}).

As mentioned above, the most striking trend in the complexation energies is the increasing stability of the XB complexes when going down in the periodic table for the halogen substituent, in contrast to the constant stability of the lp···π complexes, resulting in an inversion of the relative stabilities when going from chlorine (lp···π bonding is stronger) to bromine (both types of interaction are isoenergetic) and to iodine (halogen bonding is stronger). As expected for weak interactions, ΔE_{strain} varies within 0.1 – 0.7 kJ mol^{-1} indicating a negligible contribution from geometry distortions upon complex formation. Rather, it is the interaction energy between monomers, ΔE_{int}, that determines the stability of the studied complexes. For both types of complexes it can be concluded in general that all four terms contribute notably to the stabilization, and none of the contributing factors really dominates the formation of these systems.

For the lp···π complexes, except for C_2F_4, all four terms remain relatively constant at about 17 kJ mol^{-1} for steric repulsion, -15 kJ mol^{-1} for electrostatic attraction, -8 kJ mol^{-1} for orbital interaction and -11 kJ mol^{-1} for dispersion, indeed

supporting an important electrostatic interaction contribution in line with the modelled molecular electrostatic potentials (Figure 7.1) and also demonstrating an apparent dispersion contribution. Moreover, such consistency of terms indicates that changing the halogen substituent does not significantly change the acceptor properties of the π* orbital of the C=C bond and, accordingly, the nature of lp···π interactions is very similar to each other in these systems. For C_2F_4, whose complex has a characteristically different geometry than the other lp···π complexes, steric repulsion between monomers drops by about 5 kJ mol^{-1} with respect to the other lp···π complexes, representing a driving force for the structural distortion. All attractive terms, however, also become less attractive in the C_2F_4·DME lp···π complex compared to the other lp···π complexes.

Table 7.7. Interaction energy (ΔE_{int}) and its components, (ΔE_{Pauli}, ΔV_{elst} and ΔE_{oi}) and dispersion (E_{disp}) at the PBE/TZ2P level. The gas phase complexation energy at the CCSD(T)/CBS (ΔE (CCSD(T))) level is also given for comparison. All values are in kJ mol^{-1}.

lp···π	C_2F_4·DME	C_2F_3Cl·DME	C_2F_3Br·DME	C_2F_3I·DME
ΔE_{Pauli}	13.2	17.1	17.5	18.0
ΔV_{elst}	-13.3	-14.8	-15.0	-15.4
ΔE_{oi}	-5.6	-7.4	-7.7	-8.1
E_{disp}	-7.9	-10.8	-11.3	-11.5
ΔE_{int}	-13.7	-16.0	-16.4	-17.1
ΔE_{strain}	0.1	0.1	0.1	0.1
ΔE_{DFT}	-13.6	-15.9	-16.3	-17.0
ΔE (CCSD(T))	-13.7	-15.9	-16.4	-16.7
XB	C_2F_3Cl·DME	C_2F_3Br·DME		C_2F_3I·DME
ΔE_{Pauli}	13.4	23.8		37.0
ΔV_{elst}	-13.6	-23.7		-35.5
ΔE_{oi}	-6.9	-12.2		-19.5
E_{disp}	-5.1	-5.5		-5.8
ΔE_{int}	-12.2	-17.5		-23.8
ΔE_{strain}	0.2	0.3		0.7
ΔE_{DFT}	-12.0	-17.2		-23.1
ΔE (CCSD(T))	-11.7	-16.8		-22.5

Since the halogen bond donor properties, both electrostatic and orbital π-holes, vary with the halogen substituent, the strength of the halogen bonds and accordingly the contributing terms also vary for C_2F_3X systems (X = Cl, Br, and I). When going from Cl to Br and to I, both electrostatic and orbital interactions become more attractive, while dispersion remains constant and relatively unimportant, at about -5 kJ mol^{-1}. Admittedly, steric repulsion increases in the same order, nevertheless, the strength of halogen bonding increases when going down in the periodic table for the halogen substituent X. It is important to notice that the same trends and conclusions have been reached in a previous study on C(sp^3)-X···B XB complexes (where B is the O, N, S or P atom of a Lewis base) and the proposed rationalization of such behaviour is directly transferable to the C(sp^2)-X···O XB complexes investigated in this study. Both local softness and hardness of carbon-bonded halogen atoms systematically increase in the order of F < Cl < Br < I and accordingly they tend to develop stronger hard-hard (electrostatics) and stronger soft-soft (charge transfer) interactions that are clearly manifested in the computed ΔV_{elst} and ΔE_{oi} values, respectively. Side-by-side comparison of lp···π and XB complexes pinpoints that dispersion is typically about twice as large for the former than for the latter.

The orbital interaction energy ΔE_{oi} computed in the EDA embodies the stabilization caused by charge transfer between the occupied molecular orbitals on one fragment and the unoccupied molecular orbitals of the other fragment, as well as by the mixing of occupied and virtual orbitals within the same fragment (intrafragment polarization) upon complex formation. In this process, an important quantity is the deformation density; the NOCVs [31-32], ψ_{i}, are defined as the eigenvectors that diagonalize this deformation density. In this study the term "NOCV" is simply used for the density deformation, $\Delta\rho_{\text{i}}$, which actually represents a complementary NOCV pair (more details can be found in publications of Pinter et al. [33-34] and Mitoraj et al. [31, 35]).

$$\Delta\rho_i(r) = \nu_i\left[-\psi_{-i}^2(r) + \psi_i^2(r)\right] \tag{7.1}$$

We found that only one significant NOCV (Figure S7.5) determines the electron density deformation for lp···π and for halogen bond formations, as shown in Figure

7.8a for representative interactions between C_2F_3Br and DME, with the corresponding charge transfer values and stabilization energies. For halogen bonding the density depletion (orange) – accumulation (green) pattern characterizes an accumulating electron density between the O and X contact atoms originating mostly from DME and at some extent from C_2F_3Br. As already described for other systems, there is a density accumulation not only between the contact atoms but also on the antibonding orbital of the C-X bond. For lp···π interactions the dominant NOCV describes an electron flow from the oxygen's lone pair of DME to the π* orbital of the substituted ethene together with an intrafragment π→π* charge distribution rearrangement in the latter. The density rearrangement is larger and accordingly more stabilizing upon halogen bond formation than upon lp···π bond formation and while it is increasing along the Cl < Br < I series for the former, it remains steady, about 0.09 *e*, for the latter.

Since the investigated systems exhibit noncovalent interactions it is plausible to apply the NCI framework, introduced by Yang and co-workers to describe noncovalent interactions based on the relationship of the electron density and the reduced density gradient, for the direct comparison of halogen and lp···π bonding. This concept was demonstrated to provide valuable insights into many types of weak interactions, including halogen bonding as well as hydrogen bonding, however, to the best of our knowledge, no side-by-side comparison study on halogen vs. lp···π bonding was carried out with this technique so far. The results of this analysis for all investigated molecules are given in Figure S7.6 and Figure S7.7.

For XB complexes, the plots of the reduced density gradient, *s*, versus ρ for these complexes all exhibit the characteristic feature of one spike in the low-energy, low density region, a typical footprint of noncovalent interactions (Figure 7.8b, for C_2F_3I·DME interactions). Plotting these points in real space with respect to the geometry of the complex one can easily identify an attractive noncovalent region about midway between contact atoms of the acceptor and the donor (Figure 7.8c). The *s* versus ρ plots indicate the observed strengthening of halogen bonds when going from C_2F_3Cl to C_2F_3Br and to C_2F_3I (Figure S7.7), which can be easily monitored with the shift of the characteristic peak towards larger values on the *s* versus ρ plots. The

several sharp peaks observed for lp···π complexes (Figure 7.8b, right) indicate dispersion in these systems beyond lp···π interactions. The plotted NCI index indeed shows extended surfaces between the monomers representing dispersion interactions. The bluish pigmentation (attractive) of the solid green isosurfaces indicates that the strength of the interaction along the C···O axis, which is identified as the lp···π interaction, is slightly stronger than the extended dispersion in the van der Waals regime (green, $\rho < 0.005$ a.u).

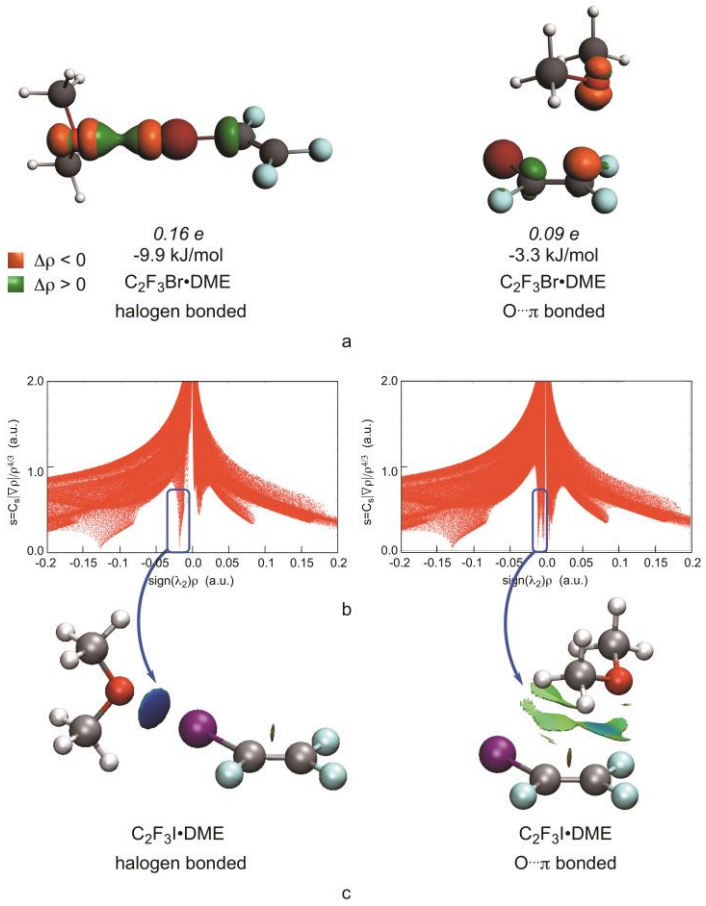

Figure 7.8: (a) Dominant NOCV with the corresponding density change and associated energy upon halogen (left) and lp···π (right) bond formations between C_2F_3Br and DME, (b) plots of the reduced density gradient versus the electron density multiplied by the sign of the second Hessian eigenvalue and (c) gradient isosurfaces (s = 0.5 a.u.) for halogen (left) and lp···π (right) bonding between C_2F_3I and DME.

7.3 Discussion

Analysis of the IR and Raman spectra of C_2F_3I with DME has shown that complexation bands, consistent with the formation of a C-I···O halogen bond, are observed in multiple areas of the spectra. No indications of the presence of lp···π complex were observed, which is consistent with the large difference in calculated complexation enthalpy in solution between both geometries.

It should, however, come as no surprise that in the mixtures of C_2F_3Br with DME a small band due to the formation of the lp···π complex is observed, since the calculated difference in strength in solution between both complexes is a mere 3.9 kJ mol^{-1} (or about 38 % of the strength of the XB complex), while in a previous study of CHF_2I with TMA, the simultaneous existence of a halogen and hydrogen bond with an experimental enthalpy difference of 4.3 kJ mol^{-1} (23 % of the XB complex) at similar conditions was proven. [21] The larger difference in relative strength for the present case, however, means that only a very small amount of the weakest (lp···π) complex is observed, which is not sufficient for further thermodynamic analysis.

For the solutions containing a combination of C_2F_3Cl and DME, two distinct complex bands can be observed for multiple vibrational modes. The shifts of these bands are in good agreement with the calculated complexation shifts for the XB complex and lp···π complex, thus proving the simultaneous coexistence of both complex geometries in solution. At the lowest temperatures a third small band between both complex bands is observed for the C=C stretching mode, while for the antisymmetric CF_2 stretching the subtraction lead to a small depression in the lp···π complex band. As an explanation for these phenomena, frequencies of the 1:2 complex with two DME molecules were calculated. When reviewing the shifts of C_2F_3Cl in this 1:2 complex, it can be seen that these are indeed very close to the frequency of the monomer band, which may complicate the subtraction process when using these areas as a reference. Based on the calculated shifts for the 1:2 complex additional measurement were made to study the areas where the 1:2 complex has a shift which is significantly different from both 1:1

complexes and the monomer band. However, no further evidence of the presence of 1:2 complex was found during these measurements.

For the mixtures involving C_2F_4 and DME a single complex band is observed for the IR forbidden C=C stretch using Raman spectroscopy. Furthermore, a single complex band is also observed for ν_9 in FTIR spectra. In both cases, as well as in the case of multiple other (combination) bands, these values are in agreement with the shifts calculated for the lp···π complex. Furthermore, the experimentally derived complexation enthalpy for these bands is compatible with the theoretically derived value, thus supporting the finding that this is indeed the lp···π complex. It is also noteworthy that for the lp···π complex involving C_2F_4 a geometry is calculated that is clearly different from the other complexes since the DME monomer is rotated as compared to the C_2F_3X moiety (angle ψ in Figure 7.2). This structural distortion can be explained by the lack of a secondary – dispersion like – interaction with the barely polarizable fluorine substituent, in contrast to heavier halogens for which the NCI index clearly indicates weak interactions between the halogen substituent and DME. When this secondary interaction is absent, the C_2F_4·DME complex gets stabilized by the release of filled-filled orbital repulsion (steric effects) between DME and C_2F_4 upon rotation, as can be seen in the EDA. This finding actually highlights that the influence of secondary interactions on the geometry and stability should not be underestimated.

When comparing the complexation enthalpies, a favourable agreement between experiment and theory can be observed for the XB complexes of C_2F_3Br·DME and C_2F_3I·DME as well as for the lp···π C_2F_4·DME complex.

Comparison of the experimental complexation enthalpies for the C_2F_3X and CF_3X halogen bonds with DME reveals similar stabilities when passing from C(sp^3)-X to C(sp^2)-X halogen bond donors, the former being on average 1.1 kJ mol^{-1} larger. These results are in line with the theoretical data obtained above, and compare favourably with the theoretical observations reported by Li et al. [9] At first sight, this might seem inconsistent with previous studies showing that halogen atoms which are covalently

bonded to an atom with higher *s* character tend to form stronger halogen bonds. Even though this is indeed the case for non-perfluorinated cases (e.g. when comparing CH_3X with C_2H_3X and HCCX), for perfluorinated cases, the presence of fluorine atoms in the direct vicinity of the bonding halogen atom, seems to counteract the effect of hybridization. This can be understood by comparing sp^3 CF_3X systems, for which three strongly electron withdrawing fluorine atoms are positioned geminal to the halogen atom forming the halogen bond, whereas only one geminal fluorine atom found in the case of C_2F_3X. It is thus not straightforward to say that halogen bonding is enhanced by an increased *s* character of the covalently bonded atom, since effects intrinsically linked to this change in hybridization may counteract this effect completely.

Analysis of the complexes with the NCI program has revealed the presence of secondary interactions for the lp···π complexes of C_2F_3Cl, C_2F_3Br and C_2F_3I with DME, which are lacking in the complex formed between C_2F_4 and DME. The lack of these secondary interactions explains the deviating geometry of the latter complex, in which DME is rotated compared to the C_2F_4 moiety and the methyl groups are also rotated farther away from C_2F_4.

NOCV analysis characterizes an accumulating electron density between the O and X contact atoms for XB complexes originating mostly from DME and partially from C_2F_3X, whereas an electron flow from the oxygen's lone pair of DME to the π* orbital of the substituted ethene together with an intrafragment π→π* charge distribution rearrangement was revealed in systems exhibiting lp···π type interactions. The charge transfer and the associated stabilization are slightly more relevant in the latter species.

7.4 Conclusions

Inspection of the electrostatic potential of C_2F_3X (X = Cl, Br, I) revealed the presence of two separate electrophilic regions. The first region is situated in the immediate vicinity of the chlorine, bromine and iodine atoms and, in agreement with the vast literature of σ-hole formation, leads to $C(sp^2)$-X···Y halogen bonding. The second electrophilic region is related to the π system of the C=C double bond and, in analogy with the interactions between hexafluorobenzene and typical Lewis bases such as water, DME and ammonia, can form complexes stabilized by so-called lp···π interactions. Furthermore, analysis of the electrostatic surface potential of C_2F_4 yielded only one region of positive electrostatic potential, perpendicular to the molecular plane, through which lp···π complexes can be formed.

Experimental studies, supported by *ab initio* calculations, in which the complexes of DME and the various C_2F_3X (X = F, Cl, Br, I) halogen bond donors formed in cryosolutions are studied using infrared and Raman spectroscopy, reveal that, in cryosolutions, mixtures of DME with C_2F_3I lead solely to XB complexes. For mixtures of C_2F_3Br with DME, apart from the complex band assigned to the formation a XB complex, a small secondary band is observed in the C=C stretching area at the lowest temperatures, which is consistent with the formation of a lp···π interaction. This band, however, was deemed too small for further analysis. In mixtures containing C_2F_3Cl and DME, two clear complex bands were observed in several spectroscopic areas, which were fully consistent with the simultaneous coexistence of both the XB and lp···π complex in solution. Using spectra recorded at different temperatures between 120 and 156 K, experimental information on the relative stability was obtained by determining the standard complexation enthalpy. For the XB complexes, the resulting values of -14.2(5) kJ mol^{-1} for C_2F_3I·DME and -9.3(5) kJ mol^{-1} for C_2F_3Br·DME, agree favourably with the predicted values of -14.6 and -10.4 kJ mol^{-1} for the complexation enthalpies in solution, derived from the CCSD(T)/CBS complexation energies. These experimental values are also similar to those reported for the complexes of DME with CF_3I and CF_3Br, with values of -15.5(1) and -10.2(1) kJ mol^{-1} respectively. Therefore,

the results reported in this study lead to the first experimental confirmation that, at least for fluorinated halogen bond donors, the hybridization of the carbon atom involved hardly has an influence on the intrinsic properties of the halogen bond studied, since the number of strong electron withdrawing fluorine atoms geminal to the involved halogen atom is reduced across the sp^3-sp^2-sp series.

Furthermore, the study also enabled a determination of the complexation enthalpy of -5.5(3) kJ mol^{-1} for the C_2F_4·DME lp···π complex in LAr, which is also in excellent agreement with the calculated value of -5.4 kJ mol^{-1} derived from the CCSD(T)/CBS calculations.

The experimental studies for the complexes of DME with C_2F_3X (X = Cl, Br, I) not only allowed to experimentally characterize and rationalize the effects of hybridization on halogen bonding but, for the first time ever, also allowed the competition of C-X···Y halogen bonding and lp···π interactions to be studied experimentally. Additional information on the complexes of the C_2F_3X (X = F, Cl, Br, and I) halogen bond donors with another Lewis base, TMA, allowing further characterization and rationalization of the competition between C-X···Y halogen bonding and lp···π interactions, is the following chapter.

7.5 References

1 P. Metrangolo, F. Meyer, T. Pilati, G. Resnati, G. Terraneo, *Angew. Chem., Int. Ed.*, 2008, ***47***, 6114-6127.

2 P. Metrangolo, G. Resnati, *Cryst. Growth Des.*, 2012, ***12***, 5835-5838.

3 N. F. Valadares, L. B. Salum, I. Polikarpov, A. D. Andricopulo, R. C. Garratt, *J. Chem. Inf. Model.*, 2009, ***49***, 2606-2616.

4 Y. X. Lu, H. Y. Li, X. Zhu, H. L. Liu, W. L. Zhu, *J. Mol. Model.*, 2012, ***18***, 3311-3320.

5 Y. X. Lu, Y. T. Liu, Z. J. Xu, H. Y. Li, H. L. Liu, W. L. Zhu, *Expert Opin. Drug Discovery*, 2012, ***7***, 375-383.

6 R. Wilcken, M. O. Zimmermann, A. Lange, A. C. Joerger, F. M. Boeckler, *J. Med. Chem.*, 2012, ***56***, 1363-1388.

7 L. P. Wolters, P. Schyman, M. J. Pavan, W. L. Jorgensen, F. M. Bickelhaupt, S. Kozuch, *WIREs Comput. Mol. Sci.*, 2014.

8 J. W. Zou, Y. J. Jiang, M. Guo, G. X. Hu, B. Zhang, H. C. Liu, Q. S. Yu, *Chem. - Eur. J.*, 2005, ***11***, 740-751.

9 Q.-Z. Li, R. Li, S.-N. Jiang, W.-Z. Li, J.-B. Cheng, *J. Fluorine Chem.*, 2012, ***135***, 207-212.

10 K. Gao, N. S. Goroff, *J. Am. Chem. Soc.*, 2000, ***122***, 9320-9321.

11 P. Politzer, J. S. Murray, M. C. Concha, *J. Mol. Model.*, 2007, ***13***, 643-650.

12 A. Sun, J. W. Lauher, N. S. Goroff, *Science*, 2006, ***312***, 1030-1034.

13 H. M. Yamamoto, R. Maeda, J.-I. Yamaura, R. Kato, *J. Mater. Chem.*, 2001, ***11***, 1034-1041.

14 D. Hauchecorne, A. Moiana, B. J. van der Veken, W. A. Herrebout, *Phys. Chem. Chem. Phys.*, 2011, ***13***, 10204-10213.

15 D. Hauchecorne, N. Nagels, B. J. van der Veken, W. A. Herrebout, *Phys. Chem. Chem. Phys.*, 2012, ***14***, 681-690.

16 D. Hauchecorne, B. J. van der Veken, A. Moiana, W. A. Herrebout, *Chem. Phys.*, 2010, ***374***, 30-36.

17 D. Hauchecorne, R. Szostak, W. A. Herrebout, B. J. van der Veken, *ChemPhysChem* 2009, ***10***, 2105-2115.

18 J. C. Amicangelo, B. W. Gung, D. G. Irwin, N. C. Romano, *Phys. Chem. Chem. Phys.*, 2008, ***10***, 2695-2705.

19 B. W. Gung, Y. Zou, Z. G. Xu, J. C. Amicangelo, D. G. Irwin, S. Q. Ma, H. C. Zhou, *J. Org. Chem.*, 2008, ***73***, 689-693.

20 J. C. Amicangelo, D. G. Irwin, C. J. Lee, N. C. Romano, N. L. Saxton, *J. Phys. Chem. A*, 2013, ***117***, 1336-1350.

21 N. Nagels, Y. Geboes, B. Pinter, F. De Proft, W. A. Herrebout, *Chem. - Eur. J.*, 2014, ***20***, 8433-8443.

22 J. S. Murray, P. Lane, T. Clark, K. E. Riley, P. Politzer, *J. Mol. Model.*, 2012, ***18***, 541-548.

23 S. N. Delanoye, W. A. Herrebout, B. J. van der Veken, *J. Am. Chem. Soc.*, 2002, ***124***, 7490-7498.

24 P. Van Ginderen, W. A. Herrebout, B. J. van der Veken, *J. Phys. Chem. A*, 2003, ***107***, 5391-5396.
25 W. A. Herrebout, S. N. Delanoye, B. U. W. Maes, B. J. van der Veken, *J. Phys. Chem. A*, 2006, ***110***, 13759-13768.
26 B. Michielsen, W. A. Herrebout, B. J. van der Veken, *ChemPhysChem*, 2007, ***8***, 1188-1198.
27 S. Grimme, J. Antony, S. Ehrlich, H. Krieg, *J. Chem. Phys.*, 2010, ***132***, 154104.
28 G. Herzberg, *Infrared and Raman Spectra of Polyatomic Molecules*, 12th ed., D. Van Nostrand Company Inc., Princeton, NJ, USA, **1945**.
29 N. Tasinato, A. Pietropolli Charmet, P. Stoppa, S. Giorgianni, A. Gambi, *Chem. Phys.*, 2012, ***397***, 55-64.
30 D. E. Mann, N. Acquista, E. K. Plyler, *J. Chem. Phys.*, 1954, ***22***, 1199-1202.
31 M. P. Mitoraj, A. Michalak, T. Ziegler, *J. Chem. Theory Comput.*, 2009, ***5***, 962-975.
32 M. P. Mitoraj, M. Parafiniuk, M. Srebro, M. Handzlik, A. Buczek, A. Michalak, *J. Mol. Model.*, 2011, ***17***, 2337-2352.
33 B. Pinter, V. Van Speybroeck, M. Waroquier, P. Geerlings, F. De Proft, *Phys. Chem. Chem. Phys.*, 2013, ***15***, 17354-17365.
34 B. Pinter, L. Broeckaert, J. Turek, A. Ruzicka, F. De Proft, *Chem. - Eur. J.*, 2014, ***20***, 734-744.
35 M. P. Mitoraj, A. Michalak, *J. Mol. Model.*, 2007, ***13***, 347-355.

7.6 Supporting information

Table S7.1.1: Cartesian coordinates of the optimized geometry of C_2F_4.

D_{2h}	X	Y	Z
C_2F_4			
C	0.316718	0.587967	0.000000
C	-0.316718	-0.587967	0.000000
F	-1.642148	-0.702698	0.000000
F	0.316718	-1.757875	0.000000
F	1.642148	0.702698	0.000000
F	-0.316718	1.757875	0.000000

Table S7.1.2: Cartesian coordinates of the optimized geometry of C_2F_3Cl.

C_s	X	Y	Z
C_2F_3Cl			
C	0.000000	0.474053	0.000000
C	-0.672455	-0.686202	0.000000
F	-0.091077	-1.880175	0.000000
F	-1.999532	-0.759966	0.000000
F	-0.676665	1.639573	0.000000
Cl	1.702365	0.604588	0.000000

Table S7.1.3: Cartesian coordinates of the optimized geometry of C_2F_3Br.

C_s	X	Y	Z
C_2F_3Br			
C	0.000000	0.578257	0.000000
C	1.338899	0.495676	0.000000
F	2.014503	-0.647878	0.000000
F	2.137386	1.558739	0.000000
F	-0.586120	1.795157	0.000000
Br	-1.146438	-0.879936	0.000000

Table S7.1.4: Cartesian coordinates of the optimized geometry of C_2F_3I.

C_s	X	Y	Z
C_2F_3I			
C	0.000000	0.895394	0.000000
C	1.289409	1.271052	0.000000
F	2.312902	0.423368	0.000000
F	1.687498	2.539797	0.000000
F	-0.954377	1.858636	0.000000
I	-0.663220	-1.064054	0.000000

Table S7.1.5: Cartesian coordinates of the optimized geometry of DME.

C_{2v}	X	Y	Z
DME			
O	0.000000	0.000000	0.607066
C	0.000000	1.169581	-0.202099
H	0.000000	2.032636	0.474896
H	0.898418	1.208635	-0.845282
H	-0.898418	1.208635	-0.845282
C	0.000000	-1.169581	-0.202099
H	0.898418	-1.208635	-0.845282
H	0.000000	-2.032636	0.474896
H	-0.898418	-1.208635	-0.845282

Table S7.2.1: Cartesian coordinates of the optimized geometry of the lp···π complex between C_2F_4 and DME.

C_1	X	Y	Z
C_2F_4			
C	-1.669831	0.198613	-0.139988
C	-0.792763	-0.614776	0.451480
F	-0.198062	-0.325432	1.607023
F	-0.441672	-1.796750	-0.043876
F	-2.269801	-0.083432	-1.294313
F	-2.016141	1.385451	0.359679
DME			
O	1.789538	0.255209	-0.634730
C	2.059147	1.523469	-0.045787
H	1.236928	2.193774	-0.327205
H	2.108473	1.446452	1.055643
H	3.012832	1.939000	-0.418689
C	2.810571	-0.680704	-0.302822
H	2.546688	-1.630968	-0.782894
H	3.794652	-0.341495	-0.674135
H	2.872470	-0.826577	0.791195

Table S7.2.2: Cartesian coordinates of the optimized geometry of the XB complex between C_2F_3Cl and DME.

C_s	X	Y	Z
C_2F_3Cl			
C	2.491739	-0.322103	-0.001221
C	1.411263	0.472387	0.001857
F	2.437022	-1.649733	-0.008035
F	3.739845	0.139084	0.002256
F	1.575855	1.813093	0.008844
Cl	-0.204870	-0.078191	-0.002410
DME			
O	-3.127079	-0.602907	-0.005628
C	-3.557384	0.070348	1.173824
H	-4.659801	0.135715	1.211870
H	-3.196823	-0.513432	2.029747
H	-3.137017	1.091676	1.222739
C	-3.559140	0.096542	-1.169088
H	-3.199877	-0.467954	-2.038387
H	-4.661610	0.162732	-1.204006
H	-3.138821	1.118712	-1.195793

Table S7.2.3: Cartesian coordinates of the optimized geometry of the lp···π complex between C_2F_3Cl and DME.

C_1	X	Y	Z
C_2F_3Cl			
C	0.551734	0.946597	-0.525177
C	1.229599	0.130701	0.294877
F	0.254867	0.647204	-1.782654
F	0.132686	2.151896	-0.163582
F	1.493835	0.517183	1.561553
Cl	1.780339	-1.431014	-0.129989
DME			
O	-2.173639	0.083260	0.005786
C	-2.369566	-1.143350	-0.691533
H	-3.319050	-1.622409	-0.390986
H	-2.402723	-0.905433	-1.761813
H	-1.538407	-1.846437	-0.497338
C	-2.118783	-0.141148	1.410859
H	-1.948144	0.831781	1.888630
H	-3.066864	-0.571588	1.781062
H	-1.291862	-0.828105	1.671961

Table S7.2.4: Cartesian coordinates of the optimized geometry of the XB complex between C_2F_3Br and DME.

C_s	X	Y	Z
C_2F_3Br			
C	-2.606268	-0.352964	-0.001087
C	-1.568464	0.497060	0.002031
F	-2.485455	-1.677090	-0.006837
F	-3.879106	0.038044	0.001252
F	-1.819481	1.828427	0.007883
Br	0.221299	-0.001260	-0.001033
DME			
O	3.078324	-0.536063	-0.003944
C	3.639537	0.060481	-1.171734
H	4.731919	-0.099006	-1.207821
H	3.170732	-0.421885	-2.038217
H	3.433823	1.145982	-1.198623
C	3.638039	0.038805	1.175378
H	3.168138	-0.459478	2.032206
H	4.730377	-0.121331	1.209906
H	3.432275	1.123627	1.222048

Table S7.2.5: Cartesian coordinates of the optimized geometry of the lp···π complex between C_2F_3Br and DME.

C_1	X	Y	Z
C_2F_3Br			
C	-0.172350	1.228806	-0.557712
C	0.709047	0.710742	0.310407
F	-0.339376	0.784987	-1.796580
F	-0.952720	2.262428	-0.270592
F	0.806818	1.239192	1.552445
Br	1.814072	-0.738275	-0.044677
DME			
O	-2.503939	-0.405173	0.022303
C	-2.363232	-1.649958	-0.655751
H	-3.136992	-2.368407	-0.329248
H	-2.479583	-1.449385	-1.727899
H	-1.366175	-2.090937	-0.470935
C	-2.362238	-0.580272	1.428357
H	-2.460058	0.410179	1.890443
H	-3.146109	-1.250472	1.825431
H	-1.371935	-1.005334	1.678231

Table S7.2.6: Cartesian coordinates of the optimized geometry of the XB complex between C_2F_3Br and DME.

C_s	X	Y	Z
C_2F_3I			
C	-1.776952	0.504396	0.000376
C	-2.790076	-0.377139	-0.000245
F	-2.629226	-1.698355	-0.001260
F	-4.077048	-0.033001	0.000083
F	-2.089350	1.829180	0.001400
I	0.242359	0.020967	-0.000096
DME			
O	3.135951	-0.492824	-0.000562
C	3.761166	0.021931	1.176244
H	3.237408	-0.412591	2.036434
H	4.826371	-0.266401	1.208436
H	3.683105	1.123210	1.213925
C	3.761408	0.025585	-1.175635
H	4.826619	-0.262648	-1.208502
H	3.237826	-0.406262	-2.037277
H	3.683356	1.126975	-1.209909

Table S7.2.7: Cartesian coordinates of the optimized geometry of the lp···π complex between C_2F_3Br and DME.

C_1	X	Y	Z
C_2F_3I			
C	-0.732988	1.284653	-0.578798
C	0.217370	0.954162	0.310590
F	-0.805022	0.785076	-1.806263
F	-1.688146	2.171829	-0.332742
F	0.191241	1.536549	1.537742
I	1.721403	-0.427551	-0.020874
DME			
O	-2.765314	-0.690822	0.030351
C	-2.476482	-1.921893	-0.625265
H	-3.156566	-2.722585	-0.281790
H	-2.619254	-1.757168	-1.700379
H	-1.432826	-2.235228	-0.437400
C	-2.595547	-0.819192	1.438421
H	-2.813399	0.160392	1.882407
H	-3.287992	-1.573658	1.853958
H	-1.558614	-1.112434	1.688421

Table S7.3: MP2/aug-cc-pVDZ vibrational frequencies, in cm^{-1}, infrared intensities, in km mol^{-1}, and Raman intensities, in $Å^4$ amu^{-1}, for the lp···π complex of C_2F_4 and DME and both monomers, as well as the complexation shift Δν.

	Monomer			lp···π complex			
	Frequency	IR int.	Raman int.	Frequency	Δν	IR int.	Raman int.
C_2F_4							
ν_1 (A_g)	1920.1	0.0	10.3	1925.9	5.8	0.3	10.1
ν_2 (A_g)	773.9	0.0	11.2	772.3	-1.6	0.1	10.0
ν_3 (A_g)	389.0	0.0	2.0	388.3	-0.7	0.0	1.7
ν_4 (A_u)	201.7	0.0	0.0	207.7	6.0	0.1	0.0
ν_5 (B_{1g})	1332.0	0.0	0.3	1329.8	-2.2	55.7	0.2
ν_6 (B_{1g})	550.0	0.0	2.1	549.8	-0.2	0.0	1.7
ν_7 (B_{1u})	416.4	3.8	0.0	425.9	9.5	8.2	0.2
ν_8 (B_{2g})	525.4	0.0	9.1	521.0	-4.3	2.0	12.5
ν_9 (B_{2u})	1328.2	409.7	0.0	1323.1	-5.1	311.7	0.1
ν_{10} (B_{2u})	209.0	4.6	0.0	209.4	0.4	3.9	0.0
ν_{11} (B_{3u})	1171.1	351.6	0.0	1168.7	-2.5	301.2	0.0
ν_{12} (B_{3u})	541.6	3.4	0.0	541.8	0.2	3.9	0.2
DME							
ν_1 (A_1)	3188.7	20.1	87.6	3190.2	1.5	17.9	60.1
ν_2 (A_1)	3024.8	58.6	320.3	3028.2	3.5	55.9	305.5
ν_3 (A_1)	1505.9	2.9	5.6	1505.1	-0.8	3.8	6.1
ν_4 (A_1)	1473.5	0.0	2.2	1473.5	0.0	0.1	4.2
ν_5 (A_1)	1261.1	6.6	0.5	1261.3	0.2	7.0	0.5
ν_6 (A_1)	942.4	34.7	9.8	938.5	-3.9	41.4	8.7
ν_7 (A_1)	416.8	2.3	1.0	416.0	-0.8	1.3	0.7
ν_8 (A_2)	3096.2	0.0	14.7	3102.7	6.5	1.8	15.3
ν_9 (A_2)	1474.8	0.0	11.4	1474.3	-0.6	0.1	8.2
ν_{10} (A_2)	1157.2	0.0	1.5	1156.7	-0.6	0.0	1.6
ν_{11} (A_2)	195.2	0.0	0.2	193.7	-1.5	0.0	0.2
ν_{12} (B_1)	3089.5	107.8	94.2	3096.0	6.4	95.8	94.9
ν_{13} (B_1)	1489.2	13.0	0.0	1488.6	-0.6	13.9	0.3
ν_{14} (B_1)	1187.2	7.2	0.0	1187.3	0.1	30.4	0.3
ν_{15} (B_1)	260.2	5.1	0.0	262.3	2.0	6.6	0.0
ν_{16} (B_2)	3187.3	24.6	59.2	3182.6	-4.7	20.5	49.4
ν_{17} (B_2)	3018.4	55.2	0.6	3022.3	3.9	49.5	4.3
ν_{18} (B_2)	1490.1	10.3	1.0	1489.5	-0.5	10.7	0.7
ν_{19} (B_2)	1441.5	2.5	1.3	1441.3	-0.2	2.1	1.5
ν_{20} (B_2)	1191.9	98.1	0.7	1188.3	-3.6	87.2	0.4
ν_{21} (B_2)	1113.8	35.0	1.6	1111.9	-1.9	31.6	1.8

Van der Waals vibrations: 11.1 cm^{-1}, 0.7 km mol^{-1}, 0.3 $Å^4$ amu^{-1}, 29.2 cm^{-1}, 0.5 km mol^{-1}, 0.2 $Å^4$ amu^{-1}, 47.0 cm^{-1}, 1.3 km mol^{-1}, 0.3 $Å^4$ amu^{-1}, 54.2 cm^{-1}, 0.6 km mol^{-1}, 0.3 $Å^4$ amu^{-1}, 65.2 cm^{-1}, 0.7 km mol^{-1}, 0.5 $Å^4$ amu^{-1}, 87.1 cm^{-1}, 3.9 km mol^{-1}, 0.2 $Å^4$ amu^{-1}.

Table S7.4: MP2/aug-cc-pVDZ vibrational frequencies, in cm^{-1}, infrared intensities, in km mol^{-1}, and Raman intensities, in $Å^4$ amu^{-1}, for the XB complex of C_2F_3Cl and DME and both monomers, as well as the complexation shift Δν.

	Monomer			XB complex			
	Frequency	IR int.	Raman int.	Frequency	Δν	IR int.	Raman int.
C_2F_3Cl							
ν_1 (A')	1843.6	50.2	13.4	1840.9	-2.8	59.9	13.8
ν_2 (A')	1323.6	174.3	0.4	1319.3	-4.3	170.1	0.4
ν_3 (A')	1203.3	184.4	0.6	1197.1	-6.2	176.2	0.5
ν_4 (A')	1062.6	234.1	1.9	1062.0	-0.6	247.7	1.4
ν_5 (A')	687.7	2.1	9.2	686.0	-1.8	1.0	10.9
ν_6 (A')	511.3	1.0	1.1	512.0	0.7	0.8	1.3
ν_7 (A')	462.5	1.3	2.3	461.2	-1.3	3.9	4.7
ν_8 (A')	336.8	1.3	1.9	338.8	2.0	1.2	2.2
ν_9 (A')	184.9	2.6	0.4	189.9	5.1	3.4	0.7
ν_{10} (A")	544.5	2.2	5.8	544.3	-0.2	1.7	6.3
ν_{11} (A")	368.9	1.0	0.1	374.9	6.0	1.3	0.1
ν_{12} (A")	172.0	0.1	0.01	176.7	4.6	0.05	0.01
DME							
ν_1 (A_1)	3188.7	20.1	87.6	3189.1	0.5	18.3	73.5
ν_2 (A_1)	3024.8	58.6	320.3	3027.7	3.0	53.5	327.8
ν_3 (A_1)	1505.9	2.9	5.6	1504.9	-1.0	6.1	6.1
ν_4 (A_1)	1473.5	0.0008	2.2	1473.2	-0.3	0.2	2.3
ν_5 (A_1)	1261.1	6.6	0.5	1260.9	-0.2	6.5	0.4
ν_6 (A_1)	942.4	34.7	9.8	937.4	-5.0	42.3	9.5
ν_7 (A_1)	416.8	2.3	1.0	416.4	-0.4	2.2	0.9
ν_8 (A_2)	3096.2	0.0	14.7	3102.1	5.9	0.3	14.1
ν_9 (A_2)	1474.8	0.0	11.4	1473.7	-1.1	0.2	10.7
ν_{10} (A_2)	1157.2	0.0	1.5	1156.7	-0.5	0.003	1.7
ν_{11} (A_2)	195.2	0.0	0.2	193.4	-1.8	0.0003	0.1
ν_{12} (B_1)	3089.5	107.8	94.2	3095.7	6.2	109.8	105.0
ν_{13} (B_1)	1489.2	13.0	0.04	1488.6	-0.6	16.2	0.1
ν_{14} (B_1)	1187.2	7.2	0.04	1187.7	0.6	5.4	0.2
ν_{15} (B_1)	260.2	5.1	0.002	263.2	3.0	9.4	0.05
ν_{16} (B_2)	3187.3	24.6	59.2	3187.8	0.5	18.9	47.1
ν_{17} (B_2)	3018.4	55.2	0.6	3021.9	3.6	47.2	2.0
ν_{18} (B_2)	1490.1	10.3	1.0	1489.0	-1.0	8.4	0.8
ν_{19} (B_2)	1441.5	2.5	1.3	1441.3	-0.2	1.2	1.5
ν_{20} (B_2)	1191.9	98.1	0.7	1187.0	-4.9	85.7	0.5
ν_{21} (B_2)	1113.8	35.0	1.6	1110.7	-3.1	37.3	1.7

Van der Waals vibrations: 2.0 cm^{-1}, 0.8 km mol^{-1}, 0.9 $Å^4$ amu^{-1}, 24.1 cm^{-1}, 1.5 km mol^{-1}, 0.03 $Å^4$ amu^{-1}, 27.6 cm^{-1}, 0.001 km mol^{-1}, 1.1 $Å^4$ amu^{-1}, 555 cm^{-1}, 0.7 km mol^{-1}, 0.08 $Å^4$ amu^{-1}, 66.9 cm^{-1}, 0.2 km mol^{-1}, 0.02 $Å^4$ amu^{-1}, 93.3 cm^{-1}, 9.2 km mol^{-1}, 0.3 $Å^4$ amu^{-1}.

Table S7.5: MP2/aug-cc-pVDZ vibrational frequencies, in cm^{-1}, infrared intensities, in km mol^{-1}, and Raman intensities, in $Å^4$ amu^{-1}, for the lp···π complex of C_2F_3Cl and DME and both monomers, as well as the complexation shift Δν.

	Monomer			lp···π complex			
	Frequency	IR int.	Raman int.	Frequency	Δν	IR int.	Raman int.
C_2F_3Cl							
ν_1 (A')	1843.6	50.2	13.4	1846.3	2.7	48.5	11.2
ν_2 (A')	1323.6	174.3	0.4	1330.3	6.7	151.4	0.4
ν_3 (A')	1203.3	184.4	0.6	1197.4	-5.9	213.4	0.4
ν_4 (A')	1062.6	234.1	1.9	1062.9	0.3	200.2	1.5
ν_5 (A')	687.7	2.1	9.2	686.8	-1.0	2.2	8.1
ν_6 (A')	511.3	1.0	1.1	511.6	0.3	0.8	1.0
ν_7 (A')	462.5	1.3	2.3	461.8	-0.7	1.2	2.2
ν_8 (A')	336.8	1.3	1.9	336.1	-0.7	1.2	1.6
ν_9 (A')	184.9	2.6	0.4	185.2	0.3	2.1	0.4
ν_{10} (A")	544.5	2.2	5.8	548.2	3.7	9.3	7.4
ν_{11} (A")	368.9	1.0	0.1	373.1	4.2	2.8	0.1
ν_{12} (A")	172.0	0.1	0.01	180.6	8.6	0.03	0.01
DME							
ν_1 (A_1)	3188.7	20.1	87.6	3189.7	1.0	16.0	63.2
ν_2 (A_1)	3024.8	58.6	320.3	3025.1	0.3	46.7	290.2
ν_3 (A_1)	1505.9	2.9	5.6	1505.5	-0.3	6.4	5.3
ν_4 (A_1)	1473.5	0.0008	2.2	1472.2	-1.3	0.1	4.0
ν_5 (A_1)	1261.1	6.6	0.5	1260.4	-0.7	5.6	0.4
ν_6 (A_1)	942.4	34.7	9.8	938.0	-4.4	26.6	8.2
ν_7 (A_1)	416.8	2.3	1.0	416.6	-0.2	1.7	0.8
ν_8 (A_2)	3096.2	0.0	14.7	3098.6	2.4	4.1	14.1
ν_9 (A_2)	1474.8	0.0	11.4	1473.6	-1.2	0.1	7.9
ν_{10} (A_2)	1157.2	0.0	1.5	1156.5	-0.7	0.02	1.8
ν_{11} (A_2)	195.2	0.0	0.2	200.1	4.9	0.03	0.1
ν_{12} (B_1)	3089.5	107.8	94.2	3092.0	2.5	108.7	84.0
ν_{13} (B_1)	1489.2	13.0	0.04	1487.7	-1.5	14.5	0.4
ν_{14} (B_1)	1187.2	7.2	0.04	1187.9	0.7	15.2	0.3
ν_{15} (B_1)	260.2	5.1	0.002	263.5	3.3	7.6	0.008
ν_{16} (B_2)	3187.3	24.6	59.2	3186.1	-1.2	16.3	49.7
ν_{17} (B_2)	3018.4	55.2	0.6	3018.6	0.3	43.3	11.2
ν_{18} (B_2)	1490.1	10.3	1.0	1489.7	-0.4	8.9	0.8
ν_{19} (B_2)	1441.5	2.5	1.3	1441.1	-0.4	1.9	1.1
ν_{20} (B_2)	1191.9	98.1	0.7	1186.0	-5.9	21.5	0.4
ν_{21} (B_2)	1113.8	35.0	1.6	1110.5	-3.3	27.7	1.5

Van der Waals vibrations: 10.1 cm^{-1}, 0.6 km mol^{-1}, 0.7 $Å^4$ amu^{-1}, 41.5 cm^{-1}, 0.1 km mol^{-1}, 0.9 $Å^4$ amu^{-1}, 49.8 cm^{-1}, 0.06 km mol^{-1}, 0.2 $Å^4$ amu^{-1}, 58.9cm^{-1}, 1.6 km mol^{-1}, 0.4 $Å^4$ amu^{-1}, 73.2 cm^{-1}, 0.06 km mol^{-1}, 0.4 $Å^4$ amu^{-1}, 95.0 cm^{-1}, 7.1 km mol^{-1}, 0.07 $Å^4$ amu^{-1}.

Table S7.6: MP2/aug-cc-pVDZ-PP vibrational frequencies, in cm^{-1}, infrared intensities, in km mol^{-1}, and Raman intensities, in $Å^4$ amu^{-1}, for the XB complex of C_2F_3Br and DME and both monomers, as well as the complexation shift Δν.

	Monomer			XB complex			
	Frequency	IR int.	Raman int.	Frequency	Δν	IR int.	Raman int.
C_2F_3Br							
ν_1 (A')	1827.9	81.1	14.6	1823.7	-4.1	99.2	13.2
ν_2 (A')	1318.6	166.4	0.7	1312.0	-6.7	163.2	0.7
ν_3 (A')	1186.2	174.2	0.4	1177.8	-8.3	166.5	0.5
ν_4 (A')	1029.4	207.2	2.7	1028.2	-1.2	212.2	1.8
ν_5 (A')	659.6	3.5	7.4	657.5	-2.1	1.9	9.1
ν_6 (A')	504.0	1.5	1.0	504.6	0.6	1.4	1.0
ν_7 (A')	371.8	0.5	3.1	367.2	-4.6	0.7	0.2
ν_8 (A')	313.4	2.5	1.3	314.5	1.1	3.2	1.4
ν_9 (A')	161.2	1.6	0.6	166.2	5.0	2.4	0.9
ν_{10} (A")	554.1	2.9	4.9	554.4	0.3	2.3	5.4
ν_{11} (A")	359.9	0.5	0.1	367.7	7.8	3.0	7.0
ν_{12} (A")	159.3	0.1	0.01	164.3	5.0	0.1	0.01
DME							
ν_1 (A_1)	3188.7	20.1	87.6	3191.1	2.4	18.5	65.7
ν_2 (A_1)	3024.8	58.6	320.3	3031.3	6.5	57.3	318.8
ν_3 (A_1)	1505.9	2.9	5.6	1504.3	-1.6	5.8	6.0
ν_4 (A_1)	1473.5	0.0008	2.2	1473.2	-0.3	0.6	3.3
ν_5 (A_1)	1261.1	6.6	0.5	1261.1	0.1	6.9	0.5
ν_6 (A_1)	942.4	34.7	9.8	933.4	-9.0	55.9	10.9
ν_7 (A_1)	416.8	2.3	1.0	416.4	-0.4	3.2	0.8
ν_8 (A_2)	3096.2	0.0	14.7	3108.0	11.8	0.4	14.1
ν_9 (A_2)	1474.8	0.0	11.4	1473.6	-1.2	0.3	9.9
ν_{10} (A_2)	1157.2	0.0	1.5	1156.2	-1.0	0.004	1.6
ν_{11} (A_2)	195.2	0.0	0.2	190.4	-4.9	0.001	0.1
ν_{12} (B_1)	3089.5	107.8	94.2	3101.8	12.3	96.9	119.2
ν_{13} (B_1)	1489.2	13.0	0.04	1488.8	-0.4	16.9	0.1
ν_{14} (B_1)	1187.2	7.2	0.04	1187.9	0.8	5.7	0.1
ν_{15} (B_1)	260.2	5.1	0.002	264.6	4.3	10.3	0.1
ν_{16} (B_2)	3187.3	24.6	59.2	3189.7	2.4	15.7	43.2
ν_{17} (B_2)	3018.4	55.2	0.6	3026.0	7.7	44.2	2.8
ν_{18} (B_2)	1490.1	10.3	1.0	1488.6	-1.5	9.1	0.7
ν_{19} (B_2)	1441.5	2.5	1.3	1441.4	-0.1	0.7	1.5
ν_{20} (B_2)	1191.9	98.1	0.7	1184.4	-7.5	80.4	0.5
ν_{21} (B_2)	1113.8	35.0	1.6	1108.8	-5.0	40.2	2.0

Van der Waals vibrations: 1.9 cm^{-1}, 0.7 km mol^{-1}, 0.8 $Å^4$ amu^{-1}, 23.0 cm^{-1}, 1.8 km mol^{-1}, 0.02 $Å^4$ amu^{-1}, 28.9 cm^{-1}, 0.003 km mol^{-1}, 0.8 $Å^4$ amu^{-1}, 55.8 cm^{-1}, 0.7 km mol^{-1}, 0.06 $Å^4$ amu^{-1}, 75.0 cm^{-1}, 0.2 km mol^{-1}, 0.01 $Å^4$ amu^{-1}, 100.9 cm^{-1}, 10.1 km mol^{-1}, 0.8 $Å^4$ amu^{-1}.

Table S7.7: MP2/aug-cc-pVDZ-PP vibrational frequencies, in cm^{-1}, infrared intensities, in km mol^{-1}, and Raman intensities, in $Å^4$ amu^{-1}, for the lp···π complex of C_2F_3Br and DME and both monomers, as well as the complexation shift Δν.

	Monomer			lp···π complex			
	Frequency	IR int.	Raman int.	Frequency	Δν	IR int.	Raman int.
C_2F_3Br							
ν_1 (A')	1827.9	81.1	14.6	1830.8	3.0	77.6	12.5
ν_2 (A')	1318.6	166.4	0.7	1325.6	7.0	144.6	0.7
ν_3 (A')	1186.2	174.2	0.4	1179.5	-6.6	82.8	0.3
ν_4 (A')	1029.4	207.2	2.7	1030.6	1.2	178.7	2.0
ν_5 (A')	659.6	3.5	7.4	659.2	-0.5	3.5	6.5
ν_6 (A')	504.0	1.5	1.0	504.3	0.3	1.3	0.8
ν_7 (A')	371.8	0.5	3.1	371.8	0.0	0.6	2.8
ν_8 (A')	313.4	2.5	1.3	312.8	-0.6	2.3	1.0
ν_9 (A')	161.2	1.6	0.6	161.6	0.4	1.3	0.5
ν_{10} (A")	554.1	2.9	4.9	557.6	3.5	10.5	6.8
ν_{11} (A")	359.9	0.5	0.1	364.6	4.7	1.8	0.2
ν_{12} (A")	159.3	0.1	0.01	170.3	10.9	0.1	0.0
DME							
ν_1 (A_1)	3188.7	20.1	87.6	3189.3	0.6	15.9	63.1
ν_2 (A_1)	3024.8	58.6	320.3	3025.0	0.2	46.0	298.3
ν_3 (A_1)	1505.9	2.9	5.6	1505.2	-0.7	6.4	5.4
ν_4 (A_1)	1473.5	0.0008	2.2	1472.1	-1.4	0.1	4.3
ν_5 (A_1)	1261.1	6.6	0.5	1260.4	-0.6	5.5	0.4
ν_6 (A_1)	942.4	34.7	9.8	938.0	-4.4	25.3	8.1
ν_7 (A_1)	416.8	2.3	1.0	416.5	-0.3	1.7	0.8
ν_8 (A_2)	3096.2	0.0	14.7	3098.5	2.3	4.1	13.8
ν_9 (A_2)	1474.8	0.0	11.4	1473.5	-1.3	0.1	7.5
ν_{10} (A_2)	1157.2	0.0	1.5	1156.4	-0.9	0.02	1.9
ν_{11} (A_2)	195.2	0.0	0.2	200.2	4.9	0.04	0.1
ν_{12} (B_1)	3089.5	107.8	94.2	3091.9	2.4	111.7	83.0
ν_{13} (B_1)	1489.2	13.0	0.04	1487.5	-1.8	14.1	0.4
ν_{14} (B_1)	1187.2	7.2	0.04	1187.0	-0.2	54.5	0.3
ν_{15} (B_1)	260.2	5.1	0.002	263.4	3.2	7.8	0.01
ν_{16} (B_2)	3187.3	24.6	59.2	3185.5	-1.7	15.9	48.3
ν_{17} (B_2)	3018.4	55.2	0.6	3018.5	0.1	43.0	11.6
ν_{18} (B_2)	1490.1	10.3	1.0	1489.5	-0.6	8.5	0.8
ν_{19} (B_2)	1441.5	2.5	1.3	1440.9	-0.6	1.7	1.1
ν_{20} (B_2)	1191.9	98.1	0.7	1188.2	-3.7	103.3	0.5
ν_{21} (B_2)	1113.8	35.0	1.6	1110.6	-3.2	26.7	1.5

Van der Waals vibrations: 14.7 cm^{-1}, 0.6 km mol^{-1}, 0.6 $Å^4$ amu^{-1}, 36.9 cm^{-1}, 0.09 km mol^{-1}, 0.6 $Å^4$ amu^{-1}, 49.2 cm^{-1}, 0.06 km mol^{-1}, 0.17 $Å^4$ amu^{-1}, 57.9 cm^{-1}, 1.8 km mol^{-1}, 0.4 $Å^4$ amu^{-1}, 74.1 cm^{-1}, 0.01 km mol^{-1}, 0.5 $Å^4$ amu^{-1}, 94.8 cm^{-1}, 7.2 km mol^{-1}, 0.08 $Å^4$ amu^{-1}.

Table S7.8: MP2/aug-cc-pVDZ-PP vibrational frequencies, in cm^{-1}, infrared intensities, in km mol^{-1}, and Raman intensities, in $Å^4$ amu^{-1}, for the XB complex of C_2F_3I and DME and both monomers, as well as the complexation shift Δν.

	Monomer			XB complex			
	Frequency	IR int.	Raman int.	Frequency	Δν	IR int.	Raman int.
C_2F_3I							
ν_1 (A')	1805.0	129.7	16.7	1799.7	-5.3	159.9	13.4
ν_2 (A')	1312.3	157.3	1.4	1303.3	-8.9	155.4	1.5
ν_3 (A')	1166.5	159.9	0.5	1156.4	-10.2	152.8	0.8
ν_4 (A')	1004.0	186.5	2.6	1002.6	-1.4	182.1	1.6
ν_5 (A')	645.4	3.6	7.1	643.2	-2.1	1.7	9.1
ν_6 (A')	500.0	1.7	0.9	500.4	0.4	1.6	0.9
ν_7 (A')	324.1	0.9	3.8	319.7	-4.4	2.5	8.0
ν_8 (A')	289.8	3.7	1.3	288.5	-1.3	8.2	2.4
ν_9 (A')	144.8	1.4	0.8	149.9	5.1	1.9	1.3
ν_{10} (A")	553.8	3.5	3.9	554.4	0.6	2.9	4.4
ν_{11} (A")	346.7	0.2	0.1	355.0	8.3	0.3	0.3
ν_{12} (A")	147.4	0.1	0.02	153.9	6.6	0.1	0.0
DME							
ν_1 (A_1)	3188.7	20.1	87.6	3193.3	4.7	18.0	56.5
ν_2 (A_1)	3024.8	58.6	320.3	3035.5	10.8	60.4	312.5
ν_3 (A_1)	1505.9	2.9	5.6	1503.8	-2.1	5.9	5.8
ν_4 (A_1)	1473.5	0.0008	2.2	1473.2	-0.3	1.3	5.3
ν_5 (A_1)	1261.1	6.6	0.5	1261.6	0.6	7.2	0.7
ν_6 (A_1)	942.4	34.7	9.8	928.3	-14.1	72.7	13.6
ν_7 (A_1)	416.8	2.3	1.0	416.9	0.1	4.9	0.8
ν_8 (A_2)	3096.2	0.0	14.7	3115.2	19.0	0.4	14.1
ν_9 (A_2)	1474.8	0.0	11.4	1473.4	-1.4	0.5	9.1
ν_{10} (A_2)	1157.2	0.0	1.5	1155.7	-1.5	0.0	1.5
ν_{11} (A_2)	195.2	0.0	0.2	188.3	-7.0	0.0	0.2
ν_{12} (B_1)	3089.5	107.8	94.2	3109.1	19.6	84.8	134.2
ν_{13} (B_1)	1489.2	13.0	0.0	1489.0	-0.2	17.6	0.2
ν_{14} (B_1)	1187.2	7.2	0.0	1188.2	1.0	4.9	0.2
ν_{15} (B_1)	260.2	5.1	0.0	265.8	5.6	10.7	0.1
ν_{16} (B_2)	3187.3	24.6	59.2	3192.0	4.7	12.1	38.1
ν_{17} (B_2)	3018.4	55.2	0.6	3031.0	12.6	40.3	4.0
ν_{18} (B_2)	1490.1	10.3	1.0	1488.1	-1.9	9.6	0.6
ν_{19} (B_2)	1441.5	2.5	1.3	1441.6	0.1	0.3	1.5
ν_{20} (B_2)	1191.9	98.1	0.7	1181.1	-10.8	73.3	0.4
ν_{21} (B_2)	1113.8	35.0	1.6	1106.3	-7.5	43.3	2.5

Van der Waals vibrations: 2.7 cm^{-1}, 0.6 km mol^{-1}, 0.7 $Å^4$ amu^{-1}, 25.0 cm^{-1}, 1.5 km mol^{-1}, 0.02 $Å^4$ amu^{-1}, 32.1 cm^{-1}, 0.005 km mol^{-1}, 0.7 $Å^4$ amu^{-1}, 61.2 cm^{-1}, 0.5 km mol^{-1}, 0.1 $Å^4$ amu^{-1}, 87.1 cm^{-1}, 0.1 km mol^{-1}, 0.05 $Å^4$ amu^{-1}, 107.1 cm^{-1}, 13.6 km mol^{-1}, 1.2 $Å^4$ amu^{-1}.

Table S7.9: MP2/aug-cc-pVDZ-PP vibrational frequencies, in cm^{-1}, infrared intensities, in km mol^{-1}, and Raman intensities, in $Å^4$ amu^{-1}, for the lp···π complex of C_2F_3I and DME and both monomers, as well as the complexation shift Δν.

	Monomer			lp···π complex			
	Frequency	IR int.	Raman int.	Frequency	Δν	IR int.	Raman int.
C_2F_3I							
ν_1 (A')	1805.0	129.7	16.7	1808.1	3.1	123.1	15.3
ν_2 (A')	1312.3	157.3	1.4	1319.7	7.4	136.5	1.3
ν_3 (A')	1166.5	159.9	0.5	1161.1	-5.5	126.8	0.6
ν_4 (A')	1004.0	186.5	2.6	1005.9	1.9	163.2	1.7
ν_5 (A')	645.4	3.6	7.1	645.1	-0.2	3.5	6.3
ν_6 (A')	500.0	1.7	0.9	500.4	0.4	1.4	0.8
ν_7 (A')	324.1	0.9	3.8	324.7	0.6	0.7	3.4
ν_8 (A')	289.8	3.7	1.3	289.1	-0.7	3.5	1.1
ν_9 (A')	144.8	1.4	0.8	145.5	0.7	1.0	0.7
ν_{10} (A")	553.8	3.5	3.9	557.7	3.9	11.7	6.2
ν_{11} (A")	346.7	0.2	0.1	351.5	4.7	1.1	0.2
ν_{12} (A")	147.4	0.1	0.02	160.6	13.2	0.1	0.04
DME							
ν_1 (A_1)	3188.7	20.1	87.6	3188.6	0.0	15.7	62.8
ν_2 (A_1)	3024.8	58.6	320.3	3024.7	-0.1	44.8	313.8
ν_3 (A_1)	1505.9	2.9	5.6	1504.7	-1.2	6.4	5.6
ν_4 (A_1)	1473.5	0.0008	2.2	1473.4	-0.2	0.2	7.1
ν_5 (A_1)	1261.1	6.6	0.5	1260.5	-0.6	5.3	0.4
ν_6 (A_1)	942.4	34.7	9.8	937.9	-4.5	24.0	8.1
ν_7 (A_1)	416.8	2.3	1.0	416.3	-0.5	1.7	0.8
ν_8 (A_2)	3096.2	0.0	14.7	3098.2	2.0	3.4	12.9
ν_9 (A_2)	1474.8	0.0	11.4	1471.9	-2.9	0.1	4.6
ν_{10} (A_2)	1157.2	0.0	1.5	1156.2	-1.1	0.1	2.0
ν_{11} (A_2)	195.2	0.0	0.2	199.2	3.9	0.04	0.1
ν_{12} (B_1)	3089.5	107.8	94.2	3091.8	2.3	117.4	83.1
ν_{13} (B_1)	1489.2	13.0	0.04	1487.2	-2.0	13.8	0.5
ν_{14} (B_1)	1187.2	7.2	0.04	1186.6	-0.5	44.9	0.4
ν_{15} (B_1)	260.2	5.1	0.002	263.1	2.8	8.0	0.02
ν_{16} (B_2)	3187.3	24.6	59.2	3185.2	-2.1	15.3	45.8
ν_{17} (B_2)	3018.4	55.2	0.6	3018.3	-0.1	42.1	10.7
ν_{18} (B_2)	1490.1	10.3	1.0	1489.1	-1.0	8.0	0.8
ν_{19} (B_2)	1441.5	2.5	1.3	1440.7	-0.7	1.5	1.0
ν_{20} (B_2)	1191.9	98.1	0.7	1187.6	-4.3	55.6	0.4
ν_{21} (B_2)	1113.8	35.0	1.6	1110.6	-3.2	25.0	1.4

Van der Waals vibrations: 18.0 cm^{-1}, 0.6 km mol^{-1}, 0.6 $Å^4$ amu^{-1}, 35.6 cm^{-1}, 0.09 km mol^{-1}, 0.6 $Å^4$ amu^{-1}, 47.8 cm^{-1}, 0.1 km mol^{-1}, 0.1 $Å^4$ amu^{-1}, 56.4 cm^{-1}, 2.1 km mol^{-1}, 0.4 $Å^4$ amu^{-1}, 75.1 cm^{-1}, 0.007 km mol^{-1}, 0.7 $Å^4$ amu^{-1}, 93.2 cm^{-1}, 7.2 km mol^{-1}, 0.1 $Å^4$ amu^{-1}.

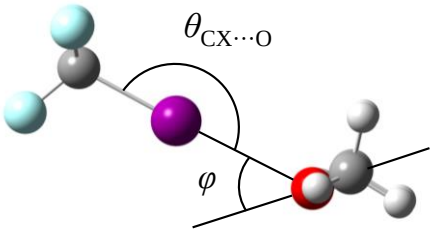

Figure S7.1: MP2/aug-cc-pVDZ(-PP) equilibrium geometries for the XB complexes of CF_3X (X = Cl, Br and I) with DME.

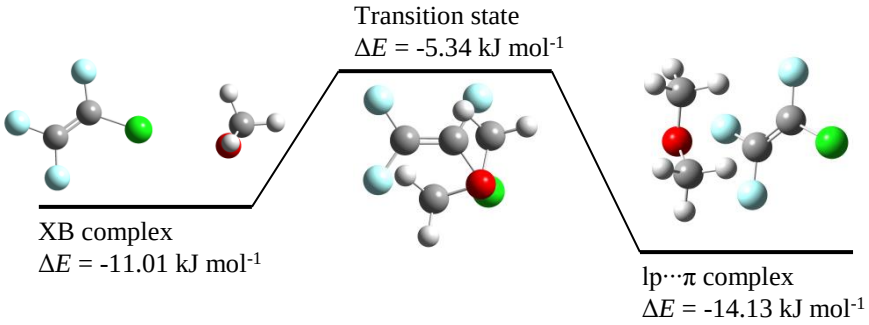

Figure S7.2: Energy diagram for the C_2F_3Cl·DME complexes and corresponding transition state.

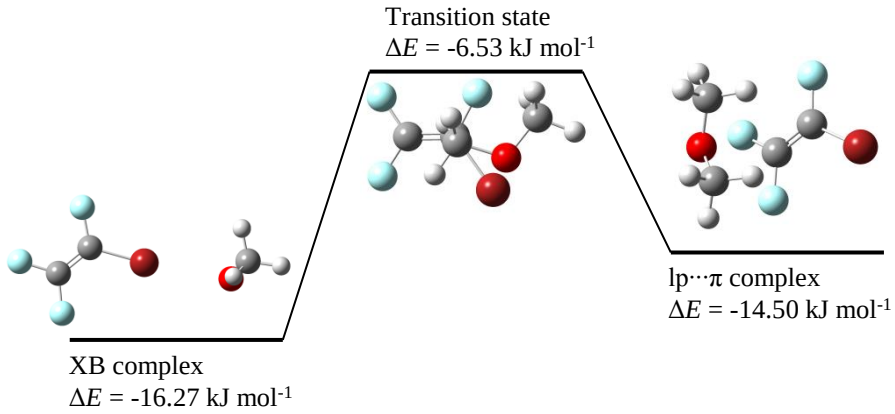

Figure S7.3: Energy diagram for the C_2F_3Br·DME complexes and corresponding transition state.

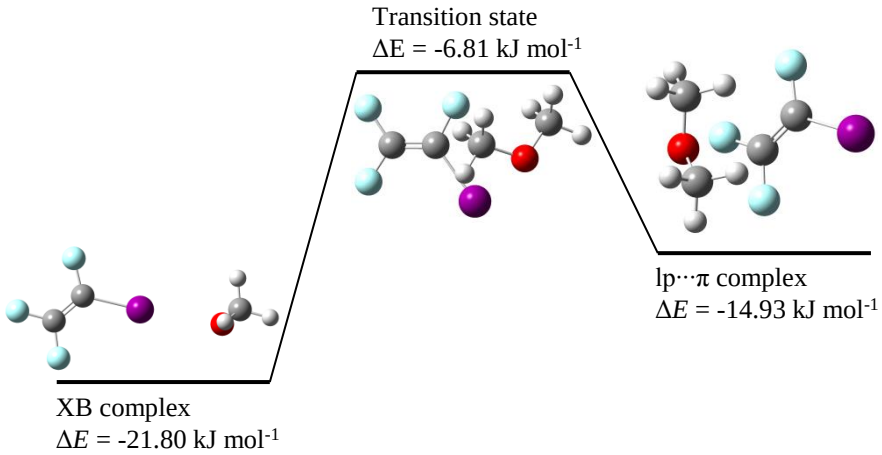

Figure S7.4: Energy diagram for the C_2F_3I·DME complexes and corresponding transition state.

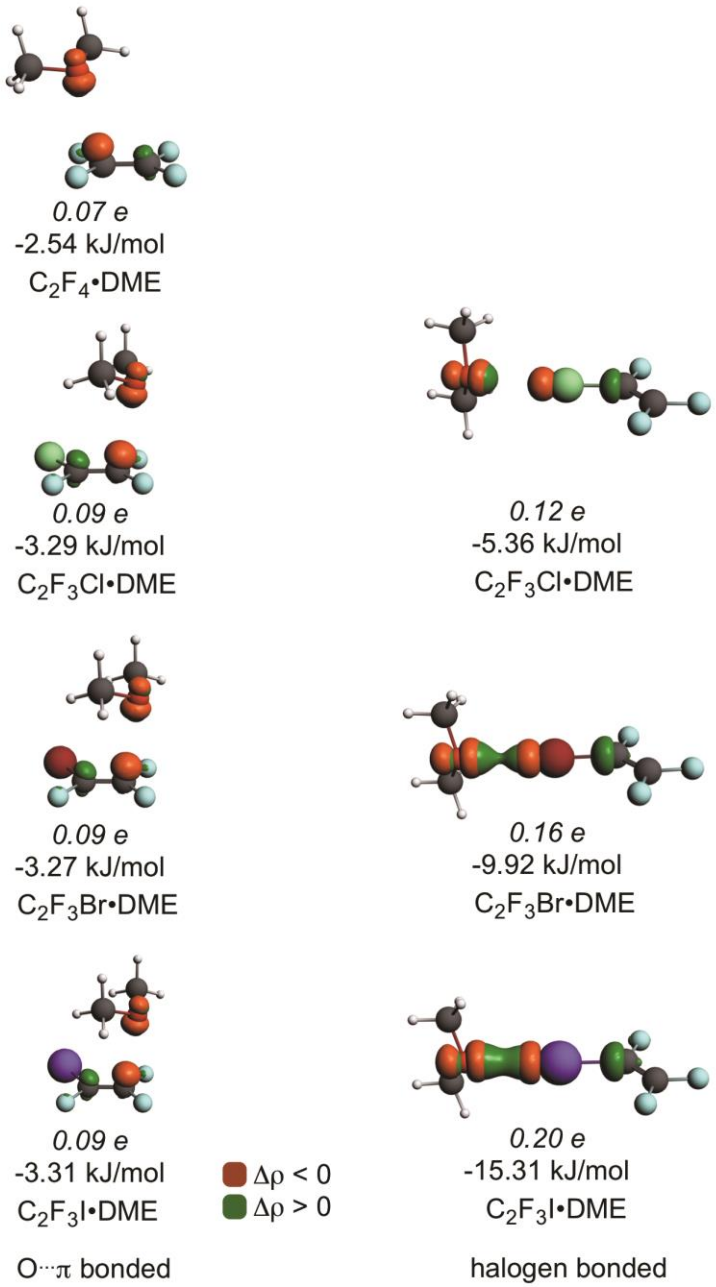

Figure S7.5: Dominant NOCV with the corresponding density change and associated energy upon halogen (right) and lp···π (left) bond formations.

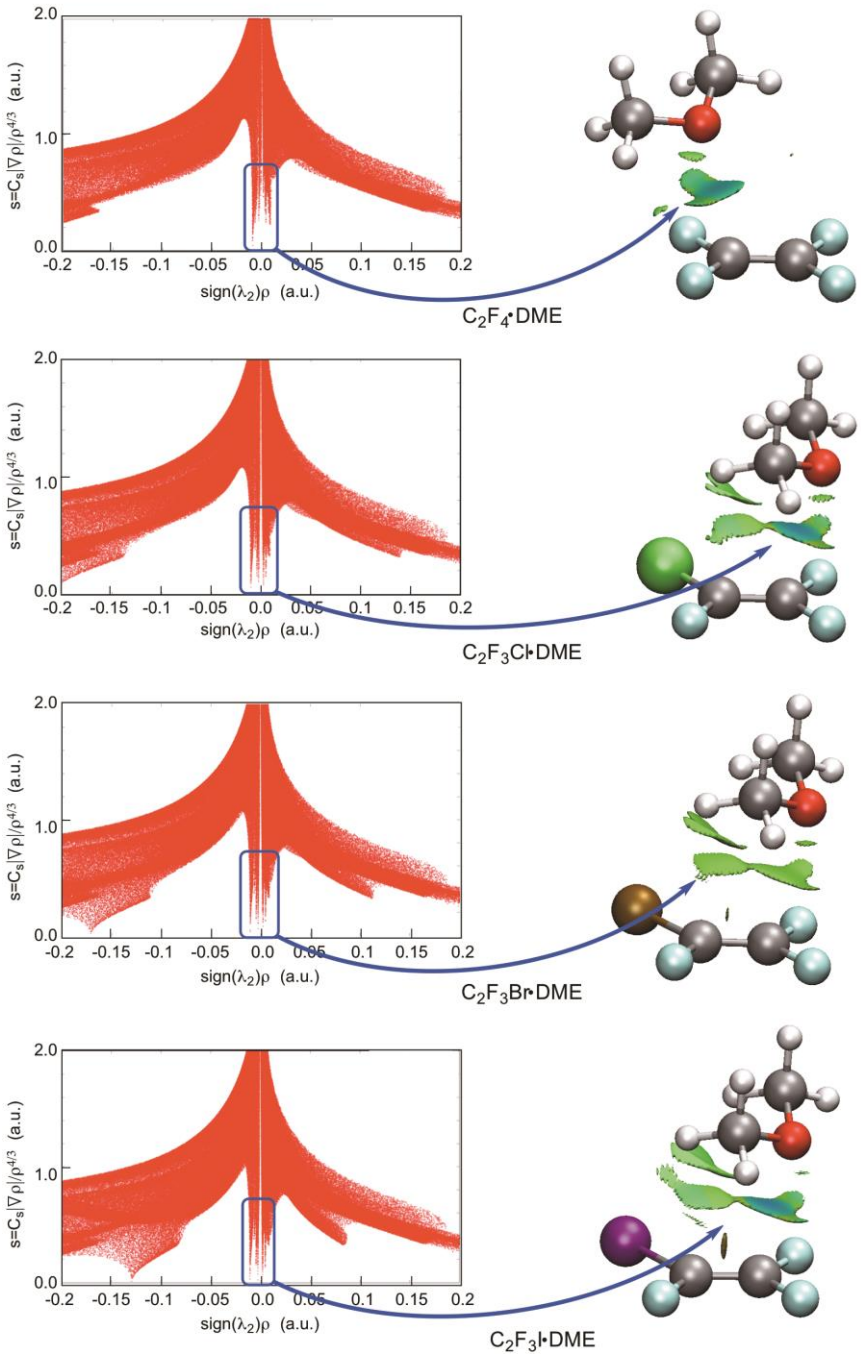

Figure S7.6: Plots of the reduced density gradient versus the electron density multiplied by the sign of the second Hessian eigenvalue (left) and gradient isosurfaces (s = 0.5 a.u., right) for lp···π-bonded species.

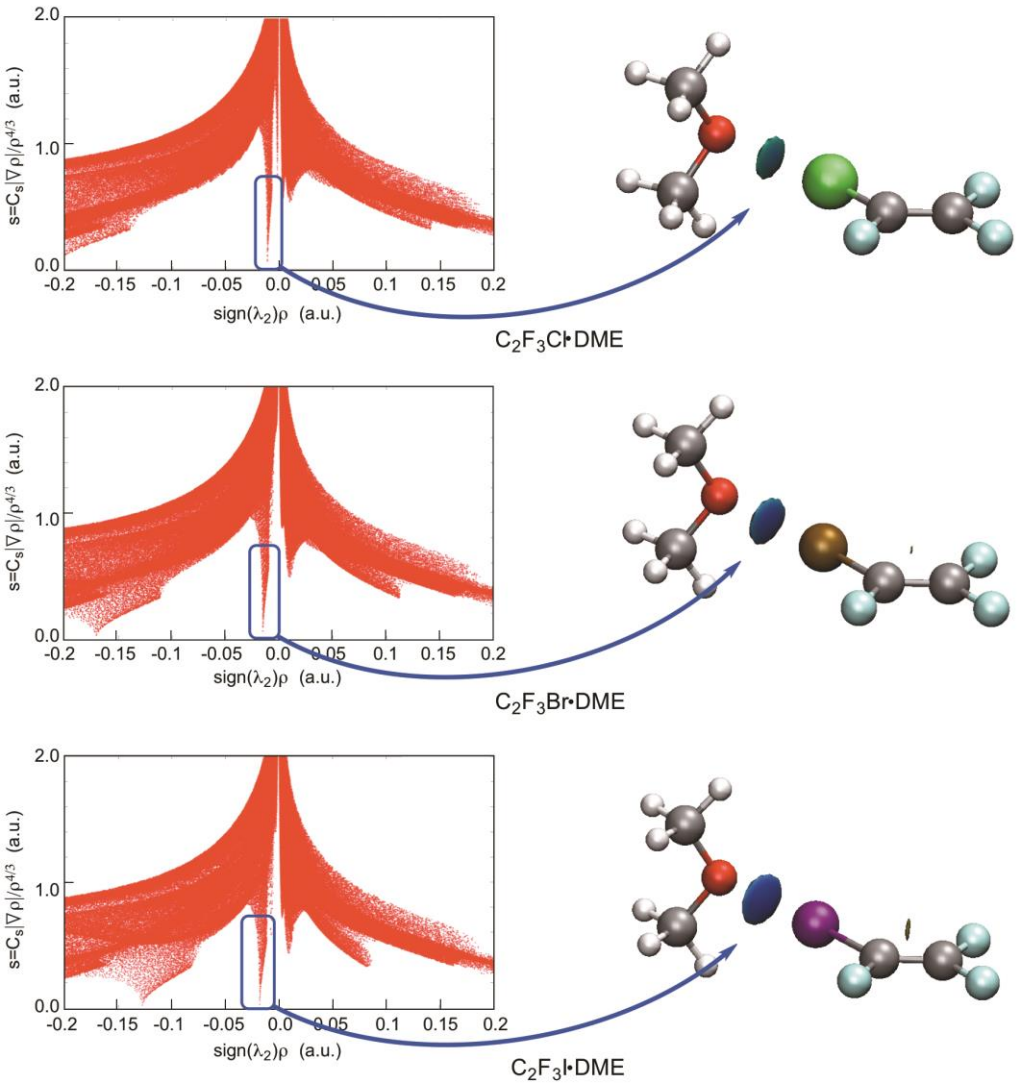

Figure S7.7: Plots of the reduced density gradient versus the electron density multiplied by the sign of the second Hessian eigenvalue (left) and gradient isosurfaces (s = 0.5 a.u., right) for XB species.

Chapter 8

Halogen bonding and lone pair···π interactions: competitive noncovalent interaction with a nitrogen lone pair.

Complexes of C_2F_3X (X = F, Cl, Br, I) with TMA.

This chapter has been published as:

Geboes, Y.; De Proft, F.; Herrebout, W. A., Expanding Lone Pair···π Interactions to Nonaromatic Systems and Nitrogen Bases: Complexes of C_2F_3X (X = F, Cl, Br, I) and TMA(-d_9), *The Journal of Physical Chemistry A* **2015**, *119*, 5597-5606.

Abstract

The molecular electrostatic potential surface of unsaturated, locally electron deficient molecules shows a positive region perpendicular to (a part of) the molecular framework. In recent years it has been shown both theoretically and experimentally that molecules are able to form noncovalent interactions with Lewis bases through this π-hole. When studying unsaturated perfluorohalogenated molecules containing a higher halogen atom, a second electropositive region is also observed near the halogen atom. This region, often denoted as a σ-hole, allows the molecules to interact with Lewis bases and form a halogen bond.

To experimentally characterize the competition between both these noncovalent interactions, FTIR and Raman spectra of LNg solutions containing perfluorohalogenated ethylene derivatives (C_2F_3X; X = F, Cl, Br or I) and TMA($-d_9$) were investigated. Analysis of the spectra shows that in mixed solutions of TMA($-d_9$) and C_2F_4 or C_2F_3Cl lp$\cdots\pi$ complex is present, while evidence for XB complex is found in solutions containing TMA($-d_9$) and C_2F_3Cl, C_2F_3Br or C_2F_3I. For all complexes observed, complexation enthalpies were determined, the values varying between -4.9(1) and -24.4(2) kJ mol^{-1}.

8.1 Introduction

Halogen bonds have gained a large increase in interest during the past decade in the fields of supramolecular chemistry and crystal engineering [1] as well as biochemistry, molecular recognition and rational drug design. [2-3] Thanks to this increased interest, halogen bonds have now been studied extensively both theoretically and experimentally.

The existence of halogen bonding has been characterized theoretically by the presence of a positive region in the electrostatic potential surface near the halogen atom, opposite to the covalent bond, the so-called σ-hole. [4] Since the strength of halogen bonds strongly depends on both the involved halogen atom and the properties of the molecule to which it is covalently bonded, it is possible to tune the strength of the noncovalent interaction by altering the halogen atom or the properties of the covalently bonded molecule. [5-6] In many applications relatively strong interactions are preferred, which has, especially in the field of supramolecular chemistry, led to the use of molecules containing strong electron withdrawing moieties, such as highly halogenated, or more specifically highly fluorinated, molecules as halogen bond donors. Thanks to the work of Resnati and Metrangolo, perfluorohalocarbons (PFHC's) are nowadays considered "iconic" halogen bond donors. [7-8]

However, when the locally strongly electron deficient molecules are also unsaturated, they can exhibit a region of positive electrostatic potential perpendicular to the molecular plane. In analogy with the term σ-hole, such a positive region, perpendicular to a portion of the molecular framework, is called a π-hole. [9] To illustrate this π-hole, as well as the σ-hole, the electrostatic potential surfaces of C_2F_4, C_2F_3Cl, C_2F_3Br and C_2F_3I are shown in Figure 7.1.

In recent years, attractive noncovalent interactions between these regions of positive electrostatic potential and electron rich sites in Lewis bases, often called lone pair···π interactions (lp···π), have also been observed in theoretical [10-12] and experimental studies. [13-18] These studies have demonstrated that lp···π interactions occur most

commonly through oxygen, [19-20] largely because of the overwhelming biological importance of water. [13-14] Theoretical and experimental information on lp···π interactions involving other electron donors, such as nitrogen, still remains scarce. [21-24]

Furthermore, in nearly all of these studies the π-system in the bond donor molecule is based on an aromatic ring structure. [25] The effect of electron withdrawing groups leading to electron deficiency in the π-system, is however not restricted to aromatic compounds. In the previous chapter, we have demonstrated the lp···π bonding possibility of a non-aromatic system of the C_2F_3X (X = F, Cl, Br, I) type with the oxygen lone pair of DME. [26] The choice for DME was based on the biochemical significance of the oxygen···π interaction with the water molecule, as well as the limitations of the used experimental equipment and techniques, which don't allow for the straightforward analysis of complexes involving strong self-associating molecules such as water.

The aim of this study is to build further on the findings of Gou et al.,[27] in which the existence of the lp···π complex of $C_2F_3Cl{\cdot}NH_3$ was demonstrated using pulsed-jet FTMW spectroscopy, and expand the field of lp···π interactions at thermodynamic equilibrium to systems with a non-aromatic bond donor and the lone pair of a nitrogen atom. This is achieved by experimentally studying mixtures of a trifluorohaloethylene-moiety C_2F_3X (X = F, Cl , Br or I), which has an electron deficient π-system, with the Lewis base TMA in noble gas solutions using FTIR and Raman spectroscopy. In order to avoid spectral congestion and aid assignment of the complex bands, measurements are performed using regular TMA and fully deuterated TMA-d_9. When referring to (measurements or results of) both undeuterated and fully deuterated TMA the notation TMA(-d_9) is used in the remainder of this chapter. The final aim of this study is to investigate whether lp···π interactions involving the lp of a nitrogen atom can be observed in an environment at thermodynamic equilibrium and if they are able to coexist and/or compete with competitive halogen bonds under these conditions.

8.2 Results

8.2.1 *Ab initio* calculations

Geometries of both types of complexes with their respective angles are shown in Figure 8.1. Intermolecular bonding distances and angles as well as calculated energetics for all calculated C_2F_3X·TMA complex geometries have been summarized in Table 8.1. Cartesian coordinates of all monomers and complex geometries are given in Tables S8.1 and S8.2 of the SI. To enable comparison with XB complexes formed through C(sp^3) bonded halogen atoms, theoretical results using an identical computational method and experimental results [28] for the equivalent CF_3X·TMA (X = Cl, Br, I) XB complexes have also been included in these tables. Explanation of the intermolecular properties is given in Figure S8.1 of the SI. As in the previous chapter on the C_2F_3X·DME complexes, no stationary point could be found for a XB geometry between C_2F_4 and TMA, which is consistent with the lack of σ-hole in the electrostatic potential surface in the vicinity of the fluorine atom. [26]

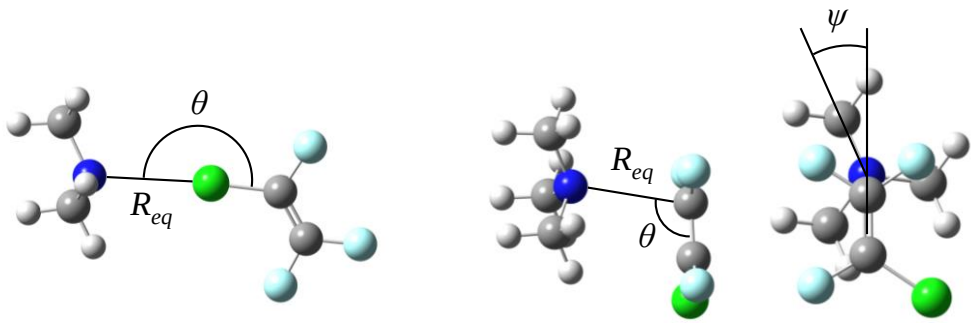

Figure 8.1: MP2/aug-cc-pVDZ(-PP) equilibrium geometries for the halogen (left) and lp···π (right) bonded complexes of C_2F_3X (X = F, Cl, Br and I) with TMA, including the designation of the angles given in Table 8.1.

For the C_2F_3X (X = Cl, Br, I) XB complexes a strong increase in bonding energy is observed from -15.1 kJ mol^{-1} to -36.0 kJ mol^{-1} at the CCSD(T)/CBS level going from chlorine to iodine, combined with a decrease in bond distance from 2.98 Å to 2.84 Å. For all XB complexes a nearly linear C-X···N bonding geometry is observed, the

bonding angles lying between 176.4 and 179.0°. From Table 8.1 it is also clear to see that the complexation energy for the lp···π complexes of C_2F_3Cl, C_2F_3Br and C_2F_3I is quite similar, the values lying between -19.6 kJ mol^{-1} and -20.6 kJ mol^{-1} at the CCSD(T)/CBS level, with a slight increase towards the complexes involving donors with a more polarizable halogen atom. For the lp···π complex with C_2F_4, the lower value of -16.8 kJ mol^{-1} can be explained by the lack of secondary C-H···F interactions, whereas secondary C-H···X (X = Cl, Br, I) interactions are present in the other lp···π complexes (*vide infra*).

Table 8.1: Intermolecular distance R_{eq} (Å), bond angles and dihedrals (°) and the MP2/aug-cc-pVDZ(-PP) ΔE(DZ) and CCSD(T)/CBS Δ*E*(CCSD(T)) complexation energies (kJ mol^{-1}) for the complexes of C_2F_3X (X = F, Cl, Br, I) with TMA. For completeness, the corresponding values for the complexes of CF_3X (X = Cl, Br, I) with TMA are also given.

lp···π	C_2F_4·TMA	C_2F_3Cl·TMA	C_2F_3Br·TMA	C_2F_3I·TMA
$R_{eq}=R_{C=C\cdots N}$	2.95	2.92	2.92	2.92
$\theta_{C=C\cdots N}$	102.2	100.3	100.4	100.9
$\varphi_{C\cdots N\text{-}C}$	116.9	117.6	116.9	115.3
$\psi_{C=C\cdots N\text{-}C}$	180.0	155.3	152.1	150.2
ΔE (DZ)	-15.1	-18.1	-18.5	-19.1
ΔE (CCSD(T))	-16.8	-19.6	-20.1	-20.6
XB	C_2F_3Cl·TMA		C_2F_3Br·TMA	C_2F_3I·TMA
$R_{eq}=R_{X\cdots N}$	2.98		2.85	2.84
$\theta_{C\text{-}X\cdots N}$	176.4		179.0	178.9
$\varphi_{C\text{-}N\cdots X}$	118.4		108.4	108.4
ΔE (DZ)	-14.7		-24.6	-36.3
ΔE (CCSD(T))	-15.1		-24.8	-36.0
XB	CF_3Cl·TMA		CF_3Br·TMA	CF_3I·TMA
$R_{eq}=R_{X\cdots N}$	2.96		2.83	2.82
$\theta_{C\text{-}X\cdots N}$	180.0		180.0	180.0
$\psi_{F\text{-}C\cdots N\text{-}C}$	58.3		0.1	0.0
ΔE (DZ)	-15.2		-25.0	-37.1
ΔE (CCSD(T))	-15.6		-25.0	-36.5

In order to study these secondary interactions, the lp···π complexes were analysed using the NCI index visualized using NCIPLOT [29-30], for which the results are given in Figure S8.2 of the SI. These images show that apart from the intermolecular interaction surface caused by the lp···π interaction, two additional intermolecular interaction surfaces appear between the hydrogens of TMA and the higher halogen atoms of C_2F_3Cl, C_2F_3Br and C_2F_3I, corresponding to these secondary C-H···X (X = Cl, Br, I) interactions. As mentioned in the previous study of C_2F_3X·DME, the existence of secondary interaction also influences the geometry of the formed lp···π complex. Here, a deviation from the linear C=C···N-C torsion angle ψ of the complex with C_2F_4 is observed for the other three lp···π complexes, with the torsion angle decreasing from 155.3° to 150.2° going from the chlorine to the iodine substituted donor molecule. From the $\theta_{C=C\cdots N}$ angle, which lies between 100.3° and 102.2°, it is also clear that the nitrogen atom does not lie directly above the C(sp^2) atom, but slightly further along the C=C axis, which corresponds to the position of the π* orbital. An overview of the calculated CCSD(T)/CBS complexation energies and calculated complex enthalpies in the vapour phase and in solution is given in Table 8.2.

Table 8.2: Values of the CCSD(T)/CBS complexation energies, the calculated vapour phase complexation enthalpies, the calculated complexation enthalpies in LKr or LXe and the corresponding experimentally obtained complexation enthalpies for the complexes of C_2F_3X (X = F, Cl, Br, I) with TMA in kJ mol^{-1}. For completeness, the corresponding values for the XB complexes of CF_3X (X = Cl, Br, I) with TMA, determined in LAr, LKr or LXe are also given.

	lp···π				XB			XB		
	C_2F_4	C_2F_3Cl	C_2F_3Br	C_2F_3I	C_2F_3Cl	C_2F_3Br	C_2F_3I	CF_3Cl	CF_3Br	CF_3I
Δ*E* (CCSD(T))	-16.8	-19.6	-20.1	-20.6	-15.1	-24.8	-36.0	-15.6	-25.0	-36.5
Δ*H*° (vap,calc)	-14.5	-17.2	-17.7	-17.3	-12.7	-22.2	-32.1	-13.7	-22.4	-32.6
Δ*H*° (LXe,calc)				-9.2			-31.6			-32.2
Δ*H*° (LKr,calc)	-7.8	-9.3	-9.5		-9.5	-19.7			-19.9	
Δ*H*° (LAr,calc)								-10.2		
Experimental										
Δ*H*° (LXe)							-24.4(2)			-28.7(1)
Δ*H*° (LKr)	-4.9(2)	-4.9(1)			-8.3(4)	-15.7(3)			-18.3(1)	
Δ*H*° (LAr)								-8.9(2)		

8.2.2 Infrared and Raman measurements

In order to distinguish the different complex geometries, vibrational modes in which both isomers have sufficiently different calculated complexation shifts, preferably one redshifted and the other blueshifted, have been selected for further experimental study. By analysing the *ab initio* calculated shifts, given in Tables S8.3 to S8.9 of the SI, three modes of interest were selected for further experimental study. The numbering of the fundamental vibrational modes of all compounds follows the numbering scheme of Herzberg. [31]

The first mode concerns the C=C stretching vibration, which for all four C_2F_3X (X = F, Cl, Br, I) compounds has a calculated blueshift for the lp···π complex and a redshift for the XB complex. The observation that the lp···π interactions cause a blueshift for the C=C stretching mode contradicts with the general expectation [32] that these types of complexes are characterized by a charge transfer from the lone pair to the π* orbital and thus should be characterized by a weakening of the C=C bond. To shed more light on the underlying nature of this contradiction, an NBO analysis of the lp···π interaction was attempted. Unfortunately, due to many different energetic contributions to the interaction energy, this analysis did not offer a clear indication whether the interaction can be ascribed solely to a pure n→π* interaction.

The calculated blueshifts for the lp···π complex are 3.2 cm^{-1}, 4.0 cm^{-1}, 4.0 cm^{-1} and 3.9 cm^{-1} for the complexes involving C_2F_4, C_2F_3Cl, C_2F_3Br and C_2F_3I respectively, while the calculated redshifts for the XB complexes of the latter three compounds are -5.3 cm^{-1}, -8.7 cm^{-1} and -12.1 cm^{-1} respectively. It should however also be noted that this vibrational mode has A_g symmetry for C_2F_4, and thus has no IR intensity. Experimental study of this vibrational mode will therefore be conducted using Raman spectroscopy.

IR spectra of the C=C stretching region of the C_2F_3X (X = F, Cl, Br, I) are shown in Figure 8.2 for the complexes with TMA and in Figure S8.3 of the SI for the complexes with TMA-d_9. Raman spectra for the same spectral regions are also given in Figures 8.3 (TMA) and S8.4 (TMA-d_9).

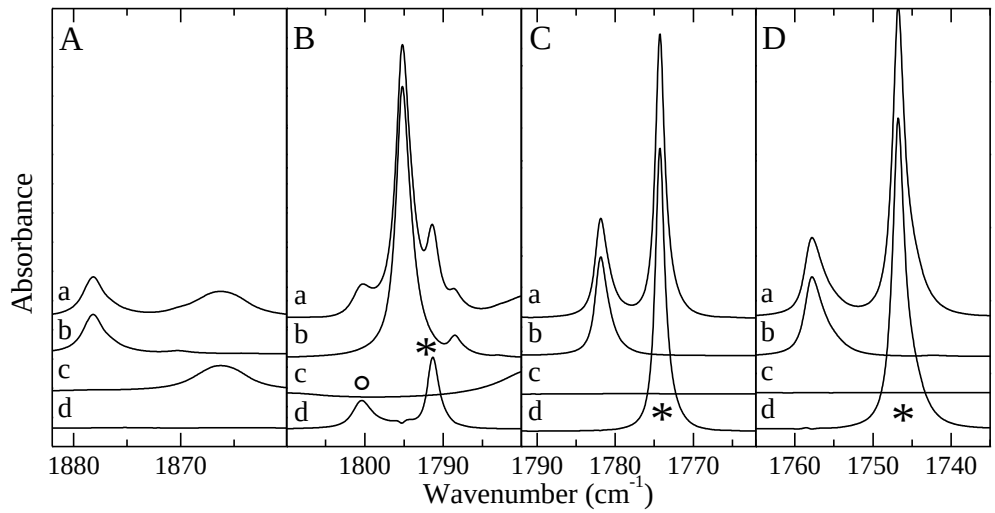

Figure 8.2: Infrared spectra of the $\nu_{C=C}$ spectral region of C_2F_3X (X = F, Cl, Br, I) for solutions of mixtures of TMA with C_2F_4 (panel A), C_2F_3Cl (panel B), C_2F_3Br (panel C) and C_2F_3I (panel D) dissolved in LKr at 120 K for panels A-C and LXe at 170 K for panel D. In each panel, trace *a* represents the mixed solution, while traces *b* and *c* show the solution containing only C_2F_3X or TMA, respectively. Trace *d* represents the spectrum of the complex and is obtained by subtracting the rescaled traces *b* and *c* from trace *a*. New bands due to the 1:1 C(sp^2)-X···N XB and the 1:1 lp···π complexes are marked with an asterisk (*) and an open circle (°), respectively.

In the Raman spectra of C_2F_4·TMA(-d_9), shown in panels 8.3A and S8.4A, a weak blueshifted complex band can be observed in the spectra of the mixtures. This band, which is blueshifted by 5.1 cm^{-1}, corresponds well to the calculated shift of 3.2 cm^{-1} for the lp···π complex.

For the mixtures of C_2F_3Cl and TMA(-d_9), shown in panels 8.2B, 8.3B, S8.3B and S8.4B, two complex bands are observed in the C=C stretching region upon subtraction. The blueshifted band with a complexation shift of 5.2 cm^{-1} can be assigned to the lp···π complex with a calculated shift of 4.0 cm^{-1}, whereas the -3.9 cm^{-1} redshifted band corresponds to the XB complex with a calculated shift of -5.3 cm^{-1}.

For the mixtures involving C_2F_3Br, shown in panels 8.2C, 8.3C, S8.3C and S8.4C, only a -7.5 cm^{-1} redshifted band is observed in the C=C stretching region, which is in good agreement with the calculated value of -8.7 cm^{-1} for the XB complex. No blueshifted

band corresponding to the lp···π complex, which has a calculated shift of 4.0 cm^{-1}, is observed in any of the spectra.

Due to the relatively high complexation strength of the C_2F_3I·TMA complex, combined with the necessity to retain a discernible amount of both monomers for the temperature studies, FTIR measurements of this complex were performed in LXe, enabling the use of a higher temperatures. [33] In the IR (panels 8.2D and S8.3D) and Raman (panels 8.3D and S8.4D) spectra, a strong complex band is observed with a -11.0 cm^{-1} redshift which is assigned to the XB complex with a calculated shift of -12.1 cm^{-1}. Again, no indications were found for the presence of the lp···π complex for this bond donor.

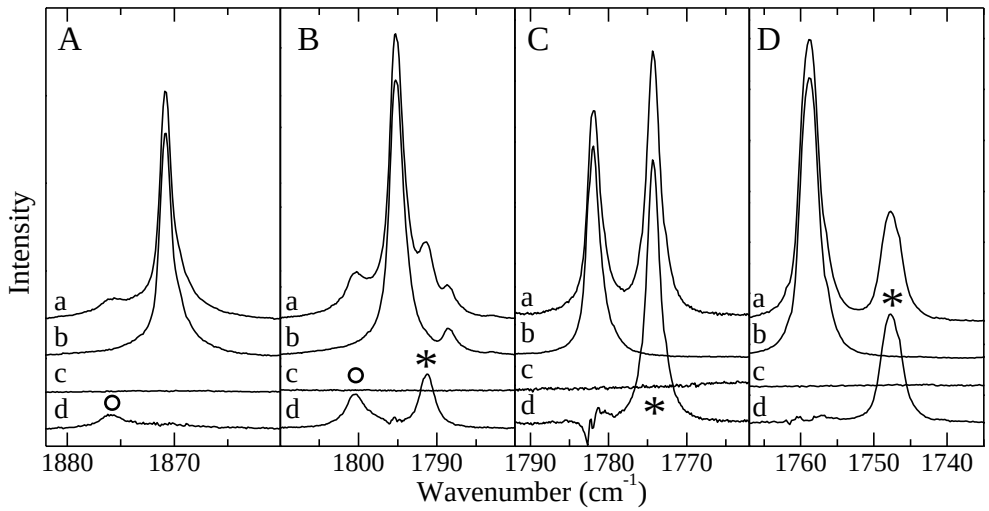

Figure 8.3: Raman spectra of the $\nu_{C=C}$ spectral region of C_2F_3X (X = F, Cl, Br, I) for solutions of mixtures of TMA with C_2F_4 (panel A), C_2F_3Cl (panel B), C_2F_3Br (panel C) and C_2F_3I (panel D) dissolved in LKr at 120 K. In each panel, trace *a* represents the mixed solution, while traces *b* and *c* show the solution containing only C_2F_3X or TMA, respectively. Trace *d* represents the spectrum of the complex and is obtained by subtracting the rescaled traces *b* and *c* from trace *a*. New bands due to the 1:1 C(sp^2)-X···N XB and the 1:1 lp···π complexes are marked with an asterisk (*) and an open circle (°), respectively.

A second region where both complex geometries can be distinguished based on the frequency calculations is found in the region of the antisymmetric CF_2 stretching mode, shown in Figure 8.4 for complexes involving TMA and Figure S8.5 of the SI for the complexes of TMA-d_9. For this vibrational mode, a redshift of -8.8, -12.8 and -18.0 cm^{-1} is predicted for the XB complexes with C_2F_3Cl, C_2F_3Br and C_2F_3I respectively, whereas blueshifts of 3.1, 3.4 and 3.7 cm^{-1} are predicted for the equivalent lp···π complexes. For C_2F_4, the *cis* and *trans* C-F stretching vibrations (ν_9 and ν_5 respectively) can be found in this spectral region. However, since the *trans* C-F stretching vibration ν_5 is IR inactive, only the *cis* C-F stretching mode is observed in IR, which has a calculated complexation shift of -10.6 cm^{-1} for the lp···π complex. Since the vibrational modes in this spectral region have a limited Raman intensity, they were not studied experimentally using Raman spectroscopy.

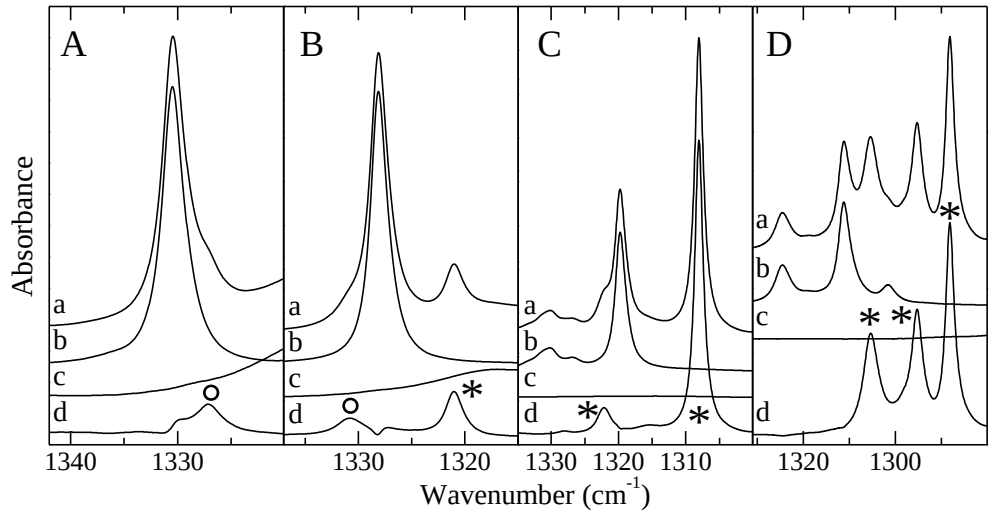

Figure 8.4: Infrared spectra of the C-F stretching region of C_2F_3X (X = F, Cl, Br, I) for solutions of mixtures of TMA with C_2F_4 (panel A), C_2F_3Cl (panel B), C_2F_3Br (panel C) and C_2F_3I (panel D) dissolved in LKr at 120 K for panels A-C and LXe at 170 K for panel D. In each panel, trace *a* represents the mixed solution, while traces *b* and *c* show the solution containing only C_2F_3X or TMA, respectively. Trace *d* represents the spectrum of the complex and is obtained by subtracting the rescaled traces *b* and *c* from trace *a*. New bands due to the 1:1 C(sp^2)-X···N XB and the 1:1 lp···π complexes are marked with an asterisk (*) and an open circle (°), respectively.

For C_2F_4, spectra of the *cis* C-F stretching region (ν_9) are shown in panels 8.4A and S8.5A. For this transition, a complex band with a redshift of -3.4 cm^{-1} is isolated using the subtraction method, which is assigned to the lp···π complex with a calculated redshift of -10.6 cm^{-1}.

For the ν_2 antisymmetric CF_2 stretching mode of C_2F_3Cl, shown in panels 8.4B and S8.5B, two complex bands with shifts of -7.1 cm^{-1} and 2.7 cm^{-1} are observed, which are assigned to the XB complex with a calculated shift of -8.8 cm^{-1} and the lp···π complex with a calculated complexation shift of 3.5 cm^{-1} respectively. For the mixtures involving TMA and C_2F_3I or C_2F_3Br, shown in panels 8.4D and 8.4C respectively, only redshifted complexation bands are observed, corresponding to the XB isomers, the calculated and experimental complexation shifts being -18.0 cm^{-1} and -15.9 cm^{-1} for C_2F_3I and -12.8 cm^{-1} and -11.7 cm^{-1} for C_2F_3Br.

Further indication of the coexistence of the lp···π and XB complex in $C_2F_3Cl{\cdot}TMA(\text{-}d_9)$ mixtures is found for the ν_{10} vibrational mode, of which the spectral region is shown in Figure 8.5. Subtraction yields two complex bands with experimental shifts of -0.5 and -2.0 cm^{-1}, corresponding to the XB and lp···π complex respectively, which have calculated shifts of -1.4 and -9.1 cm^{-1}.

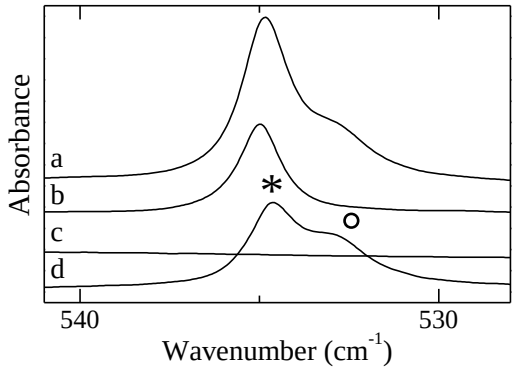

Figure 8.5: Infrared spectra of the ν_{10} vibrational mode of a C_2F_3Cl mixtures with TMA, dissolved in LKr at 120 K. Trace *a* represents the mixed solution, while traces *b* and *c* show the solution containing only C_2F_3Cl or TMA, respectively. Trace *d* represents the spectrum of the complex and is obtained by subtracting the rescaled traces *b* and *c* from trace *a*. New bands due to the 1:1 $C(sp^2)$-X···N XB and the 1:1 lp···π complexes are marked with an asterisk (*) and an open circle (°), respectively.

A full overview of the assignment of the vibrational modes for all monomers and complexes is given in Tables 8.3 to 8.6 for the complexes involving TMA and Tables S8.10 to S8.13 for the complexes involving TMA-d_9.

Table 8.3: Experimental vibrational frequencies for the monomer and complexes, as well as experimental complexation shifts ($\Delta\nu_{exp}$) and MP2/aug-cc-pVDZ calculated complexation shifts ($\Delta\nu_{calc,\ lp\cdots\pi}$), in cm^{-1}, for the lp···π complex of C_2F_4 with TMA dissolved in LKr at 120 K.

Assignment		$\nu_{monomer}$	$\nu_{complex}$	$\Delta\nu_{exp}$	$\Delta\nu_{calc,lp\cdots\pi}$
C_2F_4	$\nu_1 + \nu_9$	3196.6	3196.6	0.0	-7.5
	$\nu_1 + \nu_{11}$	3045.3	3048.4	3.1	-1.0
	ν_1	1870.8	1875.9	5.1	3.2
	ν_9	1330.5	1327.1	-3.4	-10.6
	ν_{11}	1179.5	1177.9	-1.6	-4.1
	ν_2	778.1	777.8	-0.3	-3.3
	ν_{12}	554.7	554.4	-0.3	-0.9
	ν_6	549.9	550.0	0.1	-0.4
	ν_8	505.5	501.0	-4.5	-13.6
	ν_3	395.5	395.4	-0.1	-0.9
TMA	ν_{12}	2977.0	2980.8	3.8	-3.1
	ν_1	2944.4	2947.1	2.7	-0.4
	ν_{13}	2944.4	2947.1	2.7	-3.9
	$2\ \nu_4$	2818.3	2822.0	3.7	1.7
	ν_2	2768.6	2778.7	10.1	6.9
	ν_{14}	2768.6	2778.7	10.1	7.6
	$\nu_{20} + \nu_{21}$	1474.8	1472.7	-2.1	0.9
	ν_{15}	1467.6	1470.1	2.5	0.7
	ν_3	1454.8	1454.5	-0.3	-0.8
	ν_4	1438.8	1440.6	1.8	0.8
	ν_{16}	1438.8	1440.6	1.8	-1.1
	ν_5	1184.3	[a]		2.3
	ν_{19}	1098.5	1099.0	0.5	-1.2
	ν_{20}	1041.4	1040.0	-1.4	-0.2
	ν_6	828.1	826.1	-2.0	-2.0

[a] Band could not be isolated due to overlap with C_2F_4 modes.

Table 8.4 : Experimental vibrational frequencies for the monomer and complexes, as well as experimental complexation shifts ($\Delta\nu_{exp}$) and MP2/aug-cc-pVDZ calculated complexation shifts ($\Delta\nu_{calc}$), in cm^{-1}, for the XB complex and lp···π complex of C_2F_3Cl with TMA dissolved in LKr at 120 K.

Assignment		$\nu_{monomer}$	$\nu_{complex}$	$\Delta\nu_{exp,XB}$	$\Delta\nu_{calc,XB}$	$\nu_{complex}$	$\Delta\nu_{exp,lp\cdots\pi}$	$\Delta\nu_{calc,lp\cdots\pi}$
C_2F_3Cl	ν_1	1795.2	1791.3	-3.9	-5.3	1800.4	5.2	4.0
	ν_1 (^{13}C)	1788.5	[a]		-5.3	[a]		4.0
	ν_2	1328.1	1321.0	-7.1	-8.8	1330.8	2.7	3.1
	ν_3	1214.3	1210.6	-3.7	-8.1	1210.6	-3.7	-7.9
	$2\nu_{10}$	1074.8	1073.1	-1.7		1073.1	-1.7	
	ν_4	1053.7	[b]		-3.9	1052.6	-1.1	-1.9
	ν_5 (^{35}Cl)	691.2	689.3	-1.9	-4.7	691.0	-0.2	-2.1
	ν_5 (^{37}Cl)	689.6	687.6	-2.0	-4.7	689.3	-0.3	-2.1
	ν_{10}	535.0	534.5	-0.5	-1.4	533.0	-2.0	-9.1
	ν_6	516.3	516.7	0.4	0.7	516.0	-0.3	0.1
	ν_7 (^{35}Cl)	462.4	458.3	-4.1	-5.8	462.0	-0.4	-1.0
	ν_7 (^{37}Cl)	456.5	452.4	-4.1	-5.8	456.3	-0.2	-1.0
	ν_8	338.1	340.1	2.0	2.6	[a]		-1.1
	ν_9	189.8	[a]		8.6	[a]		-0.1
TMA	ν_{12}	2977.0	2978.2	1.2	-1.0	2978.2	1.2	-2.6
	ν_1	2944.4	2945.4	1.0	0.4	2945.4	1.0	-0.4
	ν_{13}	2944.4	2945.4	1.0	-0.3	2945.4	1.0	-3.3
	$2\nu_4$	2818.6	2822.4	3.8	1.5	2822.4	3.8	0.8
	ν_2	2769.0	2772.6	3.6	8.5	2772.6	3.6	7.1
	ν_{14}	2769.0	2772.6	3.6	9.6	2772.6	3.6	7.8
	$\nu_{20} + \nu_{21}$	1474.8	1473.8	-1.0	-1.8	1473.8	-1.0	-1.8
	ν_{15}	1467.6	1468.1	0.5	0.4	1468.1	0.5	0.5
	ν_3	1454.8	1454.6	-0.2	-0.4	1454.6	-0.2	-1.1
	ν_4	1438.8	1439.3	0.5	0.8	1439.3	0.5	0.4
	ν_{16}	1438.8	1439.3	0.5	-0.8	1439.3	0.5	-1.5
	ν_{17}	1405.3	1406.3	1.0	0.5	1406.3	1.0	0.0
	ν_{18}	1273.3	1271.8	-1.5	-0.3	1271.8	-1.5	-0.6
	ν_5	1184.3	1187.7	3.4	3.4	1187.7	3.4	2.7
	ν_{19}	1098.5	1098.7	0.2	-1.0	1098.7	0.2	-1.3
	ν_{20}	1041.5	[b]		-0.7	[b]		-0.7
	ν_6	828.1	827.4	-0.7	-2.1	827.4	-0.7	-2.3
	ν_{21}	424.0	422.4	-1.6	-1.1	422.4	-1.6	-1.1
	ν_7	372.6	380.2	7.6	5.8	380.2	7.6	6.1

[a] Complex band has not been observed.

[b] Bands could not be isolated due to overlap between the C_2F_3Cl ν_4-mode and TMA ν_{20}-mode.

Table 8.5: Experimental vibrational frequencies, experimental complexation shifts and MP2/aug-cc-pVDZ-PP calculated complexation shifts ($\Delta\nu_{calc,XB}$), in cm^{-1}, for the XB complex of C_2F_3Br with TMA dissolved in LKr at 120 K. For completeness, the MP2/aug-cc-pVDZ-PP calculated complexation shifts of the lp···π complexes ($\Delta\nu_{calc,lp\cdots\pi}$) are also given.

Assignment		$\nu_{monomer}$	$\nu_{complex}$	$\Delta\nu_{exp}$	$\Delta\nu_{calc,XB}$	$\Delta\nu_{calc,lp\cdots\pi}$
C_2F_3Br	ν_1	1781.8	1774.3	-7.5	-8.7	4.0
	$2\nu_5$	1330.2	1322.2	-8.0	-11.5	-2.9
	ν_2	1319.8	1308.1	-11.7	-12.8	3.4
	ν_3	1197.2	1184.9	-12.3	-12.9	-7.1
	$2\nu_{10}$	1072.6	1071.7	-0.9	-0.8	-20.1
	$\nu_5 + \nu_7$ (^{79}Br)	1034.4	1024.3	-10.1	-6.2	-1.2
	$\nu_5 + \nu_7$ (^{81}Br)	1033.3	1024.3	-9.0	-6.2	-1.2
	$2\nu_6$	1018.8	1018.6	-0.2	0.8	0.2
	ν_4	1016.6	1006.9	-9.7	-6.2	-1.2
	ν_5	663.9	659.3	-4.6	-5.7	-1.4
	ν_{10}	535.2	534.7	-0.5	-0.4	-10.0
	ν_6	509.1	509.7	0.6	0.4	0.1
	ν_7	365.8	352.3	-13.5	-14.6	0.5
	ν_8	311.1	310.8	-0.3	-0.3	-1.0
	ν_9	162.2	168.8	6.6	9.9	0.2
TMA	ν_{12}	2977.0	2980.3	3.3	1.2	-2.7
	ν_1	2944.4	2952.8	8.4	3.1	-0.5
	ν_{13}	2944.4	2952.8	8.4	3.4	-3.4
	$2\nu_4$	2818.6	2827.9	9.3	1.3	0.4
	ν_2	2769.0	2778.8	9.8	17.9	6.6
	ν_{14}	2769.0	2778.8	9.8	19.8	7.3
	$\nu_{20} + \nu_{21}$	1474.8	1472.8	-2.0	-4.4	-1.9
	ν_{15}	1467.6	1468.3	0.7	0.4	0.3
	ν_3	1454.8	1453.5	-1.3	0.2	-1.2
	ν_4	1438.8	1440.0	1.2	0.7	0.2
	ν_{16}	1438.8	1440.0	1.2	-0.9	-1.6
	ν_{18}	1273.3	1270.2	-3.1	-1.3	-0.7
	ν_5	1184.3	1192.4	8.1	7.3	2.6
	ν_{19}	1098.5	1098.6	0.1	-1.4	-1.3
	ν_{20}	1041.5	1037.9	-3.6	-2.6	-0.8
	ν_6	828.1	826.2	-1.9	-4.0	-2.3
	ν_{21}	424.0	422.1	-1.9	-1.8	-1.1
	ν_7	372.6	388.9	16.3	14.7	5.8
	ν_{22}	277.9	272.2	-5.7	-6.6	-2.2

Table 8.6: Experimental vibrational frequencies, experimental complexation shifts and MP2/aug-cc-pVDZ-PP calculated complexation shifts ($\Delta\nu_{calc,XB}$), in cm^{-1}, for the XB complex of C_2F_3I with TMA dissolved in LXe at 170 K. For completeness, the MP2/aug-cc-pVDZ-PP calculated complexation shifts of the lp···π complexes ($\Delta\nu_{calc,lp\cdots\pi}$) are also given.

Assignment		$\nu_{monomer}$	$\nu_{complex}$	$\Delta\nu_{exp}$	$\Delta\nu_{calc,XB}$	$\Delta\nu_{calc,lp\cdots\pi}$
C_2F_3I	ν_1	1757.8	1746.8	-11.0	-12.1	3.9
	ν_1 (^{13}C)	1742.3	1731.5	-10.8	-12.1	3.9
	$\nu_4 + \nu_7$	1324.6	1305.4	-19.2	-21.2	-0.2
	ν_2	1311.2	1295.3	-15.9	-18.0	3.7
	$2\nu_5$	1301.6	1288.2	-13.4	-11.9	-2.3
	ν_3	1173.9	1158.7	-15.2	-17.3	-6.5
	$\nu_5 + \nu_6$	1155.2	1146.3	-8.9	-5.9	-1.0
	$2\nu_{10}$	1076.4	1075.0	-1.4	-0.7	-20.5
	$2\nu_6$	1012.5	1011.2	-1.3	0.1	0.3
	ν_4	1001.2	995.6	-5.6	-7.2	-0.8
	ν_5	651.4	646.3	-5.1	-5.9	-1.1
	ν_{10}	537.5	536.6	-0.9	-0.3	-10.2
	ν_6	506.4	505.7	-0.7	0.03	0.1
	ν_7	321.1	307.4	-13.7	-14.0	0.6
	ν_8	286.8	276.7	-10.1	-9.8	-1.0
TMA	ν_{12}	2977.0	2979.9	2.9	5.2	-2.8
	ν_1	2944.4	2951.3	6.9	8.6	-0.5
	ν_{13}	2944.4	2951.3	6.9	9.1	-3.6
	$2\nu_4$	2818.3	2838.7	20.4	0.3	0.1
	ν_2	2768.6	2782.6	14.0	31.0	6.3
	ν_{14}	2768.6	2782.6	14.0	33.9	6.9
	$\nu_{20} + \nu_{21}$	1474.8	1470.2	-4.6	-9.0	-2.1
	ν_{15}	1467.6	1467.1	-0.5	0.2	0.1
	ν_3	1454.8	1450.1	-4.7	1.3	-1.3
	ν_4	1438.8	1440.3	1.5	0.1	0.0
	ν_{16}	1438.8	1440.3	1.5	-0.9	-1.8
	ν_{18}	1273.4	1267.0	-6.4	-4.2	-0.8
	ν_5	1184.3	1196.8	12.5	12.4	2.5
	ν_{19}	1098.5	1097.7	-0.8	-2.0	-1.5
	ν_{20}	1041.4	1033.3	-8.1	-6.3	-0.9
	ν_6	828.1	825.5	-2.6	-7.2	-2.4
	ν_{21}	424.0	421.4	-2.6	-2.7	-1.2
	ν_7	372.6	403.1	30.5	28.0	5.7

8.3.3 van ‘t Hoff plots and complexation enthalpies

After these assignments, complex enthalpies were determined by creating van ‘t Hoff plots. An illustration of these van ‘t Hoff plots is given in Figures S8.6 and S8.7 of the SI. For the XB complexes of C_2F_3I·TMA(-d_9) in LXe and C_2F_3Br·TMA(-d_9) in LKr, average complexation enthalpies of -24.4(2) kJ mol^{-1} and -15.7(3) kJ mol^{-1} respectively were determined. For the complexes of C_2F_3Cl and TMA(-d_9) a complexation enthalpy of -8.3(4) kJ mol^{-1} was found for the XB complex, whereas the lp···π complex had a complexation enthalpy of -4.9(1) kJ mol^{-1}. For the lp···π complex with C_2F_4 an experimental complexation enthalpy of -4.9(2) kJ mol^{-1} was found. An overview of all experimental complexation enthalpies is given in Table 8.2.

8.3 Discussion

Mixtures involving C_2F_4 and TMA(-d_9) yield complex bands which, based on the *ab initio* frequency calculations, can all be assigned to the lp···π complex. Using these complex bands, an experimental complexation enthalpy of -4.9(2) kJ mol^{-1} was determined. Consistent with the lack of σ-hole in the electrostatic potential surface, no XB complex is formed in these mixtures.

For the mixtures of C_2F_3Cl and TMA(-d_9), well separated complex bands for both complex isomers are observed for several vibrational modes, thus proving the coexistence of the XB and lp···π complexes in these solutions. Complexation enthalpies of -8.3(4) kJ mol^{-1} and -4.9(1) kJ mol^{-1} were measured for the XB and lp···π complex respectively.

As opposed to the previous chapter on the complexes formed with DME, [26] no indications at all were found for the presence of lp···π complex in the mixtures of C_2F_3Br and TMA. This is in line with the calculated difference in complexation enthalpy of 10.2 kJ mol^{-1} between both complexes at the CCSD(T)/CBS level, as

opposed to 3.9 kJ mol^{-1} for the complexes involving DME. For the XB complex, an experimental complexation enthalpy in LKr was determined of -15.7(3) kJ mol^{-1}.

When using C_2F_3I as a bond donor molecule, only bands assigned to the XB complex can be observed. The absence of lp···π complex can be explained by the 22.4 kJ mol^{-1} difference in calculated enthalpy in LXe with the XB complex, resulting in the weaker complex not being able to compete at thermodynamic equilibrium. For the XB complex, a complexation enthalpy of -24.4(2) kJ mol^{-1} was determined in LXe.

From the experimental complexation enthalpies it is clear that the strength of the halogen bond is strongly influenced by the size of the halogen atom involved, with an increase in complexation enthalpy from -8.3(4) kJ mol^{-1} for C_2F_3Cl to -15.7(3) kJ mol^{-1} for C_2F_3Br and -24.4(2) kJ mol^{-1} for C_2F_3I. The influence of the halogen atom on the strength of the lp···π interaction is much smaller, yielding lp···π complexes of similar strength for C_2F_4·TMA(-d_9) and C_2F_3Cl·TMA(-d_9).

Extrapolation of the MP2/aug-cc-pVDZ(-pp) energies to the CCSD(T)/CBS level yields only a limited difference in complexation strength. Comparison of the experimental complexation enthalpies with the calculated enthalpies, determined using the extrapolated complexation energies, shows that the latter values are all higher, but follow the same complexation strength order. It is therefore noteworthy that, even though large basis sets are required in order to obtain accurate energetics for weak intermolecular interactions, the use of smaller basis set also yields correct trends, since these trends are fairly insensitive to the basis set size. [20]

When comparing the experimental results to those of the study involving DME, [26] it is clear that the C(sp²)X XB complexes with TMA still follow the Cl < Br < I bond strength order, but are about 70 % stronger (-9.3(5) vs. -15.7(3) kJ mol^{-1} for Br and -14.2(5) vs. -24.4(2) kJ mol^{-1} for I). For the lp···π complexes, too little data is currently available to reach conclusions concerning bond strength orders. More experimental data involving complexes with other Lewis bases is needed to obtain definitive conclusions concerning the influence of the changing halogen atom on the strength of the lp···π complex.

The experimental confirmation of the existence of the lp···π C_2F_3Cl·TMA(-d_9) complex is also in line with the recent report of Gou et al. [27], in which the C_2F_3Cl·NH_3 lp···π complex was found experimentally using pulsed-jet FTMW. Since the FTMW measurements take place in supersonic expansion, and not at thermodynamic equilibrium, only the complex with the largest complexation energy can be observed, thus disabling the identification of the XB complex with this technique. Indeed, from the results of our calculations shown in Table 8.2, it can be seen that the lp···π complex has a higher binding energy than the XB complex for C_2F_3Cl·TMA (-19.6 kJ mol^{-1} vs. -15.1 kJ mol^{-1}) at the CCSD(T)/CBS level. However, when applying solvent corrections, this strength order is reversed, leading to a $\Delta H°$ (LKr,calc) of -9.3 kJ mol^{-1} for the lp···π complex and -9.5 kJ mol^{-1} for the XB complex. This comparison also clearly shows that in order to study competing interactions, measurements have to be performed at thermodynamic equilibrium.

Finally, comparison of the experimental complexation enthalpies of the XB complexes with those of the equivalent CF_3X (Cl, Br, I) complexes shows a slight decrease in bonding strength when the halogen atom is bonded to a sp^2 rather than a sp^3 hybridized carbon atom, which was also observed in the study of C_2F_3X·DME and can be ascribed to the decreased number of electron withdrawing fluorine atoms geminal to the involved halogen atom.

8.4 Conclusions

Ab initio calculations of the interactions between C_2F_3X (X=F, Cl, Br, I) and TMA yielded lp···π complexes for all four donor molecules, whereas XB complexes were only found for donor molecules containing Cl or higher halogens. For the XB complexes, a significant increase in complexation energy, from -15.6 kJ mol^{-1} to -36.5 kJ mol^{-1} at the CCSD(T)/CBS level, is observed going from Cl to I. For the lp···π complexes, complexation energies between -19.6 kJ mol^{-1} and -20.6 kJ mol^{-1} are calculated for the complexes with C_2F_3Cl, C_2F_3Br and C_2F_3I, whereas a complexation energy of -16.8 kJ mol^{-1} is found for the complex with C_2F_4. This discrepancy can be attributed to the presence of secondary interactions with the diffuse heavier halogens Cl, Br and I. Experimental assignment of the complexes in the subtracted IR and Raman spectra was aided by harmonic *ab initio* frequency calculations.

Experimentally, lp···π complexes have been observed in noble gas solutions containing C_2F_4 or C_2F_3Cl and TMA($-d_9$) at thermodynamic equilibrium using FTIR and Raman spectroscopy, which clearly demonstrates that formation of lp···π interactions is definitely not limited to oxygen based Lewis bases. Moreover, as demonstrated by the simultaneous observation of the C_2F_3Cl·TMA($-d_9$) XB and lp···π complex, these noncovalent interaction are able to coexist. Furthermore, solutions containing C_2F_3Br and TMA($-d_9$) in LKr or C_2F_3I and TMA($-d_9$) in LXe only yielded XB complexes.

From temperature studies, complexation enthalpies in LKr were found to be -4.9(1) and -4.9(2) kJ mol^{-1} for the C_2F_4·TMA($-d_9$) and C_2F_3Cl·TMA($-d_9$) lp···π complex respectively, whereas the C_2F_3Cl·TMA($-d_9$) XB complex has a complexation enthalpy of -8.3(4) kJ mol^{-1}. Complexation enthalpies of the XB complexes of C_2F_3Br and TMA($-d_9$) in LKr or C_2F_3I and TMA($-d_9$) in LXe have been determined as -15.7(3) kJ mol^{-1} and -24.4(2) kJ mol^{-1} respectively.

The observed complexation strength tendencies are found to be similar to those of the complexes involving DME [26] and are in line with the calculated values at the CCSD(T)/CBS level. However, the absolute strength of the XB complexes involving

TMA were found to be stronger than the DME complexes. For the lp···π complexes too little experimental data is currently available to assess whether the difference in strength between the DME and TMA complexes is negligible. From the experiments it is also clear that lp···π interactions are able to compete with weak halogen bonds at thermodynamic equilibrium, which makes them an interesting tool in supramolecular chemistry, crystal engineering and rational drug design. Even though the high directionality of halogen bonds is one of their greatest advantages in these fields of research, it might well be their biggest weakness when competing with other noncovalent interactions, since the high directionality often does not allow for the formation of additional stabilizing interactions, whereas these are commonly found with HB complexes or lp···π complexes.

8.5 References

1 A. C. Legon, *Phys. Chem. Chem. Phys.*, 2010, ***12***, 7736-7747.
2 S. Sirimulla, J. B. Bailey, R. Vegesna, M. Narayan, *J. Chem. Inf. Model.*, 2013, ***53***, 2781-2791.
3 Y. X. Lu, Y. T. Liu, Z. J. Xu, H. Y. Li, H. L. Liu, W. L. Zhu, *Expert Opin. Drug Discovery*, 2012, ***7***, 375-383.
4 T. Clark, M. Hennemann, J. S. Murray, P. Politzer, *J. Mol. Model.*, 2007, ***13***, 291-296.
5 K. J. Donald, B. K. Wittmaack, C. Crigger, *J.Phys. Chem. A*, 2010, ***114***, 7213-7222.
6 M. Tawfik, K. J. Donald, *J. Phys. Chem. A*, 2014, ***118***, 10090-10100.
7 P. Metrangolo, G. Resnati, T. Pilati, S. Biella, *Struct. Bond.*, 2008, ***126***, 105-136.
8 R. W. Troff, T. Mäkelä, F. Topić, A. Valkonen, K. Raatikainen, K. Rissanen, *Eur. J. Org. Chem.*, 2013, ***2013***, 1617-1637.
9 J. S. Murray, P. Lane, T. Clark, K. E. Riley, P. Politzer, *J. Mol. Model.*, 2012, ***18***, 541-548.
10 I. Alkorta, I. Rozas, J. Elguero, *J. Org. Chem.*, 1997, ***62***, 4687-4691.
11 I. Alkorta, I. Rozas, M. L. Jimeno, J. Elguero, *Struct. Chem.*, 2001, ***12***, 459-464.
12 M. Raimondi, G. Calderoni, A. Famulari, L. Raimondi, F. Cozzi, *J. Phys. Chem. A*, 2003, ***107***, 772-774.
13 T. J. Mooibroek, P. Gamez, J. Reedijk, *CrystEngComm*, 2008, ***10***, 1501-1515.
14 J. C. Amicangelo, D. G. Irwin, C. J. Lee, N. C. Romano, N. L. Saxton, *J. Phys. Chem. A*, 2013, ***117***, 1336-1350.
15 N. Ma, Y. Zhang, B. Ji, A. Tian, W. Wang, *ChemPhysChem*, 2012, ***13***, 1411-1414.
16 B. W. Gung, Y. Zou, Z. G. Xu, J. C. Amicangelo, D. G. Irwin, S. Q. Ma, H. C. Zhou, *J. Org. Chem.*, 2008, ***73***, 689-693.
17 T. Korenaga, T. Shoji, K. Onoue, T. Sakai, *Chem. Commun.*, 2009, 4678-4680.
18 M. Egli, S. Sarkhel, *Acc. Chem. Res.*, 2007, ***40***, 197-205.
19 Y. Danten, T. Tassaing, M. Besnard, *J. Phys. Chem. A*, 1999, ***103***, 3530-3534.
20 J. C. Amicangelo, B. W. Gung, D. G. Irwin, N. C. Romano, *Phys. Chem. Chem. Phys.*, 2008, ***10***, 2695-2705.
21 S. Tsuzuki, K. Honda, T. Uchimaru, M. Mikami, K. Tanabe, *J. Am. Chem. Soc.*, 2000, ***122***, 11450-11458.
22 S. Kawahara, S. Tsuzuki, T. Uchimaru, *Chem. - Eur. J.*, 2005, ***11***, 4458-4464.
23 T. Yang, J. J. An, X. Wang, D. Y. Wu, W. Chen, J. S. Fossey, *Phys. Chem. Chem. Phys.*, 2012, ***14***, 10747-10753.
24 C. Estarellas, A. Frontera, D. Quiñonero, P. M. Deyà, *Cent. Eur. J. Chem.*, 2010, ***9***, 25-34.
25 G. Berger, J. Soubhye, A. van der Lee, C. Vande Velde, R. Wintjens, P. Dubois, S. Clément, F. Meyer, *ChemPlusChem*, 2014, ***79***, 552-558.

26 Y. Geboes, N. Nagels, B. Pinter, F. De Proft, W. A. Herrebout, *J. Phys. Chem. A*, 2015, ***119***, 2502-2516.
27 Q. Gou, L. Spada, Y. Geboes, W. A. Herrebout, S. Melandri, W. Caminati, *Phys. Chem. Chem. Phys.*, 2015, ***17***, 7694-7698.
28 D. Hauchecorne, B. J. van der Veken, A. Moiana, W. A. Herrebout, *Chem. Phys.*, 2010, ***374***, 30-36.
29 E. R. Johnson, S. Keinan, P. Mori-Sánchez, J. Contreras-García, A. J. Cohen, W. Yang, *J. Am. Chem. Soc.*, 2010, ***132***, 6498-6506.
30 J. Contreras-García, E. R. Johnson, S. Keinan, R. Chaudret, J.-P. Piquemal, D. N. Beratan, W. Yang, *J. Chem. Theory Comput.*, 2011, ***7***, 625-632.
31 G. Herzberg, *Infrared and Raman Spectra of Polyatomic Molecules*, 12th ed., D. Van Nostrand Company Inc., Princeton, NJ, USA, **1945**.
32 S. K. Singh, A. Das, *Phys. Chem. Chem. Phys.*, 2015, ***17***, 9596-9612.
33 W. A. Herrebout, *Top. Curr. Chem.*, 2015, ***358***, 79-154.

8.6 Supporting information

Table S8.1.1: Cartesian coordinates of the MP2/aug-cc-pVDZ optimized geometry of C_2F_4.

D_{2h}	X	Y	Z
C_2F_4			
C	0.316718	0.587967	0.000000
C	-0.316718	-0.587967	0.000000
F	-1.642148	-0.702698	0.000000
F	0.316718	-1.757875	0.000000
F	1.642148	0.702698	0.000000
F	-0.316718	1.757875	0.000000

Table S8.1.2: Cartesian coordinates of the MP2/aug-cc-pVDZ optimized geometry of C_2F_3Cl.

C_s	X	Y	Z
C_2F_3Cl			
C	0.000000	0.474053	0.000000
C	-0.672455	-0.686202	0.000000
F	-0.091077	-1.880175	0.000000
F	-1.999532	-0.759966	0.000000
F	-0.676665	1.639573	0.000000
Cl	1.702365	0.604588	0.000000

Table S8.1.3: Cartesian coordinates of the MP2/aug-cc-pVDZ-PP optimized geometry of C_2F_3Br.

C_s	X	Y	Z
C_2F_3Br			
C	0.000000	0.578257	0.000000
C	1.338899	0.495676	0.000000
F	2.014503	-0.647878	0.000000
F	2.137386	1.558739	0.000000
F	-0.586120	1.795157	0.000000
Br	-1.146438	-0.879936	0.000000

Table S8.1.4: Cartesian coordinates of the MP2/aug-cc-pVDZ-PP optimized geometry of C_2F_3I.

C_s	X	Y	Z
C_2F_3I			
C	0.000000	0.895394	0.000000
C	1.289409	1.271052	0.000000
F	2.312902	0.423368	0.000000
F	1.687498	2.539797	0.000000
F	-0.954377	1.858636	0.000000
I	-0.663220	-1.064054	0.000000

Table S8.1.5: Cartesian coordinates of the MP2/aug-cc-pVDZ optimized geometry of TMA.

C_{3v}	X	Y	Z
TMA			
N	0.000000	0.000000	0.410619
C	0.000000	1.379959	-0.066347
H	-0.892330	1.901918	0.309142
H	0.892330	1.901918	0.309142
H	0.000000	1.440847	-1.178318
C	1.195079	-0.689979	-0.066347
H	2.093274	-0.178178	0.309142
H	1.200944	-1.723740	0.309142
H	1.247810	-0.720423	-1.178318
C	-1.195079	-0.689979	-0.066347
H	-1.200944	-1.723740	0.309142
H	-2.093274	-0.178178	0.309142
H	-1.247810	-0.720423	-1.178318

Table S8.2.1: Cartesian coordinates of the MP2/aug-cc-pVDZ optimized geometry of the lp···π complex between C_2F_4 and TMA.

C_s	X	Y	Z
C_2F_4			
C	-1.801931	-0.291177	0.000000
C	-1.085165	0.834930	-0.000001
F	-0.716791	1.460715	-1.113179
F	-0.716787	1.460714	1.113177
F	-2.179558	-0.920645	1.113934
F	-2.179562	-0.920644	-1.113933
TMA			
N	1.686389	-0.189331	-0.000001
C	2.756812	0.804237	-0.000015
H	2.668986	1.441161	-0.892555
H	2.668987	1.441183	0.892510
H	3.766540	0.335983	-0.000010
C	1.772906	-1.021558	-1.196933
H	0.948332	-1.750760	-1.202146
H	1.684252	-0.390221	-2.093412
H	2.733341	-1.580918	-1.253650
C	1.772908	-1.021528	1.196950
H	1.684256	-0.390169	2.093414
H	0.948335	-1.750731	1.202183
H	2.733344	-1.580887	1.253679

Table S8.2.2: Cartesian coordinates of the MP2/aug-cc-pVDZ optimized geometry of the XB complex between C_2F_3Cl and TMA.

C_s	X	Y	Z
C_2F_3Cl			
C	1.848688	0.565730	-0.006706
C	2.712265	-0.460391	0.000331
F	2.345620	-1.739207	-0.001384
F	4.034905	-0.309281	0.009960
F	2.327646	1.829414	-0.004058
Cl	0.146026	0.411278	-0.019041
TMA			
N	-2.797640	-0.039468	-0.004405
C	-3.674754	1.087346	-0.312929
H	-3.514229	1.892228	0.419360
H	-3.439420	1.475600	-1.314797
H	-4.749924	0.801211	-0.290574
C	-3.081072	-0.544440	1.336882
H	-2.399126	-1.375551	1.570576
H	-2.920703	0.255476	2.074764
H	-4.127424	-0.909884	1.435906
C	-2.980942	-1.103274	-0.988860
H	-2.745993	-0.721860	-1.993558
H	-2.298199	-1.936292	-0.764370
H	-4.022598	-1.494526	-0.995753

Table S8.2.3: Cartesian coordinates of the MP2/aug-cc-pVDZ optimized geometry of the lp···π complex between C_2F_3Cl and TMA.

C_1	X	Y	Z
C_2F_3Cl			
C	0.723806	0.995773	-0.450233
C	1.535134	0.225429	0.288012
F	1.769890	0.538744	1.581018
F	0.156211	2.102555	0.014249
F	0.449127	0.767019	-1.727473
Cl	2.276733	-1.210807	-0.269392
TMA			
N	-1.845187	-0.291088	0.084319
C	-1.926261	-1.477360	-0.764452
H	-2.030983	-1.172765	-1.816220
H	-1.002938	-2.067658	-0.663656
H	-2.789410	-2.127472	-0.497978
C	-1.676040	-0.685631	1.480489
H	-0.757174	-1.282166	1.588635
H	-1.584398	0.211515	2.110895
H	-2.531047	-1.292362	1.853552
C	-3.051579	0.518688	-0.065762
H	-2.971295	1.419878	0.559845
H	-3.158136	0.831392	-1.115017
H	-3.970171	-0.035289	0.230912

Table S8.2.4: Cartesian coordinates of the MP2/aug-cc-pVDZ-PP optimized geometry of the XB complex between C_2F_3Br and TMA.

C_s	X	Y	Z
C_2F_3Br			
C	-1.871658	0.493138	0.000004
C	-2.793545	-0.481349	-0.000003
F	-2.504214	-1.780915	0.000006
F	-4.107730	-0.260063	-0.000019
F	-2.295355	1.781855	-0.000006
Br	-0.023389	0.229736	0.000026
TMA			
N	2.804891	-0.122529	0.000003
C	3.188330	-0.869845	-1.197024
H	2.688752	-1.849801	-1.195701
H	2.871020	-0.317593	-2.093777
H	4.286654	-1.033285	-1.252866
C	3.189517	-0.861142	1.202040
H	2.873085	-0.302403	2.095078
H	2.689949	-1.841084	1.208316
H	4.287897	-1.024170	1.257984
C	3.433423	1.197823	-0.005096
H	3.116095	1.753779	-0.899574
H	3.116972	1.760257	0.885634
H	4.543246	1.131600	-0.005400

Table S8.2.5: Cartesian coordinates of the MP2/aug-cc-pVDZ-PP optimized geometry of the lp···π complex between C_2F_3Br and TMA.

C_1	X	Y	Z
C_2F_3Br			
C	0.092482	1.225808	-0.517521
C	1.006428	0.713604	0.319356
F	1.108138	1.206880	1.576026
F	-0.704157	2.237191	-0.191199
F	-0.076426	0.820671	-1.769225
Br	2.131492	-0.705412	-0.089668
TMA			
N	-2.196447	-0.481178	0.096640
C	-2.065481	-1.724554	-0.658965
H	-2.212303	-1.523120	-1.730364
H	-1.055277	-2.137695	-0.518026
H	-2.806360	-2.491305	-0.339564
C	-1.971835	-0.733258	1.517759
H	-0.964703	-1.152553	1.665177
H	-2.040334	0.211663	2.077402
H	-2.712450	-1.447857	1.941149
C	-3.523294	0.094537	-0.107422
H	-3.604209	1.040932	0.447332
H	-3.674550	0.303648	-1.176771
H	-4.334695	-0.585548	0.235928

Table S8.2.6: Cartesian coordinates of the MP2/aug-cc-pVDZ-PP optimized geometry of the XB complex between C_2F_3I and TMA.

C_s	X	Y	Z
C_2F_3I			
C	-2.018743	-0.471605	0.000000
C	-2.946698	0.499011	-0.000010
F	-2.661927	1.801554	0.000003
F	-4.263056	0.282977	-0.000036
F	-2.460172	-1.762342	-0.000019
I	0.056658	-0.183454	0.000044
TMA			
N	2.872324	0.150203	0.000004
C	3.495052	-1.175526	-0.021184
H	3.176312	-1.745443	0.863689
H	3.173015	-1.718455	-0.921693
H	4.603546	-1.109746	-0.022232
C	3.261291	0.874592	1.212342
H	2.765064	1.855854	1.229319
H	2.942910	0.306024	2.098171
H	4.359599	1.030012	1.264549
C	3.256803	0.910905	-1.191342
H	2.935116	0.369320	-2.092748
H	2.760544	1.892193	-1.176836
H	4.354913	1.067926	-1.242916

Table S8.2.7: Cartesian coordinates of the MP2/aug-cc-pVDZ-PP optimized geometry of the lp···π complex between C_2F_3I and TMA.

C_1	X	Y	Z
C_2F_3I			
C	-0.427479	1.317701	-0.547708
C	0.531911	0.961501	0.321415
F	0.531437	1.522442	1.559304
F	-1.356208	2.228419	-0.277794
F	-0.519417	0.848572	-1.785614
I	1.989122	-0.460196	-0.045490
TMA			
N	-2.507759	-0.621448	0.101429
C	-2.273509	-1.876901	-0.607764
H	-2.434505	-1.728009	-1.685748
H	-1.233055	-2.200089	-0.452814
H	-2.949492	-2.689672	-0.259329
C	-2.263485	-0.800378	1.530400
H	-1.224754	-1.127845	1.690481
H	-2.410869	0.155944	2.054396
H	-2.942083	-1.557942	1.982161
C	-3.877985	-0.166458	-0.120355
H	-4.037960	0.789793	0.399184
H	-4.045659	-0.010487	-1.196337
H	-4.629804	-0.898851	0.249997

Table S8.3A: MP2/aug-cc-pVDZ vibrational frequencies, in cm^{-1}, infrared intensities, in km mol^{-1}, and Raman intensities, in $Å^4$ amu^{-1}, for the lp···π complex of C_2F_4 and TMA and both monomers, as well as the complexation shift Δν.

	Monomer			lp···π complex			
	Frequency	IR int.	Raman int.	Frequency	Δν	IR int.	Raman int.
C_2F_4							
ν_1 (A_g)	1920.1	0.0	10.3	1923.3	3.2	0.003	11.3
ν_2 (A_g)	773.9	0.0	11.2	770.6	-3.3	0.4	10.4
ν_3 (A_g)	389.0	0.0	2.0	388.1	-0.9	2.2	1
ν_4 (A_u)	201.7	0.0	0.0	210.0	8.3	0.0	0.02
ν_5 (B_{1g})	1332.0	0.0	0.3	1332.5	0.6	109.8	0.3
ν_6 (B_{1g})	550.0	0.0	2.1	549.6	-0.4	0.001	1.6
ν_7 (B_{1u})	416.4	3.8	0.0	418.9	2.6	4.9	0.4
ν_8 (B_{2g})	525.4	0.0	9.1	511.8	-13.6	6.2	19.2
ν_9 (B_{2u})	1328.2	409.7	0.0	1317.5	-10.6	232.5	0.2
ν_{10} (B_{2u})	209.0	4.6	0.0	209.3	0.3	3.7	0.009
ν_{11} (B_{3u})	1171.1	351.6	0.0	1167.0	-4.1	302.6	0.1
ν_{12} (B_{3u})	541.6	3.4	0.0	540.8	-0.9	3.6	0.2
TMA							
ν_1 (A_1)	3111.8	42.4	235.1	3111.4	-0.4	29.1	95.8
ν_2 (A_1)	2962.3	167.2	390.2	2969.1	6.9	175.2	431.7
ν_3 (A_1)	1499.0	23.4	0.4	1498.2	-0.8	26.1	0.3
ν_4 (A_1)	1464.0	1.6	2.3	1464.9	0.8	1.3	2.7
ν_5 (A_1)	1204.0	24.9	5.6	1206.2	2.3	24.0	5.7
ν_6 (A_1)	853.0	22.9	12.0	851.0	-2.0	30.1	10.0
ν_7 (A_1)	383.8	7.6	1.1	385.4	1.6	6.6	1.6
ν_8 (A_2)	3163.7	0.0	0.0	3159.5	-4.2	5.1	9.4
ν_9 (A_2)	1477.7	0.0	0.0	1478.0	0.2	0.0	0.002
ν_{10} (A_2)	1057.3	0.0	0.0	1057.5	0.2	0.03	0.008
ν_{11} (A_2)	243.9	0.0	0.0	240.6	-3.2	0.0004	0.004
ν_{12} (E)	3166.8	34.6	87.1	3163.8	-3.1	26.8	65.2
ν_{13} (E)	3111.1	26.1	27.8	3107.2	-3.9	28.7	65.8
ν_{14} (E)	2955.2	44.4	18.3	2962.8	7.6	43.8	24.9
ν_{15} (E)	1500.8	9.8	5.5	1501.5	0.7	11.1	5.7
ν_{16} (E)	1475.1	5.7	8.8	1474.0	-1.1	5.4	8.1
ν_{17} (E)	1421.1	0.7	1.6	1421.4	0.4	0.7	1.5
ν_{18} (E)	1303.4	14.9	1.7	1303.5	0.1	13.0	1.4
ν_{19} (E)	1115.9	9.1	0.4	1114.7	-1.2	6.8	0.5
ν_{20} (E)	1066.2	13.6	2.7	1066.1	-0.2	11.6	2.6
ν_{21} (E)	423.6	0.0	0.7	424.8	1.1	3.1	0.5
ν_{22} (E)	290.9	0.4	0.6	286.6	-4.3	0.4	0.5

Van der Waals vibrations: 9.7 cm^{-1}, 0.0002 km mol^{-1}, 0.03 $Å^4$ amu^{-1}, 21.7 cm^{-1}, 0.08 km mol^{-1}, 0.05 $Å^4$ amu^{-1}, 31.2 cm^{-1}, 0.1 km mol^{-1}, 0.02 $Å^4$ amu^{-1}, 56.6 cm^{-1}, 0.002 km mol^{-1}, 0.7 $Å^4$ amu^{-1}, 69.0 cm^{-1}, 0.2 km mol^{-1}, 0.6 $Å^4$ amu^{-1}, 69.5 cm^{-1}, 0.01 km mol^{-1}, 0.5 $Å^4$ amu^{-1}.

Table S8.3B: MP2/aug-cc-pVDZ vibrational frequencies, in cm^{-1}, infrared intensities, in km mol^{-1}, and Raman intensities, in $Å^4$ amu^{-1}, for the lp···π complex of C_2F_4 and TMA-d_9 and both monomers, as well as the complexation shift Δν.

	Monomer			lp···π complex			
	Frequency	IR int.	Raman int.	Frequency	Δν	IR int.	Raman int.
C_2F_4							
ν_1 (A_g)	1920.1	0.0	10.3	1923.3	3.1	0.005	11.5
ν_2 (A_g)	773.9	0.0	11.2	770.6	-3.3	0.2	9.7
ν_3 (A_g)	389.0	0.0	2.0	387.5	-1.4	0.05	1.6
ν_4 (A_u)	201.7	0.0	0.0	209.9	8.3	0.2	0.04
ν_5 (B_{1g})	1332.0	0.0	0.3	1332.8	0.8	113.2	0.2
ν_6 (B_{1g})	550.0	0.0	2.1	549.6	-0.4	0.0008	1.6
ν_7 (B_{1u})	416.4	3.8	0.0	423.2	6.8	9.6	0.2
ν_8 (B_{2g})	525.4	0.0	9.1	511.8	-13.6	6.3	19.2
ν_9 (B_{2u})	1328.2	409.7	0.0	1317.9	-10.3	234.2	0.1
ν_{10} (B_{2u})	209.0	4.6	0.0	209.4	0.3	3.7	0.03
ν_{11} (B_{3u})	1171.1	351.6	0.0	1167.5	-3.7	286.7	0.4
ν_{12} (B_{3u})	541.6	3.4	0.0	540.7	-0.9	3.6	0.2
TMA-d_9							
ν_1 (A_1)	2286.9	51.7	81.2	2285.9	-1.0	46.5	53.3
ν_2 (A_1)	2142.3	72.7	232.7	2146.1	3.8	75.3	246.4
ν_3 (A_1)	1151.7	0.2	5.9	1151.2	-0.5	8.3	4.5
ν_4 (A_1)	1079.2	12.6	0.2	1078.6	-0.6	15.2	0.2
ν_5 (A_1)	1018.9	33.5	3.4	1021.4	2.5	35.2	3.4
ν_6 (A_1)	756.9	12.4	9.6	755.4	-1.5	17.0	8.8
ν_7 (A_1)	323.0	4.6	0.8	326.0	3.1	6.3	0.8
ν_8 (A_2)	2345.4	0.0	0.0	2342.2	-3.2	1.7	3.6
ν_9 (A_2)	1067.7	0.0	0.0	1067.4	-0.3	0.004	0.007
ν_{10} (A_2)	801.3	0.0	0.0	801.8	0.6	0.001	0.0009
ν_{11} (A_2)	173.1	0.0	0.0	170.8	-2.3	0.001	0.002
ν_{12} (E)	2349.0	17.4	46.2	2346.6	-2.4	13.9	35.1
ν_{13} (E)	2287.5	8.1	21.2	2287.6	0.1	10.6	25.9
ν_{14} (E)	2135.6	36.1	4.2	2139.6	4.1	33.9	6.3
ν_{15} (E)	1252.4	33.4	1.0	1252.7	0.4	29.9	0.9
ν_{16} (E)	1078.6	2.1	2.4	1078.1	-0.5	4.2	2.4
ν_{17} (E)	1073.1	0.2	0.4	1073.2	0.1	0.5	0.4
ν_{18} (E)	1063.4	1.6	3.7	1062.7	-0.7	0.3	3.4
ν_{19} (E)	886.2	7.4	2.6	886.1	-0.1	6.4	2.4
ν_{20} (E)	839.0	0.03	1.0	838.4	-0.6	0.01	1.2
ν_{21} (E)	352.0	0.007	0.5	351.1	-0.9	0.01	0.5
ν_{22} (E)	210.6	0.2	0.3	207.6	-3.0	0.1	0.3

Van der Waals vibrations: 8.8 cm^{-1}, 0.0001 km mol^{-1}, 0.04 $Å^4$ amu^{-1}, 19.4 cm^{-1}, 0.1 km mol^{-1}, 0.04 $Å^4$ amu^{-1}, 28.2 cm^{-1}, 0.1 km mol^{-1}, 0.01 $Å^4$ amu^{-1}, 53.9 cm^{-1}, 0.002 km mol^{-1}, 0.6 $Å^4$ amu^{-1}, 66.3 cm^{-1}, 0.2 km mol^{-1}, 0.6 $Å^4$ amu^{-1}, 66.8 cm^{-1}, 0.02 km mol^{-1}, 0.4 $Å^4$ amu^{-1}.

Table S8.4A: MP2/aug-cc-pVDZ vibrational frequencies, in cm^{-1}, infrared intensities, in km mol^{-1}, and Raman intensities, in $Å^4$ amu^{-1}, for the XB complex of C_2F_3Cl and TMA and both monomers, as well as the complexation shift Δν.

	Monomer			XB complex			
	Frequency	IR int.	Raman int.	Frequency	Δν	IR int.	Raman int.
C_2F_3Cl							
ν_1 (A')	1843.6	50.2	13.4	1838.4	-5.3	63.0	12.3
ν_2 (A')	1323.6	174.3	0.4	1314.9	-8.8	168.5	0.4
ν_3 (A')	1203.3	184.4	0.6	1195.1	-8.1	184.2	0.3
ν_4 (A')	1062.6	234.1	1.9	1058.7	-3.9	240.0	0.8
ν_5 (A')	687.7	2.1	9.2	683.1	-4.7	0.7	17.7
ν_6 (A')	511.3	1.0	1.1	512.0	0.7	0.9	1.5
ν_7 (A')	462.5	1.3	2.3	456.6	-5.8	6.7	11.7
ν_8 (A')	336.8	1.3	1.9	339.4	2.6	1.1	1.9
ν_9 (A')	184.9	2.6	0.4	193.5	8.6	4.1	0.4
ν_{10} (A")	544.5	2.2	5.8	543.1	-1.4	1.4	6.2
ν_{11} (A")	368.9	1.0	0.1	378.0	9.0	1.4	0.2
ν_{12} (A")	172.0	0.1	0.01	179.2	7.1	0.03	0.007
TMA							
ν_1 (A_1)	3111.8	42.4	235.1	3112.3	0.4	33.2	126.5
ν_2 (A_1)	2962.3	167.2	390.2	2970.8	8.5	196.0	473.3
ν_3 (A_1)	1499.0	23.4	0.4	1498.7	-0.4	26.0	0.4
ν_4 (A_1)	1464.0	1.6	2.3	1464.8	0.8	0.5	6.0
ν_5 (A_1)	1204.0	24.9	5.6	1207.3	3.4	21.7	8.3
ν_6 (A_1)	853.0	22.9	12.0	850.9	-2.1	41.8	10.6
ν_7 (A_1)	383.8	7.6	1.1	389.6	5.8	15.1	1.0
ν_8 (A_2)	3163.7	0.0	0.0	3162.4	-1.3	1.4	2.9
ν_9 (A_2)	1477.7	0.0	0.0	1477.6	-0.2	0.004	0.003
ν_{10} (A_2)	1057.3	0.0	0.0	1058.0	0.7	0.2	0.001
ν_{11} (A_2)	243.9	0.0	0.0	239.4	-4.5	0.0001	0.001
ν_{12} (E)	3166.8	34.6	87.1	3165.8	-1.0	28.8	70.0
ν_{13} (E)	3111.1	26.1	27.8	3110.8	-0.3	26.2	56.5
ν_{14} (E)	2955.2	44.4	18.3	2964.8	9.6	42.1	25.8
ν_{15} (E)	1500.8	9.8	5.5	1501.2	0.4	11.6	6.1
ν_{16} (E)	1475.1	5.7	8.8	1474.3	-0.8	3.7	8.5
ν_{17} (E)	1421.1	0.7	1.6	1421.5	0.5	0.2	1.7
ν_{18} (E)	1303.4	14.9	1.7	1303.1	-0.3	13.1	1.4
ν_{19} (E)	1115.9	9.1	0.4	1114.9	-1.0	8.1	0.5
ν_{20} (E)	1066.2	13.6	2.7	1065.5	-0.7	12.4	2.7
ν_{21} (E)	423.6	0.006	0.7	422.6	-1.1	0.03	0.7
ν_{22} (E)	290.9	0.4	0.6	286.4	-4.6	0.4	0.6

Van der Waals vibrations: 0.7 cm^{-1}, 0.01 km mol^{-1}, 0.2 $Å^4$ amu^{-1}, 10.6 cm^{-1}, 0.1 km mol^{-1}, 0.1 $Å^4$ amu^{-1}, 18.7 cm^{-1}, 0.05 km mol^{-1}, 0.5 $Å^4$ amu^{-1}, 55.5 cm^{-1}, 0.2 km mol^{-1}, 0.1 $Å^4$ amu^{-1}, 67.5 cm^{-1}, 0.05 km mol^{-1}, 0.2 $Å^4$ amu^{-1}, 67.7 cm^{-1}, 0.5 km mol^{-1}, 1.0 $Å^4$ amu^{-1}.

Table S8.4B: MP2/aug-cc-pVDZ vibrational frequencies, in cm^{-1}, infrared intensities, in km mol^{-1}, and Raman intensities, in $Å^4$ amu^{-1}, for the XB complex of C_2F_3Cl and TMA-d_9 and both monomers, as well as the complexation shift Δν.

	Monomer			XB complex			
	Frequency	IR int.	Raman int.	Frequency	Δν	IR int.	Raman int.
C_2F_3Cl							
ν_1 (A')	1843.6	50.2	13.4	1838.4	-5.3	63.2	12.4
ν_2 (A')	1323.6	174.3	0.4	1314.9	-8.8	167.5	0.5
ν_3 (A')	1203.3	184.4	0.6	1195.2	-8.1	181.6	0.3
ν_4 (A')	1062.6	234.1	1.9	1058.6	-4.0	239.4	0.7
ν_5 (A')	687.7	2.1	9.2	683.1	-4.7	0.7	17.7
ν_6 (A')	511.3	1.0	1.1	512.0	0.7	0.9	1.5
ν_7 (A')	462.5	1.3	2.3	456.6	-5.9	6.4	11.7
ν_8 (A')	336.8	1.3	1.9	339.2	2.4	1.3	1.9
ν_9 (A')	184.9	2.6	0.4	193.4	8.5	4.0	0.4
ν_{10} (A")	544.5	2.2	5.8	543.1	-1.4	1.4	6.2
ν_{11} (A")	368.9	1.0	0.1	378.1	9.2	1.4	0.2
ν_{12} (A")	172.0	0.1	0.01	179.0	7.0	0.03	0.009
TMA-d_9							
ν_1 (A_1)	2286.9	51.7	81.2	2288.6	1.6	52.6	72.3
ν_2 (A_1)	2142.3	72.7	232.7	2147.2	4.9	85.5	263.2
ν_3 (A_1)	1151.7	0.2	5.9	1151.0	-0.7	1.6	7.6
ν_4 (A_1)	1079.2	12.6	0.2	1079.1	-0.1	12.4	0.2
ν_5 (A_1)	1018.9	33.5	3.4	1023.0	4.2	42.3	4.5
ν_6 (A_1)	756.9	12.4	9.6	755.4	-1.5	23.3	8.6
ν_7 (A_1)	323.0	4.6	0.8	328.9	5.9	10.2	0.8
ν_8 (A_2)	2345.4	0.0	0.0	2344.5	-0.9	0.4	0.8
ν_9 (A_2)	1067.7	0.0	0.0	1067.3	-0.5	0.001	0.0001
ν_{10} (A_2)	801.3	0.0	0.0	802.1	0.8	0.0001	0.0007
ν_{11} (A_2)	173.1	0.0	0.0	169.9	-3.2	0.0001	0.0006
ν_{12} (E)	2349.0	17.4	46.2	2348.2	-0.8	14.6	37.5
ν_{13} (E)	2287.5	8.1	21.2	2289.4	1.9	7.2	22.5
ν_{14} (E)	2135.6	36.1	4.2	2141.0	5.4	33.2	7.0
ν_{15} (E)	1252.4	33.4	1.0	1251.3	-1.0	31.2	0.9
ν_{16} (E)	1078.6	2.1	2.4	1078.1	-0.5	3.0	2.6
ν_{17} (E)	1073.1	0.2	0.4	1073.4	0.3	0.3	0.4
ν_{18} (E)	1063.4	1.6	3.7	1063.0	-0.5	0.7	3.6
ν_{19} (E)	886.2	7.4	2.6	886.2	0.0	7.0	2.5
ν_{20} (E)	839.0	0.03	1.0	838.4	-0.6	0.01	1.2
ν_{21} (E)	352.0	0.007	0.5	351.3	-0.7	0.01	0.5
ν_{22} (E)	210.6	0.2	0.3	207.4	-3.1	0.2	0.3

Van der Waals vibrations: 0.7 cm^{-1}, 0.01 km mol^{-1}, 0.3 $Å^4$ amu^{-1}, 9.5 cm^{-1}, 0.1 km mol^{-1}, 0.1 $Å^4$ amu^{-1}, 16.8 cm^{-1}, 0.03 km mol^{-1}, 0.5 $Å^4$ amu^{-1}, 52.3 cm^{-1}, 0.1 km mol^{-1}, 0.1 $Å^4$ amu^{-1}, 64.6 cm^{-1}, 0.1 km mol^{-1}, 0.4 $Å^4$ amu^{-1}, 64.6 cm^{-1}, 0.3 km mol^{-1}, 0.8 $Å^4$ amu^{-1}.

Table S8.5A: MP2/aug-cc-pVDZ vibrational frequencies, in cm^{-1}, infrared intensities, in km mol^{-1}, and Raman intensities, in $Å^4$ amu^{-1}, for the lp···π complex of C_2F_3Cl and TMA and both monomers, as well as the complexation shift Δν.

	Monomer			lp···π complex			
	Frequency	IR int.	Raman int.	Frequency	Δν	IR int.	Raman int.
C_2F_3Cl							
ν_1 (A')	1843.6	50.2	13.4	1847.6	4.0	46.7	13.7
ν_2 (A')	1323.6	174.3	0.4	1326.7	3.1	142.4	0.4
ν_3 (A')	1203.3	184.4	0.6	1195.3	-7.9	159.9	0.4
ν_4 (A')	1062.6	234.1	1.9	1060.7	-1.9	172.2	2.0
ν_5 (A')	687.7	2.1	9.2	685.6	-2.1	2.5	8.9
ν_6 (A')	511.3	1.0	1.1	511.4	0.1	0.6	1.0
ν_7 (A')	462.5	1.3	2.3	461.5	-1.0	1.2	2.1
ν_8 (A')	336.8	1.3	1.9	335.7	-1.1	1.1	1.5
ν_9 (A')	184.9	2.6	0.4	184.7	-0.1	1.4	0.3
ν_{10} (A")	544.5	2.2	5.8	535.4	-9.1	18.8	18.3
ν_{11} (A")	368.9	1.0	0.1	372.8	3.8	0.6	0.2
ν_{12} (A")	172.0	0.1	0.01	186.1	14.0	0.7	0.1
TMA							
ν_1 (A_1)	3111.8	42.4	235.1	3111.4	-0.4	29.0	98.3
ν_2 (A_1)	2962.3	167.2	390.2	2969.4	7.1	175.8	433.1
ν_3 (A_1)	1499.0	23.4	0.4	1498.0	-1.1	26.0	0.4
ν_4 (A_1)	1464.0	1.6	2.3	1464.4	0.4	1.6	3.0
ν_5 (A_1)	1204.0	24.9	5.6	1206.7	2.7	24.0	6.0
ν_6 (A_1)	853.0	22.9	12.0	850.7	-2.3	29.9	10.0
ν_7 (A_1)	383.8	7.6	1.1	389.9	6.1	13.4	0.9
ν_8 (A_2)	3163.7	0.0	0.0	3158.8	-4.8	9.6	19.7
ν_9 (A_2)	1477.7	0.0	0.0	1477.8	0.04	0.03	0.01
ν_{10} (A_2)	1057.3	0.0	0.0	1057.3	0.04	0.02	0.01
ν_{11} (A_2)	243.9	0.0	0.0	242.3	-1.5	0.01	0.02
ν_{12} (E)	3166.8	34.6	87.1	3164.3	-2.6	23.6	57.9
ν_{13} (E)	3111.1	26.1	27.8	3107.8	-3.3	27.6	59.3
ν_{14} (E)	2955.2	44.4	18.3	2963.0	7.8	44.6	29.0
ν_{15} (E)	1500.8	9.8	5.5	1501.3	0.5	11.1	5.9
ν_{16} (E)	1475.1	5.7	8.8	1473.6	-1.5	4.3	8.0
ν_{17} (E)	1421.1	0.7	1.6	1421.1	0.0	0.4	1.6
ν_{18} (E)	1303.4	14.9	1.7	1302.8	-0.6	10.9	1.4
ν_{19} (E)	1115.9	9.1	0.4	1114.7	-1.3	8.1	0.5
ν_{20} (E)	1066.2	13.6	2.7	1065.5	-0.7	21.1	2.4
ν_{21} (E)	423.6	0.006	0.7	422.5	-1.1	0.04	0.5
ν_{22} (E)	290.9	0.4	0.6	288.7	-2.2	0.4	0.5

Van der Waals vibrations: 9.7 cm^{-1}, 0.02 km mol^{-1}, 0.08 $Å^4$ amu^{-1}, 34.5 cm^{-1}, 0.1 km mol^{-1}, 0.2 $Å^4$ amu^{-1}, 46.3 cm^{-1}, 0.1 km mol^{-1}, 0.3 $Å^4$ amu^{-1}, 55.4 cm^{-1}, 0.1 km mol^{-1}, 0.6 $Å^4$ amu^{-1}, 68.5 cm^{-1}, 0.04 km mol^{-1}, 0.3 $Å^4$ amu^{-1}, 76.2 cm^{-1}, 0.2 km mol^{-1}, 1.1 $Å^4$ amu^{-1}.

Table S8.5B: MP2/aug-cc-pVDZ vibrational frequencies, in cm^{-1}, infrared intensities, in km mol^{-1}, and Raman intensities, in $Å^4$ amu^{-1}, for the lp···π complex of C_2F_3Cl and TMA-d_9 and both monomers, as well as the complexation shift Δν.

	Monomer			lp···π complex			
	Frequency	IR int.	Raman int.	Frequency	Δν	IR int.	Raman int.
C_2F_3Cl							
ν_1 (A')	1843.6	50.2	13.4	1847.6	3.9	46.7	13.8
ν_2 (A')	1323.6	174.3	0.4	1327.1	3.5	140.5	0.3
ν_3 (A')	1203.3	184.4	0.6	1195.6	-7.6	156.4	0.4
ν_4 (A')	1062.6	234.1	1.9	1059.7	-2.9	154.2	2.0
ν_5 (A')	687.7	2.1	9.2	685.6	-2.1	2.6	8.9
ν_6 (A')	511.3	1.0	1.1	511.3	0.0	0.6	1.0
ν_7 (A')	462.5	1.3	2.3	461.5	-1.0	1.2	2.1
ν_8 (A')	336.8	1.3	1.9	335.8	-1.0	1.2	1.4
ν_9 (A')	184.9	2.6	0.4	184.7	-0.2	1.3	0.3
ν_{10} (A")	544.5	2.2	5.8	535.4	-9.1	18.9	18.3
ν_{11} (A")	368.9	1.0	0.1	375.3	6.3	3.8	0.2
ν_{12} (A")	172.0	0.1	0.01	185.9	13.9	0.8	0.1
TMA-d_9							
ν_1 (A_1)	2286.9	51.7	81.2	2285.7	-1.2	32.2	36.5
ν_2 (A_1)	2142.3	72.7	232.7	2146.1	3.8	76.6	248.5
ν_3 (A_1)	1151.7	0.2	5.9	1151.0	-0.7	0.3	5.2
ν_4 (A_1)	1079.2	12.6	0.2	1078.6	-0.6	11.0	0.9
ν_5 (A_1)	1018.9	33.5	3.4	1021.9	3.0	35.3	3.7
ν_6 (A_1)	756.9	12.4	9.6	755.2	-1.6	16.7	8.0
ν_7 (A_1)	323.0	4.6	0.8	327.5	4.5	6.2	0.8
ν_8 (A_2)	2345.4	0.0	0.0	2342.0	-3.5	3.2	6.5
ν_9 (A_2)	1067.7	0.0	0.0	1067.3	-0.4	0.04	0.004
ν_{10} (A_2)	801.3	0.0	0.0	801.7	0.5	0.002	0.004
ν_{11} (A_2)	173.1	0.0	0.0	172.0	-1.1	0.008	0.01
ν_{12} (E)	2349.0	17.4	46.2	2346.9	-2.1	12.8	32.5
ν_{13} (E)	2287.5	8.1	21.2	2288.2	0.7	17.6	32.6
ν_{14} (E)	2135.6	36.1	4.2	2139.7	4.2	33.3	7.1
ν_{15} (E)	1252.4	33.4	1.0	1251.5	-0.8	30.3	0.9
ν_{16} (E)	1078.6	2.1	2.4	1078.2	-0.4	3.4	2.2
ν_{17} (E)	1073.1	0.2	0.4	1073.0	-0.1	0.6	0.5
ν_{18} (E)	1063.4	1.6	3.7	1062.7	-0.7	20.6	3.0
ν_{19} (E)	886.2	7.4	2.6	886.0	-0.2	6.2	2.3
ν_{20} (E)	839.0	0.03	1.0	838.2	-0.8	0.01	1.2
ν_{21} (E)	352.0	0.007	0.5	350.8	-1.2	0.02	0.4
ν_{22} (E)	210.6	0.2	0.3	209.1	-1.4	0.2	0.3

Van der Waals vibrations: 8.8 cm^{-1}, 0.02 km mol^{-1}, 0.1 $Å^4$ amu^{-1}, 31.4 cm^{-1}, 0.1 km mol^{-1}, 0.2 $Å^4$ amu^{-1}, 42.8 cm^{-1}, 0.1 km mol^{-1}, 0.2 $Å^4$ amu^{-1}, 51.9 cm^{-1}, 0.1 km mol^{-1}, 0.7 $Å^4$ amu^{-1}, 64.8 cm^{-1}, 0.03 km mol^{-1}, 0.4 $Å^4$ amu^{-1}, 72.3 cm^{-1}, 0.2 km mol^{-1}, 1.1 $Å^4$ amu^{-1}.

Table S8.6A: MP2/aug-cc-pVDZ-PP vibrational frequencies, in cm^{-1}, infrared intensities, in km mol^{-1}, and Raman intensities, in $Å^4$ amu^{-1}, for the XB complex of C_2F_3Br and TMA and both monomers, as well as the complexation shift Δν.

	Monomer			XB complex			
	Frequency	IR int.	Raman int.	Frequency	Δν	IR int.	Raman int.
C_2F_3Br							
ν_1 (A')	1827.9	81.1	14.6	1819.1	-8.7	120.2	11.0
ν_2 (A')	1318.6	166.4	0.7	1305.8	-12.8	164.6	1.1
ν_3 (A')	1186.2	174.2	0.4	1173.2	-12.9	166.7	1.5
ν_4 (A')	1029.4	207.2	2.7	1023.2	-6.2	198.3	0.9
ν_5 (A')	659.6	3.5	7.4	653.9	-5.7	0.9	17.4
ν_6 (A')	504.0	1.5	1.0	504.4	0.4	1.4	1.2
ν_7 (A')	371.8	0.5	3.1	357.2	-14.6	9.2	22.1
ν_8 (A')	313.4	2.5	1.3	313.2	-0.3	3.5	1.5
ν_9 (A')	161.2	1.6	0.6	171.1	9.9	4.0	1.1
ν_{10} (A'')	554.1	2.9	4.9	553.7	-0.4	1.9	5.6
ν_{11} (A'')	359.9	0.5	0.1	370.8	10.9	0.8	0.3
ν_{12} (A'')	159.3	0.1	0.01	168.0	8.6	0.05	0.01
TMA							
ν_1 (A_1)	3111.8	42.4	235.1	3114.9	3.1	42.9	181.3
ν_2 (A_1)	2962.3	167.2	390.2	2980.2	17.9	205.0	504.4
ν_3 (A_1)	1499.0	23.4	0.4	1499.2	0.2	26.1	0.7
ν_4 (A_1)	1464.0	1.6	2.3	1464.7	0.7	0.0	12.7
ν_5 (A_1)	1204.0	24.9	5.6	1211.3	7.3	20.7	13.7
ν_6 (A_1)	853.0	22.9	12.0	849.0	-4.0	55.2	10.8
ν_7 (A_1)	383.8	7.6	1.1	398.4	14.7	23.0	1.1
ν_8 (A_2)	3163.7	0.0	0.0	3164.9	1.3	0.0003	0.0005
ν_9 (A_2)	1477.7	0.0	0.0	1477.0	-0.7	0.0001	0.001
ν_{10} (A_2)	1057.3	0.0	0.0	1058.6	1.3	0.0001	0.0001
ν_{11} (A_2)	243.9	0.0	0.0	236.4	-7.5	0.0	0.0001
ν_{12} (E)	3166.8	34.6	87.1	3168.1	1.2	25.4	63.5
ν_{13} (E)	3111.1	26.1	27.8	3114.5	3.4	15.0	20.1
ν_{14} (E)	2955.2	44.4	18.3	2975.0	19.8	38.3	28.2
ν_{15} (E)	1500.8	9.8	5.5	1501.2	0.4	13.0	6.0
ν_{16} (E)	1475.1	5.7	8.8	1474.2	-0.9	2.6	8.3
ν_{17} (E)	1421.1	0.7	1.6	1421.9	0.9	0.01	1.7
ν_{18} (E)	1303.4	14.9	1.7	1302.1	-1.3	9.7	1.2
ν_{19} (E)	1115.9	9.1	0.4	1114.5	-1.4	7.6	0.7
ν_{20} (E)	1066.2	13.6	2.7	1063.7	-2.6	13.1	2.7
ν_{21} (E)	423.6	0.006	0.7	421.8	-1.8	0.01	0.7
ν_{22} (E)	290.9	0.4	0.6	284.4	-6.6	0.4	0.6

Van der Waals vibrations: 1.2 cm^{-1}, 0.03 km mol^{-1}, 0.2 $Å^4$ amu^{-1}, 24.1 cm^{-1}, 0.06 km mol^{-1}, 0.09 $Å^4$ amu^{-1}, 27.8 cm^{-1}, 0.03 km mol^{-1}, 0.4 $Å^4$ amu^{-1}, 75.1 cm^{-1}, 1.1 km mol^{-1}, 0.7 $Å^4$ amu^{-1}, 79.8 cm^{-1}, 1.5 km mol^{-1}, 1.4 $Å^4$ amu^{-1}, 82.4 cm^{-1}, 0.002 km mol^{-1}, 0.004 $Å^4$ amu^{-1}.

Table S8.6B: MP2/aug-cc-pVDZ-PP vibrational frequencies, in cm^{-1}, infrared intensities, in km mol^{-1}, and Raman intensities, in $Å^4$ amu^{-1}, for the XB complex of C_2F_3Br and TMA-d_9 and both monomers, as well as the complexation shift Δν.

	Monomer			XB complex			
	Frequency	IR int.	Raman int.	Frequency	Δν	IR int.	Raman int.
C_2F_3Br							
ν_1 (A')	1827.9	81.1	14.6	1819.1	-8.8	120.7	11.1
ν_2 (A')	1318.6	166.4	0.7	1305.8	-12.9	159.8	1.1
ν_3 (A')	1186.2	174.2	0.4	1173.2	-12.9	166.7	1.4
ν_4 (A')	1029.4	207.2	2.7	1023.1	-6.3	219.4	1.3
ν_5 (A')	659.6	3.5	7.4	653.9	-5.7	0.9	17.4
ν_6 (A')	504.0	1.5	1.0	504.4	0.4	1.4	1.2
ν_7 (A')	371.8	0.5	3.1	357.5	-14.3	5.7	21.0
ν_8 (A')	313.4	2.5	1.3	313.0	-0.4	3.6	1.5
ν_9 (A')	161.2	1.6	0.6	170.7	9.5	4.0	1.1
ν_{10} (A")	554.1	2.9	4.9	553.7	-0.4	1.9	5.6
ν_{11} (A")	359.9	0.5	0.1	371.5	11.6	0.8	0.3
ν_{12} (A")	159.3	0.1	0.01	167.6	8.3	0.04	0.009
TMA-d_9							
ν_1 (A_1)	2286.9	51.7	81.2	2292.8	5.8	51.9	89.6
ν_2 (A_1)	2142.3	72.7	232.7	2152.6	10.4	90.2	265.8
ν_3 (A_1)	1151.7	0.2	5.9	1149.5	-2.2	4.7	11.9
ν_4 (A_1)	1079.2	12.6	0.2	1079.6	0.4	17.2	0.3
ν_5 (A_1)	1018.9	33.5	3.4	1028.2	9.3	21.2	6.6
ν_6 (A_1)	756.9	12.4	9.6	754.0	-2.9	31.0	8.7
ν_7 (A_1)	323.0	4.6	0.8	336.5	13.6	19.6	2.1
ν_8 (A_2)	2345.4	0.0	0.0	2346.4	1.0	0.0	0.0002
ν_9 (A_2)	1067.7	0.0	0.0	1066.7	-1.1	0.0	0.0005
ν_{10} (A_2)	801.3	0.0	0.0	802.5	1.3	0.0	0.0
ν_{11} (A_2)	173.1	0.0	0.0	167.7	-5.4	0.0007	0.0003
ν_{12} (E)	2349.0	17.4	46.2	2350.1	1.1	12.7	33.7
ν_{13} (E)	2287.5	8.1	21.2	2293.6	6.1	4.0	17.7
ν_{14} (E)	2135.6	36.1	4.2	2147.0	11.5	30.0	8.4
ν_{15} (E)	1252.4	33.4	1.0	1249.0	-3.4	28.9	0.8
ν_{16} (E)	1078.6	2.1	2.4	1077.7	-0.9	3.3	2.6
ν_{17} (E)	1073.1	0.2	0.4	1073.8	0.6	0.3	0.4
ν_{18} (E)	1063.4	1.6	3.7	1062.9	-0.5	0.5	3.3
ν_{19} (E)	886.2	7.4	2.6	886.0	-0.2	6.6	2.5
ν_{20} (E)	839.0	0.03	1.0	837.6	-1.3	0.001	1.4
ν_{21} (E)	352.0	0.007	0.5	350.7	-1.3	0.003	0.5
ν_{22} (E)	210.6	0.2	0.3	206.1	-4.4	0.2	0.3

Van der Waals vibrations: 1.1 cm^{-1}, 0.03 km mol^{-1}, 0.3 $Å^4$ amu^{-1}, 22.2 cm^{-1}, 0.03 km mol^{-1}, 0.1 $Å^4$ amu^{-1}, 25.5 cm^{-1}, 0.01 km mol^{-1}, 0.4 $Å^4$ amu^{-1}, 69.7 cm^{-1}, 0.5 km mol^{-1}, 0.4 $Å^4$ amu^{-1}, 74.7 cm^{-1}, 1.7 km mol^{-1}, 1.5 $Å^4$ amu^{-1}, 76.7 cm^{-1}, 0.0 km mol^{-1}, 0.002 $Å^4$ amu^{-1}.

Table S8.7A: MP2/aug-cc-pVDZ-PP vibrational frequencies, in cm^{-1}, infrared intensities, in km mol^{-1}, and Raman intensities, in $Å^4$ amu^{-1}, for the lp···π complex of C_2F_3Br and TMA and both monomers, as well as the complexation shift Δν.

	Monomer			lp···π complex			
	Frequency	IR int.	Raman int.	Frequency	Δν	IR int.	Raman int.
C_2F_3Br							
ν_1 (A')	1827.9	81.1	14.6	1831.9	4.0	75.6	15.6
ν_2 (A')	1318.6	166.4	0.7	1322.0	3.4	137.2	0.6
ν_3 (A')	1186.2	174.2	0.4	1179.0	-7.1	150.9	0.4
ν_4 (A')	1029.4	207.2	2.7	1028.2	-1.2	168.4	2.1
ν_5 (A')	659.6	3.5	7.4	658.2	-1.4	3.8	7.2
ν_6 (A')	504.0	1.5	1.0	504.1	0.1	1.0	0.8
ν_7 (A')	371.8	0.5	3.1	372.3	0.5	0.6	2.3
ν_8 (A')	313.4	2.5	1.3	312.4	-1.0	2.1	1.0
ν_9 (A')	161.2	1.6	0.6	161.4	0.2	1.3	0.5
ν_{10} (A")	554.1	2.9	4.9	544.0	-10.0	20.8	18.2
ν_{11} (A")	359.9	0.5	0.1	364.0	4.1	0.7	0.7
ν_{12} (A")	159.3	0.1	0.01	176.5	17.1	0.2	0.05
TMA							
ν_1 (A_1)	3111.8	42.4	235.1	3111.4	-0.5	28.6	97.0
ν_2 (A_1)	2962.3	167.2	390.2	2968.9	6.6	178.6	437.9
ν_3 (A_1)	1499.0	23.4	0.4	1497.9	-1.2	25.9	0.4
ν_4 (A_1)	1464.0	1.6	2.3	1464.3	0.2	1.9	3.2
ν_5 (A_1)	1204.0	24.9	5.6	1206.5	2.6	24.1	6.2
ν_6 (A_1)	853.0	22.9	12.0	850.7	-2.3	30.1	9.9
ν_7 (A_1)	383.8	7.6	1.1	389.5	5.8	12.4	0.9
ν_8 (A_2)	3163.7	0.0	0.0	3158.6	-5.0	9.5	19.7
ν_9 (A_2)	1477.7	0.0	0.0	1477.6	-0.2	0.03	0.008
ν_{10} (A_2)	1057.3	0.0	0.0	1057.3	0.0	0.1	0.01
ν_{11} (A_2)	243.9	0.0	0.0	242.4	-1.5	0.02	0.03
ν_{12} (E)	3166.8	34.6	87.1	3164.2	-2.7	23.5	57.9
ν_{13} (E)	3111.1	26.1	27.8	3107.6	-3.4	27.7	59.4
ν_{14} (E)	2955.2	44.4	18.3	2962.5	7.3	44.8	29.9
ν_{15} (E)	1500.8	9.8	5.5	1501.1	0.3	10.9	6.0
ν_{16} (E)	1475.1	5.7	8.8	1473.5	-1.6	4.1	8.0
ν_{17} (E)	1421.1	0.7	1.6	1420.9	-0.2	0.4	1.6
ν_{18} (E)	1303.4	14.9	1.7	1302.7	-0.7	10.3	1.4
ν_{19} (E)	1115.9	9.1	0.4	1114.6	-1.3	7.6	0.5
ν_{20} (E)	1066.2	13.6	2.7	1065.5	-0.8	12.6	2.5
ν_{21} (E)	423.6	0.006	0.7	422.5	-1.1	0.04	0.6
ν_{22} (E)	290.9	0.4	0.6	288.7	-2.2	0.4	0.5

Van der Waals vibrations: 12.7 cm^{-1}, 0.02 km mol^{-1}, 0.06 $Å^4$ amu^{-1}, 33.3 cm^{-1}, 0.1 km mol^{-1}, 0.3 $Å^4$ amu^{-1}, 45.6 cm^{-1}, 0.08 km mol^{-1}, 0.3 $Å^4$ amu^{-1}, 52.8 cm^{-1}, 0.2 km mol^{-1}, 0.3 $Å^4$ amu^{-1}, 68.6 cm^{-1}, 0.06 km mol^{-1}, 0.3 $Å^4$ amu^{-1}, 77.6 cm^{-1}, 0.1 km mol^{-1}, 1.3 $Å^4$ amu^{-1}.

Table S8.7B MP2/aug-cc-pVDZ-PP vibrational frequencies, in cm^{-1}, infrared intensities, in km mol^{-1}, and Raman intensities, in $Å^4$ amu^{-1}, for the lp···π complex of C_2F_3Br and TMA-d_9 and both monomers, as well as the complexation shift Δν.

	Monomer			lp···π complex			
	Frequency	IR int.	Raman int.	Frequency	Δν	IR int.	Raman int.
C_2F_3Br							
ν_1 (A')	1827.9	81.1	14.6	1831.9	4.0	75.5	15.6
ν_2 (A')	1318.6	166.4	0.7	1322.3	3.7	134.1	0.6
ν_3 (A')	1186.2	174.2	0.4	1179.4	-6.8	147.8	0.4
ν_4 (A')	1029.4	207.2	2.7	1028.1	-1.3	170.2	1.9
ν_5 (A')	659.6	3.5	7.4	658.2	-1.4	3.9	7.2
ν_6 (A')	504.0	1.5	1.0	504.1	0.1	1.0	0.8
ν_7 (A')	371.8	0.5	3.1	372.5	0.7	0.9	2.4
ν_8 (A')	313.4	2.5	1.3	312.4	-1.0	2.1	1.0
ν_9 (A')	161.2	1.6	0.6	161.4	0.2	1.3	0.5
ν_{10} (A")	554.1	2.9	4.9	544.0	-10.1	20.9	18.2
ν_{11} (A")	359.9	0.5	0.1	366.1	6.2	2.4	0.5
ν_{12} (A")	159.3	0.1	0.01	176.3	16.9	0.2	0.04
TMA-d_9							
ν_1 (A_1)	2286.9	51.7	81.2	2285.6	-1.3	32.5	35.9
ν_2 (A_1)	2142.3	72.7	232.7	2145.8	3.5	78.1	251.3
ν_3 (A_1)	1151.7	0.2	5.9	1150.8	-0.9	0.5	5.4
ν_4 (A_1)	1079.2	12.6	0.2	1078.5	-0.7	14.8	0.4
ν_5 (A_1)	1018.9	33.5	3.4	1021.7	2.8	37.2	3.8
ν_6 (A_1)	756.9	12.4	9.6	755.2	-1.6	16.9	8.0
ν_7 (A_1)	323.0	4.6	0.8	327.6	4.7	6.3	0.7
ν_8 (A_2)	2345.4	0.0	0.0	2341.8	-3.6	3.1	6.5
ν_9 (A_2)	1067.7	0.0	0.0	1067.2	-0.5	0.03	0.004
ν_{10} (A_2)	801.3	0.0	0.0	801.7	0.4	0.002	0.005
ν_{11} (A_2)	173.1	0.0	0.0	172.0	-1.1	0.01	0.02
ν_{12} (E)	2349.0	17.4	46.2	2346.8	-2.2	12.7	32.5
ν_{13} (E)	2287.5	8.1	21.2	2288.1	0.6	17.6	32.7
ν_{14} (E)	2135.6	36.1	4.2	2139.4	3.9	33.2	7.4
ν_{15} (E)	1252.4	33.4	1.0	1251.5	-0.9	29.4	0.9
ν_{16} (E)	1078.6	2.1	2.4	1077.9	-0.7	1.9	2.5
ν_{17} (E)	1073.1	0.2	0.4	1072.9	-0.3	0.3	0.5
ν_{18} (E)	1063.4	1.6	3.7	1062.3	-1.1	1.1	3.3
ν_{19} (E)	886.2	7.4	2.6	886.0	-0.2	6.1	2.3
ν_{20} (E)	839.0	0.03	1.0	838.1	-0.9	0.009	1.2
ν_{21} (E)	352.0	0.007	0.5	350.7	-1.3	0.04	0.4
ν_{22} (E)	210.6	0.2	0.3	209.1	-1.4	0.2	0.2

Van der Waals vibrations: 11.3 cm^{-1}, 0.02 km mol^{-1}, 0.07 $Å^4$ amu^{-1}, 30.6 cm^{-1}, 0.08 km mol^{-1}, 0.2 $Å^4$ amu^{-1}, 42.0 cm^{-1}, 0.05 km mol^{-1}, 0.3 $Å^4$ amu^{-1}, 48.6 cm^{-1}, 0.2 km mol^{-1}, 0.3 $Å^4$ amu^{-1}, 64.8 cm^{-1}, 0.04 km mol^{-1}, 0.4 $Å^4$ amu^{-1}, 73.2 cm^{-1}, 0.2 km mol^{-1}, 1.3 $Å^4$ amu^{-1}.

Table S8.8A: MP2/aug-cc-pVDZ-PP vibrational frequencies, in cm^{-1}, infrared intensities, in km mol^{-1}, and Raman intensities, in $Å^4$ amu^{-1}, for the XB complex of C_2F_3I and TMA and both monomers, as well as the complexation shift Δν.

	Monomer			XB complex			
	Frequency	IR int.	Raman int.	Frequency	Δν	IR int.	Raman int.
C_2F_3I							
ν_1 (A')	1805.0	129.7	16.7	1793.0	-12.1	201.3	10.4
ν_2 (A')	1312.3	157.3	1.4	1294.3	-18.0	145.2	2.2
ν_3 (A')	1166.5	159.9	0.5	1149.3	-17.3	150.0	3.7
ν_4 (A')	1004.0	186.5	2.6	996.8	-7.2	164.8	1.2
ν_5 (A')	645.4	3.6	7.1	639.4	-5.9	0.7	18.4
ν_6 (A')	500.0	1.7	0.9	500.0	0.0	1.5	1.2
ν_7 (A')	324.1	0.9	3.8	310.2	-14.0	5.6	18.5
ν_8 (A')	289.8	3.7	1.3	280.0	-9.8	16.1	10.8
ν_9 (A')	144.8	1.4	0.8	156.7	11.9	4.8	1.5
ν_{10} (A'')	553.8	3.5	3.9	553.5	-0.3	2.6	4.5
ν_{11} (A'')	346.7	0.2	0.1	358.7	12.0	0.3	0.5
ν_{12} (A'')	147.4	0.1	0.02	160.0	12.6	0.1	0.02
TMA							
ν_1 (A_1)	3111.8	42.4	235.1	3120.4	8.6	39.8	171.9
ν_2 (A_1)	2962.3	167.2	390.2	2993.2	31.0	203.3	539.2
ν_3 (A_1)	1499.0	23.4	0.4	1500.3	1.3	26.6	1.2
ν_4 (A_1)	1464.0	1.6	2.3	1464.2	0.1	1.0	23.0
ν_5 (A_1)	1204.0	24.9	5.6	1216.4	12.4	16.0	24.7
ν_6 (A_1)	853.0	22.9	12.0	845.8	-7.2	71.9	11.6
ν_7 (A_1)	383.8	7.6	1.1	411.8	28.0	33.6	0.8
ν_8 (A_2)	3163.7	0.0	0.0	3168.9	5.2	0.004	0.02
ν_9 (A_2)	1477.7	0.0	0.0	1476.1	-1.7	0.0004	0.005
ν_{10} (A_2)	1057.3	0.0	0.0	1059.2	1.9	0.01	0.003
ν_{11} (A_2)	243.9	0.0	0.0	234.5	-9.4	0.0	0.0002
ν_{12} (E)	3166.8	34.6	87.1	3172.0	5.2	20.0	53.7
ν_{13} (E)	3111.1	26.1	27.8	3120.1	9.1	9.7	16.4
ν_{14} (E)	2955.2	44.4	18.3	2989.1	33.9	33.3	32.6
ν_{15} (E)	1500.8	9.8	5.5	1501.0	0.2	14.8	5.9
ν_{16} (E)	1475.1	5.7	8.8	1474.2	-0.9	1.4	7.8
ν_{17} (E)	1421.1	0.7	1.6	1422.3	1.2	0.1	1.7
ν_{18} (E)	1303.4	14.9	1.7	1299.2	-4.2	14.6	1.1
ν_{19} (E)	1115.9	9.1	0.4	1113.9	-2.0	7.4	0.9
ν_{20} (E)	1066.2	13.6	2.7	1059.9	-6.3	13.2	2.9
ν_{21} (E)	423.6	0.006	0.7	421.0	-2.7	0.01	0.7
ν_{22} (E)	290.9	0.4	0.6	285.4	-5.5	0.4	0.8

Van der Waals vibrations: 1.1 cm^{-1}, 0.05 km mol^{-1}, 0.2 $Å^4$ amu^{-1}, 33.4 cm^{-1}, 0.08 km mol^{-1}, 0.08 $Å^4$ amu^{-1}, 37.5 cm^{-1}, 0.03 km mol^{-1}, 0.2 $Å^4$ amu^{-1}, 90.3 cm^{-1}, 6.5 km mol^{-1}, 1.2 $Å^4$ amu^{-1}, 101.8 cm^{-1}, 1.0 km mol^{-1}, 1.0 $Å^4$ amu^{-1}, 104.0 cm^{-1}, 0.005 km mol^{-1}, 0.1 $Å^4$ amu^{-1}.

Table S8.8B: MP2/aug-cc-pVDZ-PP vibrational frequencies, in cm^{-1}, infrared intensities, in km mol^{-1}, and Raman intensities, in $Å^4$ amu^{-1}, for the XB complex of C_2F_3I and TMA-d_9 and both monomers, as well as the complexation shift Δν.

	Monomer			XB complex			
	Frequency	IR int.	Raman int.	Frequency	Δν	IR int.	Raman int.
C_2F_3I							
ν_1 (A')	1805.0	129.7	16.7	1793.0	-12.1	202.1	10.5
ν_2 (A')	1312.3	157.3	1.4	1294.4	-17.9	153.2	2.5
ν_3 (A')	1166.5	159.9	0.5	1149.3	-17.3	150.4	3.9
ν_4 (A')	1004.0	186.5	2.6	996.8	-7.2	168.8	1.3
ν_5 (A')	645.4	3.6	7.1	639.4	-6.0	0.7	18.5
ν_6 (A')	500.0	1.7	0.9	500.0	0.0	1.4	1.1
ν_7 (A')	324.1	0.9	3.8	309.8	-14.3	7.0	18.5
ν_8 (A')	289.8	3.7	1.3	279.9	-9.9	17.3	11.4
ν_9 (A')	144.8	1.4	0.8	155.2	10.4	4.8	1.6
ν_{10} (A")	553.8	3.5	3.9	553.5	-0.4	2.6	4.5
ν_{11} (A")	346.7	0.2	0.1	361.0	14.3	0.3	0.6
ν_{12} (A")	147.4	0.1	0.02	158.7	11.3	0.1	0.02
TMA-d_9							
ν_1 (A_1)	2286.9	51.7	81.2	2299.3	12.4	46.2	107.2
ν_2 (A_1)	2142.3	72.7	232.7	2160.1	17.8	90.9	265.8
ν_3 (A_1)	1151.7	0.2	5.9	1146.9	-4.8	10.5	17.8
ν_4 (A_1)	1079.2	12.6	0.2	1080.7	1.4	21.8	0.7
ν_5 (A_1)	1018.9	33.5	3.4	1034.4	15.5	35.2	14.4
ν_6 (A_1)	756.9	12.4	9.6	751.9	-5.0	40.8	9.3
ν_7 (A_1)	323.0	4.6	0.8	348.6	25.6	22.5	0.6
ν_8 (A_2)	2345.4	0.0	0.0	2349.4	4.0	0.0009	0.004
ν_9 (A_2)	1067.7	0.0	0.0	1065.7	-2.0	0.0	0.001
ν_{10} (A_2)	801.3	0.0	0.0	803.0	1.7	0.0	0.0
ν_{11} (A_2)	173.1	0.0	0.0	166.4	-6.7	0.0	0.0001
ν_{12} (E)	2349.0	17.4	46.2	2353.3	4.3	10.0	28.4
ν_{13} (E)	2287.5	8.1	21.2	2300.2	12.7	2.4	15.9
ν_{14} (E)	2135.6	36.1	4.2	2155.2	19.7	25.4	10.5
ν_{15} (E)	1252.4	33.4	1.0	1243.4	-9.0	27.0	0.7
ν_{16} (E)	1078.6	2.1	2.4	1076.9	-1.6	4.1	2.5
ν_{17} (E)	1073.1	0.2	0.4	1073.9	0.7	0.3	0.4
ν_{18} (E)	1063.4	1.6	3.7	1062.9	-0.5	0.2	3.1
ν_{19} (E)	886.2	7.4	2.6	885.6	-0.6	6.4	2.5
ν_{20} (E)	839.0	0.03	1.0	836.4	-2.6	0.02	1.5
ν_{21} (E)	352.0	0.007	0.5	349.8	-2.3	0.04	0.4
ν_{22} (E)	210.6	0.2	0.3	207.0	-3.5	0.2	0.3

Van der Waals vibrations: 1.0 cm^{-1}, 0.05 km mol^{-1}, 0.2 $Å^4$ amu^{-1}, 31.4 cm^{-1}, 0.05 km mol^{-1}, 0.09 $Å^4$ amu^{-1}, 35.3 cm^{-1}, 0.01 km mol^{-1}, 0.3 $Å^4$ amu^{-1}, 84.7 cm^{-1}, 5.2 km mol^{-1}, 1.0 $Å^4$ amu^{-1}, 92.1 cm^{-1}, 1.1 km mol^{-1}, 0.9 $Å^4$ amu^{-1}, 94.2 cm^{-1}, 0.01 km mol^{-1}, 0.07 $Å^4$ amu^{-1}.

Table S8.9A: MP2/aug-cc-pVDZ-PP vibrational frequencies, in cm^{-1}, infrared intensities, in km mol^{-1}, and Raman intensities, in $Å^4$ amu^{-1}, for the lp···π complex of C_2F_3I and TMA and both monomers, as well as the complexation shift Δν.

	Monomer			lp···π complex			
	Frequency	IR int.	Raman int.	Frequency	Δν	IR int.	Raman int.
C_2F_3I							
ν_1 (A')	1805.0	129.7	16.7	1808.9	3.9	121.4	19.3
ν_2 (A')	1312.3	157.3	1.4	1316.0	3.7	131.9	1.2
ν_3 (A')	1166.5	159.9	0.5	1160.0	-6.5	138.8	0.6
ν_4 (A')	1004.0	186.5	2.6	1003.2	-0.8	154.5	1.8
ν_5 (A')	645.4	3.6	7.1	644.2	-1.1	3.9	7.0
ν_6 (A')	500.0	1.7	0.9	500.1	0.1	1.2	0.8
ν_7 (A')	324.1	0.9	3.8	324.7	0.6	0.8	3.2
ν_8 (A')	289.8	3.7	1.3	288.8	-1.0	3.8	1.2
ν_9 (A')	144.8	1.4	0.8	145.4	0.6	1.2	0.6
ν_{10} (A")	553.8	3.5	3.9	543.6	-10.2	22.9	18.9
ν_{11} (A")	346.7	0.2	0.1	351.8	5.1	0.5	0.3
ν_{12} (A")	147.4	0.1	0.02	167.8	20.4	0.2	0.1
TMA							
ν_1 (A_1)	3111.8	42.4	235.1	3111.3	-0.5	27.9	93.7
ν_2 (A_1)	2962.3	167.2	390.2	2968.5	6.3	183.1	447.7
ν_3 (A_1)	1499.0	23.4	0.4	1497.7	-1.3	26.0	0.3
ν_4 (A_1)	1464.0	1.6	2.3	1464.1	0.0	2.1	3.6
ν_5 (A_1)	1204.0	24.9	5.6	1206.5	2.5	24.4	6.4
ν_6 (A_1)	853.0	22.9	12.0	850.7	-2.4	30.7	10.0
ν_7 (A_1)	383.8	7.6	1.1	389.5	5.7	11.9	0.9
ν_8 (A_2)	3163.7	0.0	0.0	3158.5	-5.2	9.1	19.1
ν_9 (A_2)	1477.7	0.0	0.0	1477.3	-0.4	0.03	0.008
ν_{10} (A_2)	1057.3	0.0	0.0	1057.2	0.0	0.1	0.01
ν_{11} (A_2)	243.9	0.0	0.0	242.0	-1.9	0.02	0.04
ν_{12} (E)	3166.8	34.6	87.1	3164.0	-2.8	23.5	58.5
ν_{13} (E)	3111.1	26.1	27.8	3107.5	-3.6	27.9	60.7
ν_{14} (E)	2955.2	44.4	18.3	2962.1	6.9	44.7	31.0
ν_{15} (E)	1500.8	9.8	5.5	1500.8	0.1	10.5	6.2
ν_{16} (E)	1475.1	5.7	8.8	1473.3	-1.8	3.8	7.9
ν_{17} (E)	1421.1	0.7	1.6	1420.7	-0.3	0.4	1.7
ν_{18} (E)	1303.4	14.9	1.7	1302.6	-0.8	9.1	1.4
ν_{19} (E)	1115.9	9.1	0.4	1114.5	-1.5	7.1	0.5
ν_{20} (E)	1066.2	13.6	2.7	1065.4	-0.9	11.9	2.4
ν_{21} (E)	423.6	0.006	0.7	422.4	-1.2	0.03	0.5
ν_{22} (E)	290.9	0.4	0.6	288.6	-2.4	0.2	0.4

Van der Waals vibrations: 14.8 cm^{-1}, 0.03 km mol^{-1}, 0.05 $Å^4$ amu^{-1}, 34.1 cm^{-1}, 0.1 km mol^{-1}, 0.3 $Å^4$ amu^{-1}, 44.3 cm^{-1}, 0.09 km mol^{-1}, 0.3 $Å^4$ amu^{-1}, 52.7 cm^{-1}, 0.3 km mol^{-1}, 0.3 $Å^4$ amu^{-1}, 68.9 cm^{-1}, 0.09 km mol^{-1}, 0.4 $Å^4$ amu^{-1}, 78.8 cm^{-1}, 0.1 km mol^{-1}, 1.5 $Å^4$ amu^{-1}.

Table S8.9B: MP2/aug-cc-pVDZ-PP vibrational frequencies, in cm^{-1}, infrared intensities, in km mol^{-1}, and Raman intensities, in $Å^4$ amu^{-1}, for the lp···π complex of C_2F_3I and TMA-d_9 and both monomers, as well as the complexation shift Δν.

	Monomer			lp···π complex			
	Frequency	IR int.	Raman int.	Frequency	Δν	IR int.	Raman int.
C_2F_3I							
ν_1 (A')	1805.0	129.7	16.7	1808.9	3.8	121.2	19.3
ν_2 (A')	1312.3	157.3	1.4	1316.2	3.9	126.4	1.1
ν_3 (A')	1166.5	159.9	0.5	1160.4	-6.1	134.4	1.0
ν_4 (A')	1004.0	186.5	2.6	1003.1	-0.9	157.3	1.7
ν_5 (A')	645.4	3.6	7.1	644.2	-1.1	3.9	7.0
ν_6 (A')	500.0	1.7	0.9	500.1	0.1	1.2	0.8
ν_7 (A')	324.1	0.9	3.8	324.2	0.1	1.7	3.6
ν_8 (A')	289.8	3.7	1.3	288.8	-1.0	3.4	1.1
ν_9 (A')	144.8	1.4	0.8	145.4	0.6	1.2	0.6
ν_{10} (A")	553.8	3.5	3.9	543.5	-10.3	23.0	18.9
ν_{11} (A")	346.7	0.2	0.1	355.8	9.1	1.5	0.4
ν_{12} (A")	147.4	0.1	0.02	167.5	20.1	0.2	0.07
TMA-d_9							
ν_1 (A_1)	2286.9	51.7	81.2	2285.6	-1.3	34.0	36.2
ν_2 (A_1)	2142.3	72.7	232.7	2145.5	3.3	80.3	256.6
ν_3 (A_1)	1151.7	0.2	5.9	1150.6	-1.1	1.8	5.5
ν_4 (A_1)	1079.2	12.6	0.2	1078.3	-0.9	15.3	0.3
ν_5 (A_1)	1018.9	33.5	3.4	1021.8	2.9	35.4	3.9
ν_6 (A_1)	756.9	12.4	9.6	755.2	-1.7	17.4	8.0
ν_7 (A_1)	323.0	4.6	0.8	328.2	5.2	5.3	0.2
ν_8 (A_2)	2345.4	0.0	0.0	2341.7	-3.7	3.1	6.2
ν_9 (A_2)	1067.7	0.0	0.0	1067.0	-0.7	0.03	0.009
ν_{10} (A_2)	801.3	0.0	0.0	801.6	0.4	0.004	0.007
ν_{11} (A_2)	173.1	0.0	0.0	171.9	-1.2	0.009	0.02
ν_{12} (E)	2349.0	17.4	46.2	2346.7	-2.3	12.7	32.9
ν_{13} (E)	2287.5	8.1	21.2	2287.9	0.4	17.1	32.5
ν_{14} (E)	2135.6	36.1	4.2	2139.1	3.6	32.8	7.8
ν_{15} (E)	1252.4	33.4	1.0	1251.3	-1.1	28.5	0.9
ν_{16} (E)	1078.6	2.1	2.4	1077.7	-0.9	1.9	2.6
ν_{17} (E)	1073.1	0.2	0.4	1072.8	-0.4	0.4	0.5
ν_{18} (E)	1063.4	1.6	3.7	1062.2	-1.3	0.9	3.3
ν_{19} (E)	886.2	7.4	2.6	885.9	-0.3	6.0	2.2
ν_{20} (E)	839.0	0.03	1.0	838.0	-0.9	0.01	1.1
ν_{21} (E)	352.0	0.007	0.5	349.7	-2.3	0.3	0.4
ν_{22} (E)	210.6	0.2	0.3	209.0	-1.5	0.2	0.2

Van der Waals vibrations: 13.1 cm^{-1}, 0.03 km mol^{-1}, 0.06 $Å^4$ amu^{-1}, 31.7 cm^{-1}, 0.09 km mol^{-1}, 0.2 $Å^4$ amu^{-1}, 40.4 cm^{-1}, 0.04 km mol^{-1}, 0.3 $Å^4$ amu^{-1}, 48.0 cm^{-1}, 0.3 km mol^{-1}, 0.2 $Å^4$ amu^{-1}, 65.1 cm^{-1}, 0.06 km mol^{-1}, 0.4 $Å^4$ amu^{-1}, 74.2 cm^{-1}, 0.2 km mol^{-1}, 1.5 $Å^4$ amu^{-1}.

Table S8.10: Experimental vibrational frequencies for the monomer and complexes, as well as experimental complexation shifts ($\Delta\nu_{exp}$) and MP2/aug-cc-pVDZ calculated complexation shifts ($\Delta\nu_{calc,\ lp\cdots\pi}$), in cm^{-1}, for lp···π complex of C_2F_4 with TMA-d_9 dissolved in LKr at 120 K.

Assignment		$\nu_{monomer}$	$\nu_{complex}$	$\Delta\nu_{exp}$	$\Delta\nu_{calc,lp\cdots\pi}$
C_2F_4	$\nu_1 + \nu_9$	3196.6	3198.0	1.4	-7.1
	$\nu_1 + \nu_{11}$	3045.3	3048.6	3.3	-0.5
	ν_1	1870.8	1876.0	5.2	3.1
	ν_9	1330.5	1327.5	-3.0	-10.3
	ν_{11}	1179.5	1177.9	-1.6	-3.7
	ν_2	778.1	777.6	-0.5	-3.3
	ν_{12}	554.7	554.3	-0.4	-0.9
	ν_6	549.9	550.3	0.4	-0.4
	ν_8	505.5	500.9	-4.6	-13.6
	ν_3	395.5	395.8	0.3	-1.4
TMA-d_9	ν_{12}	2233.0	2235.5	2.5	-2.4
	ν_1	2182.1	2184.1	2.0	-1.0
	ν_{13}	2182.1	2184.1	2.0	0.1
	ν_2	2029.5	2039.1	9.6	3.8
	ν_{14}	2029.5	2039.1	9.6	4.1
	ν_{15}	1220.9	[a]		0.4
	ν_4	1063.3	1064.4	1.1	-0.6
	ν_{16}	1062.3	1063.0	0.7	-0.5
	ν_{17}	1055.7	[a]		0.1
	ν_{18}	1047.7	[a]		-0.7
	ν_5	1004.0	1007.0	3.0	2.5
	ν_{19}	873.9	873.5	-0.4	-0.1
	ν_{20}	832.8	[a]		
	ν_6	741.1	739.5	-1.6	-1.5
	ν_{21}	351.1	[a]		-0.9
	ν_7	314.2	[a]		3.1
	ν_{22}	201.3	[a]		-3.0

[a] Complex band has not been observed.

Table S8.11: Experimental vibrational frequencies for the monomer and complexes, as well as experimental complexation shifts ($\Delta\nu_{exp}$) and MP2/aug-cc-pVDZ calculated complexation shifts ($\Delta\nu_{calc}$), in cm^{-1}, for the XB complex and lp···π complex of C_2F_3Cl with TMA-d_9 dissolved in LKr at 120 K.

Assignment		$\nu_{monomer}$	$\nu_{complex,XB}$	$\Delta\nu_{exp,XB}$	$\Delta\nu_{calc,XB}$	$\nu_{complex,lp\cdots\pi}$	$\Delta\nu_{exp,lp\cdots\pi}$	$\Delta\nu_{calc,lp\cdots\pi}$
C_2F_3Cl	ν_1	1795.2	1791.3	-3.9	-5.3	1800.5	5.3	3.9
	ν_1 (^{13}C)	1788.5	[a]		-5.3	[a]		3.9
	ν_2	1328.1	1321.0	-7.1	-8.8	1331.3	3.2	3.5
	ν_3	1214.3	[b]		-8.1	[b]		-7.6
		1200.1	1195.4	-4.7		1195.4	-4.7	
	$2\nu_{10}$	1074.8	1073.0	-1.8	-2.8	[b]		-18.3
	ν_4	1053.7	[b]		-4.0	[b]		-2.9
	ν_5 (^{35}Cl)	691.2	690.7	-0.5	-4.7	690.7	-0.5	-2.1
	ν_5 (^{37}Cl)	689.6	689.1	-0.5	-4.7	689.1	-0.5	-2.1
	ν_{10}	535.0	534.4	-0.6	-1.4	533.1	-1.9	-9.1
	ν_6	516.3	516.7	0.4	0.7	516.0	-0.3	0.0
	ν_7 (^{35}Cl)	462.4	458.3	-4.1	-5.9	462.0	-0.4	-1.0
	ν_7 (^{37}Cl)	456.5	452.5	-4.0	-5.9	456.3	-0.2	-1.0
	ν_8	338.1	340.4	2.3	2.4	[a]		-1.0
	ν_9	189.8	[a]		8.5	[a]		-0.2
TMA-d_9	ν_{12}	2233.0	2233.8	0.8	-0.8	2233.8	0.8	-2.1
	ν_1	2182.2	2184.5	2.3	1.6	2184.5	2.3	-1.2
	ν_{13}	2182.2	2184.5	2.3	1.9	2184.5	2.3	0.7
	ν_2	2029.5	2033.1	3.6	4.9	2033.1	3.6	3.8
	ν_{14}	2029.5	2033.1	3.6	5.4	2033.1	3.6	4.2
	$\nu_{19} + \nu_{21}$	1226.5	[b]		-0.7	[b]		-1.4
	ν_{15}	1220.8	[b]		-1.0	[b]		-0.8
	ν_3	1139.4	[a]		-0.7	[a]		-0.7
	ν_4	1063.3	[b]		-0.1	[b]		-0.6
	ν_{16}	1062.3	[b]		-0.5	[b]		-0.4
	ν_{17}	1055.7	[b]		0.3	[b]		-0.1
	ν_{18}	1047.7	[b]		-0.5	[b]		-0.7
	ν_5	1004.0	1008.1	4.1	4.2	1008.1	4.1	3.0
	ν_{19}	873.9	873.8	-0.1	0.0	873.8	-0.1	-0.2
	ν_{20}	832.8	[a]		-0.6	[a]		-0.8
	ν_6	741.1	740.5	-0.6	-1.5	740.5	-0.6	-1.6
	ν_{21}	351.1	351.5	0.4	-0.7	351.5	0.4	-1.2
	ν_7	314.2	318.6	4.4	5.9	318.6	4.4	4.5
	ν_{22}	201.3	[a]		-3.1	[a]		-1.4

[a] Complex band has not been observed.

[b] Bands could not be assigned due to overlap with other complex bands.

Table S8.12: Experimental vibrational frequencies, experimental complexation shifts and MP2/aug-cc-pVDZ-PP calculated complexation shifts ($\Delta\nu_{calc,XB}$), in cm^{-1}, for the XB complex of C_2F_3Br with TMA-d_9 dissolved in LKr at 120 K. For completeness, the MP2/aug-cc-pVDZ-PP calculated complexation shifts of the lp···π complexes ($\Delta\nu_{calc,lp\cdots\pi}$) are also given.

Assignment		$\nu_{monomer}$	$\nu_{complex}$	$\Delta\nu_{exp}$	$\Delta\nu_{calc,XB}$	$\Delta\nu_{calc,lp\cdots\pi}$
C_2F_3Br	ν_1	1781.8	1774.2	-7.6	-8.8	4.0
	$\nu_4 + \nu_8 / 2\nu_5$	1330.3	1322.0	-10.3		
	ν_2	1319.8	1307.9	-11.9	-12.9	3.7
	ν_3	1197.2	1184.8	-12.4	-12.9	-6.8
		1171.0	1166.3	-4.7		
	$2\nu_{10}$	1072.6	1071.7	-0.9	-0.9	-20.1
	$\nu_5 + \nu_7$ (^{79}Br)	1034.4	1024.3	-10.1	-6.3	-1.3
	$\nu_5 + \nu_7$ (^{81}Br)	1033.3	1024.3	-9.0	-6.3	-1.3
	$2\nu_6$	1018.8	1018.5	-0.3	0.8	0.3
	ν_4	1016.6	1006.9	-9.7	-6.3	-1.3
	ν_5	663.9	659.2	-4.7	-5.7	-1.4
	ν_{10}	535.2	534.7	-0.5	-0.4	-10.1
	ν_6	509.1	509.7	0.6	0.4	0.1
	ν_7	365.8	352.6	-13.2	-14.3	0.7
	ν_8	311.1	310.8	-0.3	-0.4	-1.0
	ν_9	162.2	168.7	6.5	9.5	0.2
TMA-d_9	ν_{12}	2233.0	2235.2	2.2	1.1	-2.2
	ν_1	2182.2	2187.9	5.7	5.8	-1.3
	ν_{13}	2182.2	2187.9	5.7	6.1	0.6
	ν_2	2029.5	2039.0	9.5	10.4	3.5
	ν_{14}	2029.5	2039.0	9.5	11.5	3.9
	$\nu_{19} + \nu_{21}$	1226.5	1224.9	-1.6	-1.5	-1.6
	ν_{15}	1220.8	1217.7	-3.1	-3.4	-0.9
	ν_3	1139.4	[a]		-2.2	-0.9
	ν_4	1063.3	1063.1	-0.2	0.4	-0.7
	ν_{16}	1062.3	1062.1	-0.2	-0.9	-0.7
	ν_{17}	1055.7	[a]		0.6	-0.3
	ν_{18}	1047.7	[a]		-0.5	-1.1
	ν_5	1004.0	1013.4	9.4	9.3	2.8
	ν_{19}	873.9	873.7	-0.2	-0.2	-0.2
	ν_{20}	832.8	[a]		-1.3	-0.9
	ν_6	741.1	739.2	-1.9	-2.9	-1.6
	ν_{21}	351.1	[b]		-1.3	-1.3
	ν_7	314.2	328.2	16.0	13.6	4.7
	ν_{22}	201.3	198.8	-3.5	-4.4	-1.4

[a] Complex band has not been observed.

[b] Band could not be assigned due to overlap with the ν_7 complex band of C_2F_3Br.

Table S8.13: Experimental vibrational frequencies, experimental complexation shifts and MP2/aug-cc-pVDZ-PP calculated complexation shifts ($\Delta\nu_{calc,XB}$), in cm^{-1}, for the XB complex of C_2F_3I with TMA-d_9 dissolved in LXe at 170 K. For completeness, the MP2/aug-cc-pVDZ-PP calculated complexation shifts of the lp···π complexes ($\Delta\nu_{calc,lp\cdots\pi}$) are also given.

Assignment		$\nu_{monomer}$	$\nu_{complex}$	$\Delta\nu_{exp}$	$\Delta\nu_{calc,XB}$	$\Delta\nu_{calc,lp\cdots\pi}$
C_2F_3I	ν_1	1757.8	1746.6	-11.2	-12.1	3.8
	ν_1 (^{13}C)	1742.3	1731.4	-10.9	-12.1	3.8
		1732.3	1721.5	-10.8		
		1720.2	1708.8	-11.4		
	$\nu_4 + \nu_7$	1324.6	1304.8	-19.8	-21.6	-0.9
	ν_2	1311.2	1294.9	-16.3	-17.9	3.9
	$2\nu_5$	1301.6	1288.0	-13.6	-11.9	-2.3
	ν_3	1173.9	1158.5	-15.4	-17.3	-6.1
	$\nu_5 + \nu_6$	1155.2	1146.1	-8.9	-6.0	-1.0
	$2\nu_{10}$	1076.4	1074.9	-1.5	-0.7	-20.5
	$2\nu_6$	1012.5	1011.3	-1.2	0.0	0.3
	ν_4	1001.2	995.5	-5.7	-7.2	-0.9
	$\nu_5 + \nu_7$	981.5	[a]		-20.3	-1.1
	$\nu_5 + \nu_8$	972.4	[a]		-15.9	-2.1
	ν_5	651.2	[a]		-6.0	-1.1
	ν_{10}	537.5	536.6	-0.9	-0.4	-10.3
	ν_6	506.4	505.7	-0.7	0.0	0.1
	ν_{11}	348.3	[a]		14.3	9.1
	ν_7	321.1	307.3	-13.8	-14.3	0.1
	ν_8	286.8	276.6	-10.2	-9.9	-1.0
TMA-d_9	ν_{12}	2229.9	2234.9	5.0	4.3	-2.3
	ν_1	2179.5	2189.5	10.0	12.4	-1.3
	ν_{13}	2179.5	2189.5	10.0	12.7	0.4
	ν_2	2027.9	2043.8	15.9	17.8	3.3
	ν_{14}	2027.9	2043.8	15.9	19.7	3.6
	$\nu_{19} + \nu_{21}$	1225.2	1222.3	-2.9	-2.9	-2.6
	ν_{15}	1219.9	1208.0	-11.9	-9.0	-1.1
	ν_4	1061.5	1062.2	0.7	1.4	-0.9
	ν_{16}	1061.5	1062.2	0.7	-1.6	-0.9
	ν_{18}	1046.6	[a]		-0.5	-1.3
	ν_5	1002.7	1018.8	16.1	15.5	2.9
	ν_{19}	873.3	872.8	-0.5	-0.6	-0.3
	ν_6	740.5	737.2	-3.3	-5.0	-1.7
	ν_{21}	351.3	349.8	-1.5	-2.3	-0.9
	ν_7	314.5	341.8	27.3	25.6	5.2
	ν_{22}	202.5	[a]		-3.5	-1.5

[a] Complex band has not been observed.

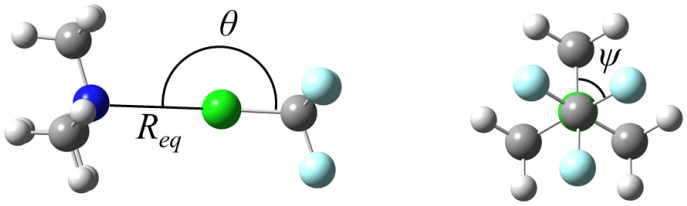

Figure S8.1: MP2/aug-cc-pVDZ(-PP) equilibrium geometries for the XB complexes of CF_3X (X = Cl, Br and I) with TMA.

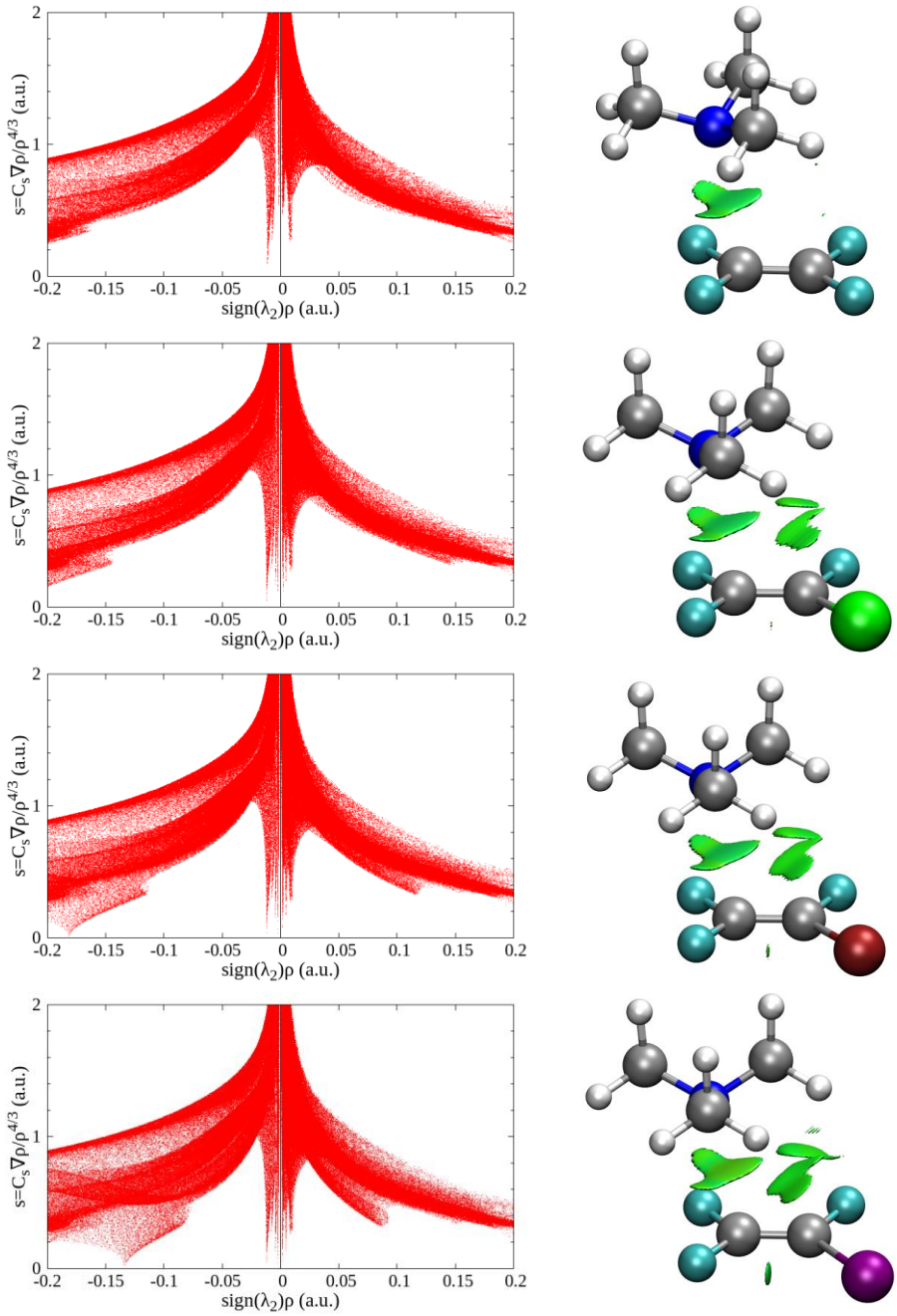

Figure S8.2: Plots of the reduced density gradient versus the electron density multiplied by the sign of the second Hessian eigenvalue (left) and gradient isosurfaces (s = 0.5 a.u., right) for lp···π species between TMA and C_2F_4 (top), C_2F_3Cl, C_2F_3Br and C_2F_3I (bottom).

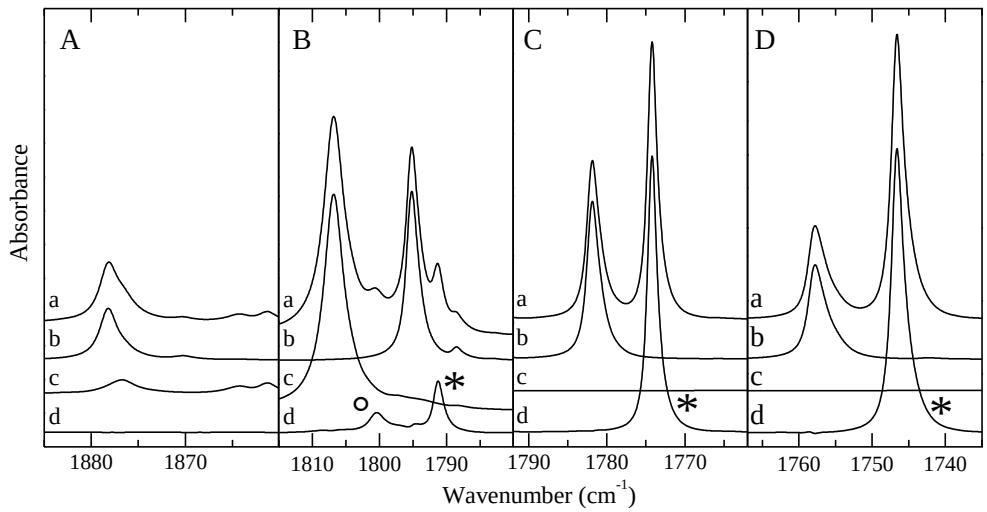

Figure S8.3: Infrared spectra of the $\nu_{C=C}$ spectral region of C_2F_3X (X = F, Cl, Br, I) for solutions of mixtures of TMA-d_9 with C_2F_4 (panel A), C_2F_3Cl (panel B), C_2F_3Br (panel C) and C_2F_3I (panel D) dissolved in LKr at 120 K for panels A-C and LXe at 170 K for panel D. In each panel, trace *a* represents the mixed solution, while traces *b* and *c* show the solution containing only C_2F_3X or TMA-d_9, respectively. Trace *d* represents the spectrum of the complex and is obtained by subtracting the rescaled traces *b* and *c* from trace *a*. New bands due to the 1:1 C(sp^2)-X···N XB and the 1:1 lp···π complexes are marked with an asterisk (*) and an open circle (°), respectively.

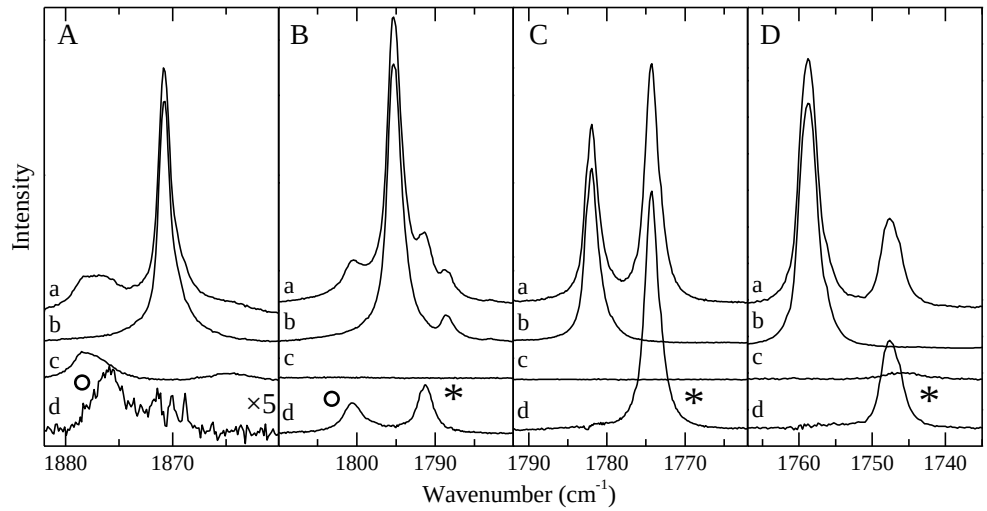

Figure S8.4: Raman spectra of the $\nu_{C=C}$ spectral region of C_2F_3X (X = F, Cl, Br, I) for solutions of mixtures of TMA-d_9 with C_2F_4 (panel A), C_2F_3Cl (panel B), C_2F_3Br (panel C) and C_2F_3I (panel D) dissolved in LKr at 120 K. In each panel, trace *a* represents the mixed solution, while traces *b* and *c* show the solution containing only C_2F_3X or TMA-d_9, respectively. Trace *d* represents the spectrum of the complex and is obtained by subtracting the rescaled traces *b* and

c from trace *a*. New bands due to the 1:1 C(sp^2)-X···N XB and the 1:1 lp···π complexes are marked with an asterisk (*) and an open circle (°), respectively.

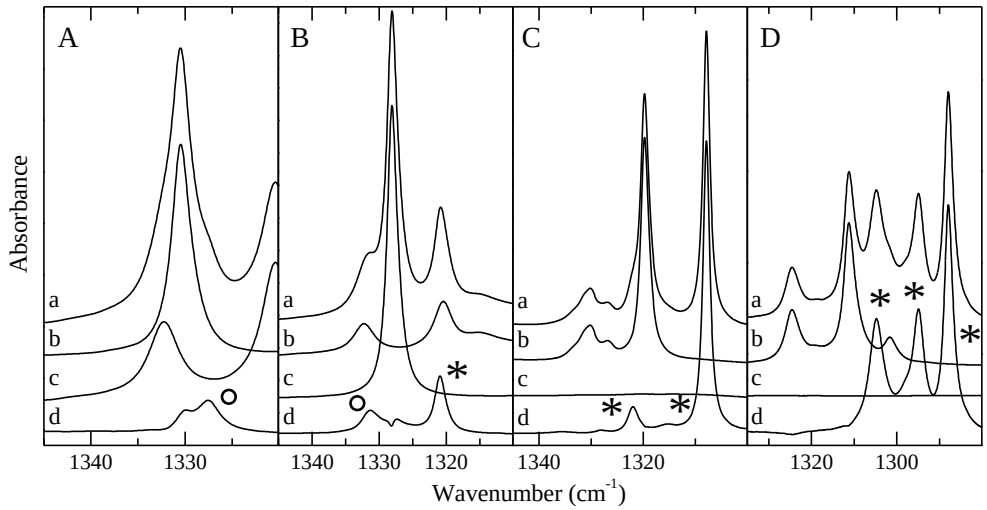

Figure S8.5: Infrared spectra of the the antisymmetric CF_2 stretching region of C_2F_3X (X = F, Cl, Br, I) for solutions of mixtures of TMA-d_9 with C_2F_4 (panel A), C_2F_3Cl (panel B), C_2F_3Br (panel C) and C_2F_3I (panel D) dissolved in LKr at 120 K for panels A-C and LXe at 170 K for panel D. In each panel, trace *a* represents the mixed solution, while traces *b* and *c* show the solution containing only C_2F_3X or TMA-d_9, respectively. Trace *d* represents the spectrum of the complex and is obtained by subtracting the rescaled traces *b* and *c* from trace *a*. New bands due to the 1:1 C(sp^2)-X···N XB and the 1:1 lp···π complexes are marked with an asterisk (*) and an open circle (°), respectively.

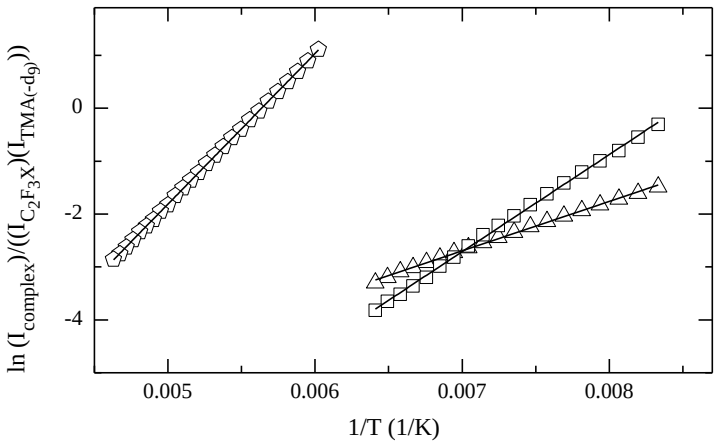

Figure S8.6: Typical van 't Hoff plots of the XB complexes of TMA(-d_9) with C_2F_3Cl (Δ) and C_2F_3Br (□) in LKr and C_2F_3I (⌓) in LXe.

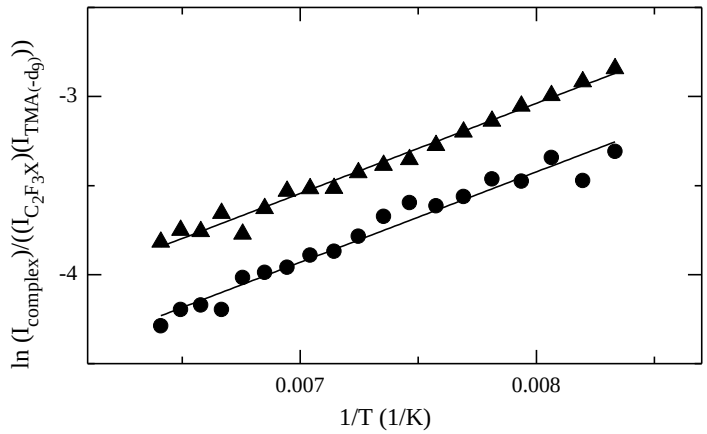

Figure S8.7: Typical van 't Hoff plots of the lp···π complexes of TMA(-d_9) with C_2F_4 (●) and C_2F_3Cl (▲) in LKr.

Chapter 9

Lone pair···π interactions involving an aromatic π-system.

Complexes of C_6F_6 with DME and TMA.

This chapter has been published as:

Geboes, Y.; De Proft, F.; Herrebout, W. A., Lone pair···π interactions involving an aromatic π-system: Complexes of hexafluorobenzene with dimethyl ether and trimethylamine, *Chemical Physics Letters* **2016**, *647*, 26-30.

Abstract

The formation of complexes between C_6F_6 and the Lewis bases DME, DME-d_6, TMA and TMA-d_9 was investigated experimentally using FTIR spectroscopy on solutions of LKr. Additional bands found in the spectra of mixtures were assigned to lp···π complexes using *ab initio* calculations at the MP2/aug-cc-pVDZ level. By constructing van 't Hoff plots, experimental complexation enthalpies were determined of -6.0(6) kJ mol^{-1} for the complex with DME(-d_6) and -6.7(9) kJ mol^{-1} for the complex with TMA(-d_9).

9.1 Introduction

The electrostatic potential on the molecular surface of unsaturated, locally electron deficient molecules shows a region of positive electrostatic potential, perpendicular to (a part of) the molecular framework, often denoted as a π-hole. [1] In recent years it has been shown both theoretically [2-3] and experimentally [4-5] that molecules are able to form noncovalent interactions with anions and lone pairs of Lewis bases through this π-hole, forming anion···π and lp···π complexes, respectively. A review concerning these noncovalent interactions has recently been published by Bauzá et al. [6]

The most studied lp···π complex is undoubtedly the C_6F_6·H_2O complex, which has been described in much detail both theoretically [7-8] and experimentally. [9-13] The interest in C_6F_6 can be attributed to its use as a solvent in several spectroscopic techniques as well as its use as a standard in ^{19}F NMR and ^{13}C NMR. Furthermore, C_6F_6 acts as a good model compound for perfluorinated aromatic rings in larger organic compounds, such as perfluorohalocarbons (PFHC's), which are often used in the fields of crystal engineering and supramolecular chemistry.[14-15] Therefore, a good understanding of the nature of the interactions with these compounds is crucial. Furthermore, as halogen atoms are often used to withdraw electrons from the π-system, lp···π interactions are often found in systems where halogen bonds are also present. To illustrate the influence of halogenation on the π-system, the electrostatic potential on the molecular surfaces of benzene and C_6F_6 are shown in Figure 9.1.

It should be noted however that the formation of lp···π complexes is not limited to aromatic bond donors, such as C_6F_6, but can also be found for non-aromatic donors containing an electron deficient π-system, such as the C_2F_3X (X = F, Cl, Br, I) systems. The existence of lp···π complex at thermodynamic equilibrium between the donor molecules C_2F_4 and C_2F_3Cl and Lewis bases DME [16] and TMA [17] has already been demonstrated. Furthermore, lp···π complex was also found experimentally using pulsed-jet Fourier transform microwave spectroscopy for the complexes of C_2F_3Cl with water, [18] DME [19] and ammonia. [20]

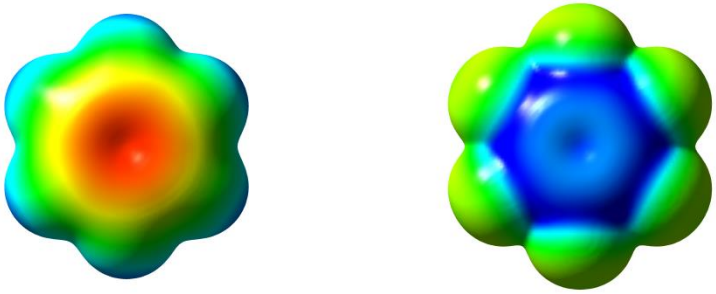

Figure 9.1: Electrostatic potential on the 0.001 electrons Bohr^{-3} contour of the electron density of benzene (left) and C_6F_6 (right), with positive, neutral and negative regions shown in blue, green and red, respectively.

Even though the complexes between C_6F_6 and different Lewis bases have been described theoretically, [21-22] experimental results supporting these findings, apart from the complex formed with water, are still scarce. [23] In this study the complexes between C_6F_6 and DME or TMA have been evaluated at equilibrium conditions using FTIR spectroscopy of liquid noble gas solutions.

9.2 Results and discussion

From the *ab initio* MP2/aug-cc-pVDZ calculations, only one stable complex isomer was found for both Lewis bases, in which the lone pair of the Lewis base faces the centre of the C_6F_6 ring. The MP2/aug-cc-pVDZ optimized structures of both complexes are given in Figure 9.2, whereas intermolecular parameters of the complexes as well as calculated complexation energies and calculated and experimental complexation enthalpies are given in Table 9.1. Cartesian coordinates of the monomer and complex geometries are given in Tables S9.1-S9.3 of the SI.

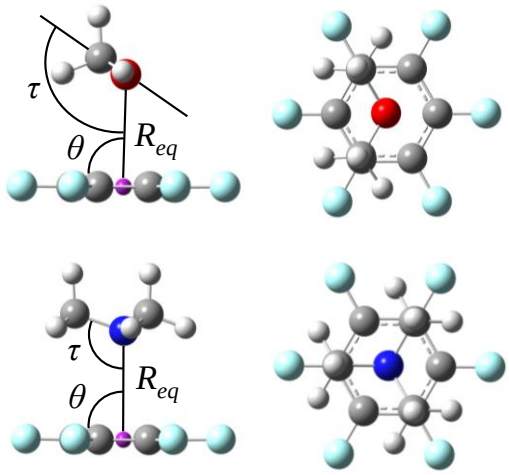

Figure 9.2: MP2/aug-cc-pVDZ equilibrium geometries for the lp···π complex between C_6F_6 and DME (top) and lp···π complex between C_6F_6 and TMA (bottom), including the designation of the binding distance and angles given in Table 9.1. The centroid of the C_6F_6 ring is shown in purple.

Table 9.1: Intermolecular distance R_{eq} (Å) between the donor atom and the centroid of the C_6F_6 ring, bond angles and dihedrals (°), calculated complexation energies at different levels of theory and experimental complexation enthalpies (kJ mol^{-1}) for the complexes of C_6F_6 with DME and TMA.

lp···π complex	C_6F_6·DME	C_6F_6·TMA
Symmetry	C_s	C_{3v}
R_{eq}	2.99	3.02
θ	91.0	90.0
τ	121.6	108.9
ΔE (DZ) [a]	-19.8	-25.8
ΔE (CCSD(T)) [b]	-19.6	-24.3
$\Delta H°$ (vap,calc) [c]	-17.4	-22.4
$\Delta H°$ (LKr,calc) [c]	-7.8	-9.3
Experimental [d]		
$\Delta H°$ (LKr)	-6.0(6)	-6.7(9)

[a] MP2/aug-cc-pVDZ energy, [b] CCSD(T)/CBS extrapolated energy, [c] based on CCSD(T)/CBS energies, [d] values determined in the 120 K - 156 K temperature interval.

From the complex geometry shown in Figure 9.2 and the geometrical parameters in Table 9.1 it can be clearly seen that the lone pair of oxygen faces towards the π-system

of C_6F_6, resulting in a lp···π interaction formed through the centre of the ring, the angle θ between the oxygen-centroid line and the molecular plane of C_6F_6 being 91.0°. The angle between the DME bisector and the oxygen-centroid line (τ) of 121.6° shows that the DME molecule is tilted towards the C_6F_6 molecular plane and is also consistent with the rabbit-ear configuration of the lone pairs on the oxygen atom. This tilted position also enables the formation of secondary interactions between the methyl groups of DME and C_6F_6. In order to visualize these secondary interactions, the lp···π complexes were analysed using the NCI index visualized by NCIPLOT [24-25], for which the results are given in Figure S9.1 of the SI. In this figure the presence of interaction surfaces between the methyl groups and C_6F_6 can be seen, adjoined to the bowl-like surface caused by the lp···π interaction. Optimization of this complex with and without imposing C_s symmetry yielded the same complexation geometry and energy. Rotation of DME above the C_6F_6 molecular plane yields a transition state with an increase in energy of 0.12 kJ mol^{-1} compared to the ground state. For this transition state, a single imaginary frequency was found of 10.9*i* cm^{-1}. As this energy barrier is smaller than the kT value at 120 K, the existence of large amplitude motions is expected.

For the complex between C_6F_6 and TMA, shown in Figure 9.2, a complex geometry with C_{3v} symmetry, in which the lone pair of the Lewis base faces directly to the centroid of the C_6F_6 ring is observed, the angle between the nitrogen atom, C_6F_6 centroid and C_6F_6 carbon atom (θ) being 90.0°. Optimization without symmetry restrictions yielded the same complex geometry. Apart from the bowl-like surface caused by the lp···π interaction, only very small secondary interaction surfaces between the methyl groups and C_6F_6 are observed for this complex in the gradient isosurfaces shown in Figure S9.1. The complex geometry in which C_6F_6 and TMA have been rotated 60° from each other, leading to a staggered configuration with C_{3v} symmetry, increased the energy by 0.09 kJ mol^{-1} and yielded one imaginary frequency (8.6*i* cm^{-1}). Also here the existence of large amplitude motions is expected.

When comparing the complexation energies of both complexes, a decrease in complexation energy of 0.2 kJ mol^{-1} and 1.5 kJ mol^{-1} for the complexes with DME and TMA respectively can be observed when going from the MP2/aug-cc-pVDZ level to

the (extrapolated) CCSD(T)/CBS level. Upon correction of the CCSD(T)/CBS energies for zero-point energy, thermal and solvent effects to obtain complex enthalpies $\Delta H°$(LKr,calc), the complex with TMA remains stronger than the complex with DME, the difference in strength between both complexes, however, diminishes from 4.7 to 1.6 kJ mol^{-1}.

In order to determine the nature of the attractive interaction, an NBO analysis of both complexes was performed. However, as in a previous study [17], this analysis did not yield clear results as to which electron transfers are responsible for the attractive interaction. It was found that the charge transfer for both complexes is smaller than 0.001, which indicates that the attraction is mainly electrostatic, rather than due to charge transfer.

Experimental assignment of the vibrational modes of the Lewis bases is based on assignments of liquefied noble gas solutions found in the literature. [26-28] To aid the assignment of the DME-d_6 modes, the anharmonic force field of DME-d_6 was also calculated using Gaussian09 at the MP2/aug-cc-pVDZ level. For the assignment of C_6F_6, gas phase [29-30] and matrix isolation frequencies [10] found in the literature were used.

From the *ab initio* calculated frequencies, given in Tables S9.4 and S9.5 of the SI, it is clear that only 4 out of 20 vibrational modes are IR active, of which ν_4 and ν_{14} lie outside the studied spectral range. The remaining vibrational modes ν_{12} and ν_{13} have a large IR intensity, resulting in the use of diluted solutions for the study of these vibrational modes. Apart from these fundamental transitions, two further bands at 1024.8 cm^{-1} and 1016.9 cm^{-1} are observed in these solutions, which are the result of a complex Fermi resonance in this spectral range and have been described before in the gas phase. Possible assignments are the double combination $\nu_{11} + \nu_{19}$, the triple combination $\nu_{14} + \nu_{17} + \nu_{18}$ and the quadruple combinations $\nu_8 + 2\nu_{14} + \nu_{20}$, $\nu_{10} + \nu_{11} + \nu_{14} + \nu_{20}$ and $\nu_{14} + \nu_{17} + 2\nu_{20}$. It should also be noted that the relative intensity of the bands in this spectral region differs strongly with those observed previously in a solid N_2 matrix, where the band at 1016.9 cm^{-1} is not observed, [10] and

the low resolution gas phase spectra, in which the band with the highest frequency has the largest intensity. [30] The infrared spectrum of the ν_{12} and ν_{13} spectral region of C_6F_6 for a C_6F_6 solution in LKr is given in Figure 9.3.

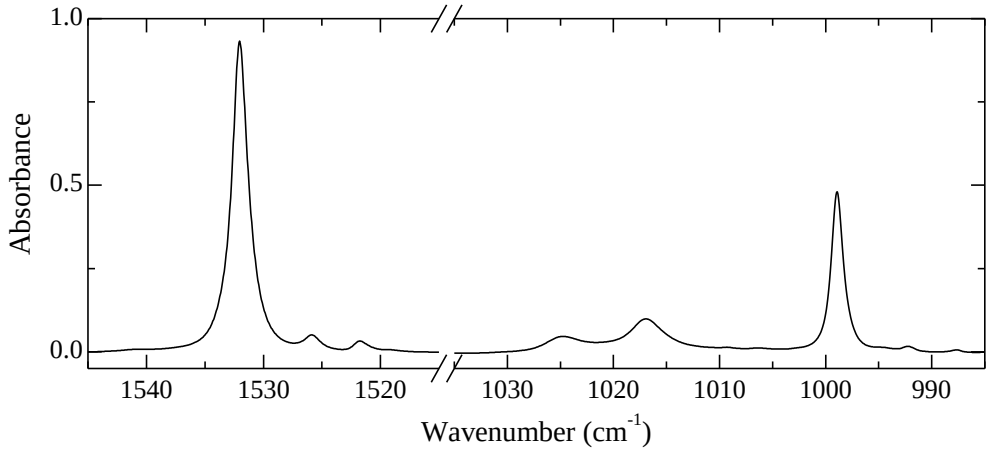

Figure 9.3: Infrared spectrum of a 1.9×10^{-5} mole fraction C_6F_6 solution in LKr at 120 K in the C_6F_6 ν_{12} and ν_{13} spectral region.

Estimated mole fractions of the solutions varied between 1.9×10^{-5} and 1.9×10^{-2} for C_6F_6, 6.6×10^{-4} and 2.8×10^{-2} for DME($-d_6$) and 5.6×10^{-4} and 1.5×10^{-2} for TMA($-d_9$). In order to obtain spectra in which the bands of interest have a maximal absorbance of 1, combined with the necessity to retain an appreciable amount of complex, solutions containing a limited amount of the molecule of interest with a large excess of the other molecule were prepared.

For both observable fundamental bands of C_6F_6, shown in panels A and B of Figure 9.4, an additional band is observed in the spectra of mixtures of C_6F_6 with DME upon subtraction. For the ν_{12} mode (panel A), a blueshifted band with a shift of 0.9 cm^{-1} is observed, whereas a redshifted band with a shift of -1.2 cm^{-1} appears near the ν_{13} band (panel B). Both complexation shifts are in agreement with the calculated complexation shifts for the lp$\cdots\pi$ complex of 1.3 cm^{-1} and -2.8 cm^{-1}, respectively. To study complex bands of the DME($-d_6$) modes, solutions with increased concentrations of C_6F_6 were measured. A spectrum of the ν_6 spectral region of DME is also shown in Figure 9.4, panel C, in which a complex band with a -3.9 cm^{-1} redshift, corresponding to the

calculated shift of -6.1 cm^{-1} for the lp···π complex, can be observed. Spectra of the above mentioned spectral ranges for C_6F_6·DME-d_6 mixtures are given in Figure S9.2 of the SI. An assignment of the monomers and corresponding complex bands is given in Table 9.2 for DME and in Table S9.6 for DME-d_6.

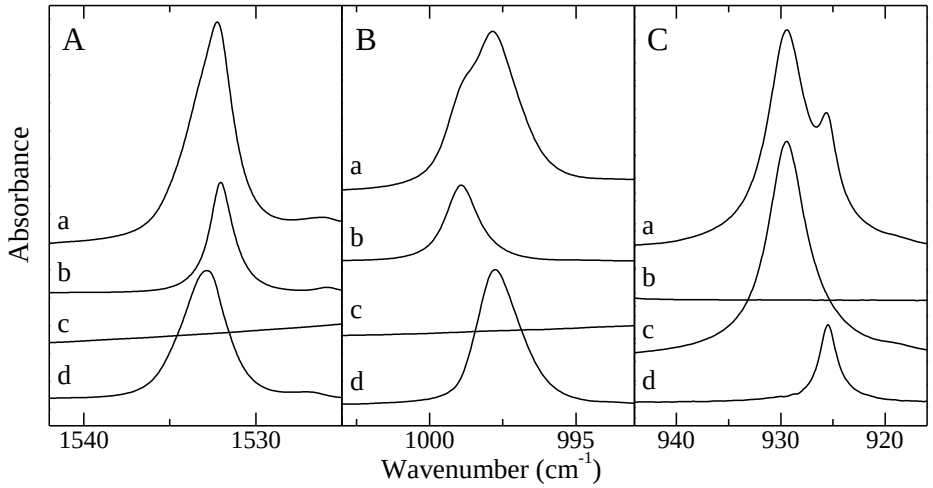

Figure 9.4: Infrared spectra of the C_6F_6 ν_{12} spectral region (panel A), C_6F_6 ν_{13} spectral region (panel B) and DME ν_6 spectral region (panel C) of solutions of mixtures of C_6F_6 and DME dissolved in LKr at 120 K. In each panel, trace *a* represents the mixed solution, while traces *b* and *c* show the solution containing only C_6F_6 or DME, respectively. Trace *d* represents the spectrum of the complex and is obtained by subtracting the rescaled traces *b* and *c* from trace *a*.

Table 9.2: Experimental IR frequencies in LKr at 120 K for the monomer and complex, as well as experimental complexation shifts ($\Delta\nu_{exp}$) and MP2/aug-cc-pVDZ calculated complexation shifts ($\Delta\nu_{calc,lp\cdots\pi}$), in cm^{-1}, for the lp$\cdots\pi$ complex of C_6F_6 with DME.

Assignment		Symmetry	$\nu_{monomer}$	$\nu_{complex}$	$\Delta\nu_{exp}$	$\Delta\nu_{calc,lp\cdots\pi}$
C_6F_6	ν_{12}	E_{1u}	1532.0	1532.9	0.9	1.3
	ν_{12} ^{13}C	E_{1u}	1525.9	1527.1	1.2	1.3
			1024.8	1024.9	0.1	
			1016.9	1017.0	0.1	
	ν_{13}	E_{1u}	999.0	997.8	-1.2	-2.8
DME	ν_1	A_1	2990.4	2990.5	0.1	-8.5
	ν_{16}	B_2	2990.4	2990.5	0.1	-8.6
	ν_{12}	B_1	2916.6	2919.5	2.9	1.8
	ν_2	A_1	2811.9	2816.1	4.2	-2.7
	ν_3	A_1	1475.0	1475.2	0.2	-0.4
	ν_{18}	B_2	1457.7	1458.4	0.7	-0.1
	ν_{13}	B_1	1454.9	1454.7	-0.2	-2.3
	ν_{19}	B_2	1426.3	1425.3	-1.0	-0.7
	ν_5	A_1	1245.1	1245.9	0.8	-2.0
	ν_{20}	B_2	1172.1	-		-6.9
	ν_{21}	B_2	1099.1	-		-4.0
	ν_6	A_1	929.4	925.5	-3.9	-6.1

For mixtures of C_6F_6 with TMA(-d_9), spectra of the fundamental bands of C_6F_6 are given in Figures 9.5 (TMA) and S9.3 of the SI (TMA-d_9). The C_6F_6 ν_{13} spectral region of the mixture with TMA-d_9 is not given due to overlap with the ν_5 mode of TMA-d_9. As with DME, a blueshifted complex band, with a shift of 0.8 cm^{-1} is observed in the ν_{12} spectral region (panel 9.5A), as well as a -2.5 cm^{-1} redshifted complex band in the ν_{13} region (panel 9.5B). Both bands are again in agreement with the calculated values for the lp$\cdots\pi$ complex of 1.3 cm^{-1} and -3.9 cm^{-1}, respectively. An assignment of the monomers and corresponding complex bands is given in Table 9.3 for TMA and Table S9.7 for TMA-d_9.

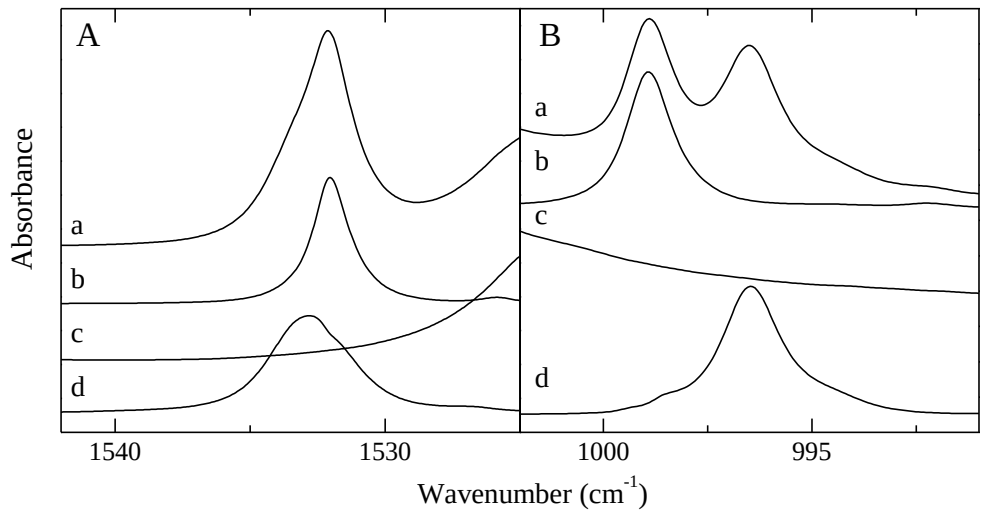

Figure 9.5: Infrared spectra of the C_6F_6 ν_{12} spectral region (panel A) and C_6F_6 ν_{13} spectral region (panel B) of solutions of mixtures of C_6F_6 and TMA dissolved in LKr at 120 K. In each panel, trace *a* represents the mixed solution, while traces *b* and *c* show the solution containing only C_6F_6 or TMA, respectively. Trace *d* represents the spectrum of the complex and is obtained by subtracting the rescaled traces *b* and *c* from trace *a*.

Even though calculated and experimental shifts agree with each other for most vibrational modes, some discrepancies can be found in Tables 9.2, 9.3, S9.6 and S9.7 regarding the complexation shift direction. Many of the vibrational modes with inconsistent shifts are found in the C-H stretching region (around 3000 cm^{-1} for the undeuterated and 2000 cm^{-1} for the deuterated Lewis bases), where, apart from the fundamentals, many overtones and combination bands are found. Therefore the complexation shifts in this region are often perturbed by Fermi resonances, and the assignment of these complex bands is rather difficult. For the DME ν_{18} mode both the calculated and experimental shifts are very small, whereas the DME ν_5 mode (CH_3-rocking mode) is very sensitive to the orientation of the DME molecule towards C_6F_6 in the complex, which might be influenced by the small rotational barrier discussed before. For DME-d_6 the vibrational modes ν_{13}, ν_{20} and ν_{19} have a large overlap, so that the spectra had to be decomposed in order to determine frequencies. For TMA the discrepancy for the ν_4 mode can be explained by the overlap with ν_{16} mode, which has a redshift, as calculated.

Table 9.3: Experimental IR frequencies in LKr at 120 K for the monomer and complex, as well as experimental complexation shifts ($\Delta\nu_{exp}$) and MP2/aug-cc-pVDZ calculated complexation shifts ($\Delta\nu_{calc,\ lp\cdots\pi}$), in cm^{-1}, for the lp···π complex of C_6F_6 with TMA.

Assignment		Symmetry	$\nu_{monomer}$	$\nu_{complex}$	$\Delta\nu_{exp}$	$\Delta\nu_{calc,\ lp\cdots\pi}$
C_6F_6	ν_{12}	E_{1u}	1532.0	1532.8	0.8	1.3
	ν_{12} ^{13}C	E_{1u}	1525.9	1527.1	1.2	1.3
			1024.8	1021.5	-3.3	
			1016.9	1014.4	-2.5	
	ν_{13}	E_{1u}	999.0	996.5	-2.5	-3.9
TMA	ν_{12}	E	2977.0	2978.4	1.4	-11.1
	ν_1	A_1	2944.4	2944.2	-0.2	-9.2
	ν_{13}	E	2944.4	2944.2	-0.2	-9.1
	$2\ \nu_4$	A_1	2818.6	2822.6	4.0	1.4
	ν_2	A_1	2769.0	2773.1	4.1	7.3
	ν_{14}	E	2769.0	2773.1	4.1	8.5
	$\nu_{20} + \nu_{21}$	E	1474.8	1472.8	-2.0	-4.1
	ν_{15}	E	1467.6	1468.7	1.1	1.7
	ν_3	A_1	1454.8	1454.3	-0.5	-3.2
	ν_4	A_1	1438.8	1437.6	-1.2	0.7
	ν_{16}	E	1438.8	1437.6	-1.2	-3.8
	ν_{17}	E	1405.3	-		0.1
	ν_{18}	E	1273.3	1271.4	-1.9	-2.1
	ν_5	A_1	1184.3	1187.1	2.8	0.9
	ν_{19}	E	1098.5	1098.4	-0.1	-2.2
	ν_{20}	E	1041.5	1039.3	-2.2	-1.8
	ν_6	A_1	828.1	826.5	-1.6	-3.8

By constructing van 't Hoff plots from measurements between 120 K and 156 K, seven experimental complexation enthalpies between -5.0 and -6.8 kJ mol^{-1} have been determined for the lp···π complex of C_6F_6 with DME($-d_6$), the average being -6.0(6) kJ mol^{-1}. For the lp···π complex with TMA($-d_9$), five experimental complexation enthalpies were determined between -5.6 kJ mol^{-1} and -8.1 kJ mol^{-1}, with an average value of -6.7(9) kJ mol^{-1}. An example of a van 't Hoff plot for each complex is shown in Figure S9.4 of the SI.

Apart from the 1:1 complexes described above, 1:2 complexes in which two Lewis base molecules form an anti-cooperative sandwich complex on opposite sides of the

C_6F_6 molecular plane can be envisaged. Such complexes have been observed experimentally in studies involving benzene and a large excess of the donor molecules CF_3I [31] and halothane [32]. The existence of (an appreciable amount of) 1:2 complex typically results in the formation of complex bands at the lowest temperatures near the C_6F_6 monomer bands with shifts greater than those of the 1:1 complex. Indeed, MP2/aug-cc-pVDZ *ab initio* calculations of the C_6F_6·2DME complex with C_{2h} symmetry and C_6F_6·2TMA complexes with D_{3h} or S_6 symmetry, for which the Cartesian coordinates are given in Tables S9.3 of the SI, confirm that the complexation shifts of the ν_{12} and ν_{13} modes of C_6F_6 are about two times larger than the complexation shift of the 1:1 complexes. Calculation of the vibrational frequencies confirmed that both complex geometries are real minima. Complexation energies at the MP2/aug-cc-pVDZ level are -38.7 kJ mol^{-1} and -49.5 kJ mol^{-1} for the complexes involving two DME and two TMA molecules, respectively. These values are slightly smaller than double the complexation energies of the 1:1 complexes reported in Table 9.1 (-39.7 kJ mol^{-1} and -50.6 kJ mol^{-1}), indicating a small anti-cooperative effect. The fact that this anti-cooperative effect is rather minute is consistent with the small charge transfer from the Lewis bases towards C_6F_6 observed in the previously mentioned NBO-analysis.

To demonstrate the stoichiometry of the complex present in the solutions, a concentration study [33] in which mixtures with different concentrations are measured at 120 K was performed. By plotting the integrated intensity of a complex band against the product of integrated intensities of the monomers, for different ratios of the monomers, the stoichiometry of the complex can be determined. The results of these concentration studies are given in Figures S9.5 and S9.6 of the SI. The data clearly show that for both Lewis bases a linear correlation is found only for a proposed 1:1 stoichiometry, which supports the idea that in the solutions mainly 1:1 complexes are formed. The appearance of weak spectral features redshifted from the 999.0 cm^{-1} monomer transition and from the 997.8 cm^{-1} and 996.5 cm^{-1} transitions assigned to the 1:1 complexes with DME and TMA respectively, also indicates the formation of 1:2 complex, albeit with an equilibrium concentration substantially smaller than that for

the 1:1 complex. As an example, the spectra of the complex bands of C_6F_6·TMA mixtures with different TMA concentrations, as well as their differential spectrum, is given in Figure S9.7. Further indication that 1:2 complex is only present in a small amount compared to the 1:1 complex is supported by the fact that the gradients of the van ‘t Hoff plots are not influenced by omitting the measurements at the lowest temperatures. We have therefore retained the results of the lowest temperatures in the construction of the van ‘t Hoff plot, even though these are most likely to contain some intensity of the 1:2 complex.

9.3 Conclusions

The existence of an attractive interaction between C_6F_6 and the Lewis bases DME(-d_6) and TMA(-d_9) has been demonstrated experimentally through the use of FTIR on LKr solutions. By comparing experimental complexation shifts with shifts obtained from *ab initio* calculations, it was found that the 1:1 complexes are formed through lp···π type interactions. Furthermore, indications for the presence of a small amount of 1:2 complex, involving two Lewis base molecules on opposite sides of the C_6F_6 molecular plane were found for mixtures with both DME(-d_6) and TMA(-d_9). For the complex with DME, a complex geometry with C_s symmetry was calculated in which the methyl groups of DME are tilted towards C_6F_6, enabling the formation of secondary interactions, which have been visualized using NCIPlot. For the interaction with TMA, a complex with C_{3v} geometry was obtained, in which the methyl groups of TMA are eclipsed with the carbon atoms of C_6F_6. From the construction of van ‘t Hoff plots, experimental complexation enthalpies of -6.0(6) kJ mol^{-1} and -6.7(9) kJ mol^{-1} were determined for the 1:1 complexes involving DME(-d_6) and TMA(-d_9), respectively.

9.4 References

1 J. S. Murray, P. Lane, T. Clark, K. E. Riley, P. Politzer, *J. Mol. Model.*, 2012, ***18***, 541-548.
2 G. Berger, J. Soubhye, A. van der Lee, C. Vande Velde, R. Wintjens, P. Dubois, S. Clément, F. Meyer, *ChemPlusChem*, 2014, ***79***, 552-558.
3 J. Ran, P. Hobza, *J. Chem. Theory Comput.*, 2009, ***5***, 1180-1185.
4 T. Korenaga, T. Shoji, K. Onoue, T. Sakai, *Chem. Commun.*, 2009, 4678-4680.
5 T. J. Mooibroek, P. Gamez, J. Reedijk, *CrystEngComm*, 2008, ***10***, 1501-1515.
6 A. Bauzá, T. J. Mooibroek, A. Frontera, *ChemPhysChem*, 2015, ***16***, 2496-2517.
7 M. Raimondi, G. Calderoni, A. Famulari, L. Raimondi, F. Cozzi, *J. Phys. Chem. A*, 2003, ***107***, 772-774.
8 K. Pluhackova, P. Jurecka, P. Hobza, *Phys. Chem. Chem. Phys.*, 2007, ***9***, 755-760.
9 Y. Danten, T. Tassaing, M. Besnard, *J. Phys. Chem. A*, 1999, ***103***, 3530-3534.
10 J. C. Amicangelo, D. G. Irwin, C. J. Lee, N. C. Romano, N. L. Saxton, *J. Phys. Chem. A*, 2013, ***117***, 1336-1350.
11 C. J. Wormald, B. Wurzberger, *Phys. Chem. Chem. Phys.*, 2000, ***2***, 5133-5137.
12 M. Besnard, Y. Danten, T. Tassaing, *J. Chem. Phys.*, 2000, ***113***, 3741-3748.
13 M. Allesch, E. Schwegler, G. Galli, *J. Phys. Chem. B*, 2007, ***111***, 1081-1089.
14 P. Metrangolo, G. Resnati, T. Pilati, S. Biella, *Struct. Bond.*, 2008, ***126***, 105-136.
15 R. W. Troff, T. Mäkelä, F. Topić, A. Valkonen, K. Raatikainen, K. Rissanen, *Eur. J. Org. Chem.*, 2013, ***2013***, 1617-1637.
16 Y. Geboes, N. Nagels, B. Pinter, F. De Proft, W. A. Herrebout, *J. Phys. Chem. A*, 2015, ***119***, 2502-2516.
17 Y. Geboes, F. De Proft, W. A. Herrebout, *J. Phys. Chem. A*, 2015, ***119***, 5597-5606.
18 Q. Gou, G. Feng, L. Evangelisti, W. Caminati, *Angew. Chem. Int. Ed.*, 2013, ***52***, 11888-11891.
19 L. Spada, Q. Gou, Y. Geboes, W. A. Herrebout, S. Melandri, W. Caminati, *J. Phys. Chem. A*, 2016, ***120***, 4939-4943.
20 Q. Gou, L. Spada, Y. Geboes, W. A. Herrebout, S. Melandri, W. Caminati, *Phys. Chem. Chem. Phys.*, 2015, ***17***, 7694-7698.
21 I. Alkorta, I. Rozas, J. Elguero, *J. Org. Chem.*, 1997, ***62***, 4687-4691.
22 J. C. Amicangelo, B. W. Gung, D. G. Irwin, N. C. Romano, *Phys. Chem. Chem. Phys.*, 2008, ***10***, 2695-2705.
23 I. Alkorta, I. Rozas, M. L. Jimeno, J. Elguero, *Struct. Chem.*, 2001, ***12***, 459-464.
24 E. R. Johnson, S. Keinan, P. Mori-Sánchez, J. Contreras-García, A. J. Cohen, W. Yang, *J. Am. Chem. Soc.*, 2010, ***132***, 6498-6506.
25 J. Contreras-García, E. R. Johnson, S. Keinan, R. Chaudret, J.-P. Piquemal, D. N. Beratan, W. Yang, *J. Chem. Theory Comput.*, 2011, ***7***, 625-632.

26 D. Hauchecorne, R. Szostak, W. A. Herrebout, B. J. van der Veken, *ChemPhysChem*, 2009, ***10***, 2105-2115.
27 D. Hauchecorne, B. J. van der Veken, A. Moiana, W. A. Herrebout, *Chem. Phys.*, 2010, ***374***, 30-36.
28 N. Nagels, Y. Geboes, B. Pinter, F. De Proft, W. A. Herrebout, *Chem. - Eur. J.*, 2014, ***20***, 8433-8443.
29 J. H. S. Green, D. J. Harrison, *J. Chem. Thermodyn.*, 1976, ***8***, 529-544.
30 P. B. Davies, G. M. Hansford, T. C. Killian, *J. Mol. Spectrosc.*, 1994, ***163***, 138-158.
31 N. Nagels, D. Hauchecorne, W. A. Herrebout, *Molecules*, 2013, ***18***, 6829-6851.
32 B. Michielsen, J. J. J. Dom, B. J. van der Veken, S. Hesse, Z. Xue, M. A. Suhm, W. A. Herrebout, *Phys. Chem. Chem. Phys.*, 2010, ***12***, 14034-14044.
33 J. J. J. Dom, B. Michielsen, B. U. W. Maes, W. A. Herrebout, B. J. van der Veken, *Chem. Phys. Lett.*, 2009, ***469***, 85-89.

9.5 Supporting information

Table S9.1.1: Cartesian coordinates of the MP2/aug-cc-pVDZ optimized geometry of C_6F_6.

D_{6h}	X	Y	Z
C_6F_6			
C	0.000000	1.399839	0.000000
C	1.212296	0.699919	0.000000
C	1.212296	-0.699919	0.000000
C	0.000000	-1.399839	0.000000
C	-1.212296	-0.699919	0.000000
C	-1.212296	0.699919	0.000000
F	0.000000	-2.744497	0.000000
F	-2.376804	-1.372248	0.000000
F	-2.376804	1.372248	0.000000
F	0.000000	2.744497	0.000000
F	2.376804	1.372248	0.000000
F	2.376804	-1.372248	0.000000

Table S9.1.2: Cartesian coordinates of the MP2/aug-cc-pVDZ optimized geometry of DME.

C_{2v}	X	Y	Z
DME			
O	0.000000	0.000000	0.607066
C	0.000000	1.169581	-0.202099
H	0.000000	2.032636	0.474896
H	0.898418	1.208635	-0.845282
H	-0.898418	1.208635	-0.845282
C	0.000000	-1.169581	-0.202099
H	0.898418	-1.208635	-0.845282
H	0.000000	-2.032636	0.474896
H	-0.898418	-1.208635	-0.845282

Table S9.1.3: Cartesian coordinates of the MP2/aug-cc-pVDZ optimized geometry of TMA.

C_{3v}	X	Y	Z
TMA			
N	0.000000	0.000000	0.410619
C	0.000000	1.379959	-0.066347
H	-0.892330	1.901918	0.309142
H	0.892330	1.901918	0.309142
H	0.000000	1.440847	-1.178318
C	1.195079	-0.689979	-0.066347
H	2.093274	-0.178178	0.309142
H	1.200944	-1.723740	0.309142
H	1.247810	-0.720423	-1.178318
C	-1.195079	-0.689979	-0.066347
H	-1.200944	-1.723740	0.309142
H	-2.093274	-0.178178	0.309142
H	-1.247810	-0.720423	-1.178318

Table S9.2.1: Cartesian coordinates of the MP2/aug-cc-pVDZ optimized geometry of the 1:1 lp···π complex between C_6F_6 and DME.

C_s	X	Y	Z
C_6F_6			
C	-0.957184	-0.062993	1.211084
C	-1.353545	-0.639750	0.000000
C	-0.957184	-0.062993	-1.211084
C	-0.158979	1.085606	-1.210775
C	0.239633	1.661022	0.000000
C	-0.158979	1.085606	1.210775
F	0.236030	1.628805	-2.377507
F	1.016467	2.758484	0.000000
F	0.236030	1.628805	2.377507
F	-1.329069	-0.624597	2.377654
F	-2.109208	-1.755361	0.000000
F	-1.329069	-0.624597	-2.377654
DME			
O	1.928282	-1.142386	0.000000
C	1.900186	-1.952508	-1.171379
H	0.979207	-2.564550	-1.209382
H	1.924498	-1.276361	-2.035959
H	2.775462	-2.625911	-1.210378
C	1.900186	-1.952508	1.171379
H	1.924498	-1.276361	2.035959
H	0.979207	-2.564550	1.209382
H	2.775462	-2.625911	1.210378

Table S9.2.2: Cartesian coordinates of the MP2/aug-cc-pVDZ optimized geometry of the 1:1 lp···π complex between C_6F_6 and TMA.

C_{3v}	X	Y	Z
C_6F_6			
C	0.000000	-1.398454	-0.949902
C	1.210826	-0.699071	-0.947581
C	1.211097	0.699227	-0.949902
C	0.000000	1.398142	-0.947581
C	-1.211097	0.699227	-0.949902
C	-1.210826	-0.699071	-0.947581
F	0.000000	2.745300	-0.926788
F	-2.377432	1.372611	-0.930561
F	-2.377500	-1.372650	-0.926788
F	0.000000	-2.745222	-0.930561
F	2.377500	-1.372650	-0.926788
F	2.377432	1.372611	-0.930561
TMA			
N	0.000000	0.000000	2.073175
C	1.197400	0.691319	2.545390
H	2.095406	0.178561	2.167568
H	1.202341	1.725394	2.167568
H	1.256390	0.725377	3.656158
C	0.000000	-1.382638	2.545390
H	-0.893064	-1.903955	2.167568
H	0.893064	-1.903955	2.167568
H	0.000000	-1.450755	3.656158
C	-1.197400	0.691319	2.545390
H	-1.202341	1.725394	2.167568
H	-2.095406	0.178561	2.167568
H	-1.256390	0.725377	3.656158

Table S9.3.1: Cartesian coordinates of the MP2/aug-cc-pVDZ optimized geometry of the 1:2 lp···π complex between C_6F_6 and DME.

C_{2h}	X	Y	Z
C_6F_6			
C	0.001588	0.698839	1.209683
C	-0.002410	1.398839	-0.000002
C	0.001588	0.698838	-1.209686
C	-0.001588	-0.698840	-1.209683
C	0.002410	-1.398839	0.000001
C	-0.001588	-0.698840	1.209685
F	-0.001616	-1.371343	-2.378574
F	0.004320	-2.745977	0.000001
F	-0.001615	-1.371339	2.378579
F	0.001616	1.371341	2.378575
F	-0.004320	2.745977	-0.000004
F	0.001615	1.371339	-2.378579
DME 1			
O	-3.011287	-0.065949	-0.000001
C	-3.421446	0.632859	-1.170990
H	-2.976151	1.645172	-1.206462
H	-3.074145	0.052008	-2.035423
H	-4.521791	0.727775	-1.213039
C	-3.421446	0.632855	1.170991
H	-3.074145	0.052001	2.035421
H	-2.976150	1.645167	1.206465
H	-4.521791	0.727770	1.213039
DME 2			
O	3.011287	0.065949	0.000001
C	3.421446	-0.632855	-1.170990
H	3.074144	-0.052003	-2.035421
H	4.521791	-0.727770	-1.213039
H	2.976152	-1.645169	-1.206463
C	3.421446	-0.632857	1.170991
H	4.521791	-0.727772	1.213039
H	3.074144	-0.052006	2.035423
H	2.976151	-1.645170	1.206463

Table S9.3.2: Cartesian coordinates of the MP2/aug-cc-pVDZ optimized geometry of the 1:2 lp···π complex between C_6F_6 and TMA with D_{3h}-symmetry.

D_{3h}	X	Y	Z
C_6F_6			
C	1.210084	0.698642	0.000000
C	0.000000	1.396640	0.000000
C	-1.210084	0.698642	0.000000
C	-1.209526	-0.698320	0.000000
C	0.000000	-1.397284	0.000000
C	1.209526	-0.698320	0.000000
F	-2.378570	-1.373268	0.000000
F	0.000000	-2.746378	0.000000
F	2.378570	-1.373268	0.000000
F	2.378433	1.373189	0.000000
F	0.000000	2.746536	0.000000
F	-2.378433	1.373189	0.000000
TMA 1			
N	0.000000	0.000000	3.042546
C	-1.197525	0.691392	3.512025
H	-1.201764	1.724887	3.132383
H	-2.094678	0.178315	3.132383
H	-1.258924	0.726840	4.622922
C	1.197525	0.691392	3.512025
H	2.094678	0.178315	3.132383
H	1.201764	1.724887	3.132383
H	1.258924	0.726840	4.622922
C	0.000000	-1.382783	3.512025
H	-0.892914	-1.903201	3.132383
H	0.892914	-1.903201	3.132383
H	0.000000	-1.453680	4.622922
TMA 2			
N	0.000000	0.000000	-3.042546
C	-1.197525	0.691392	-3.512025
H	-2.094678	0.178315	-3.132383
H	-1.201764	1.724887	-3.132383
H	-1.258924	0.726840	-4.622922
C	1.197525	0.691392	-3.512025
H	1.201764	1.724887	-3.132383
H	2.094678	0.178315	-3.132383
H	1.258924	0.726840	-4.622922
C	0.000000	-1.382783	-3.512025
H	0.892914	-1.903201	-3.132383
H	-0.892914	-1.903201	-3.132383
H	0.000000	-1.453680	-4.622922

Table S9.3.3: Cartesian coordinates of the MP2/aug-cc-pVDZ optimized geometry of the 1:2 lp···π complex between C_6F_6 and TMA with S_6-symmetry.

S_6	X	Y	Z
C_6F_6			
C	-1.187814	0.735251	0.002290
C	0.042845	1.396299	-0.002292
C	1.230662	0.661052	0.002292
C	1.187822	-0.735259	-0.002291
C	-0.042834	-1.396306	0.002292
C	-1.230657	-0.661054	-0.002293
F	2.335238	-1.445508	-0.003319
F	-0.084219	-2.745127	0.003323
F	-2.419461	-1.299621	-0.003322
F	-2.335231	1.445504	0.003317
F	0.084232	2.745119	-0.003322
F	2.419465	1.299625	0.003323
TMA 1			
N	-0.000002	0.000001	-3.041902
C	1.204330	0.679390	-3.511364
H	1.218948	1.712782	-3.131865
H	2.096342	0.157328	-3.132052
H	1.266086	0.714355	-4.622262
C	-1.190533	0.703290	-3.511364
H	-2.092782	0.199251	-3.131863
H	-1.184420	1.736827	-3.132054
H	-1.251693	0.739287	-4.622262
C	-0.013805	-1.382676	-3.511362
H	0.873829	-1.912026	-3.131860
H	-0.911930	-1.894154	-3.132054
H	-0.014397	-1.453641	-4.622260
TMA 2			
N	-0.000003	0.000001	3.041903
C	1.190538	-0.703274	3.511362
H	1.184434	-1.736810	3.132050
H	2.092783	-0.199228	3.131862
H	1.251699	-0.739273	4.622260
C	0.013787	1.382676	3.511364
H	0.911908	1.894162	3.132054
H	-0.873853	1.912017	3.131863
H	0.014380	1.453642	4.622262
C	-1.204329	-0.679399	3.511364
H	-2.096349	-0.157346	3.132057
H	-1.218935	-1.712789	3.131862
H	-1.266082	-0.714369	4.622262

Table S9.4A: MP2/aug-cc-pVDZ vibrational frequencies, in cm^{-1}, and IR intensities, in km mol^{-1} for C_6F_6, DME and the 1:1 lp···π complex of C_6F_6 with DME, as well as the complexation shift Δν.

	Monomer		lp···π complex		
	Frequency	IR intensity	Frequency	Δν	IR intensity
C_6F_6					
ν_1 (A_{1g})	1516.1	0.0	1514.0	-2.2	0.7
ν_2 (A_{1g})	554.7	0.0	554.4	-0.4	0.01
ν_3 (A_{2g})	783.0	0.0	784.3	1.3	0.0001
ν_4 (A_{2u})	211.0	4.8	215.3	4.2	6.7
ν_5 (B_{1u})	1283.7	0.0	1277.6	-6.1	0.01
ν_6 (B_{1u})	588.7	0.0	588.0	-0.7	0.0008
ν_7 (B_{2g})	427.0	0.0	408.7	-18.3	0.006
ν_8 (B_{2g})	177.9	0.0	176.0	-1.8	0.0001
ν_9 (B_{2u})	1475.5	0.0	1488.4	12.9	0.03
ν_{10} (B_{2u})	276.3	0.0	276.2	0.0	0.0
ν_{11} (E_{1g})	359.6	0.0	367.1	7.5	0.006
ν_{12} (E_{1u})	1553.4	328.2	1554.7	1.3	299.1
ν_{13} (E_{1u})	1000.4	246.8	997.6	-2.8	224.4
ν_{14} (E_{1u})	313.5	1.5	313.0	-0.4	1.2
ν_{15} (E_{2g})	1692.9	0.0	1694.9	2.0	0.1
ν_{16} (E_{2g})	1148.3	0.0	1144.7	-3.6	0.1
ν_{17} (E_{2g})	436.3	0.0	436.2	-0.1	0.003
ν_{18} (E_{2g})	265.2	0.0	265.0	-0.2	0.1
ν_{19} (E_{2u})	605.7	0.0	600.0	-5.7	0.02
ν_{20} (E_{2u})	136.6	0.0	135.7	-0.8	0.0008
DME					
ν_1 (A_1)	3188.7	20.1	3180.2	-8.5	19.9
ν_2 (A_1)	3024.8	58.6	3022.1	-2.7	42.2
ν_3 (A_1)	1505.9	2.9	1505.5	-0.4	12.3
ν_4 (A_1)	1473.5	0.0	1472.9	-0.6	0.3
ν_5 (A_1)	1261.1	6.6	1259.1	-2.0	5.8
ν_6 (A_1)	942.4	34.7	936.3	-6.1	30.8
ν_7 (A_1)	416.8	2.3	416.8	0.0	1.7
ν_8 (A_2)	3096.2	0.0	3097.6	1.4	2.2
ν_9 (A_2)	1474.8	0.0	1471.4	-3.4	1.4
ν_{10} (A_2)	1157.2	0.0	1155.4	-1.8	0.02
ν_{11} (A_2)	195.2	0.0	208.5	13.3	0.01
ν_{12} (B_1)	3089.5	107.8	3091.3	1.8	101.5
ν_{13} (B_1)	1489.2	13.0	1486.9	-2.3	15.9
ν_{14} (B_1)	1187.2	7.2	1185.5	-1.6	6.5
ν_{15} (B_1)	260.2	5.1	269.5	9.3	6.1
ν_{16} (B_2)	3187.3	24.6	3178.7	-8.6	12.7
ν_{17} (B_2)	3018.4	55.2	3016.4	-1.9	39.0
ν_{18} (B_2)	1490.1	10.3	1490.0	-0.1	7.6
ν_{19} (B_2)	1441.5	2.5	1440.8	-0.7	0.1
ν_{20} (B_2)	1191.9	98.1	1185.0	-6.9	76.6
ν_{21} (B_2)	1113.8	35.0	1109.8	-4.0	33.0

Van der Waals vibrations: 10.5 cm^{-1}, 0.06 km mol^{-1}, 28.3 cm^{-1}, 0.3 km mol^{-1}, 33.1 cm^{-1}, 0.02 km mol^{-1}, 70.8 cm^{-1}, 0.02 km mol^{-1}, 71.3 cm^{-1}, 0.7 km mol^{-1}, 93.2 cm^{-1}, 5.6 km mol^{-1}.

Table S9.4B: MP2/aug-cc-pVDZ vibrational frequencies, in cm^{-1}, and IR intensities, in km mol^{-1} for C_6F_6, DME-d_6 and the 1:1 lp···π complex of C_6F_6 with DME-d_6, as well as the complexation shift Δν.

	Monomer		lp···π complex		
	Frequency	IR intensity	Frequency	Δν	IR intensity
C_6F_6					
ν_1 (A_{1g})	1516.1	0.0	1513.9	-2.3	0.6
ν_2 (A_{1g})	554.7	0.0	554.4	-0.4	0.01
ν_3 (A_{2g})	783.0	0.0	784.3	1.3	0.0001
ν_4 (A_{2u})	211.0	4.8	216.1	5.1	10.4
ν_5 (B_{1u})	1283.7	0.0	1277.7	-6.0	0.009
ν_6 (B_{1u})	588.7	0.0	588.0	-0.7	0.0009
ν_7 (B_{2g})	427.0	0.0	408.7	-18.3	0.008
ν_8 (B_{2g})	177.9	0.0	176.0	-1.8	0.0001
ν_9 (B_{2u})	1475.5	0.0	1488.5	13.0	0.008
ν_{10} (B_{2u})	276.3	0.0	276.2	0.0	0.0
ν_{11} (E_{1g})	359.6	0.0	367.3	7.6	0.03
ν_{12} (E_{1u})	1553.4	328.2	1554.7	1.2	299.9
ν_{13} (E_{1u})	1000.4	246.8	997.5	-2.9	223.4
ν_{14} (E_{1u})	313.5	1.5	313.0	-0.4	1.2
ν_{15} (E_{2g})	1692.9	0.0	1694.9	2.0	0.1
ν_{16} (E_{2g})	1148.3	0.0	1144.9	-3.4	0.6
ν_{17} (E_{2g})	436.3	0.0	436.2	-0.1	0.003
ν_{18} (E_{2g})	265.2	0.0	265.1	-0.2	0.0008
ν_{19} (E_{2u})	605.7	0.0	600.0	-5.7	0.02
ν_{20} (E_{2u})	136.6	0.0	135.7	-0.9	0.0007
DME-d_6					
ν_1 (A_1)	2364.1	17.0	2358.5	-5.6	15.6
ν_2 (A_1)	2171.1	32.1	2169.1	-2.0	24.2
ν_3 (A_1)	1153.5	5.3	1151.0	-2.5	4.4
ν_4 (A_1)	1085.9	0.1	1085.1	-0.8	1.2
ν_5 (A_1)	1058.5	17.5	1057.3	-1.2	19.8
ν_6 (A_1)	834.8	16.9	831.0	-3.8	16.8
ν_7 (A_1)	351.5	1.5	351.3	-0.2	1.1
ν_8 (A_2)	2297.2	0.0	2298.0	0.8	0.8
ν_9 (A_2)	1065.8	0.0	1063.3	-2.5	0.002
ν_{10} (A_2)	877.6	0.0	876.1	-1.6	0.1
ν_{11} (A_2)	139.5	0.0	149.0	9.5	0.005
ν_{12} (B_1)	2290.4	65.1	2291.5	1.1	60.0
ν_{13} (B_1)	1077.4	4.3	1075.1	-2.3	5.9
ν_{14} (B_1)	937.8	9.9	936.3	-1.5	9.3
ν_{15} (B_1)	200.5	4.6	207.5	7.0	2.2
ν_{16} (B_2)	2360.7	10.6	2355.0	-5.7	5.3
ν_{17} (B_2)	2164.0	44.9	2162.5	-1.5	32.4
ν_{18} (B_2)	1170.3	134.3	1162.8	-7.5	105.4
ν_{19} (B_2)	1077.4	0.5	1076.5	-0.8	0.4
ν_{20} (B_2)	1066.1	1.6	1065.3	-0.9	3.1
ν_{21} (B_2)	860.9	0.1	859.0	-1.9	0.1

Van der Waals vibrations: 9.2 cm^{-1}, 0.4 km mol^{-1}, 27.3 cm^{-1}, 0.3 km mol^{-1}, 32.0 cm^{-1}, 0.02 km mol^{-1}, 62.4 cm^{-1}, 0.01 km mol^{-1}, 64.4 cm^{-1}, 1.2 km mol^{-1}, 81.4 cm^{-1}, 2.5 km mol^{-1}.

Table S9.5A: MP2/aug-cc-pVDZ vibrational frequencies, in cm^{-1}, and IR intensities, in km mol^{-1}, for C_6F_6, TMA and the 1:1 lp···π complex of C_6F_6 with TMA, as well as the complexation shift Δν.

	Monomer		lp···π complex		
	Frequency	IR intensity	Frequency	Δν	IR intensity
C_6F_6					
ν_1 (A_{1g})	1516.1	0.0	1512.6	-3.5	2.2
ν_2 (A_{1g})	554.7	0.0	554.2	-0.6	0.0001
ν_3 (A_{2g})	783.0	0.0	784.1	1.0	0.0
ν_4 (A_{2u})	211.0	4.8	213.1	2.1	5.7
ν_5 (B_{1u})	1283.7	0.0	1276.0	-7.8	0.02
ν_6 (B_{1u})	588.7	0.0	588.1	-0.6	0.002
ν_7 (B_{2g})	427.0	0.0	405.5	-21.5	0.007
ν_8 (B_{2g})	177.9	0.0	175.2	-2.6	0.0
ν_9 (B_{2u})	1475.5	0.0	1492.8	17.3	0.0
ν_{10} (B_{2u})	276.3	0.0	276.2	-0.1	0.0
ν_{11} (E_{1g})	359.6	0.0	368.7	9.1	0.01
ν_{12} (E_{1u})	1553.4	328.2	1554.7	1.3	285.5
ν_{13} (E_{1u})	1000.4	246.8	996.5	-3.9	214.4
ν_{14} (E_{1u})	313.5	1.5	312.7	-0.8	1.1
ν_{15} (E_{2g})	1692.9	0.0	1695.4	2.5	0.002
ν_{16} (E_{2g})	1148.3	0.0	1143.0	-5.3	0.02
ν_{17} (E_{2g})	436.3	0.0	435.8	-0.6	0.0001
ν_{18} (E_{2g})	265.2	0.0	264.9	-0.3	0.0
ν_{19} (E_{2u})	605.7	0.0	595.0	-10.7	0.003
ν_{20} (E_{2u})	136.6	0.0	134.8	-1.8	0.0
TMA					
ν_1 (A_1)	3111.8	42.4	3102.6	-9.2	59.2
ν_2 (A_1)	2962.3	167.2	2969.5	7.3	173.8
ν_3 (A_1)	1499.0	23.4	1495.9	-3.2	29.8
ν_4 (A_1)	1464.0	1.6	1464.7	0.7	1.2
ν_5 (A_1)	1204.0	24.9	1204.9	0.9	22.8
ν_6 (A_1)	853.0	22.9	849.2	-3.8	31.4
ν_7 (A_1)	383.8	7.6	387.4	3.6	10.1
ν_8 (A_2)	3163.7	0.0	3152.5	-11.1	0.0
ν_9 (A_2)	1477.7	0.0	1479.1	1.3	0.0
ν_{10} (A_2)	1057.3	0.0	1055.8	-1.5	0.0
ν_{11} (A_2)	243.9	0.0	249.2	5.3	0.0
ν_{12} (E)	3166.8	34.6	3155.7	-11.1	24.4
ν_{13} (E)	3111.1	26.1	3102.0	-9.1	11.8
ν_{14} (E)	2955.2	44.4	2963.8	8.5	40.7
ν_{15} (E)	1500.8	9.8	1502.5	1.7	16.0
ν_{16} (E)	1475.1	5.7	1471.3	-3.8	0.4
ν_{17} (E)	1421.1	0.7	1421.2	0.1	0.1
ν_{18} (E)	1303.4	14.9	1301.3	-2.1	12.3
ν_{19} (E)	1115.9	9.1	1113.7	-2.2	7.8
ν_{20} (E)	1066.2	13.6	1064.4	-1.8	13.3
ν_{21} (E)	423.6	0.006	421.4	-2.2	0.01
ν_{22} (E)	290.9	0.4	292.7	1.7	0.5

Van der Waals vibrations: 6.3 cm^{-1}, 0.0 km mol^{-1}, 32.0 cm^{-1}, 0.08 km mol^{-1}, 32.0 cm^{-1}, 0.08 km mol^{-1}, 57.0 cm^{-1}, 0.006 km mol^{-1}, 57.0 cm^{-1}, 0.006 km mol^{-1}, 71.6 cm^{-1}, 0.005 km mol^{-1}.

Table S9.5B: MP2/aug-cc-pVDZ vibrational frequencies, in cm^{-1}, and IR intensities, in km mol^{-1}, for C_6F_6, TMA-d_9 and the 1:1 lp···π complex of C_6F_6 with TMA-d_9, as well as the complexation shift Δν.

	Monomer		lp···π complex		
	Frequency	IR intensity	Frequency	Δν	IR intensity
C_6F_6					
ν_1 (A_{1g})	1516.1	0.0	1512.5	-3.6	1.5
ν_2 (A_{1g})	554.7	0.0	554.2	-0.6	0.0
ν_3 (A_{2g})	783.0	0.0	784.1	1.0	0.0
ν_4 (A_{2u})	211.0	4.8	212.8	1.8	5.5
ν_5 (B_{1u})	1283.7	0.0	1276.1	-7.7	0.0004
ν_6 (B_{1u})	588.7	0.0	588.1	-0.6	0.002
ν_7 (B_{2g})	427.0	0.0	405.5	-21.5	0.009
ν_8 (B_{2g})	177.9	0.0	175.2	-2.6	0.0
ν_9 (B_{2u})	1475.5	0.0	1492.8	17.3	0.0
ν_{10} (B_{2u})	276.3	0.0	276.2	-0.1	0.0
ν_{11} (E_{1g})	359.6	0.0	369.2	9.6	0.009
ν_{12} (E_{1u})	1553.4	328.2	1554.6	1.2	286.4
ν_{13} (E_{1u})	1000.4	246.8	996.4	-4.0	217.6
ν_{14} (E_{1u})	313.5	1.5	312.7	-0.8	1.1
ν_{15} (E_{2g})	1692.9	0.0	1695.4	2.5	0.001
ν_{16} (E_{2g})	1148.3	0.0	1143.3	-5.1	0.03
ν_{17} (E_{2g})	436.3	0.0	435.8	-0.6	0.0001
ν_{18} (E_{2g})	265.2	0.0	264.9	-0.3	0.0002
ν_{19} (E_{2u})	605.7	0.0	595.0	-10.7	0.003
ν_{20} (E_{2u})	136.6	0.0	134.7	-1.8	0.0
TMA-d_9					
ν_1 (A_1)	2286.9	51.7	2282.8	-4.1	65.2
ν_2 (A_1)	2142.3	72.7	2145.6	3.3	71.3
ν_3 (A_1)	1151.7	0.2	1150.9	-0.8	0.2
ν_4 (A_1)	1079.2	12.6	1076.8	-2.4	17.0
ν_5 (A_1)	1018.9	33.5	1019.7	0.8	34.2
ν_6 (A_1)	756.9	12.4	754.2	-2.7	18.2
ν_7 (A_1)	323.0	4.6	327.3	4.4	6.7
ν_8 (A_2)	2345.4	0.0	2337.1	-8.4	0.0
ν_9 (A_2)	1067.7	0.0	1068.1	0.4	0.0
ν_{10} (A_2)	801.3	0.0	800.7	-0.5	0.0
ν_{11} (A_2)	173.1	0.0	176.8	3.7	0.0
ν_{12} (E)	2349.0	17.4	2340.7	-8.3	12.2
ν_{13} (E)	2287.5	8.1	2283.6	-3.9	2.7
ν_{14} (E)	2135.6	36.1	2139.3	3.8	30.6
ν_{15} (E)	1252.4	33.4	1250.2	-2.1	28.3
ν_{16} (E)	1078.6	2.1	1078.7	0.1	2.9
ν_{17} (E)	1073.1	0.2	1072.6	-0.5	0.3
ν_{18} (E)	1063.4	1.6	1061.1	-2.3	0.8
ν_{19} (E)	886.2	7.4	885.1	-1.1	5.0
ν_{20} (E)	839.0	0.03	837.6	-1.3	0.001
ν_{21} (E)	352.0	0.007	349.5	-2.5	0.02
ν_{22} (E)	210.6	0.2	211.8	1.2	0.2

Van der Waals vibrations: 5.6 cm^{-1}, 0.0 km mol^{-1}, 30.5 cm^{-1}, 0.06 km mol^{-1}, 30.5 cm^{-1}, 0.06 km mol^{-1}, 50.5 cm^{-1}, 0.01 km mol^{-1}, 50.5 cm^{-1}, 0.01 km mol^{-1}, 67.7 cm^{-1}, 0.01 km mol^{-1}.

Table S9.6: Experimental infrared frequencies for the monomer and complex, as well as experimental complexation shifts ($\Delta\nu_{exp}$) and MP2/aug-cc-pVDZ calculated complexation shifts ($\Delta\nu_{calc,lp\cdots\pi}$), in cm^{-1}, for the lp···π complex of C_6F_6 with DME-d_6 dissolved in LKr at 120 K.

Assignment		Symmetry	$\nu_{monomer}$	$\nu_{complex}$	$\Delta\nu_{exp,lp\cdots\pi}$	$\Delta\nu_{calc,lp\cdots\pi}$
C_6F_6	ν_{12}	E_{1u}	1532.0	1532.5	0.5	1.2
	ν_{12} ^{13}C	E_{1u}	1525.9	1526.8	0.9	1.2
			1024.8			
			1016.9	1017.1	0.2	
	ν_{13}	E_{1u}	999.0	997.9	-1.1	-2.9
DME-d_6	ν_1	A_1	2243.6	2245.4	1.8	-5.6
	ν_{16}	B_2	2243.6	2245.4	1.8	-5.7
	ν_{12}	B_1	2180.0	2185.3	5.3	1.1
	ν_2	A_1	2054.3	2057.0	2.7	-2.0
	ν_{17}	B_2	2049.8	2052.6	2.8	-1.5
	ν_{18}	B_2	1153.4	1148.1	-5.3	-7.5
	ν_3	A_1	1144.7	1143.3	-1.4	-2.5
	ν_{13}	B_1	1060.7	1061.1	0.4	-2.3
	ν_{19}	B_2	1057.9	1058.0	0.1	-0.8
	ν_{20}	B_2	1057.9	1058.0	0.1	-0.9
	ν_5	A_1	1050.8	1051.2	0.4	-1.2
	ν_{14}	B_1	929.2	929.1	-0.1	-1.5
	ν_{21}	B_2	857.9			-1.9
	ν_6	A_1	826.4	824.4	-2.0	-3.8

Table S9.7: Experimental infrared frequencies for the monomer and complex, as well as experimental complexation shifts ($\Delta\nu_{exp}$) and MP2/aug-cc-pVDZ calculated complexation shifts ($\Delta\nu_{calc,\ lp\cdots\pi}$), in cm^{-1}, for the lp···π complex of C_6F_6 with TMA-d_9 dissolved in LKr at 120 K.

Assignment		Symmetry	$\nu_{monomer}$	$\nu_{complex}$	$\Delta\nu_{exp,lp\cdots\pi}$	$\Delta\nu_{calc,\ lp\cdots\pi}$
C_6F_6	ν_{12}	E_{1u}	1532.0	1532.8	0.8	1.2
	ν_{12} ^{13}C	E_{1u}	1525.9	1527.1	1.2	1.2
			1024.8	1021.5	-3.3	
			1016.9	1014.4	-2.5	
	ν_{13}	E_{1u}	999.0	996.5	-2.5	-4.0
TMA-d_9	ν_{12}	E	2233.0	2232.4	-0.6	-8.3
	ν_1	A_1	2182.2	2183.7	1.5	-4.1
	ν_{13}	E	2182.2	2183.7	1.5	-3.9
	ν_2	A_1	2029.5	2033.2	3.7	3.3
	ν_{14}	E	2029.5	2033.2	3.7	3.8
	$\nu_{19} + \nu_{21}$	E	1226.5	1224.5	-2.0	-3.6
	ν_{15}	E	1220.8	1218.3	-2.5	-2.1
	ν_4	A_1	1063.0	1064.0	1.0	-2.4
	ν_{16}	E	1063.0	1062.6	-0.4	0.1
	ν_{17}	E	1055.7			-0.5
	ν_{18}	E	1047.7	1048.0	0.3	-2.3
	ν_5	A_1	1004.0	-		0.8
	ν_{19}	E	873.9	873.5	-0.4	-1.1
	ν_6	A_1	741.1	740.0	-1.1	-2.7

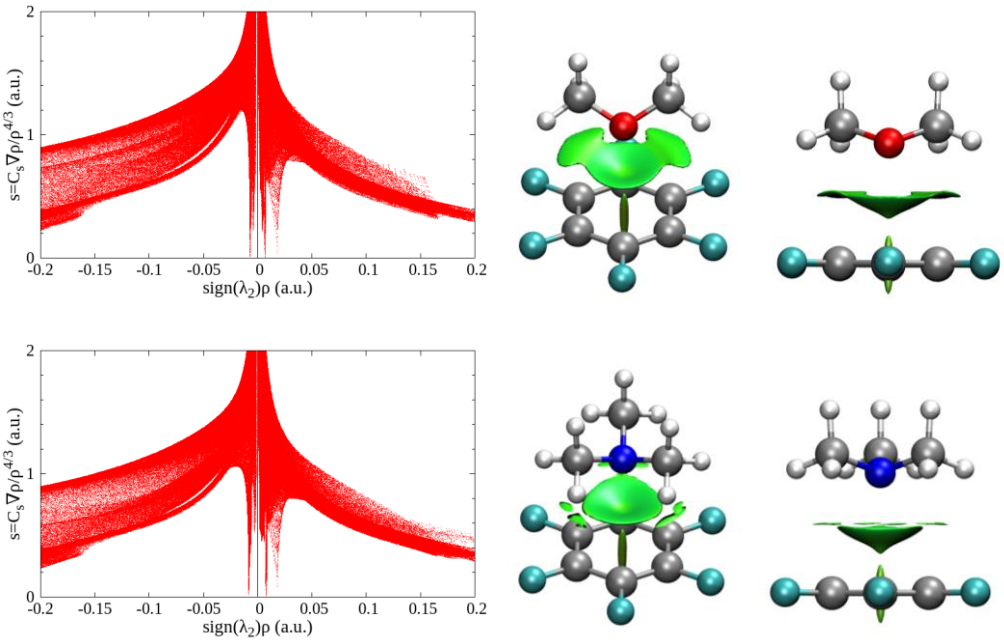

Figure S9.1: Plots of the reduced density gradient versus the electron density multiplied by the sign of the second Hessian eigenvalue (left) and gradient isosurfaces (s = 0.5 a.u., right) for the C_6F_6·DME lp···π complex (top) and C_6F_6·TMA lp···π complex (bottom).

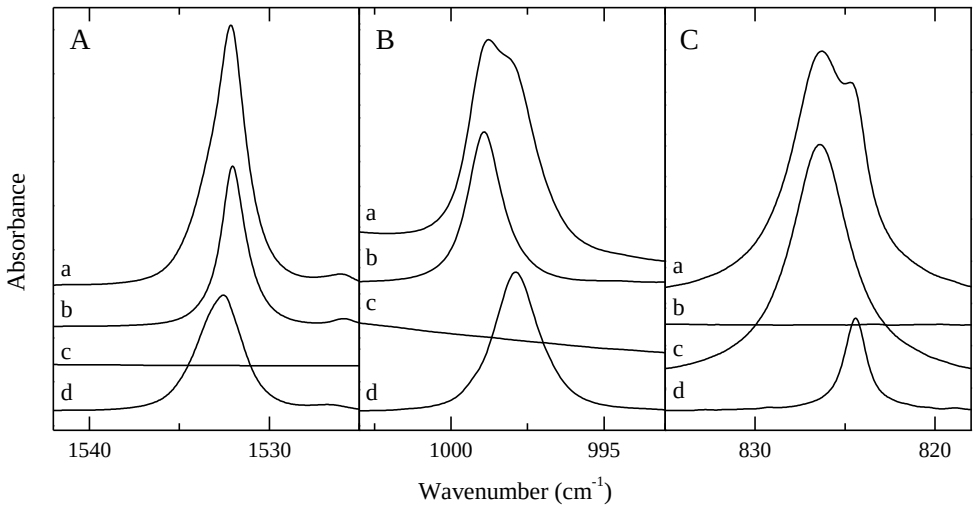

Figure S9.2: Infrared spectra of the C_6F_6 ν_{12} spectral region (panel A), C_6F_6 ν_{13} spectral region (panel B) and DME-d_6 ν_6 spectral region (panel C) of solutions of mixtures of C_6F_6 and DME-d_6 dissolved in LKr at 120 K. In each panel, trace *a* represents the mixed solution, while traces *b* and *c* show the solution containing only C_6F_6 or DME-d_6, respectively. Trace *d* represents the spectrum of the complex and is obtained by subtracting the rescaled traces *b* and *c* from trace *a*.

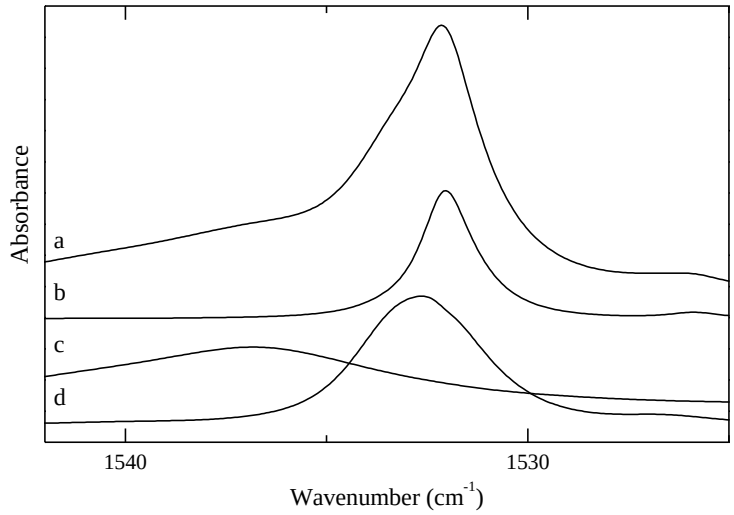

Figure S9.3: Infrared spectra of the C_6F_6 ν_{12} spectral region of mixtures of C_6F_6 and TMA-d_9 dissolved in LKr at 120 K. Trace *a* represents the mixed solution, while traces *b* and *c* show the solution containing only C_6F_6 or TMA-d_9, respectively. Trace *d* represents the spectrum of the complex and is obtained by subtracting the rescaled traces *b* and *c* from trace *a*.

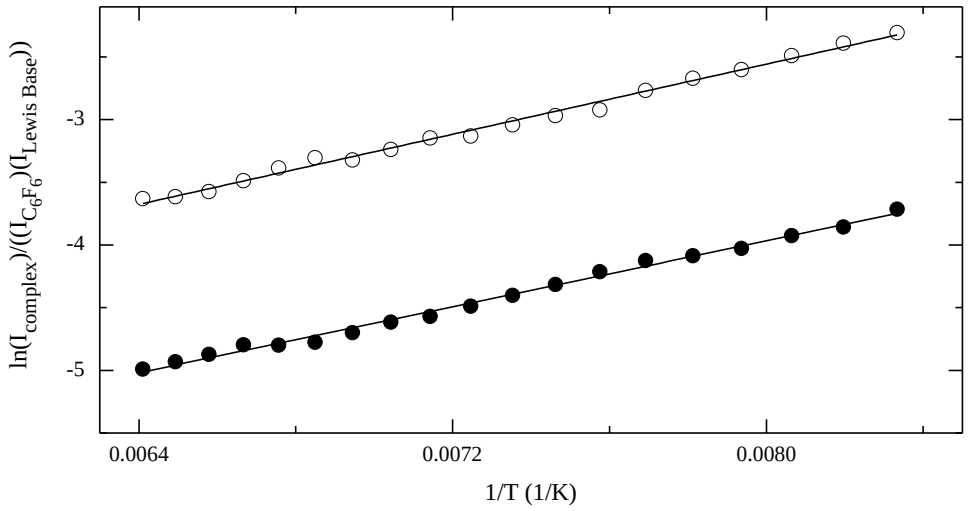

Figure S9.4: Typical van 't Hoff plot of the lp···π complexes of C_6F_6 with DME(-d_6) (●) and TMA(-d_9) (○) in LKr.

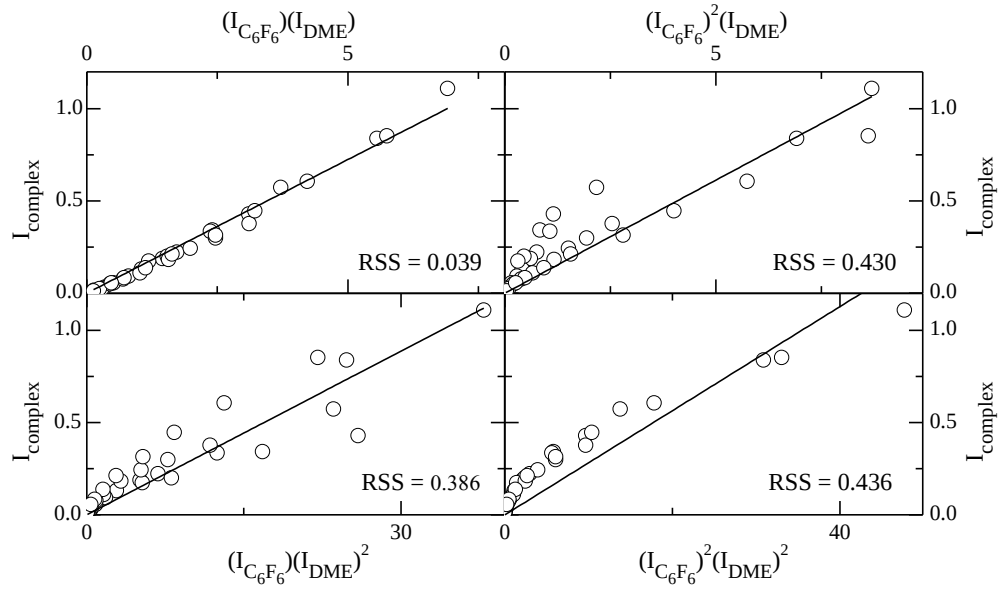

Figure S9.5: Concentration studies for the C_6F_6 ν_{13} complex band for mixed solutions in LKr at 120 K containing C_6F_6 and DME. The integrated band areas of the complex bands were plotted against the intensity products corresponding to a 1:1 (top left), 2:1 (top right), 1:2 (bottom left) and 2:2 (bottom right) stoichiometry. Additionally, residual sum of square values (RSS) have been included.

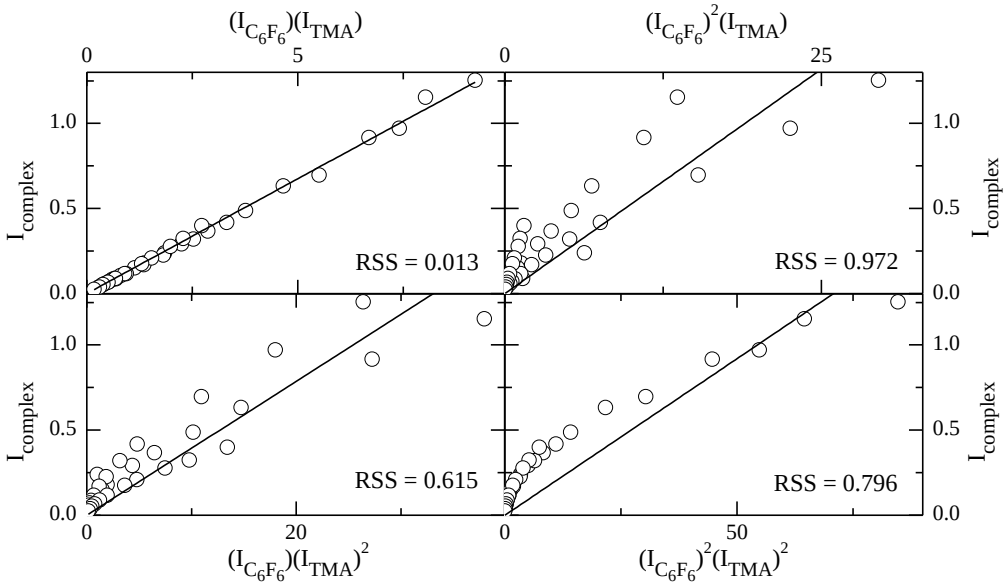

Figure S9.6: Concentration studies for the C_6F_6 ν_{13} complex band for mixed solutions in LKr at 120 K containing C_6F_6 and TMA. The integrated band areas of the complex bands were plotted against the intensity products corresponding to a 1:1 (top left), 2:1 (top right), 1:2 (bottom left) and 2:2 (bottom right) stoichiometry. Additionally, residual sum of square values (RSS) have been included.

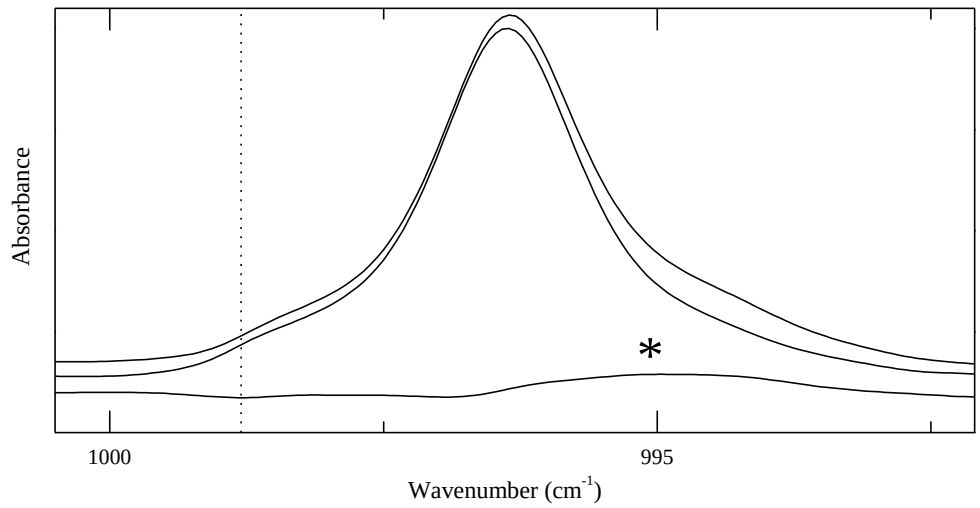

Figure S9.7: Subtracted spectra of C_6F_6·TMA mixtures, measured at 120 K, with different TMA concentrations. The top trace shows the complex band of the solution with the highest TMA concentration, whereas the middle trace shows the complex band of a solution with a lower TMA concentration. To ease comparison, the middle spectrum was rescaled in order to obtain a similar band maximum as the top spectrum. The bottom trace shows the difference between the top and middle spectrum, which reveals the presence of a very weak 1:2 complex band (*). The dotted line indicates the frequency of the band maximum of the C_6F_6 monomer ν_{13} mode.

To achieve anything, you must be prepared to dabble on the boundary of disaster.

– Sir Stirling Moss

Chapter 10

Lone pair···π interactions with carbonyl π-systems.

Complexes of COF_2 and COFCl with DME.

This chapter has been published as:

Geboes, Y.; De Proft, F.; Herrebout, W. A., Lone pair···π interactions involving carbonyl π-systems: Experimental and theoretical study of the complexes of COF_2 and COFCl with dimethyl ether, *Chemical Physics* **2016**, *476*, 1-8.

Abstract

In this theoretical and experimental study, the ability of COF_2 and COFCl to form noncovalent interactions with the Lewis base DME is assessed. From *ab initio* calculations, two stable complexes are found for COF_2·DME, both formed through a lp···π interaction. FTIR measurements on liquefied noble gas solutions, supported by *ab initio* calculations, statistical thermodynamics and MC-FEP simulations, show that a 1:1 lp···π bonded complex is found in solution, with an experimental complexation enthalpy of -14.5(3) kJ mol^{-1}. For COFCl·DME three lp···π complexes, as well as a Cl···O XB complex, are found from *ab initio* calculations. Experimentally, clear complex bands for 1:1 lp···π complexes are observed, with an experimental complexation enthalpy of -11.4(2) kJ mol^{-1}. Furthermore, indications of the presence of a small amount of the XB complex are also observed.

10.1 Introduction

The existence of an attractive noncovalent interaction between the lone pair of a Lewis base and an electron deficient π-system, called a lone pair···π interaction (lp···π), has been demonstrated both theoretically and experimentally in recent years for aromatic and non-aromatic π-systems. [1-3] The best studied lp···π complex is undoubtedly the one between hexafluorobenzene, an ideal model compound for aromatic electron deficient compounds, and water, because of its biological importance. [4-8]

During many of these studies, research was focused on homoatomic π-systems, such as ethylene or benzene containing moieties. However, the first descriptions of lp···π interactions involved the π-hole of carbonyl groups. [9-10] As electron withdrawing groups near the π-system greatly enhance the strength of the noncovalent interaction, [10] phosgene-like compounds are ideal candidates for the study of lp···π interactions involving carbonyl groups. Indeed, attractive intermolecular interactions between COF_2 and Ar, [11-12] N_2, [12] Cl_2, [13] IF [14] and BrF [15] have already been described experimentally. Here, the complexes with Ar and N_2 are of the lp···π type, the Cl_2 complex is halogen-bonded and in the cases of IF and BrF the lp···π complex is an intermediary state to the formation of a XB complex between iodine/bromine and oxygen. Even though the lp···π interactions with HCN [16] and H_2O [17] have also been described theoretically, experimental studies involving phosgene-like compounds and traditional Lewis bases capable of forming stronger intermolecular interactions have not been described.

10.2 Results and discussion

10.2.1 *Ab initio* calculations

Ab initio calculations at the MP2/aug-cc-pVDZ level yield an attractive interaction between COF_2 and DME in which the oxygen atom of the DME moiety faces towards the carbon atom of COF_2, thus forming a lp···π complex with C_s symmetry. Apart from

this global minimum, a local minimum is also found when the DME molecule is rotated above the COF_2 molecular plane, located only 0.8 kJ mol^{-1} higher in energy. The result of the relaxed potential energy scan in which the DME molecule rotates above the COF_2 molecular plane and solely the dihedral angle between the C=O axis and the DME bisector is fixed during optimization is shown in Figure 10.1. The geometries of the global and local minima are also shown in Figure 10.2 while major geometrical intermolecular parameters and complexation energies and enthalpies are summarized Table 10.1. Cartesian coordinates of all monomers and complexes are given in Tables S10.1 and S10.2 of the SI.

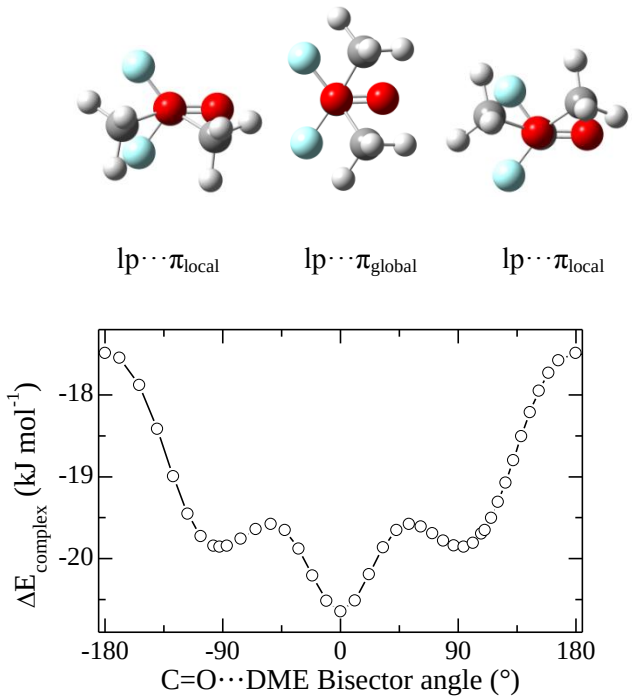

Figure 10.1 MP2/aug-cc-pVDZ calculated complexation energies for the COF_2·DME complex, obtained from a relaxed potential energy scan, plotted against the dihedral angle between the C=O axis and the bisector of DME. The geometries of the global and local minima are also shown above the graph.

For COFCl·DME, *ab initio* calculations yielded a Cl···O XB complex as well as three lp···π complex geometries, in which the DME oxygen directly faces towards the COFCl carbon atom. The geometries of the lp···π complexes are shown in Figure 10.3, while the XB complex is shown in Figure 10.2. Major geometrical intermolecular

parameters and complexation energies and enthalpies can be found in Table 10.1. The different stable lp···π complex geometries are again the consequence of the rotation of the DME moiety above the COFCl molecular plane. The relaxed potential energy scan in which the DME molecule rotates above the COFCl molecular plane and solely the dihedral angle between the C=O axis and the DME bisector is fixed during optimization is given in Figure 10.3.

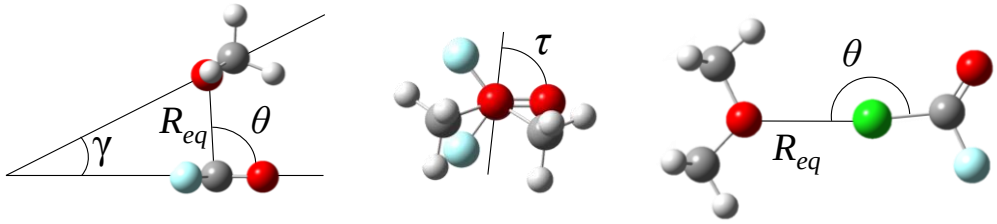

Figure 10.2: MP2/aug-cc-pVDZ equilibrium geometries for the lp···π complex between COF_2 and DME on the left (global minimum) and middle (local minimum) and the XB complex between COFCl and DME on the right, including the designation of the binding distances and angles given in Table 10.1.

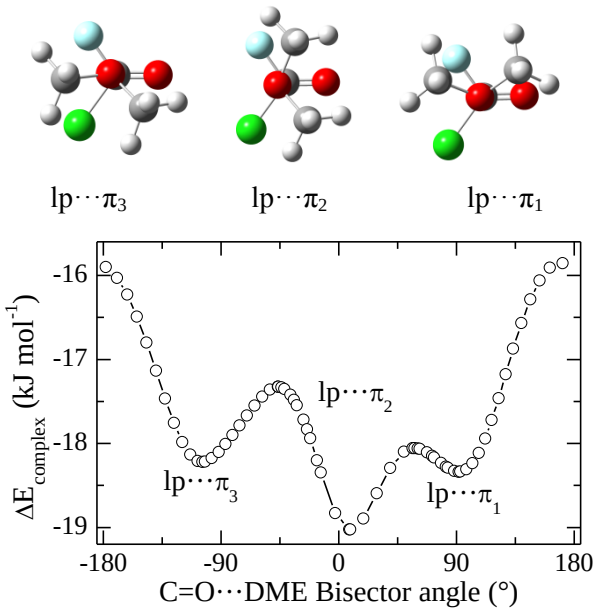

Figure 10.3: MP2/aug-cc-pVDZ calculated complexation energies for the COFCl·DME complex, obtained from a relaxed potential energy scan, plotted against the dihedral angle between the C=O axis and the bisector of DME.

Table 10.1: Intermolecular distance R_{eq} (Å), bond angles and dihedrals (°), calculated complexation energies at different levels of theory as well as theoretical and experimental complexation enthalpies (kJ mol^{-1}) for the complexes of COF_2 and COFCl with DME.

	COF_2·DME		COFCl·DME			
	lp···π_{global}	lp···π_{local}	lp···π_1	lp···π_2	lp···π_3	XB
Symmetry	C_s	C_1	C_1	C_1	C_1	C_s
R_{eq} [a]	2.64	2.63	2.74	2.75	2.72	2.94
θ	96.0	96.6	94.6	92.9	94.2	174.7
γ [b]	33.9	46.6	34.9	26.9	44.8	
τ [c]	0.0	(-)92.4 [i]	156.2	66.3	-45.6	
ΔE (DZ) [d]	-20.6	-19.9	-18.3	-19.0	-18.2	-11.3
ΔE (TZ) [e]	-22.7	-21.6	-19.9	-21.0	-20.1	-12.0
ΔE (CCSD(T)) [f]	-23.8	-22.6	-20.2	-21.3	-20.2	-12.4
$\Delta H°$ (vap,calc) [g]	-20.8	-19.7	-17.5	-18.5	-17.5	-9.9
$\Delta H°$ (LKr,calc) [g]	-16.2	-15.4	-11.5	-12.4	-12.0	-7.4
Experimental [h]						
$\Delta H°$ (LKr)	-14.5(3)	-14.5(3)	-11.4(2)	-11.4(2)	-11.4(2)	

[a] R_{eq} = $R_{C\cdots O}$ for lp···π complexes and R_{eq} = $R_{Cl\cdots O}$ for the XB complex [b] Angle between the approximate COFX (X = F, Cl) molecular plane defined by the atoms C, O and F and the DME bisector [c] Dihedral angle between the O=C bond and DME bisector [d] MP2/aug-cc-pVDZ energies, [e] MP2/aug-cc-pVDZ//MP2/aug-cc-pVTZ energies [f] CCSD(T)/CBS extrapolated energies, [g] Values based on CCSD(T) energies, [h] Values determined in the 120 K – 156 K temperature interval, given with one standard uncertainty in parentheses. [i] Depending on the local minimum observed this value can be either 92.4° or -92.4°.

Even though optimizations were initiated from a structure in which the DME molecular plane is nearly perpendicular to the COFX (X = F, Cl) molecular plane, the C-O-C plane of the DME molecule is tilted towards the COFX (X = F, Cl) molecular plane during optimization in all lp···π complexes, as can be seen on the left side of Figure 10.2 for the global minimum of the complex with COF_2, as well as Table 10.1. This is consistent with the rabbit-ear like configuration of the lone pairs on oxygen and furthermore enables the formation of secondary interactions. As the COFX (X = F, Cl) molecules lose their planarity upon complexation, the plane used to assess the angle between the approximate molecular plane of COFX (X = F, Cl) and the DME bisector is defined by the atoms in the carbonyl bond as well as the first fluorine atom, as given

in the Cartesian coordinates in Tables S10.2 of the SI. Slightly different angles will be obtained when using the other halogen atom (F or Cl) to define the molecular plane.

In an attempt to rationalize the differences in observed stability, the topology of the electron density was examined for all complexes studied using the Atoms in Molecules approach. [18] For all complexes, a single bond path due to the intermolecular interaction was found. The values for the electron density at the corresponding bond critical points and the extrapolated CCSD(T)/CBS complexation energies have been plotted in Figure S10.1 of the SI. From the data given it is clear that in general a high degree of linearity between both properties is observed. However, subtle differences in complexation energies and electron densities are observed when comparing the different lp···π complexes, making further use of the AIM approach less straightforward. The reason for the small discrepancies can most presumably be ascribed to weak secondary effects that escape detection in the AIM approach. To further investigate the effect of secondary interactions on the complexation energy, these secondary interactions have been studied using the NCI index visualized using NCIPLOT [19-20], as shown in Figure S10.2 for the COF_2·DME complexes and Figure S10.3 for the COFCl·DME complexes. For the global minimum of the COF_2·DME complex two smaller isosurfaces between the oxygen atom of COF_2 and the hydrogens of the methyl groups of DME are observed, apart from the isosurface caused by the lp···π interaction, whereas only one small isosurface due to a secondary hydrogen bond is found for the local minimum. For each of the lp···π complexes between COFCl and DME several isosurfaces caused by secondary weak hydrogen bonds are found, apart from the central isosurface caused by the lp···π interaction, whereas, due to its linearity, a single isosurface is obtained for the Cl···O XB complex. The absence of additional isosurfaces for the highly directional halogen bond is consistent with previous observations for XB complexes. [1, 21]

10.2.2 COF_2·DME spectra

The numbering of the fundamental vibrational modes of COF_2, DME and DME-d_6 follows the numbering scheme of Herzberg. [22-24] The spectra of DME and DME-d_6 and their assignments have been discussed in previous chapters. The assignment of the vibrational modes of COF_2 was aided by the assignments found in the literature, [13, 24-25] as well as the performed *ab initio* calculations. The assignment of the complex bands was aided by the *ab initio* calculations performed at the MP2/aug-cc-pVDZ level of theory, of which the results are reported in Tables S10.3 and S10.4 of the SI. Estimated mole fractions of the solutions varied between 5.6×10^{-5} and 5.6×10^{-4} for COF_2 and 1.9×10^{-4} and 1.9×10^{-3} for DME and DME-d_6

Upon investigation of spectra of COF_2·DME, shown in Figure 10.4, clearly resolved complex bands are observed. Most noticeably, complex bands are found in the COF_2 ν_6 spectral range (panel 10.4D) with a -20.8 cm^{-1} redshifted complex band ($\Delta\nu_{calc,lp\cdots\pi,\ global}$ = -30.0 cm^{-1}), the COF_2 ν_1 spectral region (panel 10.4A) with a -4.0 cm^{-1} redshift ($\Delta\nu_{calc,lp\cdots\pi,\ global}$ = -6.4 cm^{-1}) and COF_2 ν_2 / DME ν_6 spectral range (panel 10.4C), with complex shifts of -2.1 cm^{-1} and -3.5 cm^{-1} respectively (corresponding to calculated values of $\Delta\nu_{calc,lp\cdots\pi,\ global}$ = -2.4 cm^{-1} and $\Delta\nu_{calc,lp\cdots\pi,\ global}$ = -7.3 cm^{-1}). These shifts are thus all in agreement with the MP2/aug-cc-pVDZ calculated complex shifts for the lp···π complex at the global minimum. An overview of the experimental complexation shifts and corresponding calculated values is given in Table 10.2. Inspection of the spectra and comparison with the calculated shifts given in Table 10.2 also shows some differences between the calculated and experimental complexation shifts. The difference between the experimental shift of 0.4 cm^{-1} of the ν_4 mode of COF_2, shown in panel 10.4B, and the calculated shifts of 5.7 cm^{-1} and -3.9 cm^{-1} for the global and local minimum respectively can be explained by a mechanical coupling with the asymmetric O-CH_3 stretching mode ν_{20} mode of DME (ν_{18} in case of DME-d_6) in the calculations. The overestimation of the calculated shift of the ν_{12} mode of DME can be ascribed to the presence of multiple overtones and combination bands in the DME C-H stretching region, which causes resonant effects and greatly complicates the assignment of these modes. As in our previous study on lp···π interactions, [1] small experimental blueshifts

are found for the DME modes ν_3 and ν_{18} as opposed to the calculated redshifts. As the solutions are at thermodynamic equilibrium, the different calculated geometries are expected to occur in the solution in a Boltzmann-weighted ratio. Nevertheless only a single complex band is found for each vibrational mode, which can be explained by a nearly free rotation between the global and local minimum, the rotational barrier being similar to the RT at 120 K, as shown in Figure 10.1, which leads to an averaged structure being observed experimentally. Spectra of multiple spectral ranges for COF_2·DME-d_6 mixtures are given in Figure S10.4 of the SI. A full assignment of the monomers and corresponding complex bands, including the calculated complexation shifts, is given in Table 10.2 for COF_2·DME and in Table S10.8 for COF_2·DME-d_6.

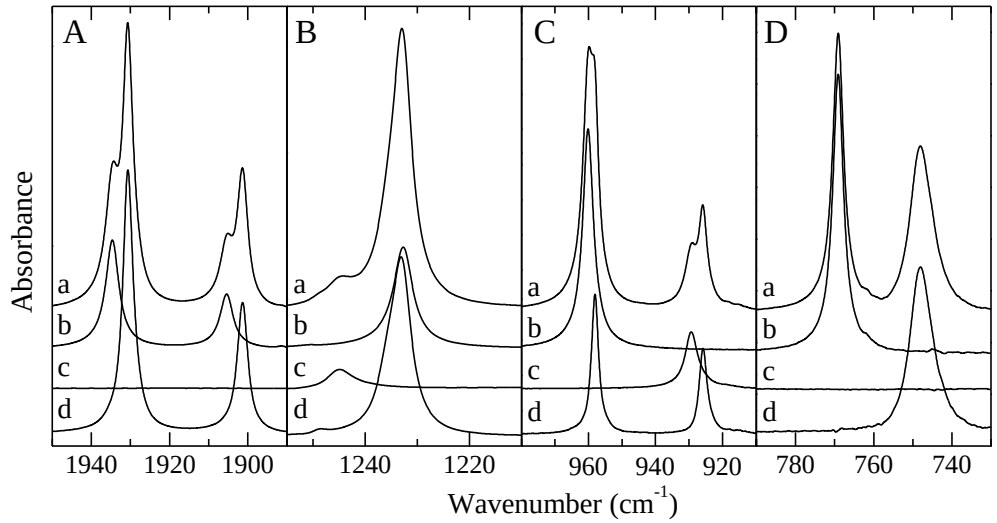

Figure 10.4: Infrared spectra of selected spectral regions of mixtures of COF_2 and DME dissolved in LKr at 120 K. In each panel, trace *a* represents the mixed solution, while traces *b* and *c* show the solution containing only COF_2 or DME, respectively. Trace *d* represents the spectrum of the complex and is obtained by subtracting the rescaled traces *b* and *c* from trace *a*. Estimated mole fractions of the solutions of the mixtures are 5.6×10^{-5} for COF_2 and 5.6×10^{-4} for DME in panels A and D and 5.6×10^{-4} for COF_2 and 1.9×10^{-4} for DME in panels B and C.

Table 10.2: Experimental infrared frequencies for the monomer and complex, as well as experimental complexation shifts ($\Delta\nu_{exp}$) and MP2/aug-cc-pVDZ calculated complexation shifts for the global ($\Delta\nu_{calc,\ lp\cdots\pi\ global}$) and local minimum ($\Delta\nu_{calc,\ lp\cdots\pi\ local}$), in cm^{-1}, of the lp···π complex of COF_2 with DME dissolved in LKr at 120 K.

Assignment		Symmetry	$\nu_{monomer}$	$\nu_{complex}$	$\Delta\nu_{exp}$	$\Delta\nu_{calc,\ lp\cdots\pi\ global}$	$\Delta\nu_{calc,\ lp\cdots\pi\ local}$
COF_2	ν_1	A_1	1934.6	1930.6	-4.0	-6.4	0.3
	$2\nu_2$	A_1	1905.4	1901.3	-4.1	-4.8	-10.4
	ν_4	B_1	1232.7	1233.1	0.4	5.7	-3.9
	ν_2	A_1	960.1	958.0	-2.1	-2.4	-5.2
	ν_6	B_2	769.0	748.2	-20.8	-30.0	-29.2
	ν_5	B_1	662.7	662.6	-0.1	1.4	-0.5
	ν_3	A_1	580.5	580.7	0.2	-1.2	-0.2
DME	ν_1	A_1	2990.0	2995.8	5.8	4.0	6.8
	ν_{16}	B_2	2990.0	2995.8	5.8	4.0	2.4
	ν_{12}	B_1	2916.2	2921.3	5.1	17.7	15.0
	ν_2	A_1	2811.5	2820.0	8.5	10.3	8.8
	ν_3	A_1	1474.7	1475.1	0.4	-1.4	-0.9
	ν_{18}	B_2	1457.4	1457.8	0.4	-1.1	-1.2
	ν_{13}	B_1	1454.7	1456.1	1.4	1.8	0.8
	ν_{19}	B_2	1426.1	1428.3	2.2	0.2	0.6
	ν_5	A_1	1244.9	1248.5	3.6	1.4	2.5
	ν_{20}	B_2	1172.0	1168.8	-3.2	-10.4	-6.2
	ν_{21}	B_2	1099.1	1096.8	-2.3	-5.9	-2.8
	ν_6	A_1	929.4	925.9	-3.5	-7.3	-5.6

By measuring mixtures with different concentrations of each of the monomers at a constant temperature of 120 K, the 1:1 complex stoichiometry was determined experimentally by plotting the integrated intensity of the complex band against the product of the integrated intensities of the monomers at different ratios. The procedure has been described in more detail in the recent review by Herrebout.[26] The results of this concentration study can be found in Figure 10.5.

By constructing van 't Hoff plots from measurements between 120 K and 156 K, 13 experimental complexation enthalpies between -14.1 and -15.0 kJ mol^{-1} have been determined for the lp···π complex of COF_2 with DME and DME-d_6, the average being -14.5(3) kJ mol^{-1}. An example of a van 't Hoff plot for the COF_2·DME and

COFCl·DME complexes is shown in Figure 10.6 while an overview of all performed temperature studies for the COF_2·DME complex can be found in Table S10.11 of the SI.

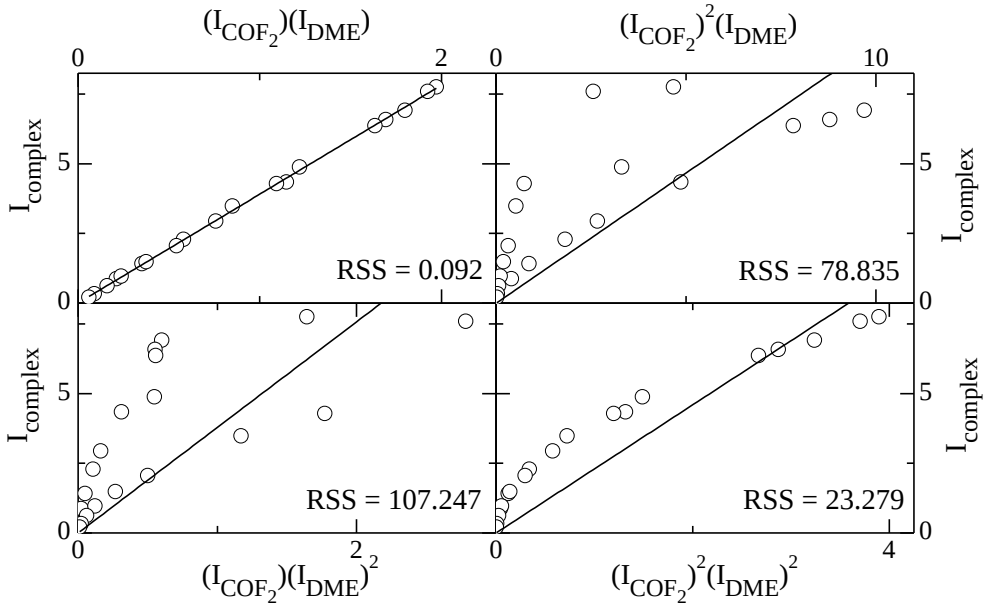

Figure 10.5: Concentration study plots of the COF_2·DME lp···π complex at 120 K in LKr. Integrated intensity of the complex is plotted against the product of monomer intensities $\left(I_{COF_2}\right)^m (DME)^n$. Top left: $m = 1, n = 1$, top right: $m = 2, n = 1$, bottom left $m = 1, n = 2$ and bottom right $m = 2, n = 2$. Additionally, residual sum of square values (RSS) have been included.

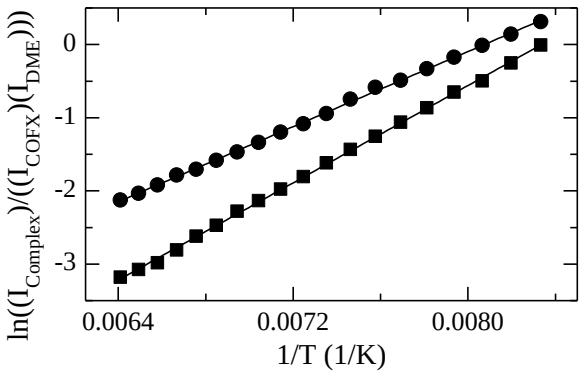

Figure 10.6: Typical van 't Hoff plots of the lp···π complexes between of COF_2 and DME (square) and COFCl and DME (round) in LKr.

10.2.3 COFCl·DME spectra

Upon initial spectroscopic evaluation of the COFCl sample, it was clear that this sample also contained a considerable amount of CO_2, which can, as published in a previous article by van Ginderen et al., [27] form a lp···π complex with DME in liquefied noble gas solutions. To account for CO_2 and its complex with DME and enable their subtraction from the COFCl·DME spectra, spectra of CO_2 and CO_2·DME mixtures were measured and studied separately. A more complete description of the performed subtraction procedure has been included in the SI. Assignment of the vibrational modes of the COFCl monomer follows the numbering scheme of Herzberg [22-24] and was aided by assignments found in the literature, [13, 25] as well as the *ab initio* calculations reported in Tables S10.5 to S10.8 of the SI. A full assignment of the CO_2·DME complex can be found in the article of van Ginderen et al. [27] Estimated mole fractions of the solutions varied between 5.6×10^{-5} and 1.9×10^{-3} for COFCl and 1.5×10^{-4} and 4.7×10^{-3} for DME and DME-d_6

Upon first inspection of the spectra of COFCl·DME mixtures, two complex bands can be seen near the ν_6 vibrational mode of COFCl, one blueshifted, and a more intense one with a large redshift. The shifts of these bands are in agreement with the calculated values of the XB complex and lp···π complexes of COFCl·DME. However, these complex shifts also correspond well to the calculated complex shifts of the degenerate π_u mode of CO_2. Subtraction of the CO_2 monomer and CO_2·DME complex spectra was performed using a rescaling factor determined for the σ_u^+ mode near 2340 cm^{-1}, as shown in panel A of Figure 10.7. Upon subtraction of the rescaled CO_2 and CO_2·DME spectra, most of the redshifted band in the COFCl ν_6 spectral region is retained, whereas only a very small amount of blueshifted band is retained, as can be seen in panel D of Figure 10.7. With experimental shifts of -13.8 cm^{-1} and 4.4 cm^{-1} these bands correspond to the calculated values given in Table 10.3 for the lp···π complexes (between -20.8 and -21.9 cm^{-1}) and XB complex (5.3 cm^{-1}) respectively. The retention of a small blueshifted band indicates the presence of a small amount of XB complex. Also in other spectral ranges, such as the ν_1 and ν_3 spectral ranges of COFCl, which are shown in panels B and C of Figure 10.7, small complex bands are retained apart from

those assigned to the lp···π complexes. With experimental shifts of -7.4 cm^{-1} and 2.3 cm^{-1}, these values correspond to the calculated shifts of -10.3 cm^{-1} and 2.2 cm^{-1} for the ^{12}COFCl·DME XB complex. Additional spectra of interesting spectral regions of the COFCl·DME complex are given in Figures S10.5 and S10.6 of the SI. The spectral regions discussed above for mixtures containing DME-d_6 are shown in Figure S10.7 of the SI.

In order to aid assignment of the other vibrational modes and help identify the lp···π complex or complexes present in solution, behaviour of the complexation shifts upon rotation of DME above the COFCl molecular plane was evaluated. The dependence of the complexation shifts upon rotation and the corresponding complexation energies are given in Figure 10.8. The complexation shift of the ν_6 mode remains stable at around -21 cm^{-1}, which is consistent with the assignment of the -13.8 cm^{-1} redshifted band to the lp···π complex. The overestimation of the calculated complexation shifts for the lp···π complexes is believed to be a consequence of the harmonic approximation which has been used in all frequency calculations. Upon further inspection of Figure 10.8, it becomes clear that the ν_1, ν_2 and ν_3 modes of COFCl show a large dependence on the C=O···C-O-C bisector angle, all having both blueshifts and redshifts at different dihedral angles. Comparison of these calculated shifts with the experimental shifts, given in Table 10.3, shows that no exact match is found for either of the three calculated energy minima. A mean absolute deviations (MAD) analysis, in which the average of the absolute deviation between the experimental and calculated shifts is calculated, yielded the lowest value of 2.3 cm^{-1} for the lp···π_2 complex when looking at the seven assigned COFCl modes, whereas values of 7.4 and 3.5 cm^{-1} were found for lp···π_1 and lp···π_3 , respectively. These values indicate a clear preference for a major contribution of the lp···π_2 complex, as can expected from the calculated complexation energies. However, when including the shifts for the assigned DME modes, values of 4.8, 2.7 and 2.6 cm^{-1} are obtained for lp···π_1, lp···π_2 and lp···π_3 respectively and the preference of lp···π_2 over lp···π_3 diminishes.

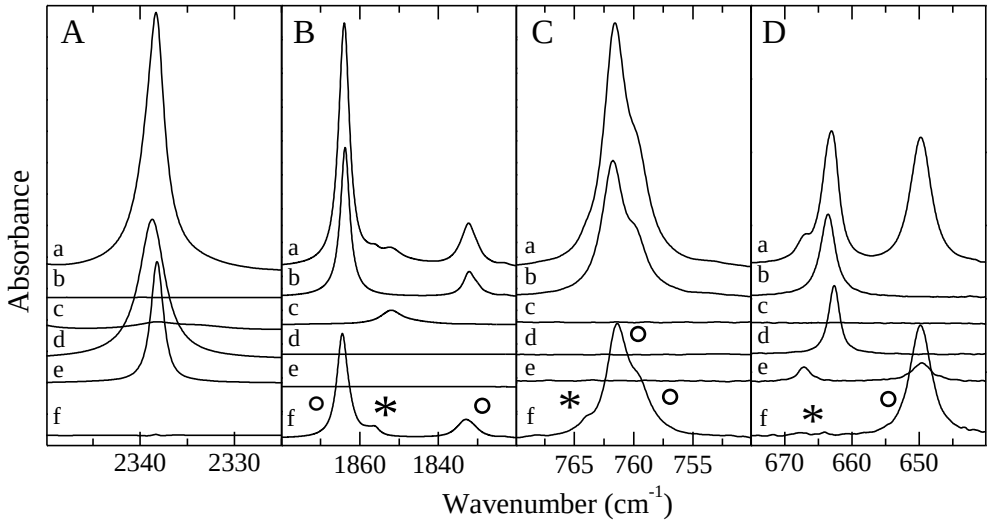

Figure 10.7: Infrared spectra of selected spectral regions of mixtures of COFCl and DME dissolved in LKr at 120 K. In each panel, trace *a* represents the mixed solution of COFCl with DME, while traces *b* and *c* show the solution containing only COFCl or DME, respectively. Trace *d* shows the rescaled spectrum of CO_2, whereas trace *e* shows the spectrum of the rescaled CO_2·DME complex, which has obtained from a separate measurement. Finally, trace *f* shows the spectrum of the COFCl·DME complex, obtained by subtracting traces *b-e* from trace *a*. Bands due to the lp···π complex and XB complex observed in trace *f* are marked with an open circle (°) or asterisk (*), respectively. Estimated mole fractions of the solutions of the mixtures are 1.9×10^{-4} for COFCl and 4.7×10^{-3} for DME in panels A, B and D and 5.6×10^{-5} for COFCl and 4.7×10^{-3} for DME in panel C.

To assess whether the discrepancies between experimental and calculated shifts of the lp···π complexes can be ascribed to the method used, calculations of these complexes were also performed using MP2 with the aug-cc-pVTZ basis set and B3LYP (including a GD3 correction for dispersion) with the aug-cc-pVDZ and aug-cc-pVTZ basis sets. Results of the MAD analysis of these calculations are given in Table S10.13 of the SI. From this analysis it becomes clear that MAD values increase when going from MP2 to B3LYP and, for both methods, when going from the aug-cc-pVDZ to the aug-cc-pVTZ basis set, while the relative values of the different lp···π complexes stay similar throughout the used methods. Hence, the best correspondence between experimental and calculated shifts is obtained for the MP2/aug-cc-pVDZ calculated values.

Again, as the rotational barrier between the different calculated minima, shown in Figures 10.6 and 10.8, is similar to the RT value at 120 K, nearly free rotation between the three complex geometries is expected and an average structure is observed experimentally, rather than three individual structures with individual complex bands.

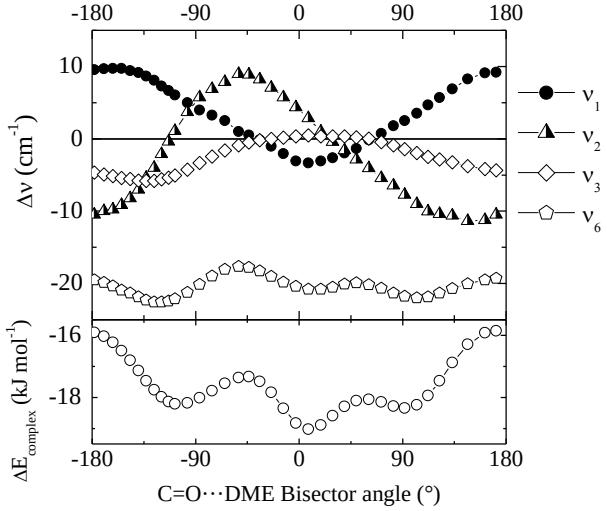

Figure 10.8: MP2/aug-cc-pVDZ calculated complexation shifts for the ν_1, ν_2, ν_3 and ν_6 modes of COFCl and complexation energy for the COFCl·DME complex, obtained from a relaxed potential energy scan, plotted against the dihedral angle between the C=O axis and the bisector of DME.

A full experimental assignment of all observed vibrational modes for the monomers and corresponding complex bands, including the calculated complexation shifts, can be found in Table 10.3 for COFCl·DME and Table S10.10 for COFCl·DME-d_6.

Table 10.3: Experimental infrared frequencies for the monomer and complex, as well as experimental complexation shifts ($\Delta\nu_{exp}$) and MP2/aug-cc-pVDZ calculated complexation shifts ($\Delta\nu_{calc}$), in cm^{-1}, for the lp···π complexes and XB complex of COFCl with DME dissolved in LKr at 120 K.

Assignment	Sym	$\nu_{monomer}$	$\nu_{complex,lp\cdots\pi}$	$\Delta\nu_{exp,lp\cdots\pi}$	$\Delta\nu_{calc,lp\cdots\pi1}$	$\Delta\nu_{calc,lp\cdots\pi2}$	$\Delta\nu_{calc,lp\cdots\pi3}$	$\nu_{complex,XB}$	$\Delta\nu_{exp,XB}$	$\Delta\nu_{calc,XB}$
COFCl										
$2\nu_2$	A’	2158.0	2161.4	3.4	-15.5	5.2	4.0	-		-7.3
ν_1	A’	1863.8	1864.5	0.7	2.6	-3.4	5.7	1856.4	-7.4	-10.3
$\nu_2+\nu_3$	A’	1832.1	1832.9	0.8	-9.2	2.9	-2.8	1832.9	0.8	-1.4
		1823.2	1823.9	0.7				-		
ν_2	A’	1083.9	1085.2	1.3	-7.7	2.6	2.0	1081.1	-2.8	-3.7
ν_2 (^{13}C)	A’	1056.4	1057.9	1.5	-8.0	2.4	2.4	1052.9	-3.5	-4.5
ν_3 (^{35}Cl)	A’	761.8	761.4	-0.4	-1.4	0.4	-4.8	764.1	2.3	2.2
ν_3 (^{37}Cl)	A’	759.8	759.6	-0.2	-1.4	0.4	-4.6	761.4	1.6	2.1
ν_6	A”	663.6	649.8	-13.8	-21.8	-20.8	-21.9	668.0	4.4	5.3
DME								-		
ν_1	A_1	2990.0	2992.2	2.2	4.7	3.8	2.4	2992.2	2.2	0.3
ν_{16}	B_2	2990.0	2992.2	2.2	-0.8	0.1	0.9	2992.2	2.2	-0.5
ν_{12}	B_1	2916.2	2919.1	2.9	12.0	13.2	9.7	2919.1	2.9	8.8
ν_2	A_1	2811.5	2817.5	6.0	6.7	7.3	4.8	2817.5	6.0	5.1
ν_3	A_1	1474.7	1474.6	-0.1	-1.6	-1.5	-1.8	1474.6	-0.1	0.0
ν_{18}	B_2	1457.4	1457.5	0.1	-1.8	-1.4	-1.9	1457.5	0.1	0.1
ν_{13}	B_1	1454.7	1455.5	0.8	-0.3	-0.3	0.7	1455.5	0.8	-0.3
ν_{19}	B_2	1426.1	-		-0.2	-0.5	-0.5	-		0.8
ν_5	A_1	1244.9	1247.5	2.6	1.2	0.6	1.3	1247.5	2.6	1.6
ν_{20}	B_2	1172.0	1169.3	-2.7	-6.7	-8.3	-5.5	1169.3	-2.7	-3.3
ν_{21}	B_2	1099.1	1097.6	-1.5	-3.1	-5.0	-2.8	1097.6	-1.5	-1.1
ν_6	A_1	929.4	925.8	-3.6	-6.4	-7.0	-5.6	925.8	-3.6	-4.3

The construction of van ‘t Hoff plots from temperature studies yielded ten experimental complexation enthalpies, varying between -11.0 and -11.7 kJ mol^{-1}, with an average of -11.4(2) kJ mol^{-1}. An example of a van ‘t Hoff plot is given in Figure 10.6, while an overview of the parameters used in the van ‘t Hoff plots is given in Table S10.12 of the SI. Furthermore the 1:1 complex stoichiometry of the lp···π complex was confirmed experimentally by a concentration study of which the results can be found in Figure 10.9.

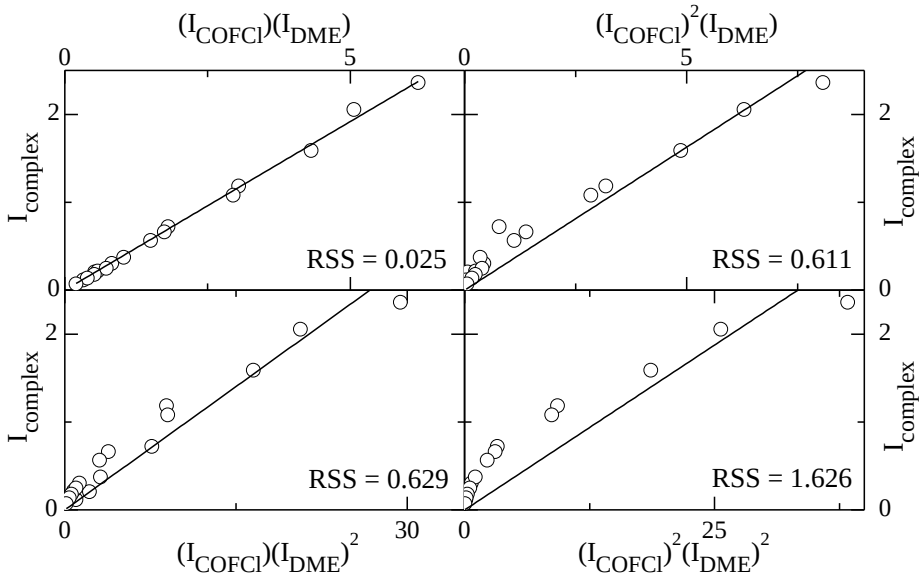

Figure 10.9: Concentration study plots of the COFCl·DME lp···π complex at 120 K in LKr. Integrated intensity of the complex is plotted against the product of monomer intensities $(I_{COFCl})^m(DME)^n$. Top left: $m = 1, n = 1$, top right: $m = 2, n = 1$, bottom left $m = 1, n = 2$ and bottom right $m = 2, n = 2$. Additionally, residual sum of square values (RSS) have been included.

10.3 Conclusions

Ab initio calculations at the MP2/aug-cc-pVDZ level of theory yielded two stable complexes between COF_2 and DME formed through a lp···π interaction, the difference in energy being a mere 0.8 kJ mol^{-1}. The existence and stoichiometry of a 1:1 lp···π complex was verified experimentally by means of FTIR measurements on liquefied krypton solutions, the assignment was aided by the complexation shifts of the *ab initio* calculations. As the rotational barrier between the global and local minimum is comparable to the RT value at 120 K, an averaged structure is observed in the spectra. Furthermore, a complexation enthalpy of -14.5(3) kJ mol^{-1} was determined experimentally by means of a temperature study, which corresponds well with the CCSD(T)/CBS extrapolated values after correction for thermal and solvent effects of -16.2 kJ mol^{-1} and -15.4 kJ mol^{-1} for the lp···π complex at the global and local minima, respectively.

For the combination of COFCl with DME, *ab initio* calculations yielded a XB complex geometry, as well as three complex geometries bonded by a lp···π interaction. These latter three complexes are the result of a rotation of DME above the COFCl molecular plane, with a rotational barrier comparable to the RT value at 120 K, impeding experimental differentiation between the different lp···π geometries. Despite the presence of CO_2 in the COFCl sample, the formation of a 1:1 lp···π complex with a complexation enthalpy of -11.4(2) kJ mol^{-1} between COFCl and DME or DME-d_6 were demonstrated experimentally. Furthermore, clear indications for the formation of XB complex between COFCl and DME or DME-d_6 were also observed. Unfortunately, due to the low intensity of the bands belonging to the XB complex, neither the complexation enthalpy nor the complexation stoichiometry could be verified experimentally.

10.4 References

1 Y. Geboes, N. Nagels, B. Pinter, F. De Proft, W. A. Herrebout, *J. Phys. Chem. A*, 2015, ***119***, 2502-2516.
2 Y. Geboes, F. De Proft, W. A. Herrebout, *J. Phys. Chem. A*, 2015, ***119***, 5597-5606.
3 A. Bauzá, T. J. Mooibroek, A. Frontera, *ChemPhysChem*, 2015, ***16***, 2496-2517.
4 J. C. Amicangelo, D. G. Irwin, C. J. Lee, N. C. Romano, N. L. Saxton, *J. Phys. Chem. A*, 2013, ***117***, 1336-1350.
5 Y. Danten, T. Tassaing, M. Besnard, *J. Phys. Chem. A*, 1999, ***103***, 3530-3534.
6 M. Besnard, Y. Danten, T. Tassaing, *J. Chem. Phys.*, 2000, ***113***, 3741-3748.
7 M. Raimondi, G. Calderoni, A. Famulari, L. Raimondi, F. Cozzi, *J. Phys. Chem. A*, 2003, ***107***, 772-774.
8 C. J. Wormald, B. Wurzberger, *Phys. Chem. Chem. Phys.*, 2000, ***2***, 5133-5137.
9 H. B. Bürgi, J. D. Dunitz, E. Shefter, *J. Am. Chem. Soc.*, 1973, ***95***, 5065-5067.
10 J. S. Murray, P. Lane, T. Brinck, P. Politzer, P. Sjoberg, *J. Phys. Chem.*, 1991, ***95***, 844-848.
11 J. A. Shea, E. J. Campbell, *J. Chem. Phys.*, 1983, ***79***, 4724-4729.
12 A. A. Stolov, W. A. Herrebout, B. J. van der Veken, *J. Phys. Chem. A*, 1999, ***103***, 5291-5300.
13 Y. Bouteiller, O. Abdelaoui, A. Schriver, L. Schriver-Mazzuoli, *J. Chem. Phys.*, 1995, ***102***, 1731-1739.
14 L. Andrews, M. Hawkins, R. Withnall, *Inorg. Chem.*, 1985, ***24***, 4234-4239.
15 H. Lorenzen-Schmidt, R. Weller, O. Schrems, *J. Mol. Struct.*, 1995, ***349***, 333-336.
16 X. Guo, L. Cao, Q. Li, W. Li, J. Cheng, *J. Mol. Model.*, 2014, ***20***, 2493.
17 N. Tanaka, T. Tamezane, H. Nishikiori, T. Fujii, W. N. Sisk, *Chem. Phys.*, 2004, ***306***, 25-34.
18 R. F. W. Bader, *Atoms in Molecules - A Quantum Theory*, Oxford University Press, Oxford, U.K., **1990**.
19 E. R. Johnson, S. Keinan, P. Mori-Sánchez, J. Contreras-García, A. J. Cohen, W. Yang, *J. Am. Chem. Soc.*, 2010, ***132***, 6498-6506.
20 J. Contreras-García, E. R. Johnson, S. Keinan, R. Chaudret, J.-P. Piquemal, D. N. Beratan, W. Yang, *J. Chem. Theory Comput.*, 2011, ***7***, 625-632.
21 N. Nagels, Y. Geboes, B. Pinter, F. De Proft, W. A. Herrebout, *Chem. - Eur. J.*, 2014, ***20***, 8433-8443.
22 G. Herzberg, *Infrared and Raman Spectra of Polyatomic Molecules*, 12th ed., D. Van Nostrand Company Inc., Princeton, NJ, USA, **1945**.
23 T. Shimanouchi, *Tables of Molecular Vibrational Frequencies Consolidated Volume I, Vol. 39*, Nat. Stand. Ref. Data Ser., Nat. Bur. Stand., Washington, D.C., USA, **1972**.
24 T. Shimanouchi, *J. Phys. Chem. Ref. Data*, 1977, ***6***, 993-1102.
25 A. H. Nielsen, T. G. Burke, P. J. H. Woltz, E. A. Jones, *J. Chem. Phys.*, 1952, ***20***, 596-604.
26 W. A. Herrebout, *Top. Curr. Chem.*, 2015, ***358***, 79-154.
27 P. Van Ginderen, W. A. Herrebout, B. J. van der Veken, *J. Phys. Chem. A*, 2003, ***107***, 5391-5396.

10.5 Supporting information

Table S10.1.1: Cartesian coordinates of the MP2/aug-cc-pVDZ optimized geometry of COF_2.

C_{2v}	X	Y	Z
COF_2			
C	0.000000	0.000000	0.148815
O	0.000000	0.000000	1.334592
F	0.000000	1.073442	-0.642757
F	0.000000	-1.073442	-0.642757

Table S10.1.2: Cartesian coordinates of the MP2/aug-cc-pVDZ optimized geometry of COFCl.

C_s	X	Y	Z
COFCl			
C	0.000000	0.503758	0.000000
O	-0.794527	1.388686	0.000000
F	1.338047	0.690833	0.000000
Cl	-0.334483	-1.197031	0.000000

Table S10.1.3: Cartesian coordinates of the MP2/aug-cc-pVDZ optimized geometry of DME.

C_{2v}	X	Y	Z
DME			
O	0.000000	0.000000	0.607066
C	0.000000	1.169581	-0.202099
H	0.000000	2.032636	0.474896
H	0.898418	1.208635	-0.845282
H	-0.898418	1.208635	-0.845282
C	0.000000	-1.169581	-0.202099
H	0.898418	-1.208635	-0.845282
H	0.000000	-2.032636	0.474896
H	-0.898418	-1.208635	-0.845282

Table S10.2.1: Cartesian coordinates of the MP2/aug-cc-pVDZ optimized geometry of the global minimum lp···π complex between COF_2 and DME.

C_s	X	Y	Z
COF_2			
C	0.446473	-1.238034	0.000000
O	1.556787	-0.816310	0.000000
F	-0.274213	-1.556818	1.075014
F	-0.274213	-1.556818	-1.075014
DME			
O	-0.744237	1.117259	0.000000
C	-0.274213	1.781064	-1.173003
H	0.829959	1.776852	-1.210974
H	-0.673110	1.233581	-2.035715
H	-0.633274	2.824855	-1.201338
C	-0.274213	1.781064	1.173003
H	-0.673110	1.233581	2.035715
H	0.829959	1.776852	1.210974
H	-0.633274	2.824855	1.201338

Table S10.2.2: Cartesian coordinates of the MP2/aug-cc-pVDZ optimized geometry of the local minimum lp···π complex between COF_2 and DME.

C_1	X	Y	Z
COF_2			
C	1.379102	0.129643	0.029753
O	1.485532	1.303606	-0.104794
F	1.161372	-0.513938	1.181268
F	1.536864	-0.795169	-0.915657
DME			
O	-1.213082	0.005821	-0.413785
C	-1.838516	1.202125	0.047884
H	-1.864391	1.232097	1.152144
H	-1.241832	2.042704	-0.32628
H	-2.870196	1.277419	-0.338535
C	-1.912084	-1.146429	0.051165
H	-1.381459	-2.024873	-0.33643
H	-1.925004	-1.181311	1.155439
H	-2.951856	-1.151514	-0.321002

Table S10.2.3: Cartesian coordinates of the MP2/aug-cc-pVDZ optimized geometry of the lp···π complex between COFCl and DME, indicated with the label lp···π_1 in the remainder of this chapter.

C_1	X	Y	Z
COFCl			
C	-1.070520	0.581881	0.200504
O	-0.954142	1.649502	-0.310715
F	-0.704564	0.314446	1.475958
Cl	-1.791808	-0.833167	-0.491408
DME			
O	1.449063	-0.258228	-0.46932
C	2.270913	0.906590	-0.427406
H	1.801327	1.656596	-1.075343
H	2.340058	1.303102	0.601833
H	3.287868	0.682358	-0.795604
C	1.980406	-1.283056	0.366430
H	1.301283	-2.142055	0.296494
H	2.988528	-1.583464	0.029060
H	2.038577	-0.945386	1.416994

Table S10.2.4: Cartesian coordinates of the MP2/aug-cc-pVDZ optimized geometry of the lp···π complex between COFCl and DME, indicated with the label lp···π_2 in the remainder of this chapter.

C_1	X	Y	Z
COFCl			
C	-1.003116	-0.496266	0.369164
O	-0.630887	-0.576025	1.497330
F	-0.921327	-1.506302	-0.522740
Cl	-1.795602	0.856134	-0.369183
DME			
O	1.474235	0.290897	-0.538929
C	1.851764	1.344480	0.345252
H	1.202771	2.201006	0.123852
H	1.715749	1.042017	1.399382
H	2.906159	1.632118	0.185257
C	2.282469	-0.863117	-0.314550
H	1.955724	-1.630170	-1.027130
H	3.349495	-0.633259	-0.483792
H	2.153802	-1.238837	0.716796

Table S10.2.5: Cartesian coordinates of the MP2/aug-cc-pVDZ optimized geometry of the lp···π complex between COFCl and DME, indicated with the label lp···π_3 in the remainder of this chapter.

C_1	X	Y	Z
COFCl			
C	-1.204666	-0.466259	-0.211942
O	-1.187745	-1.594426	0.163311
F	-1.209093	-0.093866	-1.506906
Cl	-1.321430	0.953929	0.786777
DME			
O	1.503240	-0.258655	-0.337441
C	2.093013	1.007677	-0.617732
H	1.630430	1.382699	-1.539162
H	1.905747	1.721632	0.205189
H	3.183320	0.910394	-0.766328
C	2.041656	-0.816697	0.858915
H	1.536538	-1.776674	1.022296
H	3.129219	-0.982541	0.760428
H	1.856923	-0.151191	1.722119

Table S10.2.6: Cartesian coordinates of the MP2/aug-cc-pVDZ optimized geometry of the XB complex between COFCl and DME.

C_s	X	Y	Z
COFCl			
C	2.361484	0.121929	0.000009
O	2.991185	1.133056	0.000069
F	2.932724	-1.108456	-0.000064
Cl	0.642334	-0.043677	0.000001
DME			
O	-2.30152	-0.056092	-0.000018
C	-2.923349	1.225458	-0.000055
H	-2.121764	1.974637	-0.000112
H	-3.551703	1.360165	-0.898959
H	-3.551648	1.360243	0.898877
C	-3.277358	-1.093371	0.000061
H	-2.736144	-2.047533	0.000086
H	-3.917429	-1.034314	0.898879
H	-3.917487	-1.034395	-0.898721

Table S10.3A: MP2/aug-cc-pVDZ vibrational frequencies, in cm^{-1}, infrared intensities, in km mol^{-1}, and Raman intensities, in $Å^4$ amu^{-1}, for the global minimum lp···π complex of COF_2 and DME and both monomers, as well as the complexation shift Δν.

	Monomer			lp···π complex			
	Frequency	IR int.	Raman int.	Frequency	Δν	IR int.	Raman int.
COF_2							
ν_1 (A_1)	1932.2	422.4	12.8	1925.8	-6.4	356.9	11.5
ν_2 (A_1)	934.1	66.3	9.1	931.7	-2.4	56.3	9.1
ν_3 (A_1)	563.4	6.0	1.1	562.2	-1.2	4.1	0.8
ν_4 (B_1)	1201.6	417.7	1.4	1207.3	5.7	410.4	1.4
ν_5 (B_1)	600.2	5.7	2.0	601.6	1.4	4.1	1.5
ν_6 (B_2)	768.0	32.7	0.4	738.1	-30.0	91.4	3.8
DME							
ν_1 (A_1)	3188.7	20.1	87.6	3192.6	4.0	16.0	68.6
ν_2 (A_1)	3024.8	58.6	320.3	3035.1	10.3	46.2	289.0
ν_3 (A_1)	1505.9	2.9	5.6	1504.5	-1.4	8.6	5.7
ν_4 (A_1)	1473.5	0.0008	2.2	1474.1	0.6	0.1	1.9
ν_5 (A_1)	1261.1	6.6	0.5	1262.5	1.4	6.1	0.4
ν_6 (A_1)	942.4	34.7	9.8	935.1	-7.3	30.4	8.9
ν_7 (A_1)	416.8	2.3	1.0	418.8	2.0	2.6	0.9
ν_8 (A_2)	3096.2	0.0	14.7	3113.0	16.8	0.2	12.1
ν_9 (A_2)	1474.8	0.0	11.4	1475.7	0.9	0.02	10.3
ν_{10} (A_2)	1157.2	0.0	1.5	1157.3	0.1	0.1	1.6
ν_{11} (A_2)	195.2	0.0	0.2	191.7	-3.5	0.0	0.1
ν_{12} (B_1)	3089.5	107.8	94.2	3107.2	17.7	83.3	87.7
ν_{13} (B_1)	1489.2	13.0	0.04	1491.0	1.8	16.5	0.2
ν_{14} (B_1)	1187.2	7.2	0.04	1190.5	3.4	5.9	0.3
ν_{15} (B_1)	260.2	5.1	0.002	272.2	11.9	9.9	0.03
ν_{16} (B_2)	3187.3	24.6	59.2	3191.3	4.0	16.6	44.3
ν_{17} (B_2)	3018.4	55.2	0.6	3029.8	11.5	44.2	1.3
ν_{18} (B_2)	1490.1	10.3	1.0	1488.9	-1.1	8.4	0.7
ν_{19} (B_2)	1441.5	2.5	1.3	1441.7	0.2	2.1	1.2
ν_{20} (B_2)	1191.9	98.1	0.7	1181.5	-10.4	16.5	0.1
ν_{21} (B_2)	1113.8	35.0	1.6	1107.9	-5.9	35.7	1.8

Van der Waals vibrations: 23.6 cm^{-1}, 1.1 km mol^{-1}, 0.4 $Å^4$ amu^{-1}, 79.0 cm^{-1}, 0.2 km mol^{-1}, 0.01 $Å^4$ amu^{-1}, 81.7 cm^{-1}, 3.8 km mol^{-1}, 0.4 $Å^4$ amu^{-1}, 95.7 cm^{-1}, 4.8 km mol^{-1}, 0.6 $Å^4$ amu^{-1}, 121.9 cm^{-1}, 0.03 km mol^{-1}, 0.6 $Å^4$ amu^{-1}, 147.0 cm^{-1}, 2.2 km mol^{-1}, 0.4 $Å^4$ amu^{-1}.

Table S10.3B: MP2/aug-cc-pVDZ vibrational frequencies, in cm^{-1}, infrared intensities, in km mol^{-1}, and Raman intensities, in $Å^4$ amu^{-1}, for the global minimum lp···π complex of COF_2 and DME-d_6 and both monomers, as well as the complexation shift Δν.

	Monomer			lp···π complex			
	Frequency	IR int.	Raman int.	Frequency	Δν	IR int.	Raman int.
COF_2							
ν_1 (A_1)	1932.2	422.4	12.8	1925.7	-6.6	356.9	11.1
ν_2 (A_1)	934.1	66.3	9.1	931.5	-2.6	52.3	8.6
ν_3 (A_1)	563.4	6.0	1.1	562.2	-1.2	4.0	0.8
ν_4 (B_1)	1201.6	417.7	1.4	1207.7	6.1	395.4	1.4
ν_5 (B_1)	600.2	5.7	2.0	601.6	1.4	4.1	1.5
ν_6 (B_2)	768.0	32.7	0.4	737.8	-30.3	92.9	3.9
DME-d_6							
ν_1 (A_1)	2364.1	17.0	37.1	2368.0	4.0	13.5	30.5
ν_2 (A_1)	2171.1	32.1	166.2	2177.7	6.6	27.1	148.5
ν_3 (A_1)	1153.5	5.3	2.6	1149.2	-4.3	4.0	2.4
ν_4 (A_1)	1085.9	0.09	2.5	1085.2	-0.7	1.0	2.3
ν_5 (A_1)	1058.5	17.5	1.8	1059.5	1.0	19.4	1.6
ν_6 (A_1)	834.8	16.9	7.7	831.3	-3.5	13.7	7.3
ν_7 (A_1)	351.5	1.5	0.7	353.9	2.4	1.9	0.6
ν_8 (A_2)	2297.2	0.0	7.5	2310.2	13.0	0.06	6.1
ν_9 (A_2)	1065.8	0.0	4.2	1066.1	0.3	5.0	2.7
ν_{10} (A_2)	877.6	0.0	2.2	877.6	-0.1	0.03	2.1
ν_{11} (A_2)	139.5	0.0	0.1	137.7	-1.8	0.002	0.1
ν_{12} (B_1)	2290.4	65.1	51.2	2304.3	13.9	51.2	47.0
ν_{13} (B_1)	1077.4	4.3	0.003	1077.9	0.6	5.6	0.2
ν_{14} (B_1)	937.8	9.9	0.1	941.4	3.6	12.9	0.5
ν_{15} (B_1)	200.5	4.6	0.0	220.7	20.2	9.8	0.07
ν_{16} (B_2)	2360.7	10.6	31.7	2364.6	3.9	7.4	24.0
ν_{17} (B_2)	2164.0	44.9	0.03	2171.6	7.6	36.4	0.3
ν_{18} (B_2)	1170.3	134.3	0.9	1155.1	-15.3	62.7	0.6
ν_{19} (B_2)	1077.4	0.5	0.2	1076.6	-0.8	0.9	0.09
ν_{20} (B_2)	1066.1	1.6	1.1	1065.0	-1.1	1.1	2.0
ν_{21} (B_2)	860.9	0.08	0.9	860.3	-0.6	0.3	0.9

Van der Waals vibrations: 21.8 cm^{-1}, 0.9 km mol^{-1}, 0.3 $Å^4$ amu^{-1}, 71.5 cm^{-1}, 3.5 km mol^{-1}, 0.3 $Å^4$ amu^{-1}, 72.5 cm^{-1}, 0.1 km mol^{-1}, 0.01 $Å^4$ amu^{-1}, 92.4 cm^{-1}, 3.5 km mol^{-1}, 0.4 $Å^4$ amu^{-1}, 117.2 cm^{-1}, 0.06 km mol^{-1}, 0.5 $Å^4$ amu^{-1}, 131.7 cm^{-1}, 0.1 km mol^{-1}, 0.5 $Å^4$ amu^{-1}.

Table S10.4A: MP2/aug-cc-pVDZ vibrational frequencies, in cm^{-1}, infrared intensities, in km mol^{-1}, and Raman intensities, in $Å^4$ amu^{-1}, for the local minimum lp···π complex of COF_2 and DME and both monomers, as well as the complexation shift Δν.

	Monomer			lp···π complex			
	Frequency	IR int.	Raman int.	Frequency	Δν	IR int.	Raman int.
COF_2							
ν_1 (A_1)	1932.2	422.4	12.8	1932.5	0.3	368.3	13.2
ν_2 (A_1)	934.1	66.3	9.1	928.9	-5.2	50.5	11.0
ν_3 (A_1)	563.4	6.0	1.1	563.2	-0.2	4.1	0.9
ν_4 (B_1)	1201.6	417.7	1.4	1197.7	-3.9	358.8	1.1
ν_5 (B_1)	600.2	5.7	2.0	599.7	-0.5	4.2	1.5
ν_6 (B_2)	768.0	32.7	0.4	738.9	-29.2	90.5	4.7
DME							
ν_1 (A_1)	3188.7	20.1	87.6	3195.5	6.8	13.2	52.1
ν_2 (A_1)	3024.8	58.6	320.3	3033.6	8.8	55.4	298.6
ν_3 (A_1)	1505.9	2.9	5.6	1505.0	-0.9	3.2	5.9
ν_4 (A_1)	1473.5	0.0008	2.2	1473.9	0.4	0.4	4.5
ν_5 (A_1)	1261.1	6.6	0.5	1263.5	2.5	5.9	0.5
ν_6 (A_1)	942.4	34.7	9.8	936.8	-5.6	39.0	6.9
ν_7 (A_1)	416.8	2.3	1.0	418.0	1.2	3.4	0.9
ν_8 (A_2)	3096.2	0.0	14.7	3110.7	14.5	0.6	14.0
ν_9 (A_2)	1474.8	0.0	11.4	1475.0	0.2	0.2	8.0
ν_{10} (A_2)	1157.2	0.0	1.5	1157.1	-0.1	0.003	1.5
ν_{11} (A_2)	195.2	0.0	0.2	190.1	-5.1	0.01	0.2
ν_{12} (B_1)	3089.5	107.8	94.2	3104.6	15.0	88.7	98.0
ν_{13} (B_1)	1489.2	13.0	0.04	1490.0	0.8	15.4	0.09
ν_{14} (B_1)	1187.2	7.2	0.04	1189.3	2.2	6.3	0.1
ν_{15} (B_1)	260.2	5.1	0.002	265.3	5.1	7.2	0.009
ν_{16} (B_2)	3187.3	24.6	59.2	3189.7	2.4	17.3	54.6
ν_{17} (B_2)	3018.4	55.2	0.6	3028.2	9.9	44.6	2.2
ν_{18} (B_2)	1490.1	10.3	1.0	1488.8	-1.2	10.7	0.9
ν_{19} (B_2)	1441.5	2.5	1.3	1442.1	0.6	0.3	1.4
ν_{20} (B_2)	1191.9	98.1	0.7	1185.7	-6.2	76.4	0.3
ν_{21} (B_2)	1113.8	35.0	1.6	1110.9	-2.8	40.3	2.0

Van der Waals vibrations: 16.5 cm^{-1}, 0.5 km mol^{-1}, 0.2 $Å^4$ amu^{-1}, 44.8 cm^{-1}, 2.5 km mol^{-1}, 0.1 $Å^4$ amu^{-1}, 70.3 cm^{-1}, 1.5 km mol^{-1}, 0.04 $Å^4$ amu^{-1}, 98.8 cm^{-1}, 1.0 km mol^{-1}, 0.2 $Å^4$ amu^{-1}, 123.8 cm^{-1}, 1.3 km mol^{-1}, 0.4 $Å^4$ amu^{-1}, 131.7 cm^{-1}, 1.3 km mol^{-1}, 1.0 $Å^4$ amu^{-1}.

Table S10.4B: MP2/aug-cc-pVDZ vibrational frequencies, in cm^{-1}, infrared intensities, in km mol^{-1}, and Raman intensities, in $Å^4$ amu^{-1}, for the local minimum lp···π complex of COF_2 and DME-d_6 and both monomers, as well as the complexation shift Δν.

	Monomer			lp···π complex			
	Frequency	IR int.	Raman int.	Frequency	Δν	IR int.	Raman int.
COF_2							
ν_1 (A_1)	1932.2	422.4	12.8	1932.4	0.2	366.8	13.2
ν_2 (A_1)	934.1	66.3	9.1	929.0	-5.1	51.7	8.6
ν_3 (A_1)	563.4	6.0	1.1	563.2	-0.2	4.1	0.9
ν_4 (B_1)	1201.6	417.7	1.4	1198.1	-3.5	351.9	1.1
ν_5 (B_1)	600.2	5.7	2.0	599.7	-0.5	4.2	1.5
ν_6 (B_2)	768.0	32.7	0.4	738.5	-29.5	92.0	4.8
DME-d_6							
ν_1 (A_1)	2364.1	17.0	37.1	2369.3	5.2	11.6	25.7
ν_2 (A_1)	2171.1	32.1	166.2	2176.8	5.7	31.6	153.2
ν_3 (A_1)	1153.5	5.3	2.6	1150.5	-3.0	5.2	2.4
ν_4 (A_1)	1085.9	0.09	2.5	1084.1	-1.8	2.1	2.7
ν_5 (A_1)	1058.5	17.5	1.8	1060.6	2.0	21.9	1.9
ν_6 (A_1)	834.8	16.9	7.7	832.3	-2.4	15.3	7.2
ν_7 (A_1)	351.5	1.5	0.7	353.5	2.0	2.5	0.6
ν_8 (A_2)	2297.2	0.0	7.5	2308.3	11.1	0.2	7.0
ν_9 (A_2)	1065.8	0.0	4.2	1065.6	-0.2	0.02	3.6
ν_{10} (A_2)	877.6	0.0	2.2	877.4	-0.3	0.06	2.1
ν_{11} (A_2)	139.5	0.0	0.1	135.8	-3.7	0.01	0.1
ν_{12} (B_1)	2290.4	65.1	51.2	2302.1	11.8	54.0	52.7
ν_{13} (B_1)	1077.4	4.3	0.003	1077.6	0.3	4.7	0.02
ν_{14} (B_1)	937.8	9.9	0.1	940.0	2.2	10.3	0.2
ν_{15} (B_1)	200.5	4.6	0.0	211.4	10.8	7.0	0.03
ν_{16} (B_2)	2360.7	10.6	31.7	2364.0	3.3	8.6	25.7
ν_{17} (B_2)	2164.0	44.9	0.03	2170.6	6.6	37.7	0.5
ν_{18} (B_2)	1170.3	134.3	0.9	1161.0	-9.3	118.6	0.8
ν_{19} (B_2)	1077.4	0.5	0.2	1075.7	-1.7	0.7	0.2
ν_{20} (B_2)	1066.1	1.6	1.1	1067.0	0.9	3.1	1.2
ν_{21} (B_2)	860.9	0.08	0.9	861.2	0.3	0.2	1.1

Van der Waals vibrations: 15.1 cm^{-1}, 0.4 km mol^{-1}, 0.09 $Å^4$ amu^{-1}, 38.7 cm^{-1}, 1.7 km mol^{-1}, 0.08 $Å^4$ amu^{-1}, 64.3 cm^{-1}, 1.1 km mol^{-1}, 0.03 $Å^4$ amu^{-1}, 95.1 cm^{-1}, 1.0 km mol^{-1}, 0.2 $Å^4$ amu^{-1}, 115.3 cm^{-1}, 0.4 km mol^{-1}, 0.3 $Å^4$ amu^{-1}, 127.6 cm^{-1}, 0.6 km mol^{-1}, 1.0 $Å^4$ amu^{-1}.

Table S10.5A: MP2/aug-cc-pVDZ vibrational frequencies, in cm^{-1}, infrared intensities, in km mol^{-1}, and Raman intensities, in $Å^4$ amu^{-1}, for the lp···π complex of COFCl and DME (lp···π_1) and both monomers, as well as the complexation shift Δν.

	Monomer			lp···π complex (lp···π_1)			
	Frequency	IR int.	Raman int.	Frequency	Δν	IR int.	Raman int.
COFCl							
ν_1 (A')	1863.0	345.9	16.5	1865.6	2.6	304.1	14.8
ν_2 (A')	1058.0	425.3	2.2	1050.3	-7.7	377.9	1.6
ν_3 (A')	749.9	74.2	11.0	748.5	-1.4	61.1	10.4
ν_4 (A')	499.1	0.3	5.6	498.0	-1.1	0.2	4.9
ν_5 (A')	410.4	0.6	1.8	411.2	0.8	0.3	1.3
ν_6 (A")	662.8	13.5	0.1	641.0	-21.8	42.4	3.2
DME							
ν_1 (A_1)	3188.7	20.1	87.6	3193.4	4.7	14.2	50.2
ν_2 (A_1)	3024.8	58.6	320.3	3031.5	6.7	57.2	297.2
ν_3 (A_1)	1505.9	2.9	5.6	1504.3	-1.6	3.7	6.0
ν_4 (A_1)	1473.5	0.0008	2.2	1473.4	-0.2	0.5	5.7
ν_5 (A_1)	1261.1	6.6	0.5	1262.2	1.2	6.4	0.5
ν_6 (A_1)	942.4	34.7	9.8	936.0	-6.4	41.6	9.1
ν_7 (A_1)	416.8	2.3	1.0	417.8	1.0	2.8	0.9
ν_8 (A_2)	3096.2	0.0	14.7	3107.7	11.5	0.6	14.3
ν_9 (A_2)	1474.8	0.0	11.4	1473.9	-0.9	0.4	6.5
ν_{10} (A_2)	1157.2	0.0	1.5	1156.5	-0.8	0.1	1.5
ν_{11} (A_2)	195.2	0.0	0.2	190.6	-4.7	0.03	0.2
ν_{12} (B_1)	3089.5	107.8	94.2	3101.5	12.0	89.9	101.0
ν_{13} (B_1)	1489.2	13.0	0.04	1488.9	-0.3	14.8	0.1
ν_{14} (B_1)	1187.2	7.2	0.04	1188.5	1.4	6.7	0.1
ν_{15} (B_1)	260.2	5.1	0.002	264.9	4.7	7.2	0.01
ν_{16} (B_2)	3187.3	24.6	59.2	3186.5	-0.8	18.1	47.1
ν_{17} (B_2)	3018.4	55.2	0.6	3025.9	7.5	44.7	2.9
ν_{18} (B_2)	1490.1	10.3	1.0	1488.2	-1.8	10.1	0.9
ν_{19} (B_2)	1441.5	2.5	1.3	1441.3	-0.2	0.2	1.4
ν_{20} (B_2)	1191.9	98.1	0.7	1185.2	-6.7	77.5	0.3
ν_{21} (B_2)	1113.8	35.0	1.6	1110.7	-3.1	37.3	2.1

Van der Waals vibrations: 17.8 cm^{-1}, 0.8 km mol^{-1}, 0.3 $Å^4$ amu^{-1}, 54.5 cm^{-1}, 4.0 km mol^{-1}, 0.4 $Å^4$ amu^{-1}, 64.3 cm^{-1}, 0.6 km mol^{-1}, 0.2 $Å^4$ amu^{-1}, 87.0 cm^{-1}, 0.2 km mol^{-1}, 0.1 $Å^4$ amu^{-1}, 105.7 cm^{-1}, 0.7 km mol^{-1}, 1.2 $Å^4$ amu^{-1}, 117.3 cm^{-1}, 2.5 km mol^{-1}, 0.6 $Å^4$ amu^{-1}.

Table S10.5B: MP2/aug-cc-pVDZ vibrational frequencies, in cm^{-1}, infrared intensities, in km mol^{-1}, and Raman intensities, in $Å^4$ amu^{-1}, for the lp···π complex of COFCl and DME-d_6 (lp···π_1) and both monomers, as well as the complexation shift Δν.

	Monomer			lp···π complex (lp···π_1)			
	Frequency	IR int.	Raman int.	Frequency	Δν	IR int.	Raman int.
COFCl							
ν_1 (A')	1863.0	345.9	16.5	1865.5	2.5	303.2	14.8
ν_2 (A')	1058.0	425.3	2.2	1049.1	-8.9	383.3	1.7
ν_3 (A')	749.9	74.2	11.0	748.4	-1.5	61.2	10.5
ν_4 (A')	499.1	0.3	5.6	498.0	-1.1	0.2	4.9
ν_5 (A')	410.4	0.6	1.8	411.3	0.9	0.3	1.4
ν_6 (A")	662.8	13.5	0.1	640.9	-21.9	42.6	3.3
DME-d_6							
ν_1 (A_1)	2364.1	17.0	37.1	2367.6	3.5	12.2	24.5
ν_2 (A_1)	2171.1	32.1	166.2	2175.3	4.2	32.4	151.8
ν_3 (A_1)	1153.5	5.3	2.6	1150.2	-3.4	7.6	2.6
ν_4 (A_1)	1085.9	0.09	2.5	1085.1	-0.8	6.1	2.8
ν_5 (A_1)	1058.5	17.5	1.8	1059.5	1.0	6.6	1.8
ν_6 (A_1)	834.8	16.9	7.7	831.6	-3.2	20.4	7.0
ν_7 (A_1)	351.5	1.5	0.7	353.0	1.5	2.0	0.6
ν_8 (A_2)	2297.2	0.0	7.5	2306.1	8.9	0.2	7.2
ν_9 (A_2)	1065.8	0.0	4.2	1064.8	-1.0	1.0	3.2
ν_{10} (A_2)	877.6	0.0	2.2	877.0	-0.6	0.003	2.0
ν_{11} (A_2)	139.5	0.0	0.1	136.3	-3.2	0.02	0.1
ν_{12} (B_1)	2290.4	65.1	51.2	2299.8	9.4	54.5	54.5
ν_{13} (B_1)	1077.4	4.3	0.003	1076.8	-0.5	4.8	0.04
ν_{14} (B_1)	937.8	9.9	0.1	939.3	1.5	8.8	0.2
ν_{15} (B_1)	200.5	4.6	0.0	210.1	9.6	7.1	0.03
ν_{16} (B_2)	2360.7	10.6	31.7	2361.5	0.9	9.0	22.8
ν_{17} (B_2)	2164.0	44.9	0.03	2168.8	4.9	37.0	0.7
ν_{18} (B_2)	1170.3	134.3	0.9	1160.9	-9.4	112.5	0.8
ν_{19} (B_2)	1077.4	0.5	0.2	1075.5	-1.8	1.4	0.2
ν_{20} (B_2)	1066.1	1.6	1.1	1066.3	0.1	3.7	1.2
ν_{21} (B_2)	860.9	0.08	0.9	860.6	-0.3	0.2	1.1

Van der Waals vibrations: 16.2 cm^{-1}, 0.7 km mol^{-1}, 0.2 $Å^4$ amu^{-1}, 47.3 cm^{-1}, 2.8 km mol^{-1}, 0.2 $Å^4$ amu^{-1}, 60.2 cm^{-1}, 0.7 km mol^{-1}, 0.2 $Å^4$ amu^{-1}, 81.5 cm^{-1}, 0.2 km mol^{-1}, 0.2 $Å^4$ amu^{-1}, 99.6 cm^{-1}, 0.5 km mol^{-1}, 1.0 $Å^4$ amu^{-1}, 111.1 cm^{-1}, 0.9 km mol^{-1}, 0.9 $Å^4$ amu^{-1}.

Table S10.6A: MP2/aug-cc-pVDZ vibrational frequencies, in cm^{-1}, infrared intensities, in km mol^{-1}, and Raman intensities, in $Å^4$ amu^{-1}, for the lp···π complex of COFCl and DME (lp···π_2) and both monomers, as well as the complexation shift Δν.

	Monomer			lp···π complex (lp···π_2)			
	Frequency	IR int.	Raman int.	Frequency	Δν	IR int.	Raman int.
COFCl							
ν_1 (A')	1863.0	345.9	16.5	1859.6	-3.4	298.4	13.4
ν_2 (A')	1058.0	425.3	2.2	1060.6	2.6	334.1	1.5
ν_3 (A')	749.9	74.2	11.0	750.3	0.4	64.0	10.2
ν_4 (A')	499.1	0.3	5.6	498.8	-0.3	0.2	5.0
ν_5 (A')	410.4	0.6	1.8	411.2	0.8	0.1	1.1
ν_6 (A")	662.8	13.5	0.1	642.0	-20.8	42.4	2.7
DME							
ν_1 (A_1)	3188.7	20.1	87.6	3192.5	3.8	15.9	57.6
ν_2 (A_1)	3024.8	58.6	320.3	3032.1	7.3	48.5	291.3
ν_3 (A_1)	1505.9	2.9	5.6	1504.4	-1.5	9.5	5.6
ν_4 (A_1)	1473.5	0.0008	2.2	1473.5	0.0	0.06	2.1
ν_5 (A_1)	1261.1	6.6	0.5	1261.7	0.6	5.7	0.4
ν_6 (A_1)	942.4	34.7	9.8	935.4	-7.0	37.5	9.1
ν_7 (A_1)	416.8	2.3	1.0	419.0	2.2	2.5	1.0
ν_8 (A_2)	3096.2	0.0	14.7	3108.7	12.5	0.4	12.7
ν_9 (A_2)	1474.8	0.0	11.4	1474.7	-0.2	0.3	9.9
ν_{10} (A_2)	1157.2	0.0	1.5	1157.1	-0.2	0.2	1.6
ν_{11} (A_2)	195.2	0.0	0.2	192.8	-2.4	0.003	0.1
ν_{12} (B_1)	3089.5	107.8	94.2	3102.7	13.2	86.9	90.1
ν_{13} (B_1)	1489.2	13.0	0.04	1490.0	0.7	16.5	0.3
ν_{14} (B_1)	1187.2	7.2	0.04	1189.6	2.5	5.8	0.3
ν_{15} (B_1)	260.2	5.1	0.002	269.9	9.7	9.0	0.04
ν_{16} (B_2)	3187.3	24.6	59.2	3187.4	0.1	17.9	45.1
ν_{17} (B_2)	3018.4	55.2	0.6	3026.5	8.2	44.7	2.4
ν_{18} (B_2)	1490.1	10.3	1.0	1488.7	-1.4	8.4	0.7
ν_{19} (B_2)	1441.5	2.5	1.3	1441.0	-0.5	1.2	1.3
ν_{20} (B_2)	1191.9	98.1	0.7	1183.6	-8.3	91.7	0.5
ν_{21} (B_2)	1113.8	35.0	1.6	1108.8	-5.0	57.0	2.0

Van der Waals vibrations: 23.8 cm^{-1}, 1.1 km mol^{-1}, 0.5 $Å^4$ amu^{-1}, 68.3 cm^{-1}, 2.0 km mol^{-1}, 0.5 $Å^4$ amu^{-1}, 84.1 cm^{-1}, 0.4 km mol^{-1}, 0.3 $Å^4$ amu^{-1}, 87.2 cm^{-1}, 5.1 km mol^{-1}, 0.7 $Å^4$ amu^{-1}, 100.8 cm^{-1}, 0.3 km mol^{-1}, 0.7 $Å^4$ amu^{-1}, 132.0 cm^{-1}, 2.7 km mol^{-1}, 0.5 $Å^4$ amu^{-1}.

Table S10.6B: MP2/aug-cc-pVDZ vibrational frequencies, in cm^{-1}, infrared intensities, in km mol^{-1}, and Raman intensities, in $Å^4$ amu^{-1}, for the lp···π complex of COFCl and DME-d_6 (lp···π_2) and both monomers, as well as the complexation shift Δν.

	Monomer			lp···π complex (lp···π_2)			
	Frequency	IR int.	Raman int.	Frequency	Δν	IR int.	Raman int.
COFCl							
ν_1 (A')	1863.0	345.9	16.5	1859.5	-3.5	299.4	13.1
ν_2 (A')	1058.0	425.3	2.2	1056.3	-1.7	250.1	1.7
ν_3 (A')	749.9	74.2	11.0	750.2	0.3	64.0	10.2
ν_4 (A')	499.1	0.3	5.6	498.8	-0.3	0.2	5.0
ν_5 (A')	410.4	0.6	1.8	411.4	1.0	0.3	1.3
ν_6 (A")	662.8	13.5	0.1	641.9	-20.8	42.7	2.7
DME-d_6							
ν_1 (A_1)	2364.1	17.0	37.1	2367.0	2.9	12.7	28.1
ν_2 (A_1)	2171.1	32.1	166.2	2175.8	4.6	27.8	149.0
ν_3 (A_1)	1153.5	5.3	2.6	1149.3	-4.3	4.6	2.5
ν_4 (A_1)	1085.9	0.09	2.5	1084.9	-0.9	1.2	2.2
ν_5 (A_1)	1058.5	17.5	1.8	1059.0	0.5	19.4	1.5
ν_6 (A_1)	834.8	16.9	7.7	831.0	-3.8	18.5	7.2
ν_7 (A_1)	351.5	1.5	0.7	353.7	2.2	1.6	0.6
ν_8 (A_2)	2297.2	0.0	7.5	2306.8	9.6	0.1	6.4
ν_9 (A_2)	1065.8	0.0	4.2	1069.7	3.9	80.1	3.0
ν_{10} (A_2)	877.6	0.0	2.2	877.4	-0.2	0.04	2.0
ν_{11} (A_2)	139.5	0.0	0.1	138.4	-1.1	0.0009	0.1
ν_{12} (B_1)	2290.4	65.1	51.2	2300.8	10.4	52.7	48.6
ν_{13} (B_1)	1077.4	4.3	0.003	1077.4	0.0	10.7	0.3
ν_{14} (B_1)	937.8	9.9	0.1	940.2	2.4	9.8	0.3
ν_{15} (B_1)	200.5	4.6	0.0	216.0	15.5	8.9	0.06
ν_{16} (B_2)	2360.7	10.6	31.7	2362.1	1.4	8.7	21.9
ν_{17} (B_2)	2164.0	44.9	0.03	2169.3	5.3	36.5	0.5
ν_{18} (B_2)	1170.3	134.3	0.9	1158.2	-12.1	146.1	0.9
ν_{19} (B_2)	1077.4	0.5	0.2	1076.5	-0.9	0.1	0.1
ν_{20} (B_2)	1066.1	1.6	1.1	1064.8	-1.3	4.4	1.6
ν_{21} (B_2)	860.9	0.08	0.9	860.1	-0.8	0.3	0.9

Van der Waals vibrations: 21.6 cm^{-1}, 0.9 km mol^{-1}, 0.4 $Å^4$ amu^{-1}, 64.9 cm^{-1}, 2.2 km mol^{-1}, 0.5 $Å^4$ amu^{-1}, 75.1 cm^{-1}, 1.8 km mol^{-1}, 0.3 $Å^4$ amu^{-1}, 81.7 cm^{-1}, 2.2 km mol^{-1}, 0.3 $Å^4$ amu^{-1}, 94.0 cm^{-1}, 0.3 km mol^{-1}, 0.7 $Å^4$ amu^{-1}, 119.1 cm^{-1}, 0.3 km mol^{-1}, 0.8 $Å^4$ amu^{-1}.

Table S10.7A: MP2/aug-cc-pVDZ vibrational frequencies, in cm^{-1}, infrared intensities, in km mol^{-1}, and Raman intensities, in $Å^4$ amu^{-1}, for the lp···π complex of COFCl and DME (lp···π_3) and both monomers, as well as the complexation shift Δν.

	Monomer			lp···π complex (lp···π_3)			
	Frequency	IR int.	Raman int.	Frequency	Δν	IR int.	Raman int.
COFCl							
ν_1 (A')	1863.0	345.9	16.5	1868.7	5.7	300.1	15.1
ν_2 (A')	1058.0	425.3	2.2	1060.0	2.0	363.2	1.8
ν_3 (A')	749.9	74.2	11.0	745.1	-4.8	68.4	10.0
ν_4 (A')	499.1	0.3	5.6	494.4	-4.7	0.2	5.2
ν_5 (A')	410.4	0.6	1.8	410.8	0.4	0.3	1.4
ν_6 (A")	662.8	13.5	0.1	640.9	-21.9	43.0	3.0
DME							
ν_1 (A_1)	3188.7	20.1	87.6	3191.1	2.4	13.3	51.1
ν_2 (A_1)	3024.8	58.6	320.3	3029.6	4.8	53.2	289.2
ν_3 (A_1)	1505.9	2.9	5.6	1504.1	-1.8	5.7	5.6
ν_4 (A_1)	1473.5	0.0008	2.2	1472.8	-0.7	0.2	2.6
ν_5 (A_1)	1261.1	6.6	0.5	1262.4	1.3	5.9	0.4
ν_6 (A_1)	942.4	34.7	9.8	936.8	-5.6	35.9	8.8
ν_7 (A_1)	416.8	2.3	1.0	417.2	0.4	2.6	0.8
ν_8 (A_2)	3096.2	0.0	14.7	3105.4	9.2	1.3	14.3
ν_9 (A_2)	1474.8	0.0	11.4	1474.2	-0.6	0.5	9.4
ν_{10} (A_2)	1157.2	0.0	1.5	1156.3	-0.9	0.05	1.6
ν_{11} (A_2)	195.2	0.0	0.2	192.8	-2.4	0.01	0.2
ν_{12} (B_1)	3089.5	107.8	94.2	3099.2	9.7	95.8	98.1
ν_{13} (B_1)	1489.2	13.0	0.04	1489.4	0.1	15.6	0.2
ν_{14} (B_1)	1187.2	7.2	0.04	1188.2	1.0	6.9	0.2
ν_{15} (B_1)	260.2	5.1	0.002	264.5	4.3	8.0	0.01
ν_{16} (B_2)	3187.3	24.6	59.2	3188.2	0.9	16.0	49.5
ν_{17} (B_2)	3018.4	55.2	0.6	3023.9	5.5	43.6	2.7
ν_{18} (B_2)	1490.1	10.3	1.0	1488.1	-1.9	9.8	0.9
ν_{19} (B_2)	1441.5	2.5	1.3	1440.9	-0.5	0.3	1.3
ν_{20} (B_2)	1191.9	98.1	0.7	1186.4	-5.5	80.5	0.3
ν_{21} (B_2)	1113.8	35.0	1.6	1111.0	-2.8	38.1	1.9

Van der Waals vibrations: 21.6 cm^{-1}, 0.3 km mol^{-1}, 0.6 $Å^4$ amu^{-1}, 57.3 cm^{-1}, 1.5 km mol^{-1}, 0.5 $Å^4$ amu^{-1}, 64.0 cm^{-1}, 0.5 km mol^{-1}, 0.07 $Å^4$ amu^{-1}, 89.5 cm^{-1}, 0.08 km mol^{-1}, 0.7 $Å^4$ amu^{-1}, 109.1 cm^{-1}, 5.7 km mol^{-1}, 0.2 $Å^4$ amu^{-1}, 115.8 cm^{-1}, 0.2 km mol^{-1}, 1.1 $Å^4$ amu^{-1}.

Table S10.7B: MP2/aug-cc-pVDZ vibrational frequencies, in cm^{-1}, infrared intensities, in km mol^{-1}, and Raman intensities, in $Å^4$ amu^{-1}, for the lp···π complex of COFCl and DME-d_6 (lp···π_3) and both monomers, as well as the complexation shift Δν.

	Monomer			lp···π complex (lp···π_1)			
	Frequency	IR int.	Raman int.	Frequency	Δν	IR int.	Raman int.
COFCl							
ν_1 (A')	1863.0	345.9	16.5	1868.6	5.6	299.7	15.0
ν_2 (A')	1058.0	425.3	2.2	1057.9	-0.1	288.6	1.8
ν_3 (A')	749.9	74.2	11.0	745.0	-4.9	67.9	10.1
ν_4 (A')	499.1	0.3	5.6	494.4	-4.7	0.2	5.2
ν_5 (A')	410.4	0.6	1.8	410.8	0.4	0.3	1.4
ν_6 (A")	662.8	13.5	0.1	640.9	-21.9	43.1	3.0
DME-d_6							
ν_1 (A_1)	2364.1	17.0	37.1	2366.3	2.2	12.2	25.6
ν_2 (A_1)	2171.1	32.1	166.2	2174.1	3.0	30.5	149.2
ν_3 (A_1)	1153.5	5.3	2.6	1150.2	-3.4	7.1	2.4
ν_4 (A_1)	1085.9	0.09	2.5	1084.6	-1.3	8.4	2.6
ν_5 (A_1)	1058.5	17.5	1.8	1060.3	1.8	65.5	1.2
ν_6 (A_1)	834.8	16.9	7.7	832.1	-2.6	18.5	6.7
ν_7 (A_1)	351.5	1.5	0.7	352.5	1.0	1.8	0.6
ν_8 (A_2)	2297.2	0.0	7.5	2304.2	6.9	0.4	7.0
ν_9 (A_2)	1065.8	0.0	4.2	1065.4	-0.4	4.9	3.6
ν_{10} (A_2)	877.6	0.0	2.2	876.8	-0.8	0.02	2.1
ν_{11} (A_2)	139.5	0.0	0.1	138.2	-1.3	0.007	0.1
ν_{12} (B_1)	2290.4	65.1	51.2	2297.8	7.4	57.8	51.5
ν_{13} (B_1)	1077.4	4.3	0.003	1077.2	-0.1	7.1	0.06
ν_{14} (B_1)	937.8	9.9	0.1	939.1	1.3	9.6	0.2
ν_{15} (B_1)	200.5	4.6	0.0	209.8	9.3	8.0	0.02
ν_{16} (B_2)	2360.7	10.6	31.7	2362.3	1.7	6.9	23.3
ν_{17} (B_2)	2164.0	44.9	0.03	2167.5	3.5	36.0	0.7
ν_{18} (B_2)	1170.3	134.3	0.9	1162.1	-8.2	116.4	0.8
ν_{19} (B_2)	1077.4	0.5	0.2	1075.5	-1.9	4.4	0.3
ν_{20} (B_2)	1066.1	1.6	1.1	1066.4	0.2	11.2	1.1
ν_{21} (B_2)	860.9	0.08	0.9	860.8	-0.1	0.2	1.0

Van der Waals vibrations: 19.6 cm^{-1}, 0.2 km mol^{-1}, 0.5 $Å^4$ amu^{-1}, 50.9 cm^{-1}, 1.2 km mol^{-1}, 0.4 $Å^4$ amu^{-1}, 58.5 cm^{-1}, 0.4 km mol^{-1}, 0.05 $Å^4$ amu^{-1}, 86.5 cm^{-1}, 0.09 km mol^{-1}, 0.7 $Å^4$ amu^{-1}, 96.8 cm^{-1}, 2.9 km mol^{-1}, 0.2 $Å^4$ amu^{-1}, 112.6 cm^{-1}, 0.3 km mol^{-1}, 1.1 $Å^4$ amu^{-1}.

Table S10.8A: MP2/aug-cc-pVDZ vibrational frequencies, in cm^{-1}, infrared intensities, in km mol^{-1}, and Raman intensities, in $Å^4$ amu^{-1}, for the XB complex of COFCl and DME and both monomers, as well as the complexation shift Δν.

	Monomer			XB complex			
	Frequency	IR int.	Raman int.	Frequency	Δν	IR int.	Raman int.
COFCl							
ν_1 (A')	1863.0	345.9	16.5	1852.6	-10.3	364.3	18.3
ν_2 (A')	1058.0	425.3	2.2	1054.3	-3.7	450.1	2.2
ν_3 (A')	749.9	74.2	11.0	752.1	2.2	59.7	14.8
ν_4 (A')	499.1	0.3	5.6	501.8	2.7	2.3	9.1
ν_5 (A')	410.4	0.6	1.8	416.2	5.8	0.6	1.7
ν_6 (A")	662.8	13.5	0.1	668.1	5.3	13.9	0.1
DME							
ν_1 (A_1)	3188.7	20.1	87.6	3189.0	0.3	20.2	65.8
ν_2 (A_1)	3024.8	58.6	320.3	3029.9	5.1	69.0	326.9
ν_3 (A_1)	1505.9	2.9	5.6	1505.9	0.0	1.5	6.7
ν_4 (A_1)	1473.5	0.0008	2.2	1474.3	0.8	0.1	3.8
ν_5 (A_1)	1261.1	6.6	0.5	1262.7	1.6	6.6	1.3
ν_6 (A_1)	942.4	34.7	9.8	938.1	-4.3	70.5	11.5
ν_7 (A_1)	416.8	2.3	1.0	417.7	0.9	4.8	1.0
ν_8 (A_2)	3096.2	0.0	14.7	3104.9	8.7	0.07	13.8
ν_9 (A_2)	1474.8	0.0	11.4	1474.4	-0.4	0.004	10.2
ν_{10} (A_2)	1157.2	0.0	1.5	1157.0	-0.2	0.0	1.5
ν_{11} (A_2)	195.2	0.0	0.2	193.7	-1.6	0.0	0.2
ν_{12} (B_1)	3089.5	107.8	94.2	3098.3	8.8	91.8	109.4
ν_{13} (B_1)	1489.2	13.0	0.04	1488.9	-0.3	12.4	0.2
ν_{14} (B_1)	1187.2	7.2	0.04	1187.3	0.1	7.4	0.02
ν_{15} (B_1)	260.2	5.1	0.002	258.1	-2.2	4.5	0.002
ν_{16} (B_2)	3187.3	24.6	59.2	3186.8	-0.5	19.3	50.7
ν_{17} (B_2)	3018.4	55.2	0.6	3024.3	6.0	50.4	2.0
ν_{18} (B_2)	1490.1	10.3	1.0	1490.1	0.1	11.1	0.9
ν_{19} (B_2)	1441.5	2.5	1.3	1442.3	0.8	1.2	1.6
ν_{20} (B_2)	1191.9	98.1	0.7	1188.6	-3.3	90.1	0.7
ν_{21} (B_2)	1113.8	35.0	1.6	1112.7	-1.1	38.3	2.3

Van der Waals vibrations: 11.8 cm^{-1}, 3.1 km mol^{-1}, 0.01 $Å^4$ amu^{-1}, 12.6 cm^{-1}, 1.1 km mol^{-1}, 0.02 $Å^4$ amu^{-1}, 14.7 cm^{-1}, 0.4 km mol^{-1}, 0.3 $Å^4$ amu^{-1}, 43.1 cm^{-1}, 1.6 km mol^{-1}, 1.0 $Å^4$ amu^{-1}, 62.7 cm^{-1}, 0.6 km mol^{-1}, 0.2 $Å^4$ amu^{-1}, 69.0 cm^{-1}, 0.8 km mol^{-1}, 0.2 $Å^4$ amu^{-1}.

Table S10.8B: MP2/aug-cc-pVDZ vibrational frequencies, in cm^{-1}, infrared intensities, in km mol^{-1}, and Raman intensities, in $Å^4$ amu^{-1}, for the XB complex of COFCl and DME-d_6 and both monomers, as well as the complexation shift Δν.

	Monomer			XB complex			
	Frequency	IR int.	Raman int.	Frequency	Δν	IR int.	Raman int.
COFCl							
ν_1 (A')	1863.0	345.9	16.5	1852.6	-10.4	364.5	18.2
ν_2 (A')	1058.0	425.3	2.2	1053.9	-4.1	481.0	2.1
ν_3 (A')	749.9	74.2	11.0	752.1	2.2	60.5	14.6
ν_4 (A')	499.1	0.3	5.6	501.8	2.7	2.2	9.1
ν_5 (A')	410.4	0.6	1.8	416.3	5.9	1.0	1.9
ν_6 (A")	662.8	13.5	0.1	668.1	5.3	13.9	0.1
DME-d_6							
ν_1 (A_1)	2364.1	17.0	37.1	2364.8	0.7	16.7	29.6
ν_2 (A_1)	2171.1	32.1	166.2	2174.2	3.1	38.3	166.7
ν_3 (A_1)	1153.5	5.3	2.6	1151.7	-1.9	7.0	4.2
ν_4 (A_1)	1085.9	0.09	2.5	1085.7	-0.2	0.8	3.1
ν_5 (A_1)	1058.5	17.5	1.8	1060.7	2.2	3.7	3.8
ν_6 (A_1)	834.8	16.9	7.7	832.5	-2.3	32.0	8.3
ν_7 (A_1)	351.5	1.5	0.7	352.9	1.4	3.3	0.6
ν_8 (A_2)	2297.2	0.0	7.5	2303.9	6.7	0.03	7.0
ν_9 (A_2)	1065.8	0.0	4.2	1065.3	-0.5	0.002	3.7
ν_{10} (A_2)	877.6	0.0	2.2	877.3	-0.4	0.0002	2.0
ν_{11} (A_2)	139.5	0.0	0.1	138.4	-1.1	0.0005	0.1
ν_{12} (B_1)	2290.4	65.1	51.2	2297.3	6.9	56.2	59.2
ν_{13} (B_1)	1077.4	4.3	0.003	1076.9	-0.4	4.0	0.01
ν_{14} (B_1)	937.8	9.9	0.1	937.4	-0.4	9.8	0.2
ν_{15} (B_1)	200.5	4.6	0.0	198.7	-1.8	4.1	0.005
ν_{16} (B_2)	2360.7	10.6	31.7	2361.2	0.5	8.1	26.2
ν_{17} (B_2)	2164.0	44.9	0.03	2167.8	3.8	40.9	0.2
ν_{18} (B_2)	1170.3	134.3	0.9	1165.5	-4.8	128.3	1.2
ν_{19} (B_2)	1077.4	0.5	0.2	1077.2	-0.2	0.6	0.2
ν_{20} (B_2)	1066.1	1.6	1.1	1066.8	0.7	2.5	1.3
ν_{21} (B_2)	860.9	0.08	0.9	861.1	0.3	0.1	1.1

Van der Waals vibrations: 9.9 cm^{-1}, 2.4 km mol^{-1}, 0.02 $Å^4$ amu^{-1}, 11.7 cm^{-1}, 0.4 km mol^{-1}, 0.09 $Å^4$ amu^{-1}, 13.5 cm^{-1}, 0.3 km mol^{-1}, 0.3 $Å^4$ amu^{-1}, 42.5 cm^{-1}, 1.2 km mol^{-1}, 1.0 $Å^4$ amu^{-1}, 60.3 cm^{-1}, 0.5 km mol^{-1}, 0.2 $Å^4$ amu^{-1}, 66.2 cm^{-1}, 0.7 km mol^{-1}, 0.2 $Å^4$ amu^{-1}.

Table S10.9 : Experimental infrared frequencies for the monomer and complex, as well as experimental complexation shifts ($\Delta\nu_{exp}$) and MP2/aug-cc-pVDZ calculated complexation shifts for the global ($\Delta\nu_{calc,\ lp\cdots\pi\ global}$) and local minimum ($\Delta\nu_{calc,\ lp\cdots\pi\ local}$), in cm^{-1}, of the lp···π-bonded complex of COF_2 with DME-d_6 dissolved in LKr at 120 K.

Assignment		Symmetry	$\nu_{monomer}$	$\nu_{complex}$	$\Delta\nu_{exp}$	$\Delta\nu_{calc,\ lp\cdots\pi\ global}$	$\Delta\nu_{calc,\ lp\cdots\pi\ local}$
COF_2	ν_1	A_1	1934.6	1930.5	-4.1	-6.6	0.2
	$2\nu_2$	A_1	1905.4	1901.2	-4.2	-5.2	-10.1
	ν_4	B_1	1232.7	1233.4	0.7	6.1	-3.5
	ν_2	A_1	960.1	958.0	-2.1	-2.6	-5.1
	ν_6	B_2	769.0	747.3	-21.7	-30.3	-29.5
	ν_5	B_1	662.7	662.6	-0.1	1.4	-0.5
	ν_3	A_1	580.5	580.5	0.0	-1.2	-0.2
DME-d_6	ν_1	A_1	2243.3	2249.3	6.0	4.0	5.2
	ν_{16}	B_2	2243.3	2249.3	6.0	3.9	3.3
	ν_{12}	B_1	2179.8	2190.3	10.5	13.9	11.8
	ν_2	A_1	2054.3	2059.7	5.4	6.6	5.7
	ν_{17}	B_2	2049.5	2055.7	6.2	7.6	6.6
	ν_{18}	B_2	1153.4	1146.1	-7.3	-15.3	-9.3
	ν_3	A_1	1144.7	1143.2	-1.5	-4.3	-3.0
	ν_{13}	B_1	1060.5	1061.7	1.2	0.6	0.3
	ν_{19}	B_2	1057.7	1058.5	0.8	-0.8	-1.7
	ν_{20}	B_2	1057.7	1058.5	0.8	-1.1	0.9
	ν_5	A_1	1050.7	1053.6	2.9	1.0	2.0
	ν_{14}	B_1	929.0	930.2	1.2	3.6	2.2
	ν_{21}	B_2	857.8	-		-0.6	0.3
	ν_6	A_1	826.3	825.5	-0.8	-3.5	-2.4

Table S10.10 Experimental infrared frequencies for the monomer and complex, as well as experimental complexation shifts ($\Delta\nu_{exp}$) and MP2/aug-cc-pVDZ calculated complexation shifts ($\Delta\nu_{calc}$), in cm^{-1}, for the lp···π complexes and XB complex of COFCl with DME-d_6 dissolved in LKr at 120 K.

Assignment	Sym	$\nu_{monomer}$	$\nu_{complex}$	$\Delta\nu_{exp}$	$\Delta\nu_{calc,\ lp\cdots\pi1}$	$\Delta\nu_{calc,\ lp\cdots\pi2}$	$\Delta\nu_{calc,\ lp\cdots\pi3}$	$\nu_{complex}$	$\Delta\nu_{exp,\ XB}$	$\Delta\nu_{calc,\ XB}$
COFCl										
$2\nu_2$	A'	2158.0	2164.2[b]	6.2	-17.7	-3.5[a]	-0.3[a]	-		-8.2
ν_1	A'	1863.8	1864.4	0.6	2.5	-3.5	5.6	1856.2	-7.6	-10.4
$\nu_2 + \nu_3$	A'	1832.1	1834.4	2.3	-10.3	-1.4[a]	-5.0[a]	1834.4	2.3	-1.9
		1823.2	1824.3	1.1				-		
ν_2	A'	1083.9	1086.6	2.7	-8.9	-1.7[a]	-0.1[a]	1081.0	-2.9	-4.1
ν_2 (^{13}C)	A'	1056.4	1058.4[b]	2.0	-8.5	1.4	1.9	1052.3[b]	-4.1	-4.8
ν_3 (^{35}Cl)	A'	761.8	761.4	-0.4	-1.5	0.3	-4.9	764.1	2.3	2.2
ν_3 (^{37}Cl)	A'	759.8	759.6	-0.2	-1.4	0.4	-4.7	761.8	2.0	2.1
ν_6	A''	663.6	649.6	-14.0	-21.9	-20.8	-21.9	668.2	4.6	5.3
DME-d_6										
ν_1	A_1	2243.3	2248.2	4.9	3.5	2.9	2.2	2248.2	4.9	0.7
ν_{16}	B_2	2243.3	2244.8	1.5	0.9	1.4	1.7	2244.8	1.5	0.5
ν_{12}	B_1	2179.8	2187.2	7.4	9.4	10.4	7.4	2187.2	7.4	6.9
ν_2	A_1	2054.3	2057.9	3.6	4.2	4.6	3.0	2057.9	3.6	3.1
ν_{17}	B_2	2049.5	2053.6	4.1	4.9	5.3	3.5	2053.6	4.1	3.8
ν_{18}	B_2	1153.4	1147.8	-5.6	-9.4	-12.1	-8.2	1147.8	-5.6	-4.8
ν_3	A_1	1144.7	-		-3.4	-4.3	-3.4	-		-1.9
ν_{13}	B_1	1060.5	1060.7	0.2	-0.5	0.0	-0.1	1060.7	0.2	-0.4
ν_{19}	B_2	1057.7	1058.4	0.7	-1.8	-0.9	-1.9	1058.4	0.7	-0.2
ν_{20}	B_2	1057.7	1058.4	0.7	0.1	-1.3	0.2	1058.4	0.7	0.7
ν_5	A_1	1050.7	1052.3	1.6	1.0	0.5	1.8	1052.3	1.6	2.2
ν_{14}	B_1	929.0	929.8	0.8	1.5	2.4	1.3	929.8	0.8	-0.4
ν_{21}	B_2	857.8	-		-0.3	-0.8	-0.1	-		0.3
ν_6	A_1	826.3	825.0	-1.3	-3.2	-3.8	-2.6	825.0	-1.3	-2.3

[a] Mechanical coupling between COFCl ν_2 mode and DME-d_6 modes causes deviating calculated shifts as compared to the nondeuterated species.
[b] Overlap with DME-d_6 bands.

Table S10.11: Overview of the different van 't Hoff plots constructed for the lp···π complex between COF_2 and DME or DME-d_6 in LKr in the 120-156 K temperature interval, showing the estimated mole fractions of each monomer, range of the integrated monomer and complex bands and complex enthalpies $\Delta H°$ (LKr).

x_{COF_2}	x_{DME}	Integrated COF_2 band (cm^{-1})	Integrated DME band (cm^{-1})	Integrated Complex band (cm^{-1})	$\Delta H°$ (LKr) [a]
9.4×10^{-5}	1.9×10^{-3}	1269.4 - 1202.9	2117 - 2070	1960 - 1880	-14.1(1)
9.4×10^{-5}	1.9×10^{-3}	1965 - 1886	2040 - 2006	971 - 947	-14.50(8)
5.6×10^{-5}	5.6×10^{-4}	2000 - 1820	3050 - 2770	1950 - 1891	-14.9(2)
5.6×10^{-5}	5.6×10^{-4}	1296 - 1180.5	970 - 900	1255 - 1210	-14.2(2)
9.4×10^{-5}	9.4×10^{-4}	1970 - 1880	3035 - 2965	1975 - 1876	-14.4(1)
5.6×10^{-4}	5.6×10^{-4}	1000 - 930	3050 - 2760	764 - 728	-15.00(5)
5.6×10^{-4}	5.6×10^{-4}	797 - 748	980 - 890	937 - 912	-14.83(9)
5.6×10^{-4}	1.9×10^{-4}	1000 - 930	1215 - 1140	972 - 946	-14.5(1)
5.6×10^{-4}	1.9×10^{-4}	794 - 750	3050 - 2760	1113 - 1076	-15.0(2)
5.6×10^{-4}	1.9×10^{-4} [b]	1000 - 930	2273 - 2222	971 - 947	-14.3(1)
5.6×10^{-4}	1.9×10^{-4} [b]	797 - 784	2085 - 2025	2215 - 2171	-14.37(7)
5.6×10^{-5}	5.6×10^{-4} [b]	1980 - 1880	855 - 805	1950 - 1915	-14.7(1)
5.6×10^{-5}	5.6×10^{-4} [b]	1300 - 1177	2272 - 2222	1255 - 1210	-14.3(1)

[a] Values are given with the standard deviation of the linear regression in parentheses.
[b] Measurement involving DME-d_6, rather than DME.

Table S10.12: Overview of the different van 't Hoff plots constructed for the lp···π complex between COFCl and DME or DME-d_6 in LKr in the 120-156 K temperature interval, showing the estimated mole fractions of each monomer, range of the integrated monomer and complex bands and complex enthalpies $\Delta H°$ (LKr).

x_{COF_2}	x_{DME}	Integrated COF_2 band (cm^{-1})	Integrated DME band (cm^{-1})	Integrated Complex band (cm^{-1})	$\Delta H°$ (LKr) [a]
9.4×10^{-5}	4.7×10^{-3}	1920 - 1801	2130 - 2065	1885 - 1847	-11.4(2)
9.4×10^{-5}	4.7×10^{-3}	1130 - 1045	2053 - 1993	1885 - 1847	-11.3(2)
1.9×10^{-4}	1.9×10^{-3}	682 - 652	2050 - 1990	1845 - 1819	-11.5(2)
1.9×10^{-4}	1.9×10^{-3}	778 - 748	2050 - 1990	767 - 754	-11.4(2)
9.4×10^{-4}	4.7×10^{-3}	686 - 648	2130 - 2065	662 - 637	-11.23(7)
9.4×10^{-4}	4.7×10^{-3}	2190 - 2130	2053 - 1993	662 - 637	-11.35(7)
9.4×10^{-5}	4.7×10^{-3} [b]	1920 - 1801	2315 - 2275	1885 - 1847	-11.7(2)
9.4×10^{-5}	4.7×10^{-3} [b]	1130 - 1045	1985 - 1958	1847 - 1818	-11.7(3)
9.4×10^{-4}	4.7×10^{-3} [b]	2190 - 2130	2315 - 2275	661 - 640	-11.0(1)
1.9×10^{-4}	4.7×10^{-3} [b]	683 - 652	1986 - 1958	1846.5 - 1818	-11.5(2)

[a] Values are given with the standard deviation of the linear regression in parentheses.
[b] Measurement involving DME-d_6, rather than DME.

Table S10.13: Overview of the MAD analysis of the different lp···π complexes between COFCl and DME, calculated using MP2 and B3LYP (with GD3 dispersion) at the aug-cc-pVDZ and aug-cc-pVTZ levels of theory. Values are given for the seven assigned COFCl modes with and without the eleven assigned DME modes in cm^{-1}.

MAD values in cm^{-1}	Assigned modes	lp···π_1	lp···π_2	lp···π_3
MP2/aug-cc-pVDZ	COFCl	7.4	2.3	3.5
	COFCl+DME	4.8	2.7	2.6
MP2/aug-cc-pVTZ	COFCl	8.1	3.3	4.7
	COFCl+DME	5.1	3.1	3.2
B3LYP/aug-cc-pVDZ	COFCl	7.9	3.0	4.2
	COFCl+DME	5.6	3.9	3.9
B3LYP/aug-cc-pVTZ	COFCl	6.9	3.7	4.6
	COFCl+DME	5.2	4.2	4.1

	CCSD(T)/CBS extrapolated energy (kJ mol^{-1})	Electron density in (3,-1) intermolecular bond critical point (10^{-2} a.u)
COF_2·DME lp···π local minimum	-23.8	1.45
COF_2·DME lp···π global minimum	-22.6	1.40
COFCl·DME lp···π_1	-20.2	1.20
COFCl·DME lp···π_2	-21.3	1.22
COFCl·DME lp···π_3	-20.2	1.25
COFCl·DME XB	-12.4	1.04

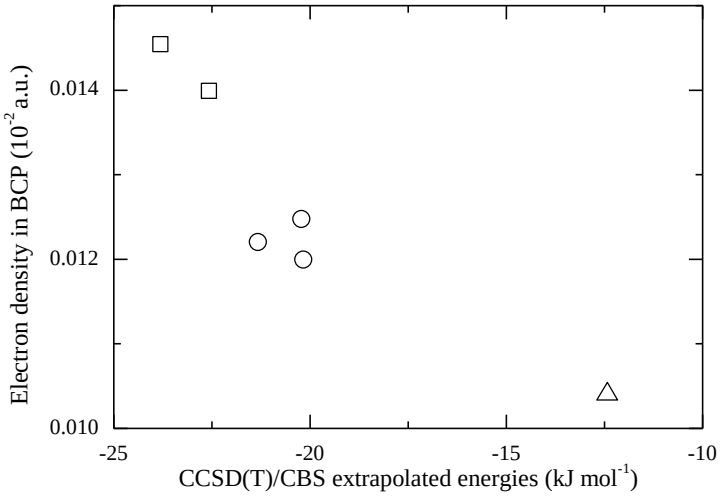

Figure S10.1: Overview of the electron densities in the (3,-1) bond critical point due to the formation of an intermolecular interaction and the corresponding extrapolated CCSD(T)/CBS complexation energies for all complexes studied, including a plot of both properties. In the plot, the COF_2·DME lp···π complexes are shown as squares, the COFCl·DME lp···π complexes as circles and the COFCl·DME XB complex as a triangle.

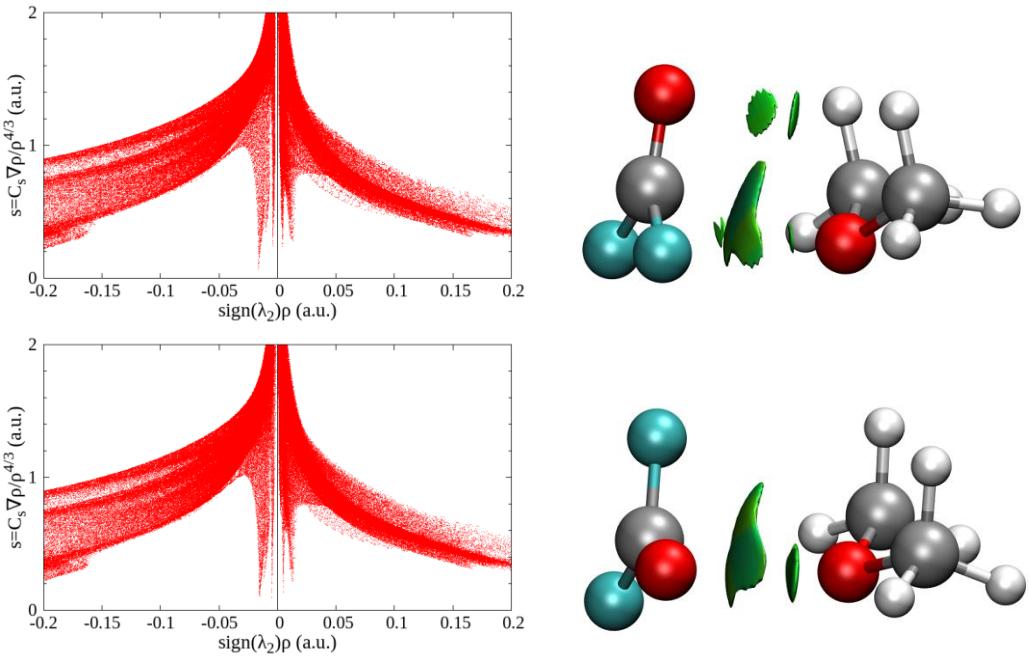

Figure S10.2: Plots of the reduced density gradient versus the electron density multiplied by the sign of the second Hessian eigenvalue (left) and gradient isosurfaces (s = 0.5 a.u., right) for the lp···π complexes between COF_2 and DME. The global minimum is shown on top, the local minimum on the bottom.

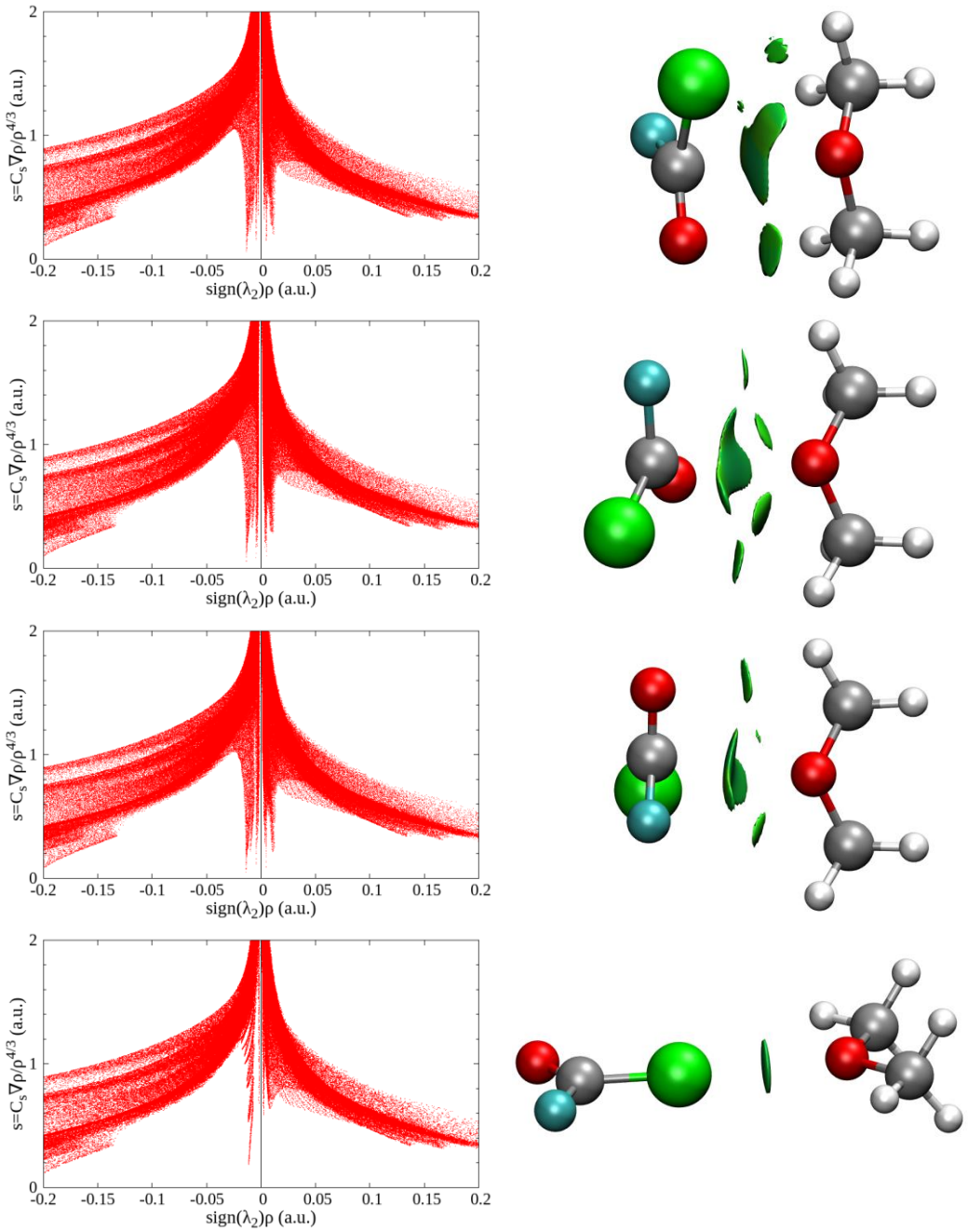

Figure S10.3: Plots of the reduced density gradient versus the electron density multiplied by the sign of the second Hessian eigenvalue (left) and gradient isosurfaces (s = 0.5 a.u., right) for the lp···π complexes (from top to second to last: lp···π_1, lp···π_2 and lp···π_3) and the XB complex (bottom) between COFCl and DME.

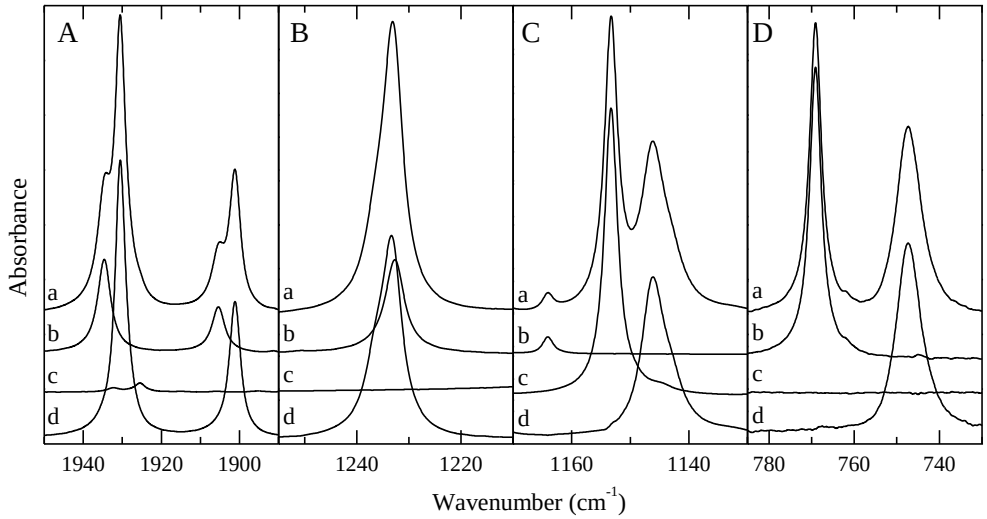

Figure S10.4: Infrared spectra of selected spectral regions of mixtures of COF_2 and DME-d_6 dissolved in LKr at 120 K. In each panel, trace *a* represents the mixed solution, while traces *b* and *c* show the solution containing only COF_2 or DME-d_6, respectively. Trace *d* represents the spectrum of the complex and is obtained by subtracting the rescaled traces *b* and *c* from trace *a*. Estimated mole fractions of the solutions of the mixtures are 5.6×10^{-5} for COF_2 and 5.6×10^{-4} for DME-d_6 in panels A and D and 5.6×10^{-4} for COF_2 and 1.9×10^{-4} for DME-d_6 in panels B and C.

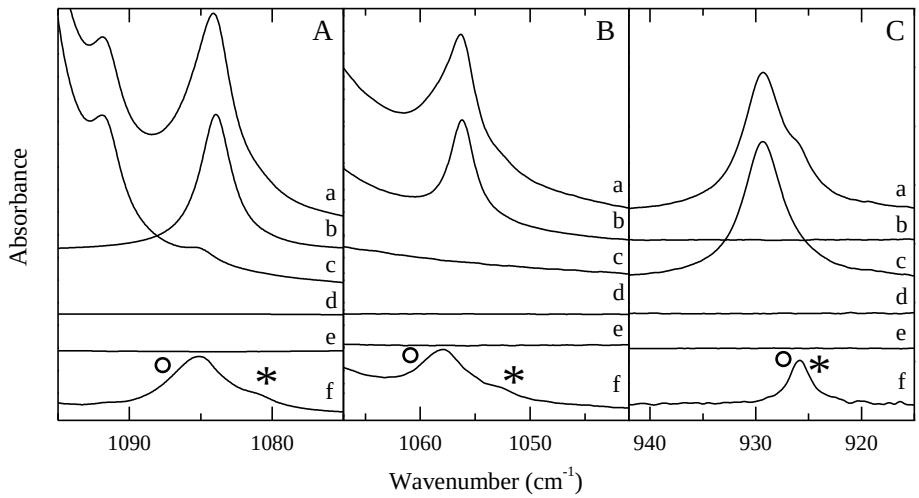

Figure S10.5: Infrared spectra of selected spectral regions of mixtures of COFCl and DME dissolved in LKr at 120 K. In each panel, trace *a* represents the mixed solution of COFCl with DME, while traces *b* and *c* show the solution containing only COFCl or DME, respectively. Trace *d* shows the rescaled spectrum of CO_2, whereas trace *e* shows the spectrum of the rescaled CO_2·DME complex, which has been obtained from a separate measurement. Finally, trace *f* shows the spectrum of the COFCl·DME complex, obtained by subtracting traces *b*-*e* from trace *a*. Bands due to the lp···π complex and XB complex observed in trace *f* are marked with an open circle (°) or asterisk (*), respectively. Estimated mole fractions of the solutions of the mixtures are 5.6×10^{-5} for COFCl and 4.7×10^{-3} for DME in panel A, 5.6×10^{-4} for COFCl and 4.7×10^{-3} for DME in panel B and 6.6×10^{-4} for COFCl and 1.5×10^{-4} for DME in panel C.

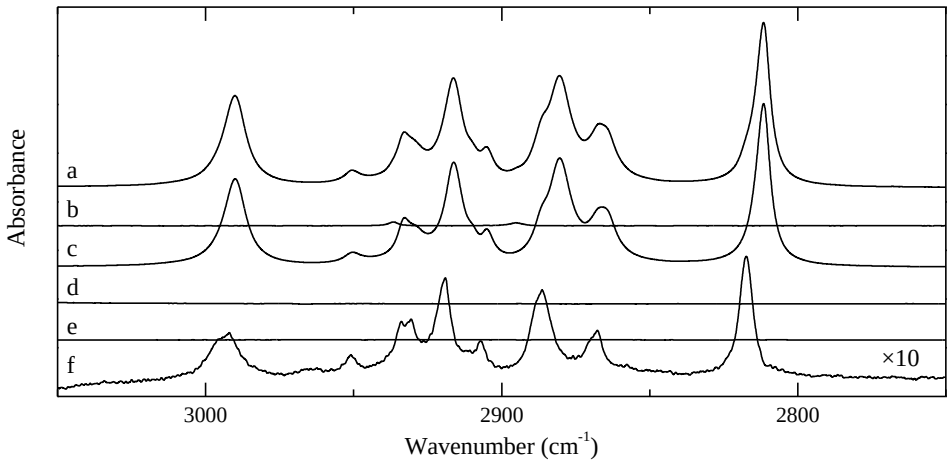

Figure S10.6: Infrared spectra of the C-H stretching region for mixtures of COFCl and DME dissolved in LKr at 120 K. Trace *a* represents the mixed solution of COFCl with DME, while traces *b* and *c* show the solution containing only COFCl or DME, respectively. Trace *d* shows the rescaled spectrum of CO_2, whereas trace *e* shows the spectrum of the rescaled CO_2·DME complex, which has been obtained from a separate measurement. Finally, trace *f* shows the spectrum of the COFCl·DME complex, obtained by subtracting traces *b*-*e* from trace *a*. For reasons of clarity, trace *f* has been multiplied by a factor of 10. Estimated mole fractions of the solution of the mixture are 6.6×10^{-4} for COFCl and 1.5×10^{-4} for DME.

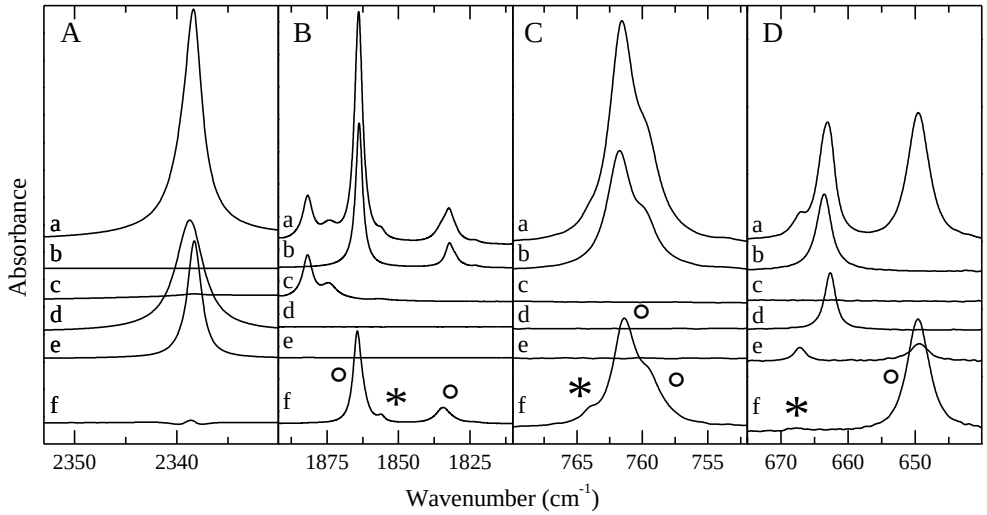

Figure S10.7: Infrared spectra of selected spectral regions of mixtures of COFCl and DME-d_6 dissolved in LKr at 120 K. In each panel, trace *a* represents the mixed solution of COFCl with DME-d_6, while traces *b* and *c* show the solution containing only COFCl or DME-d_6, respectively. Trace *d* shows the rescaled spectrum of CO_2, whereas trace *e* shows the spectrum of the rescaled CO_2·DME-d_6 complex, which has been obtained from a separate measurement. Finally, trace *f* shows the spectrum of the COFCl·DME-d_6 complex, obtained by subtracting traces *b*-*e* from trace *a*. Bands due to the lp···π complex and XB complex observed in trace *f* are marked with an open circle (°) or asterisk (*), respectively. Estimated mole fractions of the solutions of the mixtures are 1.9×10^{-4} for COFCl and 4.7×10^{-3} for DME-d_6 in panels A, C and D and 5.6×10^{-5} for COFCl and 4.7×10^{-3} for DME-d_6 in panel D.

10.5.1 Addendum: Description of the subtraction procedure for COFCl·DME(-d_6) spectra:

In order to obtain spectra of the COFCl·DME(-d_6) complex bands, spectra of both COFCl and DME(-d_6) have to be rescaled and subtracted from the spectrum of the mixture. Inspection of the spectra has of COFCl also revealed the presence of an appreciable amount of CO_2. As CO_2 is able to form complexes with DME and its π_u mode overlaps with the ν_6 mode of COFCl, bands caused by CO_2 and CO_2·DME(-d_6) complex also have to be subtracted from the spectrum of the COFCl·DME(-d_6) mixture to obtain a spectrum containing solely COFCl·DME complex bands. An example of the used subtraction procedure is given here.

As many bands of DME(-d_6) are well isolated from the CO_2 and COFCl modes, these spectral regions will only contain DME(-d_6) monomer bands and accompanying complex bands from the interactions with COFCl or CO_2. The region used to determine the subtraction factor is chosen based on *ab initio* calculated complexation shifts, so that overlap with complex bands is avoided. An example of this subtraction for DME is given in Figure S10.8.

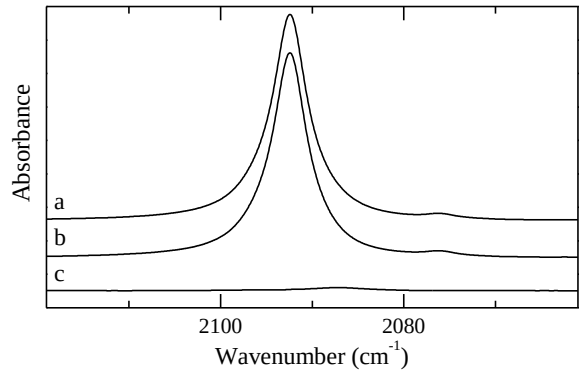

Figure S10.8: Subtraction of DME from the COFCl·DME mixture in LKr at 120 K which also contains CO_2 and its accompanying complex with DME. Trace *a* shows the spectrum of the mixture, while trace *b* shows the rescaled DME spectrum. Trace *c* shows the spectrum resulting from the subtraction procedure.

In order to perform a subtraction of the COFCl monomer in its ν_6 spectral region, CO_2 and CO_2·DME(-d_6) complex also have to be accounted for. These latter two components can be dealt with before the COFCl subtraction if the CO_2 σ_u^+ mode around 2340 cm^{-1} is in-scale, or have to be subtracted simultaneously in the COFCl ν_6 region if the σ_u^+ mode of CO_2 is out-of-scale. To subtract the CO_2·DME(-d_6) complex, a spectrum in which these complex bands are isolated has to be obtained. To this end, CO_2·DME(-d_6) mixtures were measured separately and subtracted beforehand, as shown in Figure S10.9.

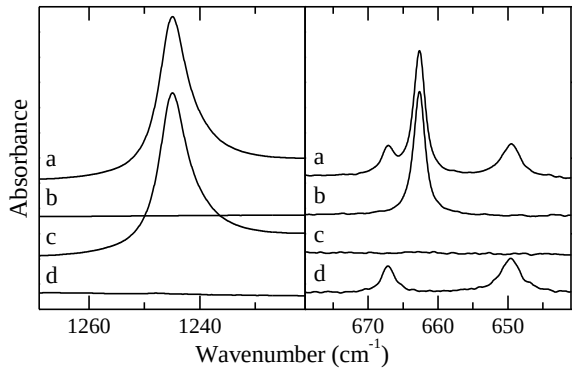

Figure S10.9: Subtraction of CO_2 and DME from the CO_2·DME mixture, measured at 120 K in LKr. Trace *a* shows the CO_2·DME mixture, while traces *b* and *c* show the rescaled CO_2 and DME spectra, respectively. Trace *d* shows the spectrum resulting from the subtraction procedure, containing solely CO_2·DME complex.

After obtaining the isolated CO_2·DME complex spectrum, this complex and the CO_2 monomer can be subtracted from the spectrum obtained in Figure S10.8, as shown in Figure S10.10.

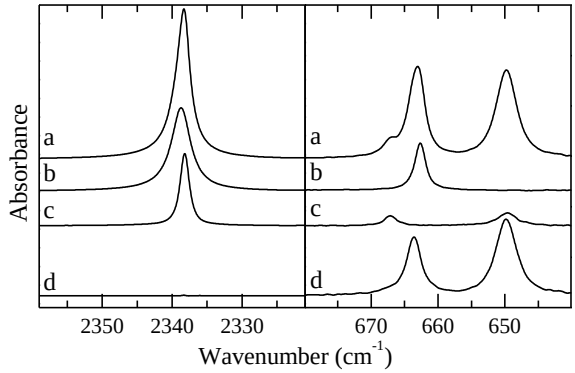

Figure S10.10: Subtraction of CO_2 and CO_2·DME complex from the spectrum obtained in Figure S10.8. Trace *a* shows the spectrum obtained in Figure S10.8, trace *b* shows the rescaled CO_2 spectrum and trace *c* shows the rescaled CO_2·DME complex spectrum, obtained in Figure S10.9. The resulting spectrum is shown in trace *d*. All measurements were performed at 120 K in LKr.

Before COFCl can be subtracted from the spectrum obtained in Figure S10.10, CO_2 also has to be subtracted from the monomer spectrum. As CO_2 and COFCl don't form any (appreciable amount of) complex, subtraction in the σ_u^+ spectral region (near 2340 cm^{-1}) of CO_2 is straightforward, as shown in Figure S10.11.

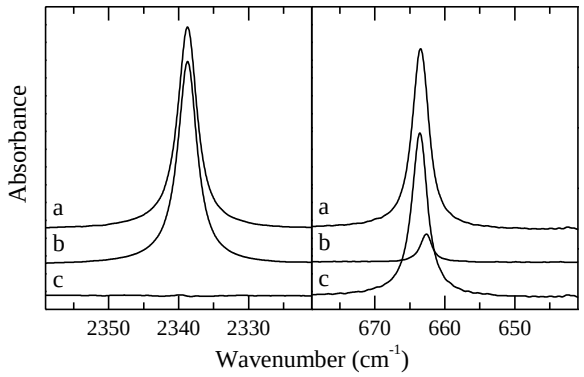

Figure S10.11: Subtraction of CO_2 from the COFCl monomer spectra. Trace *a* shows the COFCl spectrum also containing CO_2, trace *b* shows the rescaled CO_2 spectrum and trace *c* shows the resulting spectrum containing only COFCl bands. All measurements were performed at 120 K in LKr.

Finally, the CO_2 subtracted spectrum of COFCl can be subtracted from the spectrum obtained in Figure S10.10 to obtain a spectrum containing solely bands due to the COFCl·DME(-d_6) complex.

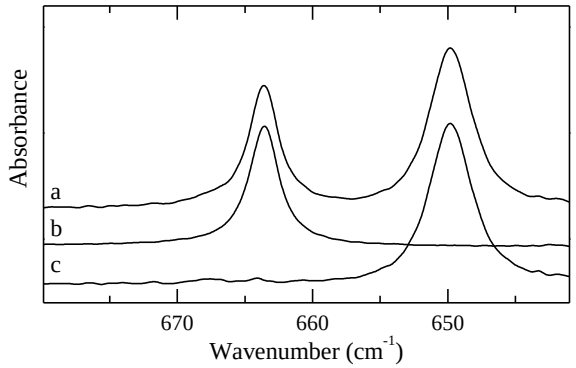

Figure S10.12: Subtraction of COFCl from the spectrum obtained in Figure S10.10, yielding a spectrum containing solely COFCl·DME complex bands. Trace *a* shows the spectrum obtained in Figure S10.10, trace *b* shows the COFCl spectrum, corrected for CO_2, obtained in Figure S10.11. The spectrum resulting from the subtraction procedure containing only COFCl·DME complex bands is shown in trace *c*.

Chapter 11

Chalcogen bonding: S···O what?

A σ-hole interaction between 2,2,4,4-tetrafluoro-1,3-dithiethane and DME.

Abstract

In the last decade halogen bonds, noncovalent interactions formed between positive regions in the electrostatic potential on halogen atoms, often referred to as σ-holes, and electron rich sites, have gained a lot of interest. Recently this interest has been expanded towards interactions with group V and group VI elements, giving rise to pnicogen and chalcogen bonds. Although chalcogen bonds have already shown some promising results for applications in crystallography and catalysis, experimental results characterizing these noncovalent interactions remain scarce. In this combined experimental and theoretical study, original data allowing the characterization of S···O chalcogen bonds is obtained by studying the 1:1 molecular complexes between $C_2F_4S_2$ and DME.

Ab initio calculations of the $C_2F_4S_2$·DME dimer yield two stable chalcogen-bonded isomers, the difference being the presence or absence of secondary F···H interactions. Liquid krypton solutions containing $C_2F_4S_2$ and DME were studied using FTIR and Raman spectroscopy. Upon subtraction of rescaled monomer spectra, clear complex bands are observed. The derived experimental complexation shifts agree favourably with the *ab initio* calculated shifts of the chalcogen-bonded complexes. The 1:1 stoichiometry of the complex is confirmed experimentally and an experimental complexation enthalpy of -13.5(1) kJ mol^{-1} is found, which is in good agreement with the calculated values. A Ziegler-Rauk EDA revealed that electrostatic interactions prominently dominate over orbital interactions. Nevertheless, significant charge transfer occurs from the oxygen in DME to one of the sulphur atoms in $C_2F_4S_2$ and the carbon along the extension of the chalcogen bond.

11.1 Introduction

For many years, noncovalent interactions formed through σ-holes, [1-2] positive regions in the electrostatic potential opposite to a covalent bond, have been studied theoretically and experimentally. Heretofore most attention has focused on interactions formed through the σ-hole on a halogen atom, the so-called halogen bonds, proving the value of these noncovalent interactions in the fields of, amongst others, crystal engineering, [3-4] supramolecular chemistry [5-6] and rational drug design. [7-8] Nevertheless, substantial evidence for the existence of interactions between electron rich sites and the σ-holes on Group VI and Group V elements, giving rise to chalcogen bonds and pnicogen bonds respectively, has been found in theoretical [9-13] and crystallographic [14] studies. In a recent study by Garrett et al. [15] the existence of tellurium based chalcogen bonds has also been described in solution for the first time using UV-VIS, ^{1}H and ^{19}F NMR experiments. Furthermore, chalcogen bonds may also be of interest in the field of catalysis, as they, just as halogen bonds, are more directional and hydrophobic than hydrogen bonds. [16]

Because of the presence of oxygen and sulphur in proteins, several studies concerning chalcogen bonds have focused specifically on S···O chalcogen bonds, suggesting that these interactions might play a role in controlling protein structures [17-19] and in the enzymatic activity of sulphur-containing compounds. [20] As chalcogen bonding can affect binding of possible drug molecules, the principle of chalcogen bonding is of interest to researchers developing new pharmaceuticals. [21] Motivated by the biochemical importance of this kind of interaction, most of the previous studies have focused on the interactions formed with an sp²-hybridized carbonyl oxygen atom. [10, 22-23]

Although S···O chalcogen bonds have already shown some promising results for applications, experimental results characterizing these noncovalent interactions remain scarce. Therefore, within this combined experimental and theoretical study, the moderately strong S···O chalcogen bond formed between $C_2F_4S_2$ and DME is investigated. The experimental study involves an infrared and Raman spectroscopic

study of the formation of S···O chalcogen-bonded $C_2S_2F_4$·DME dimers in liquid krypton. The basis for this study is the observation that, in general, cryospectroscopy in liquid noble gases forms an excellent technique to study weak noncovalent interactions, as the measurements are performed at moderately low temperatures (varying from 118 to 173 K for liquid krypton) in a solution where the solvent is only weakly interacting with the solutes, thereby creating a pseudo-gas phase experiment in which the 1:1 (or higher) adducts formed are only weakly distorted by solvent interactions. Furthermore, by working at thermodynamic equilibrium and by measuring spectra at various temperatures, thermodynamic properties of the noncovalent interactions, such as the complexation enthalpy, can be determined experimentally.

To assign the complex bands observed in the spectra, the measurements are supported by *ab initio* calculations. By performing additional MC-FEP simulations and statistical thermodynamics calculations, calculated complexation enthalpies are obtained which can be compared with the experimentally obtained values. The chalcogen bond energy is qualitatively analysed via the Ziegler-Rauk EDA by decomposing it into its different components: orbital interactions, electrostatic interactions, Pauli repulsion (often associated with steric repulsion) and dispersion interaction. The orbital interactions are further scrutinized by a NOCV analysis allowing the quantification and visualization of the charge density reorganization upon chalcogen bond formation. In addition, a NCI index analysis is performed, revealing the presence of weak interactions for one of the complex geometries that stabilize the complex.

The choice for $C_2F_4S_2$ as a chalcogen bond donor was based on the observation that, in order to obtain complexes with an appreciable strength, a highly fluorinated molecule is preferred, a strategy that has been followed extensively in studies involving halogen bonding [24-25] and has also been proven to work for chalcogen bonding. [26] The choice for $C_2F_4S_2$ was further motivated by the fact that high purity (>97 %) samples are commercially available, and by the observation that $C_2F_4S_2$ is a rigid molecule with D_{2h} symmetry. The rigidity of the chalcogen acceptor reduces the added complexity due to internal rotations or large amplitude motions, while the use of a high symmetry molecule allows to apply the principles of mutual exclusivity and thus allows the

complementarity of infrared and Raman spectroscopy to be fully exploited. As a Lewis base the choice was made for DME, a molecule containing an sp^3 hybridized oxygen atom, which has also been used extensively as an oxygen donor in previous cryospectroscopic studies. [27-29] DME has proven to possess no self-associating properties, a phenomenon which is known to limit a thorough analysis [30-31] of the cryospectroscopic data and, in contrast to acetone and ethylene oxide, is known to have a substantial solubility in liquid noble gases.

Inspection of the electrostatic potential on the molecular surface of $C_2F_4S_2$, shown in Figure 11.1, reveals the presence of four σ-holes, two on both sulphur atoms, which are equivalent due to the D_{2h} symmetry of $C_2F_4S_2$. The presence of multiple σ-holes therefore implies the ability of this molecule to simultaneously undergo interactions with multiple Lewis bases, giving rise to complexes of higher stoichiometric ratio's. On the other side, the availability of two lone pairs on the oxygen atom might also enable DME to form interactions with two $C_2F_4S_2$ molecules, although significant steric hindrance is expected for such a complex. Therefore, special interest will be given to the experimental determination of the complexation stoichiometry within this study.

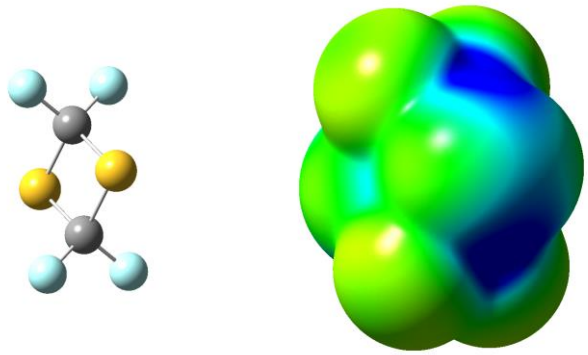

Figure 11.1: Electrostatic potential of $C_2F_4S_2$ on the molecular surface defined by the 0.001 electrons $Bohr^{-3}$ contour of the electron density, calculated at the MP2/aug-cc-pVDZ level, with positive, neutral and negative regions shown in blue, green and red, respectively.

11.2 Results

11.2.1 *Ab initio* calculations

Ab initio calculations yielded two stable isomers for the $C_2F_4S_2$ complex with DME, both of which are formed through a chalcogen bond between the oxygen and sulphur atom. Both complexes have a C_s symmetry and were optimized without imposing symmetry restrictions. The complex geometries are shown in Figure 11.2, while the main intermolecular parameters and energetics are summarized in Table 11.1. Cartesian coordinates of the monomers and complexes are given in Tables S11.1 and S11.2 of the SI. In the first complex the methyl groups of DME are facing towards the fluorine atoms of $C_2F_4S_2$, while in the other complex an interaction is formed with the other oxygen lone pair, resulting in a complex geometry where the methyl groups are facing away from the fluorine atoms. When the methyl groups are facing towards the electronegative fluorine atoms, which have a negative electrostatic potential, as seen in Figure 11.1, the formation of secondary F···H can be expected even though at 2.92 Å the F···H distance is still larger than the sum of van der Waal radii of 2.55 Å. In order to reveal these secondary interactions the NCI index was visualized using NCIPLOT [32-33]. Plots of the reduced density gradient versus the electron density multiplied by the sign of the second Hessian eigenvalue and figures showing the gradient isosurfaces are given in Figure S11.1 of the SI. When comparing the gradient isosurfaces of the complex geometries where the methyl groups are facing toward (top) and away from (bottom) the fluorine atoms, two extensions of the gradient isosurface are clearly visible between the hydrogen atoms of the methyl groups and the fluorine atoms in the top image, thus revealing the presence of these secondary interactions.

Even though the complex without secondary F···H interactions has a slightly smaller intermolecular distance, the complexation energies reveal that the complex with the secondary F···H interactions is indeed the most stable geometry, the energy difference at the CCSD(T)/CBS level of theory being 1.5 kJ mol^{-1}.

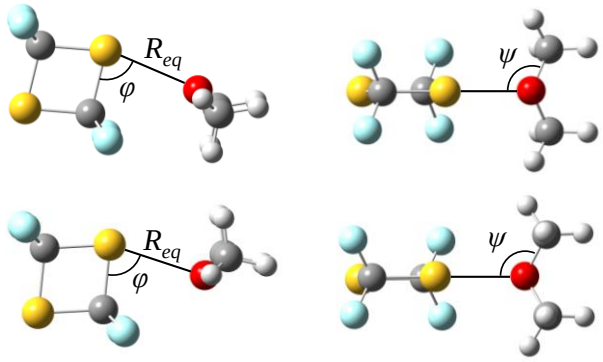

Figure 11.2: MP2/aug-cc-pVDZ geometries for the chalcogen-bonded complexes between $C_2F_4S_2$ and DME. The complex geometry with secondary C-F···H-C interactions is given at the top, while the complex geometry without the secondary interactions is given at the bottom.

Table 11.1: Intermolecular distance R_{eq} (Å) and bond angles (°) from the MP2/aug-cc-pVDZ optimized geometries, MP2/aug-cc-pVDZ ΔE(DZ) and CCSD(T)/CBS extrapolated complexation energies ΔE(CCSD(T)), calculated vapour phase complexation enthalpies $\Delta H°$ (vap,calc), the calculated complexation enthalpies in liquid krypton ($\Delta H°$ (LKr,calc)) and the corresponding experimentally obtained complexation enthalpy ($\Delta H°$ (LKr)) (kJ mol^{-1}) of the chalcogen-bonded complexes between $C_2F_4S_2$ and DME.

	Chalcogen-bonded complexes	
	With secondary interactions	Without secondary interactions
Symmetry	C_s	C_s
R_{eq}=$R_{S\cdots O}$	2.81	2.80
$R_{eq}/\Sigma r_{vdW}$	0.864	0.862
φC-S···O	80.0	77.6
ψC-O···S	121.6	106.5
ΔE (DZ)	-23.4	-22.2
ΔE (CCSD(T))	-25.0	-23.5
$\Delta H°$ (vap,calc)	-22.1	-20.8
$\Delta H°$ (LKr,calc)	-16.6	-15.2
Experimental $\Delta H°$ (LKr)	-13.5(1)	

A transition state search between both complex geometries using the Synchronous Transit-Guided Quasi-Newton method [34] yielded a transition state with a single imaginary frequency of -42 cm^{-1}, a mere 0.7 kJ mol^{-1} higher in energy at the MP2/aug-cc-pVDZ level than the complex geometry without secondary interactions. Therefore, rapid interconversion between both complex geometries and an averaged structure is expected to be observed during the experimental measurements. An energy diagram of both minima and the transition state is given in Figure S11.2 of the SI, the Cartesian coordinates of the transition state are given in Table S11.2.3 of the SI.

Table 11.2: Interaction energies (ΔE_{int}) at the PBE/TZ2P level, together with the Ziegler-Rauk energy decomposition components (ΔE_{Pauli}, ΔV_{elst}, ΔE_{oi}, E_{disp}) for the chalcogen-bonded complexes with and without secondary F···H interactions. For comparison, the EDA for the CF_3I···DME XB complex, taken from a previous study [35], has been included. All values are in kJ mol^{-1}. The relative contributions of the stabilising interactions are indicated in parentheses.

Complex	ΔE_{int}	ΔE_{Pauli}	ΔV_{elst}	ΔE_{oi}	E_{disp}
With F···H	-24.1	36.1	-32.5 (54%)	-17.7 (29%)	-9.9 (17%)
Without F···H	-23.9	40.5	-33.7 (52%)	-21.3 (33%)	-9.4 (15%)
CF_3I···DME	-24.0	38.0	-35.9 (58%)	-20.3 (33%)	-5.7 (9%)

An EDA of the interaction energy between $C_2F_4S_2$ and DME was carried out to evaluate the relative importance of electrostatic and orbital interactions, steric effects, and dispersion interactions. The results are given in Table 11.2. The PBE/TZ2P interaction energies agree well with the MP2/aug-cc-pVDZ and CCSD(T)/CBS extrapolated complexation energies in Table 11.1. However, the energy difference between the complex with and without secondary interactions is now negligible. Notably, the secondary F···H interactions only cause an extra stabilization of 0.5 kJ mol^{-1} in the dispersion energy component (E_{disp}), in accordance with the rather large F···H distance of 2.92 Å. In both complexes, the electrostatic interactions (ΔV_{elst}) clearly dominate the orbital interactions (ΔE_{oi}). The larger electrostatic and particularly orbital interaction energy values observed for the complex without secondary interactions are compensated by a larger destabilising Pauli repulsion term (ΔE_{Pauli}). The orbital interaction energy (ΔE_{oi}) represents the stabilization originating from all

interactions of occupied and unoccupied molecular orbitals between the two fragments as well as the stabilising orbital interactions within one single fragment upon complex formation. The NOCV analysis provides a special means for further decomposing and visualising the components (so-called NOCV orbitals) of the charge density reorganization resulting from the interacting orbitals of the two fragments. Only one significant NOCV determines the charge distribution rearrangement upon chalcogen-bond formation, shown in Figure 11.3. A significant charge transfer of 0.20 to 0.24 *e* takes place, being slightly more pronounced for the complex without secondary interactions, in accordance with the EDA results. The values of the charge transfer are also nearly identical to the charge transfer of 0.22 *e* for the relevant NOCV of the CF_3I·DME complex (ΔE_{NOCV} = -16.6 kJ mol^{-1}) described by Pinter et al. [35] The associated stabilization energy ranges from -12.7 to -16.4 kJ mol^{-1}, which corresponds to 72-77% of the total orbital interaction energy. It is clearly observed that electron donation takes place from DME to $C_2F_4S_2$. The electron density does not solely accumulate on the chalcogen atom, but further delocalizes into $C_2F_4S_2$, accumulating mostly on the carbon atoms adjacent to the chalcogen, and quantitatively considerably more on the carbon along the extension of the chalcogen bond. The build-up of electron density in the internuclear region strongly implies a characteristic charge transfer character for the investigated chalcogen interaction.

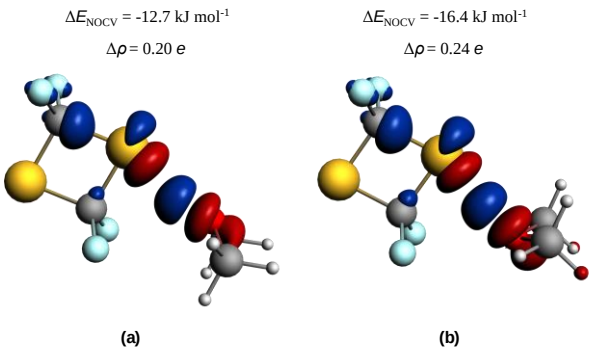

Figure 11.3: Relevant NOCVs with the corresponding orbital energy interaction and density change for the complex with secondary interactions (a) and without secondary interactions (b). Electron depletion is indicated by the red-coloured regions, while electron accumulation is represented by the blue-coloured regions.

11.2.2 Vibrational spectra

Assignment of the vibrational modes of DME has been discussed in previous chapters while the assignment of the bands of $C_2F_4S_2$ is based on the *ab initio* calculations, including anharmonic frequency calculations using Gaussian09, and assignments found in the literature. [36-38] Numbering of the vibrational modes follows the numbering scheme of Herzberg. [39] An overview of the *ab initio* calculated frequencies of the monomers and complexes is given in Tables S11.3 and S11.4 of the SI. It should be noted that, since the assignments of the ν_{11} fundamental and $\nu_2 + \nu_7$ combination band of $C_2F_4S_2$ from Raman measurements have been switched in some previous studies, these assignments have to be interpreted with the necessary prudence. Furthermore, the infrared band assigned to a ring deformation mode near 843 cm^{-1} by Durig et al. [36] and Harris et al. [37] has not been observed in any of the spectra, which is in line with the more recent theoretical study of Jensen. [38] As solubility problems occurred at lower temperatures for mixtures with increased concentrations, Raman measurements were performed at 147 K. The infrared concentration study was performed at 130 K, whereas infrared spectra and assignments given are based on measurements performed at 120 K.

11.2.2.1 Infrared spectra

Upon subtraction of the infrared spectra of $C_2F_4S_2$·DME mixtures, complex bands are observed in multiple spectral regions, of which a selection is shown in Figure 11.4. For the $C_2F_4S_2$ ν_{16} mode, shown in panel B of Figure 11.4, a -2.4 cm^{-1} redshifted complex band is observed, corresponding well to the -4.3 cm^{-1} and -1.3 cm^{-1} complex shifts for the chalcogen-bonded complexes with and without secondary F···H interactions. A 1.3 cm^{-1} blueshifted band is observed in the $C_2F_4S_2$ ν_{13} spectral range, shown on the left side of panel 11.4C, whereas only a 0.3 cm^{-1} blueshift is predicted by the *ab initio* calculations for the complex with secondary interactions. Due to a degeneracy with a DME vibrational mode in the calculations, a -1.8 cm^{-1} redshift is predicted for this vibrational mode in the complex without secondary interactions. Also for the ν_{17}

$C_2F_4S_2$ mode, shown in panel 11.4E, and the ν_8 $C_2F_4S_2$ mode redshifted complex bands were observed with shifts of -0.5 cm^{-1} and -4.3 cm^{-1}, corresponding to the calculated shifts of -1.1 and -11.2 cm^{-1} for the most stable chalcogen-bonded complex. Also noteworthy is the presence of a complex band at 836.2 cm^{-1}, corresponding to the ν_6 mode of $C_2F_4S_2$ with B_{1g} symmetry in the monomer, which becomes IR active upon complexation due to the breaking of the symmetry, as predicted in the *ab initio* calculations. The assignment of this band is confirmed by the Raman measurements in which both the monomer and complex band are visible (*vide infra*). A similar effect is calculated for the $C_2F_4S_2$ ν_{11} vibrational mode with B_{2g} symmetry, as seen in Tables S11.3 and S11.4 of the SI. Due to the nearby presence of the $\nu_2 + \nu_9$ and $\nu_7 + \nu_{17}$ combination bands of $C_2F_4S_2$ and the ν_{22} mode of DME, the appearance of this band is not clear at first sight. By combining this data with the data from the Raman measurements and an additional infrared measurement involving fully deuterated DME (DME-d_6), the band at 1087.5 cm^{-1} can be assigned to the complex band of the $C_2F_4S_2$ ν_{11} mode. Also for the DME vibrational modes, complex bands with shifts agreeing with the calculated shifts of the chalcogen-bonded complexes are observed, the best resolved bands being the 7.7 cm^{-1} blueshifted band for DME ν_2 ($\Delta\nu_{calc,\ F\cdots H}$ = 10.5 cm^{-1}) shown in panel 11.4A and the -8.0 cm^{-1} redshifted band for DME ν_6 ($\Delta\nu_{calc,\ F\cdots H}$ = -10.5 cm^{-1}), shown in panel 11.4C. An overview of the assignments of the infrared spectra is given in Table 11.3.

Apart from the bands assigned in Table 11.3, an additional shoulder at the high frequency side of the complex band of the $C_2F_4S_2$ ν_{13} mode (panel 11.4C) is observed for the lowest temperatures, which might correspond to a 1:2 complex with two DME molecules. The presence of complexes with higher stoichiometric ratio is discussed in more detail further on in this chapter.

Table 11.3: Experimental IR frequencies in LKr at 120 K for the monomers and complex, as well as experimental complexation shifts ($\Delta\nu_{exp}$) and MP2/aug-cc-pVDZ calculated shifts ($\Delta\nu_{calc}$), in cm^{-1}, for the $C_2F_4S_2$·DME chalcogen-bonded complexes.

Assignment		$\nu_{monomer}$	$\nu_{complex}$	$\Delta\nu_{exp}$	$\Delta\nu_{calc,\ F\cdots H}$	$\Delta\nu_{calc,\ no\ F\cdots H}$
$C_2F_4S_2$	$\nu_3 + \nu_{17}$	1165.2	1166.9 [a]	1.7	-0.1	0.0
	$\nu_6 + \nu_{14}$	1165.2	1166.9 [a]	1.7	3.0	-0.2
	$\nu_2 + \nu_{18}$	1116.1	1117.4	1.3	-1.5	-2.0
	ν_8	1107.9	1103.6	-4.3	-11.2	-2.0 [b]
	$\nu_2 + \nu_9$	1091.5	1092.1 [a]	0.6	1.0	0.4
	ν_{11}	-	1087.5		-10.6	-7.2
	$\nu_7 + \nu_{17}$	1082.0	1085.1	3.1	1.9	2.1
	$\nu_2 + \nu_7$	-	1075.4		0.6	0.6
	ν_{16}	1068.6	1066.2	-2.4	-4.3	-1.3
	ν_{16} (^{13}C)	1052.2	1049.8	-2.4	-4.3	-1.3
	$\nu_{12} + \nu_{17}$	1030.1	1033.9	3.8	3.7	3.9
	ν_{13}	960.3	961.6	1.3	0.3	-1.8 [b]
	ν_{13} (^{13}C)	947.4	950.1	2.7	0.3	-1.8 [b]
	ν_6	-	836.2		1.4	-1.7
	ν_{17}	652.4	651.9	-0.5	-1.1	-1.0
	ν_{18}	450.4	451.3	0.9	0.8	0.4
DME	ν_1	2990.0	2993.6	3.6	3.2	4.0
	ν_{16}	2990.0	2993.6	3.6	3.3	4.1
	$2\nu_3$	2950.3	2949.9	-0.4	-4.0	-4.8
	$\nu_3 + \nu_{18}$	2932.7	2932.1	-0.6	-4.1	-4.9
	$\nu_3 + \nu_{13}$	2929.5	2932.1	2.6	-3.3	-2.9
	ν_{12}	2916.2	2918.6	2.4	18.1	13.5
	$2\nu_4$	2910.5	-		-0.3	-4.2
	$\nu_3 + \nu_{19}$	2905.1	2907.0	1.9	-2.0	-3.4
	$\nu_{18} + \nu_{19}$	2886.8	2888.3	1.5	-2.1	-3.5
	$\nu_4 + \nu_{19}$	2880.4	2888.3	7.9	-0.2	-3.1
	ν_2	2811.5	2819.2	7.7	10.5	6.5
	$\nu_6 + \nu_{20}$	2092.4	-		-18.5	-18.6
	$\nu_6 + \nu_{21}$	2020.3	-		-15.0	-16.3
	ν_3	1474.7	1474.0	-0.7	-2.0	-2.4
	ν_{18}	1457.4	1457.0	-0.4	-2.1	-2.5
	ν_{13}	1454.7	1455.7	1.0	-1.3	-0.5
	ν_{19}	1426.1	-		0.0	-1.0
	ν_5	1244.9	1247.7	2.8	1.7	0.1
	ν_{20}	1172.0	1167.6	-4.4	-7.9	-7.9
	ν_{21}	1099.0	1095.6	-3.4	-4.4	-5.6
	ν_6	929.3	921.3	-8.0	-10.5	-10.7

[a] Determined using a mixture with DME-d_6 due to overlap with DME complex bands.
[b] Degenerate with DME mode in *ab initio* calculation.

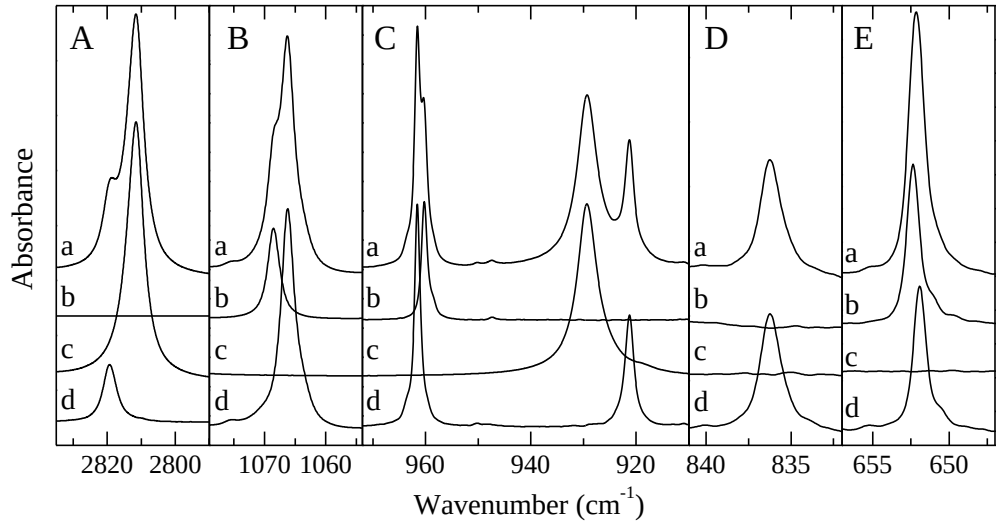

Figure 11.4: Infrared spectra of selected spectral regions for the mixtures of $C_2F_4S_2$ with DME dissolved in LKr at 120 K. In each panel, trace *a* represents the mixed solution, while traces *b* and *c* show the rescaled spectra of the solutions containing only $C_2F_4S_2$ or DME, respectively. Trace *d* represents the spectrum of the complex which is obtained by subtracting the rescaled traces *b* and *c* from trace *a*. Estimated mole fractions of the solutions of the mixtures are 1.9×10^{-4} for $C_2F_4S_2$ and 4.7×10^{-4} for DME in panels A and E, 2.8×10^{-5} for $C_2F_4S_2$ and 7.5×10^{-4} for DME in panel B, 1.3×10^{-4} for $C_2F_4S_2$ and 7.5×10^{-4} for DME in panel C and 9.4×10^{-4} for $C_2F_4S_2$ and 2.6×10^{-4} for DME in panel D.

11.2.2.2 Raman spectra

Due to the D_{2h} symmetry of $C_2F_4S_2$, Raman measurements yield data which is highly complementary to the previously discussed infrared measurements, as all but one *ungerade* vibrational modes are IR active and all *gerade* vibrational modes have an appreciable Raman intensity.

As the band at 1093.4 cm^{-1}, shown in panel A of Figure 11.5, is far more intense than the band at 1077.8 cm^{-1}, this is assigned to the ν_{11} fundamental mode of $C_2F_4S_2$, while the weaker band is assigned to the combination band $\nu_2 + \nu_7$, which is consistent with the assignments of Jensen [38] and Harris et al.[37], but contradicts the assignment of Durig et al. [36] Upon inspection of the mixtures with DME this assignment is confirmed even

further by the -5.1 cm^{-1} redshift of the complex band assigned to the ν_{11} mode, which corresponds to the calculated shifts of -10.6 cm^{-1} and -7.2 cm^{-1} for the complexes with and without secondary interactions. Despite these arguments, we insist that the assignment of both bands needs to be interpreted with the necessary prudence. The appearance of the complex band of $C_2F_4S_2$ ν_{11} at 1087.5 cm^{-1} in infrared should not be regarded as an argument for this assignment, as multiple vibrational modes are present in this region and an additional complex band is also observed at 1075.4 cm^{-1}.

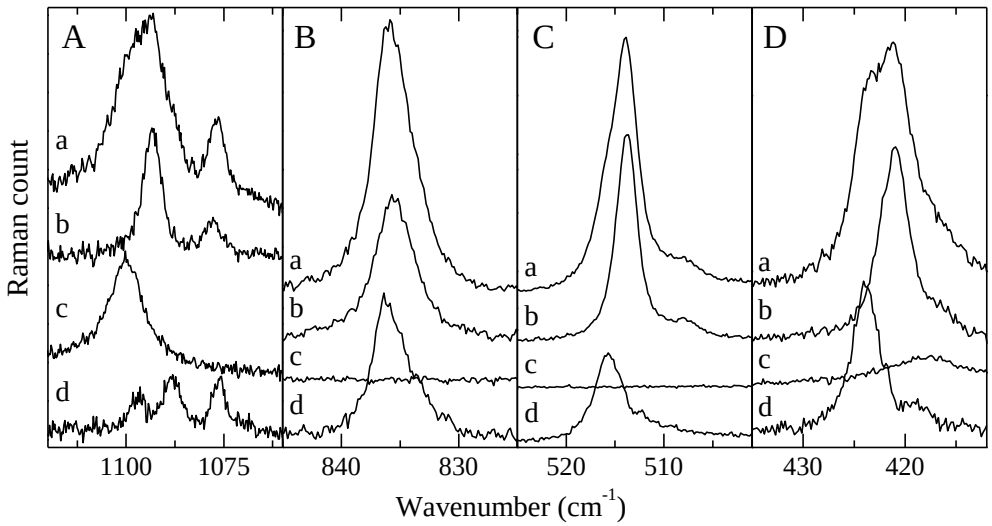

Figure 11.5: Raman spectra of selected spectral regions for the mixtures of $C_2F_4S_2$ with DME dissolved in LKr at 147 K. In each panel, trace *a* represents the mixed solution, while traces *b* and *c* show the rescaled spectra of the solutions containing only $C_2F_4S_2$ or DME, respectively. Trace *d* represents the spectrum of the complex which is obtained by subtracting the rescaled traces *b* and *c* from trace *a*. Estimated mole fractions of the mixtures are 1.1×10^{-3} for $C_2F_4S_2$ and 1.1×10^{-3} for DME in all panels. For clarity, the spectra in panel A have been multiplied by a factor of two.

In the $C_2S_4F_2$ ν_3 spectral region, shown in panel C of Figure 11.5, a 1.8 cm^{-1} blueshifted band is observed, corresponding to the calculated blueshifts of 1.0 cm^{-1}. Also for the $C_2F_4S_2$ ν_7 mode, shown in panel 11.5D, a blueshifted complex band is observed for which the experimental shift of 2.8 cm^{-1} is in good agreement with the calculated shifts of 3.0 cm^{-1} and 3.1 cm^{-1} for the complex with and without the additional F···H interactions, respectively. For the ν_6 mode of $C_2F_4S_2$, shown in panel 11.5B, an experimental complexation shift of 0.4 cm^{-1} is found, which lies in the middle of the

calculated shifts for the complex with ($\Delta\nu_{calc}$ = 1.4 cm^{-1}) and without secondary interactions ($\Delta\nu_{calc}$ = -1.7 cm^{-1}). An overview of all bands assigned using Raman spectroscopy is given in Table 11.4.

Table 11.4: Experimental Raman frequencies for the monomers and complex, as well as experimental complexation shifts ($\Delta\nu_{exp}$) and MP2/aug-cc-pVDZ calculated complexation shifts ($\Delta\nu_{calc}$), in cm^{-1}, for the chalcogen-bonded complexes of $C_2F_4S_2$ with DME dissolved in LKr at 147 K.

Assignment		$\nu_{monomer}$	$\nu_{complex}$	$\Delta\nu_{exp}$	$\Delta\nu_{calc,\ F\cdots H}$	$\Delta\nu_{calc,\ no\ F\cdots H}$
$C_2F_4S_2$	ν_1	1162.7	1158.8	-3.9	-4.0	-2.7
	ν_{11}	1093.4	1088.3	-5.1	-10.6	-7.2
	$\nu_2 + \nu_7$	1077.8	1076.2	-1.6	0.6	0.6
	ν_6	835.5	835.9	0.4	1.4	-1.7
	ν_2	666.6	665.1	-1.5	-2.4	-2.5
	$2\nu_4$	654.5	655.3	0.8	1.8	1.4
	ν_3	513.8	515.6	1.8	1.0	1.0
	ν_7	421.0	423.8	2.8	3.0	3.1
	ν_{12}	378.7	383.2	4.5	4.9	4.9
	ν_4	328.4	328.9	0.5	0.9	0.7
	ν_{15}	283.4	287.4	4.0	5.5	5.6
DME	ν_1	2990.0	2996.3	6.3	3.2	4.0
	ν_{16}	2990.0	2996.3	6.3	3.3	4.1
	$2\nu_3$	2950.0	2948.8	-1.2	-4.0	-4.8
		2927.8	2928.8	1.0		
	ν_{12}	2916.3	2917.6	1.3	18.1	13.5
		2887.3	2888.4	1.1		
		2863.7	2867.3	3.6		
	ν_2	2812.0	2818.4	6.4	10.5	6.5
	ν_3	1476.5	1475.0	-1.5	-2.0	-2.4
	ν_{18}	1456.0	1455.5	-0.5	-2.0	-2.5
	ν_9	1448.3	1445.6	-2.7	-2.1	-1.4
	ν_4	1431.6	1428.0	-3.6	-0.2	-2.1
	ν_{20}	1173.1	-		-7.9	-7.9
	ν_{10}	1145.8	-		-1.0	-1.5
	ν_{21}	1100.2	1097.0	-3.2	-4.4	-5.6
	ν_6	929.2	921.4	-7.8	-10.5	-10.7
	ν_7	417.9	418.5	0.6	0.7	-0.6

11.2.2.3 Concentration study and complex stoichiometry

Assignment of the complex bands present in the solutions and analysis of the complexation shifts of the mixtures shows that the bands are in good agreement with the calculated complexes with a 1:1 stoichiometry. To verify the stoichiometry, a concentration study was performed by systematically varying the concentrations of both species at a constant temperature of 130 K and recording the spectra. Estimated mole fractions of the solutions varied between 2.8×10^{-5} and 9.4×10^{-4} for $C_2F_4S_2$ and 2.6×10^{-4} and 7.5×10^{-4} for DME. The results of this analysis are given in Figure S11.3 of the SI. By plotting the integrated intensity of the complex against the product of the intensities of the monomers at different ratio's, a linear correlation is found for the combination where both *x* and *y* are equal to one, thus confirming the 1:1 stoichiometry of the experimentally observed complex.

Additionally, a small shoulder is observed at the high frequency side for the $C_2F_4S_2$ ν_{13} complex band at the lowest temperatures, as shown in panel C of Figure 11.4. It is suggested that this spectral feature is the consequence of the presence of a small amount of 1:2 complex with two DME molecules. However, as the observed feature largely overlaps with the 1:1 complex band and is too small to reliably determine its integrated intensity, it does not allow a robust statistical analysis. Therefore, an experimental confirmation of its stoichiometry is not possible.

11.2.2.4 Temperature study and experimental complexation enthalpy

Construction of van 't Hoff plots from measurements in the 120 - 156 K temperature interval, for which details are given in Table S11.5 of the SI, yielded seven experimental complexation enthalpies, with an average value of -13.5(1) kJ mol^{-1}. An illustration of these van 't Hoff plots is given in Figure S11.4 of the SI.

11.3 Discussion

Apart from the spectral features assigned to the monomers involved, in the infrared spectra of the solutions in liquid krypton containing mixtures of $C_2F_4S_2$ and DME, separate features due to 1:1 complexes are observed. Hence, direct spectroscopic evidence for the co-existence of monomer and complexes, each with a separate spectrum, is found. This result differs from the studies reported by Garett and co-workers in which evidence for the existence of 1:1 Te···N bonded adducts with benzatelluradiazoles were obtained indirectly by analysing shifts of the λ_{max} in the UV-vis spectra and of the magnetic shielding in the NMR spectra during titration experiments of the benzatelluradiazoles with $Bu_4N^+Cl^-$ in THF. [15] It should also be noted that observations of Garret et al. focused on the experimental observations of the stronger tellurium chalcogen bond in solution, while up to now, evidence for the sulphur based chalcogen bonding in solution is, to the best of our knowledge, still non-existing. The study of the binary complexes between $C_2F_4S_2$ and DME reported here, therefore, clearly is one of the first, and probably the most convincing, study reporting the existence of such species in solution. Moreover, due to the inert nature of the solvent used, the intrinsic properties of the complex are observed nearly free of any solvent perturbations.

Ab initio calculations yielded two stable chalcogen-bonded complex isomers, which are distinguished by the presence or absence of secondary F···H interactions. As expected from the low energy barrier between both calculated complex geometries, a single band of the averaged structure is found for each of the vibrational modes and no distinction between both calculated geometries could be found. A concentration study at 130 K also confirmed the 1:1 complex stoichiometry of the complex experimentally.

As both complex geometries are based on an S···O chalcogen bond, they are inherently very similar as reflected by the nearly identical calculated shifts for both complex geometries. The only vibrational mode for which shifts are calculated in opposite directions is the ν_6 mode of $C_2F_4S_2$, as observed in Raman spectroscopy. Here, the experimentally observed shift of 0.4 cm^{-1} is found to lie in between the blueshift

calculated for the complex geometry with the secondary interactions and the redshift calculated for the geometry without secondary interactions.

To evaluate the correspondence between the experimental results and the *ab initio* calculations, the calculated shifts for both complexes are compared with the experimental shifts assigned to the fundamental vibrational modes. An overview of this analysis can be found in Table S11.6 of the SI, while a plot of the experimental shifts against the calculated shifts can be found in Figure 11.6.

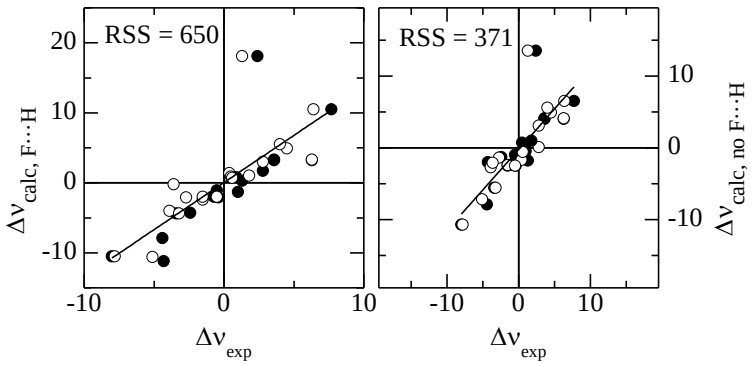

Figure 11.6: Plot of the experimental complexation shifts of the fundamental modes determined using IR (full circles) and Raman spectroscopy (open circles) against the MP2/aug-cc-pVDZ calculated complexation shifts for the complex with secondary F···H interactions (left) and without secondary F···H interactions (right). Residual sum of square values (RSS) and the adjusted R^2 values are also given.

The good correlation between the calculated and experimental values reported in Table S11.6 of the SI, the slope of the linear fit being close to 1 with an intercept close to 0, confirms the assignment of the complex bands to a chalcogen-bonded complex. The largest discrepancy is found for the DME ν_{12} mode in IR and Raman, where an experimental shift is found of 2.4 cm^{-1} in IR and 1.3 cm^{-1} in Raman, while the calculated shifts are 18.1 cm^{-1} for the chalcogen-bonded complex with F···H interactions and 13.5 cm^{-1} for the complex without secondary interactions. This discrepancy between experimental and calculated complexation shifts for the ν_{12} mode of DME has also been observed in previous chapters for HB [40] and XB complexes [28, 40] as well as lp···π complexes. [29] While the exact nature of this discrepancy is unknown, it is likely that it is the consequence of Fermi resonant effects between the C-H

fundamental stretches and combination bands and/or overtones of the C-H bending modes. Omitting these two values decreases the residual sum of squares (RSS) values to 130 for the complex with and 80 for the complex without secondary interactions. The better correlation for the complex without secondary interactions can be ascribed to the general overestimation of the complexation shifts, consistent with the overestimation of the complexation energy at the MP2/aug-cc-pVDZ level, which is more pronounced for the more stable complex with secondary interactions. The better fit for the complex without secondary interactions should therefore not be seen as an indication that this complex geometry has a larger contribution to the experimentally observed average.

Moreover, an average experimental complexation enthalpy of -13.5(1) kJ mol^{-1} has been determined from seven van 't Hoff plots in the 120 - 156 K temperature interval. This value is in agreement with the calculated complexation enthalpies of -16.6 and -15.2 kJ mol^{-1} for the chalcogen-bonded complexes with and without the F···H interactions, which are obtained by correcting the extrapolated CCSD(T)/CBS energies with zero point energies, thermal effects and solvent effects.

Comparison with the previously studied XB complexes between DME and a series of trifluorohalomethanes (CF_3X) [27] shows that this complexation enthalpy lies between the values of the XB complex formed with CF_3Br ($\Delta H°$ (LAr) = -10.2(1) kJ mol^{-1}) and the complex formed with CF_3I ($\Delta H°$ (LAr) = -15.5(1) kJ mol^{-1}). Since CF_3I·DME and $C_2F_4S_2$·DME have similar interaction energies and similar acceptor···donor distances, the EDA interaction energy components can be compared quantitatively. The EDA results for the XB complex were taken from a previous study [35] and are listed in Table 11.2. Except for a slightly larger dispersion interaction in the chalcogen-bonded complex, nearly the same energy contributions are obtained, emphasising the similarities between both types of noncovalent interactions. Analogously, the size of the charge transfer and associated energy for the relevant NOCVs of the $C_2F_4S_2$·DME complexes are nearly identical to the values obtained for the CF_3I·DME complex. [35]

It is therefore clear that sulphur chalcogen bonds can be comparable in strength with bromine and iodine halogen bonds when the interaction involves the lone pair of an sp^3 hybridized oxygen atom. Further studies are needed to assess whether this relation holds up when other Lewis bases are used. Comparison of actual results with the complexation enthalpy of the CF_3Cl·DME XB complex ($\Delta H°$ (LAr) = -6.8(3) kJ mol^{-1}) also implies that sulphur chalcogen bonding can be stronger than chlorine halogen bonding. Chalcogen bonds therefore hold great potential to form stronger noncovalent interactions than halogen bonds involving halogens from the same period of the periodic table. An important aspect in this regard is the lower electronegativity of chalcogens compared to same-period halogens, which might enhance the effect of electron withdrawing moieties on the covalently bonded group, giving rise to larger σ-holes on the chalcogen atom and stronger chalcogen bonds. The fact that divalent chalcogens form two covalent bonds yields additional possibilities to enhance the electron depletion of the chalcogen atom.

Even though chalcogen bonding involving oxygen donors have been reported to play an important role in, amongst others, the folding and interactions of biomolecules, a more thorough understanding of the chalcogen bonding concept with $C_2F_4S_2$ as a bond donor might benefit from complementary studies involving other Lewis bases including, amongst others, nitrogen bases such as NH_3 or TMA, and other Lewis bases such as DMS and TMP. Experimental studies of complexes between $C_2F_4S_2$ and NH_3 or TMA similar to those reported above were initiated but so far failed completely. Due to the low solubility of NH_3 in cryogenic liquids and due to the appearance of various oligomers hampering a detailed characterization of binary complexes, no results could be obtained for NH_3. Experiments with TMA, on the other hand, failed due to the formation of a white, yet unknown, precipitate appearing after condensing the TMA and $C_2F_4S_2$ gases. The appearance of such a solid is not surprising as it is in line with earlier observations suggesting that particularly the tellurium-bearing congeners are prone to self-association in the solid state through N···chalcogen interactions [41-44] and by the observations that co-crystallization with Lewis basic solvents and anions can appear. The appearance of a solid precipitate stable at room

temperature, hampers the preparation of cryosolutions required for spectroscopic studies, as these experiments typically involve the subsequent condensation of the compounds under study and the solvent gas into the liquid cell used.

11.4 Conclusions

Ab initio calculations at the MP2/aug-cc-pVDZ level of theory yielded two stable chalcogen-bonded complexes between $C_2F_4S_2$ and DME. Analysis of the complexes with NCIPlot revealed that the difference between both isomers is the presence or absence of secondary F···H interactions, the complex with the secondary interactions being 1.5 kJ mol^{-1} more stable at the CCSD(T)/CBS level. Due to the low energy barrier between both complexes, rapid interconversion between them is expected.

Using infrared and Raman spectroscopy on liquid krypton solutions of $C_2F_4S_2$ and DME, the presence of complex bands is revealed, the shifts being consistent with those of the *ab initio* calculations of the chalcogen-bonded complexes. A 1:1 stoichiometry is determined by performing a concentration study at 130 K in infrared. Furthermore an average experimental complex enthalpy of -13.5(1) kJ mol^{-1} is found by creating van 't Hoff plots of measurements in liquid krypton in the 120-156 K temperature interval. This value also agrees favourably with the calculated complexation enthalpy values of -16.6 and -15.2 kJ mol^{-1} for the chalcogen-bonded complex with and without secondary F···H interactions.

This study does not only show that oxygen based chalcogen bonding exists in solution at thermodynamic equilibrium, but also that, when using a highly fluorinated chalcogen bond donor, the strength of the interaction formed is of the same order as that of XB complexes formed through bromine and iodine.

11.5 References

1 J. S. Murray, P. Lane, T. Clark, K. E. Riley, P. Politzer, *J. Mol. Model.*, 2012, ***18***, 541-548.
2 J. S. Murray, P. Lane, P. Politzer, *J. Mol. Model.*, 2009, ***15***, 723-729.
3 P. Metrangolo, G. Resnati, T. Pilati, S. Biella, *Struct. Bond.*, 2008, ***126***, 105-136.
4 C. B. Aakeröy, S. Panikkattu, P. D. Chopade, J. Desper, *CrystEngComm*, 2013, ***15***, 3125-3136.
5 P. Metrangolo, F. Meyer, T. Pilati, G. Resnati, G. Terraneo, *Angew. Chem., Int. Ed.*, 2008, ***47***, 6114-6127.
6 C. B. Aakeröy, N. Schultheiss, A. Rajbanshi, J. Desper, C. Moore, *Cryst. Growth Des.*, 2009, ***9***, 432-441.
7 Y. X. Lu, Y. T. Liu, Z. J. Xu, H. Y. Li, H. L. Liu, W. L. Zhu, *Expert Opin. Drug Discovery*, 2012, ***7***, 375-383.
8 S. Sirimulla, J. B. Bailey, R. Vegesna, M. Narayan, *J. Chem. Inf. Model.*, 2013, ***53***, 2781-2791.
9 J. S. Murray, P. Lane, T. Clark, P. Politzer, *J. Mol. Model.*, 2007, ***13***, 1033-1038.
10 W. Zierkiewicz, J. Fanfrlík, P. Hobza, D. Michalska, T. Zeegers-Huyskens, *Theor. Chem. Acc.*, 2016, ***135***, 217.
11 W. Wang, B. Ji, Y. Zhang, *J. Phys. Chem. A*, 2009, ***113***, 8132-8135.
12 A. Zabardasti, A. Mahdizadeh, S. Farhadi, *J. Sulfur Chem.*, 2016, ***38***, 98-111.
13 A. Bauzá, I. Alkorta, A. Frontera, J. Elguero, *J. Chem. Theory Comput.*, 2013, ***9***, 5201-5210.
14 M. E. Brezgunova, J. Lieffrig, E. Aubert, S. Dahaoui, P. Fertey, S. Lebègue, J. G. Ángyán, M. Fourmigué, E. Espinosa, *Cryst. Growth Des.*, 2013, ***13***, 3283-3289.
15 G. E. Garrett, G. L. Gibson, R. N. Straus, D. S. Seferos, M. S. Taylor, *J. Am. Chem. Soc.*, 2015, ***137***, 4126-4133.
16 S. Benz, J. López-Andarias, J. Mareda, N. Sakai, S. Matile, *Angew. Chem., Int. Ed.*, 2017, ***56***, 812-815.
17 M. Iwaoka, S. Takemoto, S. Tomoda, *J. Am. Chem. Soc.*, 2002, ***124***, 10613-10620.
18 M. Iwaoka, N. Isozumi, *Molecules*, 2012, ***17***, 7266-7283.
19 M. Iwaoka, S. Takemoto, O. Mai, S. Tomoda, *Chem. Lett.*, 2001, ***30***, 132-133.
20 J. C. Taylor, G. D. Markham, *J. Biol. Chem.*, 1999, ***274***, 32909-32914.
21 Y. Nagao, T. Hirata, S. Goto, S. Sano, A. Kakehi, K. Iizuka, M. Shiro, *J. Am. Chem. Soc.*, 1998, ***120***, 3104-3110.
22 S. Wu, A. Greer, *J. Org. Chem.*, 2000, ***65***, 4883-4887.
23 O. V. Shishkin, I. V. Omelchenko, A. L. Kalyuzhny, B. V. Paponov, *Struct. Chem.*, 2010, ***21***, 1005-1011.
24 G. Valerio, G. Raos, S. V. Meille, P. Metrangolo, G. Resnati, *J. Phys. Chem. A*, 2000, ***104***, 1617-1620.

25 K. E. Riley, J. S. Murray, J. Fanfrlik, J. Rezac, R. J. Sola, M. C. Concha, F. M. Ramos, P. Politzer, *J. Mol. Model.*, 2011, ***17***, 3309-3318.
26 R. Shukla, D. Chopra, *J. Chem. Sci.*, 2016, ***128***, 1589-1596.
27 D. Hauchecorne, R. Szostak, W. A. Herrebout, B. J. van der Veken, *ChemPhysChem*, 2009, ***10***, 2105-2115.
28 Y. Geboes, N. Nagels, B. Pinter, F. De Proft, W. A. Herrebout, *J. Phys. Chem. A*, 2015, ***119***, 2502-2516.
29 Y. Geboes, F. De Proft, W. A. Herrebout, *Chem. Phys.*, 2016, ***476***, 1-8.
30 L. I. De Beuckeleer, W. A. Herrebout, *J. Phys. Chem. A*, 2016, ***120***, 884-894.
31 L. I. De Beuckeleer, W. A. Herrebout, *Spectrochim. Acta, Part A*, 2017, ***171***, 60-71.
32 E. R. Johnson, S. Keinan, P. Mori-Sánchez, J. Contreras-García, A. J. Cohen, W. Yang, *J. Am. Chem. Soc.*, 2010, ***132***, 6498-6506.
33 J. Contreras-García, E. R. Johnson, S. Keinan, R. Chaudret, J.-P. Piquemal, D. N. Beratan, W. Yang, *J. Chem. Theory Comput.*, 2011, ***7***, 625-632.
34 C. Peng, H. B. Schlegel, *Isr. J. Chem.*, 1993, ***33***, 449-454.
35 B. Pinter, N. Nagels, W. A. Herrebout, F. De Proft, *Chem. - Eur. J.*, 2013, ***19***, 519-530.
36 J. R. Durig, R. C. Lord, *Spectrochim. Acta*, 1963, ***19***, 769-774.
37 W. C. Harris, A. Nuernberg, *Appl. Spectrosc.*, 1973, ***27***, 44-46.
38 J. O. Jensen, *J. Mol. Struct.: THEOCHEM*, 2004, ***678***, 189-193.
39 G. Herzberg, *Infrared and Raman Spectra of Polyatomic Molecules*, 12th ed., D. Van Nostrand Company Inc., Princeton, NJ, USA, **1945**.
40 N. Nagels, Y. Geboes, B. Pinter, F. De Proft, W. A. Herrebout, *Chem. - Eur. J.*, 2014, ***20***, 8433-8443.
41 A. F. Cozzolino, I. Vargas-Baca, *J. Organomet. Chem.*, 2007, ***692***, 2654-2657.
42 G. Berionni, B. Pegot, J. Marrot, R. Goumont, *CrystEngComm*, 2009, ***11***, 986-988.
43 T. Chivers, X. Gao, M. Parvez, *Inorg. Chem.*, 1996, ***35***, 9-15.
44 N. W. Alcock, *Bonding and Structure: Structural Principles in Inorganic and Organic Chemistry, Vol. 103*, Ellis Horwood, Ltd., Harlow, U.K., **1990**.

11.6 Supporting information

Table S11.1.1: Cartesian coordinates of the MP2/aug-cc-pVDZ optimized geometry of $C_2F_4S_2$.

D_{2h}	X	Y	Z
$C_2F_4S_2$			
S	0.000000	1.387164	0.000000
C	1.191095	0.000000	0.000000
F	2.014655	0.000000	1.085309
F	2.014655	0.000000	-1.085309
S	0.000000	-1.387164	0.000000
C	-1.191095	0.000000	0.000000
F	-2.014655	0.000000	1.085309
F	-2.014655	0.000000	-1.085309

Table S11.1.2: Cartesian coordinates of the MP2/aug-cc-pVDZ optimized geometry of DME.

C_{2v}	X	Y	Z
DME			
O	0.000000	0.000000	0.607066
C	0.000000	1.169581	-0.202099
H	0.000000	2.032636	0.474896
H	0.898418	1.208635	-0.845282
H	-0.898418	1.208635	-0.845282
C	0.000000	-1.169581	-0.202099
H	0.898418	-1.208635	-0.845282
H	0.000000	-2.032636	0.474896
H	-0.898418	-1.208635	-0.845282

Table S11.2.1: Cartesian coordinates of the MP2/aug-cc-pVDZ optimized geometry of the chalcogen-bonded complex with secondary F···H interactions between $C_2F_4S_2$ and DME.

C_s	X	Y	Z
$C_2F_4S_2$			
S	-0.941573	-0.347420	0.000000
C	-1.518098	1.386540	0.000000
F	-2.283100	1.705540	1.085871
F	-2.283100	1.705540	-1.085871
S	0.107328	2.222589	0.000000
C	0.683775	0.486090	0.000000
F	1.454447	0.188153	1.086124
F	1.454447	0.188153	-1.086124
DME			
O	0.757555	-2.589095	0.000000
C	1.454447	-3.000236	-1.175404
H	1.541279	-4.100704	-1.212050
H	0.872030	-2.648676	-2.035901
H	2.464592	-2.555308	-1.209819
C	1.454447	-3.000236	1.175404
H	2.464592	-2.555308	1.209819
H	0.872030	-2.648676	2.035901
H	1.541279	-4.100704	1.212050

Table S11.2.2: Cartesian coordinates of the MP2/aug-cc-pVDZ optimized geometry of the chalcogen-bonded complex without secondary F···H interactions between $C_2F_4S_2$ and DME.

C_s	X	Y	Z
$C_2F_4S_2$			
S	0.826807	-0.123871	0.000000
C	0.469489	-1.915942	0.000000
F	0.977506	-2.571660	1.085840
F	0.977506	-2.571660	-1.085840
S	-1.355271	-1.835427	0.000000
C	-1.000053	-0.037283	0.000000
F	-1.517795	0.597674	1.087123
F	-1.517795	0.597674	-1.087123
DME			
O	0.356324	2.635676	0.000000
C	0.977506	3.152584	-1.175988
H	2.044989	2.868780	-1.216809
H	0.449831	2.719491	-2.034609
H	0.896858	4.253445	-1.208389
C	0.977506	3.152584	1.175988
H	0.896858	4.253445	1.208389
H	0.449831	2.719491	2.034609
H	2.044989	2.868780	1.216809

Table S11.2.3: Cartesian coordinates of the transition state between the chalcogen-bonded complexes between $C_2F_4S_2$ and DME with and without secondary F···H interactions, calculated at the MP2/aug-cc-pVDZ level of theory.

C_s	X	Y	Z
$C_2F_4S_2$			
S	-0.134528	-0.910861	0.001655
C	-1.939506	-0.629974	0.001078
F	-2.573168	-1.164109	1.087683
F	-2.572984	-1.167378	-1.084030
S	-1.939846	1.196495	-0.001688
C	-0.128767	0.918461	-0.001570
F	0.483264	1.467342	1.084589
F	0.482834	1.463575	-1.089831
DME			
O	2.612787	-0.317891	0.000305
C	3.397006	-0.499296	-1.176133
H	3.824861	-1.517275	-1.212527
H	2.729931	-0.349900	-2.034096
H	4.218523	0.237932	-1.216499
C	3.397726	-0.489366	1.177766
H	4.219357	0.248084	1.211309
H	2.731214	-0.332639	2.034849
H	3.825525	-1.507037	1.222498

Table S11.3: MP2/aug-cc-pVDZ vibrational frequencies, in cm^{-1}, infrared intensities, in km mol^{-1}, and Raman intensities, in $Å^4$ amu^{-1}, for the chalcogen-bonded complex with secondary F···H interactions between $C_2F_4S_2$ and DME and both monomers, as well as the complexation shift Δν.

	Monomer			Chalcogen-bonded complex			
	Frequency	IR int.	Raman int.	Frequency	Δν	IR int.	Raman int.
$C_2F_4S_2$							
ν_1 (A_g)	1160.9	0.0	8.6	1156.9	-4.0	1.3	8.1
ν_2 (A_g)	651.0	0.0	15.5	648.6	-2.4	0.5	16.1
ν_3 (A_g)	513.3	0.0	14.7	514.4	1.0	0.7	16.7
ν_4 (A_g)	323.4	0.0	3.0	324.3	0.9	0.1	2.9
ν_5 (A_u)	231.2	0.0	0.0	236.6	5.4	0.01	0.02
ν_6 (B_{1g})	839.9	0.0	8.4	841.3	1.4	7.4	12.1
ν_7 (B_{1g})	422.6	0.0	5.3	425.6	3.0	2.0	7.3
ν_8 (B_{1u})	1095.1	320.6	0.0	1083.9	-11.2	257.4	0.002
ν_9 (B_{1u})	428.3	0.4	0.0	431.7	3.4	0.4	0.02
ν_{10} (B_{1u})	56.3	1.2	0.0	62.7	6.4	0.5	0.1
ν_{11} (B_{2g})	1079.3	0.0	4.9	1068.7	-10.6	1.5	4.8
ν_{12} (B_{2g})	377.9	0.0	1.3	382.7	4.9	0.03	1.2
ν_{13} (B_{2u})	970.0	128.0	0.0	970.3	0.3	119.8	0.5
ν_{14} (B_{2u})	335.3	4.5	0.0	336.9	1.6	6.9	0.1
ν_{15} (B_{3g})	282.2	0.0	2.1	287.7	5.5	0.004	1.9
ν_{16} (B_{3u})	1065.2	732.2	0.0	1060.9	-4.3	725.4	0.1
ν_{17} (B_{3u})	638.7	15.9	0.0	637.5	-1.1	10.0	0.6
ν_{18} (B_{3u})	445.4	2.1	0.0	446.3	0.8	6.6	0.5
DME							
ν_1 (A_1)	3188.7	20.1	87.6	3191.9	3.2	18.6	55.1
ν_2 (A_1)	3024.8	58.6	320.3	3035.2	10.5	66.7	313.1
ν_3 (A_1)	1505.9	2.9	5.6	1503.9	-2.0	4.1	6.3
ν_4 (A_1)	1473.5	0.0	2.2	1473.4	-0.2	0.5	4.3
ν_5 (A_1)	1261.1	6.6	0.5	1262.8	1.7	6.5	0.8
ν_6 (A_1)	942.4	34.7	9.8	931.9	-10.5	75.2	11.3
ν_7 (A_1)	416.8	2.3	1.0	417.5	0.7	2.6	1.3
ν_8 (A_2)	3096.2	0.0	14.7	3113.7	17.5	0.06	12.7
ν_9 (A_2)	1474.8	0.0	11.4	1472.8	-2.0	0.2	9.3
ν_{10} (A_2)	1157.2	0.0	1.5	1156.2	-1.0	0.005	1.5
ν_{11} (A_2)	195.2	0.0	0.2	200.4	5.1	0.006	0.2
ν_{12} (B_1)	3089.5	107.8	94.2	3107.7	18.1	83.7	110.5
ν_{13} (B_1)	1489.2	13.0	0.0	1487.9	-1.3	14.7	0.3
ν_{14} (B_1)	1187.2	7.2	0.0	1187.8	0.6	5.7	0.3
ν_{15} (B_1)	260.2	5.1	0.0	265.6	5.4	6.7	0.01
ν_{16} (B_2)	3187.3	24.6	59.2	3190.6	3.3	13.5	36.3
ν_{17} (B_2)	3018.4	55.2	0.6	3030.1	11.8	43.2	4.4
ν_{18} (B_2)	1490.1	10.3	1.0	1487.9	-2.1	10.2	0.8
ν_{19} (B_2)	1441.5	2.5	1.3	1441.5	0.0	0.4	1.7
ν_{20} (B_2)	1191.9	98.1	0.7	1184.0	-7.9	84.2	0.3
ν_{21} (B_2)	1113.8	35.0	1.6	1109.3	-4.4	60.4	2.0

Van der Waals vibrations: 6.6 cm^{-1}, 0.5 km mol^{-1}, 0.4 $Å^4$ amu^{-1}, 56.3 cm^{-1}, 0.4 km mol^{-1}, 0.4 $Å^4$ amu^{-1}, 66.3 cm^{-1}, 1.9 km mol^{-1}, 0.2 $Å^4$ amu^{-1}, 87.2 cm^{-1}, 0.6 km mol^{-1}, 0.4 $Å^4$ amu^{-1}, 98.3 cm^{-1}, 0.2 km mol^{-1}, 0.2 $Å^4$ amu^{-1}, 102.2 cm^{-1}, 6.6 km mol^{-1}, 0.05 $Å^4$ amu^{-1}.

Table S11.4: MP2/aug-cc-pVDZ vibrational frequencies, in cm^{-1}, infrared intensities, in km mol^{-1}, and Raman intensities, in $Å^4$ amu^{-1}, for the chalcogen-bonded complex without secondary F···H interactions between $C_2F_4S_2$ and DME and both monomers, as well as the complexation shift Δν.

	Monomer			Chalcogen-bonded complex			
	Frequency	IR int.	Raman int.	Frequency	Δν	IR int.	Raman int.
$C_2F_4S_2$							
ν_1 (A_g)	1160.9	0.0	8.6	1158.2	-2.7	0.2	8.7
ν_2 (A_g)	651.0	0.0	15.5	648.5	-2.5	0.7	16.6
ν_3 (A_g)	513.3	0.0	14.7	514.3	1.0	0.8	18.8
ν_4 (A_g)	323.4	0.0	3.0	324.1	0.7	0.2	2.8
ν_5 (A_u)	231.2	0.0	0.0	236.7	5.5	0.02	0.01
ν_6 (B_{1g})	839.9	0.0	8.4	838.2	-1.7	8.5	12.7
ν_7 (B_{1g})	422.6	0.0	5.3	425.7	3.1	1.7	8.3
ν_8 (B_{1u})	1095.1	320.6	0.0	1093.1	-2.0	195.3	0.6
ν_9 (B_{1u})	428.3	0.4	0.0	431.1	2.8	0.3	0.02
ν_{10} (B_{1u})	56.3	1.2	0.0	63.2	6.9	0.9	0.02
ν_{11} (B_{2g})	1079.3	0.0	4.9	1072.1	-7.2	57.1	3.8
ν_{12} (B_{2g})	377.9	0.0	1.3	382.8	4.9	0.02	1.3
ν_{13} (B_{2u})	970.0	128.0	0.0	968.2	-1.8	122.7	0.6
ν_{14} (B_{2u})	335.3	4.5	0.0	336.8	1.5	7.1	0.2
ν_{15} (B_{3g})	282.2	0.0	2.1	287.8	5.6	0.002	1.9
ν_{16} (B_{3u})	1065.2	732.2	0.0	1063.9	-1.3	698.9	0.3
ν_{17} (B_{3u})	638.7	15.9	0.0	637.7	-1.0	9.8	0.8
ν_{18} (B_{3u})	445.4	2.1	0.0	445.9	0.4	5.8	0.7
DME							
ν_1 (A_1)	3188.7	20.1	87.6	3192.6	4.0	16.4	54.6
ν_2 (A_1)	3024.8	58.6	320.3	3031.3	6.5	63.7	294.1
ν_3 (A_1)	1505.9	2.9	5.6	1503.5	-2.4	5.9	6.0
ν_4 (A_1)	1473.5	0.0	2.2	1471.4	-2.1	0.6	4.8
ν_5 (A_1)	1261.1	6.6	0.5	1261.2	0.1	6.4	0.7
ν_6 (A_1)	942.4	34.7	9.8	931.7	-10.7	78.7	11.1
ν_7 (A_1)	416.8	2.3	1.0	416.2	-0.6	3.4	0.8
ν_8 (A_2)	3096.2	0.0	14.7	3109.1	12.9	0.6	13.9
ν_9 (A_2)	1474.8	0.0	11.4	1473.4	-1.4	0.3	9.0
ν_{10} (A_2)	1157.2	0.0	1.5	1155.8	-1.5	0.002	1.5
ν_{11} (A_2)	195.2	0.0	0.2	193.0	-2.3	0.0001	0.2
ν_{12} (B_1)	3089.5	107.8	94.2	3103.0	13.5	88.8	129.9
ν_{13} (B_1)	1489.2	13.0	0.0	1488.8	-0.5	14.7	0.2
ν_{14} (B_1)	1187.2	7.2	0.0	1188.2	1.1	6.2	0.2
ν_{15} (B_1)	260.2	5.1	0.0	265.5	5.2	9.5	0.2
ν_{16} (B_2)	3187.3	24.6	59.2	3191.4	4.1	12.0	35.5
ν_{17} (B_2)	3018.4	55.2	0.6	3026.1	7.8	41.2	4.1
ν_{18} (B_2)	1490.1	10.3	1.0	1487.5	-2.5	9.5	0.8
ν_{19} (B_2)	1441.5	2.5	1.3	1440.5	-1.0	0.3	1.7
ν_{20} (B_2)	1191.9	98.1	0.7	1184.0	-7.9	82.6	0.3
ν_{21} (B_2)	1113.8	35.0	1.6	1108.2	-5.6	71.8	2.2

Van der Waals vibrations: 17.5 cm^{-1}, 0.5 km mol^{-1}, 0.6 $Å^4$ amu^{-1}, 43.5 cm^{-1}, 0.02 km mol^{-1}, 0.3 $Å^4$ amu^{-1}, 45.9 cm^{-1}, 1.9 km mol^{-1}, 0.09 $Å^4$ amu^{-1}, 77.7 cm^{-1}, 0.05 km mol^{-1}, 0.2 $Å^4$ amu^{-1}, 102.5 cm^{-1}, 0.06 km mol^{-1}, 0.1 $Å^4$ amu^{-1}, 116.2 cm^{-1}, 9.8 km mol^{-1}, 0.8 $Å^4$ amu^{-1}.

Table S11.5: Overview of the different van 't Hoff plots constructed for the chalcogen-bonded complex between $C_2F_4S_2$ and DME in LKr in the 120-156 K temperature interval, showing the estimated mole fractions of each monomer, range of the integrated monomer and complex bands and complex enthalpies $\Delta H°$ (LKr).

$x_{C_2F_4S_2}$	x_{DME}	Integrated $C_2F_4S_2$ band (cm^{-1})	Integrated DME band (cm^{-1})	Integrated Complex band (cm^{-1})	$\Delta H°$ (LKr) [a]
1.9×10^{-4}	4.7×10^{-4}	656-647.5	1510-1432	966-957	-13.4(1)
1.9×10^{-4}	4.7×10^{-4}	656-647.5	975-900	926-915.5	-13.6(1)
2.8×10^{-5}	7.5×10^{-4}	1081-1059	975-895	1079-1055	-13.5(2)
2.8×10^{-5}	7.5×10^{-4}	966-953	3035-2964	967-953	-13.5(2)
9.4×10^{-4}	2.6×10^{-4}	657.3-646.5	1212-1144	1179-1155	-13.3(1)
1.3×10^{-4}	7.5×10^{-4}	972-950	990-880	972-953.5	-13.4(3)
1.3×10^{-4}	7.5×10^{-4}	1123-1097	1550-1394.5	928.5-914.9	-13.7(1)

[a] Values are given with the standard deviation of the linear regression in parentheses.

Table S11.6: Summary of the results from the plots of the experimental and MP2/aug-cc-pVDZ calculated complexation shifts for the complex with and without secondary F···H interactions, for both the plots including and excluding the DME ν_{12} mode in IR and Raman spectroscopy.

	With F···H	Without F···H
All fundamental modes		
Slope	1.3(2)	1.13(14)
Intercept	0.0(7)	-0.2(6)
Residual sum of squares (RSS)	649.6	370.8
R^2	0.58491	0.63451
Without DME ν_{12}		
Slope	1.24(9)	1.05(7)
Intercept	-0.9(3)	-0.9(3)
Residual sum of squares (RSS)	129.6	80.0
R^2	0.85672	0.87371

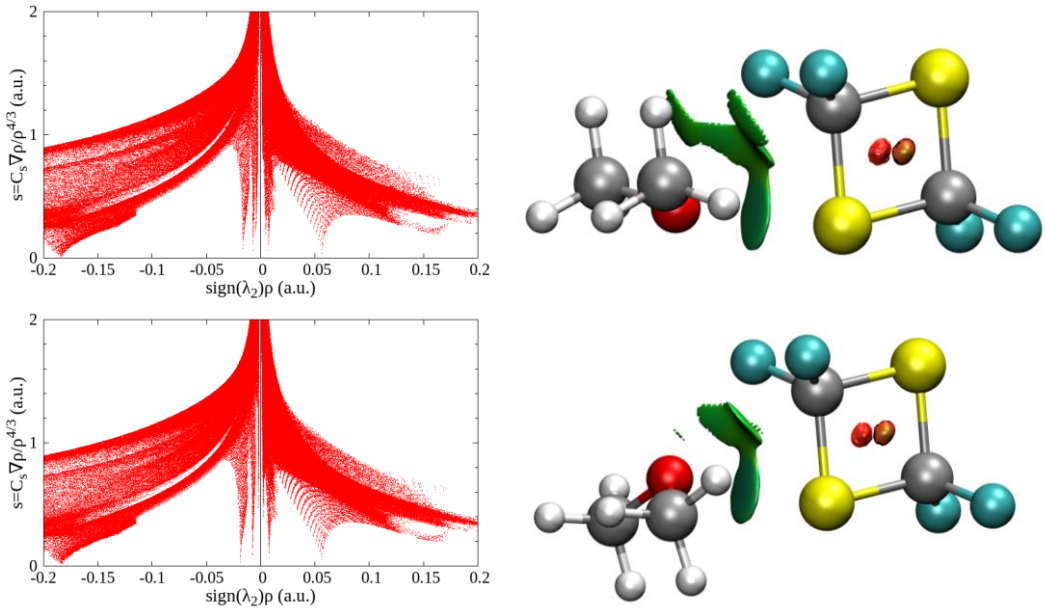

Figure S11.1: Plots of the reduced density gradient versus the electron density multiplied by the sign of the second Hessian eigenvalue (left) and gradient isosurfaces (s = 0.5 a.u., right) for the chalcogen-bonded complex between $C_2F_4S_2$ and DME with (top) and without (bottom) secondary F···H interactions.

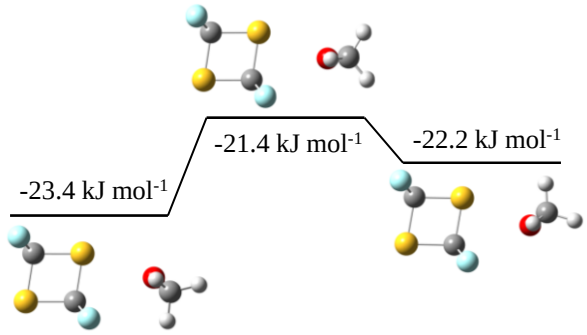

Figure S11.2: Energy diagram of the chalcogen-bonded complexes between $C_2F_4S_2$ and DME with (left) and without (and) secondary F···H interactions, and the transition state between both geometries calculated at the MP2/aug-cc-pVDZ level of theory.

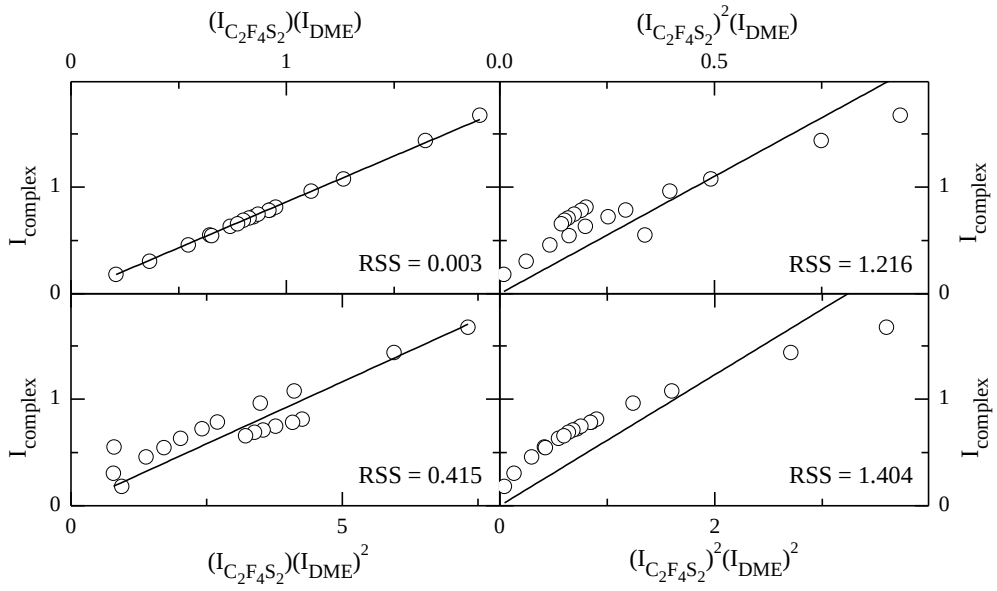

Figure S11.3: Concentration study plots of the $C_2F_4S_2$·DME chalcogen-bonded complex at 130 K in LKr. Integrated intensity of the complex is plotted against the product of monomer intensities $\left(I_{C_2F_4S_2}\right)^x (DME)^y$. Top left: x= $1, y = 1$, top right: $x = 2, y = 1$, bottom left $x = 1, y = 2$ and bottom right $x = 2, y = 2$. Additionally, residual sum of square values (RSS) have been included.

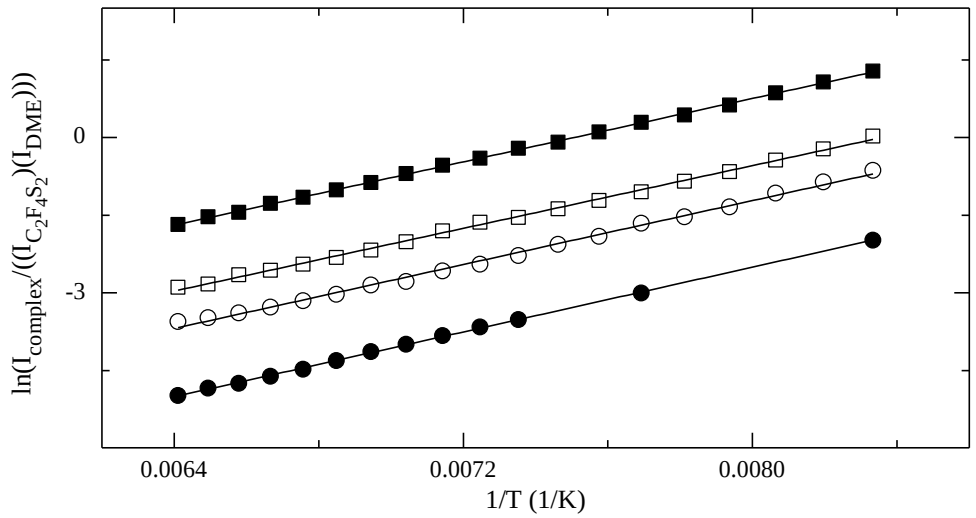

Figure S11.4: Typical van 't Hoff plots of the chalcogen-bonded complex between $C_2F_4S_2$ and DME in LKr in the 120-156 K temperature interval.

If quantum mechanics hasn't profoundly shocked you, you haven't understood it yet.

– Niels H. D. Bohr

Chapter 12

Fourier Transform Microwave Spectroscopy of weak noncovalent interactions.

From thermodynamic equilibrium to supersonic expansion.

12.1 FTMW at the University of Bologna

During the research stay at the University of Bologna, pulsed-jet FTMW measurements focused on the study of the mixtures of C_2F_3Cl with NH_3 [1] and DME [2], which were building further on a previous study by Gou et al. in which the $C_2F_3Cl{\cdot}H_2O$ mixtures were studied, thereby revealing the presence of lp···π complex. [3] Results of both studies have been published in peer reviewed papers and will not be discussed in detail within this thesis. An overview of the experimental spectroscopic parameters is given in Table 12.1 and an overview of the calculated rotational constants for the XB and lp···π complexes is given in Table 12.2. As these measurements are not performed at thermodynamic equilibrium and rapid interconversion has been proven in supersonic jets when the conformational barrier is below 400 cm^{-1} (4.8 kJ mol^{-1}), [4] the higher energetic isomers might not be observed using this technique.

Comparison of the experimental and calculated rotational constants for the mixture involving $^{14}NH_3$ clearly shows that the complex present is of the lp···π type. The observation of lp···π complex in the $C_2F_3Cl{\cdot}NH_3$ mixtures clearly demonstrated that this type of interaction can also be formed through the lone pair on a nitrogen atom, which supports the observation of lp···π complex during the cryospectroscopic study of $C_2F_3X{\cdot}$TMA mixtures reported in chapter 8, for which the geometry is given in Figure 12.1.

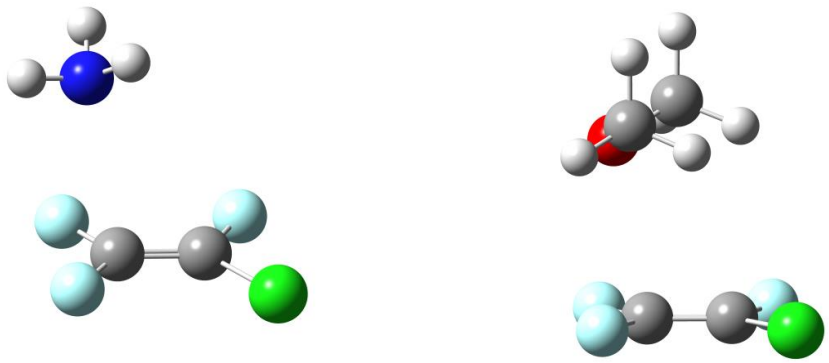

Figure 12.1: MP2/aug-cc-pVDZ geometries of the lp···π complexes between C_2F_3Cl and NH_3 (left) or DME (right).

Table 12.1: Experimental spectroscopic parameters of the complexes observed between C_2F_3Cl and the Lewis bases $^{14}NH_3$ [1] and DME [2] measured in helium, fitted using Pickett's SPFIT program [5] with Watson's S-reduction and I^r-representation, as given in equation 12.1. [6] The error is given in parentheses in units of the last digit.

	$C_2F_3{}^{35}Cl\cdot{}^{14}NH_3$	$C_2F_3{}^{37}Cl\cdot{}^{14}NH_3$	$C_2F_3{}^{35}Cl\cdot$DME	$C_2F_3{}^{37}Cl\cdot$DME
A (MHz) [c]	2236.0689(1)	2225.110(1)	1434.4456(2)	1421.3262(2)
B (MHz) [c]	1317.19498(8)	1294.36090(8)	903.5197(1)	893.0386(1)
C (MHz) [c]	1219.63324(7)	1196.9012(1)	823.4024 (1)	810.43402(9)
D_J (kHz) [d]	2.5186(8)	2.416(1)	0.9123(9)	0.9397(7)
D_{JK} (kHz) [d]	-6.710(6)	-6.27(7)	7.104(5)	6.334(4)
D_K (kHz) [d]	16.926(9)	16.926 [a]	−4.642(6)	−3.577(4)
d_1 (kHz) [d]	-0.3695(8)	-0.3695 [a]	−0.1032(6)	−0.1195(4)
d_2 (kHz) [d]	-0.1151(9)	-0.1151 [a]	0.0129(4)	0.0123(2)
χ_{aa}(Cl) (MHz) [e]	-21.817(2)	-18.71(1)	18.483(5)	13.029(6)
$\chi_{bb} - \chi_{cc}$(Cl) (MHz) [e]	-50.762(4)	-38.630(7)	−81.276(6)	−62.996(7)
χ_{ab}(Cl) (MHz) [e]	55.9(4)	46.1(8)	41.5(7)	35(1)
χ_{ac}(Cl) (MHz) [e]	10.3(3)	6.8(5)	11.0 [b]	8.8 [b]
χ_{bc}(Cl) (MHz) [e]	12(2)	-	-24.5(5)	-18.6(7)
χ_{aa}(N) (MHz) [e]	-0.404(2)	-0.404 [a]		
$\chi_{bb} - \chi_{cc}$(N) (MHz) [e]	-0.435(4)	-0.435 [a]		
χ_{ab}(N) (MHz) [e]	0.72(6)	0.72 [a]		
χ_{ac}(N) (MHz) [e]	1.8(4)	1.8 [a]		
σ (kHz) [f]	2.8	3.5	2.0	2.3
N [g]	475	176	339	330

[a] Value is fixed to the corresponding value of the parent species. [b] Fixed to *ab initio* value. [c] Rotational constant. [d] Centrifugal distortion constant. [e] Nuclear quadrupole coupling constants. [f] RMS error of the fit. [g] Number of fitted lines.

Here, Watson's S-reduction and I^r-representation is defined by the Hamiltonian

$$\hat{H} = A\hat{J}_z^2 + \frac{B+C}{2}\left(\hat{J}^2 - \hat{J}_z^2\right) + \frac{1}{4}(B-C)\left(\hat{J}_+^2 + \hat{J}_-^2\right) - D_J\hat{J}^4 - D_{JK}\hat{J}^2\hat{J}_z^2 - D_k\hat{J}_z^4 + d_1\hat{J}^2\left(\hat{J}_+^2 - \hat{J}_-^2\right) + d_2\left(\hat{J}_+^4 + \hat{J}_-^4\right) \quad (12.1)$$

to which additional terms are added to describe the nuclear quadrupole coupling of the chlorine and/or nitrogen atom(-s). [6-7]

Table 12.2: MP2/aug-cc-pVDZ calculated rotational constants for the lp···π and XB complex between $C_2F_3{}^{35}Cl$ and the Lewis bases $^{14}NH_3$ and DME.

	$C_2F_3{}^{35}Cl\cdot{}^{14}NH_3$		$C_2F_3{}^{35}Cl\cdot$DME	
	lp···π	XB	lp···π	XB
A (MHz)	2191	3839	1397	2892
B (MHz)	1281	862	900	455
C (MHz)	1192	706	823	424

The presence of $C_2F_3Cl\cdot$DME lp···π complex yields further proof of the assignments made for the same complex during the cryospectroscopic measurements reported in chapter 7. Furthermore, the fact that solely lp···π complex is observed is also in good agreement with the complexation energies reported in the same chapter, which indicate that the lp···π complex has the lowest complexation energy.

12.2 CP-FTMW at Newcastle University

During the studies at Newcastle University, under the supervision of dr. Nick Walker, we aimed to study the complexes of CHF_2I with NH_3 and TMA, to investigate the influence of methylation of the Lewis base on the HB-XB competition. *Ab initio* calculations, for which the results are shown in Figure 12.2, had indeed shown that for the complexes with NH_3, the HB complex would be more stable, while the XB complex was expected to prevail for the complex with TMA.

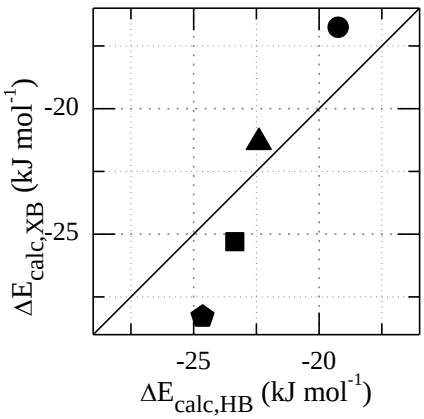

Figure 12.2: MP2/aug-cc-pVDZ-pp complexation energies for the XB and HB complexes between CHF_2I and ammonia (circle), methylamine (triangle), dimethylamine (square) and trimethylamine (pentagon). For points below the bisector, the XB complex has the highest complexation energy, while for the points above the bisector the HB complex prevails over the XB complex

The presence of a nuclear electric quadrupole on both the ^{127}I atom (I = 5/2) and ^{14}N atom (I = 1) results in a splitting of each transition into 18 component lines, thus fully exploiting the advantage of broadband FTMW, where all these lines are detected simultaneously.

Unfortunately a full assignment of all observed peaks for the mixtures with TMA, a *conditio sine qua non* for publication, has proven unattainable at this moment in time. The reason for this most probably is the presence of an internal rotor around the three fold axis of either monomer with a low barrier (resulting in a nearly free rotation)

deviating from the principal axes of inertia of the complex, shown in Figure 12.3. As this rotation cannot be described by currently available Hamiltonians, a full assignment of the observed transitions is hitherto not possible.

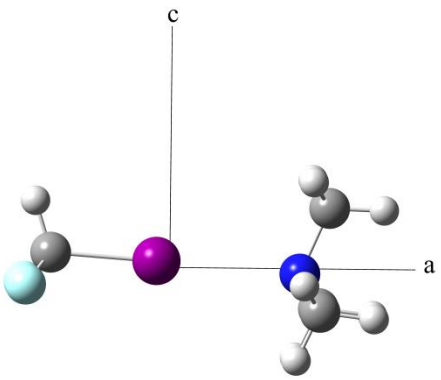

Figure 12.3: MP2/aug-cc-pVDZ-pp calculated CHF_2I·TMA halogen bond complex geometry, showing the principal axes of inertia.

A similar challenge has been observed for the HB complex between TMA and fluoroform (CF_3H), measured previously by S. Stephens but still unassigned and unpublished, which has a slightly bend complex geometry in *ab initio* calculations due to the formation of secondary C-F···H, so that the three fold axis of both molecules no longer align with the axis along the moment of inertia. We have reached out to Isabelle Kleiner of the *Laboratoire Interuniversitaire des Systèmes Atmosphériques* (LISA) in France, one of the very few experts in the field of internal rotors for the development of a suitable Hamiltonian, but are still awaiting response.

From the approximate rotational constants and the shape of the spectrum resembling a clear a-type spectrum, as shown in Figure 12.4, it is however clear that the formed complex is of the XB type. Furthermore, we were able to get a decent fit for the K = 1 transitions, for which an example is given in Figure 12.5.

The spectrum of the mixtures with NH_3 did not show a clear a-type spectrum, thus indicating the complex might be hydrogen-bonded. As the complex is found to be rather weak, assignment of the small observed peaks is also proving to be challenging

and a full assignment has not been made yet, as most resources had been focused on the assignment of the CHF_2I·TMA complex.

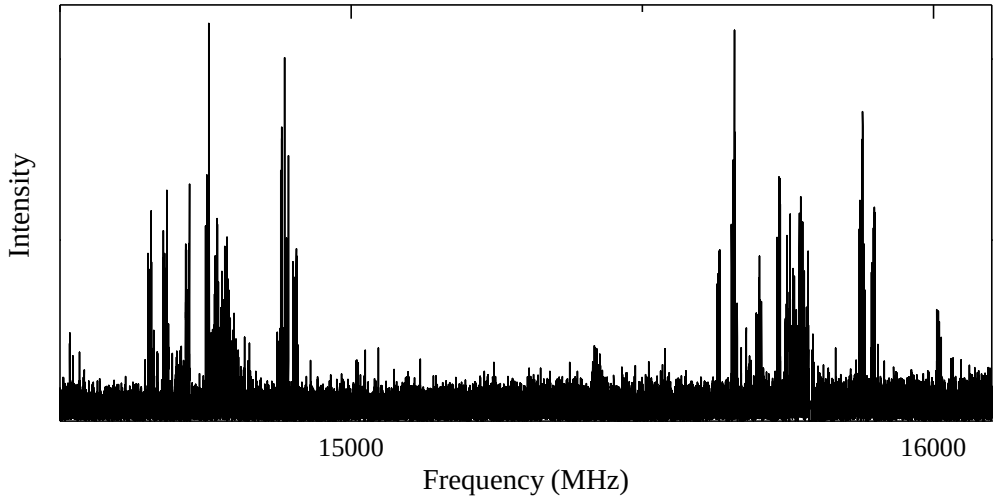

Figure 12.4: Excerpt of the CP-FTMW spectrum (261000 FIDs) of the CHF_2I·TMA complex, showing the J'-J"= 15-14 (left) and J'-J"= 16-15 (right) transitions. Lines due to the CHF_2I monomer have been cut from the spectrum to aid clarity.

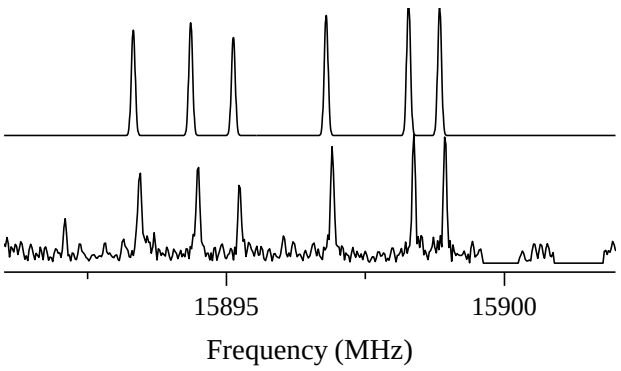

Figure 12.5: Example of the fit of the J'-J", K'-K"= 16-15, 1-1 transitions. An excerpt of the spectrum in Figure 12.4 is shown in the bottom trace, while the fitted lines are shown in the top trace. Lines due to the CHF_2I monomer have been cut from the spectrum to aid clarity, as can be seen on the right side of the bottom trace.

12.3 References

1 Q. Gou, L. Spada, Y. Geboes, W. A. Herrebout, S. Melandri, W. Caminati, *Phys. Chem. Chem. Phys.*, 2015, ***17***, 7694-7698.

2 L. Spada, Q. Gou, Y. Geboes, W. A. Herrebout, S. Melandri, W. Caminati, *J. Phys. Chem. A*, 2016, ***120***, 4939-4943.

3 Q. Gou, G. Feng, L. Evangelisti, W. Caminati, *Angew Chem Int Ed Engl*, 2013, ***52***, 11888-11891.

4 R. S. Ruoff, T. D. Klots, T. Emilsson, H. S. Gutowsky, *J. Chem. Phys.*, 1990, ***93***, 3142-3150.

5 H. M. Pickett, *J. Mol. Spectrosc.*, 1991, ***148***, 371-377.

6 J. K. G. Watson, Aspects of Quartic and Sextic Centrifugal Effects on Rotational Energy Levels, in *Vibrational Spectra and Structures*, Dekker, New York, NY, USA, **1977**.

7 H. W. Kroto, *Molecular Rotation Spectra*, Dover Publications, Inc., Mineola, NY, USA, **1992**.

Final Chapter

Summary, conclusions and future perspectives

Summary and conclusions

During the course of this thesis the competition between the noncovalent interactions hydrogen bonding, halogen bonding and lp···π interactions has been studied using FTIR and Raman spectroscopy on liquid noble gas solutions.

As a starting point for the competition between halogen bonding and hydrogen bonding, the complexes between the combined halogen and hydrogen bond donor difluoroiodomethane (CHF_2I) and the Lewis bases fluoromethane (CH_3F), dimethyl ether (DME) and trimethylamine (TMA) were studied. This study demonstrated that halogen bonding and hydrogen bonding can coexist in liquid noble gas solutions, and that either noncovalent interaction can prevail depending on the Lewis base used.

To further rationalize the influence of the Lewis base involved on the competition between halogen bonding and hydrogen bonding, an additional study was performed in which the complexes were investigated between CHF_2I and the Lewis bases chloromethane (CH_3Cl), dimethyl sulfide (DMS) and trimethylphosphine (TMP), which all contain a lone pair on an element of the third period of the periodic table. Combining the results of both studies revealed that softer Lewis bases (e.g. TMA, DMS and TMP) tend to prefer halogen bonding, while the harder Lewis bases (CH_3F) prefer HB complexes with CHF_2I.

Apart from the influence of the Lewis base involved, the effect of modifications of the combined donor on the halogen/hydrogen bond competition was investigated. As it is well known that the size of the halogen atom involved is one of the main criteria determining the size of the σ-hole, and thus the halogen bond strength, the effect of substituting the σ-hole carrying iodine atom for the smaller bromine atom was examined by investigating the complexes of bromodifluoromethane (CHF_2Br) with TMA. Despite using a Lewis base that would, based on the conclusions above, give halogen bonding the best chance of competing with hydrogen bonding, only HB complex was found in solution. Except for the absence of XB complex, it was also

found that changing iodine for bromine had no appreciable influence on the strength of the HB complex formed. It would, however, be interesting to see whether these conclusions hold up when the hydrogen and bromine halogen bond donor are placed farther apart in a larger molecule.

A second, often applied technique for controlling the strength of halogen bonding is the addition of electron withdrawing groups on the molecule which is covalently bonded to the halogen atom. Most often fluorine atoms, which, except for a limited amount of cases in certain molecules (e.g. F_2), are not able to act as halogen bond donors themselves, are used to enhance the XB complex. Therefore, the complexes of DME and TMA with fluoroiodomethane (CH_2FI) were studied. Comparison of these results with those of the study involving CHF_2I showed that the complexes of CH_2FI are indeed weaker and that the XB complex with DME is no longer observed. An energy decomposition analysis (EDA) also revealed that, despite the reduced number of fluorine atoms, the nature of the noncovalent interactions is not altered, as the different relative (or in case of dispersion absolute) energetic contributions remain identical.

The aforementioned studies also revealed the importance of secondary interactions on the halogen/hydrogen bond competition. As halogen bonds are highly directional, and are only formed along the covalent bond axis of the halogen atom, yielding very linear complexes, they are most often not able to form additional stabilizing secondary interactions when both the donor and acceptor molecules are small. Hydrogen bonds are far less directional and are able to form complexes which deviate significantly from linearity. Combined with the shorter C-H and intermolecular distance compared to the XB complexes, this can bring the covalently bonded molecule in the proximity of the Lewis base, thus enabling the formation of secondary interactions, as revealed by using the noncovalent index (NCI). This means that, even though the high linearity of XB complexes yields highly predictable complex geometries, which is of great advantage in applications in, for instance, supramolecular chemistry, its inability to form secondary interactions might well be its biggest disadvantage when having to compete with hydrogen bonds.

To investigate the influence of the hybridization of the covalently bonded carbon atom on the halogen bond strength, the complexes of trifluorohaloethenes (C_2F_3X, X = F, Cl, Br, I), where the carbon atoms have an sp^2 hybridization, with the Lewis bases DME and TMA were investigated. Contrary to previous theoretical studies on non-fluorinated halogen bond donor molecules it was found that the XB complexes formed with C_2F_3Cl, C_2F_3Br and C_2F_3I are weaker than those with their CF_3X (sp^3) counterparts for both Lewis bases. Furthermore, as the highly electron deficient, unsaturated molecules also have regions of positive electrostatic potential perpendicular to the molecular plane, they are also able to interact with the Lewis bases through these sites, thus forming lp···π interactions. These noncovalent interactions are indeed observed in the mixtures of C_2F_4 and C_2F_3Cl, alongside XB complex for the latter bond donor, while for C_2F_3Br and C_2F_3I the XB complex prevails over the lp···π complex.

To further elaborate on the concept of lp···π interactions, and to see whether these can also exist for aromatic electron deficient π-systems, mixtures of hexafluorobenzene (C_6F_6) with DME and TMA were investigated. During this study, the presence of lp···π complexes was demonstrated with both Lewis bases.

The study into lp···π concept was further expanded by investigating electron deficient heteroatomic π-systems in the form of carbonyl groups, which also formed the subject of the initial crystallographic studies into lp···π interactions thanks to their importance in biological systems, e.g. in proteins. In this study the complexes of the phosgene derivatives carbonyl fluoride (COF_2) and carbonyl chloride fluoride (COFCl) with DME were investigated in liquid krypton. For the COF_2·DME and COFCl·DME mixtures, lp···π complex was observed, while for the latter mixtures also trace amounts of Cl···O XB complex were detected, thus establishing that lp···π interactions can prevail over competitive halogen bonds in some instances.

Finally, the concept of σ-hole bonding has been expanded by the study of the S···O chalcogen-bonded complex between $C_2F_4S_2$ and DME, during which many similarities to halogen bonding were unveiled. Furthermore, as this interaction is significantly

stronger than previously studied Cl···O halogen bonds, chalcogen bonding (especially involving larger chalcogen atoms) is a promising candidate to replace halogen bonding in some applications in the fields of catalysis, supramolecular chemistry and rational drug design.

All in all, from the above it can be concluded that weak noncovalent interactions, such as halogen bonds, hydrogen bonds and lp···π complexes are able to compete and/or coexist with each other at thermodynamic equilibrium in liquid noble gas solutions. The competition between halogen bonding and hydrogen bonding can be influenced by making changes to both the bond donor and the bond acceptor, but substituting the electron-deficient bond donor for an unsaturated system might also establish the formation of competing lp···π complexes. Finally, the study of a chalcogen-bonded complex also offers new opportunities for future cryospectroscopic studies towards a more general understanding of σ-hole bonding, including pnicogen bonding and perhaps tetrel bonding.

Future perspectives

I hope the data provided in this thesis aids scientists working in crystal engineering, supramolecular chemistry and drug design to use these (novel) noncovalent interaction and their competition to develop new materials and drugs. Especially the effect of substituting fluorine atoms by hydrogen atoms to influence the strength of halogen bonding and the consequential competitive hydrogen bonds springs to mind here. I would also like to stress again the importance of the formation of secondary interactions in HB complexes when these are in competition with the far more directional halogen bonds. Additionally, I think the data provided in this manuscript can help scientists working in crystallography to rationalize and understand unexpected crystalline structures when working with materials in which these (competitive) noncovalent interactions are present. The results can also aid in the development of a unified theory to predict the crystal structure of solid materials. I would also like to suggest that researchers take a look at chalcogen bonding as an alternative to halogen bonding in the previously mentioned applications.

The data presented in this manuscript might also be of interest to computational chemists as an experimental reference in benchmarking studies of computational methodologies, as experimental data are nowadays often omitted during these studies. On the other hand, I hope the data presented encourages computational scientists to create more enhanced techniques and methods to describe these systems in LNg solutions, be it using Force Fields, Molecular Dynamics or Monte Carlo calculations or other computational techniques.

Throughout this thesis the experimental complexation enthalpies and complexation shifts have been compared with the experimentally observed values, during which it was observed that the calculated complexation enthalpies are (generally) slightly overestimated. The discrepancies between both values can be ascribed to the approximations made to obtain both values.

In order to get a better agreement between both values, a more accurate computational description with less approximations might be envisaged. In this context, the inclusion of an explicit description of the system as a non-rigid rotor and anharmonic oscillator comes to mind, in order to get a more accurate description of the influence of the LNg at moderately low temperature (as opposed to 0 K in current *ab initio* calculations) on the stability of the complex and the entropic contributions. Additionally, the effect of internal rotations, as seen in chapters 9 and 10, should also be taken into account and a weighted average of the different calculated complex geometries could be made in order to obtain more accurate results. In order to make sure all possible complex geometries are incorporated within this approach, the results from a prior search for stable (gas-phase) complex geometries using an automated algorithm, comparable to the methodology used for current VCD and ROA calculations, can be used as a starting point for the solvent calculations. To get a more accurate and detailed description of the solvent influence on the complex formation, the obtained solvated complex geometries can then be dissociated within the solvent environment instead of performing three separate calculations (one for each monomer and one for the complex), thus circumventing the FEP limitations. Furthermore, the non-iterative first-order approximation made during the solvent calculations to polarize the LNg atoms can be replaced with a more elaborate (iterative) process, which also includes induced dipole-induced dipole interactions between the solvent atoms.

Hopefully this enhanced model will also help to explain the absence of some complex geometries in the solutions, such as the CH_2FI·DME and CHF_2Br·TMA XB complexes, which is considered unexpected based on the current calculations. It can then also be applied to the complexes discussed in previous PhD theses, in particular the theses dealing with the gaseous anaesthetics, such as halothane, where the expected XB complexes were also not observed.

This enhanced system is possibly also able to described the influence of solvation and thermal effects on the vibrational frequencies and shifts, in order to explain the discrepancy between experimental and calculated shifts for some vibrational modes, as

demonstrated for the C-H stretching vibration in the CHF_2I·DMS HB complex in chapter 4.

Additional information on the complexes studied within this thesis can also be obtained using other experimental techniques. As demonstrated in chapter 12, the use of FTMW spectroscopy yields direct spectroscopic information on the geometries of the molecular complexes in supersonic expansion, although the presence of internal rotors can pose great difficulties in assigning the peaks observed. The development of new Hamiltonians able to described these internal rotations not aligned with the principal axes is of great importance in this context. Experimental data on the geometries of the complexes can also be obtained using X-ray diffraction (XRD) experiments on crystals of the molecular complexes. For the complexes studied here, this will involve the (probably complicated) formation of crystals at cryogenic temperatures, although less detailed information can also be obtained by using powder diffraction.

Publication list

Nagels, N.; Geboes, Y.; Pinter, B.; De Proft, F.; Herrebout, W. A., Tuning the Halogen/Hydrogen Bond Competition: A Spectroscopic and Conceptual DFT Study of Some Model Complexes Involving CHF_2I, *Chemistry - A European Journal* **2014**, *20*, 8433-8443.

Geboes, Y.; Nagels, N.; Pinter, B; De Proft, F.; Herrebout, W. A., Competition of $C(sp^2)$−X···O Halogen Bonding and Lone Pair···π Interactions: Cryospectroscopic Study of the Complexes of C_2F_3X (X = F, Cl, Br, and I) and Dimethyl Ether, *The Journal of Physical Chemistry A* **2015**, *119*, 2502-2516.

Geboes, Y.; De Proft, F.; Herrebout, W. A., Expanding Lone Pair···π Interactions to Nonaromatic Systems and Nitrogen Bases: Complexes of C_2F_3X (X = F, Cl, Br, I) and TMA(-d_9), *The Journal of Physical Chemistry A* **2015**, *119*, 5597-5606.

Geboes, Y.; De Proft, F.; Herrebout, W. A., Lone pair···π interactions involving an aromatic π-system: Complexes of hexafluorobenzene with dimethyl ether and trimethylamine, *Chemical Physics Letters* **2016**, *647*, 26-30.

Geboes, Y.; De Proft, F.; Herrebout, W. A., Lone pair···π interactions involving carbonyl π-systems: Experimental and theoretical study of the complexes of COF_2 and COFCl with dimethyl ether, *Chemical Physics* **2016**, *476*, 1-8.

Geboes, Y.; De Proft, F.; Herrebout, W. A., Taking the halogen bonding-hydrogen bonding competition one step further: Complexes of difluoroiodomethane with trimethylphosphine, dimethyl sulfide and chloromethane, *Acta Crystallographica B* **2017**, *B73*, 168-178.

Geboes, Y.; De Proft, F.; Herrebout, W. A., Effect of Fluorination on the Competition of Halogen Bonding and Hydrogen Bonding: Complexes of Fluoroiodomethane with Dimethyl Ether and Trimethylamine, *The Journal of Physical Chemistry A* **2017**, *121*(21), 4180-4188.

Gou, Q; Spada, L.; Geboes, Y.; Herrebout, W. A.; Melandri, S.; Caminati, W., N lone-pair···π interaction: a rotational study of chlorotrifluoroethylene···ammonia, *Physical Chemistry Chemical Physics* **2015**, *17*, 7694-7698.

Spada, L.; Gou, Q; Geboes, Y.; Herrebout, W. A.; Melandri, S.; Caminati, W., Rotational Study of Dimethyl Ether−Chlorotrifluoroethylene: Lone Pair···π Interaction Links the Two Subunits, *The Journal of Physical Chemistry A* **2016**, *120*, 4939−4943.

Samenvatting

Halogeenbruggen, waterstofbruggen en daar voorbij:

een cryospectroscopische studie naar competitieve niet-covalente interacties

De studie van zwakke niet-covalente interacties vormt reeds twee decennia het onderwerp van experimentele studies binnen de *Molecular Spectroscopy (MolSpec) group* (voorheen onderzoeksgroep Cryospectroscopie) aan de Universiteit Antwerpen. Aanvankelijk werd tijdens de studies gefocust op van der Waals complexen en waterstofbrugcomplexen, waarbij bij deze laatsten een bijzondere interesse uitging naar de interacties gevormd met gehalogeneerde anesthetica. In de laatste tien jaar verschoof de wetenschappelijke interesse naar halogeenbruggen, zwakke niet-covalente interacties tussen covalent gebonden halogeenatomen en elektronenrijke sites in een Lewisbase, waarbij de complexen tussen trifluorohalomethanen (CF_3X, X = Cl, Br, I) en Lewisbasen met vrije electronenparen of π-electronen bestudeerd werden.

In de huidige studie werden de eerdere onderzoeksinspanningen naar waterstof- en halogeenbruggen overbrugd door de competitie tussen beide niet-covalente interacties te bestuderen. Hiertoe werden, net als voorheen, infrarood- en Ramanmetingen uitgevoerd, waarbij gekeken wordt naar de moleculaire vibraties, op oplossingen in vloeibare edelgassen bij lage temperaturen (bvb. -153 °C tot -117 °C voor oplossingen in vloeibaar krypton (LKr)). Door de vorming van niet-covalente interacties wijzigt de elektronenverdeling van de interagerende moleculen, wat zich in de opgemeten spectra manifesteert als bijkomende banden die verschoven liggen t.o.v. de banden van de individuele moleculen. Door spectra op te nemen van de individuele moleculen naast de spectra van oplossingen die beide moleculen bevatten, kunnen spectra bekomen worden die enkel signalen bevatten van deze nieuw ontstane banden. Deze complexspectra worden bekomen door de spectra van de individuele monomeren te vermenigvuldigen met een schalingsfactor en vervolgens het verschil te nemen tussen het mengselspectrum en deze herschaalde monomeerspectra. Hierbij wordt de schalingsfactor zodanig gekozen dat na subtractie geen signaal van de monomeren aanwezig is in het nieuw gevormde complexspectrum. Door de verschuivingen van de complexbanden te vergelijken met de resultaten uit *ab initio* berekeningen kan vervolgens de geometrie van het complex gevormd in de oplossing bepaald worden. Vermits de metingen uitgevoerd worden bij thermodynamisch evenwicht, kunnen

daarnaast door het uitvoeren van metingen op oplossingen met verschillende concentraties bij een constante temperatuur complexatie-stoichiometrieën bepaald worden. Vervolgens kunnen, aan de hand van de van 't Hoff vergelijking, door het uitvoeren van metingen bij verschillende temperaturen, de complexatie-enthalpieën van de aanwezige complexen bepaald worden. Door het toepassen van correcties bekomen uit Monte Carlo-*Free Energy Perturbation* (MC-FEP) simulaties en statistische thermodynamica op de *ab initio* berekende complexatie energie, kan deze berekende enthalpiewaarde vergeleken worden met de experimenteel bekomen waarde. In een latere fase worden in samenwerking met de onderzoeksgroep Algemene Chemie (ALGC) aan de Vrije Universiteit Brussel de waargenomen tendensen gerationaliseerd met behulp van conceptuele kwantumchemische berekeningen, waaronder de *noncovalent interactions index* (NCI), gevisualiseerd in NCIPlot, *natural orbitals for chemical valence* (NOCV), waarin de herverdeling van de elektronen bij de vorming van het complex gevisualiseerd wordt en een energiedecompositie-analyse (EDA) van het Ziegler-Rauk type.

In tegenstelling tot vorige studies werd tijdens de huidige studie (initieel) specifiek gekeken naar moleculen die (althans theoretisch) in staat zijn om zowel halogeenbruggen als waterstofbruggen te vormen, zogenaamde gecombineerde donoren. Als startpunt werd gekozen voor de studie van difluorjoodmethaan (CHF_2I) met een reeks Lewisbasen die een vrij elekronenpaar bevatten op een element uit de tweede periode (trimethylamine (TMA), dimethylether (DME) en methylfluoride, Hoofdstuk 3) of derde periode (trimethylfosfine, dimethylsulfide en methylchloride, Hoofdstuk 4). Hieruit werd geconcludeerd dat zachtere Lewisbasen, volgens de *Hard Soft Acid Base* (HSAB) theorie van Pearson, jood halogeenbruggen verkiezen boven waterstofbruggen, terwijl hardere Lewisbasen eerder waterstofbruggen vormen.

Om de invloed van modificaties van de gecombineerde donoren op de competitie tussen halogeen- en waterstofbruggen beter te begrijpen, werd de invloed van de aanwezigheid van fluoratomen op de donormolecule bekeken door de studie van de complexen tussen fluorjoodmethaan (CH_2FI) en de Lewisbasen TMA en DME (in Hoofdstuk 5). Vergelijking met bovengenoemde studie met CHF_2I leert dat de

vermindering van het aantal elektronegatieve fluoratomen, zoals verwacht, de sterkte van de niet-covalente interacties verzwakt, maar de aard van de interacties zelf niet beïnvloedt.

De invloed van het betrokken halogeenatoom op de competitie werd eveneens bestudeerd in Hoofdstuk 6 aan de hand van de analyse van oplossingen van broomdifluormethaan (CHF_2Br) en TMA. Hierbij werd enkel een waterstofbrugcomplex teruggevonden in de spectra, met een stabiliteit die nagenoeg gelijk is aan dat van het waterstofbrugcomplex tussen CHF_2I en TMA. Hieruit blijkt tevens dat broom-gebaseerde halogeenbruggen waarschijnlijk niet in staat zijn in competitie te treden met waterstofbruggen indien beide donoratomen (H en Br) covalent gebonden zijn aan eenzelfde koolstofatoom.

Een belangrijk aspect aan de halogeenbrug/waterstofbrug competitie dat eveneens aan het licht kwam in de hiervoor beschreven studies, is de mogelijkheid tot de vorming van secundaire interacties in de waterstofbrugcomplexen, welke deze complexen extra stabiliteit verlenen. Door de hogere richtingsgevoeligheid van halogeenbruggen en de grotere bindingsafstand (ten gevolge van de grootte van het halogeenatoom zelf) is de vorming van deze bijkomend stabiliserende secundaire interacties met de Lewisbasen veel minder waarschijnlijk in halogeenbrugcomplexen. Hoewel de richtingsgevoeligheid van halogeenbruggen algemeen beschouwd wordt als één van de voornaamste voordelen van dit type interactie t.o.v. waterstofbruggen in o.a. *crystal engineering* en supramoleculaire chemie, daar ze zeer voorspelbare kristalstructuren vormen, is het gebrek aan mogelijkheden om bijkomende stabiliserende secundaire interacties aan te gaan ook één van de grote nadelen wanneer halogeenbruggen in competitie treden met waterstofbruggen.

Een derde manier waarop de sterkte van halogeenbruggen beïnvloed kan worden, is het aanpassen van de hybridisatie van het koolstofatoom waaraan het interagerende halogeenatoom covalent gebonden is. Zo werd in voorgaande (theoretische) studies gesuggereerd dat halogeenatomen die covalent gebonden zijn aan sp^2-gehybridiseerde koolstofatomen sterkere interacties vormen dan diegenen gebonden aan

sp^3-gehybridiseerde koolstofatomen. Om dit na te gaan werden de complexen tussen trifluorhaloethylenen (C_2F_3X, X = F, Cl, Br, I) en DME (Hoofdstuk 7) of TMA (Hoofdstuk 8) bestudeerd. Hieruit bleek dat, in tegenstelling tot eerdere suggesties, de gevormde halogeenbrugcomplexen zwakker zijn dan bij de CF_3X analogen, waardoor de eerdere aanname dat halogeenatomen gebonden aan sp^2-gehybridiseerde koolstofatomen sterkere halogeenbruggen vormen niet opgaat voor gefluoreerde verbindingen. Het gebruik van deze onverzadigde, elektronenarme donoren had bovendien als bijkomend gevolg dat naast de σ-holte op het halogeenatoom een tweede soort regio met positieve elektrostatische potentiaal werd gevormd boven en onder de dubbele binding, de zogenaamde π-holte, welke eveneens in staat is te interageren met de elektronenrijke site op de Lewisbase. De aanwezigheid van niet-covalente interacties tussen deze positieve regio's en de vrije elektronenparen op de Lewisbasen, welke de naam *lone pair*$\cdots\pi$ (lp$\cdots\pi$) interacties dragen, werd waargenomen in de mengsels van zowel DME als TMA met C_2F_4 en C_2F_3Cl, wat tevens aantoont dat deze niet-covalente interacties in staat zijn in competitie te treden met halogeenbruggen.

Om meer inzicht te krijgen in dit type niet-covalente interactie werden de mengsels van DME en TMA met de aromatische bindingsdonor hexafluorbenzeen (C_6F_6) eveneens bestudeerd in Hoofdstuk 9, waarbij de aanwezigheid van lp$\cdots\pi$ interacties duidelijk aangetoond werd.

In de literatuur werd echter gesuggereerd dat dit type niet-covalente interactie niet beperkt is tot de homogene π-systemen die hierboven beschreven worden, maar dat deze ook gevormd kunnen worden met heterogene π-systemen. Het bestaan van dit soort interacties werd immers voor het eerst beschreven tussen elektronenrijke sites en het π-systeem van een carbonyl-groep. Dit type lp$\cdots\pi$ interactie werd binnen deze thesis geanalyseerd met een studie naar de complexen tussen DME en carbonylfluoride (COF_2) of carbonylchloridefluoride (COFCl). Hierbij werden naast de vorming van relatief sterke lp$\cdots\pi$ interacties eveneens aanwijzingen gevonden van de aanwezigheid van een kleine hoeveelheid Cl$\cdots$O halogeenbrugcomplex in de mengseloplossingen met COFCl, wat bewijst dat deze nieuwe soort niet-covalente interacties ook sterker kan zijn dan competitieve halogeenbruggen.

Rationalisatie van halogeenbruggen heeft geleerd dat deze interacties het gevolg zijn van een anisotrope elektronenverdeling rondom het covalent gebonden halogeenatoom, waardoor een regio met positieve elektrostatische potentiaal ontstaat op het halogeenatoom in het verlengde van de covalente binding, de zogenaamde σ-holte (sigmaholte). Later werd aangetoond dat dit verschijnsel zich niet beperkt tot halogeenatomen, maar ook kan voorkomen bij elementen uit groep VI, V of zelfs IV van het periodiek systeem. Interacties tussen de σ-holtes op deze elementen en elektronenrijke sites geven dan aanleiding tot de vorming van respectievelijk chalcogeenbruggen, pnicogeenbruggen en tetrelbruggen (Eng.: chalcogen, pnicogen and tetrel bonds). Als uitbreiding van het σ-holte bindingsconcept werd binnen deze thesis het chalcogeenbrugcomplex bestudeerd tussen 2,2,4,4-tetrafluor-1,3-dithiethaan ($C_2F_4S_2$) en DME. Hierin werd aangetoond dat de stabiliteit van de gevormde niet-covalente interactie vergelijkbaar is met die van I···O halogeenbruggen, waardoor dit nieuwe type niet-covalente interactie zich opwerpt als een beloftevolle vervanger voor halogeenbruggen en/of waterstofbruggen bij toepassingen in supramoleculaire chemie, katalyse en de ontwikkeling van geneesmiddelen.

Tenslotte wordt ook nog kort ingegaan op de bereikte resultaten van de Fourier Transform microgolfspectroscopische (FTMW) studies aan de universiteiten van Bologna (Italië) en Newcastle upon Tyne (Verenigd Koninkrijk). Tijdens de metingen aan de universiteit van Bologna werden gasmengsels van chloortrifluorethyleen (C_2F_3Cl) en de Lewisbasen ammoniak (NH_3) of DME bestudeerd in supersonische expansie. Hierbij werd aangetoond dat voor beide Lewisbasen lp···π complexen gevormd werden, terwijl er bij deze metingen, die niet onder thermodynamisch evenwicht uitgevoerd werden, geen halogeenbrugcomplexen teruggevonden werden. Tijdens de FTMW metingen aan de universiteit van Newcastle, uitgevoerd met een *chirped-pulse* FTMW spectrometer, werden de complexen van CHF_2I met TMA en NH_3 bestudeerd. Door de aanwezigheid van een interne rotatie is een volledige toewijzing van alle CHF_2I·TMA lijnen tot op heden niet mogelijk, al vertoont het spectrum sterke structurele gelijkenissen met het spectrum voorspeld voor het

halogeenbrugcomplex, terwijl uit het $CHF_2I{\cdot}NH_3$ spectrum afgeleid werd dat dit waarschijnlijk een waterstofbrugcomplex vormt.

The essence of a dream is the desire to achieve it.

– Horacio Pagani